Studies on:

Roles and Therapeutic Potential of Isocitrate Dehydrogenase Mutations in Cancer and Inhibition of the SARS-CoV-2 Main Protease

A thesis submitted to the board of the Mathematical, Physical and Life Sciences Division at the University of Oxford in partial fulfilment of the requirements for the degree of Doctor of Philosophy.

Siegfried Graf Thun-Hohenstein

Supervised by Professor Christopher J. Schofield, FRS

Wolfson College

Trinity Term 2024

Dedicated to my grandfather John Douglas Young (1927 – 2023).

You were my age when you left your master's studies in Petrochemical Engineering at the University of Texas early to raise your first child. Since then, you lived a long life filled with chemistry and family.

Thank you for instilling in me a love of science and mischief. Cautionary tales were undoubtedly a strategy of reverse psychology. I remember fondly the 'secret recipe' of potassium permanganate with aluminium, which triggered your local air raid siren during World War Two, and the well-judged evacuation of a lab producing mercury fulminate, which only cost you half an ear.

Listening to you talk about your career and patents always made me proud to be your grandson. Although you were not able to see it, I hope this doctoral thesis submitted for a DPhil. in Chemistry makes you proud.

Abstract

Altered metabolism is a hallmark of cancer. Mutations in the metabolic enzymes human isocitrate dehydrogenase 1 and 2 (IDH1/2) are common in various cancers, with significant prevalence in glioma. Small-molecule inhibitors targeting IDH1 and IDH2 variants have been approved for treatment of haematological malignancies, and, recently for glioma treatment. Resistance to these inhibitors has been observed and is associated with disease relapse. The precise metabolic mechanisms linking IDH1 mutations to oncogenic drivers in glioma remain unclear. This thesis describes studies investigating the role of IDH1/2 WT and IDH1 R132H in glioma and studies seeking to identify new treatment strategies exploiting the resulting metabolic dysfunction. Work carried out to meet the urgent need for COVID-19 therapeutics is also described, that is, structure-activity studies aiming to develop a small-molecule inhibitor targeting the SARS-CoV-2 main protease.

Chapter 1 reviews the effects of the IDH1/2 mutation gain-of-function in cancer and existing therapeutic avenues. Chapter 2 describes the synthesis of inhibitors of IDH1 WT and IDH2 WT, inhibition studies on the binding kinetics of IDH1 WT, and the investigation of a novel potential scaffold for IDH1 R132H inhibitors. Chapter 3 describes metabolomic studies on the effects of the IDH1 R132H mutation on LN18 GBM cells, and the effects of IDH1 WT and IDH2 WT inhibitors on LN18 GBM cells, with and without the IDH1 R132H mutation. Chapter 4 describes the development of ebselen-type inhibitors against the SARS-CoV-2 main protease.

This thesis tentatively proposes a link between IDH1 R132H and an oncogenic driver in glioma, and proposes novel therapeutic avenues against IDH1 R132H glioma.

Declaration of Authorship

The work described in this thesis is entirely my own, unless otherwise stated.

Declaration of experiments conducted by others:

IDH1 WT and IDH1 variants used in experiments were produced by Dr Raphael Reinbold. LN18 GBM cells used in metabolomics experiments were provided by Dr Chiara Bardella and Dr Ingvild Hvinden.

Chapter 2:

e-Leaf experiments, and kinetic derivations in e-Leaf experiments and NADPH absorbance-based assays were performed by Dr Ryan Herold. Quaternary ammonium ion compounds were synthesised by Dr Shyam Basak.

Chapter 3:

LN18 GBM cell handling, and IC-MS data collection and pre-processing for metabolomics experiment 1 was conducted by Dr Ingvild Hvinden. IC-MS data collection for metabolomics experiment 2 was conducted by Rachel Williams and Kyoungeun Lee.

Chapter 4:

Protein observed mass spectrometry assays were performed by Tika R. Malla. M^{pro} was produced by Eidarus Salah. Mass spectrometry-based inhibition assays were performed by Dr Anthony Tumber and Tika R. Malla. Selected compounds were synthesised by Timothy F. Suits and are included for completeness. Flow cytometry experiments were performed by Dr Chris Moon and Dr Joanna Bacon (Public Health England).

Table of Contents

Acknowledgements

First and foremost, thank you to my supervisor, Professor Christopher J. Schofield, for providing me with the opportunity to research a passion of mine; his guidance was instrumental in shaping me as a scientist and his sincere support and patience were exemplary during challenging periods of both research and personal life. My perspectives on the life sciences and topics further afield have been forever refined as a result, and for that, I could not be more grateful.

Thank you as well to Professor James McCullagh and Professor Fraser Armstrong for their specialised advice and friendly engagement throughout the last four years, and Professor Simon Newstead for his good-natured support prior to them. In the same manner, I am immensely grateful to the many post-docs and former students who helped me to find my feet on many diverse projects; in particular, Dr. Timothy Suits, Dr. Raphael Reinbold, Dr. Ingvild Hvinden, Dr. Ryan Herold, Dr Edmond Toma, Dr Alistair Farley, and Dr. Lennart Brewitz. This work would not have been possible without them. In addition, thank you to my project collaborators, Dr. Tika Malla, Dr. Tony Tumber, Eidarus Salah, Samanpreet Atwal, Dr. John Walsby-Tickle, Rachel Williams, Kyoungeun Lee, Dr. Xiao Liu, Dr. Chris Moon and Dr. Joanna Bacon. Finally, thank you to my fearless proofreaders who sacrificed many hours for the benefit of this thesis; Dr. Timothy Suits, Dr. Ingvild Hvinden, Dr. Raphael Reinbold, Henry Ludlam-Steinke, and especially Dr. Edmond Toma who was far more generous with his time than I had any right to expect.

During the writing up period of this thesis and the last four years I have received endless support from my family, friends, and colleagues. I sincerely enjoyed the company of the entire Schofield group, and will always cherish the memories created during lunch, tea, and extra-curricular activities with Tim, Raph, Klem, Jos, Toby, Will, Eddie, Justin, Emily, Amelia, James, Freddie, Giorgia, Gayatri, Matt Bowen, Josh, Ryan, Faisal, Damon, Xingzhao, Jimmy, Alistair, and all of my compatriots in LG1/2/9/10.

Thank you to Dr. Alan Roth for fanning the flames of scientific entrepreneurship in me, and my colleagues and friends at OSE, for your support and understanding throughout the final year. Thank you to John Stewart for his advice outside of academia and career.

Thank you to my wonderful housemates Fe and Sophie who have always been there for me, night and day. Thank you tremendously to Max B and Henry, for being role models and the finest of true friends. To all my long-distance friends, for encouraging me and indulging my subject specific conversations, but most importantly, contributing to who I am today; Julien, Max B-S and all of the boys, Nic, Nat, Allegra, Sophie, and all of my friends I haven't named here (Lord forgive me if I were to forget a single name). To Hannah, my team-mate, I cannot overstate the measure by which you inspire me and have supported this journey – from the bottom of my heart, thank you.

Perhaps most importantly, thank you to my beloved family. For everything you have given me materially and spiritually; in some small way, I do everything for you. My extended family, Gladys, Nana and Pop, my wonderful siblings Punkie, Tang, and Stasi, my loving parents, Christian and Sarah, my new sibling Hillary, and my new godson Markus, even if he doesn't know he helped yet!

To my friends, family, and everyone who I have had the great fortune of sharing my life with so far, thank you for everything; I am blessed to be where I am today, and I have you all to thank for it.

List of Abbreviations

1,3PG	1,3-phosphoglycerate
2-HG	2-hydroxyglutarate
2-OG	2-oxoglutarate
2PG	2-phosphoglycerate
3PG	3-phosphoglycerate
6PGL	6-phosphogluconolactone
6PG	6-phosphogluconate
6PGD	6-phosphogluconate dehydrogenase
Å	angstrom
ADP	adeonisine diphosphate
Ala	Alanine
AM	acetoxy-methyl ester
AML	acute myeloid leukaemia
AMP	adenosine monophosphate
ASNS	asparagine synthetase
ATGL	adipose triglyceride lipase
ATP	adenosine triphosphate
BBB	blood-brain barrier
BCAA	branched-chain amino acid
BCAT	branched-chain amino acid aminotransferase
βCG	β-citryl-glutamate
BIT	benzisothiazolinone
Boc	*tert*-butyl carbonyl

BSA	bovine serum albumin
CDP	cytidine diphosphate
CE-MS	capillary electrophoresis–mass spectrometry
cf.	conferatur
CHD	coronary heart disease
CL	cell line
CLASP	CLIP-associated protein
CLIP	cytoplasmic linker protein
CNS	central nervous system
CoA	coenzyme A
COVID-19	coronavirus disease 2019
CSE	cystathionine-γ-lyase
CTP	cytidine triphosphate
CV	calcein violet
Da	dalton
DAG	diacylglycerol
dGDP	deoxyguanosine diphosphate
DHAP	dihydroxyacetone phosphate
DIPEA	diisopropylethylamine
DMEM	Dulbecco's modified Eagle medium
DMF	dimethylformamide
DMSO	dimethyl sulfoxide
DNA	deoxyribonucleic acid
DTT	dithiothreitol
E4P	erythrose-4-phosphate

E	entgegen
ESI	electrospray ionisation
eq.	equivalent
F1,6P	fructose-1,6-phosphate
F6P	fructose-6-phosphate
FAD	flavin adenine dinucleotide
$FADH_2$	reduced flavin adenine dinucleotide
FC	fold-change
FDA	food and drug administration
FDG	^{18}F-fluorodeoxyglucose
FDR	false discovery rate
FGF	fibroblast growth factor
FH	fumarate dehydrogenase
FNR	ferredoxin $NADP^+$ reductase
FRET	Förster resonance energy transfer
g	gram
G3P	glyceraldehyde-3-phosphate
G6P	glucose-6-phosphate
G6PD	glucose-6-phosphate dehydrogenase
GA	glutaric aciduria
GABA	γ-aminobutyric acid
GBM	glioblastoma multiforme
GC-MS	gas chromatography-mass spectrometry
GCP	glutamate carboxypeptidase
GHB	γ-hydroxybutyric acid

GLS	glutaminase
GLUD	glutamate dehydrogenase
GLUT	glucose transporter
GMP	guanosine monophosphate
GOT	glutamate OAA transaminase
GPAT	glutamine phosphoribosylpyrophosphate amidotransferase
GS	glutamine synthase
GSC	glioma stem cell
GSH	reduced glutathione
GSSG	oxidised glutathione
GTP	guanosine triphosphate
h	hours
HAO	L-α-hydroxyacid oxidase
HIE	hypoxic-ischemic encephalopathic
HIF	hypoxia-inducible factor
HOT	hydroxyacid oxoacid transhydrogenase
HPLC	high-performance liquid chromatography
HR-MS	high-resolution mass spectrometry
HTS	high-throughput screen
IC_{50}	half-maximal inhibitory concentration
IC-MS	ion exchange chromatography-mass spectrometry
ICT	isocitrate
IDH	isocitrate dehydrogenase
IMP	inosine monophosphate
IR	infra-red

ITO	indium tin oxide
KDM	histone lysine specific demethylase
K_d	dissociation constant
K_m	michaelis constant
L	litre
LC	liquid chromatography
LC-MS	liquid chromatography-mass spectrometry
LDH	lactate dehydrogenase
Ldt	L,D-transpeptidase
LOOCV	leave-one-out-cross-validation
Lys	lysine
M	molar
M/z	mass to charge
MAPK	mitogen-activated protein kinase
MCT	monocarboxylate transporter
MCTS	multicellular tumour spheroid
mDCR	mitochondrial 2,4-dienoyl CoA reductase
MDH	malate dehydrogenase
Me	methyl
ME	malic enzyme
MeCN	acetonitrile
µg	microgram
mg	milligram
MHz	megahertz
MIC	minimum inhibitory concentration

µL	microlitre
mL	millilitre
µM	micromolar
mM	millimolar
Mp	melting point
M^{pro}	SARS-CoV-2 main protease
MRS	magnetic resonance spectroscopy
MS	mass spectrometry
MSI	mass spectrometry imaging
MUT	mutant
NAAA	*N*-acetylated amino acid
NAAG	*N*-acetylaspartylglutamate
NAAla	*N*-acetylalanine
NAAsp	*N*-acetylaspartate
NAD	nicotinamide adenine nucleotide
NADH	reduced nicotinamide adenine nucleotide
NADP	nicotinamide adenine nucleotide phosphate
NADPH	reduced nicotinamide adenine nucleotide phosphate
NAGlu	*N*-acetylglutamate
NAGln	*N*-acetylglutamine
NAGly	*N*-acetylglycine
NAHis	*N*-acetylhistidine
NAMet	*N*-acetylmethionine
NASer	*N*-acetylserine
NAT	*N*-terminal acetyltransferases

NAThr	*N*-acetylthreonine
NGF	nerve growth factor
nM	nanomolar
NMDA	*N*-methyl-D-aspartic acid
NMP	*N*-methyl-2-pyrrolidone
NMR	nuclear magnetic resonance
NNT	nicotinamide nucleotide transhydrogenase
Nrf2	nuclear factor erythroid 2-related factor
NSP	non-structural protein
OAA	oxaloacetate
OMP	orotate monophosphate
ODC	ornithine decarboxylase
P4H	prolyl 4-hydroxylase
P5P	pyridoxal-5'-phosphate
PC	pyruvate carboxylase
PD	pharmacodynamics
PDB	protein data bank
pDCR	peroxisomal 2,4-dienoyl CoA reductase
$Pd(dppf)Cl_2$	bis(diphenylphosphino)ferrocene)palladium(II) dichloride
PDX	patient-derived xenograft
PEP	phosphoenolpyruvate
PET	positron emission tomography
PEX	peroxisomal biogenesis factor
PGE	pyrolytic graphite edge
PGP	p-glycoprotein

PHD	prolyl hydroxylase domain
PHGDH	phosphoglycerate dehydrogenase
PK	pharmacokinetics
PKC	protein kinase C
PLS-DA	partial least squares-discriminant analysis
Pl^{pro}	papain-like protease
PNS	peripheral nervous system
POMS	protein-observed mass spectrometry
PPP	pentose phosphate pathway
PROTAC	proteolysis targeting chimera
PRA	phosphoribosylamine
PRPP	phosphoribosyl pyrophosphate
PRPS	pyrophosphokinase
PSMA	prostate specific membrane antigen
PTB	patient tissue biopsy
QH_2	ubiquinol
qRT-PCR	quantitative reverse transcription polymerase chain reaction
R_f	retardation factor
R5P	ribose-5-phosphate
RIMKL	ribosomal modification protein rimK like family member
RL5P	ribulose-5-phosphate
RNA	ribonucleic acid
RNAi	RNA interference
ROS	reactive oxygen species
rt	room temperature

S7P	sedoheptulose-7-phosphate
SAR	structure-activity relationship
SARS-CoV-2	severe acute respiratory syndrome coronavirus 2
SDH	succinate dehydrogenase
SG	sytox green
SHE	standard hydrogen electrode
siRNA	small interfering RNA
S_NAr	nucleophilic aromatic subsitution
SPE-MS	solid-phase extraction mass spectrometry
SPR	surface plasmon resonance
TCA	tricarboxylic acid
TEAC	tetraethylammonium chloride
TET	ten-eleven translocation methylcytosine dioxygenase
THF	tetrahydrofuran
TLC	thin layer chromatography
TMAO	trimethylamine *N*-oxide
TME	tumour microenvironment
TNF-α	tumour necrosis factor alpha
TOF	time of flight
UDP	uridine diphosphate
UMP	uridine monophosphate
UPLC	ultra-high performance liquid chromatography
UTP	uridine triphosphate
UV	ultraviolet
v/v	volume per volume

VHL	von Hippel-Lindau
VIP	variable importance in projection
VLCFA	very long chain fatty acid
w/w	weight per weight
WHO	world health organisation
WT	wild-type
X5P	xylulose-5-phosphate
Z	zusammen

1. Isocitrate Dehydrogenases and Cancer

1.1. The Identification of Altered Metabolism as a Hallmark of Cancer

Abnormal metabolism in cancer has long been studied and has recently become a high priority from a therapeutic perspective.[1-3] Otto Warburg first described changes in the metabolism of cancer patients in 1930, though at that time metabolic studies in cancer were not yet considered urgent.[1, 2, 4, 5] Following the addition of energy metabolism perturbation as an emerging hallmark of cancer, advances in mass spectrometry based metabolomics and genome sequencing have enabled powerful metabolic studies leading to increasing interest in the field from the early 2000s. Metabolic dysfunction is now considered to be pervasive in cancer cells.[1, 3-5] Nonetheless, a comprehensive understanding of metabolic dysfunction in cancer, including its roles in tumorigenesis, is still lacking.[6, 7]

Warburg's work has since been substantiated by the discovery of glucose transporter 1 (GLUT1) upregulation and increased glucose uptake in tumours, leading to the conclusion that cancer cells experience a shift from mitochondrial oxidative phosphorylation toward cytosolic glucose oxidation and glycolysis.[1, 8-10] Today, tumours may be visualised using this 'Warburg effect' by the detection of positrons emitted from ^{18}F-fluorodeoxyglucose (FDG) injected into the bloodstream. Phosphorylated FDG metabolites accumulate in cancer cells; the ^{18}F decays into ^{18}O before the metabolites leave the cell, allowing positron emission tomography (PET) to detect the increased uptake of glucose in cancer cells.[11]

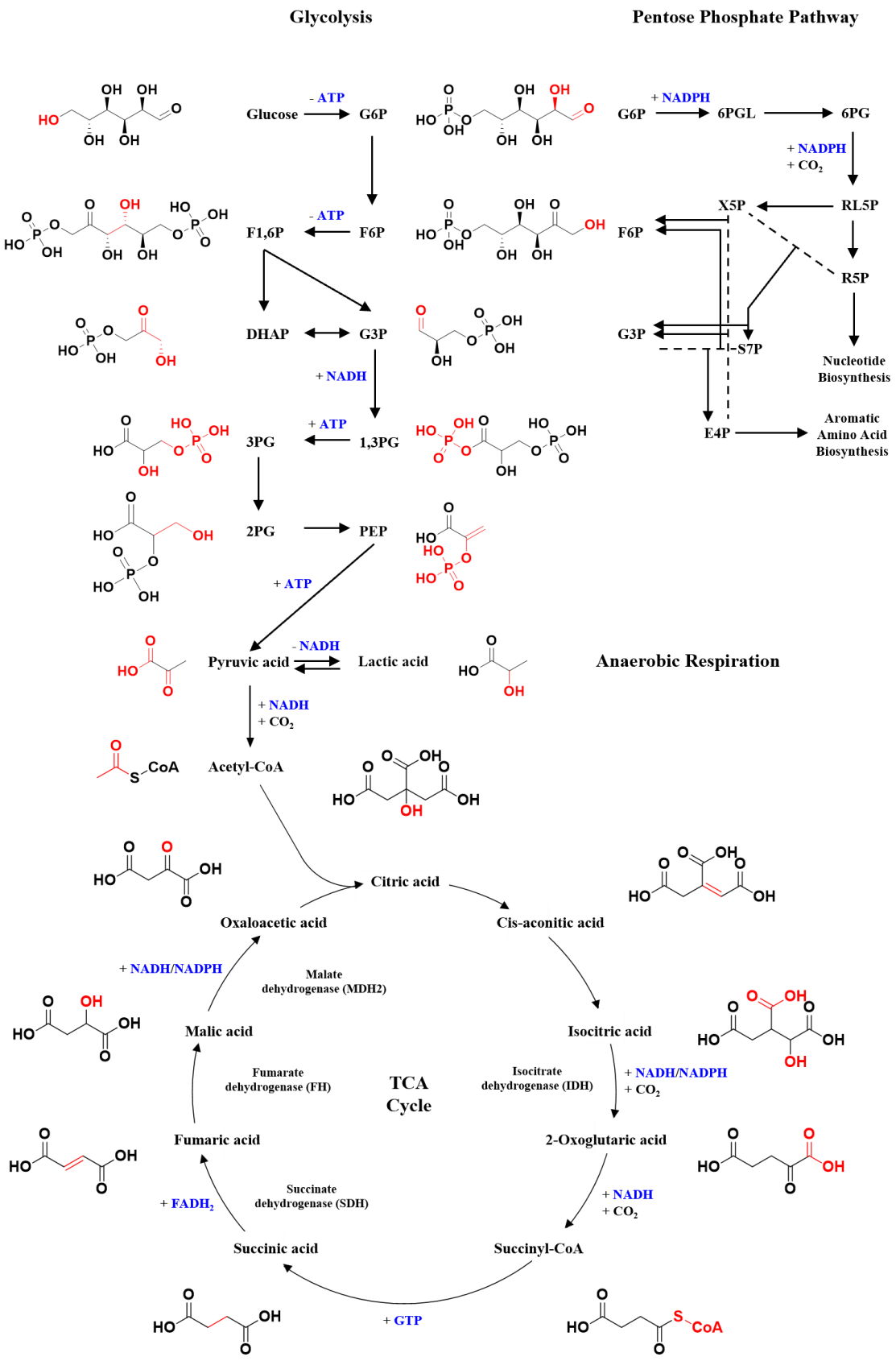

Figure 1.1 | *Glycolysis, the anaerobic production of lactic acid, and the tricarboxylic acid (TCA) cycle in humans. An overview of the pentose phosphate pathway is also included for completeness. Dashed lines represent reactions between metabolites. Products are denoted by*

solid arrows. The sites of the reaction on each metabolite are coloured red. Energy carriers are coloured blue. Only enzymes which are reported to be mutated in cancer are shown. Note, IDH1 and IDH2 also operate independently to the TCA cycle and are more frequently mutated in cancer than IDH3, which primarily operates in the TCA cycle. G6P = glucose-6-phosphate. F6P = fructose-6-phosphate. F1,6P = fructose-1,6-bisphosphate. DHAP = dihydroxyacetone phosphate. G3P = glyceraldehyde-3-phosphate. 1,3PG = 1,3-phosphoglycerate. 3PG = 3-phosphoglycerate. 2PG = 2-phosphoglycerate. PEP = phosphoenolpyruvate. 6PGL = 6-phosphogluconolactone. 6PG = 6-phosphogluconate. RL5P = ribulose-5-phosphate. R5P = ribose-5-phosphate. X5P = xylulose-5-phosphate. S7P = sedoheptulose-7-phosphate. E4P = erythrose-4-phosphate. CoA = coenzyme A. ATP = adenosine triphosphate. NADPH = nicotinamide adenine dinucleotide monophosphate. NADH = nicotinamide adenine dinucleotide. GTP = guanosine triphosphate. $FADH_2$ = flavin adenine dinucleotide.

Metabolic changes in cancer cells are not limited to impaired glycolysis and have been linked to germline mutations in TCA cycle enzymes such as succinate dehydrogenase (SDH), fumarate hydratase (FH), and malate dehydrogenase 2 (MDH2) (**Figure 1.1**). SDH catalyses the conversion of succinate to fumarate, FH converts fumarate to malate, and MDH2 converts malate to oxaloacetate (OAA). Loss-of-function mutations in SDH and FH genes are reported in several cancers such as paragangliomas and renal carcinomas, correlating with succinate and fumarate accumulation in cells, respectively.[3, 12] Mutations in MDH2 are found in paraganglioma, but do not correlate with malate accumulation in cells.[13] FH deletions are reported in neuroblastomas.[3]

The most frequently mutated metabolic enzyme in cancer occurs somatically and affects isocitrate dehydrogenase (IDH).[14, 15] IDH converts isocitrate to 2-oxoglutarate (2-OG, also known as α-ketoglutarate) (**Figure 1.1**). Originally classified as loss-of-function, a seminal paper by Dang et al. demonstrated that mutations in IDH1 and IDH2 are gain-of-function and enable the neomorphic production of (*R*)-2-hydroxyglutarate (2-HG, also known as D-2-HG) from 2-OG (**Figure 1.2**).[16] Accordingly, high concentrations of 2-HG are detected inside cells bearing mutations in IDH1 or IDH2.[16]

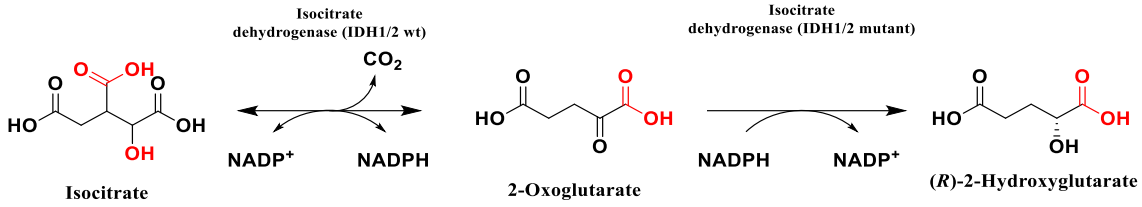

Figure 1.2 | *IDH1/2 WT catalyses the oxidative decarboxylation of isocitrate to 2-oxoglutarate. Mutant IDH1/2 is also able to catalyse the reduction of 2-oxoglutarate to (R)-2-hydroxyglutarate.*

1.2. The Role of Wild-Type IDH and Endogenous 2-Hydroxyglutarate in *Homo sapiens*

1.2.1. The Physiological roles of IDH1, IDH2, and IDH3

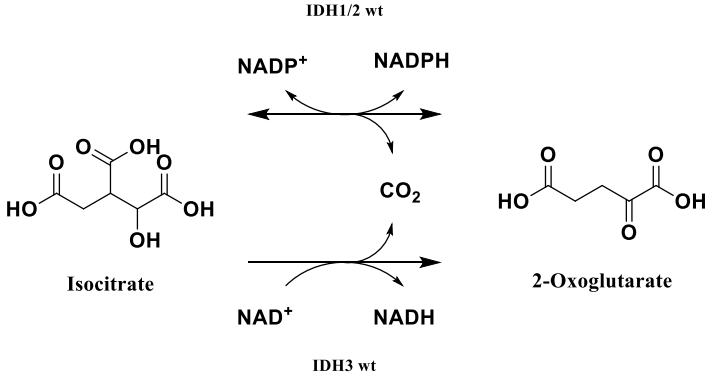

Figure 1.3 | *IDH1/2 WT catalyse the reversible oxidative decarboxylation of isocitrate to 2-oxoglutarate with concomitant reduction of $NADP^+$ to NADPH. IDH3 WT catalyses the irreversible oxidative decarboxylation of isocitrate to 2-oxoglutarate with the concomitant reduction of NAD^+ to NADH.*

IDH in humans exists as three isoforms – IDH1 WT and IDH2 WT, which share 70% sequence identity, and IDH3 WT, which is phylogenetically distinct.[17] All isoforms of IDH catalyse the oxidative decarboxylation of isocitrate to give 2-OG. IDH1 and IDH2 can operate independently to the forward-direction TCA cycle and catalyse the reaction reversibly. In contrast, the oxidation of isocitrate as catalysed by IDH3 is primarily within the TCA cycle and is apparently irreversible (**Figure 1.3**).[18] The reverse reaction catalysed by IDH1/2 entails the reductive carboxylation of 2-OG and CO_2 to isocitrate, which may be converted to citrate via the bidirectional enzyme aconitase.[19] All IDHs are

dehydrogenases that belong to the oxidoreductase enzyme superfamily and use $NAD^+/NADP^+$ as co-substrates.[17, 20] IDH1 and IDH2 are heterodimers. IDH1 and IDH2 each contain two Rossmann folds, each of which comprises an α-helix and two parallel ß-strands linked by a glycine-rich loop for pyrophosphate binding, to bind the nicotinamide and adenine rings of $NAD^+/NADP^+$ separately.[20] IDH3 is a heterooctamer and the structure is considerably more complex than those of IDH1 and IDH2.[21]

IDH1 is found in the cytosol and peroxisomes, and contains a type-1 peroxisomal targeting sequence.[18, 22] IDH1 activity and enzyme localisation have been detected in the majority in mammalian peroxisomes. Reports have suggested IDH1 may have been considered cytosolic because it leaks out during cell homogenization.[23, 24] The established role of IDH1 is to generate NADPH outside the mitochondria, alongside 2-OG synthesis.[18] The production of NADPH is particularly important in the oxidising environment of the peroxisome, where there is evidence that peroxisomal 2,4-dienoyl CoA reductase (pDCR) utilises NADPH for the reduction of 2,4-dienoyl-CoA thioesters to 3-enoyl-CoA thioesters during the β-oxidation of both short and very long chain unsaturated fatty acids (VLCFA, n > 20 carbons).[25-28] IDH1 deficiency attenuates gluconeogenesis.[29] RNA interference (RNAi) knockdown of IDH1 (by MiR-181a) activates β-oxidation genes and deactivates lipid biosynthesis genes, suggesting that IDH1 is involved in lipid metabolism regulation.[30, 31] Furthermore, mutations in IDH1 are strongly associated with cancer.[18]

IDH2 is found in the mitochondrial matrix where it is considered to provide NADPH molecules as reducing equivalents to help protect mitochondria from oxidative damage, as well as to mitochondrial 2,4-dienoyl CoA reductase (mDCR) catalysing the β-oxidation of unsaturated fatty acids (n < 20 carbons).[17, 18, 28] Despite the localisation of IDH2 to the mitochondria, the relationship between IDH2 and β-oxidation is potentially

more complicated and less direct than IDH1; one recent study reported evidence that IDH2 deficiency exacerbates weight gain, while another reported that IDH2 deficiency protects against weight gain.[32, 33] IDH2 is also involved in both hepatic glycolysis and gluconeogenesis, providing evidence that it may perform the reduction of 2-OG to isocitrate under physiological conditions.[32] Similarly to IDH1, mutations in IDH2 are frequently reported in cancer.[18]

IDH3 is thought to be a key rate-limiting enzyme in the TCA cycle, and, like IDH2, IDH3 is localised in the mitochondrial matrix.[18, 34, 35] IDH3 is a heterooctamer formed as a dimer of heterotetramers, which are in turn formed of heterodimers containing two of three subunits, α, β, and γ, in the final form $(\alpha\beta\alpha\gamma)_2$.[21, 36] Heterodimers of IDH3, αβ or αγ, associate via a CLIP-associated protein (CLASP) domain made of two antiparallel ß-sheets, into heterotetramers (αβαγ).[21] The γ-subunit *N*-terminus of one heterotetramer of IDH3 inserts into the β-subunit of the opposing heterotetramer, producing the heterooctameric quaternary structure $(\alpha\beta\alpha\gamma)_2$.[21, 35, 36] There is limited association of the IDH3α subunit, encoded by *IDH3A*, with cancer.[18, 35]

1.2.2. The Physiological Role of 2-Hydroxyglutarate

Both enantiomers of 2-hydroxyglutarate (2-HG), *R*-2-HG (D-2-HG) and *S*-2-HG (also known as L-2-HG), occur naturally at low levels in the human body (**Figure 1.4**).[37-40] Studies have reported both enantiomers in blood plasma (low micromolar concentrations) and urine (low micromolar concentrations for new-borns, low millimolar concentrations for adults).[37-40]

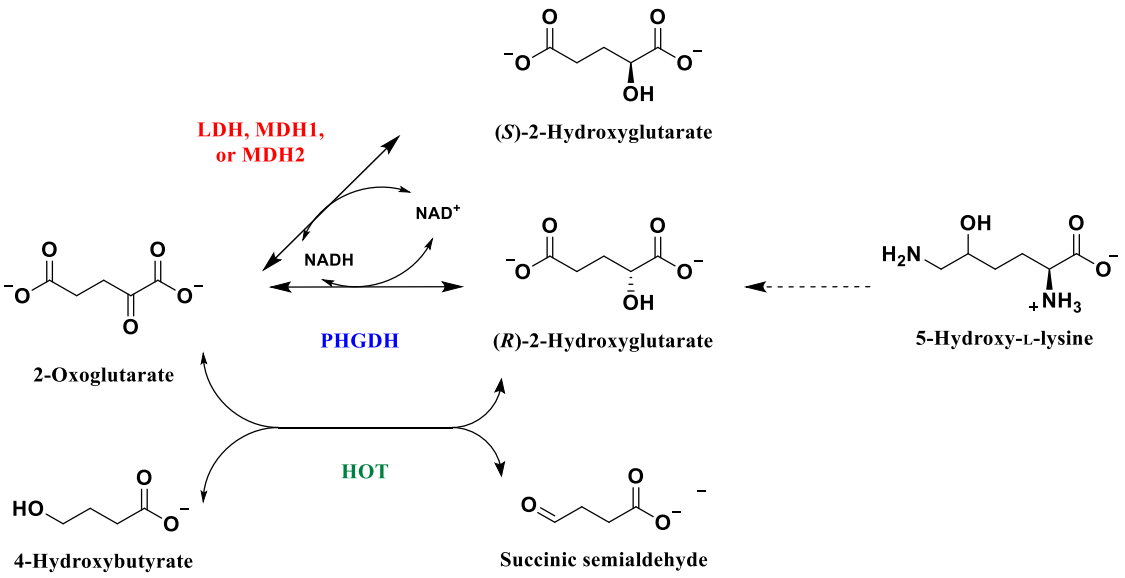

Figure 1.4 | *Metabolic routes that produce R-2-HG and S-2-HG. The dotted line indicates more than one reaction in a metabolic route. LDH = lactate dehydrogenase. MDH = malate dehydrogenase. PHGDH = phosphoglycerate dehydrogenase. HOT = hydroxyacid oxoacid transhydrogenase.*

R-2-HG may be formed by reactions in the metabolism of 5-hydroxy-L-lysine, 4-hydroxybutyrate, and by phosphoglycerate dehydrogenase (PHGDH) (**Figure 1.4**), exacerbated under acidic conditions.[41-45] *S*-2-HG, which is proposed to regulate cellular redox homeostasis in periods of stress, may be formed at low levels by malate dehydrogenase 1 (MDH1), malate dehydrogenase 2 (MDH2), and lactate dehydrogenase (LDH) (**Figure 1.4**), and, like *R*-2-HG, is exacerbated by increased acidity and hypoxia.[45-48] Under normal physiological conditions, low levels of *R*-2-HG and *S*-2-HG are converted to 2-OG by the corresponding dehydrogenase, D2HGDH or L2HGDH. A deficiency in the respective mitochondrial 2-HG dehydrogenase for either *R*-2-HG or *S*-2-HG leads to the corresponding aciduria with accumulation of 2-HG in the plasma, urine, and cerebrospinal fluid.[49-54] This in turn correlates with cardiomyopathy (*R*-2-HG only), cerebral ataxia, epilepsy, and neurological and developmental abnormalities.[50-55] Interestingly, despite the status of *R*-2-HG as an oncometabolite, *R*-2-HG aciduria is not associated with the same cancers as IDH mutations.[56] By contrast, *S*-2-HG is associated with sporadic cases of central nervous system tumours.[57-60] It is plausible that some of

these reactions may be reversible under suitable conditions, such as a shift in redox balance or pH.

1.3. The Discovery of Mutated IDH and Elevated 2-HG in Gliomas

The first IDH mutations in cancer were reported in 2008, and involved IDH1 point mutations in grade II and III glioma, and secondary glioblastoma multiforme (GBM) (now 'Astrocytoma, IDH-mutant CNS WHO grade 4').[61-63] In acute myeloid leukaemia (AML), IDH1 and the more prevalent IDH2 mutations were discovered in 2009.[63-67] The most common substitution in IDH2 found in AML is R140Q.[63-67] Since then, mutations of IDH1 and IDH2 have been shown to be prevalent in a wide array of cancers, including grade 2/3 gliomas (> 75%), secondary GBM (55 – 88%), AML (14 – 33%), chondrosarcoma (17 – 70%), angioimmunoblastic T-cell lymphoma (20 – 33%), sinonasal undifferentiated carcinoma (35 – 80%), solid papillary carcinoma with reverse polarity (> 77%), and intrahepatic cholangiocarcinoma (7.5 – 41%).[19, 61-107]

Gliomas make up 30 – 40% of brain tumours and derive from glial cells, non-neuronal brain cells that are required for neuronal survival and function.[108, 109] The major types of glial cells in the central nervous system (CNS) are astrocytes, oligodendrocytes, microglia, and ependymal cells; examples in the peripheral nervous system (PNS) include Schwann cells.[109-111] Glial functions include facilitating neurotransmission, metabolism, inflammation, and formation of the blood-brain barrier.[109-111] As an unfortunate result, gliomas are intra-axial and grow intermixed with healthy brain tissue.[112] The aggressiveness of a resulting glioma is classified as low-grade (grades 1 and 2) or high-grade (grades 3 and 4).[113, 114] IDH1 and IDH2 mutations are not common in primary GBM (now 'Glioblastoma, IDH-wild-type, CNS WHO grade 4') and mutations in either

isoform were included in the diagnostic criteria for CNS tumours in 2016. Therefore, in 2021, the World Health Organisation (WHO) changed IDH-mutation status to a requirement for the diagnosis of certain adult-type diffuse gliomas, such as astrocytoma (grade 2-4) and oligodendroglioma (grade 2 and 3).[61, 62, 67-71, 115, 116]

The tumour type strongly correlates with the nature of the IDH mutation.[117] Solid tumours present early mutations in IDH1 or IDH2 during their development. Co-mutation of IDH1 with IDH2 is exceedingly rare and often considered mutually exclusive.[68, 70, 71, 85, 118] IDH1 is the most frequently mutated isoform, particularly in gliomas and secondary GBM, whereas IDH2 mutations are more common in AML.[17, 63, 117] Known IDH1 mutations in gliomas lead to the substitutions R132H, R132C, R132S, R132L, R132G, R132V, and R100Q. Of these mutations, the most commonly found in grade 2/3 gliomas and secondary GBM is the substitution R132H (85 – 90%), followed by R132C, R132S, R132L, R132G, R132V (5 – 8%), and most infrequently R100Q (< 1%).[62, 63, 106, 119] R100Q is reported to have the lowest catalytic efficiency.[120] IDH2 mutations are rarer in gliomas than IDH1 mutations, and lead to the substitutions R172K, R172M, R172W, R172S, R172G (3 – 5 %), of which R172K is the most common.[62, 106, 119]

Soon after discovery the initial discovery of IDH mutations in cancer, studies identified that IDH1 mutations negatively impacted the ability of the enzyme to catalyse isocitrate to 2-OG turnover and a dominant negative phenotype was observed.[67, 121] Work by Dang et al. reported the IDH1 R132H mutation to cause a gain-of-function and enable the reduction of 2-OG to *R*-2-HG, driving a detectable accumulation of *R*-2-HG in IDH-mutated cancer cells.[16] Later, IDH2 R172K and IDH2 R140Q were also found to catalyse the synthesis of *R*-2-HG, driving *R*-2-HG accumulation.[66] From this point on, *R*-2-HG is referred to as 2-HG unless otherwise specified.

1.4. The Structure and Mechanism of Action of Wild-type and Mutant IDH1

1.4.1. The Structure of IDH1 WT

IDH1 WT forms a homodimer (**Figure 1.5**),[122] each monomer consisting of three domains: a large domain (233 residues: 1-103, and 286-414) (**Figure 1.5.C**), a small domain (133 residues: 104-136, and 186-285) (**Figure 1.5.D**), and a CLASP domain (two double-stranded antiparallel β-sheets) (**Figure 1.5.E**).[122] The large domains each contain a dinucleotide-binding Rossmann fold. The small domains form the dimer-interface via both α9 and α10 helices (**Figure 1.5.D**). The CLASP domain of each monomer interlock to hold the two monomers together, and two symmetrical active sites are formed in the clefts between the small and large domains of each monomer, utilising residues from both monomers (**Figure 1.5.E**, **Figure 1.5.A**).[122] The homodimer can assume two established conformations: inactive and active, in addition to one putative semi-active conformation.[122] The inactive conformation exhibits active site distances (Cα – Cα) of 18.8 Å (L250 monomer A – I76 monomer B) and 21.2 Å (I76 monomer A – L250 monomer B) (**Figure 1.6.A**).[122] Residues D275, D279N, and K212 from monomer A are far from the active site. In particular, D275 and D279N are in the α10 helix, which is not well resolved, flexible and loop-like. Together, these features define an 'open' active site cleft compared to the active conformation, hence this conformation is referred to as the 'open-inactive' conformation.[123] Only $NADP^+$ is bound in this conformation.[122]

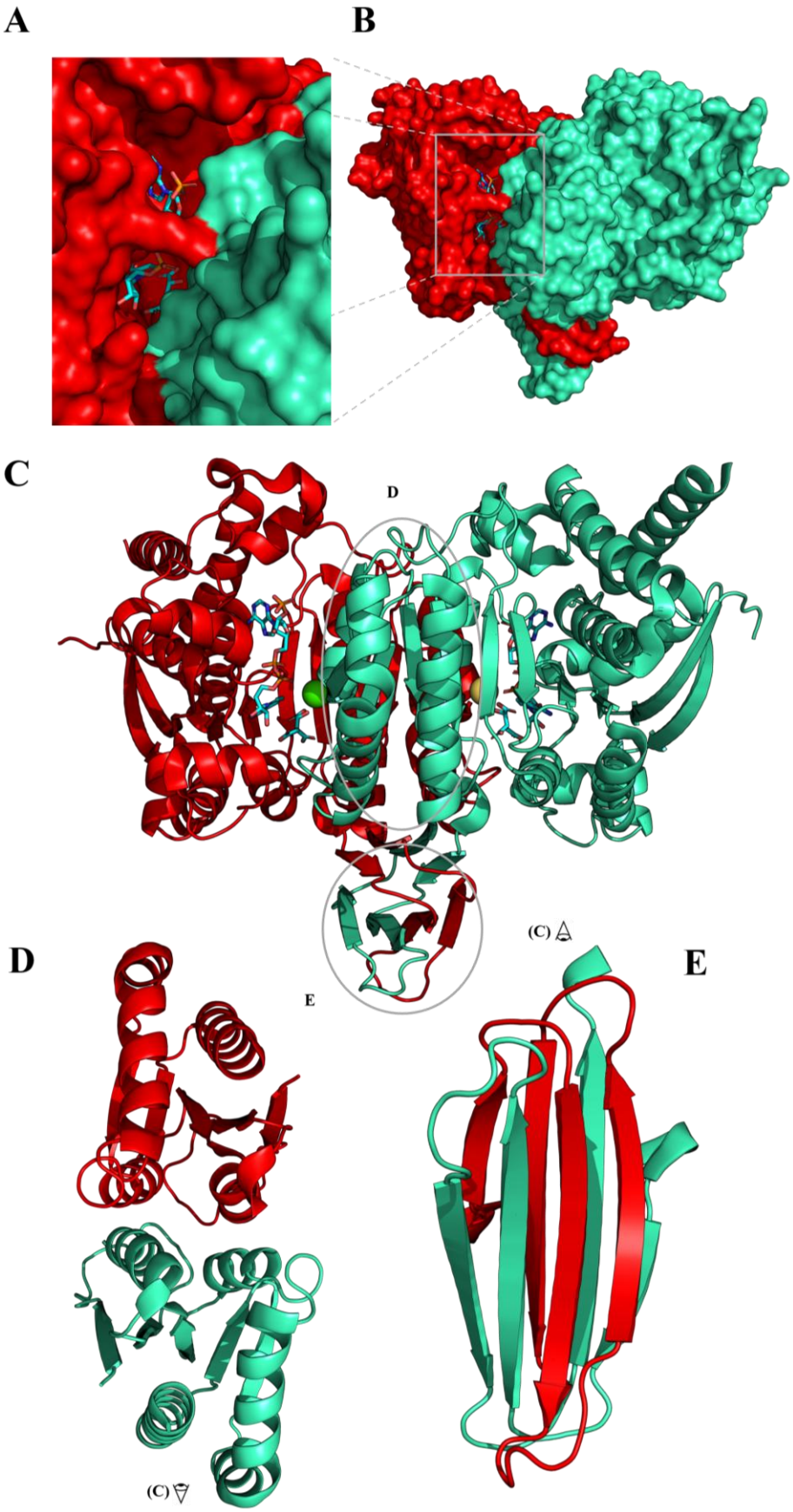

Figure 1.5 | *Views from a crystal structure of IDH1 WT homodimer in the closed-active conformation (pdb: 1T0L).*[122] *The backbone of the monomer A subunit is teal, the backbone of*

the monomer B subunit is crimson. Substrate carbons (ICT and $NADP^+$) are coloured cyan. In all small molecules present as sticks, oxygen atoms are coloured red, nitrogen atoms are coloured blue, and sulfur atoms are coloured orange. Metal ions are coloured green. ***A.*** *The entrance to one of two symmetrical active sites in IDH1 WT, located in the cleft between the large domain of monomer B (crimson) and the small domain of monomer A (teal). Stick representations of $NADP^+$ (cyan) and isocitrate (cyan) can be seen within.* ***B.*** *Surface render of the 3D structure of an IDH1 WT homodimer, viewed from the front.* ***C.*** *Cartoon secondary structure of the 3D structure of an IDH1 WT homodimer, viewed from the front. The large domains of monomers A (teal, right) and B (crimson, left) flank the small domains (**D**). The small domains (**D**), and the CLASP domains (**E**) of monomers A (teal) and B (crimson) are circled.* ***D.*** *Top-down view of the small domains of monomers A (teal, bottom) and B (crimson, top). The dimer interface can be seen as a gap between α-helices of monomer A (teal, bottom) and monomer B (crimson, top). The perspective displayed in **C** is indicated.* ***E.*** *Bottom-up view of the CLASP domains of monomers A (teal) and B (crimson). The perspective displayed in **C** is indicated.*

The binding of an isocitrate-metal complex (likely isocitrate–magnesium under physiological conditions) to IDH1 WT in the open-inactive conformation is able to trigger a structural transformation to the active conformation.[124, 125] Residues K212, D275, and D279N are recruited to the active site by the substrate complex and in turn are proposed to move the α10 helix towards the active site.[122] This proposal is supported by experiments in which pre-incubation removes a lag-phase commonly observed at the beginning of turnover assays.[124] The active conformation accordingly exhibits shorter active site distances (Cα – Cα) than the open-inactive conformation, 13.4 Å (L250 monomer A – I76 monomer B, cf. 18.8 Å) and 12.6 Å (I76 monomer A – L250 monomer B, cf. 21.2 Å) (**Figure 1.6.B**).[122] As a result, the active conformation is referred to as the 'closed-active' conformation.

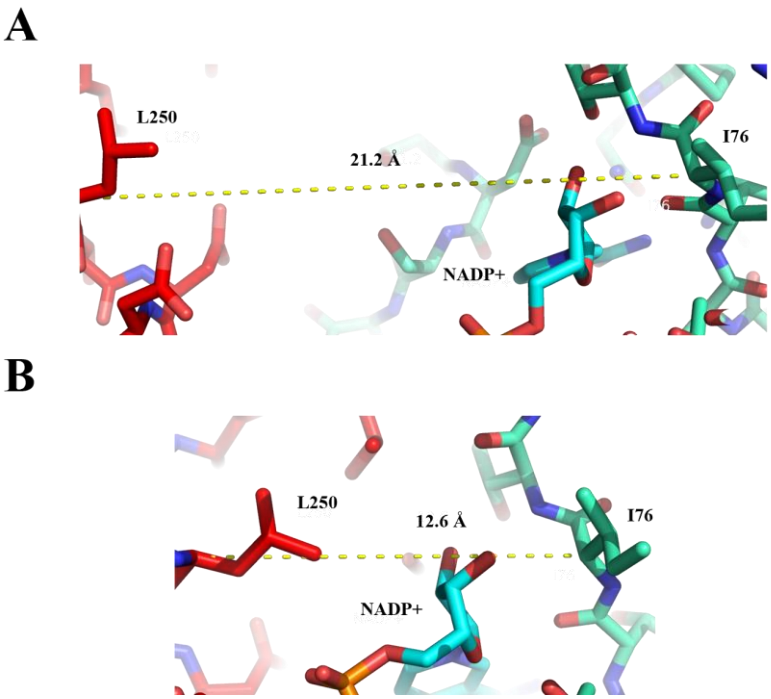

Figure 1.6 *| Views of the active site distances (Cα – Cα) from a crystal structure of IDH1 WT homodimer in the open-inactive and closed-active conformations. The backbone of the monomer A subunit is teal, the backbone of the monomer B subunit is crimson. Substrate carbons (ICT and NADP⁺) are coloured cyan. In all small molecules present as sticks, oxygen atoms are coloured red, nitrogen atoms are coloured blue, and sulfur atoms are coloured orange. Metal ions are coloured green.* ***A.*** *Open-inactive conformation, I76 monomer A – L250 monomer B (pdb: 1T09).* ***B.*** *Closed-active conformation, I76 monomer A – L250 monomer B (pdb: 1T0L).* [122]

Once bound, eight residues from both monomers are involved in binding isocitrate (monomer A – K212, T214, D252; monomer B – T77, R100, R109, R132, and D275) (**Figure 1.7.A**) and three residues coordinate the metal ion (monomer A, α9 – D252; monomer B, α10 – D275 and D279) (**Figure 1.7.B**).[122, 124] The metal ion is also coordinated by the C1 carboxyl and C2 hydroxyl groups of isocitrate (**Figure 1.7.B**). [124]

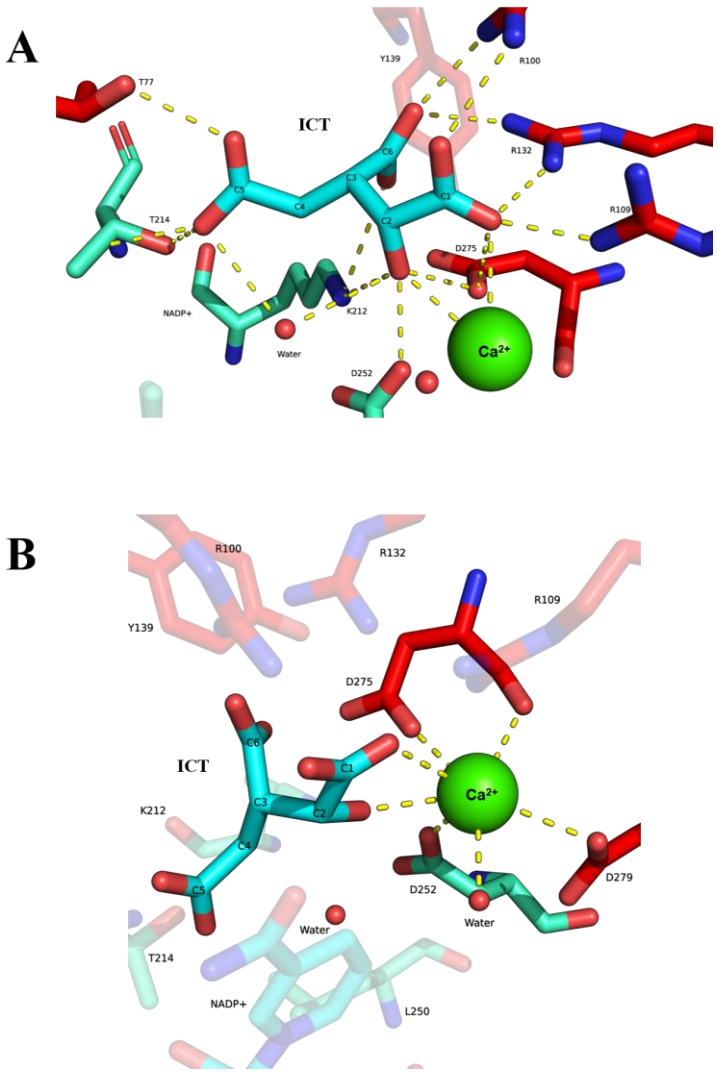

Figure 1.7 *| Views of the active site of IDH1 WT (pdb: 1T0L). Amino acid carbons from the monomer A subunit are coloured teal, amino acid carbons from the monomer B subunit are coloured crimson, and substrate carbons (ICT and NADP$^+$) are coloured cyan. In all chemical structures represented as sticks, oxygen atoms are coloured red, and nitrogen atoms are coloured blue. Metal ions are coloured green.* ***A.*** *Isocitrate (ICT, cyan) bound by D252, K212, and T214 of monomer A (teal), R100, R132, R109, D275, and T77 of monomer B (crimson), and Ca^{2+} (green).* ***B.*** *Metal ion (here Ca^{2+}, green) bound by D252 of monomer A (teal), D275 and D279 of monomer B (crimson), and the C1 carboxyl and C2 hydroxyl of isocitrate (ICT, cyan). Note, Ca^{2+} is a catalytically-inactive substitute for Mg^{2+}.*[122]

At the active site of IDH1 WT, NADPH is coordinated within the large domain similarly in open-inactive and closed-active conformations.[122] Before isocitrate binding, D-279 coordinates via hydrophobic interactions with the nicotinamide ring.[122] This interaction is then sustained by the substrate upon isocitrate binding, ready for electron transfer.[122]

1.4.2. The Mechanism of IDH1 WT

Isocitrate and magnesium bind to IDH1 WT as a complex with high affinity, adjacent to $NADP^+$/NADPH (**Figure 1.8**).[125] NADPH typically copurifies with IDH1 WT. Initial time-dependent studies reported that one molecule of NADPH per homodimer was released into solution after long-term incubation without turnover. The release of only one NADPH molecule suggests that the second active site does not exchange substrates with the solution, and implies half-site reactivity of the enzyme by extension.[124] This proposal has been further supported by absorbance and crystallographic studies.[124]

The catalytic mechanism of IDH1 WT is currently proposed to involve the following steps: D-279 deprotonates K212, which in turn deprotonates the C2 alcohol of isocitrate (**Figure 1.9.A**);[126] $NADP^+$ abstracts a hydride from the C2 position of isocitrate (**Figure 1.9.B**), oxidising the alcohol to a ketone; then decarboxylation at C3 (**Figure 1.9.C**) produces an enolate, finally deprotonating Y-139 (**Figure 1.9.D**) to form 2-OG (**Figure 1.9.E**).[124, 126, 127]

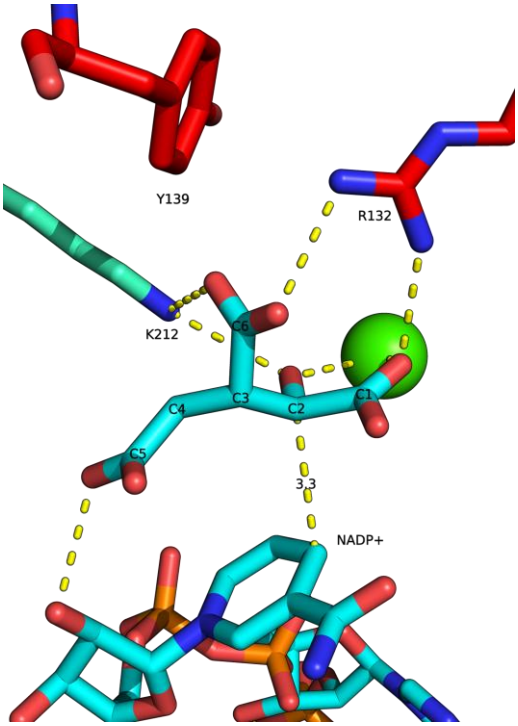

Figure 1.8 *| A view of the interactions of $NADP^+$ and the IDH1 WT active site residues which react with isocitrate (ICT, cyan), K212 (teal) and Y139 (crimson) (pdb: 1T0L). Amino acid carbons from the monomer A subunit are coloured teal, amino acid carbons from the monomer B subunit are coloured crimson, and substrate carbons (ICT and $NADP^+$) are coloured cyan. In all chemical structures represented by sticks, oxygen atoms are coloured red, nitrogen atoms are coloured blue, and sulfur atoms are coloured orange. Metal ions are coloured green. R132 (crimson) can be seen coordinating the C1 and C6 carboxyls. The metal ion (here Ca^{2+}, green) can be seen behind ICT (cyan), coordinated by the C1 carboxyl and C2 hydroxyl.*[122]

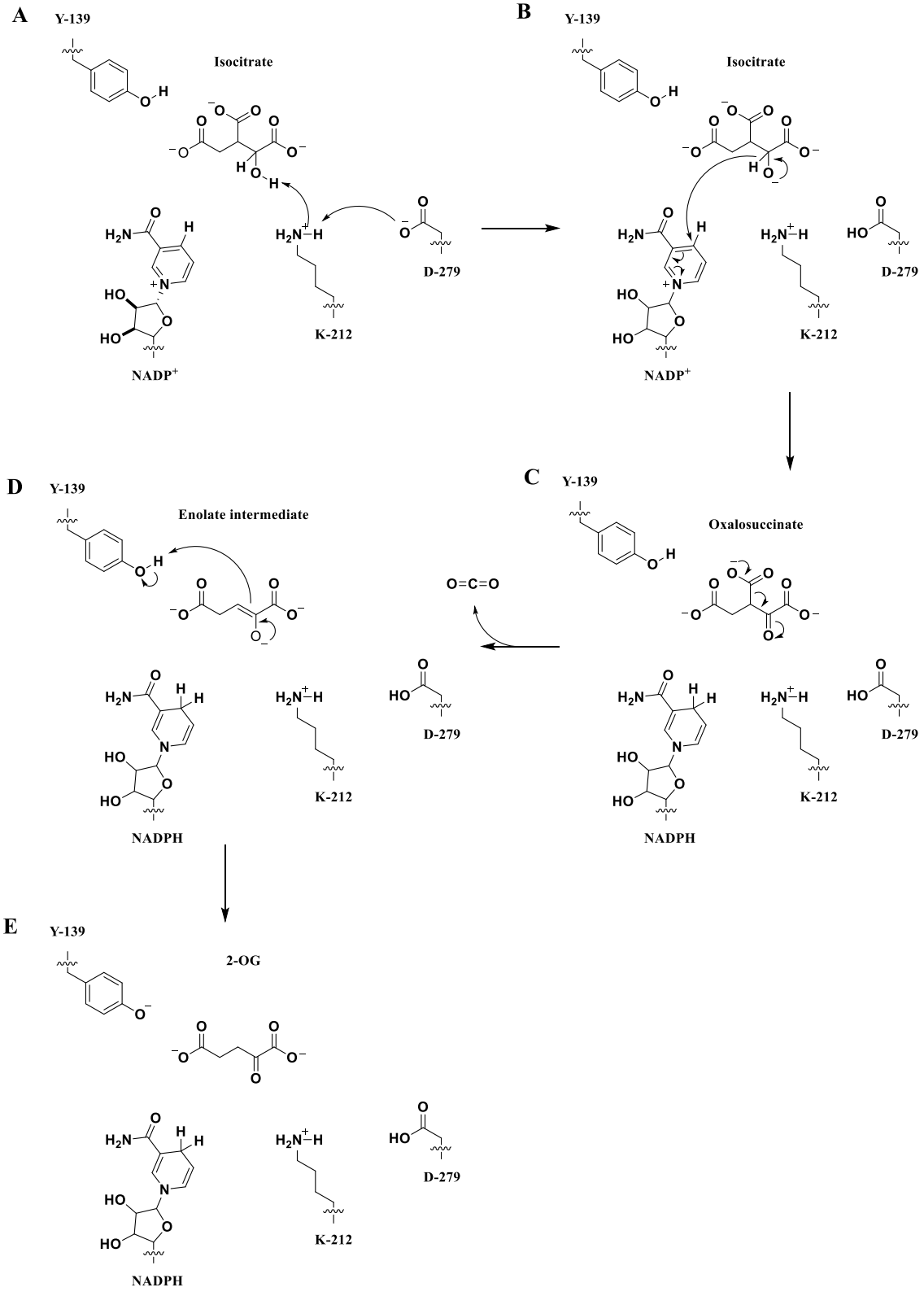

Figure 1.9 *| The proposed catalytic mechanism of IDH1 WT.* ***A.*** *Isocitrate is deprotonated.* ***B.*** *Isocitrate is oxidised to oxalosuccinate.* ***C.*** *Oxalosuccinate is decarboxylated to give an enolate intermediate.* ***D.*** *The enolate abstracts a proton from Tyr-139 (Y-139) to form 2-OG (**E.**).*

1.4.3. Structural and Mechanistic Effect of the R132 Substitution

IDH1 R132H catalyses the turnover of isocitrate to 2-OG and subsequently reduces 2-OG in the active site to 2-HG, as shown by NMR studies.[125] IDH1 R132H can also catalyse the reduction of 2-OG not derived from isocitrate as shown by absorbance assays and NMR.[125] This gain-of-function is proposed to be due to differences in the geometries of IDH1 R132H leading to a subtly different closed-active conformation compared to IDH1 WT.

The observed gain-of-function R132 substitutions replace arginine with histidine, cysteine, serine, or a number of other short side chain residues.[62, 63, 106, 119] It is proposed that binding of the isocitrate C3 carboxylate by R132 is lost when arginine is replaced with a shorter side chain because the distance is too far to form favourable interactions (**Figure 1.8**, **Figure 1.10**).[122] The 2-OG reduction gain-of-function is similar for seven different mutations, supporting the conclusion that it is the lack of arginine that drives the observed phenotype.[60] In IDH1 R132H, residues D252, D275, and D279 are displaced compared to IDH1 WT, and Y139 coordinates 2-OG (**Figure 1.10**). IDH1 WT can catalyse the reduction of 2-OG with carboxylation at C3 to form isocitrate, enabled by the coordination of CO_2 by R132 at the appropriate position adjacent to C3 (**Figure 1.8**).[19, 60] Short amino acid side chains such as H132 of IDH1 R132H are unable to coordinate CO_2 (**Figure 1.10**), allowing for the reduction of 2-OG to 2-HG, but not the requisite carboxylation in the reverse reaction to form isocitrate.[19, 60]

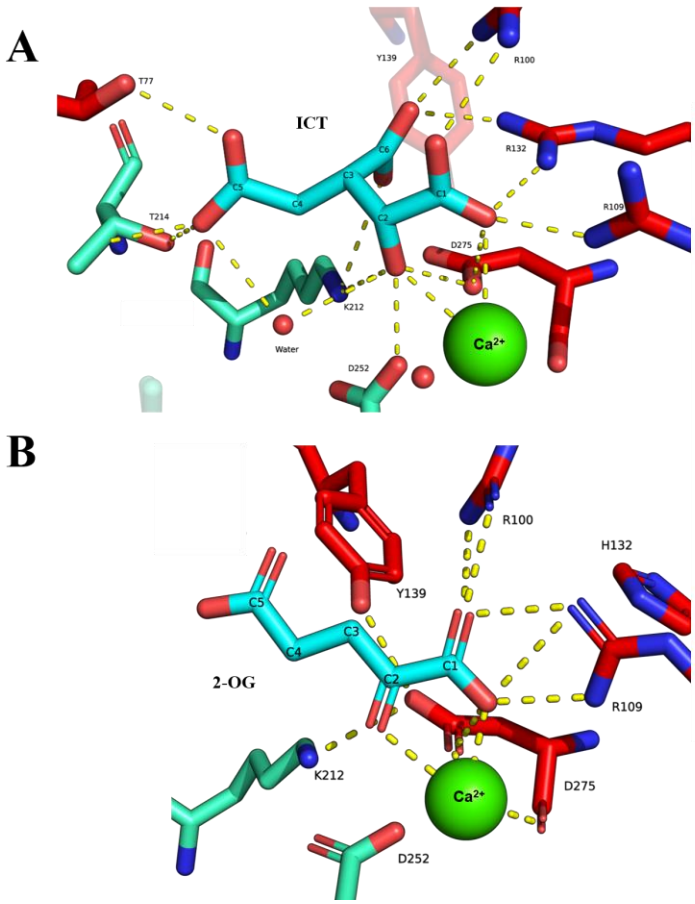

Figure 1.10 *| Comparative views of ICT bound in the active site of IDH1 WT (**A**, pdb: 1T0L, **Figure 1.7.A**) and 2-OG bound in the active site of IDH1 R132H (**B**, pdb: 4KZO).*[122, 128] *Amino acid carbons from the monomer A subunit are coloured teal, amino acid carbons from the monomer B subunit are coloured crimson, and substrate carbons (ICT and NADP*$^{+}$*) are coloured cyan. In all molecules, oxygen atoms are coloured red, and nitrogen atoms are coloured blue. Metal ions are coloured green. Note that in IDH1 R132H, H132 (crimson) does not coordinate the substrate (here 2-OG, cyan), and Y139 (crimson) has moved substantially closer to the substrate.*

1.5. The Physiological Effects of Mutated IDH in Glioma

The presence of mutated IDH in cells impairs the physiological function of wild-type IDH, and introduces the neormorphic function of mutated isoforms, for example IDH1 R132H. [16, 67, 121] Due to the dominant negative effect of IDH1 R132H in IDH1 heterodimers, it is possible that one quarter of IDH1 dimers (IDH1 WT homodimers) may result in the production 2-OG, while three quarters of IDH1 dimers may result in a net production of 2-HG (25% IDH1 R132H homodimers, 50% IDH1 WT/IDH1 R132H heterodimers). As a result, there is less overall production of 2-OG and NADPH by IDH1

WT in afflicted cells.[129] The neomorphic 2-HG forming reaction has three immediate consequences: the consumption of 2-OG, the consumption of NADPH, and the production of 2-HG.[16, 130] Therefore, it follows that the effects of mutated IDH1 and IDH2 in glioma will be derived from these catalysed reactions. The decreased production of 2-OG and NADPH by IDH1 WT, and increased consumption of 2-OG and NADPH by IDH1 R132H, is cumulative. Thus, at least simplistically, the causes of potential effects of IDH mutation can be classed as being due to lowered levels of 2-OG, lowered levels of NADPH, and higher levels of 2-HG. Note, however, that compensatory adaptation mechanisms may restore levels of these metabolites.

Low levels of 2-OG could impair the function of 2-OG dependent enzymes, including prolyl-hydroxylases (PHDs), collagen prolyl hydroxylases (P4Hs) lysine demethylases (KDMs), and 10,11-translocases (TETs).[131-134] Along with many other metabolites, however, decreased levels of 2-OG are inconsistently detected in IDH1 and IDH2 mutant cells, making it hard to draw conclusions.[130, 135-141] It is likely in any case that 2-OG is at least partly replenished by glutamate dehydrogenase as both GLUD1 and GLUD2 have been observed to be upregulated in gliomas.[20]

Low levels of NADPH impair fatty acid metabolism and the ability of a cell to respond to oxidative stress.[142, 143] NADPH and $NADP^+$ are required to metabolise unsaturated fatty acids in the peroxisome, and conduct fatty acid biosynthesis.[26, 27, 143] Glutathione is a free-radical scavenging, anti-oxidant, tripeptide possessing a free thiol that forms a disulfide bridge with another glutathione molecule after an oxidation event.[144] NADPH is necessary to regenerate the reduced form of glutathione (GSH) from oxidised glutathione (GSSG) and uphold cellular redox homeostasis.[142] IDH1 WT has been reported to produce ~65% of total NADPH in glioblastoma tissue, with R132H substitution resulting in a ~40% decrease of NADPH production.[145] In addition to global

redox dysregulation, the depletion of NADPH as a cofactor may contribute to downstream effects in IDH mutant glioma such as altered metabolism, which are discussed in **Sections 1.5.2**, **1.5.3**, **1.5.4**, and **1.5.5**.

Normal physiological levels of 2-HG are usually low, in part due to 2-HG dehydrogenase activity, as discussed in **Section 1.2.2**. It is proposed that IDH1 and IDH2 mutations overwhelm the capacity of the 2-HG dehydrogenases, leading to the accumulation of 2-HG (5 – 35 μmol g^{-1}, 5 – 35 mM at an assumed tissue density of 1g mL^{-1}).[16, 17] In turn, high levels of 2-HG can inhibit 2-OG dependent enzymes (**Section 1.5.1**), and may also contribute to downstream effects in the cell such as altered metabolism (**Sections 1.5.2**, **1.5.3**, **1.5.4**, and **1.5.5**).

Metabolism in glioma cells, in addition to the relative levels of 2-OG, NADPH, and 2-HG, has been consistently reported as being altered in samples from patient tissue biopsies (PTB), patient-derived xenograft mouse models (PDX), and multiple cell lines (CL).[130, 135-141, 146-151] These changes are discussed in **Sections 1.5.2**, **1.5.3**, **1.5.4**, and **1.5.5**. Interestingly, although levels of 2-HG appear to increase in higher grade brain tumours, the levels are consistent across all brain tumour grades when normalised according to tumour cellularity.[152, 153]

1.5.1. Effects of Mutated IDH on 2-OG Dependent Oxygenases

Similar to the dicarboxylic acids succinate and fumarate, *in vitro* studies have shown high levels of 2-HG are able to inhibit 2-OG dependent oxygenases such as prolyl hydroxylase domain-containing protein 2 (PHD2) (IC_{50} = 7.3 mM), and the predominantly nuclear enzymes lysine-specific demethylase 4A (KDM4A) (IC_{50} = 24 μM) and tet methylcytosine dioxygenase 2 (TET2) (IC_{50} = 5.3 mM).[3, 12, 132, 154, 155] While *in cellulo* studies reporting nuclear effects of 2-HG have commonly utilised octyl-2-HG as a

treatment substitute to ensure cell permeability, 2-HG has been detected in tumour interstitial fluid and in non-brain tumour samples from IDH1 R132H glioma-bearing mice, suggesting that 2-HG may distribute across multiple compartments, possibly via protein carriers or other transport mechanisms.[123, 156, 157] Furthermore, the *S*-enantiomer of 2-HG (*S*-2-HG) was recently detected directly within the nucleus using a bespoke biosensor, providing further evidence that 2-HG species may access different cellular compartments *in vivo*.[158] Although definitive evidence for the direct *in vivo* modulation of 2-OG-dependent oxygenases by 2-HG remains to be established, it is nonetheless prudent to consider how IDH mutations may contribute to gliomagenesis through the dysregulation of PHD2, KDM4A, and TET2.

PHD2 is an essential enzyme in the physiological response to hypoxia in animals.[159] Under normoxic conditions, 2-OG and molecular oxygen are utilised by PHD2 to hydroxylate the hypoxia-inducible factor alpha (HIFα) isoforms.[160] The hydroxylated form of HIFα is recognised by von Hippel-Lindau (VHL) protein and consequently ubiquitinylated for degradation by the proteosome.[160] Under hypoxic conditions, low levels of O_2 prevent PHD2 from efficiently hydroxylating HIFα.[160] HIFα that is not recognised by VHL is able to associate with the HIFβ monomer, forming the HIFαβ heterodimer.[160] HIFαβ binds hypoxia-response elements in the promoter regions of multiple genes, leading to the transcription and subsequent expression of proteins necessary for the cellular hypoxic response.[160] Inhibition of PHD2 by sufficiently high concentrations of metabolites such as 2-HG, succinate, and fumarate could in part mimic low levels of O_2, leading to a pseudohypoxic response.[12, 161] Pseudohypoxia aids tumour growth by triggering angiogenesis, upregulation of glucose uptake, and glycolysis.[161] Nonetheless, the potential for PHD2 inhibition by 2-HG is not conclusive evidence that IDH mutation directly causes HIFα stabilisation. 2-HG is not a potent PHD2 inhibitor

(IC_{50} = 7.3 mM) and some studies suggest 2-HG is an activator of PHD2, while others suggest non-enzymatic conversion of 2-HG to complicate matters.[132, 162, 163] Gliomas with IDH mutations also do not show a consistent link with HIF upregulation: HIF levels have been found to be elevated, decreased, or unchanged.[17] While HIFα has been proposed as an oncogene in some cancers, especially kidney tumours, it may actually act as a tumour suppressor in cancers with IDH mutations, such as glioma and leukaemia.[120, 164, 165] Indeed, PHD inhibitor mediated HIFα upregulation is a potential treatment for AML.[166]

KDM4A and TET2 are 2-OG dependent oxygenases which participate in DNA regulation via catalysing demethylation. KDM4A demethylates *N*-methylated lysines on histones, and TET2 oxidises 5-methyl-cytosine to 5-hydroxymethylcytosine in DNA.[167, 168] 2-HG inhibits both enzymes to different degrees (KDM4A, IC_{50} = 24 μM; TET2, IC_{50} = 5.3 mM).[132, 154] Inhibition of KDM4A and TET2 leads to a hypermethylation phenotype and widespread gene silencing, which can be oncogenic by hindering cellular differentiation.[17] Hypermethylation has been reported in cancers with IDH mutations, such as gliomas and leukaemia.[17, 168] It is plausible that 2-HG accumulation (≥ 5 mM) could exacerbate epigenetic changes, given that this concentration exceeds the KDM4A IC_{50} (24 μM) and approaches that of TET2 (5.3 mM).[16, 17, 132, 154] However, the local availability of 2-HG within specific cellular compartments, and its potential binding to additional proteins, may substantially influence its effective concentration. Further studies are thus required to confirm whether these in vitro IC_{50} values reliably translate into physiologically relevant inhibition *in vivo*.

1.5.2. Alterations in Glycolytic and TCA Cycle Metabolites in IDH Mutated Glioma

Enzyme levels measured in IDH1 R132H PTBs and PDXs exhibit a shift away from reliance on glycolysis, and towards mitochondrial pathways (see **Figure 1.1** for outline of the glycolysis pathway).[146, 169, 170] Further reports suggest that IDH1 R132H gliomas favour glutamate and potentially lactate as anaplerotic substrates, rather than glucose, glutamine, and acetate putatively favoured by IDH1 WT glioma (also see **Section 1.5.3**).[146, 169-172] A shift away from glycolysis in glioma cells is supported by reports that glucose uptake is reduced, mono-carboxylate exporters (MCT-1, MCT-4; export lactate and other mono-carboxylate metabolites) and lactate dehydrogenase-A (LDHA; catalyses pyruvate to lactate) are downregulated, and lactate dehydrogenase-B (LDHB; catalyses lactate to pyruvate) is upregulated.[146, 169, 170, 173-176] Pyruvate carboxylase (PC) is reported to be upregulated in glioma cells while pyruvate dehydrogenase is reported to be downregulated, leading to the majority of pyruvate in IDH1 R132H gliomas fuelling OAA synthesis instead of acetyl-CoA.[177, 178] At the time of writing, the levels of lactate were reported to be decreased in four out of five studies using the NHA astrocyte cell line, and U87, and LN18 glioma cell lines. PDX studies reported either decreased or unchanged levels of lactate, and studies of HOG cell lines and PTBs reported no change in lactate (**Table 1.1**). In PTBs, this may be due to the mixing of extracellular and intracellular lactate during tissue homogenisation, where cell line harvesting avoids mixing.[135-139, 141, 147] Alterations of metabolites involved in glycolysis are shown below (**Table 1.1**). Many intermediates are inconsistently altered across studies, suggesting no clear change overall. Ribulose-5-phosphate and 3-phosphoglycerate showed decreased levels overall, and acetyl-CoA showing increased levels (**Table 1.1**). With the exception of acetyl-CoA, the absence of consistent changes in the levels of glycolytic metabolites

across studies supports previous reports that IDH1 R132H PTBs and PDXs may rely less on glycolysis and to a greater degree on mitochondrial pathways, in turn suggesting that IDH mutations may promote the utilisation of alternative fuel sources by the cell.[146, 169, 170] While levels of acetyl-CoA were reported by one study to be consistently increased in the presence of either IDH1 or IDH2 mutations in HOG cells, studies utilising additional disease models are required to confidently conclude that IDH mutations consistently lead to altered levels of acetyl-CoA.

Alteration	IDH Mutation	Model	Analysis method	Source
Glucose-1-phosphate -				
-	$IDH1^{R132H}$	PTB	CE-MS	135
-	$IDH1^{R132H}$	CL (LN18)	IC-MS	138
Glucose-6-phosphate -				
-	$IDH1^{R132H}$	PTB	CE-MS	135
-	$IDH1^{R132H}$	PTB	GC-MS/LC-MS	141
↓	$IDH1^{R132H}$	CL (U87)	NMR	136
-	$IDH2^{R172K}$	CL (U87)	NMR	136
6-Phospho-gluconate				
-	$IDH1^{R132H}$	PTB	CE-MS	135
↓	$IDH1^{R132H}$	PTB	GC-MS/LC-MS	141
Ribulose-5-phosphate ↓				
-	$IDH1^{R132H}$	PTB	CE-MS	135
↓	$IDH1^{R132H}$	CL (LN18)	IC-MS	138
↓	$IDH1^{R132H}$	CL (U87)	NMR	136
↑	$IDH2^{R172K}$	CL (U87)	NMR	136
Ribose-5-phosphate -				
-	$IDH1^{R132H}$	PTB	CE-MS	135
-	$IDH1^{R132H}$	PTB	GC-MS/LC-MS	141
↓	$IDH1^{R132H}$	CL (LN18)	IC-MS	138
Seduheptulose-7-phosphate -				
-	$IDH1^{R132H}$	PTB	CE-MS	135
-	$IDH1^{R132H}$	PDX	MSI/LC-MS	137
↓	$IDH1^{R132H}$	CL (LN18)	IC-MS	138
Fructose-1,6-bisphosphate -				
↓	$IDH1^{R132H}$	PTB	GC-MS/LC-MS	141

(Fructose-1,6-bisphosphate) cont.				
-	IDH1^{R132H}	CL (LN18)	IC-MS	138
Fructose-6-phosphate -				
-	IDH1^{R132H}	PTB	CE-MS	135
-	IDH1^{R132H}	PTB	GC-MS/LC-MS	141
-	IDH1^{R132H}	CL (LN18)	IC-MS	138
-	IDH1^{R132H}	CL (U87)	NMR	136
-	IDH2^{R172K}	CL (U87)	NMR	136
Dihydroxyacetone phosphate -				
-	IDH1^{R132H}	PTB	CE-MS	135
Glyceraldehyde-3-phosphate -				
-	IDH1^{R132H}	PTB	CE-MS	135
↑	IDH1^{R132H}	CL (LN18)	IC-MS	138
Phosphoenolpyruvate -				
-	IDH1^{R132H}	PTB	CE-MS	135
↓	IDH1^{R132H}	PTB	GC-MS/LC-MS	141
↑	IDH1^{R132H}	CL (LN18)	IC-MS	138
3-Phospho-glycerate ↓				
-	IDH1^{R132H}	PTB	CE-MS	135
↓	IDH1^{R132H}	PTB	GC-MS/LC-MS	141
↓	IDH1^{R132H}	CL (LN18)	IC-MS	138
Acetyl-CoA ↑				
↑	IDH1^{R132H}	CL (HOG)	LC-MS	139
↑	IDH2^{R172K}	CL (HOG)	LC-MS	139
Pyruvate -				
-	IDH1^{R132H}	PTB	CE-MS	135
-	IDH1^{R132H}	PDX	MSI/LC-MS	137
-	IDH1^{R132H}	CL (HOG)	LC-MS	139
-	IDH1^{R132H}	CL (LN18)	IC-MS	138
↓	IDH1^{R132H}	PTB	GC-MS/LC-MS	141
↓	IDH1^{R132H}	PTB	LC-MS	137
-	IDH2^{R172K}	CL (HOG)	LC-MS	139
Lactate -				
-	IDH1^{R132H}	PTB	CE-MS	135
-	IDH1^{R132H}	PTB	GC-MS/LC-MS	141
-	IDH1^{R132H}	PTB	LC-MS	137
-	IDH1^{R132H}	PDX	MSI/LC-MS	137
-	IDH1^{R132H}	CL (HOG)	LC-MS	139
↓	IDH1^{R132H}	PDX	MRSI	146

(Lactate cont.)

↓	$IDH1^{R132H}$	CL (U87)	NMR	147
↓	$IDH1^{R132H}$	CL (NHA)	NMR	147
↓	$IDH1^{R132H}$	CL (LN18)	IC-MS	138
↑	$IDH1^{R132H}$	CL (U87)	NMR	136
-	$IDH2^{R172K}$	CL (HOG)	LC-MS	139
↓	$IDH2^{R172K}$	CL (U87)	NMR	136

Table 1.1 | *Table summarising the alterations of glycolytic and pentose phosphate pathway metabolites in IDH mutant samples w.r.t IDH WT samples. A red arrow (↑) represents a significant increase in metabolite level. A blue arrow (↓) represents a significant decrease in metabolite level. A black dash (-) represents no significant change. The overall change of a metabolite observed across studies is indicated next to the metabolite name. PTB = Patient tumour biopsy. PDX = Patient-derived (mouse) xenograft. CL = Cell line. Table adapted from Hvinden et al. with permission under the Creative Commons CC-BY 4.0 license, https://creativecommons.org/licenses/by/4.0/.*[19]

TCA cycle metabolite levels on the whole exhibit decreases or no change in levels across the metabolomic studies included in **Table 1.2**, involving 2-OG, OAA, citrate, cis-aconitate, isocitrate, succinate, fumarate, and malate; individual exceptions were OAA in IDH1 R132H U87 cells, citrate in IDH2 R172K HOG cells, malate in IDH1 R132H U251 cells, and three instances of succinate in IDH1 R132H HOG, U251, and U87 cells (**Table 1.2**). The most prominent trends are the decrease of 2-OG and malate, but the remaining metabolites exhibited studies with no changes, or opposing changes. (**Table 1.2**). The alterations of TCA cycle intermediates in mutant IDH cell samples compared to wild-type IDH cell samples are shown below (**Table 1.2**).

Alteration	IDH Mutation	Model	Analysis method	Source
2-HG ↑				
↑	$IDH1^{R132H}$	PTB	CE-MS	135
↑	$IDH1^{R132H}$	CL (U87)	NMR	136
↑	$IDH1^{R132H}$	PTB	GC-MS/LC-MS	141
↑	$IDH1^{R132H}$	PTB	LC-MS	137
↑	$IDH1^{R132H}$	PDX	MSI/LC-MS	137
↑	$IDH1^{R132H}$	CL (LN18)	IC-MS	138

(2-HG cont.)				
↑	IDH1^{R132H}	CL (HOG)	LC-MS	139
↑	IDH1^{R132H}	CL (LN18)	IC-MS	140
↑	IDH2^{R172K}	CL (HOG)	LC-MS	139
↑	IDH2^{R172K}	CL (U87)	NMR	136
2-OG ↓				
-	IDH1^{R132H}	PTB	CE-MS	135
-	IDH1^{R132H}	CL (U87)	NMR	136
-	IDH1^{R132H}	CL (U251)	LC-MS	130
↓	IDH1^{R132H}	PTB	GC-MS/LC-MS	141
↓	IDH1^{R132H}	PTB	LC-MS	137
↓	IDH1^{R132H}	PDX	MSI/LC-MS	137
↓	IDH1^{R132H}	CL (LN18)	IC-MS	138
↓	IDH1^{R132H}	CL (HOG)	LC-MS	139
↓	IDH1^{R132H}	CL (LN18)	IC-MS	140
-	IDH2^{R172K}	CL (HOG)	LC-MS	139
↓	IDH2^{R172K}	CL (U87)	NMR	136
OAA -				
-	IDH1^{R132H}	PTB	GC-MS/LC-MS	141
↑	IDH1^{R132H}	CL (U87)	NMR	135
↓	IDH2^{R172K}	CL (U87)	NMR	135
Citrate -				
-	IDH1^{R132H}	PTB	CE-MS	135
-	IDH1^{R132H}	PTB	GC-MS/LC-MS	141
-	IDH1^{R132H}	PTB	LC-MS	137
-	IDH1^{R132H}	PDX	MSI/LC-MS	137
-	IDH1^{R132H}	CL (U87)	NMR	135
-	IDH1^{R132H}	CL (LN18)	IC-MS	138
-	IDH1^{R132H}	CL (U251)	LC-MS	130
↓	IDH1^{R132H}	CL (HOG)	LC-MS	139
↑	IDH2^{R172K}	CL (HOG)	LC-MS	139
↓	IDH2^{R172K}	CL (U87)	NMR	135
Cis-aconitate -				
-	IDH1^{R132H}	PTB	CE-MS	135
↓	IDH1^{R132H}	CL (HOG)	LC-MS	139
Isocitrate -				
-	IDH1^{R132H}	PTB	CE-MS	135
↓	IDH1^{R132H}	PTB	GC-MS/LC-MS	141

Succinate -				
-	$IDH1^{R132H}$	PTB	CE-MS	135
-	$IDH1^{R132H}$	PTB	LC-MS	137
-	$IDH1^{R132H}$	PDX	MSI/LC-MS	137
↓	$IDH1^{R132H}$	CL (LN18)	IC-MS	138
↑	$IDH1^{R132H}$	CL (HOG)	LC-MS	139
↑	$IDH1^{R132H}$	CL (U251)	LC-MS	130
↑	$IDH1^{R132H}$	CL (U87)	NMR	135
↓	$IDH2^{R172K}$	CL (U87)	NMR	135
↓	$IDH2^{R172K}$	CL (HOG)	LC-MS	139
Fumarate -				
-	$IDH1^{R132H}$	PTB	CE-MS	135
-	$IDH1^{R132H}$	PTB	GC-MS/LC-MS	141
-	$IDH1^{R132H}$	CL (U87)	NMR	135
-	$IDH1^{R132H}$	CL (U251)	LC-MS	130
↓	$IDH1^{R132H}$	CL (HOG)	LC-MS	139
↓	$IDH1^{R132H}$	CL (LN18)	IC-MS	138
-	$IDH2^{R172K}$	CL (U87)	NMR	135
↓	$IDH2^{R172K}$	CL (HOG)	LC-MS	139
Malate ↓				
-	$IDH1^{R132H}$	PTB	LC-MS	137
-	$IDH1^{R132H}$	CL (U87)	NMR	135
↓	$IDH1^{R132H}$	PDX	MSI/LC-MS	137
↓	$IDH1^{R132H}$	CL (LN18)	IC-MS	138
↓	$IDH1^{R132H}$	CL (HOG)	LC-MS	139
↑	$IDH1^{R132H}$	CL (U251)	LC-MS	130
-	$IDH2^{R172K}$	CL (U87)	NMR	135
↓	$IDH2^{R172K}$	CL (HOG)	LC-MS	139

Table 1.2 | *Table summarising the alterations of TCA cycle metabolites in IDH mutant samples w.r.t IDH WT samples. A red arrow (↑) represents a significant increase in metabolite level. A blue arrow (↓) represents a significant decrease in metabolite level. A black dash (-) represents no significant change. The overall change of a metabolite observed across studies is indicated next to the metabolite name. PTB = Patient tumour biopsy. PDX = Patient derived xenograft. CL = Cell line. Table adapted from Hvinden et al. with permission under the Creative Commons CC-BY 4.0 license, https://creativecommons.org/licenses/by/4.0/.*[19]

1.5.3. Alterations in Amino Acid Metabolites in IDH Mutated Glioma

IDH mutated glioma cells are proposed to utilise glutamate as an anaplerotic substrate.[146, 169, 170, 172] GLUD1 and GLUD2 catalyse the conversion of glutamate to 2-OG and are upregulated in IDH1 R132H glioma, and IDH1 R132H glioma growth is enhanced by nerve-specific GLUD2 upregulation.[146, 169, 170, 179, 180] The observation that levels of glutamate are reported to be decreased in the majority of studies supports this proposal (**Table 1.3**).

Cytosolic branched chain amino acid transaminase 1 (BCAT1) catalyses the transamination of a branched chain amino acid (BCAA; leucine, isoleucine, valine) and 2-OG, forming the respective branched chain keto-acid (BCKA; α-ketoisocaproate, L-α-keto-β-methylvalerate, α-ketoisovalerate) and glutamate.[181, 182] BCAT1 is widely expressed in the brain because BCAAs are a major source of nitrogen in the brain.[181, 183-185] PTBs and PDXs of IDH1 R132H gliomas consistently show decreased levels of BCAT1, possibly because it would be counterproductive to utilise glutamate-derived 2-OG to produce glutamate.[146, 169, 186] In addition, 2-HG has been reported to inhibit BCAT1 and BCAT2 at high concentrations ([2-HG] > 3 mM).[187]

It is noteworthy that leucine is reported to activate GLUD1 via an allosteric binding site.[188, 189] Levels of isoleucine and valine are reported to be elevated in the majority of studies in **Table 1.3**, as expected, but leucine was found to vary between elevated, decreased, and unchanged.

Glutaminolysis, the process of energy release from glutamine degradation, is a hallmark of some cancers but a key enzyme, glutaminase (GLS, which catalyses glutamine → glutamate + NH_3), is reported to have unchanged expression in IDH1 R132H glioma patient samples.[146, 169] The fate of glutamine is of particular interest in

glioma because an essential function of astrocytes is the conversion of glutamate to glutamine for use by neurons.[190] Indeed, glutamine synthase (GS) has been reported to be exclusively expressed in astrocytes.[190] When not under depolarisation, astrocytes convert ≥ 85% of up taken glutamate to glutamine for recycling to neurons, which are unable to synthesise glutamate from sources other than glutamine.[191-193] Together, glutamine and concomitant GS activity have been reported to enable malignancy, fuel nucleotide biosynthesis, mediate the immune response, and mediate the surrounding tumour microenvironment (TME) in GBM, but the role of GS in IDH mutant glioma is not yet fully understood.[194-198] Asparagine synthetase (ASNS, which catalyses glutamine + aspartate → glutamate + asparagine) and glutamate OAA transaminase (GOT, which catalyses 2-OG + aspartate ↔ glutamate + OAA) are upregulated in IDH1 R132H glioma patient samples.[199] GLS inhibition did not substantially decrease proliferation in patient-derived cell cultures, likely because glutamate was produced from glutamine, aspartate, and potentially 2-OG instead.[199] Alternatively, ASNS may serve as an alternate route for converting glutamine to glutamate, while GOT may provide an alternative route for glutamate to 2-OG, consuming OAA produced from pyruvate by PC (**Section 1.5.2**). Levels of glutamine and OAA do not show overall trends in alterations, however aspartate is decreased and asparagine is increased in the majority of studies as would be expected from the function of ASNS (**Table 1.2**, **Table 1.3**).

Most proteinogenic amino acids (13/20) display altered levels in IDH mutant glioma samples and cell cultures across metabolomic studies included in **Table 1.3**. Of these, the levels of glutamate, aspartate, alanine, glycine, and phenylalanine (5/13) show overall decreases across metabolomic studies, and the levels of asparagine, isoleucine, lysine, methionine, threonine, tryptophan, tyrosine, and valine (8/13) are elevated overall across metabolomic studies (**Table 1.3**). Arginine, cysteine, glutamine, histidine, leucine,

proline, and serine (7/20) did not display an overall change in a particular direction in the majority of metabolomic studies (**Table 1.3**). The alterations of proteinogenic amino acids in IDH mutated cell samples compared to wild-type IDH cell samples are shown below (**Table 1.3**).

Alteration	IDH Mutation	Model	Analysis method	Source
Glutamate ↓				
-	$IDH1^{R132H}$	PTB	GC-MS/LC-MS	141
-	$IDH1^{R132H}$	PDX	MRSI	146
↓	$IDH1^{R132H}$	PTB	CE-MS	135
↓	$IDH1^{R132H}$	PTB	LC-MS	137
↓	$IDH1^{R132H}$	PTB	NMR	148
↓	$IDH1^{R132H}$	CL (U87)	NMR	136
↓	$IDH1^{R132H}$	CL (HOG)	LC-MS	139
↓	$IDH1^{R132H}$	CL (U87)	NMR	147
↓	$IDH1^{R132H}$	CL (NHA)	NMR	147
↑	$IDH1^{R132H}$	CL (U251)	LC-MS	130
-	$IDH2^{R172K}$	CL (HOG)	LC-MS	139
↑	$IDH2^{R172K}$	CL (U87)	NMR	136
Aspartate ↓				
-	$IDH1^{R132H}$	PTB	CE-MS	135
-	$IDH1^{R132H}$	PTB	GC-MS/LC-MS	141
-	$IDH1^{R132H}$	CL (NHA)	NMR	147
↓	$IDH1^{R132H}$	PTB	LC-MS	137
↓	$IDH1^{R132H}$	CL (HOG)	LC-MS	139
↓	$IDH1^{R132H}$	CL (U87)	NMR	147
↓	$IDH2^{R172K}$	CL (HOG)	LC-MS	139
Alanine ↓				
-	$IDH1^{R132H}$	PTB	CE-MS	135
↓	$IDH1^{R132H}$	PTB	GC-MS/LC-MS	141
↓	$IDH1^{R132H}$	CL (U87)	NMR	136
↑	$IDH1^{R132H}$	CL (HOG)	LC-MS	139
↓	$IDH2^{R172K}$	CL (U87)	NMR	136
↑	$IDH2^{R172K}$	CL (HOG)	LC-MS	139
Arginine -				
-	$IDH1^{R132H}$	PTB	CE-MS	135
↑	$IDH1^{R132H}$	CL (HOG)	LC-MS	139

(Arginine cont.)				
↓	IDH2^{R172K}	CL (HOG)	LC-MS	139
Asparagine ↑				
↓	IDH1^{R132H}	PTB	CE-MS	135
↑	IDH1^{R132H}	PTB	GC-MS/LC-MS	141
↑	IDH1^{R132H}	CL (HOG)	LC-MS	139
↑	IDH1^{R132H}	CL (LN18)	LC-MS	140
↑	IDH2^{R172K}	CL (HOG)	LC-MS	139
Cysteine -				
-	IDH1^{R132H}	PTB	CE-MS	135
-	IDH1^{R132H}	CL (HOG)	LC-MS	139
↑	IDH1^{R132H}	CL (LN18)	LC-MS	140
-	IDH2^{R172K}	CL (HOG)	LC-MS	139
Glutamine -				
-	IDH1^{R132H}	PTB	GC-MS/LC-MS	141
-	IDH1^{R132H}	PTB	LC-MS	137
-	IDH1^{R132H}	CL (NHA)	NMR	147
↓	IDH1^{R132H}	PTB	CE-MS	135
↓	IDH1^{R132H}	CL (U87)	NMR	147
↑	IDH1^{R132H}	PDX	MRSI	141
↑	IDH1^{R132H}	CL (HOG)	LC-MS	139
↑	IDH2^{R172K}	CL (HOG)	LC-MS	139
Glycine ↓				
-	IDH1^{R132H}	PTB	CE-MS	135
↓	IDH1^{R132H}	PTB	GC-MS/LC-MS	141
↓	IDH1^{R132H}	CL (U87)	NMR	136
↑	IDH1^{R132H}	CL (HOG)	LC-MS	139
↓	IDH2^{R172K}	CL (U87)	NMR	136
↑	IDH2^{R172K}	CL (HOG)	LC-MS	139
Histidine -				
-	IDH1^{R132H}	PTB	CE-MS	135
↑	IDH1^{R132H}	CL (HOG)	LC-MS	139
↑	IDH1^{R132H}	CL (LN18)	LC-MS	140
-	IDH2^{R172K}	CL (HOG)	LC-MS	139
Isoleucine ↑				
-	IDH1^{R132H}	PTB	CE-MS	135
↓	IDH1^{R132H}	CL (U87)	NMR	136
↑	IDH1^{R132H}	CL (HOG)	LC-MS	139
↑	IDH1^{R132H}	CL (LN18)	LC-MS	140

(Isoleucine cont.)				
↑	IDH2^{R172K}	CL (HOG)	LC-MS	139
↑	IDH2^{R172K}	CL (U87)	NMR	136
Leucine -				
-	IDH1^{R132H}	PTB	CE-MS	135
↓	IDH1^{R132H}	CL (U87)	NMR	136
↑	IDH1^{R132H}	CL (HOG)	LC-MS	139
↓	IDH2^{R172K}	CL (U87)	NMR	136
↑	IDH2^{R172K}	CL (HOG)	LC-MS	139
Lysine ↑				
-	IDH1^{R132H}	PTB	CE-MS	135
↑	IDH1^{R132H}	CL (HOG)	LC-MS	139
↑	IDH2^{R172K}	CL (HOG)	LC-MS	139
Methionine ↑				
-	IDH1^{R132H}	PTB	CE-MS	135
↑	IDH1^{R132H}	CL (HOG)	LC-MS	139
↑	IDH1^{R132H}	CL (LN18)	LC-MS	140
↑	IDH2^{R172K}	CL (HOG)	LC-MS	139
Phenylalanine ↓				
↓	IDH1^{R132H}	PTB	CE-MS	135
(Phenylalanine cont.)				
↓	IDH1^{R132H}	CL (U87)	NMR	136
↑	IDH1^{R132H}	CL (HOG)	LC-MS	139
↓	IDH2^{R172K}	CL (U87)	NMR	136
↑	IDH2^{R172K}	CL (HOG)	LC-MS	139
Proline -				
-	IDH1^{R132H}	PTB	CE-MS	135
-	IDH1^{R132H}	CL (HOG)	LC-MS	139
↓	IDH2^{R172K}	CL (HOG)	LC-MS	139
Serine -				
↓	IDH1^{R132H}	PTB	GC-MS/LC-MS	141
↑	IDH1^{R132H}	CL (HOG)	LC-MS	139
-	IDH2^{R172K}	CL (HOG)	LC-MS	139
Threonine ↑				
-	IDH1^{R132H}	PTB	CE-MS	135
↓	IDH1^{R132H}	CL (U87)	NMR	136
↑	IDH1^{R132H}	CL (HOG)	LC-MS	139
↑	IDH2^{R172K}	CL (U87)	NMR	136
↑	IDH2^{R172K}	CL (HOG)	LC-MS	139

Tryptophan ↑				
-	IDH1^{R132H}	PTB	CE-MS	[135]
↑	IDH1^{R132H}	CL (HOG)	LC-MS	[139]
↑	IDH2^{R172K}	CL (HOG)	LC-MS	[139]
Tyrosine ↑				
-	IDH1^{R132H}	PTB	CE-MS	[135]
↑	IDH1^{R132H}	CL (HOG)	LC-MS	[139]
↑	IDH2^{R172K}	CL (HOG)	LC-MS	[139]
Valine ↑				
-	IDH1^{R132H}	PTB	CE-MS	[135]
↓	IDH1^{R132H}	CL (U87)	NMR	[136]
↑	IDH1^{R132H}	CL (HOG)	LC-MS	[139]
↑	IDH1^{R132H}	CL (U87)	NMR	[147]
↑	IDH1^{R132H}	CL (NHA)	NMR	[147]
↑	IDH2^{R172K}	CL (U87)	NMR	[136]
↑	IDH2^{R172K}	CL (HOG)	LC-MS	[139]

Table 1.3 | *Table summarising the alterations of amino acid metabolites in IDH mutant samples w.r.t IDH WT samples. A red arrow (↑) represents a significant increase in metabolite level. A blue arrow (↓) represents a significant decrease in metabolite level. A black dash (-) represents no significant change. The overall change of a metabolite observed across studies is indicated next to the metabolite name. PTB = Patient tumour biopsy. PDX = Patient derived xenograft. CL = Cell line. Table adapted from Hvinden et al. with permission under the Creative Commons CC-BY 4.0 license, https://creativecommons.org/licenses/by/4.0/.*[19]

N-Acetylated amino acids (NAAAs) have been found to be consistently decreased in glioma patients by magnetic resonance spectroscopy (MRS), for both IDH mutant and IDH WT glioma.[149, 200, 201] Comparing IDH mutant and IDH WT gliomas, studies using PTBs, PDXs, and cell lines found *N*-acetylaspartylglutamate (NAAG), *N*-acetylaspartate (NAAsp), *N*-acetylalanine (NAAla), *N*-acetylglutamate (NAGlu), *N*-acetylhistidine (NAHis), *N*-acetylserine (NASer), *N*-acetylthreonine (NAThr) to be decreased in IDH mutated samples, and *N*-acetylglutamine (NAGln), *N*-acetylglycine (NAGly), *N*-acetylmethionine (NAMet), exhibit no change in the majority of studies (**Table 1.4**). Total NAAAs in IDH mutant gliomas showed no change or elevated levels compared to IDH WT gliomas (**Table 1.4**). The alterations in NAAAs are show below (**Table 1.4**).

Alteration	IDH Mutation	Model	Analysis method	Source
Total NAAA -				
	$IDH1^{R132H}$			
↑	$IDH2^{R172K}$	PTB	MRS	149
-	$IDH1^{R132H}$	PDX	MRS	146
NAAG ↓				
↑	$IDH1^{R132H}$	PTB	LC-MS	137
-	$IDH1^{R132H}$	PDX	MSI	137
↓	$IDH1^{R132H}$	CL (HOG)	LC-MS	139
↓	$IDH1^{R132H}$	CL (LN18)	IC-MS	138
↓	$IDH1^{R132H}$	CL (LN18)	IC-MS	140
↓	$IDH2^{R172K}$	CL (HOG)	LC-MS	139
NAAsp ↓				
↓	$IDH1^{R132H}$	PTB	CE-MS	135
↓	$IDH1^{R132H}$	PTB	LC-MS	137
-	$IDH1^{R132H}$	PDX	MSI	137
↓	$IDH1^{R132H}$	CL (HOG)	LC-MS	139
↓	$IDH2^{R172K}$	CL (HOG)	LC-MS	139
NAAla ↓				
↓	$IDH1^{R132H}$	CL (HOG)	LC-MS	139
↓	$IDH2^{R172K}$	CL (HOG)	LC-MS	139
NAGln -				
↓	$IDH1^{R132H}$	CL (HOG)	LC-MS	139
-	$IDH2^{R172K}$	CL (HOG)	LC-MS	139
NAGlu ↓				
↓	$IDH1^{R132H}$	PTB	CE-MS	135
↓	$IDH1^{R132H}$	CL (HOG)	LC-MS	139
↓	$IDH2^{R172K}$	CL (HOG)	LC-MS	139
NAGly -				
↑	$IDH1^{R132H}$	CL (U87)	NMR	136
↓	$IDH2^{R172K}$	CL (U87)	NMR	136
NAHis ↓				
↓	$IDH1^{R132H}$	PTB	CE-MS	135
NAMet -				
↓	$IDH1^{R132H}$	CL (HOG)	LC-MS	139

(NAMet cont.)				
↑	IDH1^{R132H}	CL (LN18)	IC-MS	[140]
-	IDH2^{R172K}	CL (HOG)	LC-MS	[139]
NASer ↓				
↓	IDH1^{R132H}	CL (HOG)	LC-MS	[139]
↓	IDH2^{R172K}	CL (HOG)	LC-MS	[139]
NAThr ↓				
↓	IDH1^{R132H}	CL (HOG)	LC-MS	[139]
↓	IDH2^{R172K}	CL (HOG)	LC-MS	[139]

Table 1.4 *| Table summarising the alterations of N-acetylated amino acid metabolites in IDH mutant samples w.r.t IDH WT samples. A red arrow (↑) represents a significant increase in metabolite level. A blue arrow (↓) represents a significant decrease in metabolite level. A black dash (-) represents no significant change. The overall change of a metabolite observed across studies is indicated next to the metabolite name. PTB = Patient tumour biopsy. PDX = Patient derived xenograft. CL = Cell line. Table adapted from Hvinden et al. with permission under the Creative Commons CC-BY 4.0 license, https://creativecommons.org/licenses/by/4.0/.*[19]

1.5.4. Alterations in Redox and Energy Metabolites in IDH Mutated Glioma

IDH1 WT, IDH2 WT, malic enzyme 1 (ME1), glucose-6-phosphate dehydrogenase (G6PD), and 6-phosphogluconate dehydrogenase (6PGD) are the primary sources of NADPH in cells (**Figure 1.1**), with IDH1 WT being of particular importance in the brain.[145, 202, 203] As mentioned in **Section 1.5**, IDH1 WT is reported to produce ~65% of the total NADPH in glioblastoma tissue, with R132H substitution resulting in a ~40% decrease in NADPH production.[145] NADPH is necessary to produce and regenerate antioxidants, such as glutathione, protecting against ROS driven dysfunction in the cytosol (IDH1 WT) and mitochondria (IDH2 WT).[142, 204-208] NADPH levels are proposed to be partially, but not completely, preserved by increased activity through the pentose phosphate pathway (G6PD, 6PGD), and NAD^+ kinase ($NAD^+ + ATP \rightarrow NADP^+ + ADP$).[129, 130, 209] By contrast, a recent study found the $NADP^+$/NADPH ratio to not be significantly changed in IDH1 R132H glioma cells.[140] Furthermore, NADH in the mitochondria may be converted to NADPH via nicotinamide

nucleotide transhydrogenase (NNT, NADH + $NADP^+$ → NAD^+ + NADPH). IDH1 mutant glioma cell lines have exhibited upregulation of enzymes involved in glutathione biosynthesis, including nuclear factor erythroid 2-related factor 2 (Nrf2) and cystathionine-γ-lyase (CSE).[210, 211] In addition, IDH1 mutant glioma cell lines have exhibited ameliorated redox homeostasis, represented by both $NADP^+$/NADPH and glutathione GSSG/GSH ratios, upon addition of extracellular glutamate.[212] An increased consumption of cysteine for glutathione synthesis would be supported by the observed decrease in levels of cystathionine, however decreased levels of glutathione, both GSSG and GSH, in the majority of studies indicate IDH mutant cells struggle to meet glutathione production demands (**Table 1.5**). Considering cysteine levels appear unchanged, the variation in reports of $NADP^+$/NADPH ratios, and that extracellular glutamate ameliorates redox homeostasis, decreased levels of glutamate, and potentially glycine, may primarily form the bottleneck that hinders the synthesis of sufficient glutathione in IDH mutant gliomas (**Table 1.3**, **Table 1.5**).[140, 212]

Decreased levels of cystathionine and glutathione, both reduced (GSH) and oxidised (GSSG), have been detected in most of the studies in **Table 1.5**. NADH has been measured as elevated, and Creatine, ATP, ADP, AMP, NAD^+, $NADP^+$, and NADPH are reported as unchanged in the majority of studies in **Table 1.5**. The alterations in redox and energy metabolites in IDH mutated cell samples compared to wild-type IDH cell samples are shown below (**Table 1.5**).

Alteration	IDH Mutation	Model	Analysis method	Source
Glutathione (GSSG / Oxidised) ↓				
↓	$IDH1^{R132H}$	CL (HOG)	LC-MS	[139]
↓	$IDH2^{R172K}$	CL (HOG)	LC-MS	[139]
Glutathione (GSH / Reduced) ↓				
-	$IDH1^{R132H}$	PTB	LC-MS	[137]

(Glutathione (GSH / Reduced) cont.)				
-	IDH1^{R132H}	PDX	MSI/LC-MS	137
-	IDH1^{R132H}	CL (NHA)	NMR	147
↓	IDH1^{R132H}	CL (HOG)	LC-MS	139
↓	IDH1^{R132H}	CL (U87)	NMR	147
↓	IDH1^{R132H}	CL (LN18)	IC-MS	138
↑	IDH1^{R132H}	CL (U87)	NMR	136
↓	IDH2^{R172K}	CL (U87)	NMR	136
↓	IDH2^{R172K}	CL (HOG)	LC-MS	139
Cystathionine ↓				
↓	IDH1^{R132H}	PDX	MSI/LC-MS	137
Creatine -				
-	IDH1^{R132H}	CL (NHA)	NMR	147
↓	IDH1^{R132H}	CL (U87)	NMR	136
↓	IDH1^{R132H}	CL (U87)	NMR	147
-	IDH2^{R172K}	CL (U87)	NMR	136
ATP				
-	IDH1^{R132H}	PTB	LC-MS	137
-	IDH1^{R132H}	CL (LN18)	IC-MS	138
↓	IDH1^{R132H}	PDX	MSI/LC-MS	137
ADP -				
-	IDH1^{R132H}	PDX	MSI/LC-MS	137
↑	IDH1^{R132H}	CL (LN18)	IC-MS	138
AMP -				
-	IDH1^{R132H}	PTB	LC-MS	137
-	IDH1^{R132H}	PDX	MSI/LC-MS	137
-	IDH1^{R132H}	CL (LN18)	IC-MS	138
NAD$^+$ -				
↓	IDH1^{R132H}	CL (U87)	NMR	136
↑	IDH2^{R172K}	CL (U87)	NMR	136
NADH ↑				
↑	IDH1^{R132H}	CL (LN18)	IC-MS	138
NADPH -				
-	IDH1^{R132H}	CL (LN18)	LC-MS	140
NADP$^+$ -				
-	IDH1^{R132H}	CL (LN18)	LC-MS	140

Table 1.5 | *Table summarising the alterations of redox and energy metabolites in IDH mutant samples w.r.t IDH WT samples. A red arrow (↑) represents a significant increase in metabolite*

level. A blue arrow (↓) represents a significant decrease in metabolite level. A black dash (-) represents no significant change. The overall change of a metabolite observed across studies is indicated next to the metabolite name. PTB = Patient tumour biopsy. PDX = Patient derived xenograft. CL = Cell line. Table adapted with permission from Hvinden et al. under the Creative Commons CC-BY 4.0 license, https://creativecommons.org/licenses/by/4.0/.[19]

1.5.5. Alterations in Lipid Metabolism in IDH Mutated Glioma

Acetyl-CoA for fatty acid synthesis can be supplied by IDH1 WT and IDH2 WT by the reductive carboxylation of 2-OG to isocitrate, followed by the conversion of isocitrate to citrate via cis-aconitate, and ultimately the conversion of citrate to acetyl-CoA and OAA (**Figure 1.1**).[32, 213, 214] NADPH is also required for fatty acid synthesis and unsaturated fatty acid metabolism.[26, 27, 215] Mutations in either isoform of IDH hinder NADPH production, prevent reductive carboxylation of 2-OG, and are proposed to sensitise cells to ferroptosis (iron dependent cell-death mediated through lipid peroxide accumulation).[216-219] The treatment of cells with exogenous 2-HG also promotes the accumulation of lipid peroxides.[218, 219] As mentioned in **Section 1.2.1**, IDH1 WT and IDH2 WT have been consistently linked to lipid metabolism, and their dysfunction has been consistently implicated in lipid dysregulation.[30, 31, 220-223]

Phosphocholine and phosphoethanolamine levels have been reported to be decreased overall across studies in **Table 1.6**, glycerophosphocholine and phosphatidylinositol have been reported as increased overall across studies in **Table 1.6**, and glycerophosphoethanolamine has been reported to have no change in all studies (**Table 1.6**). The alterations in phosphorylated lipid metabolites in IDH mutant cell samples compared to wild-type IDH cell samples are shown below (**Table 1.6**).

Alteration	IDH Mutation	Model	Analysis method	Source
Phosphocholine ↓				
↑	IDH1^{R132H}	PTB	1H NMR	148
-	IDH1^{R132H}	PTB	31P NMR	150
-	IDH1^{R132H}	PDX	31P MRI	150
↑	IDH1^{R132H}	CL (U251)	31P NMR	150
↓	IDH1^{R132H}	CL (HOG)	LC-MS	139
↓	IDH1^{R132H}	CL (U87)	1H NMR	147
↓	IDH1^{R132H}	CL (NHA)	1H NMR	147
↓	IDH2^{R172K}	CL (HOG)	LC-MS	139
Glycerophosphocholine ↑				
↑	IDH1^{R132H}	PTB	1H NMR	148
↑	IDH1^{R132H}	PTB	31P NMR	150
↑	IDH1^{R132H}	PDX	31P MRI	150
↑	IDH1^{R132H}	CL (U251)	31P NMR	150
↑	IDH1^{R132H}	CL (HOG)	LC-MS	139
↑	IDH1^{R132H}	CL (U87)	1H NMR	147
-	IDH1^{R132H}	CL (NHA)	1H NMR	147
↓	IDH2^{R172K}	CL (HOG)	LC-MS	139
Phosphoethanolamine ↓				
-	IDH1^{R132H}	PTB	1H MRI	151
↓	IDH1^{R132H}	PTB	31P NMR	150
↓	IDH1^{R132H}	PDX	31P MRI	150
↓	IDH1^{R132H}	CL (U251)	31P NMR	150
Glycerophospho-ethanolamine -				
-	IDH1^{R132H}	PTB	31P NMR	150
-	IDH1^{R132H}	PDX	31P MRI	150
-	IDH1^{R132H}	CL (U251)	31P NMR	150
Phosphatidylinositol ↑				
↑	IDH1^{R132H}	PDX	MSI	137

Table 1.6 | *Table summarising the alterations of phosphorylated lipid metabolites in IDH mutant samples w.r.t IDH WT samples. A red arrow (↑) represents a significant increase in metabolite level. A blue arrow (↓) represents a significant decrease in metabolite level. A black dash (-) represents no significant change. The overall change of a metabolite observed across studies is indicated next to the metabolite name. PTB = Patient tumour biopsy. PDX = Patient derived xenograft. CL = Cell line. Table adapted with permission from Hvinden et al. under the Creative Commons CC-BY 4.0 license, https://creativecommons.org/licenses/by/4.0/.*[19]

1.5.6. Alterations in the Levels of β-Citryl-Glutamate in IDH Mutated Glioma

β-Citryl-glutamate (βCG) is a small-molecule metabolite that was first discovered in the brains of newborn rats.[224] βCG consists of one glutamate molecule *N*-linked to one citric acid molecule at C-β (**Figure 1.11**).[224] βCG is a metal-chelator and is reported to chelate iron to activate aconitase.[225] Studies on mice have shown that βCG is synthesised by RIMKLB, an isoform of RIMKLA which synthesises the most abundant peptide neurotransmitter in the brain NAAG.[226] βCG is hydrolysed by glutamate carboxypeptidase 3 (GCP3), an isoform of GCP2, also known as prostate specific membrane antigen (PSMA).[226-228] Similar to NAAG, βCG is found predominantly in the brain.[224, 229] βCG is also found in the testes and, at a lower level, in the eyes.[224, 230] βCG appears at high concentrations during neuronal growth and differentiation, then decreases during neuronal maturation, controlled by the expression and activity of RIMKLB and GCP3.[224, 225, 231] βCG is proposed to play a regulatory role during the development of neurons.[224, 225, 231]

Recent work by Dr John Walsby-Tickle (Department of Chemistry, University of Oxford) and Dr Ingvild Hvinden (Department of Chemistry, University of Oxford) identified levels of βCG to be consistently decreased in IDH R132H glioma cell lines (LN18), and to be increased after the inhibition of IDH1 R132H.[138, 140] More widely, levels of βCG have been reported as altered in both directions in a number of studies. βCG has been reported to decrease in glioma cells (U87MG) after forming 3D multicellular tumour spheroids (MCTSs) from 2D cells, after the differentiation of muscle cells into myotubes, in the brain cortex during sleep, and in hypoxic-ischemic encephalopathic (HIE) brains.[232-235] βCG levels are reported to increase in humans after chronic resistance exercise training, in the testes upon the appearance of spermatids, in

the serum of older humans (mean age = 77.8 years) compared to younger humans (mean age = 25.8 years), and in cells with the 1q25 risk allele for coronary heart disease (CHD), type 2 diabetes, and downregulation of GS.[236-239] Furthermore, βCG levels are altered along with other 4-hydroxybutyric acid (GHB) metabolites after exogenous GHB exposure, leading to its investigation as a biomarker for GHB exposure.[240] RIMKLB mutation leads to infertility in male mice and its expression increases by 43% after acute resistance exercise.[236, 241] Despite evidence of alterations in βCG due to a multitude of conditions such as tissue differentiation, exercise, age, and cancer, the physiological role of βCG is not yet understood.

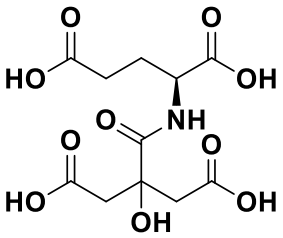

β-citryl-glutamate

Figure 1.11 *|The chemical structure of βCG.*

1.6. The Utilisation of IDH-Mutation Status for Therapeutic Benefit

1.6.1. Peptide Vaccines Targeting IDH Mutations

Glioma cells have been reported by researchers at the University Hospital Heidelberg to present tumour-specific neoantigens corresponding to IDH1 R132H on their cell surface via the major-histocompatibility complex (MHC).[242, 243] 10-mer and 15-mer peptides were therefore tested therapeutically as potential cancer-vaccines against IDH1 R132H mutant glioma in mouse models. A 15-mer peptide elicited an IDH1 R132H tumour cell-specific $CD4^+$ T cell response which inhibited tumour growth and achieved the

elimination of a subset of tumours in the treated group.[243] A Phase I clinical trial was subsequently conducted utilising standard of care glioma therapy (radiotherapy, temozolomide, or both) in addition to eight vaccinations. Over the 23-week course of treatment, ~93% of patients developed a vaccine-induced immune response with evidence of apparent infiltration into the lesions by immune cells and no vaccine-related adverse events higher than grade 1. 84% of patients survived three years or longer. By contrast, a phase II clinical trial conducted by researchers at Duke University in combination with standard of care therapy exhibited a much lower response rate of ~43% and did not disclose survival data.[244] Therefore, while early results may appear promising, contrasting phase II results suggest that the high costs associated with the development and delivery of peptide vaccines may not ultimately be economical in comparison with potentially efficacious small-molecule therapies. Nonetheless, a follow-on phase I clinical trial in combination with a checkpoint inhibitor by researchers at the University Hospital Heidelberg, is ongoing.[245]

1.6.2. Small-Molecule Inhibitors Targeting IDH Mutations

Small-molecule inhibitors of mutant IDH isoforms have been classed by Lin et al. according to their mechanisms of action.[246] Class-I inhibitors bind the active site, Class-II inhibitors bind in an allosteric pocket on mutant IDH1 (or IDH2), and Class-III inhibitors bind allosterically to both IDH1 and IDH2 mutant isoforms (**Figure 1.12**).[246] Most clinically tested small-molecule inhibitors fall into the class II category, in which there is a substantial degree of structural variability (**Figure 1.12**).

Studies of class II inhibitors with IDH1 demonstrate the ability of inhibitors to lock IDH1 into an open-inactive conformation, and to bind both variant and wild-type isoforms.[125, 247-249] The affinity of IDH1 WT for the isocitrate-magnesium complex substrate is higher than the affinity of IDH1 R132H for 2-OG and magnesium, which bind separately and

more weakly than the isocitrate-magnesium complex.[125] Mutant IDH1 and IDH2 selective inhibitors indirectly compete with magnesium, mediated via the allosteric binding pocket, and are able to outcompete magnesium binding to mutant IDH isoforms.[125] The isocitrate-magnesium complex substrate binds wild-type IDH1 and IDH2 more tightly, and with higher affinity, limiting the efficacy of inhibitor binding at the allosteric binding pocket.[125]

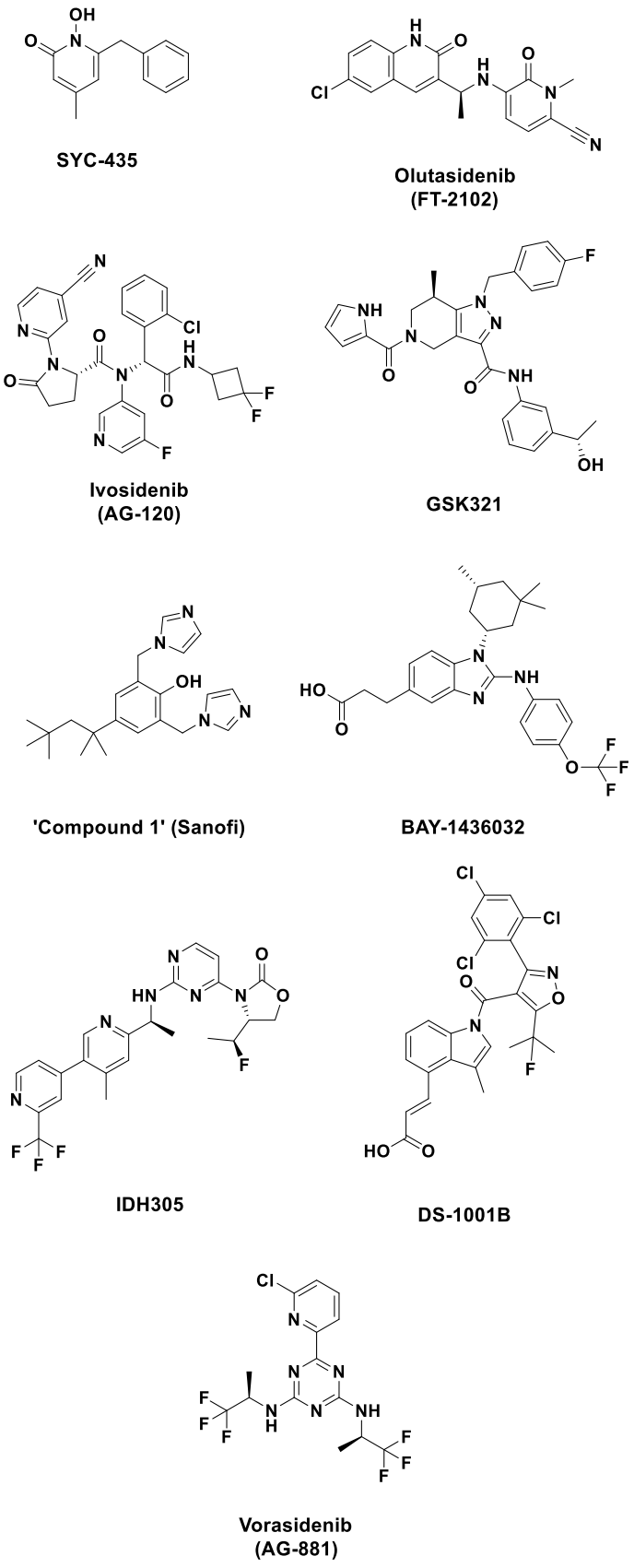

Figure 1.12 *| Structures of selected IDH1 inhibitors. Class I: SYC-435. Class II: Olutasidenib, Ivosidenib, GSK321, 'Compound 1', BAY-1436032, IDH305, DS-1001B. Class III: Vorasidenib.*

Until recently there were no approved IDH inhibitors for use in glioma. The initial development of IDH inhibitors focused on AML, reflecting in part the absence of blood-brain barrier constraints.[250, 251] In August 2024, vorasidenib (Class III) was approved 'for adult and pediatric patients 12 years and older with Grade 2 astrocytoma or oligodendroglioma with a susceptible IDH1 or IDH2 mutation, following surgery including biopsy, sub-total resection, or gross total resection'; daily treatment with vorasidenib (40 mg) led to a longer median progression-free survival of 27.7 months compared to 11.1 months under placebo treatment.[252-254] For AML containing mutations in IDH1 and IDH2, there are three clinically approved small-molecule inhibitors: olutasidenib (FT-2102, IDH1 specific), ivosidenib (AG-120, IDH1 specific), and enasidenib (AG-221, IDH2 specific).[251, 255-257] There are also a number of pre-clinical inhibitors published, which are discussed in greater detail later in **Chapter 2**.

Clinically approved inhibitors have demonstrated efficacy against initial mutations in IDH1 and IDH2, however several important limitations restrict their overall therapeutic potential. Although IDH variant inhibitors suppress the production of 2-HG, they may fail to fully reverse epigenetic changes associated with the initial stages of oncogenesis in the presence of variant IDH isoforms.[258] The persistence of certain chromatin states established during tumour initiation may not be fully reversible through inhibition of 2-HG production alone, and may necessitate combinatorial strategies involving direct targeting of chromatin-modifying enzymes.[259] Additionally, IDH variant inhibitors may inadvertently contribute to resistance against DNA-damaging therapies, including radiotherapy and alkylating chemotherapy, although the mechanistic basis for this phenomenon remains incompletely understood.[258, 259] IDH variant inhibitors have also demonstrated relatively limited efficacy in more advanced, contrast-enhancing, gliomas,

where tumours may have acquired genetic and epigenetic alterations that render them less dependent on IDH variant activity. [259, 260]

Finally, patient responses to IDH inhibitors are variable, highlighting a need for improved predictive biomarkers to identify the most likely beneficiaries.[260] In particular relapse is frequently defined by additional resistance-associated mutations which can restore 2-HG production and render first-generation inhibitors ineffective. [260-264] Therefore, there is a need for next-generation treatment strategies tailored to address these limitations in gliomas containing IDH mutations.

1.6.3. Resistance to IDH Inhibitor Treatments of IDH Mutated Cancer

Documented cases of resistance are comprised of isoform switching, transallelic mutations, and second-site mutations, in each case restoring the production of 2-HG in the cell.[261-264]

Isoform switching follows treatment with a selective inhibitor for mutated IDH1 or IDH2.[261] A mutation occurs in the uninhibited, previously wild-type, isoform of IDH and causes novel homo- and heterodimers to be expressed. [261] Three AML patients treated with ivosidenib experienced relapse after initially exhibiting the IDH1 R132C mutation. The patients acquired IDH2 R140Q mutations in two cases, and IDH2 R172K in the third.[261] Similarly, a case of IDH2 R140Q AML responded well to enasidenib in one patient until they acquired an IDH1 R132C mutation.[261]

Transallelic mutations occur on the opposing allele to the original mutation within the same gene.[264] Typically, the substituted residue is located at the allosteric binding site of the inhibitor, the dimer-interface, and restores activity in the presence of the inhibitor.[264] IDH1 R132C AML patients treated with ivosidenib have been reported to gain D279N or S280F substitutions, and IDH2 R140Q AML patients treated with enasidenib have

been reported to gain Q316E or I319M (homologous to S280F) substitutions.[262-264] After acquiring a resistance enabling mutation, 2-HG levels rose to previously observed levels.[264] Some transallelic mutations have only been observed once to date, that is R119P, G131A, G289D, and H315D.[262]

Second-site mutations are similar to transallelic mutations, because they restore activity in the presence of an inhibitor, but differ because the second mutation occurs on the same allele as the original mutation.[262-264] The most common second-site mutation entails the S280F substitution in IDH1, observed as IDH1 R132C S280F.[262-264] This substitution interferes with the activity of ivosidenib, raising the IC_{50} value from 19 nM (IDH1 R312C), to >100 μM.(IDH1 R132C S280F).[262-264]

The dimer-interface mutations restore activity by preventing the efficacious binding of inhibitors. AGI-14686 (an ivosidenib analogue) was modelled into IDH1 R132H, before the S280F substitution was introduced. The novel phenylalanine side chain, F280, was found to sterically clash with the bound inhibitor.[246] Further modelling with vorasidenib also exhibited clashes with F280, and suggested ivosidenib would previously have been able to H-bond with S280. Thus, the S280F substitution additionally loses this favourable interaction.[263] As vorasidenib nears approval, it is possible that it will already be susceptible to known and new resistance mechanisms.[253] Nonetheless, the clinical adoptions of IDH1 and IDH2 mutant inhibitors demonstrate that altered metabolism is a robust hallmark of cancer and can be targeted for therapeutic gain.[1, 265]

1.6.4. Therapeutic Avenues Targeting Metabolic Vulnerabilities in IDH Mutated Cancer

Small-molecule inhibitors of mutant IDH isoforms are frequently reported to reduce levels of 2-HG *in vivo*; however, decreased 2-HG does not always correlate with slowed

growth in glioma and chondrosarcoma cell lines.[266, 267] In addition, selective monotherapies such as ivosidenib and enasidenib are susceptible to resistance via point mutations (**Section 1.6.3**). However, regardless of the specific point-mutation, the common effect of 2-HG elevation may reveal novel therapeutic avenues.[268]

Inhibitors of glutaminase (GLS) have been reported to reduce the viability of IDH1 mutant cell lines compared to IDH1 WT.[269-272] However, patient-derived glioma cells exhibit cell-line dependent effects.[199] A clinical trial of a GLS inhibitor, telaglenastat (CB-839), in conjunction with radiotherapy and temozolomide for treatment of astrocytoma with IDH1 or IDH2 mutations is ongoing.[273] A separate study reported that telaglenastat was not cytotoxic and had a tumour stabilising effect.[274] Ultimately, glutaminase inhibitors may be most effective in patients for whom glutamine-starvation is a confirmed tumour vulnerability.[275, 276]

Glioma cells with IDH mutations are reported to express elevated levels of GLUD2, likely to fuel glutamate anaplerosis, as previously discussed in **Section 1.5.3**.[146, 169, 170, 179, 180] Chloroquine, amongst known functions as an antimalarial and autophagy inhibitor, is also a nerve-specific GLUD2 inhibitor.[277-279] Preliminary studies of chloroquine applied to IDH1 WT stem-like glioma cells increased cell death, but were inconclusive as to whether the effects of chloroquine were GLUD2 mediated or autophagy inhibition was induced.[280]

1.7. Aims of the Work Described in this Thesis

There is currently no cure for glioma. Challenges facing vorasidenib, and the development of novel mutant IDH1 and IDH2 inhibitors for treatment of gliomas, include resistance as well as a lack of understanding behind the biological functions of IDH1 and IDH2 mutations. The project aims were fourfold:

- To investigate the metabolic effect of wild-type IDH1 and IDH2 as therapeutic targets in glioma cells with mutant IDH1-induced metabolic dysfunction.
- To differentiate the effects of the dominant negative phenotype, and the gain-of-function, in glioma cells bearing IDH1 mutations.
- To investigate the metabolic link between IDH1 mutations and an oncogenic driver responsible for the tissue-specific prevalence of IDH1 mutations in glioma.
- To identify novel therapeutic avenues enabled by metabolic dysfunction for the treatment of IDH mutant gliomas.

The coronavirus disease 2019 (COVID-19) pandemic emerged in 2020 shortly before the commencement of the work in this thesis. In addition to the work conducted on glioma, work was initially conducted on COVID-19. Prior to the invention of vaccines against severe acute respiratory syndrome coronavirus 2 (SARS-CoV-2), the Schofield Group focussed on developing a potential novel small-molecule therapeutic. The project aim was singular:

- To develop an inhibitor scaffold with the potential to manifest selectivity and potency against SARS-CoV-2 main protease (M^{pro}).

2. Identification and Synthesis of Small-Molecule Tools to Investigate the Effects of Wild-Type IDH1 and IDH2 in Gliomas Containing Mutant IDH1

2.1. Introduction

Most small-molecule therapeutic interventions targeting cancers containing IDH mutations have focussed on inhibiting the resultant IDH variant enzyme isoforms (**Chapter 1**, **Section 1.6.2**). There are currently two clinically approved small molecules selective for mutations in IDH1, olutasidenib (FT-2102) and ivosidenib (AG-120).[251, 255, 281, 282] There is one clinically approved small-molecule for mutations in IDH2, enasidenib (AG-221).[256, 257] Vorasidenib (AG-881) is a dual IDH1/2 variant inhibitor, recently approved for use in treatment of patients with grade 2 glioma with IDH1/2 mutations.[252-254]

The clinical outcomes of the variant IDH inhibitors reveal extension of lifespan, however, there is documented evidence of relapses caused by acquired resistance.[283-285] This resistance can be mediated by acquired mutations in the remaining wild-type (WT) IDH isoform or additional substitutions in the already mutated variants, such as S280F in IDH1, and I319M in IDH2 (**Chapter 1**, **Section 1.6.3**).[261-264] Mutations arise during treatment and convey resistance to currently approved IDH selective treatments ivosidenib (AG-120) and enasidenib (AG-221), restoring the production of 2-hydroxyglutarate (2-HG).[261, 283]

Considering IDH variants are both gain-of-function and dominant-negative for IDH WT, it is crucial to understand the physiologically relevant roles of the WT IDH reaction in

the context of mutant IDH glioma. Indeed, it is possible that the effect of some IDH1/2 variant inhibitors may be mediated by WT IDH inhibition or inhibition of heterodimeric WT/variant complexes. This chapter describes synthetic chemistry and biochemical studies that were utilised to prepare small-molecules to investigate the effects of the inhibition of WT IDH1 and IDH2 reactions, including in gliomas containing IDH mutations.

2.2. Wild-type IDH1 and IDH2 as Drug Targets

A strategy to inhibit the cellular activities of IDH1 WT or IDH2 WT in the presence of IDH1 R132H was devised. IDH1 R132H was chosen for study as it is the most common IDH mutation in grade 2/3 gliomas and secondary GBM (85 – 90%).[62, 63, 106, 119] IDH WT activity is reported to be responsible for 65% of NADPH production capacity in human glioblastoma, which is reduced to 27% in the presence of an IDH mutation.[86, 286] IDH1 WT is reported to contribute to the reduction of glutathione in the cytosol and to protect cells against γ-ray irradiation, UVB irradiation, and singlet oxygen induced apoptosis.[287-289] IDH2 WT has been considered to be the primary source of NADPH in the mitochondria.[142, 204] siRNA knockdown of IDH2 WT is reported to sensitise gliomas and HeLa cells to γ-ray irradiation, and HeLa cells to heat shock, high-glucose, doxorubicin, actinomycin D, etoposide, and tumor necrosis factor-α (TNF-α) induced apoptosis.[204, 287, 290-293] IDH1 and IDH2 mutations appear to be mutually exclusive, with rare exceptions.[19, 68, 80, 85, 86, 294, 295] Inhibiting the corresponding IDH WT may also determine if synthetic lethality can be triggered in cells with an IDH mutation, despite the rare occurrences of concurrent mutations.[68, 80, 86] Small-molecular inhibitors of IDH1 WT or IDH2 WT were therefore identified as desirable investigative tools, which may

enable potential therapeutic avenues in glioma cells with the most frequently mutated isoform, IDH1.

To ensure that non-cancerous cells in the human body would retain at least one uninhibited isoform of $NADP^+$-dependent IDH, a dual inhibitor of IDH1 WT and IDH2 WT (class III as defined by Lin et al.) is likely not useful.[246] Indeed, selectivity between IDH1 WT and IDH2 WT was prioritised over selectivity between IDH1 WT and IDH1 mutant isoforms or IDH2 WT and IDH2 mutant isoforms, in addition to overall potency for the WT isoform. An active site inhibitor (class I as defined by Lin et al.) was ruled out due to the similarity of IDH1 WT and IDH2 WT active sites. As a result, supported by their documented selectivity as inhibitors of IDH1 and IDH2, allosteric binders (Class II as defined by Lin et al.) were assessed.[246]

2.2.1. Identification of a Potent Inhibitor of IDH1 WT

Class II IDH1 inhibitors were profiled from Agios, GSK, Sanofi, Bayer, Forma Therapeutics, Daiichi Sankyo, Lilly, and Novartis (**Figure 2.1**, the structures of class II inhibitors from **Figure 1.12** are shown again here for reference). Ivosidenib (AG-120, Agios) is reported to potently inhibit IDH1 WT (IC_{50} = 24-71 nM), however ivosidenib is a substrate for p-glycoprotein (PGP).[296] Therefore, ivosidenib is unlikely to efficiently cross the blood brain barrier (BBB).[296] GSK321 (GSK) is also reported to potently inhibit IDH1 WT (IC_{50} = 46 nM) and has been studied exclusively in haematological malignancies.[297] The bis-imidazole 'Compound 1' (Sanofi) is reported to poorly inhibit IDH1 WT (IC_{50} > 30 μM); Urban et al. also reported that 'Compound 1' was a poorer inhibitor of IDH1 R132H (IC_{50} > 13μM) than the original authors (IC_{50} = 13 nM), measured by a fluorescence assay.[296, 298] BAY-1436032 (Bayer) is reported to poorly inhibit IDH1 WT (IC_{50} = 20 μM).[299, 300] A structural analogue of BAY-1436032 was shown to form a salt bridge between its own carboxylate (in a similar position on BAY-

1436032) and H132 in complex with IDH1 R132H.[299, 300] BAY-1436032 may poorly inhibit IDH1 WT because IDH1 WT contains R132 instead of H132. FT-2102 (Forma Therapeutics) was reported to not inhibit IDH1 WT at measured concentrations (measured up to 20 μM).[246] DS-1001B (Daiichi Sankyo) was reported to not have any effect on IDH1 WT tumors and is reported to require extended preincubation in inhibition assays (IC_{50} > 10 μM). LY3410738 (Lilly) is a covalent inhibitor that is reported to selectively inhibit IDH1 variant enzymes; however, there is no available structure or structural, binding, or inhibition data for LY3410738 with any IDH isoforms.[301] IDH305 (Novartis) is reported to moderately inhibit IDH1 WT (IC_{50} = 6.1 μM) and exhibits BBB penetration properties.[302]

The Novartis series of IDH1 inhibitors were chosen for further consideration. The clinical candidate IDH305 is reported to be a moderately potent BBB-penetrant inhibitor of IDH1 WT (IC_{50} = 6.1 μM). Ivosidenib (AG-120) (IC_{50} = 24-71 nM) and GSK321 (IC_{50} = 46 nM) have greater potency against IDH1 WT, but lack any evidence of BBB penetration (a property important for glioma treatment).[296, 297] Three reports from Novartis describing the development of 3-pyrimidin-4-yl-oxazolidin-2-ones as allosteric inhibitors of mutant IDH1 were in consideration for potential IDH1 WT inhibitors, Levell et al., Cho et al., and Zhao et al. (**Figure 2.2**).[302-304]

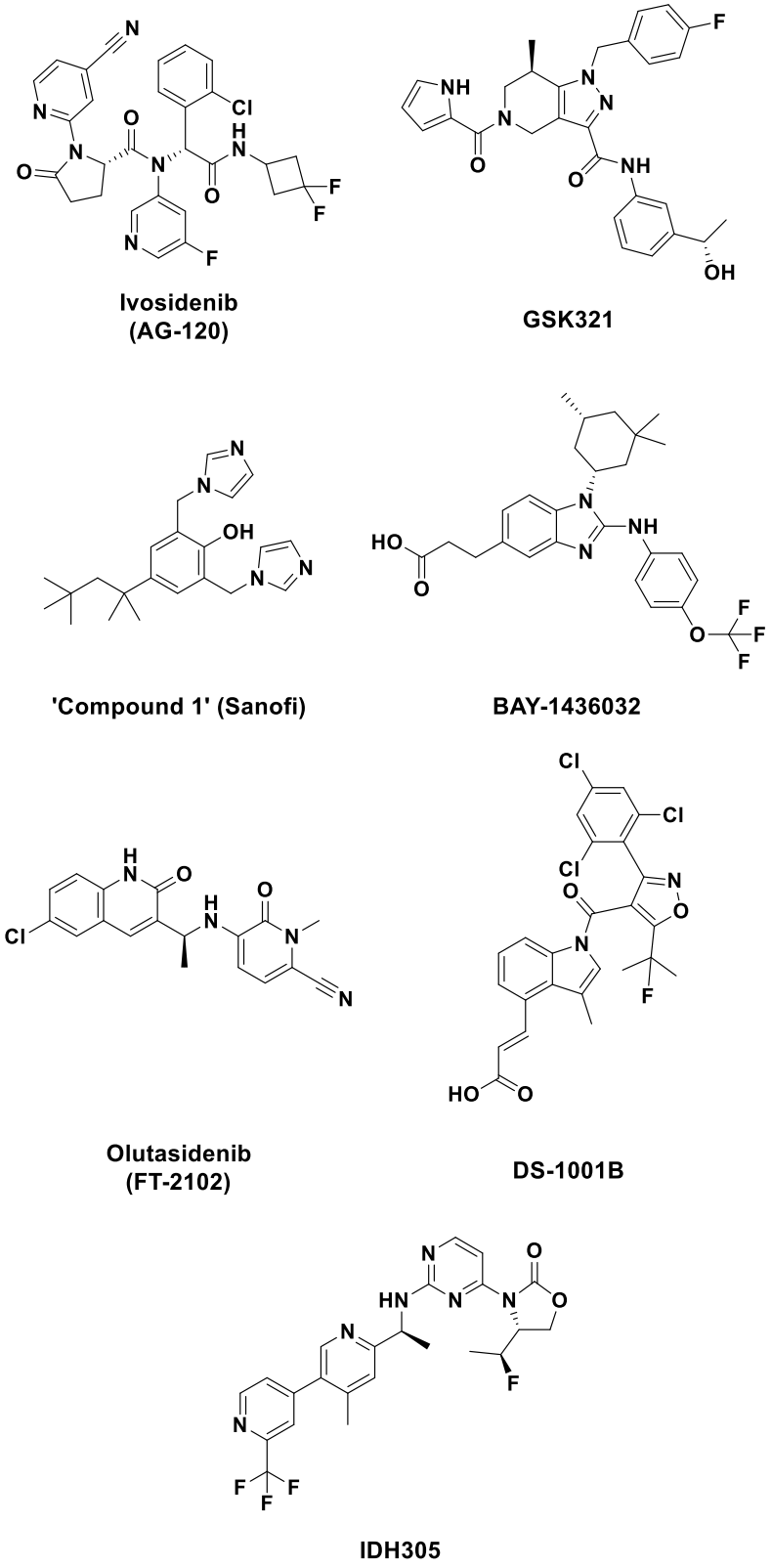

Figure 2.1 | *An overview of the structures of selected Class II IDH1 inhibitors (reproduced from* ***Figure 1.12****)*

Levell et al. identified the 3-pyrimidin-4-yl-oxazolidin-2-one IDH125 from a high-throughput screen against IDH1 R132H. IDH125 manifests moderate potency (IC_{50} = 220 nM) and BBB penetration (**Figure 2.2**).[303] The optimal stereochemistry of IDH125 was determined to be (C4-S, C13-S) (**Figure 2.2**).[303] The 3-pyrimidin-4-yl-oxazolidin-2-one scaffold was developed to improve potency, pharmacodynamic (PD), and pharmacokinetic (PK) properties, leading to the lead compound IDH889 (IC_{50} = 20 nM) (**Figure 2.2**). Further optimisation of PD and PK properties by Cho et al. led to IDH305 (IC_{50} = 27 nM), a clinical candidate with satisfactory potency, selectivity, and BBB penetration (**Figure 2.2**).[302] Zhao et al. performed subsequent structure-activity relationship (SAR) studies on 3-pyrimidin-4-yl-oxazolidin-2-one inhibitors.[304] The SAR studies focused on improving *in vitro* and *in vivo* stability and identified 'Compound 19' as a potent (IC_{50} = 21 nM), brain-penetrant, and orally bioavailable compound (**Figure 2.2**).[304] A preliminary screen of reported compounds containing 3-pyrimidin-4-yl-oxazolidin-2-one cores against IDH1 WT was conducted by a collaborator, Dr Xiao Liu.[305] The screen identified 'Compound 15' from Zhao et al. as a very potent inhibitor of IDH1 WT (IC_{50} = 20 nM).[304, 305] Compound 15 was selected for synthesis in-house for further study; it is referred to as Compound '**1**' from here on.

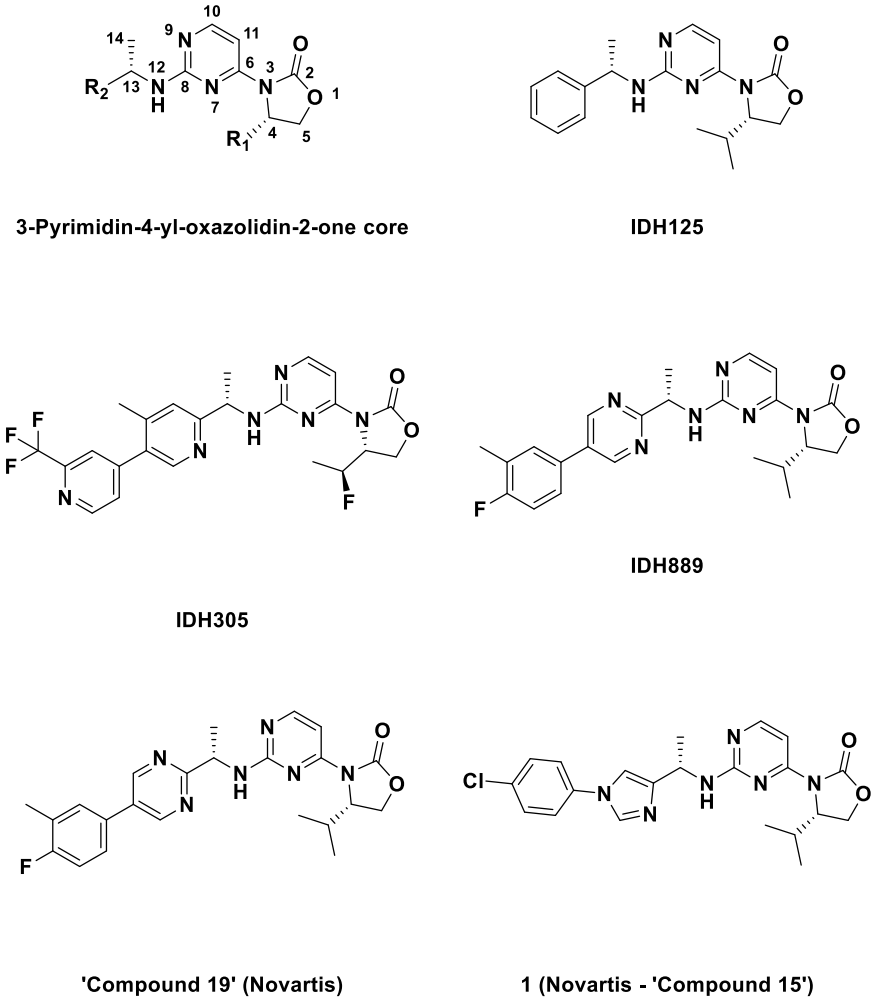

Figure 2.2 *| Structures of Novartis IDH1 inhibitors containing the 3-pyrimidin-4-yl-oxazolidin-2-one core.*

2.2.2. Identification of a Potent Inhibitor of IDH2 WT

The IDH2 variant inhibitor enasidenib (AG-221) contains a triazine core (**Figure 2.3**).[257] A follow on screen of compounds containing triazine cores against IDH2 WT was conducted by Leonard Lee (Department of Chemistry, University of Oxford) and Dr Xiao Liu. The screen identified a triazine derivative, 'Compound 16b', which is structurally related to the brain-penetrant IDH1/2 dual inhibitor vorasidenib (AG-881), which is currently in clinical trials for glioma containing mutations in IDH (**Figure 2.3**).[252, 253] 'Compound 16b' was found to be a potent inhibitor of IDH2 WT (IC_{50} = 105 nM), R140Q (IC_{50} = 13 nM), and R172K (IC_{50} = 151 nM) isoforms and, crucially, selective with

respect to IDH1 isoforms (IC_{50}s > 10μM).[305, 306] 'Compound 16b' was selected for synthesis in-house for further study and is referred to as Compound '**2'** from here on.

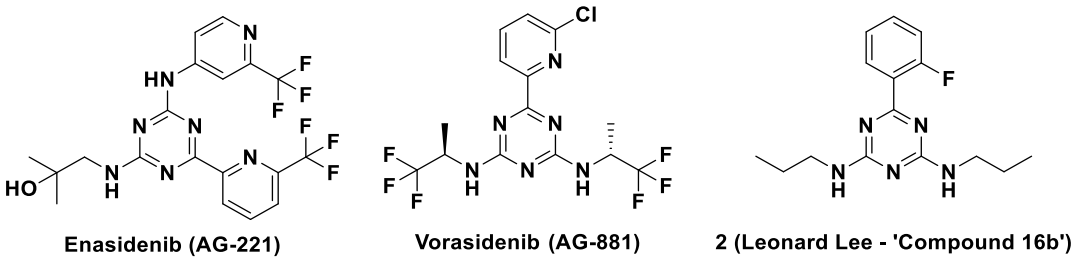

Figure 2.3 *| Structure of the Servier (formerly Agios) IDH2 variant inhibitor enasidenib (AG-221), IDH1/2 dual inhibitor vorasidenib (AG-881), and 'Compound 16b' ('**2**').*

2.3. The Synthesis of Inhibitors of IDH1 WT and IDH2 WT

2.3.1. Synthesis of Oxazolidone 1

The synthesis of Oxazolidone **1** commenced with a copper catalysed Ullman coupling of 1-chloro-4-iodobenzene and 1*H*-imidazole-4-carbaldehyde (**Figure 2.4.A-F**).[304, 307] The synthetic procedure involved six steps. The fifth step required the intermediate **11** (**Figure 2.4.F**). **11** was synthesised in (**E**) from commercially available (*S*)-4-isopropyloxazolidin-2-one (**Figure 2.4.E**, **Figure 2.7.B**).

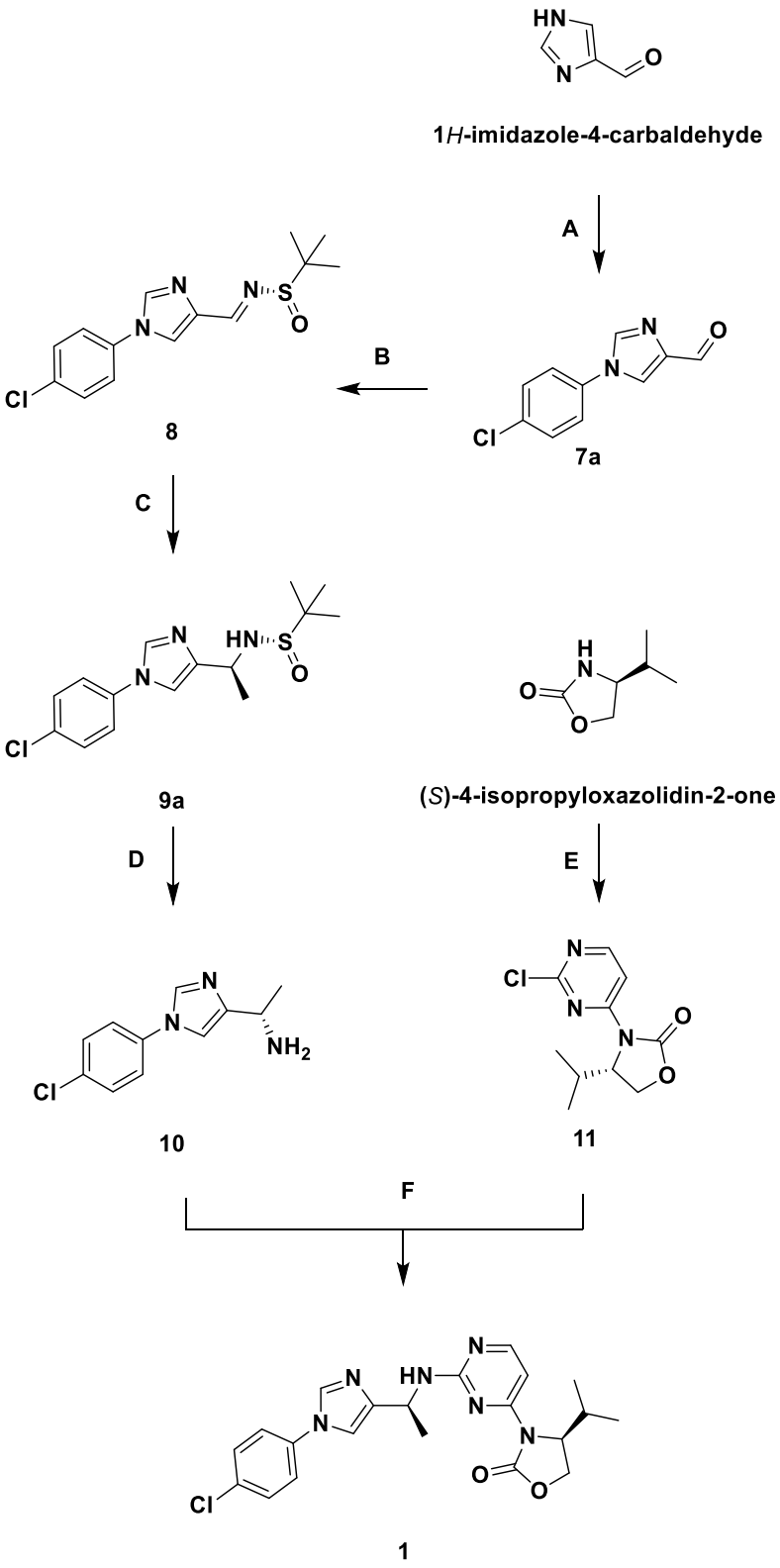

Figure 2.4 *| Overview of the synthesis of oxazolidone **1**. Reagents and conditions: **A**: 1-Chloro-4-iodobenzene, CuI/trans-(1R,2R)-N,N'-dimethyl 1,2-cyclohexane diamine, $CsCO_3$, DMF, 110 °C, 3h, 64%. **B**: (S)-2-Methylpropane-2-sulfinamide, pyrrolidine, CH_2Cl_2, 60 °C, overnight, 59-88%. **C**: MeMgBr, CH_2Cl_2, Et_2O, -70/-40/25 °C, overnight, 25-41%. **D**: HCl, MeOH, 1,4-Dioxane, rt, 1h, 50%. **E**: 2,4-Dichloropyrimidine, NaH, DMF, 0/25 °C, 18h, 20-34%. **F**: Et_3N, DMSO, 90 °C, 22h, 11%.*

Following a patent reported procedure, 1*H*-imidazole-4-carbaldahyde was coupled with 1-chloro-4-iodobenzene under Ullmann-type reaction conditions to produce aryl derivative **7a**.[307] Initially, when cuprous iodide and trans-(1*R*,2*R*)-*N*,*N*′-dimethyl 1,2-cyclohexane diamine were dissolved in anhydrous DMF, a blue colour was observed. The blue colour indicated a Cu(II) species, which could have been introduced via molecular oxygen in the solvent. Thus, poor turnover of the starting material was observed corresponding with a low yield of **7a**. Surprisingly, aldehyde **7b** was isolated in 32% yield (**Figure 2.5**). Anhydrous DMF was purged with nitrogen for 2 hours to remove molecular oxygen, and, upon dissolving trans-(1*R*,2*R*)-*N*,*N*′dimethyl 1,2-cyclohexane diamine and cuprous iodide in DMF, a green colour (Cu(I) species) was observed. The reaction was then heated for 3 hours at 110 °C, and, following full consumption of 1*H*-imidazole-4-carbaldahyde (observed by thin-layer chromatography (TLC)), purification ensued. Pleasingly, aryl **7a** was synthesised in 64% yield, superseding the reported 56% yield.[307]

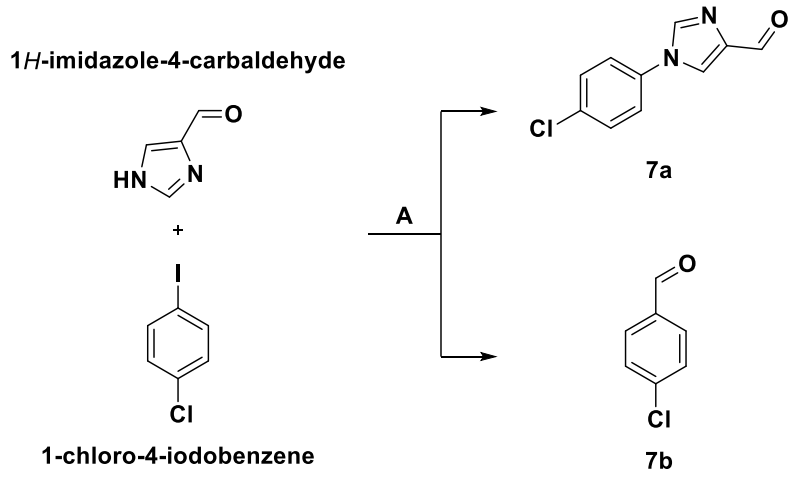

Figure 2.5 *| Synthesis of aryl* ***7a*** *and 4-chlorobenzaldehyde* ***7b****. Reagents and conditions:* ***A****: 1-chloro-4-iodobenzene, CuI, trans-(1R,2R)-N,N′-dimethyl 1,2-cyclohexane diamine,* Cs_2CO_3*, DMF, 110 °C, 3h, 64%.*

Ellman's chiral auxiliary was envisioned by Zhao, Manning and co-workers for the stereoselective addition of the methyl group to provide sulfinamide **9a** (C13-(*S*), N15-(*S*)). Aryl **7a** was condensed with (*S*)-2-methylpropane-2-sulfinamide by using pyrrolidine and heating to 60 °C in CH_2Cl_2, furnishing sulfinyl imine **8** in 88% yield (**Figure 2.6.B**). An excess of methyl magnesium bromide was added over four hours to sulfinyl imine **8** on a 20 mg scale at -70 °C; the mixture was subsequently, stirred at -40 °C for 1h. Incomplete conversion of sulfinyl imine **8** was observed, corresponding to a low yield of sulfinamide **9a** (41%). In order to have sufficient material for the ensuing reactions, the reaction was repeated on a larger scale (650 mg cf. 20 mg). Unfortunately, the larger scale produced a lower yield of sulfinyl imine **9a** (173 mg, 25% cf. 12 mg, 41%). The reaction was repeated, and in an attempt to improve the conversion, the mixture was allowed to warm to rt in an ice bath overnight after the stirring -40 °C. Full conversion of sulfinyl imine **8** was observed, and the mixture of diastereomers **9a** and **9b**—produced by the higher temperature of the reaction—were able to be separated by flash chromatography (**Figure 2.6.C**).

A large number (>100) of solvent systems were explored for the separation of the diastereomers **9a** and **9b**. The relatively non-polar solvent used was CH_2Cl_2. The concentration of the more polar solvent (99% ethyl acetate, 1% triethylamine, v/v) was increased along a gradient from 0% to 100%. Subsequently a second polar solvent (99% methanol, 1% triethylamine, v/v) was introduced and increased along a gradient from 0% to 1%. Two overlapping peaks with mixed fractions eluted in an approximate 1:1:1 ratio. To identify which peak represented diastereomer **9a,** ^{1}H NMR spectra of eluted fractions from each peak were compared with the ^{1}H NMR spectrum of a stereospecifically synthesized sample of **9a** reported by Cho et al..[308] Most of the peaks in the ^{1}H NMR spectra of **9a** and **9b** were observed to overlap.[308] The chemical shift of protons at position

14 in the ^{1}H NMR spectrum of the initially eluting fraction peak matched the reported chemical shifts corresponding to **9a**, and the peak was identified as primarily consisting of **9a** (δ = 1.57 cf. 1.58, d cf. d, *J* = 6.67 Hz cf. 6.65 Hz, 3H cf. 3H).[308] The chemical shift of protons at position 14 in the ^{1}H NMR spectrum of **9b** differed from the reported value (δ = 1.66 cf. 1.58, d cf. d, *J* = 6.79 Hz cf. 6.65 Hz, 3H cf. 3H).[308] The initially eluting fraction peak contained a mixture of **9a**:**9b** in a ratio > 99:1 and the later eluting fractions peak contained a mixture of **9b**:**9a** in a ratio > 95:5. A higher yield of sulfinamide **9a** (35% cf. 25%) and excellent diastereomeric ratio of **9a**:**9b** (>99:1) supplied sufficient material to progress.

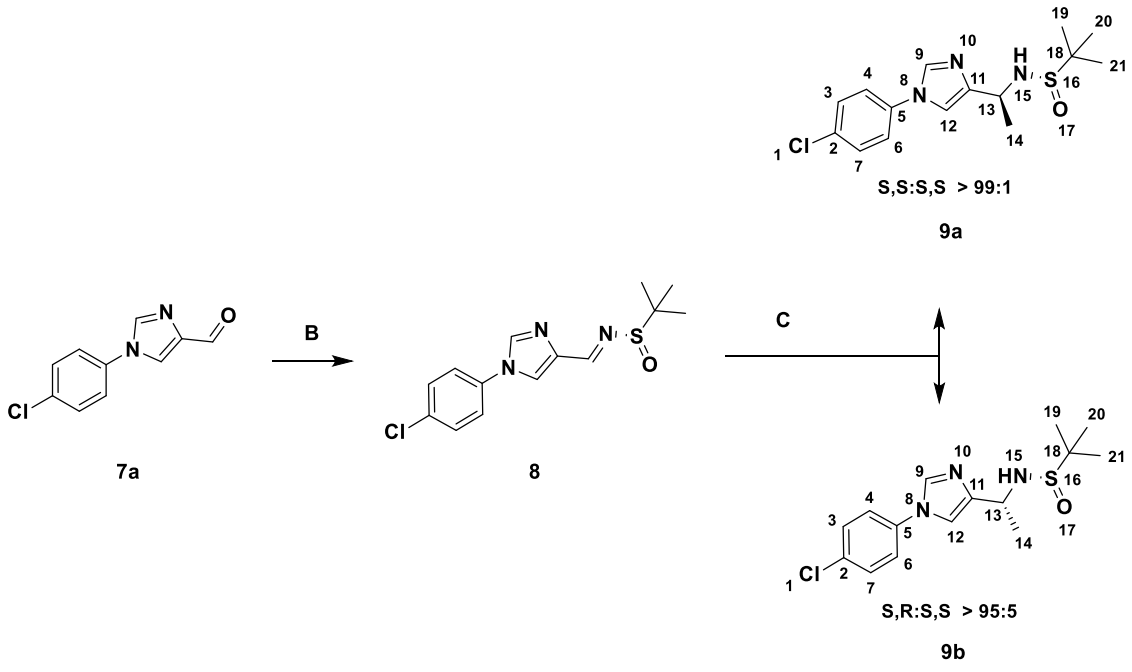

Figure 2.6 *| Synthesis of sulfinyl imine* ***8 (B)*** *and the formation of diastereomers* ***9a*** *and* ***9b (C)****. Conditions:* ***B****: (S)-2-Methylpropane-2-sulfinamide, pyrrolidine, CH_2Cl_2, 60 °C, overnight, 59-88%.* ***C****: MeMgBr, CH_2Cl_2, Et_2O, -70/-40/25 °C, overnight, 25-41%.*

Deprotection of sulfinamide **9a** by HCl in methanol and dioxane gave amine **10** in 50% yield (**Figure 2.7.A**). To produce pyrimidine **11**, (*S*)-4-isopropyloxazolidin-2-one, 2,4-dichloropyrimidine, and DMF were stirred at 0 °C, then sodium hydride was added

portion wise. The mixture was allowed to warm slowly to rt, and stirred for 18 hours to produce pyrimidine **11** in 34% yield (**Figure 2.7.B**). In the final step (**Figure 2.7.C**), amine **10** and pyrimidine **11** were heated with triethylamine in DMSO to construct **1**. The literature procedure reported removing the DMSO *in vacuo* at 80 °C; however, this was considered unfeasible with the equipment available.[304] Instead, the reaction mixture was diluted with CH_2Cl_2, heated to 40 °C, and then placed under a stream of nitrogen to evaporate the majority of the DMSO. Unfortunately, neither this procedure, nor diluting with organic solvent with aqueous washes succeed in removing the residual DMSO. DMSO removal was successfully achieved by diluting the mixture with a large excess of Et_2O and gently stirring with ice in a separatory funnel. To ensure the aqueous layer remained at 0 °C, ice was added as required. As the ice melted, the aqueous layer was separated, and this process was repeated 4 times. The crude mixture was purified using flash chromatography to give oxazolidone **1** in 11% yield). The reported ternary solvent system for chromatography of **1** was adapted, utilising ethyl acetate and methanol as before, but utilising cyclohexane in place of heptane.[304]

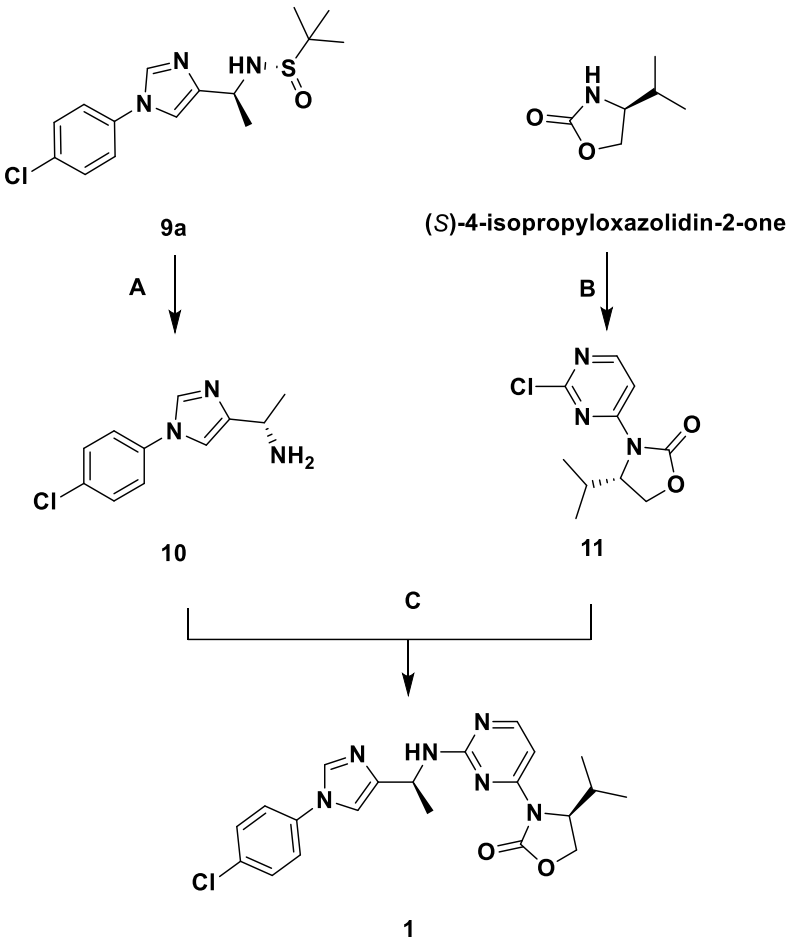

***Figure 2.7** | Synthesis of oxazolidone **1**. Reagents and conditions: **A**: HCl, MeOH, 1,4-Dioxane, rt, 1h, 50%. **B**: 2,4-Dichloropyrimidine, NaH, DMF, 0/25 °C, 18h, 20-34%. **C**: Et_3N, DMSO, 90 °C, 22h, 11%.*

2.3.2. Synthesis of 2

Triazine **2** was synthesised in two steps from cyanuric chloride as reported in Leonard Lee's Master's thesis.[306] Thus, propylamine was added dropwise to cyanuric acid in acetone and water at 0 °C, and then stirred at 45 °C for 2 hours to form the disubstituted triazine **15** intermediate (**Figure 2.8**). Crude disubstituted triazine **15**, was reacted via Suzuki-Miyaura cross-coupling with 2-fluorobenzeneboronic acid in the presence of [1,1′-bis(diphenylphosphino)-ferrocene]-dichloropalladium(II) ($Pd(dppf)Cl_2$), sodium carbonate, water, and dioxane. After stirring overnight at 115 °C, trisubstituted triazine **2** was fashioned in 41% yield over 2 steps (**Figure 2.8**).

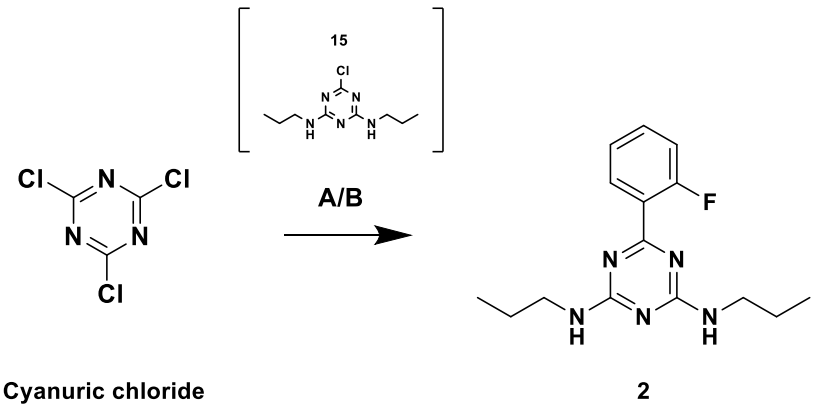

***Figure 2.8** | Synthesis of aryl **2**. Reagents and conditions: **A.** Propylamine, Acetone/H_2O, 0/45 °C, 2h. **B.** Pd(dppf)Cl_2, Na_2CO_3, H_2O, 1,4-Dioxane, 115 °C, overnight. Overall yield, 41% (over 2 steps).*[306]

2.4. The Synthesis of a Putative PROTAC-type Inhibitor targeting IDH2 WT

Preliminary work by Dr Ingvild Hvinden indicated that oxazolidone **1** and triazine **2** did not trigger a strong metabolic effect in LN18 GBM cells expressing IDH1 R132H or IDH1 WT (discussed in **Chapter 3**, **Section 3.4**, **Section 3.5**). It was hypothesised that inducing proteasomal degradation of either IDH isoform may result in a stronger metabolic effect than inhibition. However, considering IDH1 R132H inhibits IDH1 WT activity via the formation of IDH1 WT/R132H heterodimers, it was proposed that IDH1 WT degradation in cells expressing IDH1 R132H would have a reduced impact on the production of 2-OG and NADPH compared with the degradation of IDH2 WT, which is otherwise unaffected by the IDH1 R132H mutation.[67, 121] Therefore, IDH2 WT was selected for degradation to maximally arrest a target cell's IDH1/2 WT activity and achieve a stronger overall metabolic effect.

Proteolysis targeting chimeras (PROTACs) are heterobifunctional small-molecules that are able to target cellular proteins for degradation by the proteosome, typically via an E3 ligase complex.[309, 310] PROTAC-type inhibition may also help avoid second-site mutation

mediated resistance mechanisms, since it is not necessary for a PROTAC to inhibit the target protein while bound.[283, 311] Thalidomide—a synthetically appealing, well-studied, E3 ligase recruiter molecule—binds the E3 ligase substrate adapter cereblon; therefore, combining an IDH2 WT inhibitor, triazine **2**, and thalidomide for IDH2 WT degradation was conceived (**Figure 2.9**).

The design of the PROTAC warhead was guided by an analysis of synthetically accessible sites for linker attachment on the triazine core of compound **2**. Two primary positions were considered: replacement of the 2-fluorobenzene group or replacement of one of the propylamine substituents. Both strategies were pursued, yielding the warhead designs of compound **3** with the linker attached at the phenyl position, and compound **4** with the linker replacing a propylamine group (**Figure 2.9**). To incorporate a thalidomide-derived E3 ligase ligand, 4-fluoro-thalidomide **12** was selected, as it contains a halide substituent amenable to linker installation via S_NAr, providing a straightforward synthetic route.[312] In addition, PROTAC efficacy is frequently influenced by linker properties, including composition, length, attachment chemistry, and attachment site.[313] Accordingly, potential PROTACs **3** and **4**, were designed by coupling 4-fluoro-thalidomide **12** with derivatives of triazine **2** using simple four-carbon alkyl linkers and amine attachments to facilitate initial synthesis and handling, with the intention of refining linker properties at a later stage (**Figure 2.9**). Future work will focus on optimising linker length, composition, and placement to maximise the efficacy of these molecules as IDH2 WT degraders.

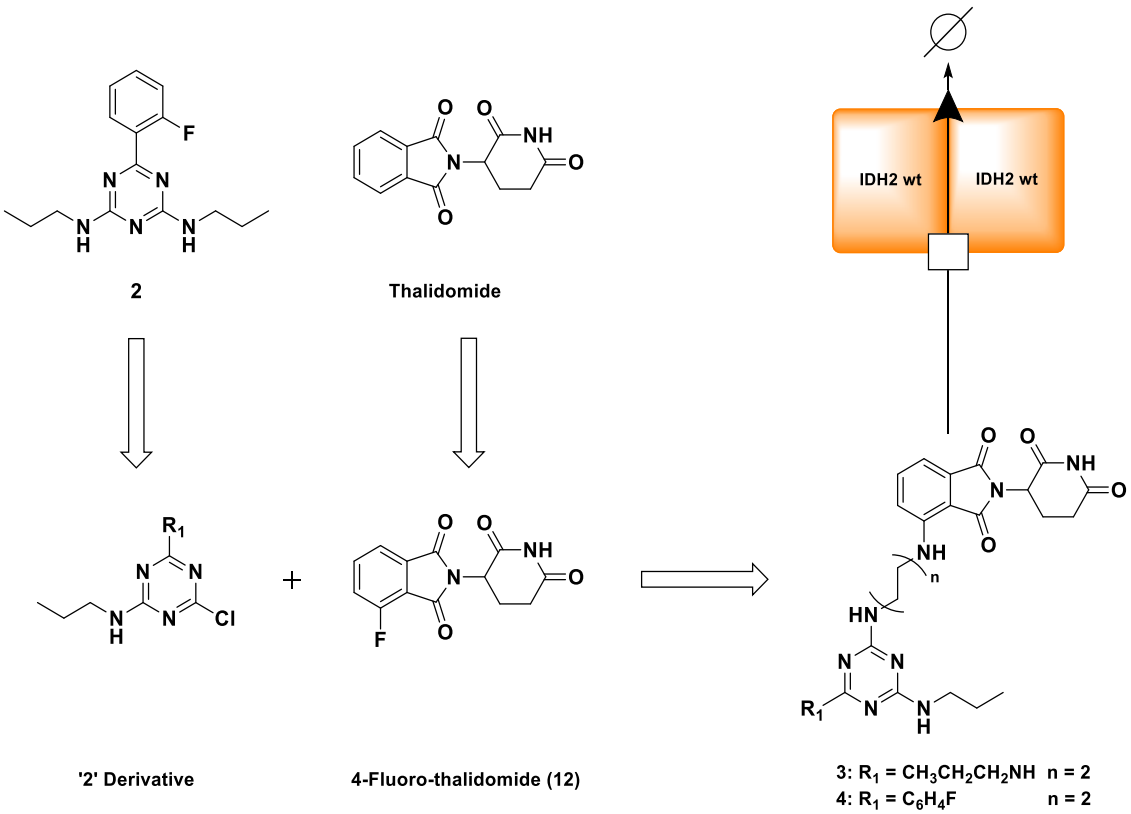

Figure 2.9 *| Simplified representation of the design of potential PROTAC inhibitors **3** and **4**, which enable the degradation of IDH2 WT homodimers. The IDH2 WT selectivity of triazine **2** and cereblon-binding activity of thalidomide were combined via derivatives of triazine **2** and 4-fluoro-thalidomide into '**2**'-thalidomide conjugates **3** and **4**. R_1 represents either a propylamine or 2-fluorobenzene substituent.*

Initially, installing a linker at the C2 position of the 2-fluorobenzene was attempted to form carbamate **6**. Three conditions were tested for reacting triazine **2** with amine **5** (**Figure 2.10**): **A.** 35 °C in CH_2Cl_2 with caesium carbonate overnight, **B.** 60 °C in dioxane with caesium carbonate overnight, and **C.** 90 °C in DMF with DIPEA overnight. The insertion of amine **5** into triazine **2** was not observed in all cases. As such, the synthesis of carbamate **6** was ultimately abandoned.

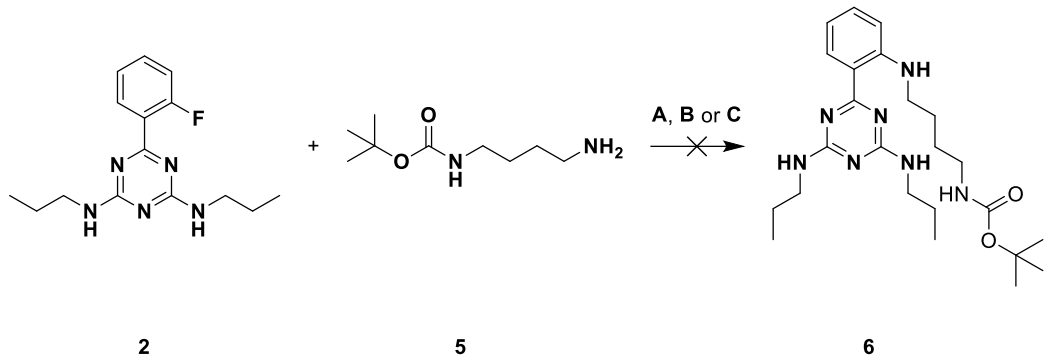

2 5 6

Figure 2.10 *| Synthesis of carbamate **6** from triazine **2**. Conditions: **A.** Amine **5**, Cs_2CO_3, CH_2Cl_2, 35 °C, overnight. **B.** Amine **5**, Cs_2CO_3, dioxane, 60 °C, overnight. **C.** Amine **5**, DIPEA, DMF, 90 °C, overnight.*

Amino thalidomide **14** was synthesised in three steps from 3-fluorophthalic anhydride (**Figure 2.11**).[314-317] Following a reported procedure for the insertion of furfurylamine into phthalic anhydride, 3-fluoropthalic anhydride and L-glutamine were heated neat at 170 °C for 6h (**Figure 2.11.A**).[314] Two main products were isolated and characterised, uncyclized thalidomide **62** in ~50% yield and glutarimide **12** in ~24% yield (**Figure 2.11.A**). A different procedure utilising 3-aminopiperidine-2,6-dione and sodium acetate in acetic acid was used to furnish glutarimide **12** in higher yields (48%) (**Figure 2.11.B**).[315]

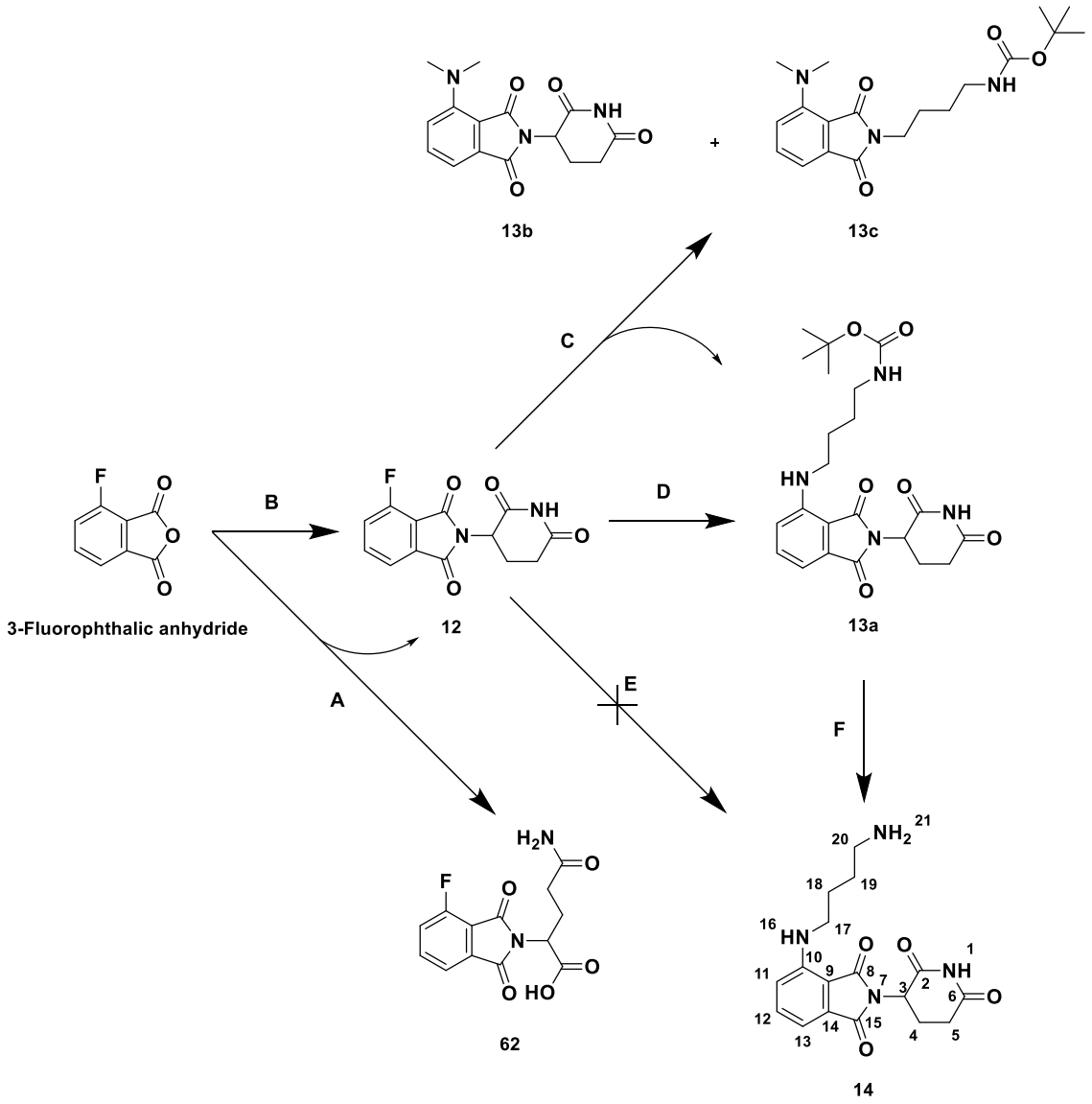

***Figure 2.11** | Synthesis of E3 ligase ligand **12** (**A** or **B**) and the instalment of the linker to produce **14** (**D**, **F**). Conditions: **A.** L-Glutamine, 170 °C, 6h, 24%.[314] **B.** 3-Aminopiperidine-2,6-dione, sodium acetate, acetic acid, reflux at 120 °C, 4h, 48%.[315] **C/D.** Amine **5**, DIPEA, DMF (**C**) or NMP (**D**), 90 °C, 12h, 16% (**D**).[316] **E.** 1,4-Diaminobutane, rt, 1h. **F.** HCl, methanol, rt, 2h, 97%.[317]*

Glutarimide **12** was reacted with *N*-Boc protected (**Figure 2.11.C** and **2.10.D)**, and unprotected 1,4-diaminobutane (**Figure 2.11.E**). Unprotected 1,4-diaminobutane did not yield the desired amino thalidomide **14** (**Figure 2.11.E**). Glutarimide **12** was instead reacted with *N*-Boc protected 1,4-diaminobutane, DIPEA in DMF and heated to 90 °C for 12h (**Figure 2.11.C**). The reaction produced three products which were readily separated by reverse-phase flash-chromatography, and identified as thalidomides **13a**, **13b**, and **13c** using LC-MS. Surprisingly, dimethylamine appeared to insert into

glutarimide **12** to form thalidomides **13b** and **13c**. Similar reactions have been reported in literature, suggestingthat side products **13b** and **13c** may have formed from the addition of dimethlyamine via S_NAr following the degradation of DMF in base.[318, 319] To avoid side products **13b** and **13c**, *N*-methyl-2-pyrrolidone (NMP) (**Figure 2.11.D**) was used as the solvent to construct thalidomide **13a** (16%). The deprotection of thalidomide **13a** with HCl in methanol produced amino thalidomide **14** in high yield (97%, **Figure 2.11.F**). The sensitivity of thalidomide to base hydrolysis and thermal degradation negatively affected the overall yield of amino thalidomide **14**.[320, 321] Considering the low amount of material produced, an alternative route was chosen to install the linker into the triazine core first, and then insert the linker into glutarimide **12** as the final step.

The synthesis of conjugate **3**, which contains a 1,4-diaminobutane linker in place of a 2-fluorobenzene substituent, was first attempted (**Figure 2.12**). Then, amine **5** was reacted with crude disubstituted triazine **15** in DIPEA and NMP at 90 °C overnight (**Figure 2.12**.**B**). The starting materials were removed by using a silica chromatography column to give *N*-Boc triazine **16** (48%) as a crude product. Without further purification, *N*-Boc triazine **16** was deprotected with HCl in methanol at rt overnight (**Figure 2.12.C**). Methanol was removed *in vacuo* and aqueous extraction of the crude residue yielded amino triazine **17** in a high 88% yield. An S_NAr reaction ensued to assemble conjugate **3** by heating amino triazine **17** and Glutarimide **12** in NMP at 90 °C over 4h without the use of base (12%, **Figure 2.12.D**).

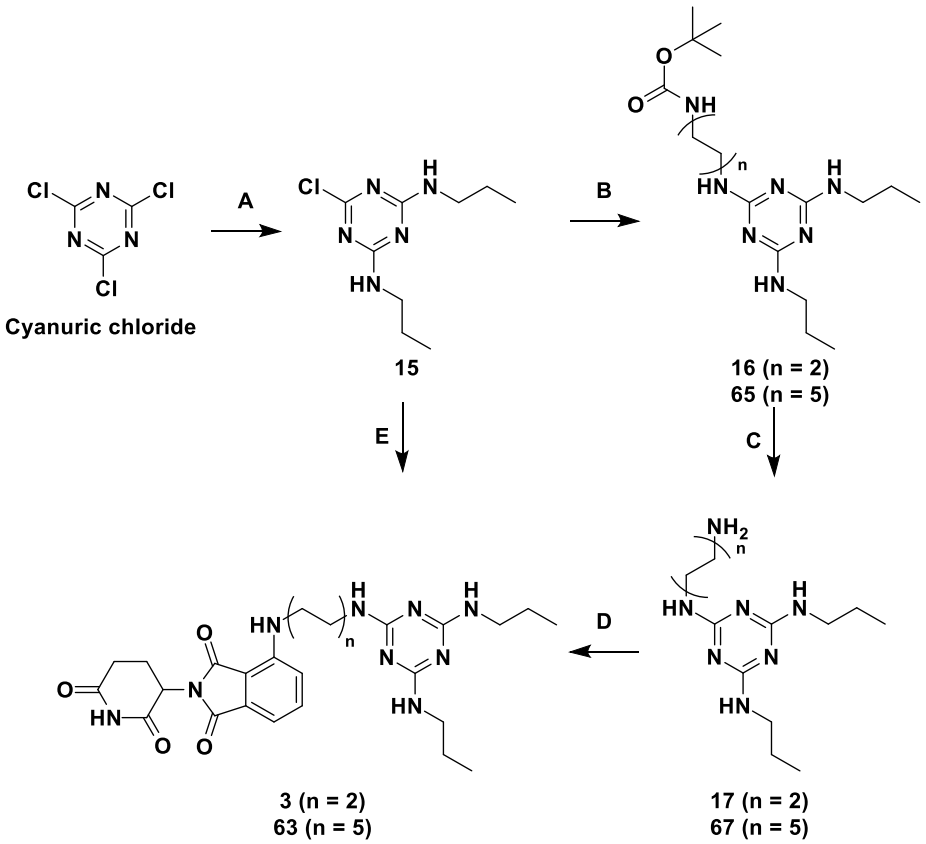

Figure 2.12 *| Synthesis of conjugate **3**. Conditions: **A.** THF, 0 °C, 2h, 66%. **B.** amine **5**, DIPEA, NMP, 90 °C, overnight, 48%. **C.** HCl, methanol, rt, overnight, 88%. **D.** Glutarimide **12**, NMP, 90 °C, 4h, 12%. **E.** Amino thalidomide **14**, DIPEA, NMP, 80 °C, overnight, 5%.*

To compare overall yields of the different routes towards conjugate **3**, another SNAr reaction was conducted by heating crude disubstituted triazine **15** and amino thalidomide **14** in NMP at 80 °C over 4h (5%, **Figure 2.12.E**). Installing the linker into glutarimide **12** first resulted in a 5-step synthesis with an overall yield of 0.4% for conjugate **3**. However, installing the linker into disubstituted triazine **15** first demonstrated a 5-step synthesis with an overall yield of 5% for conjugate **3**. Thus, installing the linker into disubstituted triazine **15** first was a more efficient and economical route.

Conjugate **4**, which contains a 1,4-diaminobutane linker in place of a propylamine substituent, was then synthesised (**Figure 2.13**). To avoid the accidental formation of the disubstituted triazine **15** by the double addition of propylamine, a stoichiometric amount of propylamine was added dropwise over 30 minutes to cyanuric chloride in THF at 0 °C

(**Figure 2.13**.**A**). The reaction mixture was stirred further at 0 °C for 2h to synthesise monosubstituted triazine **18** in 60% yield. 2-Fluorobenzeneboronic acid was cross-coupled with monosubstituted triazine **18** via Suzuki-Miyaura cross-coupling in the presence of $Pd(dppf)Cl_2$, caesium carbonate, and dioxane (**Figure 2.13.B**). The reaction mixture was stirred at 100 °C for 1h to produce aryl **19** (10%). Aryl **19** was subjected to an S_NAr reaction with amine **5** and DIPEA in NMP at 90 °C. After stirring for 6h, the starting materials were removed using a silica column to give *N*-Boc amine **20** (77%, **Figure 2.13.C**). Deprotection of *N*-Boc amine **20** with HCl in methanol supplied amine **21** (41%, **Figure 2.13.D**). Amine **21** was introduced via an S_NAr reaction with glutarimide **12** in NMP (**Figure 2.13.E**). The reaction mixture was stirred at 90 °C for 4h and flash chromatography yielded a crude product, conjugate **4** (~12%). The overall yield for the 5-step synthesis of **4** with respect to 3-fluorophthalic anhydride was ~5%.

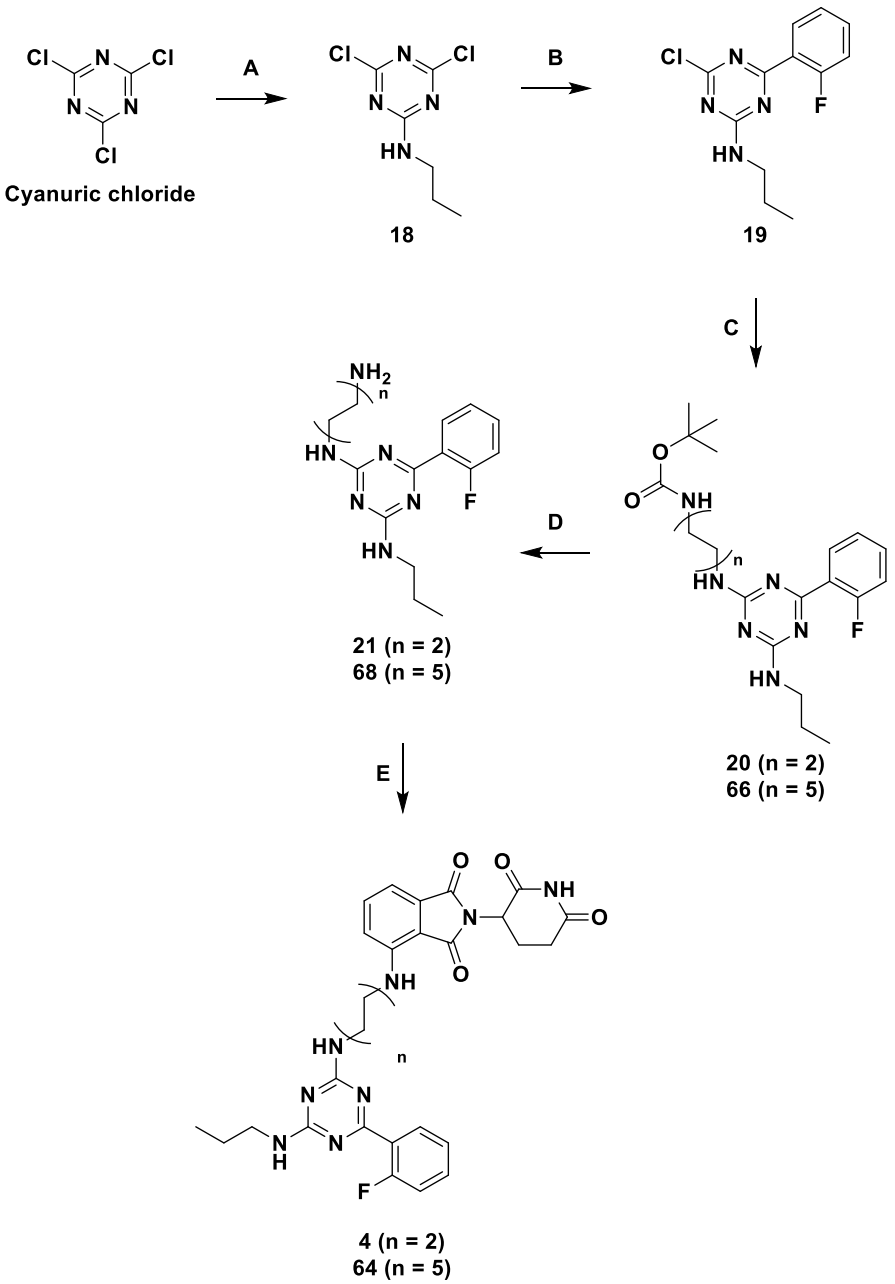

Figure 2.13 | *Synthesis of conjugate **4**. Conditions: **A.** Propylamine, DIPEA, THF, 0 °C, 2h, 60%. **B.** 2-Fluorobenzeneboronic acid, $Pd(dppf)Cl_2$, Cs_2CO_3, dioxane, 100 °C, 1h, 10%. **C.** Amine **5**, DIPEA, NMP, 90 °C, 6h, 77%. **D.** HCl, methanol, rt, overnight, 41%. **E.** Glutarimide **12**, NMP, 90 °C, 4h, 12%.*

Conjugate **3** was applied to LN18 GBM cells during the synthesis of conjugate **4**. The treatment of LN18 GBM cells with conjugate **3** exhibited a promising effect as measured in metabolomic studies discussed in **Chapter 3**, **Section 3.6**. Therefore, conjugate **4** was not pursued further, as was the case for the synthesis of conjugates with a linker length of ten carbons (**63**, **64**, **65**, **66**, **67**, **68**), which was limited to a small number of test reactions.

2.5. Biochemical Investigation of IDH1 WT Inhibition Binding Kinetics

2.5.1. Reproduction of Reported IDH1 WT inhibition by 1

The reported inhibition of IDH1 WT by Compound **1** was confirmed by NADPH-based absorbance assays (**Section 6.2.2**). Reported procedures measured the increase in concentration of NADPH over time by absorbance at 340 nm as a proxy of IDH1 WT activity (**Figure 2.14**).[125]

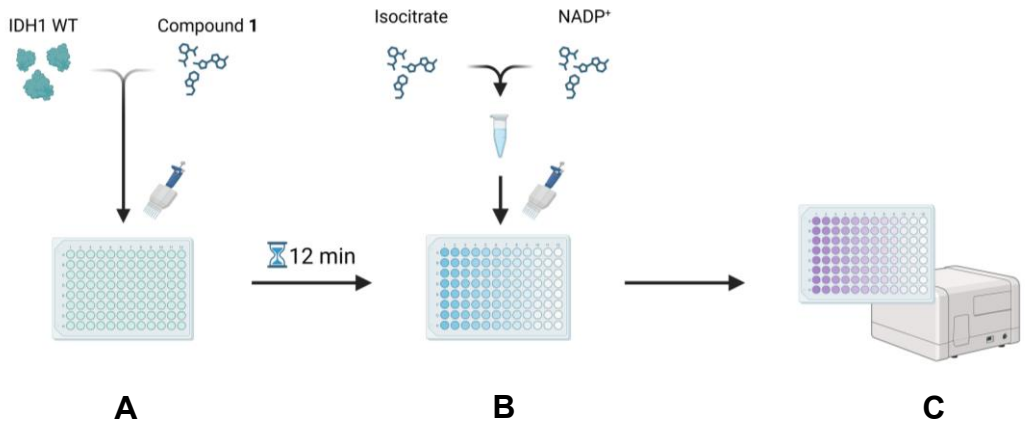

Figure 2.14 *| Overview of the NADPH-based absorbance assay methodology adapted from Liu et al.*[125] ***A.*** *Enzyme (here, IDH1 WT) and inhibitor (here, compound **1**) are dispensed in reaction buffer into an assay plate (here, 96 wells) and incubated together for 12 minutes.* ***B.*** *Substrates (here, isocitrate and $NADP^+$) are added in reaction buffer simultaneously into each reaction well to initiate the reaction.* ***C.*** *The assay plate is immediately submitted for measurement, and the change in NADPH absorbance (340 nM) over time is recorded.*

Different reaction conditions to Dr Xiao Liu's preliminary screen, including a higher concentration of IDH1 WT (4.5 nM cf. 2 nM), were employed primarily to ensure consistency with previous studies investigating the roles of metal ions in IDH1 R132H and IDH1 WT that utilised enzyme from the same production batch.[125, 305] Ideally, future work should ensure that conditions and specific enzyme activity are matched with previously reported assays to enable direct comparison.

Following procedures adapted from Liu et al, compound **1** was incubated across a range of 10 concentrations (generated by fourfold serial dilution from a maximum concentration of 100 μM, yielding a final concentration series: [**1**] = 0.38 nM – 100 μM) with IDH1 WT (final concentration: [IDH1 WT] = 4.5 nM) in reaction buffer (100mM Tris, 10 mM $MgCl_2$, 0.2mM DTT, 0.005% (v/v) Tween-20, 0.1 mg/mL BSA, pH 8.0) at rt for 12 minutes (**Figure 2.14.A**, **Figure 2.15**).[125] The reaction was initiated by addition of reaction buffer containing the enzyme substrates (final concentrations: [isocitrate (ICT)] = 150 μM, [$NADP^+$] = 75 μM) (**Figure 2.14.B**, **Figure 2.15**). Under these conditions compound **1** demonstrated potent inhibition of IDH1 WT (IC_{50} = 6 nM), similar to the previously measured inhibition by Dr Xiao Liu (IC_{50} = 19 nM) (**Figure 2.15**).[305]

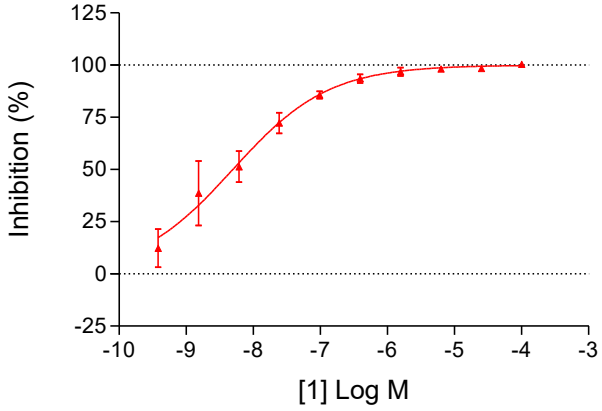

Figure 2.15 *| Plot of inhibition of IDH1 WT (%) against [**1**] Log M. Conditions: 4.5 nM IDH1 WT, 150µM ICT, 75µM NADP$^+$, reaction buffer: 100mM Tris, 10 mM $MgCl_2$, 0.2mM DTT, 0.005% (v/v) Tween-20, 0.1 mg/mL BSA, pH 8.0. No. of experiments = 2. Technical replicates (per experiment):* ***1****, n = 8; controls, n = 16.*

2.5.2. Inhibition of IDH1 WT by 1 Under Turnover Conditions Using the e-Leaf

The following experiments and derivations were conducted by a collaborator, Dr Ryan Herold (Department of Chemistry, University of Oxford). The experiments utilised a new technology for studying redox driven enzyme turnover called the e-Leaf (**Figure 2.16**).[248, 322-324] In brief, in the e-Leaf method, ferredoxin NADP$^+$ reductase (FNR) is first adsorbed onto an electrode with pores composed of indium tin oxide (ITO). Electrons from the electrode can directly tunnel into FNR and reduce/oxidise NADP$^+$/NADPH. This allows FNR and NADP$^+$/NADPH production to be directly driven by manipulating the current of the system. Introducing a second NADP$^+$/NADPH dependent enzyme into the pore, here IDH1 WT, allows for the recycling of NADP$^+$/NADPH.[249] The second enzymatic reaction can then be indirectly driven in either the forward or reverse direction, here oxidising ICT or reducing 2-OG. Conventional kinetic assays typically yield endpoint measurements or IC_{50} values, but these approaches often fail to resolve the complexities of slow-binding or multi-step inhibition under continuous turnover conditions. In contrast, the e-Leaf's real-time, activity-based readout enables direct observation of

enzyme catalysis and the dynamic effects of inhibitors introduced after turnover has been initiated, potentially providing mechanistic insights inaccessible to pre-incubation-based methods.

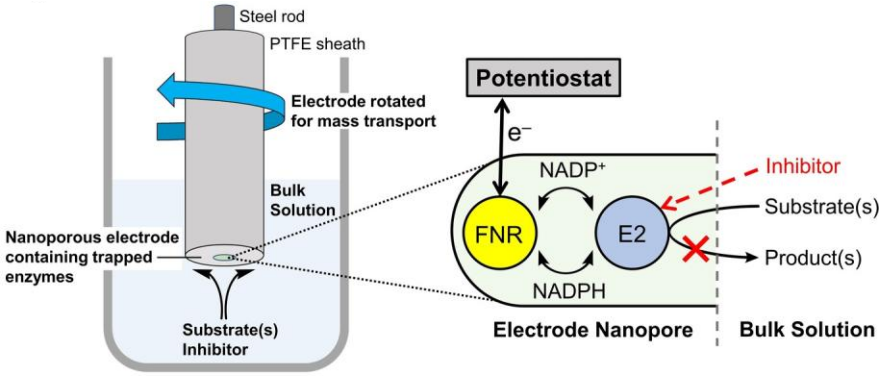

Figure 2.16 | *Overview of the experimental setup and mechanism of the e-Leaf, reproduced from Herold et al. under the Creative Commons CC BY license.*[248]

Previous work by Dr Ryan Herold used the e-Leaf to investigate the kinetics of IDH1 variant inhibition, revealing that IDH1 variant inhibitors, such as ivosidenib (AG-120) and IDH224, inhibit IDH1 R132H more slowly when introduced after the enzymatic reaction has been initiated, compared to reported IC_{50} incubation times (>12 minutes).[248, 323, 324] For example, after 12 minutes of incubation with isolated IDH1 R132H and $MgCl_2$, IDH224 displayed potent inhibition (IC_{50} = 4.3 nM). By contrast, when the reaction was initiated in the absence of IDH224, subsequent addition of a much higher concentration of IDH224 (1 µM cf. 4.3 nM) resulted in <50% inhibition of IDH1 R132H for longer than 30 minutes.[323]

The slower inhibition observed under turnover conditions may arise from the conformational dynamics of IDH1 R132H. Specifically, the open-inactive conformation of IDH1 R132H, which predominates in the absence of substrate and magnesium (as occurs during the pre-incubation phase of conventional IC_{50} assays), is proposed to allow ivosidenib to bind, but possibly the closed-active conformation does not.[125, 323] Once

substrate (ICT or 2-OG) and magnesium bind, the enzyme adopts a closed-active conformation, resulting in slower inhibition if the inhibitor is introduced after catalysis has commenced. Conversely, successful inhibitor binding of the open-inactive conformation may hinder magnesium ion binding, thereby stabilising the open-inactive state. Therefore, the allosteric inhibitors are competitive with respect to magnesium ions in the presence of substrate.[125]

Based on these findings, Dr Ryan Herold proposed a kinetic mechanism for the inhibition of IDH1 R132H by variant inhibitors, consistent for both ivosidenib and IDH224 (**Figure 2.17**).[325]

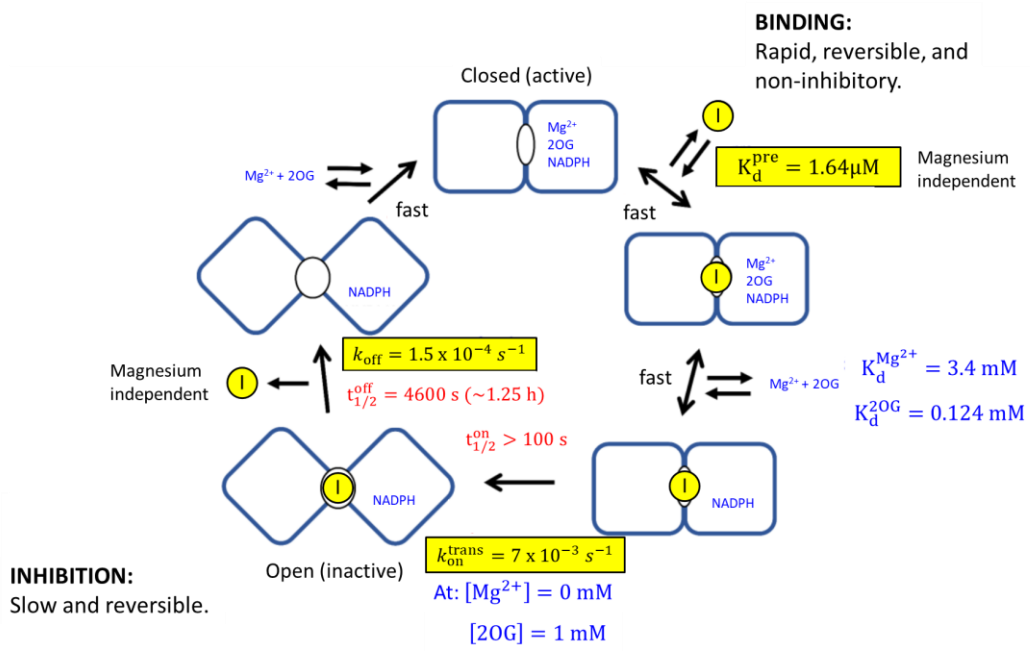

***Figure 2.17** | Proposed kinetic mechanism for the inhibition of IDH1 R132H by ivosidenib. Kinetic binding data of IDH224 with IDH1 R132H are consistent with ivosidenib. Other allosteric dimer interface-binding IDH1/2 inhibitors likely follow this mechanism. Here, the binding and dissociation steps for 2-OG and Mg^{2+} are shown in the active site of a single monomer. In reality, there is likely half-site reactivity.[124] Values for the pre-equilibrium enzyme-inhibitor complex, K_d^{pre}, K_d^{2OG}, $K_d^{Mg^{2+}}$, and $t_{1/2}$ are reported from Dr Ryan Herold's prevous work. The k_{on}^{trans} value presented is the limiting rate, determined by plotting the Mg^{2+}-dependent k_{on}^{trans} values against $[Mg^{2+}]$ and extrapolating to $[Mg^{2+}] = 0$ M. Figure adapted with permission from Dr Ryan Herold.[325]*

Given that IDH224 and **1** share a common 3-pyrimidin-4-yl-oxazolidin-2-one core (**Figure 2.18**), and that the IC_{50} values for IDH1 R132H inhibition by IDH224

(IC_{50} = 4.2 nM) and for IDH1 WT inhibition by **1** (IC_{50} = 6 nM) are similar, it was of interest to determine whether the kinetic behaviour observed by Dr Ryan Herold for IDH1 R132H would extend to IDH1 WT.[283] Therefore, using the e-Leaf, **1** was introduced into a pre-initiated reaction mixture containing IDH1 WT to investigate whether a similar reduction in potency would be observed under turnover conditions.

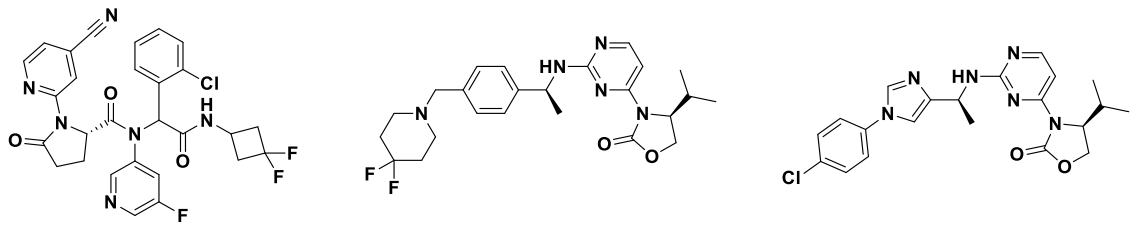

Figure 2.18 | *Structures of IDH1 R132H inhibitors ivosidenib (AG-120) and IDH224, and IDH1 WT inhibitor **1**.*

Chronoamperometry time course experiments of IDH1 WT inhibition by **1** showed slower inhibition when **1** was injected after the reaction was initiated, than the rate of inhibition observed in reported IC_{50}s. This observation agrees with previous experiments involving inhibition of IDH1 R132H by IDH224 (e-Leaf with delayed injection: [IDH224] = 1μM, <50% inhibition after 30 minutes cf. solution IC_{50} with pre-incubation: [IDH224] = 4.3 nM, ~50% inhibition after ≤ 12 minutes). The binding kinetics of IDH1 WT with **1** were much slower than IDH1 R132H and IDH224 (**Figure 2.19**). The maximum inhibition of IDH1 WT by **1** was also poorer than the inhibition of IDH1 R132H by IDH224 (**Figure 2.19**). The different potencies of **1** and IDH224 measured after delayed injection under e-Leaf conditions are notable given the comparable values of **1** and IDH224 measured after pre-incubation under solution IC_{50} conditions (IC_{50} = 6 nM, cf. 4.3 nM, respectively) (**Figure 2.19**). After 2 hours at a concentration of 1 μM, IDH224 manifested >80% inhibition, but **1** manifested <40% inhibition. Indeed, after 2 hours at a concentration of 70 μM, **1** did not achieve 80% inhibition (**Figure 2.19.B**).

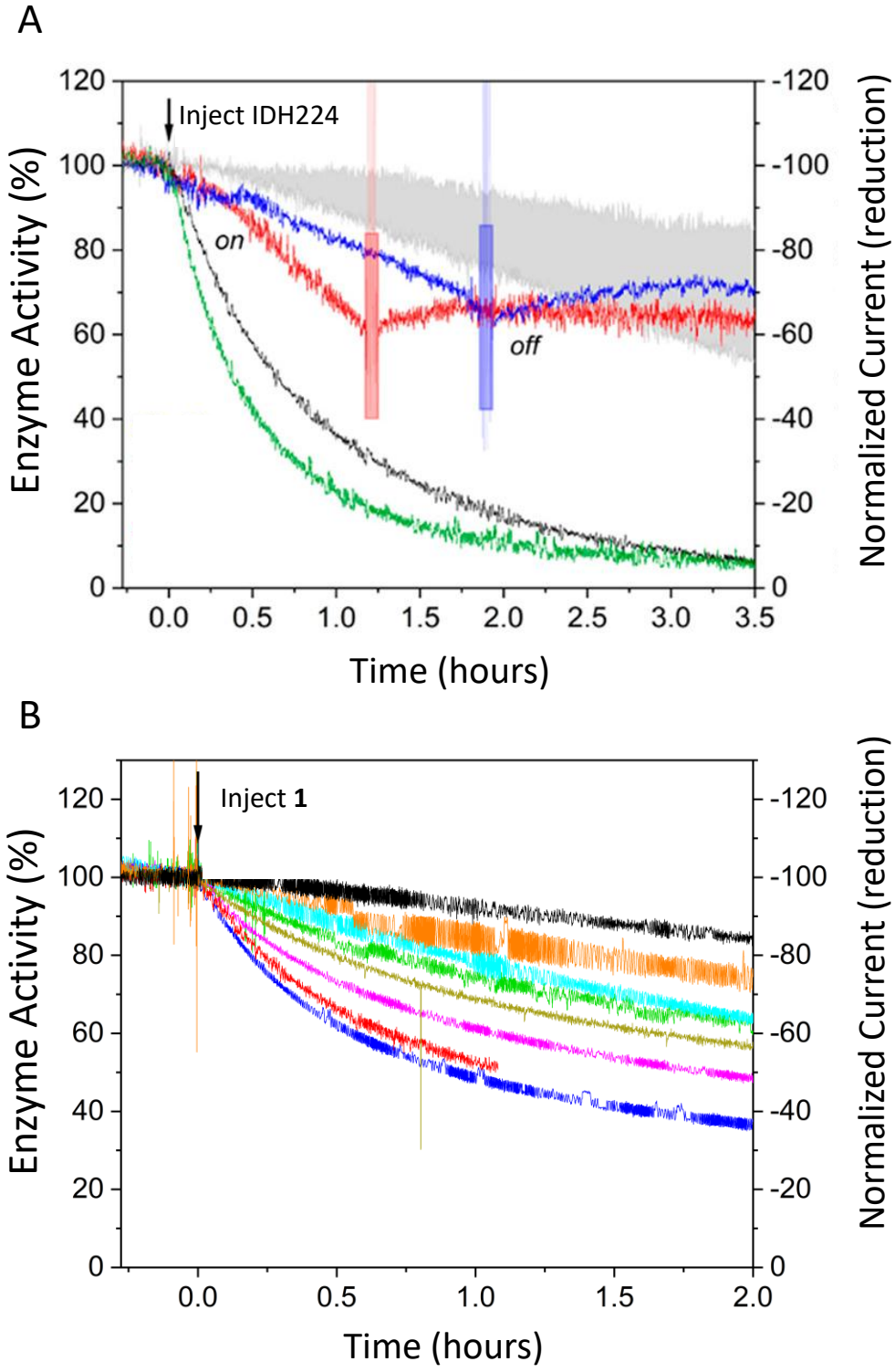

Figure 2.19 | *Chronoamperometry plots of IDH1 R132H activity in the presence of IDH224, and IDH1 WT activity in the presence of* ***1****.* ***A.*** *Different concentrations of IDH224 (0 μM, 50 nM, 100 nM, 1 μM, and 5 μM) reduce the amount of active IDH1 R132H over time. The shaded region shows the range for 3 DMSO controls. Blue (50nM) and red (100 nM) boxes represent the recovery of IDH1 R132H activity by removal of the inhibitor by buffer exchange, in each case demonstrated by a subsequent increase in enzyme activity to a level in line with controls. Conditions: (FNR + IDH1 R132H) @ ITO/PGE electrode, area = 0.06 cm², electrode rotation rate = 1000 rpm temperature = 25 °C, E = −0.513 V vs SHE, O_2 < 1 ppm, reaction buffer = 20 mM MES, 20 mM TAPS, 20 mM CHES, 10 mM $MgCl_2$, 10 μM NADPH, 10 mM 2-OG, pH =*

8, total volume = 4 mL. Enzyme loading molar ratios: FNR:IDH1 R132H = 1:2.5. Inhibitor (various concentrations, 2.5 µL DMSO) was injected at t = 0. ***B.*** *Different concentrations of* ***1*** *(0 µM, 2µM, 5µM, 10µM, 20 µM, 30 µM, 50µM, and 70µM) reduce the amount of active IDH1 WT over time. Conditions: (FNR + IDH1 WT) @ ITO/PGE electrode, electrode area = 0.03 cm^2, electrode rotation rate = 1000 rpm, temperature = 25 °C, E = +0.24 V vs SHE, O_2 < 1 ppm, reaction buffer = 100 mM HEPES, 10 µM NADP$^+$, 150 µM DL-ICT, pH = 8, total volume = 5 mL. Enzyme loading molar ratios: FNR:IDH1 WT = 1:8. Inhibitor (various concentrations, 2.5 µL DMSO) was injected at t = 0. Data in* ***B*** *are not corrected for film loss, pending further wild-type control experiments; correction will cause the time-course data in* ***B*** *to plateau at slightly higher values. Figures adapted with permission from Dr Ryan Herold, under the Creative Commons CC-BY 4.0 license, https://creativecommons.org/licenses/by/4.0.*[323, 325]

The chronoamperometry data from **Figure 2.19.B** was plotted logarithmically according to **Eq. 1**. The resulting plot demonstrated pseudo first-order binding kinetics between IDH1 WT and **1**, similar to the observed binding kinetics of IDH1 R132H and IDH224 (**Figure 2.20**).

Eq. 1

$$\ln\left(\frac{[E]_t-[E]_\infty}{[E]_0-[E]_\infty}\right) = -(k_{obs})t$$

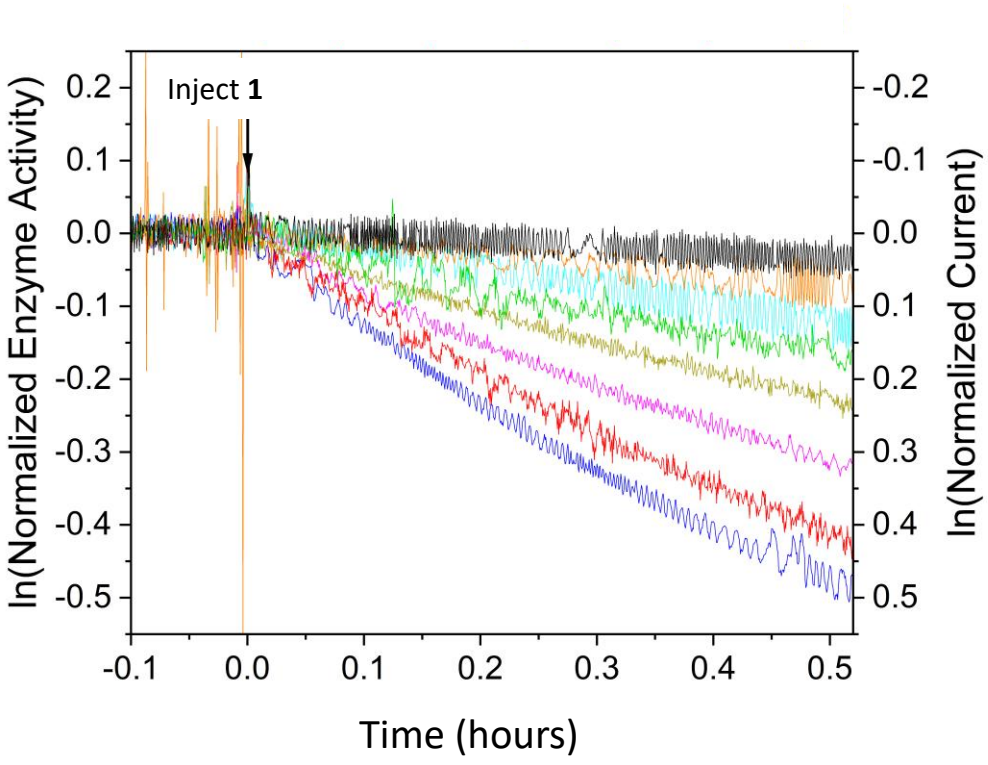

Figure 2.20 *| Chronoamperometry data of IDH1 WT in the presence of* ***1*** *(Control, 2µM, 5µM, 10µM, 20 µM, 30 µM, 50µM, and 70µM) plotted logarithmically according to* ***Eq. 1*** *(without correcting for the equilibrium value in each case). The plot shows pseudo first-order reaction kinetics of inhibition. Conditions: as described in* ***Figure 2.19.B****. Figures adapted with permission from Dr Ryan Herold.*[325]

For low concentrations of **1** (2μM – 20μM), the observed rate constant (k_{obs}) was derived from the gradient of the first 20 minutes (0 hours – 0.33 hours) of data for each concentration shown in **Figure 2.20**, then plotted against [**1**] (**Figure 2.21**). The plot showed a linear relationship that allowed forward (k_{on}) and reverse (k_{off}) rate constants to be deduced (**Figure 2.21**).

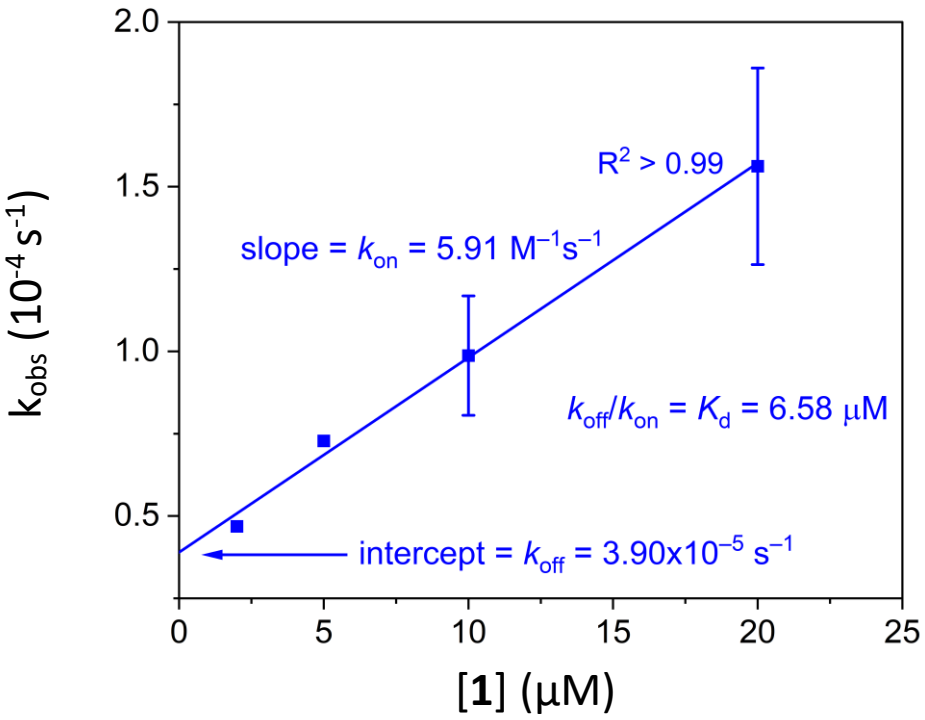

Figure 2.21 *| The observed rate constant (k_{obs}) for inhibition of IDH1 WT by* ***1,*** *plotted using data from the first 20 minutes of* ***Figure 2.20****. The forward rate constant (k_{on}) = slope = 5.91 $M^{-1}s^{-1}$. The reverse rate constant (k_{off}) = intercept = 3.90 x $10^{-5}s^{-1}$. The dissociation constant (K_d) = (k_{off})/(k_{on}) = 6.58 μM. Experiment repeats = 1-3. Figures adapted with permission from Dr Ryan Herold, CC BY 4.0.*[323, 325]

Compound **1** demonstrated substantially lower k_{on} (5.91 $M^{-1}s^{-1}$) and k_{off} (3.90 x 10^{-5} s^{-1}) values than IDH224 (k_{on}= 82 $M^{-1}s^{-1}$, k_{off} = 1.27 x 10^{-4} s^{-1}) (**Figure 2.21**).[325] The k_{off} value for IDH1 WT and **1** corresponds to a dissociation half-time ($t_{1/2}$) of ~5 hours compared to 1.5 hours for IDH224.[325] **1** binds to IDH1 WT in an inhibitory manner more slowly than IDH224 binds to IDH1 R132H, but stays bound roughly 3 times

longer. The resultant dissociation equilibrium constant (K_d) for **1** is ~7 μM, compared to ~1.5 μM for IDH224.

The e-Leaf data from ivosidenib and IDH224 inhibition implied that the observed rate constant ($k_{\mathrm{obs}}{}'$) exhibits a hyperbolic dependence on the concentration of inhibitor according to **Eq. 2**.[325] The activity of IDH1 WT and concomitant inhibition by **1** plateaus at high concentrations of inhibitor, as seen in the chronoamperometry data and the plot of k_{obs} against [**1**] (**Figure 2.19**, **Figure 2.22**). The similarities between the data for the inhibition of IDH1 R132H by IDH224, and IDH1 WT by **1** (**Figure 2.19**), suggest that the inhibitors share similar kinetic mechanisms of action (**Figure 2.17**).

Eq. 2

$$k_{\mathrm{obs}}{}' = \frac{a[1]}{b + [1]}$$

Utilising **Eq. 3**, $\frac{1}{(k_{\mathrm{obs}} - k_{\mathrm{off}})}$ can be plotted against $\frac{1}{[1]}$ to deduce the rate constant for the intramolecular isomerization reaction ($k_{\mathrm{on}}^{\mathrm{trans}}$) at the y-axis intercept and the dissociation constant for the pre-equilibrium enzyme-inhibitor complex (K_d^{pre}) at the x-axis intercept (**Figure 2.22**).

Eq. 3

$$\frac{1}{(k_{\mathrm{obs}} - k_{\mathrm{off}})} = \frac{1}{k_{\mathrm{on}}^{\mathrm{trans}}} + \frac{\mathrm{K}_d^{pre}}{k_{\mathrm{on}}^{\mathrm{trans}}} \cdot \frac{1}{[1]}$$

The non-inhibitory IDH1 WT-**1** complex is less stable ($\mathrm{K}_d^{pre} = 57.7\ \mu M$) than the IDH1 R132H-ivosidenib or IDH1 R132H-IDH224 complexes ($\mathrm{K}_d^{pre} =$ ~1.6 μM for both) (**Figure 2.22**). In addition, IDH1 WT and **1** in equilibrium ($k_{\mathrm{on}}^{\mathrm{trans}} = 4.3 \times 10^{-4} s^{-1}$) take ~16 times longer than IDH1 R132H and ivosidenib to form the inhibited open-inactive conformation ($t_{1/2}$ = ~27 minutes cf. 100 seconds) (**Figure 2.22**). The notable

difference can be clearly seen by plotting k_{obs} against [**1**] for IDH1 WT, and k_{obs} against [ivosidenib] for IDH1 R132H, on the same axes (**Figure 2.23**).

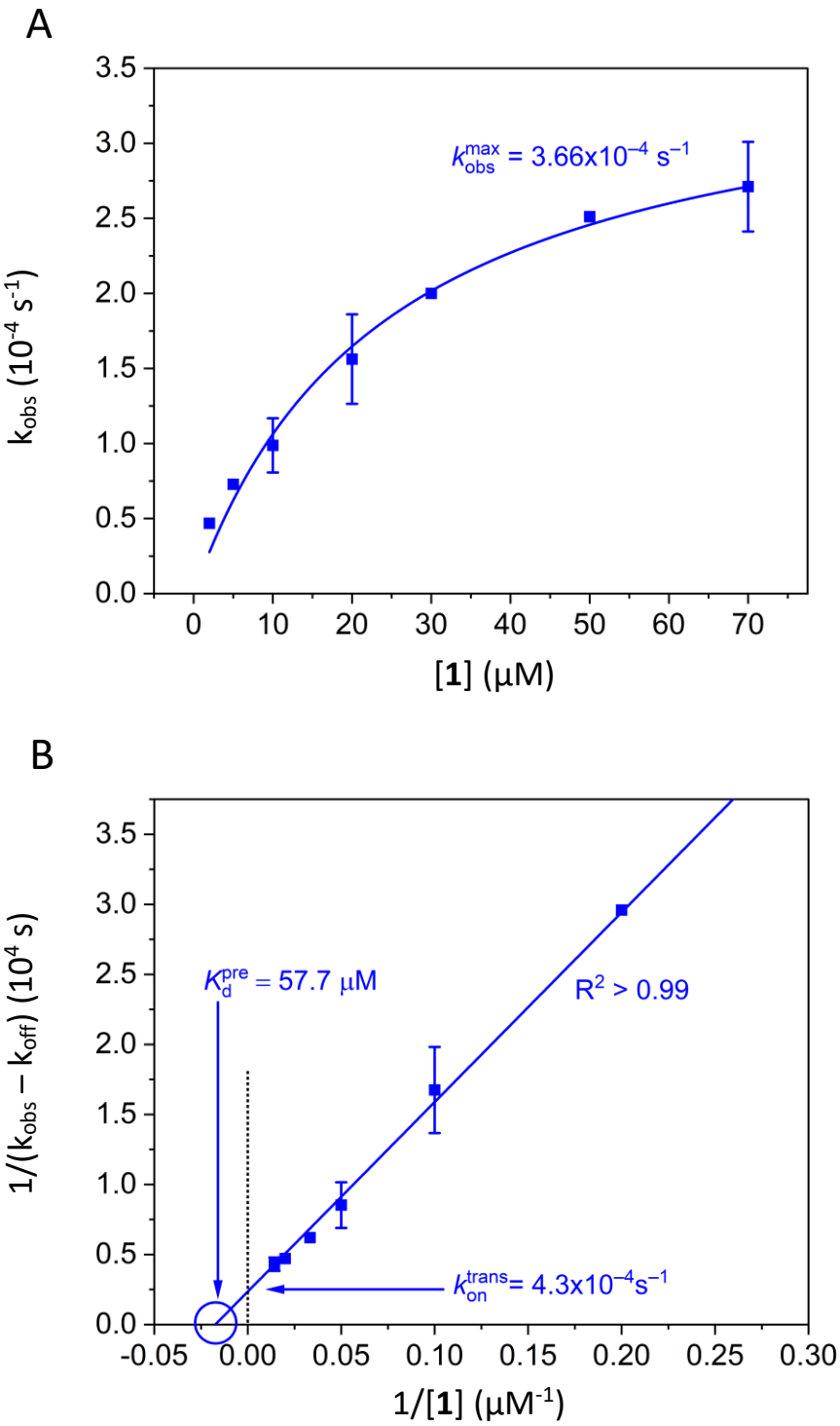

Figure 2.22 | *Data supporting the proposal that **1** likely shares a similar two-step binding-inhibition mechanism with ivosidenib and IDH224 (**Figure 2.17**). **A.** Extended k_{obs} plot from **Figure 2.21** showing a hyperbolic dependence of the rate of inhibition on the concentration of **1** according to **Eq. 2**. Experimental*

repeats, n = 1-3. ***B.*** *Data from panel* ***A*** *plotted according to* ***Eq. 3*** *to obtain k_{on}^{trans} and K_d^{pre} values. Figures adapted with permission from Dr Ryan Herold.*[325]

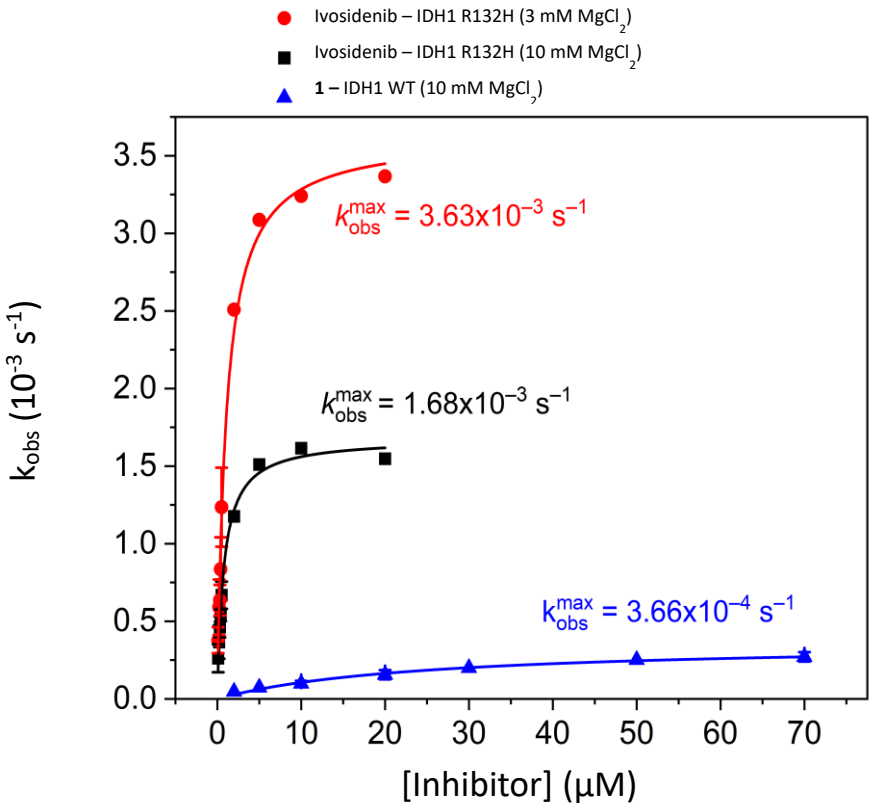

Figure 2.23 | *Comparison of the observed rate constants (k_{obs}) values for* ***1*** *and ivosidenib against IDH1 WT and IDH1 R132H. The observed rate constant (k_{obs}) values for the inhibition of IDH1 WT (blue) by* ***1*** *are plotted from* ***Figure 2.22. A****. The observed rate constant (k_{obs}) values for inhibition of IDH1 R132H by ivosidenib are given for [Mg^{2+}] = 3mM (red) and [Mg^{2+}] = 10mM (black). See* ***Figure 2.19*** *for conditions of IDH1 WT and* ***1****. Figure adapted with permission from Dr Ryan Herold.*[325]

The incubation of IDH1 WT with **1** before reaction initiation appears to lead to superior inhibition compared to the introduction of **1** after IDH1 WT has initiated the catalytic cycle. Even considering a K_d value (~7 μM) higher than the measured IC_{50} value (6 nM), concentrations up to 20 μM failed to achieve 50% inhibition. This is clearly different from ivosidenib which inhibits up to 100% at concentrations around the K_d value (~1.6 μM).[325] As previously proposed, this suggests that binding does not necessitate inhibition.[249]

One explanation for the difference in potencies between ivosidenib and **1** when introduced to a steady-state reaction could be that there is a different mechanism of

inhibition for ivosidenib and **1**. On the basis of reported crystallography studies, only 1 molecule of ivosidenib (an analogue of AGI-5198) is proposed to bind to IDH1 R132H, compared to 2 molecules of IDH224 (a partial structural analogue of **1**).[251, 302] In this case, binding of a single inhibitory molecule of **1** to IDH1 WT may be insufficient. A second molecule may be required to achieve complete inhibition. The IC_{50} value for inhibition of IDH1 WT by **1** suggests that this is unlikely because of the robust data showing 100% inhibition at close to stoichiometric concentrations of enzyme (4 nM) and inhibitor (6 nM), after 12 minute incubations. Assuming that the proposed outline for the kinetic mechanism of inhibition may be accurate (**Figure 2.17**), there is an alternative possible explanation for the difference in measured potencies of ivosidenib and **1** under e-Leaf conditions, as discussed in **Section 2.5.4**.[325]

2.5.3. The Inhibition of IDH1 WT by 1 Under Turnover Conditions Using NADPH Absorbance-based Assays in Solution

A key consideration for the comparison of solution IC_{50} assays with experiments conducted by the e-Leaf method is the reaction environment. The e-Leaf drives enzyme activity in a nano-confined space. [323] NADPH absorbance-based assays contain enzyme which is free in solution.[323] Solution experiments were thus conducted to investigate the effects of injecting **1** into reaction mixtures containing IDH1 WT after the reactions had been initiated , as measured by NADPH absorbance. For solution experiments, the concentration of IDH1 WT was reduced (250 pM) compared to the concentration of IDH1 WT utilised for IC_{50} measurement (4.5 nM). The concentration IDH1 WT was reduced in this way to slow the rate of NADPH production, extending the linear region of a graph of absorbance plotted against time. A linear region of a plot of absorbance against time facilitates the calculation of kinetic parameters under pseudo-first order

conditions. IDH1 WT was injected into a reaction mixture containing buffer (100mM Tris, 0.2mM DTT, pH 8.0), DL-ICT (150 μM) and $NADP^+$ (75 μM). The rate of increase of absorbance was allowed to linearise (3-5 minutes) before compound **1** was injected into a reaction mixture.

Compound **1** was injected at a range of final concentrations (0.1 μM, 1 μM, 5 μM, 10 μM, 25 μM, 50μM, 100 μM) into reaction mixtures containing either 1mM $MgCl_2$ (**Figure 2.24.A**), or 10 mM $MgCl_2$ (**Figure 2.24.B**). 10 mM $MgCl_2$ was chosen to enable comparisons with the previous e-Leaf experiments and IC_{50} experiments. 1 mM $MgCl_2$ was chosen as a closer approximation of the reported concentration of magnesium in astrocytic cytosol (~125 μM) and cerebrospinal fluid (CSF, ~900 μM).[326, 327] In one of the reactions containing 1 mM $MgCl_2$, compound **1** (0.1 μM) was pre-incubated with IDH1 WT for 12 minutes to enable a comparison in the absence of reported IC_{50} data. The reactions were monitored for 1 hour, then the measured absorbance was plotted against time (**Figure 2.24**).

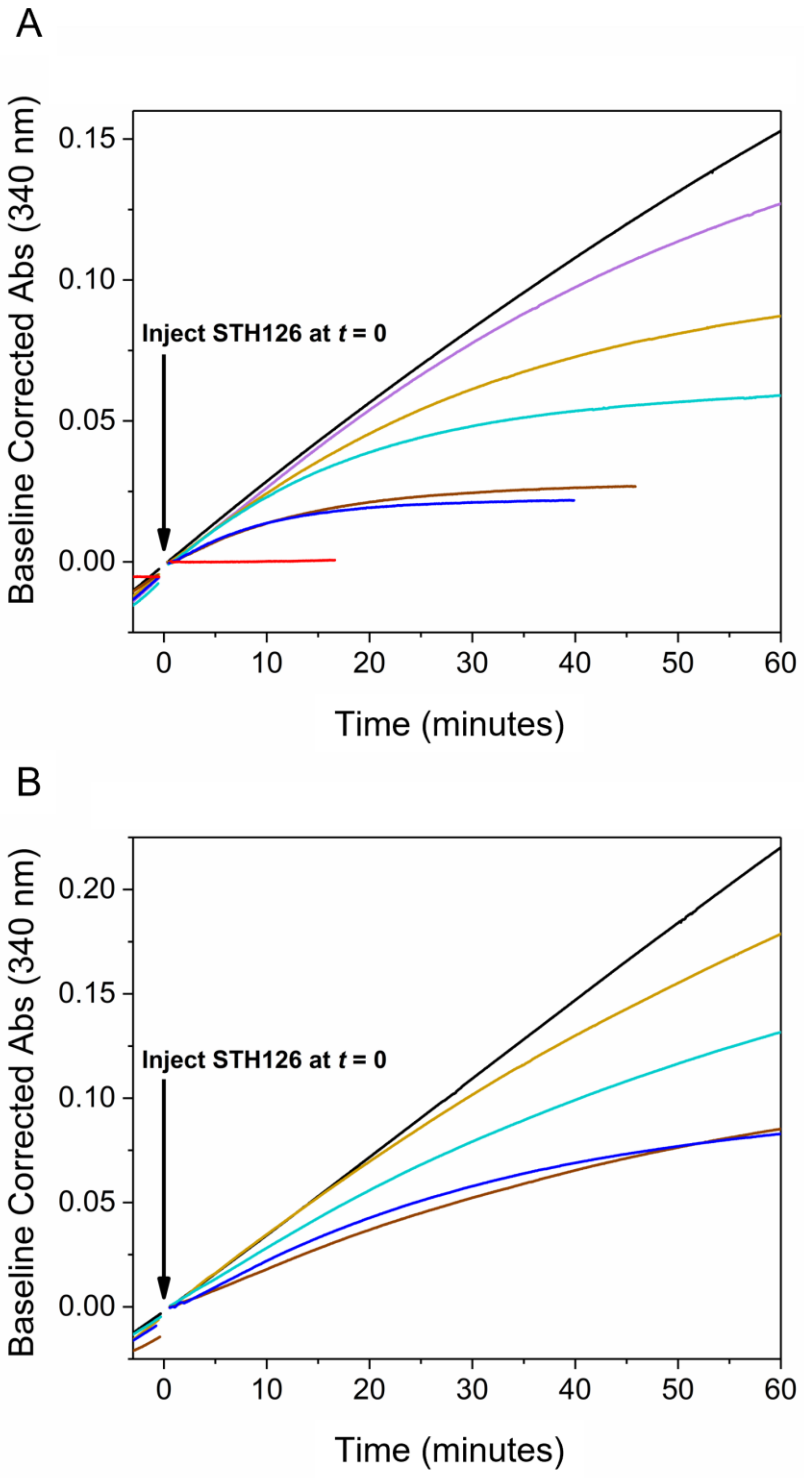

Figure 2.24 *| Plots of NADPH absorbance (340 nM) over time from reactions containing IDH1 WT (250 pM) and compound* ***1*** *(0 μM, 0.1 μM, 5 μM, 10 μM, 25 μM, 50 μM, 100 μM). Conditions: 100 mM Tris, 0.2 mM DTT, pH 8.0, 150 μM DL-ICT, and 75 μM* $NADP^+$*.* ***A.*** *Conditions: 1 mM* $MgCl_2$*.* ***B.*** *Conditions: 10 mM* $MgCl_2$*. Note that the plots for concentrations of compound* ***1*** *below 10 μM at 1 mM* $MgCl_2$ *(****A****), and below 5 μM at 10 mM* $MgCl_2$ *(****B****), could not be differentiated from noise and are omitted for clarity.*

The fraction of IDH1 WT activity was deduced by calculating the gradient of the curve at a given timepoint. The fraction of IDH1 WT activity was interpreted as the

concentration of active IDH1 WT (**Figure 2.25**). As expected, compound **1** (0.1 μM) completely inhibited IDH1 WT after 12 minutes of pre-incubation in the presence of 1 mM $MgCl_2$. The potent inhibition measured in the presence of 1 mM $MgCl_2$ (0.1 μM, 100% inhibition) supports the low IC_{50} value (6 nM) measured in the presence of 10 mM $MgCl_2$ and the proposal that inhibition occurs rapidly in the absence of substrate (**Figure 2.25.A**). For reactions without pre-incubation, the observed inhibition was reduced, supporting the observations of the previous e-Leaf experiments (**Section 2.5.2**). 30 minutes after the delayed injection of inhibitor, the fraction of active IDH1 WT activity was ~65% in the presence of 5 μM **1**, and ~5% in the presence of 100 μM **1** ([$MgCl_2$] = 1 mM, **Figure 2.25.A**). At a higher $MgCl_2$ concentration (10 mM cf. 1 mM), the plot of the concentration of normalized active IDH1 WT against time was comparable to the corresponding e-Leaf experiment (**Figure 2.25.B** cf. **Figure 2.19.B**). 30 minutes after the delayed injection of inhibitor, the measured fraction of IDH1 WT activity in the presence of **1** (100 μM) and 10 mM $MgCl_2$ was ~40% in the NADPH absorbance assay (cf. ~55% in the e-Leaf experiment, **Figure 2.25.B**). The plots of the normalised concentration of active IDH1 WT against time displayed greater inhibition by **1** in the presence of 1 mM $MgCl_2$ than 10 mM $MgCl_2$.

The results described here support the proposed mechanism of allosteric inhibition competitive with respect to magnesium ions (**Figure 2.17**).[125, 249] Nonetheless, the concentration of **1** (100 μM) required to approximate 100% inhibition in the presence of 1 mM $MgCl_2$ after 30 minutes was three orders of magnitude greater than a sufficient concentration (0.1 μM) under pre-incubation conditions. The plots of absorbance against time could not be differentiated from noise due to the low levels of inhibition for a moderate concentration of **1** (5 μM) in the presence of 10 mM $MgCl_2$, and low

concentrations of **1** (0.1 µM, 1 µM) in the presence of either 1 mM $MgCl_2$ or 10 mM $MgCl_2$ (**Figure 2.24**).

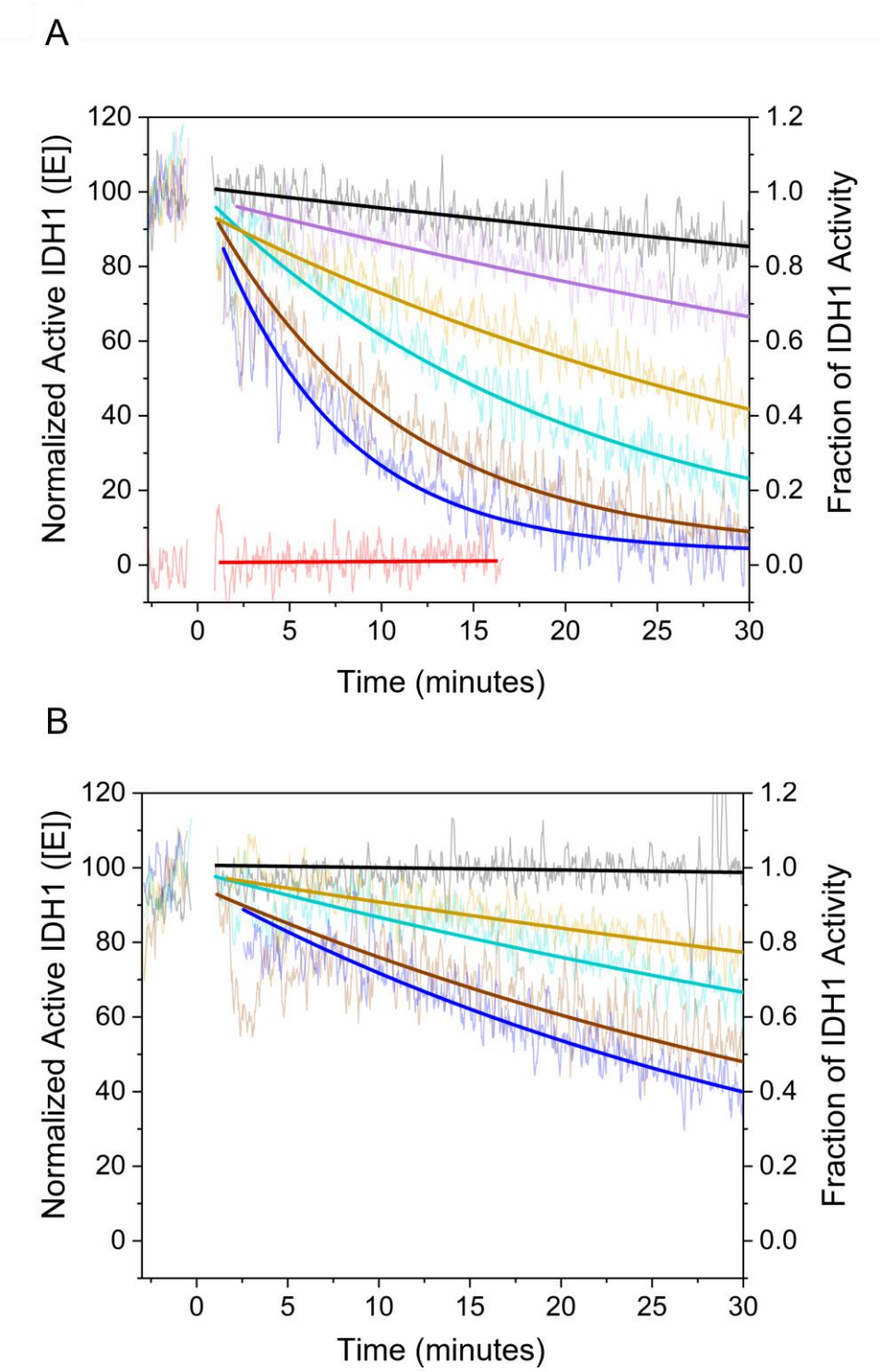

Figure 2.25 | *Plots of the normalised concentration of active IDH1 WT (fraction of IDH1 WT activity) against time from reactions containing IDH1 WT (250 pM) and compound **1** (control, 0.1 µM, 5 µM, 10 µM, 25 µM, 50 µM, 100 µM). The fraction of IDH1 WT activity for each reaction was calculated using the data*

*shown in **Figure 2.24**. Conditions: 100 mM Tris, 0.2 mM DTT, pH 8.0, DL-ICT (150 μM), and $NADP^+$ (75 μM). **A.** Conditions: 1 mM $MgCl_2$. **B.** Conditions: 10 mM $MgCl_2$.*

The observed rate constant (k_{obs}) was plotted for concentrations of **1** ≤ 50 μM in the presence of 1 mM $MgCl_2$ (**Figure 2.26.A**) and 10 mM $MgCl_2$ (**Figure 2.26.B**). The measured k_{off} values in the presence of 1 mM $MgCl_2$ (8.2 x 10^{-5} s^{-1}) and 10 mM $MgCl_2$ (7.6 x 10^{-5} s^{-1}) appeared to agree (**Figure 2.26**), supporting the proposed mechanism that inhibitor dissociation is magnesium ion independent (**Figure 2.17**). Therefore, the measured k_{off} values for **1** and IDH1 WT in the presence of 1 mM $MgCl_2$ (8.2 x 10^{-5} s^{-1}) and 10 mM $MgCl_2$ (7.6 x 10^{-5} s^{-1}) were averaged (avg k_{off} = 7.9 x 10^{-5} s^{-1}) to represent the proposed shared mechanism of magnesium-independent inhibitor dissociation. The plots from **Figure 2.26** with were then overlaid using the new y-intercept (avg k_{off}) (**Figure 2.27**).

The measured k_{on} of IDH1 WT and **1** was higher in the presence of 1 mM $MgCl_2$ (30.8 M^{-1} s^{-1}, **Figure 2.26.A**, **Figure 2.27**) than with 10 mM $MgCl_2$ (5.6 M^{-1} s^{-1}, **Figure 2.26.B**, **Figure 2.27**), supporting the proposed mechanism that inhibition is competitive with respect to magnesium (**Figure 2.17**). The measured k_{on} of IDH1 WT and **1** at 10 mM $MgCl_2$ (5.6 M^{-1} s^{-1}, **Figure 2.26.B**, **Figure 2.27**) agrees with the measured k_{on} from the e-Leaf experiment (5.91 M^{-1} s^{-1}, in the presence of 10 mM $MgCl_2$, **Figure 2.21**). The calculated avg k_{off} in the presence of either 10 mM $MgCl_2$ or 1 mM $MgCl_2$ (7.9 x 10^{-5} s^{-1}, **Figure 2.27**), was also similar to the measured k_{off} from the e-Leaf experiment (3.9 x 10^{-5} s^{-1}, **Figure 2.21**). The resulting K_d values were 2.6 μM in the presence of 1 mM $MgCl_2$, and 14.1 μM in the presence of 10 mM $MgCl_2$ (**Figure 2.27**, cf. 6.58 μM in the presence of 10 mM $MgCl_2$ in the e-Leaf experiment, **Figure 2.21**).

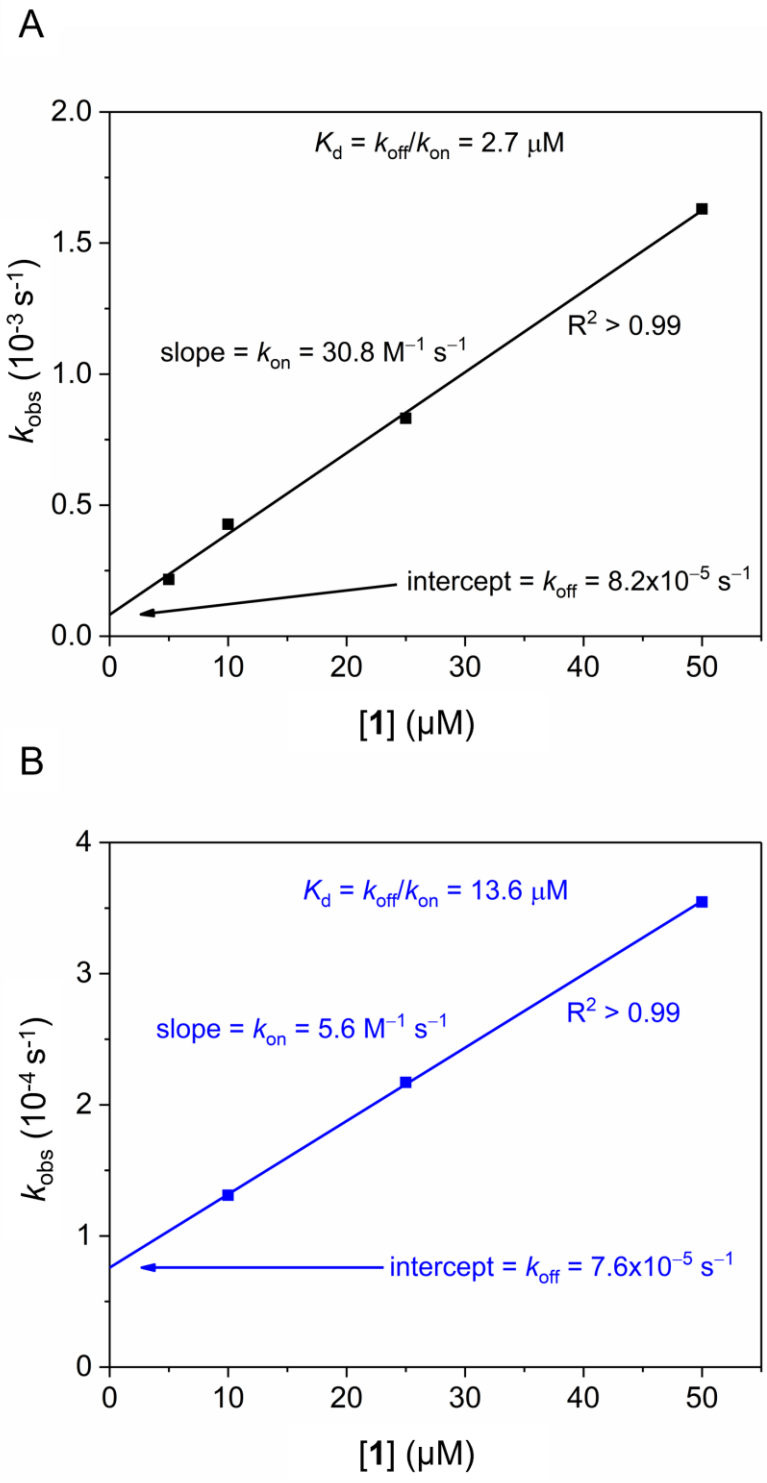

Figure 2.26 | *The observed rate constant (k_{obs}) plotted against [**1**] for inhibition of IDH1 WT by **1**. (k_{obs}) values were derived in the same manner as **Figure 2.21. A.** Conditions: 1 mM $MgCl_2$. The forward rate constant (k_{on}) = slope = 30.8 $M^{-1}s^{-1}$. The reverse rate constant (k_{off}) = intercept = 8.2 x 10^{-5} s^{-1}. The dissociation constant (K_d) = (k_{off})/(k_{on}) = 2.7 μM. **B.** Conditions: 10 mM $MgCl_2$. The forward rate constant (k_{on}) = slope = 5.6 $M^{-1}s^{1}$. The reverse rate constant (k_{off}) = intercept = 7.6 x 10^{-5} s^{-1}. The dissociation constant (K_d) = (k_{off})/(k_{on}) = 13.6 μM.*

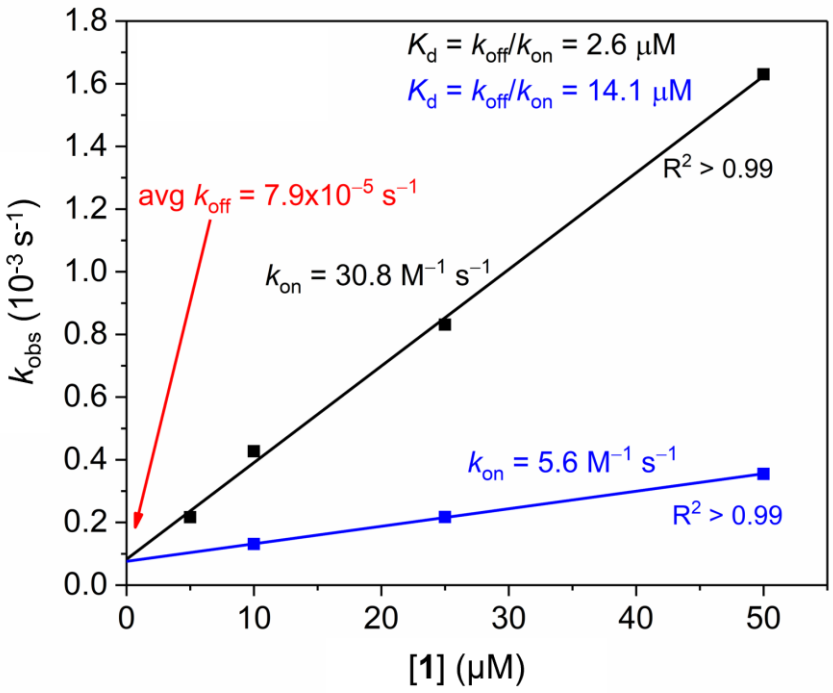

***Figure 2.27** | Overlaid plots of (k_{obs}) against [1] from **Figure 2.26**. The values of (k_{off}) from **Figure 2.26** were averaged, and the output was defined as the common y-intercept for both plots. 1 mM $MgCl_2$ (black): The forward rate constant (k_{on}) = slope = 30.8 $M^{-1}s^{-1}$. The (new) reverse rate constant (k_{off}) = intercept = 8.2 x 10^{-5} s^{-1}. The (new) dissociation constant (K_d) = (k_{off})/(k_{on}) = 2.6 µM (cf. 2.7 µM). 10 mM $MgCl_2$ (blue): The forward rate constant (k_{on}) = slope = 5.6 $M^{-1}s^{-1}$. The (new) reverse rate constant (k_{off}) = intercept = 7.9 x 10^{-5} s^{-1}. The (new) dissociation constant (K_d) = (k_{off})/(k_{on}) = 14.1 µM.*

The overall findings of the NADPH absorbance-based investigation into IDH1 WT inhibition under solution conditions appear to support the initial findings of the e-LEAF experiments (**Section 2.5.2**). In the presence of the same concentration of $MgCl_2$ (10 mM), the rate constants for association (k_{on} = 5.6 M^{-1} s^{-1}, **Figure 2.27**, cf. 5.91 M^{-1} s^{-1}, **Figure 2.21**) and dissociation (avg k_{off} = 7.9 x 10^{-5} s^{-1}, **Figure 2.27**, cf. 3.9 x 10^{-5} s^{-1}, **Figure 2.21**), and the equilibrium constant for dissociation (K_d = 14.1 µM, **Figure 2.27**, cf. 6.58 µM, **Figure 2.21**), are comparable between the e-Leaf and NADPH absorbance-based experiments. The findings of the NADPH absorbance-based assay also appear to support the proposed kinetic model of indirect competitive inhibition with respect to magnesium, and the magnesium-independent dissociation of the inhibitor

(**Figure 2.17**). The rate constant for association was higher in the presence of 1 mM $MgCl_2$ than 10 mM $MgCl_2$ (k_{on} = 30.8 M^{-1} s^{-1}, **Figure 2.26.A**, cf. 5.6 M^{-1} s^{-1}, **Figure 2.26.B**), and the rate constant for dissociation was approximately the same in 1mM $MgCl_2$ and 10 mM $MgCl_2$ (k_{off} = 7.6 x 10^{-5} s^{-1}, **Figure 2.26.A**, cf. 8.2 x 10^{-5} s^{-1}, **Figure 2.26.B**). Accordingly, the equilibrium constant for dissociation was lower in the presence of 1 mM $MgCl_2$ than 10 mM $MgCl_2$ (K_d = 2.7 μM, **Figure 2.26.A**, cf. 13.6 μM, **Figure 2.26.B**).

2.5.4. Discussion of IDH1 WT Inhibition Under Turnover Conditions

IDH1 WT and IDH1 R132H exhibit differences at the allosteric inhibitor binding pocket at the IDH1-IDH1 homodimer interface.[328] Changes in the conformation of the enzyme due to the R132H mutation are suggested to be the basis for an observed reduction in the affinity for Mg^{2+}.[125] The new active site geometries in IDH1 R132H enable the reduction of 2-OG to 2-HG.[16, 125] These conformational changes also likely affect the topology of the allosteric binding pocket, putatively conveyed by a shift in the position of the dimer-interface/active-site/magnesium binding site spanning α-10 regulatory segment.[328] Differences in the topology of the allosteric binding pocket may drive the selectivity of clinically approved IDH1 inhibitors for IDH1 mutants over IDH1 WT.[328] The approved allosteric inhibitors are competitive with respect to Mg^{2+}.[125] In the proposed kinetic binding mechanism, once inhibitor is bound, inhibition relies on the exit of Mg^{2+} from the active site and the enzyme to shift to the open-active conformation.[249] Upon shifting conformations, the enzyme is trapped in the open-inactive conformation until the inhibitor dissociates (**Figure 2.17**).[325] The lower affinity of IDH1 R132H for Mg^{2+} (K_m = 4.4 mM, reduction of 2-OG) results in the slower binding and earlier dissociation of Mg^{2+} from the active site.[125] The variant enzyme spends longer periods without

magnesium and substrate, increasing the likelihood that any enzyme with inhibitor already bound will isomerise to the open-inactive conformation and become inhibited.

In IDH1 WT, the substrate is the ICT-Mg^{2+} complex, and the affinities for Mg^{2+} (K_m = 36 μM, oxidation of ICT,) and ICT (K_m = 38 μM, oxidation of ICT) are over 100-fold greater than Mg^{2+} in IDH1 R132H, where it might bind alone.[125] Indeed, the ICT-Mg^{2+} substrate complex binds IDH1 WT tightly, while 2-OG and Mg^{2+} bind weakly and likely separately. IDH1 WT will be without substrates and co-factors less often than IDH1 R132H, affording a shorter window of opportunity in which the open-inactive conformation may form if inhibitor is bound. This does not prevent the rapid initial binding of inhibitor to IDH1 WT, and this is likely represented by the potent IC_{50} value (IC_{50} = 6 nM). Note the presence of Mg^{2+} in the reaction buffer will not prevent the conformational isomerisation of the enzyme without the presence of ICT. During the pre-incubation period, it is likely that the purified enzyme is at least partly in the open-inactive conformation; the inhibitor can bind and trap the enzyme in the open-inactive conformation for the duration of the assay (k_{off} = 3.90 x $10^{-5}s^{-1}$, $t_{1/2}$ = ~5 hours). While this effect applies to both IDH1 WT and IDH1 R132H, the 100-fold difference in affinities for Mg^{2+} (as part of ICT-Mg^{2+}) results in the isomerisation and concomitant inhibition of many fewer IDH1 WT-inhibitor complexes.

2.6. Quaternary Ammonium Ions as Ligands of Mutant IDH1

A consequence of R132H substitution in IDH1 is the neomorphic formation of 2-HG, along with decreased production of NADPH.[16] The IDH variants also conduct the WT IDH reaction, albeit at a reduced rate.[125] A dominant negative mechanism of inhibition of IDH1 WT by IDH1 R132H in WT/R132H heterodimers is proposed to result in ~25% of IDH1 dimers maintaining WT catalytic activity.[121, 329, 330] The restoration of

physiological catalytic activity in IDH1 R132H may therefore have a positive effect on the (local) concentration of NADPH within cells, which may supersede the effect of IDH1 R132H inhibition. A strategy was proposed to promote WT catalytic activity in IDH1 R132H monomers.

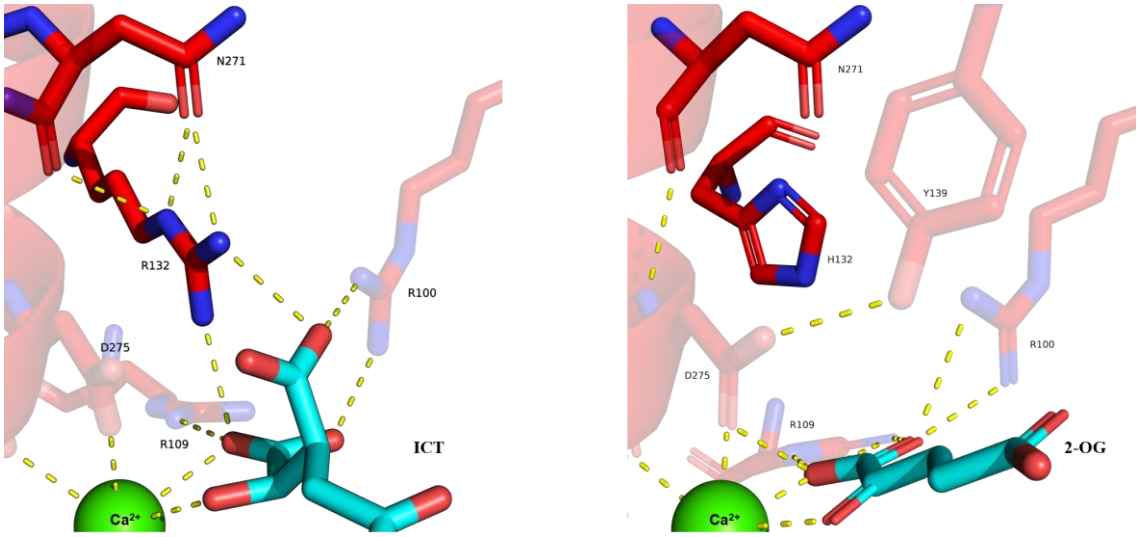

Figure 2.28 | ***A.*** *A view of the IDH1 WT active site with polar interactions between residues R132 and N271 depicted (pdb: 1T0L).*[122] *Note that R132 exhibits polar interactions with N271 and ICT.* ***B.*** *A view of the IDH1 R132H active site with residues H132 and N271 depicted (pdb: 4KZO).*[128] *Note that H132 does not sustain polar interactions with N271, and Y139 has moved to form a polar interaction with D275 (**Chapter 1**, **Section 1.4.3**).*

A recent study by Xie et al. suggested that the loss of a R132-N271 charge-charge interaction underpins the conformational change between the active site and the α10 helix that reduces Mg^{2+} affinity and enables 2-HG production (**Figure 2.28**).[328] Monovalent quaternary ammonium ions, including the tetraethylammonium ion, can replace Mg^{2+} and maintain proton-pumping ability in bacteriorhodopsin (**Figure 2.29**).[331] Trimethylamine *N*-oxide (TMAO) is a quaternary ammonium ion, produced in the human body by the oxidation of trimethylamine.[332, 333] Although neutral, TMAO stabilises compact conformations of proteins and counteracts the unfolding effects of urea *in vitro* (**Figure 2.29**).[332, 333] If TMAO or tetraethylammonium were to induce activity in IDH1 R132H in the absence of magnesium, it would suggest that some quaternary ammonium ions could

act as a functional replacement for magnesium in IDH1 R132H. IDH variant inhibition by TMAO or tetraethylammonium may suggest that quaternary ammonium ions are able to occupy the magnesium binding site, warranting further investigation. Therefore, following adapted procedures for the screening of IDH1 variant inhibitors (10 μM) using an NADPH absorbance-based assay, TMAO and tetraethylammonium chloride (TEAC) were screened (10μM) against IDH1 R132H in the presence and absence of magnesium, and in conditions for oxidation of ICT and reduction of 2-OG. [334]

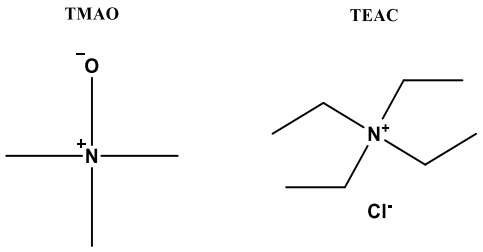

Figure 2.29 | *Chemical structures of trimethylamine n-oxide (TMAO) and tetraethylammonium chloride (TEAC).*

2.6.1. Effect of Trimethylamine-*N*-oxide and Tetraethylammonium ions on IDH1 R132H

In the absence of magnesium, TMAO and TEAC were not found to cause an increase in activity of R132H for either the WT or variant reaction, as measured by the NADPH absorbance assay (**Figure 2.30**). IDH1 R132H did not exhibit ICT oxidation in the absence of magnesium, consistent with prior reports, and neither TMAO nor TEAC were able to recapture this capability.[125] Similarly, IDH1 R132H exhibits a very low level of activity (~7%) for the reduction of 2-OG in the absence of magnesium, which was not significantly altered by TMAO (~8%) or TEAC (~7%). In combination, these results suggested that quaternary ammonium ions may not be a promising route to promote activity in IDH1 R132H. Additionally, the screened concentration of TMAO and TEAC (10 μM) was substantially lower than concentrations used in fragment-based screening

(up to 2 mM); considering the small size of TMAO and TEAC, future work should screen higher concentrations (>200 µM) to confidently rule out any low-affinity or transient interactions. [335]

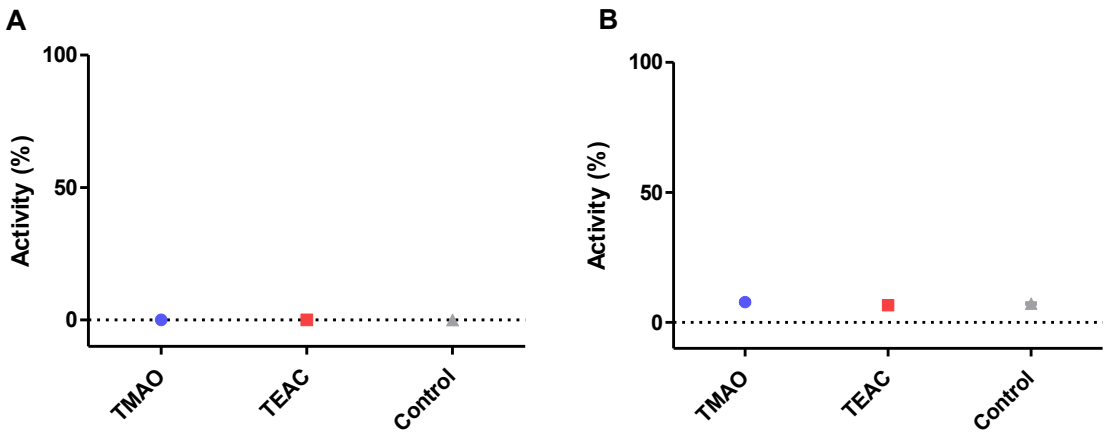

Figure 2.30 *| Activity of IDH1 R132H (400 nM) performing the oxidation of ICT or reduction of 2-OG in the absence of Mg^{2+}, and in the presence of TMAO or TEAC (10 µM). Error bars: standard error of the mean (technical replicates = 16).* ***A.*** *Oxidation of ICT (1.5 mM) and reduction of $NADP^+$ (300 µM).* ***B.*** *Reduction of 2-OG (1.5 mM) and oxidation of NADPH (300 µM). Buffer: 100 mM Tris, 0.2 mM DTT, 0.005% (v/v) Tween-20, 0.1 mg/mL BSA, pH 8.0.*

2.6.2. Inhibition of IDH1 R132H by Compounds Containing Quaternary Ammonium Ions

To investigate if quaternary ammonium ions could nonetheless interfere with the magnesium-dependent activity of the enzyme, IDH1 R132H was then incubated with TMAO and TEAC in the presence of magnesium. Inhibition of the oxidation of ICT by TMAO (~3%) and TEAC (~6%) was marginal, if any, however the inhibition of IDH1 R132H catalysed reduction of 2-OG by TMAO (~16%) and TEAC (~8%) was slightly more pronounced (**Figure 2.31**). Considering R132H has a higher affinity for ICT (K_M = 257 µM) than 2-OG (K_M = 652 µM)[125], a mechanism of competitive inhibition could explain why the oxidation of ICT was less affected by TMAO and TEAC. As mentioned previously, future work should also screen higher concentrations of TMAO and TEAC

(>200 μM) to elucidate any weak interactions that may be overlooked at lower concentrations (e.g., 10 μM). Nonetheless, increasing the IDH1 R132H affinity of a quaternary ammonium ion by employing a structural backbone mimicking aspects of 2-OG may lead to superior inhibitor of IDH1 R132H.

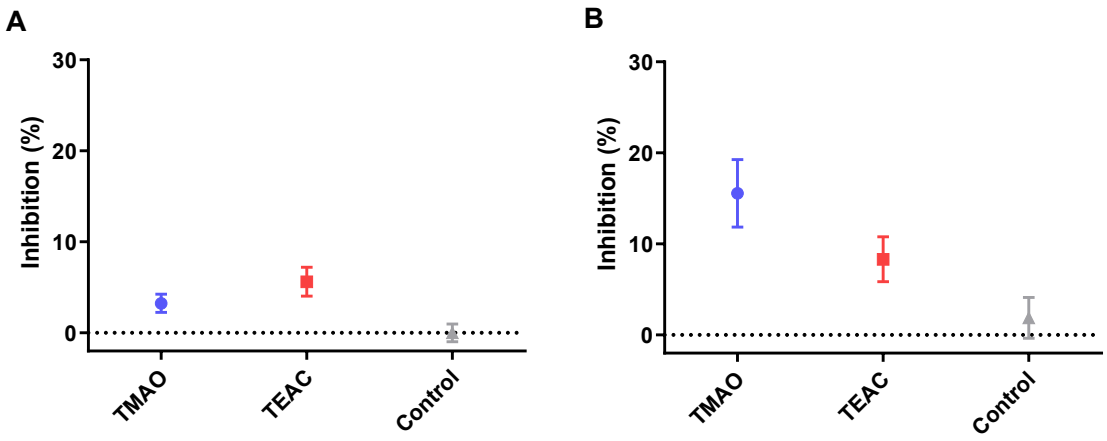

Figure 2.31 *| Inhibition of IDH1 R132H (400 nM) performing the oxidation of ICT or reduction of 2-OG in the presence of TMAO or TEAC (10 μM). Error bars: standard error of the mean (technical replicates = 16).* ***A.*** *Oxidation of ICT (1.5 mM) and reduction of* $NADP^+$ *(300 μM).* ***B.*** *Reduction of 2-OG (1.5 mM) and oxidation of NADPH (300 μM). Buffer: 100 mM Tris, 10 mM* $MgCl_2$*, 0.2 mM DTT, 0.005% (v/v) Tween-20, 0.1 mg/mL BSA, pH 8.0.*

To test this hypothesis, seven compounds containing quaternary ammonium ions and of a similar size to 2-OG were kindly provided by Dr Shyam Basak (Department of Chemistry, University of Oxford) (**Figure 2.32**). The compounds were screened (10 μM) for inhibition against IDH1 R132H in the presence of magnesium. SB11, SB15, SB17, SB18, and SB53 contain a quaternary ammonium ion and a carboxylic acid group separated by three atoms, similar to the structure of 2-OG which contains two carboxylic acid groups separated by three carbon atoms. Variations included a sulfonic acid group instead of a carboxylic acid in the backbone of SB12, a four carbon atom chain between the ammonium ion and carboxylic acid of SB69, a double bond at the C2 position of SB17, a methyl group at the C4 of SB11, an ethyl substituent at the N5 of SB15, an allyl

substituent at N5 of SB18, and an additional methylated nitrogen (N4) in the backbone of SB53.

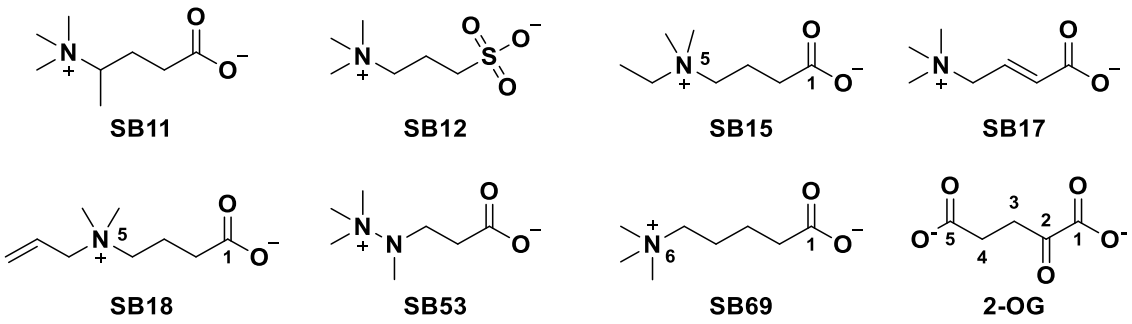

Figure 2.32 | *The structures of the compounds containing quaternary ammonium ions, SB11-SB69, and 2-OG for comparison.*

The inhibitory activity of quaternary ammonium ion-containing compounds against IDH1 R132H was poor (**Figure 2.33**). Compounds that did not have an unbranched three carbon linker between the acid group and quaternary ammonium ion exhibited very low, if any, inhibition, namely SB11 (~3%), SB53 (~2%), SB69 (~0%). The sulfonic acid SB12 (~21%), ethyl substituted ammonium SB15 (~17%), and alkene SB17 (~16%) also inhibited poorly, but less so. The backbones of SB15 (~17%) and SB69 (~0%) are eight atoms long and differ only in the position of the nitrogen atom, N5 and N6 respectively. This is sufficient to reduce inhibition from 17% to 0%, possible reflecting the sensitivity of the IDH1 R132H active site to polar groups at positions analogous to the carboxylic acids at C1 and C5 of 2-OG or ICT. Interestingly the ethyl substituted SB15 (~17%) was somewhat more potent than the allyl substituent of SB18 (~6%). SB18, like SB15, contains nitrogen at position five, but has nine backbone atoms compared to eight, suggesting the active site is also sensitive to the maximum compound length.

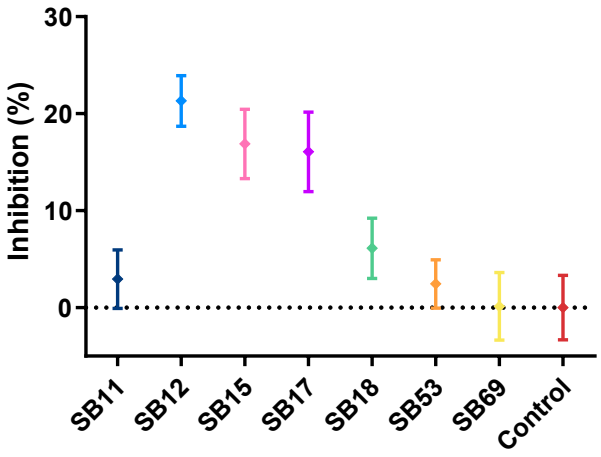

Figure 2.33 | *Inhibition of IDH1 R132H (400 nM) performing the reduction of 2-OG by compounds containing quaternary ammonium ions (10 μM). Error bars: standard error of the mean (experimental repeats = 2, technical replicates = 8). Conditions:1.5 mM 2-OG, 300 μM NADPH. Buffer: 100 mM Tris, 10 mM $MgCl_2$, 0.2 mM DTT, 0.005% (v/v) Tween-20, 0.1 mg/mL BSA, pH 8.0.*

Despite structural similarities with elements of 2-OG, the inclusion of quaternary ammonium ions into carbon backbones produced derivatives lacking inhibition (≥ 50%) at a high concentration (10 μM), and did not improve inhibition compared to TMAO (~16%). The results for SB12 (~21%), SB15 (~17%), and SB17 (~16%) demonstrated that incorporating the quaternary ammonium ion into a backbone is at best equivalent to TMAO, while SB11 (~3%), SB18 (~6%), SB53 (~2%), and SB69 (~0%) show that minor deviations can abolish inhibition completely. As a result, 2-OG analogues containing quaternary ammonium ions were not pursued further.

3. Metabolomic Studies on the Role of Wild-type IDH1/2 in Glioma Cells Containing IDH1 R132H Mutations

3.1. Introduction

Previous metabolomics work focussing on the effects of IDH mutants has mostly addressed the difference between IDH1 R132H and IDH1 WT glioma metabolism using cell lines, mouse models, and patient derived tumour samples.[19] The results manifest alterations in central carbon metabolism, amino acid metabolism, lipid metabolism, and redox homeostasis.[19] It is still unclear if the apparently causal links between mutation in IDH1 and these effects are due to direct enzyme inhibition by 2-HG, and/or indirect effects on gene transcription.

The effects of IDH1 variant inhibitors on glioma cells has primarily focussed on cellular levels of 2-HG, cell viability, and specific metabolic pathways.[105, 250, 251, 266, 297, 299, 300, 336-338] The number of metabolites and inhibitors studied in dedicated metabolic studies has also been limited.[136, 339-341] A collaborator, Dr Ingvild Hvinden (Department of Chemistry, University of Oxford), conducted a rigorous investigation of the effects of IDH1 variant inhibitors on IDH1 WT and IDH1 R132H glioma cells to investigate the cellular effects of IDH1 R132H inhibition and further understand existing therapeutic strategies.[140] The results provided an insight into the changes in glioma caused by the neomorphism of IDH1 R132H, but do not inform the changes caused by the dominant-negative phenotype of IDH1 and IDH2 mutations.

IDH1 variant inhibitors can inhibit IDH1 WT at higher concentrations, but the potential off-target effects on IDH1 WT have previously been overlooked. In addition, Dr Ingvild Hvinden reported experiments using [^{13}C]-tracer experiments indicating that most of the carbon in the total 2-HG pool is originally derived from glutamine, in IDH1 WT cells (58%) and IDH1 R132H cells (72%).[140] Dr Ingvild Hvinden applied the glutaminase (GLS) inhibitor CB-839 to glioma cells with and without IDH1 R132H mutations. The results exhibited decreased cell viability, but unperturbed 2-HG levels. The 2-HG levels may have been maintained by compensatory asparagine synthetase (ASNS) and glutamic-oxaloacetic transaminase (GOT) activity.[140]

To further investigate the role of the IDH1 R132H mutation in glioma cells, wild-type IDH1 and IDH2 were inhibited in glioma cells with and without IDH1 R132H mutations. Glioma cells were treated with small-molecule inhibitors of IDH1 WT (**1**) and IDH2 WT (**2**), and a putative PROTAC targeting IDH2 WT (**3**). The cells were then harvested and subjected to metabolomics analyses.

3.2. Methodology for the Metabolomics Experiments

The LN18 glioblastoma multiforme (GBM) cells used in metabolomics experiments were kindly provided by Dr Chiara Bardella (University of Birmingham) and Dr Ingvild Hvinden (Department of Chemistry, University of Oxford). The cells were transfected with either an empty vector or IDH1 R132H. The over expression of the IDH1 R132H gene in the latter case was confirmed by quantitative reverse transcription polymerase chain reaction (qRT-PCR).[283] In accordance with Dr Ingvild Hvinden's established protocols to capture metabolic shifts induced by IDH1 variant inhibitors, cells were grown in supplemented low-glucose DMEM (1.0 g/L glucose), initially incubated for 24 hours without treatment to permit reattachment and recovery to a uniform growth phase,

and subsequently exposed to treatment for a further 24 hours to allow stable global metabolic reprogramming, while acknowledging that earlier, transient events may remain undetected.(**Section 6.3.15**, **Section 6.3.16**). Following harvesting, the cellular contents were processed into samples to be analysed by IC-MS (**Section 6.3.17**). Relative DNA concentration was used as a proxy for cell count and the extracts were normalised accordingly by dilution with aqueous methanol (80% methanol, 20% H_2O, v/v) (**Section 6.3.18**). The samples were analysed by untargeted IC-MS (**Section 6.3.19**). The data were pre-processed using Progenesis QI (**Section 6.3.20**) and features were identified by comparing retention time, *m/z*, isotopic similarity, and fragmentation pattern to a known standard (**Section 6.3.20**). Relative abundances of identified metabolites were determined by integration of the extracted ion chromatograms (Progenesis QI). Data filtration, normalisation, univariate statistical analysis, and multivariate statistical analysis were conducted using MetaboAnalyst 6.0. www.metaboanalyst.ca (**Section 6.3.21**, **6.3.22**). Univariate analysis entailed the pairwise comparison of normalised data using a t-test, determined by the false-discovery-rate (FDR) adjusted p-value (FDR < 0.05). Abundances were considered substantially altered if the calculated relative fold-change (FC) was greater than or equal to 1.2 (FC ≥ 1.2). Multivariate analyses entailed the generation of partial least squares-discriminant analysis (PLS-DA) models using the website www.metaboanalyst.ca. PLS-DA model performance was assessed using leave-one-out-cross-validation (LOOCV) and permutation testing (**Section 6.3.24**). Validated PLS-DA models were used to generate variable importance in projection (VIP) scores. A summary of the metabolomics experiments carried out is presented in **Table 3.1**.

Expt.	Treatment(s)	DMSO (%, v/v)	IDH Mutation	Biological Replicates	Total Dishes
1	Compound **1**, and Compound **2**	0.1	IDH1 WT, IDH1 R132H	**1** (10), **2** (10), Ctrl (10) **1** (10), **2** (10), Ctrl (10	60
2	Compound **3**	0.50	IDH1 WT, IDH1 R132H	**3** (5), Ctrl (5) **3** (5), Ctrl (5)	20

Table 3.1 | *Overview of all metabolomics experiments. The table contains the experiment number, treatment applied, final percentage of DMSO in the growth media, IDH mutation status (consistent for all groups).*

Experiments **1** and **2** were performed to investigate the effect of IDH1 WT and IDH2 WT inhibition in LN18 GBM cells with and without IDH1 R132H mutations. From here on, LN18 GBM cells expressing the mutant IDH1 R132H enzyme are referred to as 'MUT' cells, and LN18 GBM cells without IDH1 R132H mutations are referred to as 'WT' cells, unless otherwise specified.

In experiment 1, IDH1 WT inhibitor **1**, and IDH2 WT inhibitor **2** were incubated for 24 hours with MUT and WT cells, which were then harvested, processed, and analysed by IC-MS; the data were pre-processed by Dr Ingvild Hvinden. Sixty biological replicates were prepared, consisting of WT cells (total n = 30) and MUT cells (total n = 30), which were each split equally between three treatment conditions: control (n = 10), **1** (10 μM, n = 10), and **2** (10 μM, n = 10) (**Table 3.1**).

In experiment 2, a putative IDH2 WT PROTAC inhibitor, **3**, was applied to MUT and WT cells as in experiment 1. After treatment and incubation, the cells were harvested, processed and normalised with aqueous methanol as described. The samples were kindly submitted for IC-MS analysis by Rachel Williams (Department of Chemistry, University of Oxford). IC-MS output data were then pre-processed to identify known metabolites before statistical analyses. Twenty biological replicates were prepared, consisting of half

WT cells (total n = 10) and half MUT cells (total n = 10). The cells of each IDH mutational status were in turn split between two treatment conditions: control (n = 5), and **3** (5 μM, n = 5) (**Table 3.1**).

For the univariate statistical analysis of each treatment, the data were median normalised (**Section 6.3.21**, **Section 6.3.22**) and experimental groups were compared pairwise in three combinations: untreated WT cells vs untreated MUT cells (control), untreated vs treated WT cells, and untreated vs treated MUT cells. The ion abundances of each compound feature were subjected to FDR adjusted t-tests (significantly altered was defined as FDR < 0.05) and relative fold-change calculations (substantially altered was defined as FC ≥ 1.2). A set of eleven 'core' metabolites (set **A**) were assessed each time univariate analysis was conducted. Ten metabolites in set **A** comprised compounds representing the Warburg Effect (glucose, lactic acid), the TCA cycle (citric acid, *cis*-aconitic acid, isocitrate, 2-oxoglutaric acid (2-OG), succinic acid), the glutamine-glutamate cycle (glutamine, glutamate), and the IDH1 R132H gain-of-function molecule 2-hydroxyglutarate (2-HG). The final metabolite in set A was β-citryl-L-glutamic acid (β-CG). Recent reports suggest that β-CG is regularly decreased in MUT cells with respect to WT cells.[138, 140] Therefore, it was decided to assess the relative abundances of β-CG each time univariate analysis was performed. Any additional identified metabolites found during univariate statistical analyses to exhibit significant differences in abundances between WT cells and MUT cells were labelled set **B**.

For the multivariate analysis of each treatment, the data were transformed and scaled in addition to normalisation. The data in experiment 1 were median normalised, log transformed, and auto scaled (**Section 6.3.22**). The data in experiment 2 were median normalised, square root transformed and mean centred (**Section 6.3.22**). PLS-DA models were generated for WT and MUT cells using control and treated groups for each treatment

(e.g., WT control, WT **1**, MUT control, MUT **1**) to investigate systematic changes between experimental groups.

3.3. The Effect of the IDH1 R132H in LN18 GBM Cells

3.3.1. Univariate Statistical Analyses of Untreated LN18 GBM Cells

T-test and relative FC analyses of untreated WT and MUT Cells

Control WT and MUT cells (DMSO = 0.1%, v/v) were compared to confirm the expression of IDH1 R132H in experiment 1 and experiment 2. The relative levels of 2-HG were used as a biomarker. Significant and substantially high levels of 2-HG were detected in MUT cells with respect to WT cells in both cases (FDR = 4.18 x 10^{-8}, FC = 141.6, experiment 1; FDR = 0.0024, FC = 110.0 experiment 2) (**Table 3.2.A**). This observation provides evidence the cells were producing recombinant active IDH1 R132H leading to accumulation of 2-HG.

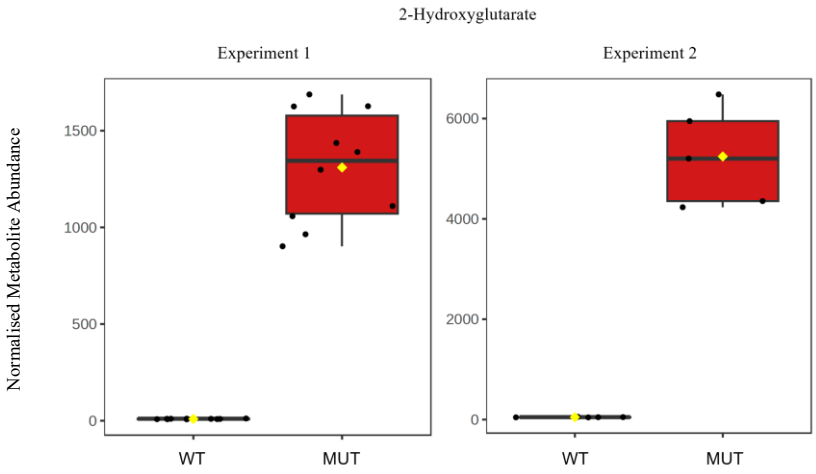

Figure 3.1 *| Box plot of the median normalised abundances of 2-hydroxyglutarate (2-HG) in WT cells (blue) and MUT cells (red). Each datapoint represents the normalised metabolite abundance for one sample. Yellow diamonds represent mean values. Box plot middle lines represent median values. Box plot limits are defined as upper and lower quartiles. Number of samples per group: experiment 1 = 10, experiment 2 = 5.*

In set **A**, in addition to 2-HG, β-CG was significantly and substantially decreased in MUT cells with respect to WT cells in experiment 1 (FDR = 0.0004, FC = 2.61, experiment 1)

(**Table 3.2.A**). There were no other metabolites in set **A** found to have significantly different abundances between MUT cells and WT cells (**Table 3.2.A**). In set **B**, 11 metabolites were found to be significantly and substantially altered (**Table 3.2.B**): 2-hydroxybutyric acid (FDR = 0.0024, FC = 6.92, experiment 2), 4-hydroxybutyric acid (FDR = 4.18×10^{-8}, FC = 54.2, experiment 1), adenylosuccinate (FDR = 0.0024, FC = 1.67, experiment 2), citramalic acid (FDR = 4.32×10^{-6}, FC = 3.93, experiment 1), erythrose-4-phosphate (E4P, FDR= 0.0498, FC = 2.08, experiment 1), glutaconic acid (FDR = 2.66×10^{-5}, FC = 1.50, experiment 1), ribose-5-phosphate (R5P, FDR = 0.0499, FC = 1.63, experiment 2), ribulose-5-phosphate (RL5P, FDR = 0.0482, FC = 1.37, experiment 2), succinic semialdehyde (FDR = 0.0024, FC = 9.61, experiment 2), *N*-acetylaspartylglutamic acid (NAAG, FDR = 0.0033, FC = 2.18, experiment 1), and valeric acid (FDR = 0.0064, FC = 1.36, experiment 1).

Metabolites	Experiment 1			Experiment 2		
	Higher in	FC	p-value (FDR)	Higher in	FC	p-value (FDR)
A						
Glucose	-	-	-	n/a	n/a	n/a
Lactic acid	-	-	-	-	-	-
Citric acid	-	-	-	-	-	-
cis-Aconitic acid	-	-	-	-	-	-
Isocitrate	-	-	-	-	-	-
2-OG	-	-	-	-	-	-
Succinic acid	-	-	-	-	-	-
Glutamine	-	-	-	-	-	-
Glutamic acid	-	-	-	-	-	-
2-HG	MUT	141.6	****	MUT	110.0	**
β-CG	WT	2.61	***	-	-	-
B						
2-Hydroxybutyric acid	-	-	-	MUT	6.92	**
4-Hydroxybutyric acid	MUT	54.2	****	-	-	-
Adenylosuccinate	-	-	-	MUT	1.67	**
Citramalic acid	MUT	3.93	****	-	-	-
Erythrose-4-phosphate	MUT	2.08	*	-	-	-
Glutaconic acid	MUT	1.50	****	-	-	-
Ribose-5-phosphate	-	-	-	MUT	1.63	*
Ribulose-5-phosphate	-	-	-	MUT	1.37	*
Succinic semialdehyde	-	-	-	MUT	9.61	**
NAAG	WT	2.18	**	-	-	-
Valeric Acid	WT	1.36	**	-	-	-

Table 3.2 | *Overview of identified metabolites that were significantly and substantially different between control WT and MUT cell samples (DMSO = 0.01%, v/v), in experiment 1 and experiment 2. Set **A**: Selected metabolites representing the Warburg Effect, TCA cycle, glutamine-glutamate cycle, IDH1 R132H gain-of-function and β-Citryl-L-glutamic acid. Set **B**: Additional significantly and substantially different metabolites. Significantly different (FDR): * < 0.05, ** < 0.01, *** < 0.001, **** < 0.0001. Substantially different: FC > 1.2. Metabolites that were not identified in an experiment are marked 'n/a'. Significantly higher abundances in IDH1 WT cells are blue. Significantly higher abundances in IDH1 R132H cells are red. Statistical tests and calculations were performed on median normalised data. 2-OG = 2-Oxoglutaric acid. 2-HG = 2-Hydroxyglutaric acid. β-CG = β-Citryl-L-glutamic acid. NAAG = N-acetylaspartylglutamic acid.*

Closer inspection of the significantly altered metabolites revealed different areas of metabolism, which may be affected by the IDH1 R132H mutation, including the pentose phosphate pathway (PPP), de novo nucleotide synthesis pathways, neurotransmitter homeostasis, amino acid degradation, and short chain fatty acid homeostasis. These metabolites are grouped, and the results associated with them described below.

Significantly altered metabolites in the pentose phosphate pathway and *de novo* nucleotide synthesis

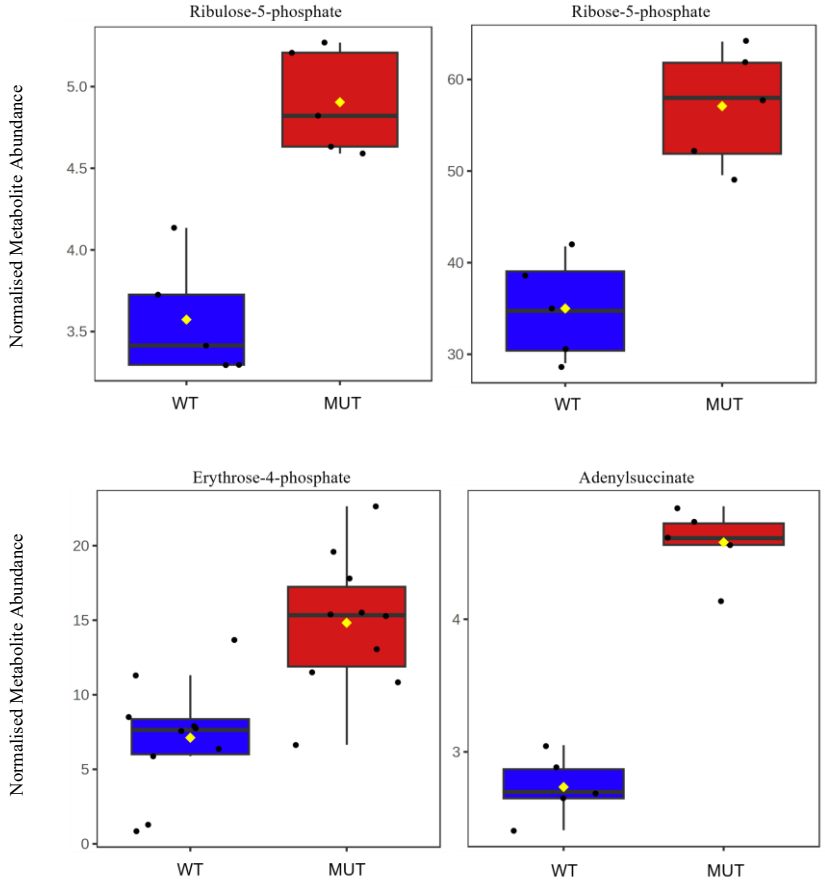

Figure 3.2 *| Box plots of the median normalised abundances of ribulose-5-phosphate (RL5P, $p < 0.05$, experiment 2), ribose-5-phosphate (R5P, $p < 0.05$, experiment 2), erythrose-4-poshpate (E4P, $p < 0.05$, experiment 1), and adenylosuccinate ($p < 0.01$, experiment 2) in WT cells (blue) and MUT cells (red). Each datapoint represents the normalised metabolite abundance for one sample. Yellow diamonds represent mean values. Box plot middle lines represent median values. Box plot limits are defined as upper and lower quartiles. Number of samples per group: experiment 1 = 10, experiment 2 = 5.*

The abundances of R5P, RL5P, E4P, and adenylosuccinate in MUT cells were found to be significantly and substantially higher than in WT cells (**Table 3.2.B**, **Figure 3.2**). In the PPP, none of the other metabolites were found to have significantly or substantially different abundances between untreated WT and MUT cells (glucose-6-phosphate (G6P, not identified in experiments 1 or 2), 6-phosphogluconolactone (not identified in experiments 1 or 2), 6-phosphogluconate, xylulose-5-phosphate (X5P, not identified in experiment 1), sedoheptulose-7-phosphate (S7P), fructose-6-phosphate (F6P, not

identified in experiment 1), and glyceraldehyde-3-phosphate (G3P, not identified in experiment 1), **Figure 3.3**). RL5P is the final metabolite in the oxidative phase of the PPP, which yields two molecules of NADPH per molecule of RL5P produced from G6P (**Figure 3.3**).[342] RL5P is then converted into either R5P by ribulose-5-phosphate isomerase, or X5P by ribulose-5-phosphate epimerase (**Figure 3.3**).[342, 343] R5P may progress through the PPP to form E4P undergoing two successive reactions catalysed by transketolase (catalyses R5P + X5P → G3P + S7P or E4P + X5P → G3P + F6P), then transaldolase (catalyses G3P + S7P ↔ F6P + E4P) (**Figure 3.3**).[342] Ultimately, E4P may re-enter glycolysis by reaction with X5P, catalysed by transketolase as previously described. Alternatively, R5P may enter *de novo* nucleotide biosynthesis pathways after phosphorylation by the ATP-dependent enzyme ribose-phosphate diphosphokinase, to form phosphoribosyl pyrophosphate (PRPP).[344] Originally derived from PRPP, inosine monophosphate (IMP) is a late stage intermediate in the *de novo* synthesis of purine nucleotides.[345-353] The reaction of IMP with aspartate by the GTP-dependent enzyme adenylosuccinate synthase produces adenylosuccinate, the penultimate intermediate in *de novo* AMP synthesis.[350]

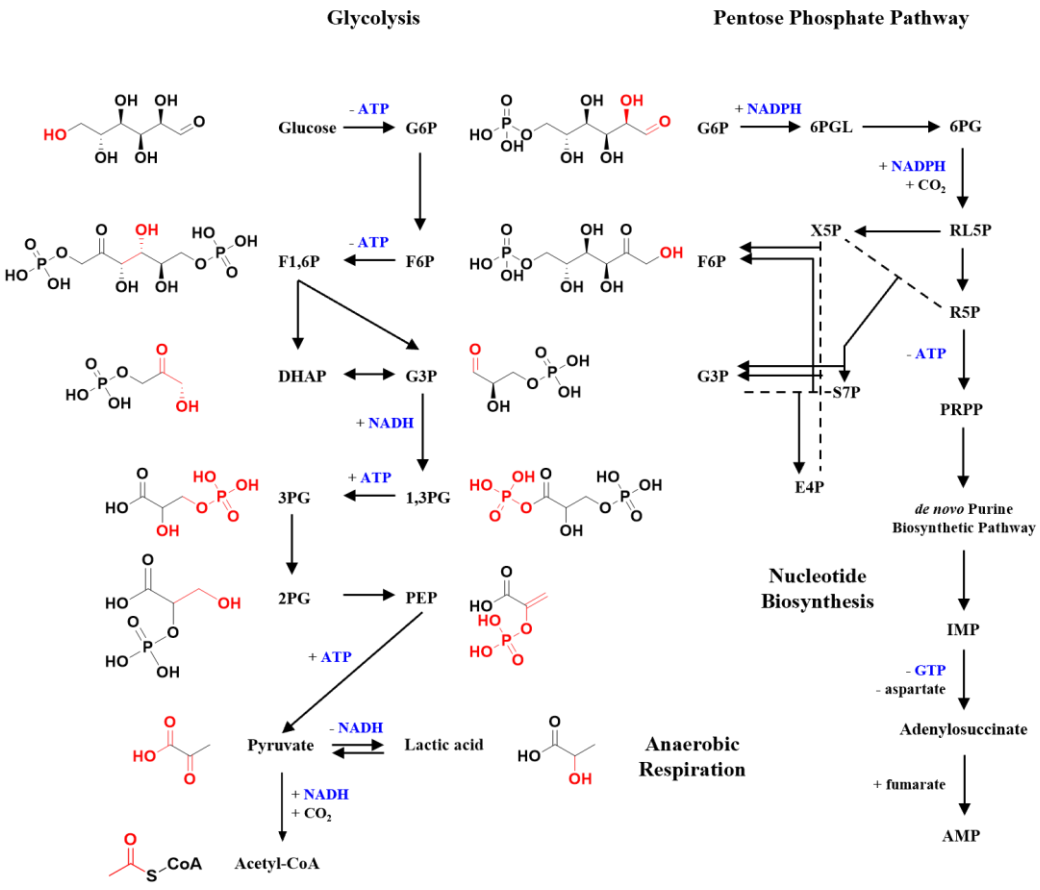

Figure 3.3 | *Overview of glycolysis and the pentose phosphate pathway. The figure is adapted from* ***Figure 1.1****. Dashed lines represent reactions between metabolites. Products are denoted by solid arrows. Energy carriers are coloured blue. G6P = glucose-6-phosphate. F6P = fructose-6-phosphate. F1,6P = fructose-1,6-bisphosphate. DHAP = dihydroxyacetone phosphate. G3P = glyceraldehyde-3-phosphate. 1,3PG = 1,3-phosphoglycerate. 3PG = 3-phosphoglycerate. 2PG = 2-phosphoglycerate. PEP = phosphoenolpyruvate. 6PGL = 6-phosphogluconolactone. 6PG = 6-phosphogluconate. RL5P = ribulose-5-phosphate. R5P = ribose-5-phosphate. X5P = xylulose-5-phosphate. S7P = sedoheptulose-7-phosphate. E4P = erythrose-4-phosphate. PRPP = phosphoribosyl pyrophosphate. IMP = inosine monophosphate. CoA = coenzyme A. ATP = adenosine triphosphate. NADPH = nicotinamide adenine dinucleotide monophosphate. NADH = nicotinamide adenine dinucleotide. GTP = guanosine triphosphate.*

Significantly altered metabolites in neurotransmitter homeostasis

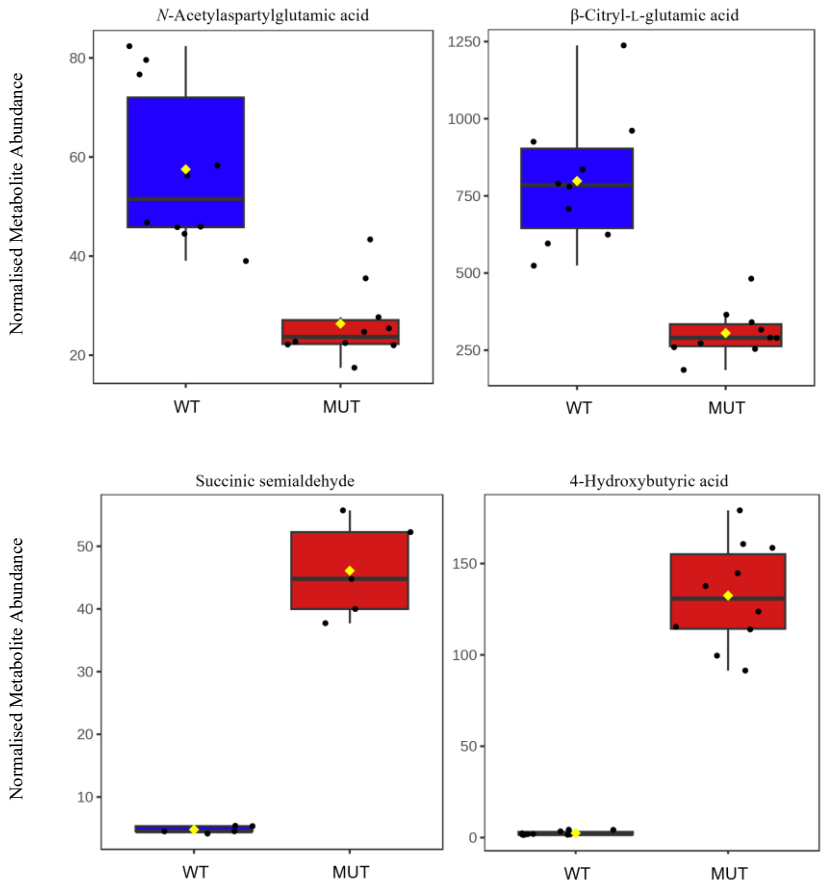

Figure 3.4 *| Box plots of the median normalised abundances of N-acetylaspartylglutamate (NAAG, $p < 0.01$, experiment 1), β-citryl-L-glutamic acid (β-CG, $p < 0.001$, experiment 1), succinic semialdehyde ($p < 0.05$, experiment 2), and 4-hydroxybutyric acid ($p < 0.0001$, experiment 1) in WT cells (blue) and MUT cells (red). Each datapoint represents the normalised metabolite abundance for one sample. Yellow diamonds represent mean values. Box plot middle lines represent median values. Box plot limits are defined as upper and lower quartiles. Number of samples per group: experiment 1 = 10, experiment 2 = 5.*

The levels of 4-hydroxybutyric acid (also known as γ-hydroxybutyrate (GHB)) and succinic semialdehyde in MUT cells were significantly and substantially increased with respect to WT cells (**Figure 3.4**). Conversely, levels of *N*-acetylaspartylglutamate (NAAG) and the closely related metabolite β-citryl-L-glutamic acid (β-CG) in MUT cells were significantly and substantially decreased compared to WT cells (**Figure 3.4**).

4-Hydroxybutyric acid is a neurotransmitter that is synthesised from succinic semialdehyde by succinic semialdehyde reductase.[354] Succinic semialdehyde and glutamate are produced by GABA transaminase from the transamination of 2-OG with

GABA, an inhibitory neurotransmitter.[355, 356] 4-Hydroxybutyric acid can be converted back to succinic semialdehyde through two different reactions; the γ-hydroxybutyrate dehydrogenase (GHB-dehydrogenase) catalysed oxidation of 4-hydroxybutyric acid directly to succinic semialdehyde, or 4-hydroxybutyric acid can react with 2-OG to form succinic semialdehyde and 2-HG, as catalysed by hydroxyacid-oxoacid transhydrogenase (HOT).[42, 357] Other reactions catalysed by HOT are reversible, such as the transhydrogenation of (*S*)-3-hydroxybutanoate and 2-oxoglutarate to form acetoacetate and 2-HG.[42] Therefore, considering the high levels of 2-HG measured in the presence of IDH1 R132H, it seems likely that at least some succinic semialdehyde may react with 2-HG to produce 4-hydroxybutyric acid and 2-OG via HOT activity.

4-Hydroxybutyric acid shares similar chromatographic properties with 2-HG in the metabolite database used for compound identification (rt = 10.65 cf. 10.90 respectively). It is therefore possible that the compound feature identified as 4-hydroxybutyric acid could be an unrecognised fragment of 2-HG; the mass of 2-HG (148) after decarboxylation (-44) equals the mass 4-hydroxybutyric acid (104). Accordingly, any conclusions regarding the relationship between 4-hydroxybutyric acid and the IDH1 R132H mutation should be considered in the context of supporting evidence, including changes in the levels of related metabolites. In this case, alterations in the levels of the related metabolite succinic semialdehyde were also observed, suggesting observed alterations in the levels of 4-hydroxybutyric acid may be relevant. Nonetheless, such conclusions should be drawn with appropriate caution.

NAAG is synthesized from *N*-acetylaspartate (NAAsp) and glutamate, predominantly by the enzyme RIMKLA, and has been found in unpublished work by Sam Atwal (Department of Chemistry, University of Oxford) to be synthesised to a lesser extent by the closely related enzyme RIMKLB (**Figure 3.5**).[226] By contrast, β-CG is synthesised

from citric acid and glutamate, predominantly by RIMKLB, and is reported to be synthesised to a lesser extent by RIMKLA, confirmed in unpublished work by Sam Atwal (**Figure 3.5**).[226] In addition, NAAG and β-CG are respectively broken down to NAAsp/citric acid and glutamate by homologous enzymes, glutamate carboxypeptidase II (GCPII, also known as prostate specific membrane antigen, PSMA) and glutamate carboxypeptidase III (GCPIII) (**Figure 3.5**).[358] The role of NAAG as a neurotransmitter and the most abundant dipeptide in the brain is documented,[230] however, although NAAG and β-CG are closely related metabolites, the precise physiological role of β-CG is not yet understood.

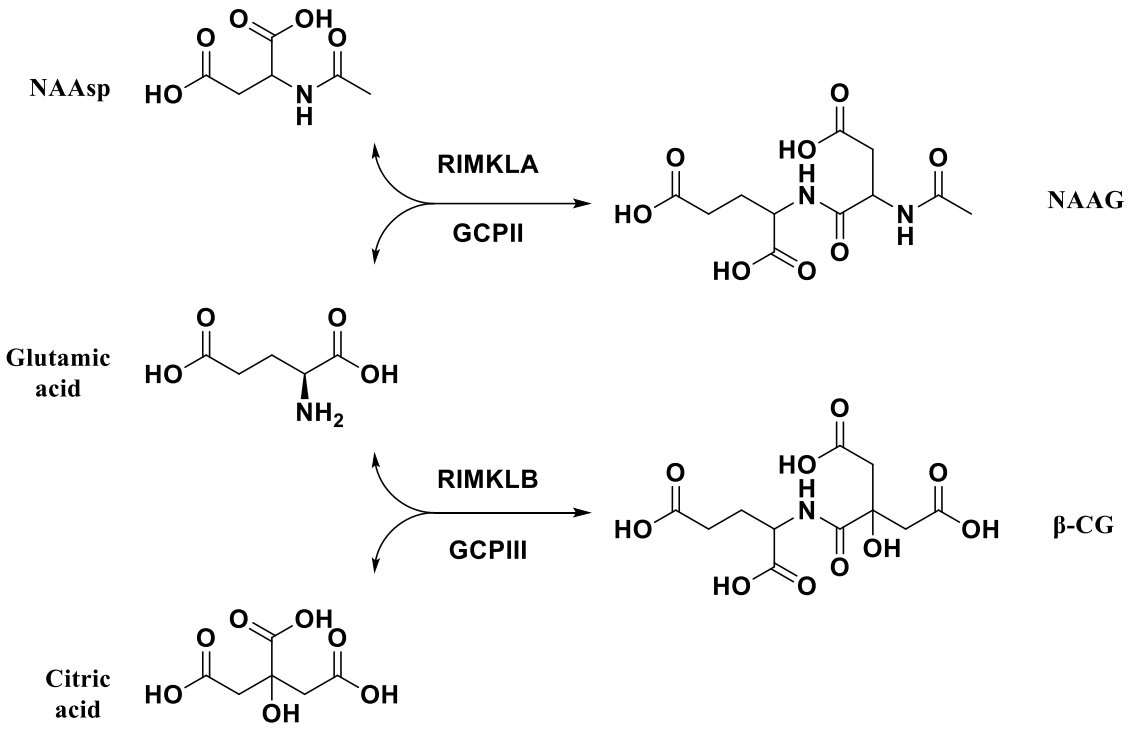

***Figure 3.5** | Overview of the synthesis and degradation of NAAG and β-CG. The synthesis and degradation of NAAG is performed by RIMKLA (predominantly), and GCPII. The synthesis and degradation of β-CG is performed by RIMKLB (predominantly), and GCPIII.*

Considering recent reports that β-CG abundances are consistently observed to be decreased in MUT cells,[140] it was unexpected that the difference between abundances of β-CG was significant in experiment 1 (FDR = 0.0004), but not experiment 2 (FDR =

0.0755) (**Figure 3.6**).[140] Therefore, the box plots of β-CG abundances in experiment 2 were examined more closely (**Figure 3.6**).

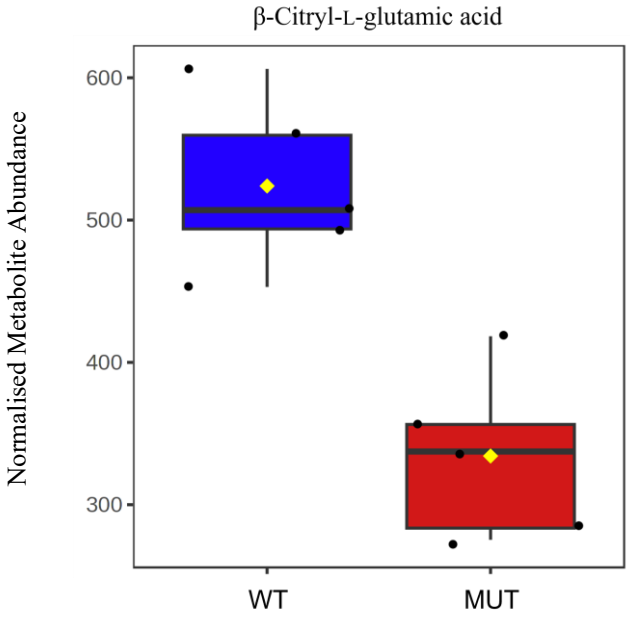

Figure 3.6 | *Box plot of the median normalised abundances of β-CG in WT cells (blue) and MUT cells (red). Each datapoint represents the normalised metabolite abundance for one sample. Yellow diamonds represent mean values. Box plot middle lines represent median values. Box plot limits are defined as upper and lower quartiles. Number of samples per group = 5.*

The relative abundance of β-CG in experiment 2 were substantially decreased in MUT cells with respect to WT cells (FC = 1.57), corroborating a recently reported FC value (FC = 1.77).[140] The raw p value of β-CG in experiment 2 was significant (p = 0.001); however, the FDR adjusted value was not (FDR = 0.0755; the significance level was defined as FDR < 0.05). The relative abundances of β-CG in four MUT samples were tightly grouped (range: 290 – 350) close to the mean abundance value (~320), but one MUT sample is notably higher in abundance (~415). The MUT sample exhibiting the highest abundance (~415) is comparable to the lowest abundance exhibited by a WT sample (~450). As the data from experiment 2 was normalised and PCA plots did not detected any outliers (**Section 6.3.21**), the high abundance of β-CG in one MUT sample may be due to 'natural' variance. It is relevant to consider that experiment 1 contained

more samples per experimental group than experiment 2 (n = 10 cf. n = 5) (**Table 3.1**). Sample size has a strong effect on significance; therefore, were future experiments to contain more samples per experimental group (n > 5), substantial differences between WT and MUT cells may be revealed as being significant, or not.

Significantly altered metabolites in amino acid degradation, and other, pathways

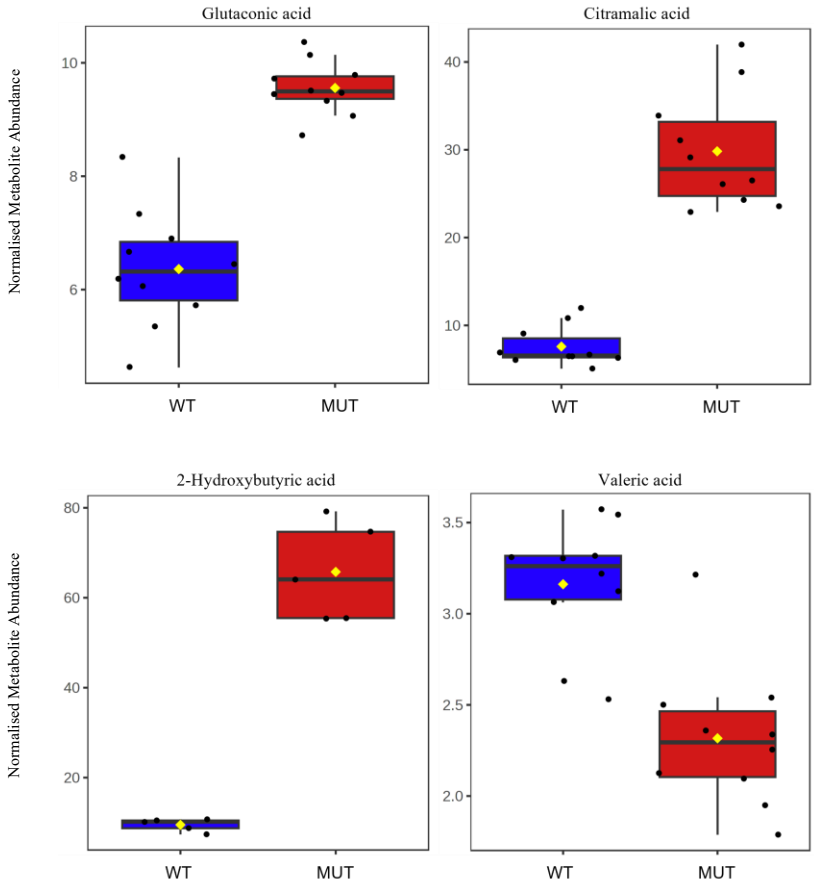

***Figure 3.7** | Box plots of the median normalised abundances of glutaconic acid ($p < 0.0001$, experiment 1), citramalic acid ($p < 0.0001$, experiment 1), 2-hydroxybutyric acid ($p < 0.01$, experiment 2) valeric acid ($p < 0.01$, experiment 1) in WT cells (blue) and MUT cells (red). Each datapoint represents the normalised metabolite abundance for one sample. Yellow diamonds represent mean values. Box plot middle lines represent median values. Box plot limits are defined as upper and lower quartiles. Number of samples per group: experiment 1 = 10, experiment 2 = 5.*

Glutaconic acid, citramalic acid, and 2-hydroxybutyric acid levels in MUT cells were found to be significantly and substantially higher than WT cells (**Figure 3.7**). Valeric acid levels were found to be significantly and substantially lower in MUT cells than WT cells (**Figure 3.7**).

Glutaconic acid is an intermediate in the shared final phase of lysine, hydroxylysine, and tryptophan degradation pathways. 2-Oxoadipic acid derived from lysine, hydroxylysine, or tryptophan, is decarboxylated and reacts with free CoA, as catalysed by 2-oxoadipic acid dehydrogenase, to form glutaryl-CoA.[359] Glutaryl-CoA is then oxidised in two steps to crotonyl-CoA, as catalysed by glutaryl-CoA dehydrogenase. The first step of this reaction involves dehydrogenation on the glutaryl- moiety to produce glutaconyl-CoA.[360] Accumulation of glutaryl/glutaconyl-CoA in the mitochondria can lead to dysregulation of the ester-CoA/free-CoA ratio and ultimately mitochondrial toxicity.[361, 362] Therefore, excess glutaconyl-CoA is reacted with carnitine to form glutaconyl-carnitine and transported across the inner mitochondrial membrane, where the free acid is released.[362]

Citramalic acid is a metabolite in the C5-dicaboxylate acid degradation pathway, which is broken down into pyruvate and acetyl-CoA by citramalyl-CoA lyase, an enzyme which is also reported to exhibit weak citramalyl-CoA synthase activity and strong malate/β-methylmalate synthase activity.[363, 364]

2-Hydroxybutyric acid is a by-product of glutathione synthesis under conditions of limiting cysteine. Homocysteine is diverted from methionine synthesis to form cystathionine via transulfuration.[365] Cystathionine is then cleaved by cystathionine γ-lyase to release cysteine for glutathione synthesis, and 2-ketobutyric acid. 2-Ketobutyric acid is then converted to 2-hydroxybutyric acid by lactate dehydrogenase (NADH dependent).[366, 367]

Valeric acid (also known as pentanoic acid) is a short chain fatty acid (SCFA) that is five carbons long; it is often derived from the diet. Valeric acid, derivatised as pentanoyl-CoA, is also a substrate and an intermediate in oxidation of odd-numbered fatty acids.[368] β-Oxidation progressively shortens fatty acid chains, releasing a molecule of acetyl-CoA

(number of carbons = 2) after each reaction cycle. Therefore, odd-numbered fatty acid chains longer than valeric acid (number of carbons > 5) necessarily progress via pentanoyl-CoA (number of carbons = 5) as the penultimate acyl-CoA intermediate before the release of propionyl-CoA (number of carbons = 3) as the final product.[368]

3.3.2. Discussion

The presence of the IDH1 R132H mutation leads to the consumption of NADPH,[16] and the oxidative phase of the PPP (G6P → RL5P) is a major source of cellular NADPH.[342] Elevated levels of metabolites in the PPP, namely RL5P, R5P, and E4P, suggest that MUT cells may have upregulated the PPP to compensate for the elevated consumption of NADPH relative to WT cells. In addition, the non-oxidative phase of the PPP, RL5P converts into R5P and indirectly E4P, then E4P ultimately returns to the glycolysis pathway in the form of G3P and F6P (**Figure 3.3**).[130, 342, 369, 370] As MUT cells are likely often rapidly dividing cancer cells, the resulting increase in R5P may supply the necessary substrate for *de novo* nucleotide biosynthesis to meet the increased demand from DNA replication. Observed elevated levels of adenylosuccinate suggest that this could be the case, at least for the production of AMP. Thus, consumption of NADPH by the IDH1 R132H mutation may promote elevated PPP which also helps fuel nucleotide biosynthesis.[130]

Astrocytes, a common progenitor of IDH1 mutated glioma, recycle neuronally derived neurotransmitters including GABA to glutamine as part of their physiological role at the synaptic cleft.[61, 69, 70, 113, 114, 190, 371, 372] The recycling pathway of GABA in particular involves the transamination of GABA and 2-OG to produce glutamate and succinic semialdehyde, which usually enters the TCA cycle via succinic acid.[355, 373] The elevated levels of succinic semialdehyde and 4-hydroxybutyric acid suggest that GABA transamination may be occurring at a higher rate, and a substantial proportion of succinic

semialdehyde is converted to 4-hydroxybutyric acid. Although this conversion can be directly catalysed by succinic semialdehyde reductase,[354] the very high concentrations of 2-HG in MUT cells would likely drive reactions with succinic semialdehyde through HOT to form 2-OG and 4-hydroxybutyric acid. Therefore, a metabolic benefit of increased HOT activity may be an indirect route to regenerate 2-OG from 2-HG. Via increasing 2-HG levels, the IDH1 R132H mutation may protect the cell against the negative effects of accumulated succinic semialdehyde and enable increased nitrogen utilisation from GABA.

The degradation pathways of lysine, hydroxylysine, and tryptophan terminate after the conversion of glutaryl-CoA to crotonyl-CoA. High levels of glutaconic acid have been observed in diseases with deficiencies in glutaryl-CoA dehydrogenase, such as glutaric aciduria 1 (GA1).[58, 361, 362] The accumulation of glutaryl-CoA in the mitochondria may also lead to oxidation events catalysed by other acyl-CoA dehydrogenases, producing glutaconyl-CoA. Whether by incomplete glutaryl-CoA dehydrogenase catalysis or overwhelming glutaryl-CoA concentrations, glutaryl-CoA accumulation leads to increased levels of glutaconyl-CoA.[361, 362, 374, 375] Interestingly, the pipecolate pathway of lysine degradation begins in the peroxisome, where IDH1 R132H is localised.[24, 376] Therefore, localised dysfunction caused by NADPH and 2-OG depletion, or 2-HG accumulation may have some effect on lysine degradation via pipecolate. However, the peroxisomal phase of the pipecolate pathway is not fully elucidated; more evidence is required to establish whether the relationship between glutaconic acid and IDH1 R132H is derived from the gain-of-function or dominant negative phenotype.

In the presence of IDH1 R132H, β-oxidation appears to be upregulated in the mitochondria, suggested by the decreased levels of valeric acid. The mitochondria is exclusively able to oxidise fatty acids with a maximum carbon chain length of 20.[26, 377]

In the peroxisome, β-oxidation occurs preferentially with very long chain fatty acids (VLCFA, number of carbons ≥ 22) and enzymatic activity decreases with carbon chain length; one third the activity observed with 20 carbon substrates was observed using eight carbon substrates, and substrates with 4 carbon chain lengths exhibited no activity.[378] Therefore, β-oxidation products originating in the peroxisome are likely released at a length between 5-8 carbons long, commonly understood to be mostly octanoyl-CoA, but potentially including pentanoyl-CoA. Decreased levels of valeric acid suggest an increased rate of consumption, which would necessarily take place in the mitochondria. The rate of lipolysis in the cell is reported to be governed by the peroxisomal sensing of β-oxidation.[379] The first step in peroxisomal β-oxidation produces H_2O_2, which leads to increased levels of reactive oxygen species (ROS) in the peroxisome. The levels of ROS are sensed by peroxisomal biogenesis factor 2 (PEX2) as a signal of β-oxidation.[379] Increased levels of ROS indicate an increased rate of β-oxidation, which causes PEX2 to promote adipose triglyceride lipase (ATGL) activity and trigger lipolysis.[379] IDH1 R132H, which is localised to the peroxisome,[24] may trigger this mechanism by depleting the local levels of NADPH; higher levels of ROS may indirectly lead to an increased rate of β-oxidation by triggering lipolysis, and resulting depletion of valeric acid. In this way, the IDH1 R132H gain-of-function may push the cell towards elevated levels of β-oxidation.

Increased oxidative stress caused by higher levels of ROS may increase the rate of glutathione synthesis sufficiently for demand to exceed the concentration of available cysteine. If so, the resultant conversion of homocysteine to cysteine via cystathionine would fulfil the demand and produce the observed increase in levels of 2-hydroxybutyric acid in the process.[366, 367] 2-Hydroxybutyric acid has also been reported to be an early indicator of type-II diabetes as a sign of fatty acid metabolic dysregulation.[380]

The enzymes which control the synthesis and degradation of NAAG and β-CG are closely related and apparently similarly affected by the presence of the IDH1 R132H mutation.[140, 227, 381] The increased conversion of glutamate to 2-OG as a result of the gain-of-function may limit the availability of glutamate for NAAG and β-CG synthesis; however, glutamate levels do not appear to be significantly altered. In neuroblastoma cells, NAAG levels are reported to decrease in direct response to application of the protein kinase C (PKC) activator, phorbol ester.[382] Phorbol esters are known mimics of the endogenous PKC activator diacylglycerol (DAG), which itself is the first intermediate in the lipolysis pathway.[383, 384] In particular, PKCδ may be activated by phorbol esters, DAG, and oxidative stress in the peroxisome (via H_2O_2 or oxidative stress signal c-Abl).[383, 385] Therefore, the speculative peroxisomal effects of IDH1 R132H may cause activation of PKCδ, leading to downregulation of NAAG; however, a direct link between NAAG, β-CG, a specific PKC, and IDH1 R132H has yet to be reported.

Elevated concentrations of citramalic acid have been reported in humans with propionyl-CoA deficiency (> 50 times above normal).[386] As previously mentioned, propionyl-CoA is the final product released from the β-oxidation of odd-numbered fatty acids, including valeric acid itself.[368] The observations of elevated levels of citramalic acid and decreased levels of valeric acid in the presence of IDH1 R132H suggest that is a link to fatty acid metabolic dysregulation, a previously reported metabolic effect of the IDH1 R132H mutation.[31, 129, 137, 141, 150, 219, 222, 223, 387-390]

Overall, the findings of experiments 1 and 2 in untreated WT and MUT cells agree with the findings of previous reports; in particular, IDH mutations cause dysregulation and alterations in the PPP, nucleotide metabolites, lipid metabolism, lysine/hydroxylysine/tryptophan degradation pathways, and levels of NAAG/β-CG.[31, 129, 130, 136, 137, 140, 141, 150, 219, 222, 223, 387-390] These cumulative effects of the IDH1 R132H

mutation may be derived from the gain-of-function or the dominant negative phenotype, however, it is difficult to distinguish which behaviour is responsible for which effect. Elevated 2-HG levels as a result of the gain-of-function may directly inhibit metabolic reactions. The gain-of-function is also likely, at least in part, responsible for increased oxidative stress via local NADPH depletion and downstream effects of 2-HG accumulation. Observed alterations in the abundances of some metabolites can tentatively be linked to the gain-of-function via the depletion of NADPH (RL5P, R5P, E4P, 2-hydroxybutyric acid), or concurrent depletion of 2-OG and accumulation of 2-HG (succinic semialdehyde, 4-hydroxybutyric acid), while valeric acid and adenylosuccinate may be speculatively linked to IDH1 R132H via NADPH depletion. Unfortunately, although a significant relationship appears to exist between the presence of the IDH1 R132H mutation and the metabolites NAAG, β-CG, glutaconic acid, and citramalic acid, there is not yet enough evidence to conclude what drives the changes in abundance observed. Indeed, the metabolic alterations reported here were observed in only two independent experiments comprising a combined total of fifteen sample replicates; therefore, further independent experiments should be conducted with a greater number of sample replicates in order to confirm these findings.

3.4. The Effect of IDH1 WT Inhibitor 1, on LN18 GBM Cells

3.4.1. Univariate Statistical Analysis of WT LN18 GBM Cells Treated with IDH1 WT Inhibitor, 1

T-test and relative FC analysis of WT Cells treated with compound 1

Control WT cells (DMSO = 0.01%, v/v) and treated WT cells (DMSO = 0.01%, v/v; [**1**] = 10 μM) were compared to investigate the effect of an IDH1 WT inhibitor, **1**, on WT cells. An FDR adjusted t-test and relative FC calculation was performed on the abundances of each metabolite pair between experimental groups.

None of the 11 metabolites in set **A** were found to have significantly different abundances between control WT cells and treated WT cells (**Table 3.3.A**). One metabolite in set **B**, glutaric acid (FDR = 0.0020, FC = 1.43) was found to be significantly and substantially altered (**Table 3.3.B**).

Metabolites	Higher in	FC	p-value (FDR)
A			
Glucose	-	-	-
Lactic acid	-	-	-
Citric acid	-	-	-
cis-Aconitic acid	-	-	-
Isocitrate	-	-	-
2-OG	-	-	-
Succinic acid	-	-	-
Glutamine	-	-	-
Glutamic acid	-	-	-
2-HG	-	-	-
β-CG	-	-	-
B			
Glutaric acid	WT **1**	1.43	**

Table 3.3 | *Overview of identified metabolites that were significantly and substantially different between control WT cell samples (DMSO = 0.01%, v/v) and treated WT cell samples (DMSO = 0.01%, v/v; [**1**] = 10 μM; treatment duration = 24 hours). Set **A**: Selected metabolites representing the Warburg Effect, TCA cycle, glutamine-glutamate cycle, IDH1 R132H gain-of-function and β-Citryl-L-glutamic acid.*

*Set **B**: Additional significantly and substantially different metabolites. Significantly different (FDR): * < 0.05, ** < 0.01, *** < 0.001, **** < 0.0001. Substantially different: FC > 1.2. Significantly higher abundances in treated WT cells are teal. Statistical tests and calculations were performed on median normalised data. 2-OG = 2-Oxoglutaric acid. 2-HG = 2-Hydroxyglutaric acid. β-CG = β-Citryl-L-glutamic acid. NAAG = N-acetylaspartylglutamic acid.*

Levels of glutaric acid are significantly altered in WT cells treated with 1

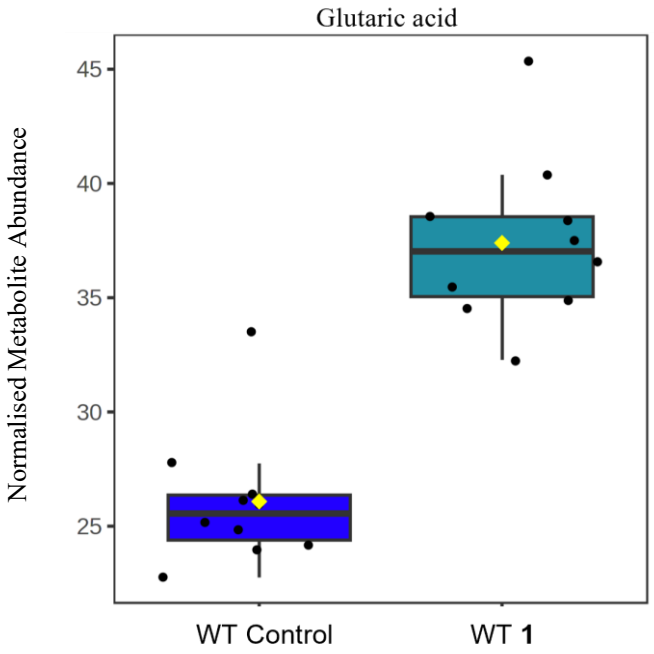

***Figure 3.8** | Box plot of the median normalised abundances of glutaric acid in control WT cells (blue) and treated WT cells (teal) (p < 0.01, experiment 1). Each datapoint represents the normalised metabolite abundance for one sample. Yellow diamonds represent mean values. Box plot middle lines represent median values. Box plot limits are defined as upper and lower quartiles. Number of samples per group = 10.*

The levels of glutarate, the free acid form of glutaryl-CoA, were found in treated WT cells to be significantly and substantially higher than in control WT cells. As discussed in **Section 3.3.1**, glutaryl-CoA is a metabolite in the shared final phase of lysine, hydroxylysine, and tryptophan degradation pathways.[359] Glutaric acid is formed from the oxidation of 2-oxoadipic acid by succinate dehydrogenase and usually progresses via glutaconyl-CoA to crotonyl-CoA. Excess glutaryl-CoA, often caused by dysfunction in the glutaryl-CoA dehydrogenase enzyme, is reacted with carnitine to release CoA and prevent mitochondrial toxicity. The glutaryl-carnitine is then transported across mitochondrial inner membrane where glutaric acid is released.

3.4.2. Univariate Statistical Analysis of MUT LN18 GBM Cells Treated with IDH1 WT Inhibitor, 1

FDR adjusted t-test and relative FC analysis of MUT Cells treated with compound 1

Control MUT cells (DMSO = 0.01%, v/v) and treated MUT cells (DMSO = 0.01%, v/v; [**1**] = 10 μM) were compared to investigate the effect of IDH1 WT inhibitor, **1**, on MUT cells. An FDR adjusted t-test and relative FC calculation was performed on the abundances of each metabolite pair between experimental groups.

Two metabolites in set **A** were found to have significantly different abundances between control MUT cells and treated MUT cells; 2-HG (FDR = 4.83×10^{-8}, FC = 64.3) and β-CG (FDR = 0.0009, FC = 1.99) (**Table 3.4.A**).

Six metabolites in set **B** were found to be significantly and substantially altered; 4-hydroxybutyric acid (FDR = 4.83×10^{-8}, FC = 34.6), citramalic acid (FDR = 2.27×10^{-5}, FC = 3.67), glutaconic acid (FDR = 4.36×10^{-7}, FC = 1.53), glutaric acid (FDR = 0.0006, FC = 1.69), NAAG (FDR = 0.0011, FC = 1.89), valeric acid (FDR = 0.0091, FC = 1.34) (**Table 3.4.B**).

Metabolites	Higher in	FC	p-value (FDR)
A			
Glucose	-	-	-
Lactic acid	-	-	-
Citric acid	-	-	-
cis-Aconitic acid	-	-	-
Isocitrate	-	-	-
2-OG	-	-	-
Succinic acid	-	-	-
Glutamine	-	-	-
Glutamic acid	-	-	-
2-HG	MUT Ctrl	64.3	****
β-CG	MUT **1**	1.99	***
B			
4-Hydroxybutyric acid	MUT Ctrl	34.7	****
Citramalic acid	MUT Ctrl	3.67	****
Glutaconic acid	MUT Ctrl	1.53	****
Glutaric acid	MUT **1**	1.69	***
NAAG	MUT **1**	1.89	**
Valeric Acid	MUT **1**	1.34	**

Table 3.4 *| Overview of identified metabolites that were significantly and substantially different between control MUT cell samples (DMSO = 0.01%, v/v) and treated MUT cell samples (DMSO = 0.01%, v/v; **[1]** = 10 µM; treatment duration = 24 hours). Set **A**: Selected metabolites representing the Warburg Effect, TCA cycle, glutamine-glutamate cycle, IDH1 R132H gain-of-function and β-Citryl-L-glutamic acid. Set **B**: Additional significantly and substantially different metabolites. Significantly different (FDR): * < 0.05, ** < 0.01, *** < 0.001, **** < 0.0001. Substantially different: FC > 1.2. Significantly higher abundances in control MUT cells are red. Significantly higher abundances in treated MUT cells are orange. Statistical tests and calculations were performed on median normalised data. 2-OG = 2-Oxoglutaric acid. 2-HG = 2-Hydroxyglutaric acid. β-CG = β-Citryl-L-glutamic acid. NAAG = N-acetylaspartylglutamic acid.*

Closer inspection of the results of statistical analyses involving MUT cells treated with **1** reveals two groups of significantly altered abundances of metabolites; glutaric acid, which was also observed after treatment of WT cells, and metabolites associated with the presence of IDH1 R132H in control MUT cells.

Levels of glutaric acid are significantly altered in MUT cells treated with compound 1

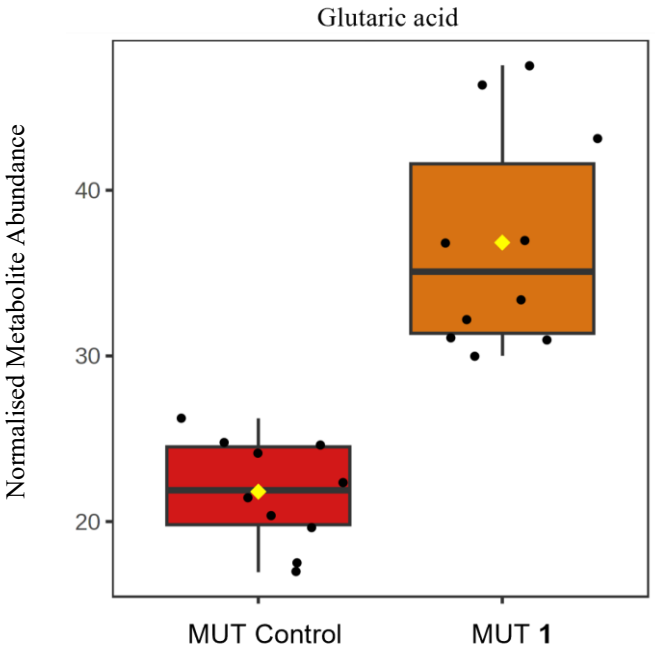

Figure 3.9 *| Box plot of the median normalised abundances of glutaric acid in control MUT cells (red) and treated MUT cells (orange) ($p < 0.01$, experiment 1). Each datapoint represents the normalised metabolite abundance for one sample. Yellow diamonds represent mean values. Box plot middle lines represent median values. Box plot limits are defined as upper and lower quartiles. Number of samples per group = 10.*

The level of glutaric acid was significantly and substantially increased in treated MUT cells compared to control MUT cells (**Figure 3.9**). A late-stage intermediate in lysine, hydroxylysine, and tryptophan degradation pathways (as described above, p.g. 136), [391] glutaric acid was elevated by a comparable amount in treated MUT cells compared to control MUT cells (FDR < 0.001, FC = 1.69), and treated WT cells compared to control WT cells (FDR < 0.01, FC = 1.43). The metabolic steps involving glutaric acid are described previously (**Section 3.3.1**, **Section 3.3.2**, **Section 3.4.1**), but in brief, glutaric acid may accumulate as a consequence of glutaryl-CoA dehydrogenase deficiency and subsequent release of the free acid outside of the mitochondria.

Levels of metabolites associated with the presence of IDH1 R132H are significantly altered in MUT cells treated with compound 1

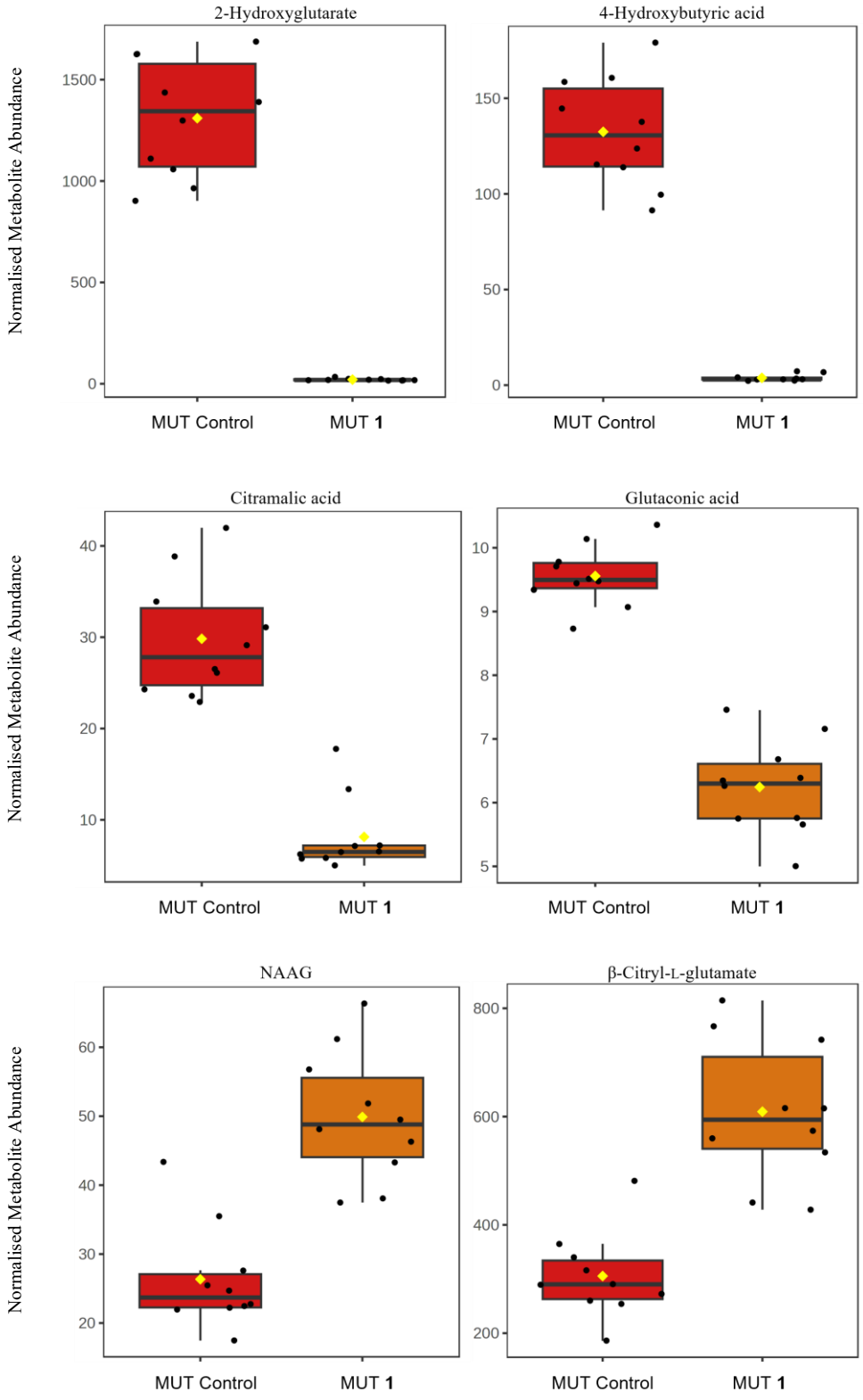

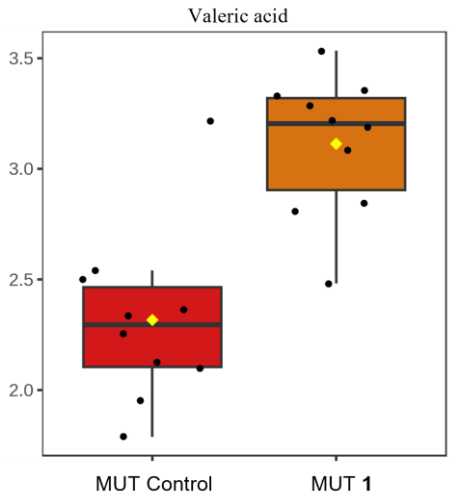

Figure 3.10 *| Box plots of the median normalised abundances of 2-HG (< 0.0001), 4-hydroxybutyric acid (< 0.0001), citramalic acid (< 0.0001), glutaconic acid (< 0.0001), NAAG (< 0.01), β-CG (< 0.001), and valeric acid (< 0.01) in control MUT cells (red) and treated MUT cells (orange). Each datapoint represents the normalised metabolite abundance for one sample. Yellow diamonds represent mean values. Box plot middle lines represent median values. Box plot limits are defined as upper and lower quartiles. Number of samples per group = 10.*

The abundances of 2-HG, 4-hydroxybutyric acid, citramalic acid, and glutaconic acid in treated MUT cells were significantly and substantially lower than in control MUT cells, while the abundances of NAAG, β-CG, and valeric acid in treated MUT cells were significantly and substantially higher than in control MUT cells (**Figure 3.10**). The abundances of 2-HG, 4-hydroxybutyric acid, citramalic acid, glutaconic acid, NAAG, β-CG, and valeric acid were also found to be significantly altered between control MUT cells and control WT cells; therefore, the respective metabolic pathways for the synthesis and/or degradation of each metabolite were previously described in greater detail (**Section 3.3.1**). Interestingly, all seven metabolites are significantly altered in treated MUT cells in the same direction as control WT cells, when compared to control MUT cells.

3.4.3. Multivariate Statistical Analysis of LN18 GBM Cells Treated with IDH1 WT Inhibitor, 1

PLS-DA model of WT and MUT Cells treated with compound 1

To better understand how altered metabolite abundances collectively led to differences between the mutant and wild type cells with and without inhibitor treatment, and identify important features relevant in unseen datasets, multivariate statistical methods were used to analyse the full dataset comparing WT and MUT cells treated with **1**.

A PLS-DA model, incorporating all experimental groups, was generated using www.metaboanalyst.ca (**Figure 3.11**). A 2D plot of the model's component scores highlighted shifts in the XY-direction for cell samples treated with compound **1** (**Figure 3.11.A**). Control WT cells (WT control) exhibited partial separation from treated WT cells (WT **1**), and control MUT cells (MUT control) exhibited partial separation from treated MUT cells (MUT **1**), in the XY-direction. The presence of the IDH1 R132H mutation also led to a shift in the XY-direction. Interestingly, the confidence regions for treated WT cells (WT **1**) and control MUT cells (MUT control) partially overlap. Treatment with **1** and the presence of IDH1 R132H both appear to lead to a shift in the XY-direction, suggesting a similar effect on LN18 GBM cells (**Figure 3.11.A**).

The model was assessed using leave-one-out cross-validation (LOOCV) and permutation testing, revealing good fit, poor validity (3 components, accuracy = 0.48, R^2 = 0.98, Q^2 = 0.22, **Figure 3.11.B**) and insignificant separation (p = 0.382, **Figure 3.11.C**). The large number of predictors and low number of samples in the model likely contributes to the discrepancy between R^2 and Q^2. VIP scores could not confidently be used as indicators of variable importance for yet unseen samples. Therefore, the model was not analysed further or used to generate VIP scores.

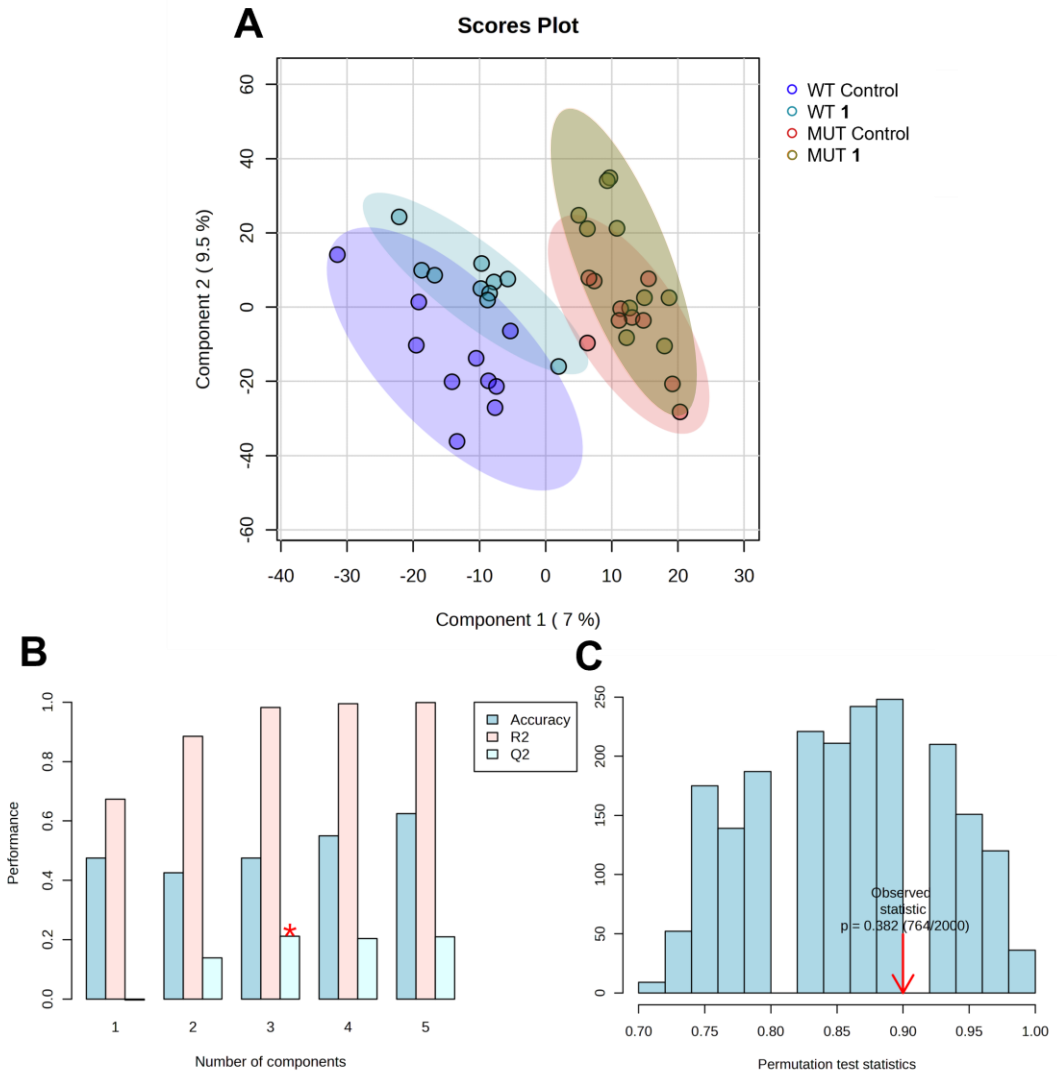

Figure 3.11 *| PLS-DA model of selected groups from experiment 1. Experimental groups: Control WT cell samples blue (n = 10); WT cell samples treated with **1** are cyan (n = 10); Control MUT cell samples are red (n = 10); MUT cell samples treated with **1** are green (n = 10). Control cells were incubated in growth media containing DMSO for 24 hours. Treated cells were incubated in growth media containing **1** (10 μM) for 24 hours.* ***A.*** *PLS-DA scores plot (X axis = component 1, Y axis = component 2). The shaded area for each experimental group represents the 95% confidence region.* ***B.*** *Bar plot summarising the performance of cross-validation (LOOCV, 5 components).* ***C.*** *Bar plot summarising the permutation test (test statistic = prediction accuracy, permutations = 2000).*

3.4.4. Discussion

The observed shift in the PLS-DA plot of treated and mutant groups in the same direction suggests that the metabolic effects of compound **1** partially mimic those of the R132H mutation. This may result from the loss of IDH1 WT activity due to the allosteric inhibition by compound **1** and the dominant negative effect of the IDH1 R132H mutation in IDH1 WT/R132H heterodimers. However, the treated MUT cells do not align closer

to control WT cells than control MUT cells, which seems unrepresentative. Notably, seven out of eight significantly altered metabolites in control MUT cells showed significant changes in the opposite direction after treatment with compound **1** (2-HG, β-CG, 4-hydroxybutyric acid, citramalic acid, glutaconic acid, glutaric acid, NAAG, valeric acid).

Compound **1** appears to have two distinct effects on LN18 GBM cells. First, it significantly altered seven metabolite abundances in MUT cells, restoring them to levels observed in control WT cells, suggesting that direct inhibition of IDH1 R132H by compound **1** is responsible.

Second, treatment with compound **1** increased glutaric acid levels across all treated cells (WT and MUT) compared to controls. This conserved effect suggests that IDH1 WT inhibition, present in both WT and MUT cells, might be involved. The IDH1 R132H mutation may lead to IDH1 WT inhibition in WT/R132H heterodimers, while compound **1** may allosterically inhibit IDH1 WT in homodimers, in addition to inhibiting IDH1 R132H. The accumulation of glutaric acid and depletion of glutaconic acid in treated MUT cells suggests that glutaric acid accumulation is linked to IDH1 WT inhibition, while glutaconic acid accumulation is associated with the IDH1 R132H gain-of-function. Although both metabolites are involved in the lysine, hydroxylysine, and tryptophan degradation pathways, IDH1 R132H mutation and IDH1 WT inhibition likely affect these pathways through different mechanisms.

As discussed in Chapter 2, compound **1** is less potent against IDH1 WT under turnover conditions than during pre-incubation. In cellular conditions, where IDH1 WT is under turnover, it may not be fully inhibited, and cellular metabolic flexibility could prevent significant widespread changes in metabolite concentrations. However, no substantial

differences in 2-OG levels were observed. The precise cause of the change in glutaric acid levels remains unclear, but it may involve homeostatic adaptation to maintain 2-OG levels or localized changes affecting glutaric acid.

Ultimately, the absolute specificity of compound **1** for IDH1 WT or IDH1 R132H in this cellular context has not been definitively confirmed, and potential off-target effects cannot be ruled out. Consequently, caution is warranted when attributing the observed metabolic changes solely to IDH1 inhibition.

3.5. The Effect of IDH2 WT Inhibitor, 2, on LN18 GBM Cells

3.5.1. Univariate Statistical Analysis of WT LN18 GBM Cells Treated with IDH1 WT Inhibitor, 2

T-test and relative FC analysis of WT Cells treated with compound 2

Control WT cells (DMSO = 0.01%, v/v) and treated WT cells (DMSO = 0.01%, v/v; [**2**] = 10 μM) were compared to investigate the effect of an IDH2 WT inhibitor, **2**, on WT cells. An FDR adjusted t-test and relative FC calculation was performed on the abundances of each metabolite pair between experimental groups.

No metabolites in set **A** were found to have significantly different abundances between control WT cells and treated WT cells (**Table 3.5.A**). One metabolite in set **B**, galactose (FDR = 0.0194, FC = 1.43) was found to be significantly and substantially altered (**Table 3.5.B**).

Metabolites	Higher in	FC	p-value (FDR)
A			
Glucose	-	-	-
Lactic acid	-	-	-
Citric acid	-	-	-
cis-Aconitic acid	-	-	-
Isocitrate	-	-	-
2-OG	-	-	-
Succinic acid	-	-	-
Glutamine	-	-	-
Glutamic acid	-	-	-
2-HG	-	-	-
β-CG	-	-	-
B			
Galactose	WT **2**	1.43	*

Table 3.5 | *Overview of identified metabolites that were significantly and substantially different between control WT cell samples (DMSO = 0.01%, v/v) and treated WT cell samples (DMSO = 0.01%, v/v; [**2**] = 10 μM; treatment duration = 24 hours). Set **A**: Selected metabolites representing the Warburg Effect, TCA cycle, glutamine-glutamate cycle, IDH1 R132H gain-of-function and β-Citryl-L-glutamic acid.*

*Set **B**: Additional significantly and substantially different metabolites. Significantly different (FDR): * < 0.05, ** < 0.01, *** < 0.001, **** < 0.0001. Substantially different: FC > 1.2. Significantly higher abundances in treated WT cells are cyan. Statistical tests and calculations were performed on median normalised data. 2-OG = 2-Oxoglutaric acid. 2-HG = 2-Hydroxyglutaric acid. β-CG = β-Citryl-L-glutamic acid. NAAG = N-acetylaspartylglutamic acid.*

The abundance of galactose is significantly altered in WT cells treated with 2

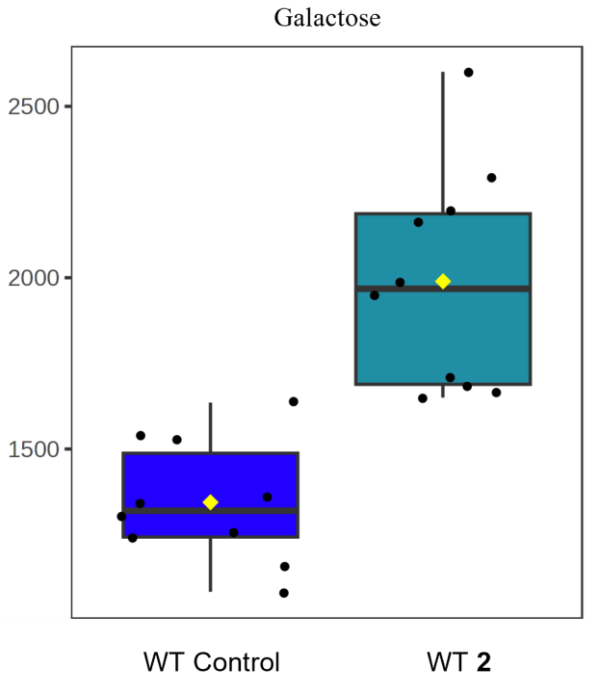

***Figure 3.12** | Box plot of the median normalised abundances of galactose in control WT cells (blue) and treated WT cells (teal) (p < 0.05, experiment 1). Each datapoint represents the normalised metabolite abundance for one sample. Yellow diamonds represent mean values. Box plot middle lines represent median values. Box plot limits are defined as upper and lower quartiles. Number of samples per group = 10.*

Galactose levels in control WT cells were found to be significantly and substantially higher than in treated WT cells. β-D-Galactose, normally derived from the hydrolysis of lactose, is taken up into the cell and reversibly converted to α-D-galactose by galactose mutarotase.[392] α-D-Galactose is phosphorylated using ATP by galactokinase to produce galactose-1-phoshphate, which enters the Leloir pathway to ultimately produce UDP-galactose.[393] UDP-galactose can then be reversibly converted by UDP-glucose-4-epimerase to UDP-glucose.[393] The reversible production of glucose-1-phosphate and UDP-galactose from UDP-glucose and galactose-1-phosphate (catalysed by galactose-1-phosphate uridyltransferase) connects galactose, via the Leloir pathway, to glycolysis.

3.5.2. Univariate Statistical Analysis of MUT LN18 GBM Cells Treated with IDH1 WT Inhibitor, 2

FDR adjusted t-test and relative FC analysis of MUT Cells treated with compound 2

Control MUT cells (DMSO = 0.01%, v/v) were compared with treated MUT cells (DMSO = 0.01%, v/v; [**2**] = 10 μM) to investigate the effect of **2**, on MUT cells. An FDR adjusted t-test and relative FC calculation was performed on the abundances of each metabolite pair between experimental groups. No metabolites in set **A** or set **B** were found to have significantly different abundances between control MUT cells and treated MUT cells.

3.5.3. Multivariate Statistical Analysis of LN18 GBM Cells Treated with IDH1 WT Inhibitor, 2

PLS-DA model of WT and MUT Cells treated with compound 2

To complement the univariate analyses (FDR-adjusted t-test and relative FC calculations) performed on WT and MUT cells treated with **2**, and identify important features relevant to treatment with **2** applicable beyond this dataset, multivariate statistical methods were performed. A PLS-DA model, incorporating all experimental groups, was generated using www.metaboanalyst.ca (**Figure 3.13**). Visualization of the model's component scores in a 2D plot highlighted shifts in the XY-direction for cell samples treated with compound **2**, irrespective of mutational status (**Figure 3.13.A**). Control MUT cells (MUT control) exhibited partial separation from treated MUT cells (MUT **2**), and control WT cells (WT control) exhibited partial separation from treated WT cells (WT **2**), in the XY-direction. The presence of the IDH1 R132H mutation defined a shift along the X-axis, leading to complete separation of MUT from WT groups. The effect of compound **2** appears to be similar in both WT and MUT cells. Interestingly, treated WT

cells (WT **2**) are closer to control MUT cells (MUT control) than control WT cells (WT control).

The validity of the model was assessed using leave-one-out cross-validation (LOOCV) and permutation testing, revealing poor validity (2 components, accuracy = 0.43, R^2 = 0.95, Q^2 = 0.51, **Figure 3.13.B**) and significant separation (p = 0.0035, **Figure 3.13.C**). The permutation test statistic suggests that the observed model performance is significantly better than random; nonetheless, the low Q^2 value suggested that variable importance in projection (VIP) scores may not be reliable indicators of variable importance for treated LN18 samples that were not included in the model. Therefore, VIP scores were not generated.

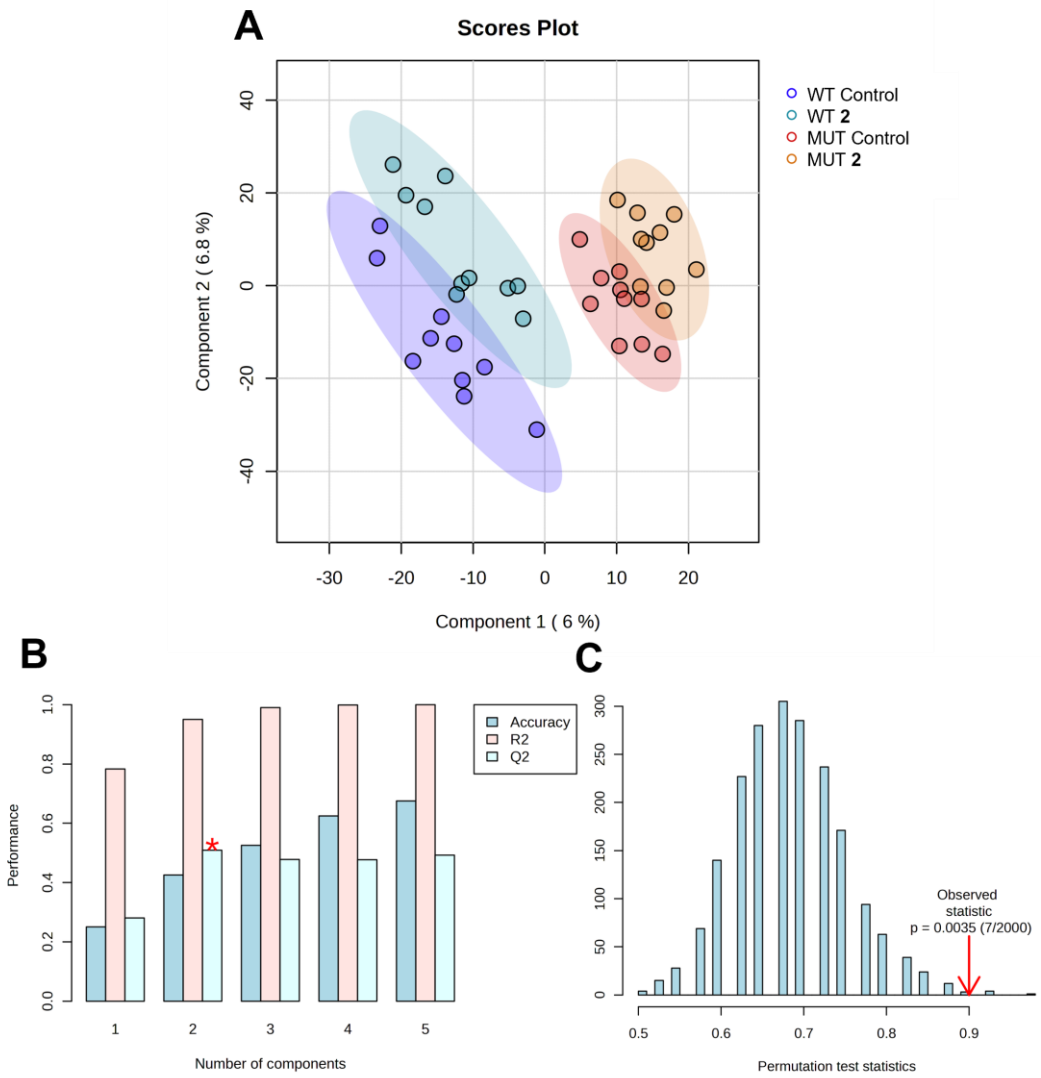

Figure 3.13 *| PLS-DA model of selected groups from experiment 1. Experimental groups: Control WT cell samples blue (n = 10); WT cell samples treated with* ***2*** *are cyan (n = 10); Control MUT cell samples are orange (n = 10); MUT cell samples treated with* ***2*** *are orange (n = 10). Control cells were incubated in growth media containing DMSO for 24 hours. Treated cells were incubated in growth media containing* ***2*** *(10 μM) for 24 hours.* ***A.*** *PLS-DA scores plot (X axis = component 1, Y axis = component 2). The shaded area for each experimental group represents the 95% confidence region.* ***B.*** *Bar plot summarising the performance of cross-validation (LOOCV, 5 components).* ***C.*** *Bar plot summarising the permutation test (test statistic = prediction accuracy, permutations = 2000.*

3.5.4. Discussion

The PLS-DA model effectively distinguished the experimental groups, as evidenced by significant separation, although it did not exhibit predictive validity (**Figure 3.13**). This differentiation indicates that systematic alterations define these groups. Notably, similar directional shifts in the 2D scores plots were observed for cells treated with **2** (WT **2** and MUT **2**) and cells with IDH1 R132H mutations (MUT control and MUT **2**), as compared

with control WT cells (**Figure 3.13.A**); shared directional shifts imply that the effects of **2** may be similar to the effects of the IDH1 R132H mutation, implying a possible shared biological impact. Similar to a previous PLS-DA model analysing control and treated glioma cells (WT control, MUT control; WT **1**, MUT **1**), a potential common mechanism is the dominant negative influence of IDH1 R132H on IDH1 WT activity in IDH1 WT/R132H heterodimers, and, here, the inhibition of IDH2 WT by **2**. Although **1** targets IDH1 WT *in vitro* and **2** inhibits IDH2 WT *in vitro*, both compounds ultimately inhibit the same enzymatic reaction. Nonetheless, because the absolute specificity of these inhibitors has not been thoroughly characterised in this cellular context, the possibility of off-target effects cannot be excluded, cautioning against definitive attribution of all observed changes to IDH1 or IDH2 inhibition alone.

Diseases caused by deficiencies in galactokinase and galactose-1-phosphate uridyltransferase are associated with galactose accumulation, suggesting that compound **2** might inadvertently inhibit these enzymes.[394, 395] The relationship between the WT IDH2 reaction and the Leloir pathway remains ambiguous, as the pathway does not use or interact directly with IDH2 WT substrates and products such as 2-OG, NADP+/NADPH, and ICT. An indirect relationship may exist through alterations in glycolysis; specifically, glycolysis has been reported to be downregulated by RNAi inhibition of IDH2 WT.[396] Regardless, the metabolic impact of the IDH1 R132H mutation seems to override any potential impact of IDH2 WT inhibition on galactose levels, as galactose abundances were not found to be significantly altered between control and treated MUT cells.

3.6. The Effect of Putative IDH2 WT PROTAC, 3 Treatment of LN18 GBM Cells

3.6.1. Univariate Statistical Analysis of WT Cells Treated with Compound 3

FDR adjusted t-test and relative FC analysis of WT Cells treated with compound 3

Control WT cells (DMSO 0.50%, v/v) were compared with treated WT cells (DMSO = 0.50%, v/v; [**3**] = 10 μM) to assess the effect of the putative IDH2 WT PROTAC inhibitor, **3**, on WT cells. The effect of PROTAC **3** was compared with that of the IDH2 WT inhibitor, **2**. An FDR-adjusted t-test and relative fold change (FC) calculation was performed on the metabolite abundances between experimental groups.

Three metabolites in set **A** exhibited significantly and substantially different abundances between control WT cells and treated WT cells: *cis*-aconitic acid (FDR = 0.0199, FC = 2.39), 2-OG (FDR = 0.0272, FC = 1.40), and β-CG (FDR = 0.0212, FC = 2.24) (**Table 3.6.A**).

26 metabolites in set **B** exhibited significantly and substantially different abundances between control WT cells and treated WT cells: 2-ketobutyric acid (FDR = 0.0264, FC = 1.40), 4-hydroxyphenylglycine (FDR = 0.0331, FC = 4.14), 4-hydroxyproline (FDR = 0.0273, FC = 2.68), 4-hydroxypyrrolidinone (FDR = 0.0272, FC = 2.07), adenosine diphosphate (ADP, FDR = 0.0182, FC = 2.25), adenosine triphosphate (ATP, FDR = 0.0272, FC = 2.21), cytidine diphosphate (CDP, FDR = 0.0182, FC = 1.76), cytidine triphosphate (CTP, FDR = 0.0272, FC = 1.67), deoxyguanosine diphosphate (dGDP, FDR = 0.0348, FC = 2.54), dihydrouracil (FDR = 0.0351, FC = 1.76), FAD (FDR = 0.0380, FC = 1.88), fumarate (FDR = 0.0272, FC = 1.70), glutamylcysteine (FDR = 0.0182, FC = 1.71), glutathione (GSH, FDR = 0.0201, FC = 1.96), guanosine diphosphate

(GDP, FDR = 0.0351, FC = 1.92), guanosine monophosphate (GMP, FDR = 0.0264, FC = 2.01), *N*-acetyl-aspartate (FDR = 0.0348, FC = 2.62), *N*-acetylglutamate (FDR = 0.0182, FC = 2.44), *N*-acetylglycine (FDR = 0.0264, FC = 1.58) *N*-acetyl-L-alanine (FDR = 0.0182, FC = 1.89), NAD^+ (FDR = 0.0331, FC = 1.90), 2-oxoadipic acid (FDR = 0.0182, FC = 2.03), pyridoxal-5'-phosphate (P5P, FDR = 0.0296, FC = 2.53), taurine (FDR = 0.0393, FC = 1.79), uridine diphosphate (UDP, FDR = 0.0264, FC = 1.85), uridine triphosphate (UTP, FDR = 0.0387, FC = 1.62) (**Table 3.6.B**).

Metabolites	Higher in	FC	p-value (FDR)
A			
Glucose	-	-	-
Lactic acid	-	-	-
Citric acid	-	-	-
cis-Aconitic acid	WT **3**	2.39	*
Isocitrate	-	-	-
2-OG	WT **3**	1.40	*
Succinic acid	-	-	-
Glutamine	-	-	-
Glutamic acid	-	-	-
2-HG	-	-	-
β-CG	WT **3**	2.24	**
B			
2-Ketobutyric acid	WT **3**	1.40	*
2-Oxoadipic acid	WT **3**	2.03	*
4-Hydroxyphenylglycine	WT **3**	4.14	*
4-Hydroxyproline	WT **3**	2.68	*
4-Hydroxypyrrolidinone	WT **3**	2.07	*
ADP	WT **3**	2.25	*
ATP	WT **3**	2.21	*
CDP	WT **3**	1.76	*
CTP	WT **3**	1.67	*
dGDP	WT **3**	2.54	*
Dihydrouracil	WT **3**	1.76	*
FAD	WT **3**	1.88	*
Fumarate	WT **3**	1.70	*
γ-Glutamylcysteine	WT **3**	1.71	*
Glutathione (GSH)	WT **3**	1.96	*
GDP	WT **3**	1.92	*
GMP	WT **3**	2.01	*
N-Acetyl-aspartate	WT **3**	2.62	*
N-Acetylglutamate	WT **3**	2.44	*
N-Acetylglycine	WT **3**	1.58	*
N-Acetyl-L-alanine	WT **3**	1.89	*
NAD^+	WT **3**	1.90	*
P5P	WT **3**	2.53	*
Taurine	WT **3**	1.79	*
UDP	WT **3**	1.85	*
UTP	WT **3**	1.62	*

Table 3.6 | *Overview of identified metabolites that were significantly and substantially different between control WT cell samples (DMSO = 0.50%, v/v) and treated WT cell samples (DMSO = 0.50%, v/v; **[3]** = 10 μM; treatment duration = 24 hours). Set **A**: Selected metabolites representing the Warburg Effect, TCA cycle, glutamine-glutamate cycle, IDH1 R132H gain-of-function and β-Citryl-L-glutamic acid. Set **B**: Additional significantly and substantially different metabolites. Significantly different*

*(FDR): * < 0.05, ** < 0.01, *** < 0.001, **** < 0.0001. Substantially different: FC > 1.2. Significantly higher abundances in treated WT cells are teal. Statistical tests and calculations were performed on median normalised data. 2-OG = 2-Oxoglutaric acid. 2-HG = 2-Hydroxyglutaric acid. β-CG = β-Citryl-L-glutamic acid. ADP = Adenosine diphosphate. ATP = Adenosine triphosphate. CDP = Cytidine diphosphate. CTP = Cytidine triphosphate. dGDP = Deoxyguanosine diphosphate. GDP = Guanosine diphosphate. GMP = Guanosine monophosphate. NAD^+ = Nicotinamide adenine dinucleotide. P5P = Pyridoxal-5'-phosphate. UDP = Uridine diphosphate. UTP = Uridine triphosphate.*

Examination of the findings reveal significantly and substantially altered abundances between the control WT cells and the WT cells treated with **3** in distinct areas of metabolism; multiple metabolites were found to be significantly altered including co-/post-translationally modified amino acids, nucleotides, redox homeostasis and glutathione synthesis metabolites, and TCA cycle metabolites. Other metabolites included 4-hydroxyphenylglycine, 4-hydroxypyrrolidinone, 2-oxodipic acid, β-CG, P5P, and taurine.

Significantly altered abundances of co-/post-translationally modified amino acids in WT cells treated with 3

N-Acetyl-aspartate, *N*-acetylglutamate, *N*-acetylglycine, *N*-acetyl-L-alanine, and 4-hydroxyproline were significantly and substantially elevated in treated WT cells compared to control WT cells. *N*-acetylation of amino acids by N-terminal acetyltransferases (NATs) occurs at the N-terminus of most proteins (~85%) and facilitates protein synthesis, stability and localisation.[397] 4-Hydroxyproline is produced by the post-translational hydroxylation of proline residues in proteins, catalysed by prolyl hydroxylases. The elevated levels of free *N*-acetylated amino acids and 4-hydroxyproline may be increased due to elevated levels of proteolysis in the cell.

Significantly altered abundances of nucleotides and related metabolites in WT cells treated with 3

ADP, ATP, CDP, CTP, GDP, GMP, dGDP, UDP, UTP, and dihydrouracil in treated WT cells were significantly and substantially higher than in control WT cells. ADP, ATP, GDP, GMP, and dGDP are purine nucleotides derived from R5P and the PPP. IMP is the final shared intermediate in the *de novo* purine biosynthesis pathway. To form GMP, IMP is dehydrogenated by IMP dehydrogenase to form xanthosine monophosphate (XMP, produces NADH), which is then reacted with glutamine by GMP synthase (ATP dependent) to yield GMP and glutamate. To form AMP, IMP is reacted with aspartate by adenylosuccinate synthetase (GTP dependent) to form adenylosuccinate, then cleaved by adenylosuccinate lyase to release AMP and fumarate.

The *de novo* purine biosynthesis pathway is regulated at the first step, catalysed by ribose-phosphate pyrophosphokinase (PRPS1, R5P + ATP → PRPP + AMP), and the second step, catalysed by glutamine phosphoribosylpyrophosphate amidotransferase (GPAT/PPAT, PRPP + glutamine + H_2O → phosphoribosylamine (PRA) + glutamate + PP_i); PRPS1 is activated by P_i and inhibited by purine nucleotides, GPAT/PPAT is activated by PRPP and inhibited by purine nucleotides. CDP, CTP, UDP, and UTP are pyrimidine nucleotides derived from glutamine and aspartate. The *de novo* pyrimidine synthesis pathway produces UMP from the decarboxylation of orotate monophosphate (OMP), then UMP undergoes two successive phosphorylation events using ATP to form UTP, then UTP is reacted with glutamine by CTP synthase (ATP dependent) to produce CTP.

The *de novo* pyrimidine biosynthesis pathway is regulated at the first step, which is the formation of carbamoyl phosphate by carbamoyl phosphatase synthase II from glutamine,

bicarbonate, ATP, and a water molecule; ATP and PRPP activate the reaction, and UTP inhibits the reaction. Dihydrouracil is reversibly produced from uracil by dihydrouracil dehydrogenase (in an NADH dependent manner).

Significantly altered abundances of glutathione synthesis and redox homeostasis metabolites in WT cells treated with 3

2-Ketobutyric acid, glutamylcysteine, glutathione, NAD^+, and FAD in treated WT cells were significantly and substantially higher than control WT cells. Reduced glutathione (GSH) is an essential endogenous antioxidant that neutralises ROS and free radicals, producing oxidised glutathione disulfides (GSSG) in the process. Glutamate and cysteine are reacted by glutamate-cysteine ligase (ATP dependent) to form γ-glutamylcysteine, then γ-glutamylcysteine is reacted with glycine by glutathione synthetase (ATP dependent) to produce glutathione. As mentioned previously (**Section 3.3.1**), the concentration of cellular cysteine may become limiting for glutathione synthesis in periods of elevated oxidative stress; homocysteine is then diverted from methionine synthesis and reacted with serine by cystathionine-β-synthase to form cystathionine, then cystathionine is cleaved by cystathionine-γ-lyase to release cysteine and 2-ketobutyric acid. NAD^+ and FAD are the oxidised forms of electron carriers NADH and $FADH_2$. The NAD^+ *de novo* synthesis pathway converts tryptophan into nicotinic acid adenine dinucleotide (NaAD), which is finally amidated to NAD^+. Riboflavin is phosphorylated by riboflavin kinase (ATP dependent) to form flavin mononucleotide (FMN), FMN is then adenylated by FAD synthase (ATP dependent) to form flavin adenine dinucleotide (FAD). NAD^+ and FAD are derived from nucleotides and are therefore also related to the significantly altered nucleotide metabolites discussed above.

Significantly altered abundances of TCA cycle metabolites in WT cells treated with 3

cis-Aconitic acid, 2-OG, and fumarate levels were significantly and substantially higher in WT cells treated with **3** than in control WT cells. Acetyl-CoA reacts with OAA, catalysed by citric acid synthase, to form citric acid (**Figure 1.1**). Citric acid is reversibly isomerised in two steps to isocitrate via the intermediate *cis*-aconitic acid, catalysed by aconitase (**Figure 1.1**). Isocitrate is decarboxylated and oxidised to produce 2-OG by IDH1/2/3 WT (IDH1/2 WT produce NADPH, IDH3 WT produces NADH), then 2-OG is decarboxylated and oxidised to succinyl-CoA by 2-OG dehydrogenase (produces NADH) (**Figure 1.1**). 2-OG can be decarboxylated by 2-OG-dependent dioxygenases in the presence of molecular oxygen to directly produce succinate and is regularly a substrate/product in transamination reactions producing/consuming glutamate. Succinic acid is released from succinyl-CoA by succinyl-CoA synthetase (produces GTP), then oxidised by succinic dehydrogenase to fumarate (produces QH_2) (**Figure 1.1**). Fumarate is a side product of the purine synthesis and salvage pathways; IMP reacts with aspartate to form adenylosuccinate (catalysed by adenylosuccinate synthase), then cleaved by adenylosuccinate lyase to release fumarate and AMP (**Figure 3.3**). Fumarate is hydrated to malate by fumarate hydratase, then malate is oxidised by malate dehydrogenase (produces NADH) to regenerate OAA (**Figure 1.1**). Fumarate may be recycled to aspartate for the synthesis of AMP; fumarate is converted to OAA via the TCA cycle, then OAA is reacted with glutamate via transamination to produce aspartate and 2-OG.

Other significantly altered metabolites in WT cells treated with 3

4-Hydroxyphenylglycine, 4-hydroxypyrrolidinone, 2-oxodipic acid, β-CG, P5P, and taurine were found in treated WT cells to be significantly and substantially higher than control WT cells.

2-Oxoadipic acid is a shared metabolite in late-phase of lysine, hydroxylysine, and tryptophan degradation pathways.[376, 391] 2-Oxoadipic acid is the precursor of glutaric acid (which found to be altered between control WT cells and WT cells treated with **1**, **Section 3.4.1**) and glutaconic acid (which was found to be altered between control WT cells and control MUT cells, **Section 3.3.1**). 2-Aminoadipate is derived from lysine or hydroxylysine and reacts with 2-OG to produce 2-oxoadipic acid and glutamate, as catalysed by kynurenine/2-aminoadipate amino transferase.[398] 2-Aminomuconate derived from tryptophan is converted to 2-oxoadipic acid, as catalysed by an unknown enzyme, in the reaction: 2-aminomuconate + NADH + H^+ + H_2O → 2-oxoadipic acid + NH_3 + NAD^+).[399] 2-Oxoadipic acid is then decarboxylated by 2-oxoadipate dehydrogenase to produce glutaryl-CoA, which may form glutaric acid and glutaconic acid in cases of metabolic dysfunction.[400-404]

β-CG levels were previously found to be significantly altered between control WT cells and control MUT cells (**Section 3.3.1**, **Section 3.3.2**). β-CG is synthesised by RIMKLB, and a lesser extent RIMKLA, from citric acid and glutamate, then cleaved by GCPIII to recover citric acid and glutamate.[227, 358, 381] β-CG is structurally related to NAAG, a neurotransmitter synthesised from *N*-acetylaspartate and glutamate by RIMKLA, and RIMKLB to a lesser extent, then cleaved by GCPII to release *N*-acetylaspartate and glutamate.[227, 229, 358, 405]

Taurine is an abundant non-proteinogenic sulfur amino acid (that makes up ~0.1% total human bodyweight), which is derived from cysteine, and which is proposed to contribute to cytoprotection, development, and neurotransmission.[406] Cysteine is oxidised by cysteine dioxygenase (O_2 dependent) to produce cysteine sulfinic acid, then cysteine sulfinic acid is decarboxylated by sulfinoalanine-decarboxylase to form hypotaurine, then hypotaurine is oxidised by hypotaurine dehydrogenase (produces NADH) to produce taurine.[407] Homocysteine may also be converted to taurine via the transulfuration pathway (discussed previously in the context of glutathione synthesis and 2-ketobutyic acid/2-hydroxybutyric acid production, **Section 3.3.1**, **Section 3.6.1**).[408]

P5P is the active form of vitamin B6 and a widespread coenzyme in enzymatic reactions (~4% of classified enzyme activities); notably, transamination, deamination, decarboxylation, and racemisation reactions. P5P cannot be synthesised in the body and is usually derived from the diet.

4-Hydroxyphenylglycine is a non-proteinogenic amino acid, similar in structure to tyrosine. 4-Hydroxypyrrolidinone is structurally related to 4-hydroxyproline. Similar to 4-hydroxybutyric acid, 2-hydroxybutyric acid, and 2-ketobutyric acid, 4-hydroxyphenylglycine and 4-hydroxypyrrolidinone are structurally related to more commonly identified biological metabolites. It may be that the compound features are caused by tyrosine and 4-hydroxyproline fragments or isomers, which were not detected by the algorithm or absent from the metabolite database used for identifications.

3.6.2. Univariate Statistical Analysis of MUT Cells Treated with Compound 3

FDR adjusted t-test and relative FC analysis of MUT Cells treated with compound 3

Control MUT cells (DMSO = 0.50%, v/v) were compared with treated MUT cells (DMSO = 0.50%, v/v; [**3**] = 10 μM) to assess the effect of **3**, on MUT cells. An FDR adjusted t-test and relative FC calculation was performed on the abundances of each metabolite pair between experimental groups. No metabolites in set **A** or set **B** were found to have significantly different abundances between the control MUT cells and MUT cells treated with **3**.

3.6.3. Multivariate Statistical Analysis of LN18 GBM Cells Treated with Compound 3

PLS-DA model of LN18 GBM Cells treated with compound 3

To supplement the findings of the univariate statistical analysis (FDR adjusted t-test and relative FC calculations), multivariate methods of statistical analysis were performed on the data from experiment 2. A PLS-DA model containing every experimental group was generated using the website www.metaboanalyst.ca (**Figure 3.14**). The PLS-DA component scores for each sample were visualised using a 2D plot of component 1 (X axis) against component 2 (Y axis) (**Figure 3.14.A**). Treatment with compound **3** appeared to lead to a shift along the X axis for cell samples regardless of mutational status. The experimental groups comprising control and treated MUT cells (MUT Control, MUT **3**) overlapped, partially separating along the X axis. Similarly, the experimental groups comprising control and treated WT cells (WT Control, WT **3**) overlapped, partially separating along the X axis. The presence of the IDH1 R132H mutation in cell samples appeared to lead to a shift along the Y axis. The experimental groups comprising MUT cells (MUT Control, MUT **3**) completely separated from the

experimental groups comprising WT cells (WT Control, WT **3**) along the Y axis. The graphical separation of cell samples in the PLS-DA scores plot suggests that both the presence of an IDH1 R132H mutation, and treatment with **3**, are associated with systematic alterations in metabolite concentrations within LN18 GBM cells.

The PLS-DA model was assessed by leave-one-out cross-validation (LOOCV) and permutation testing. LOOCV yielded acceptable parameters representing the accuracy, fit, and predictability of the model (5 components, accuracy = 0.75, $R^2 = 0.98$, $Q^2 = 0.82$, **Figure 3.14.B**). Permutation testing determined the separation to be significant ($p = 0.024$, **Figure 3.14.C**). The test results indicated that it is possible to have a degree of confidence in the predictions of the model. Variable importance in projection (VIP) scores were generated to identify the most important metabolites and compound features contributing to the model (**Table 3.7**).

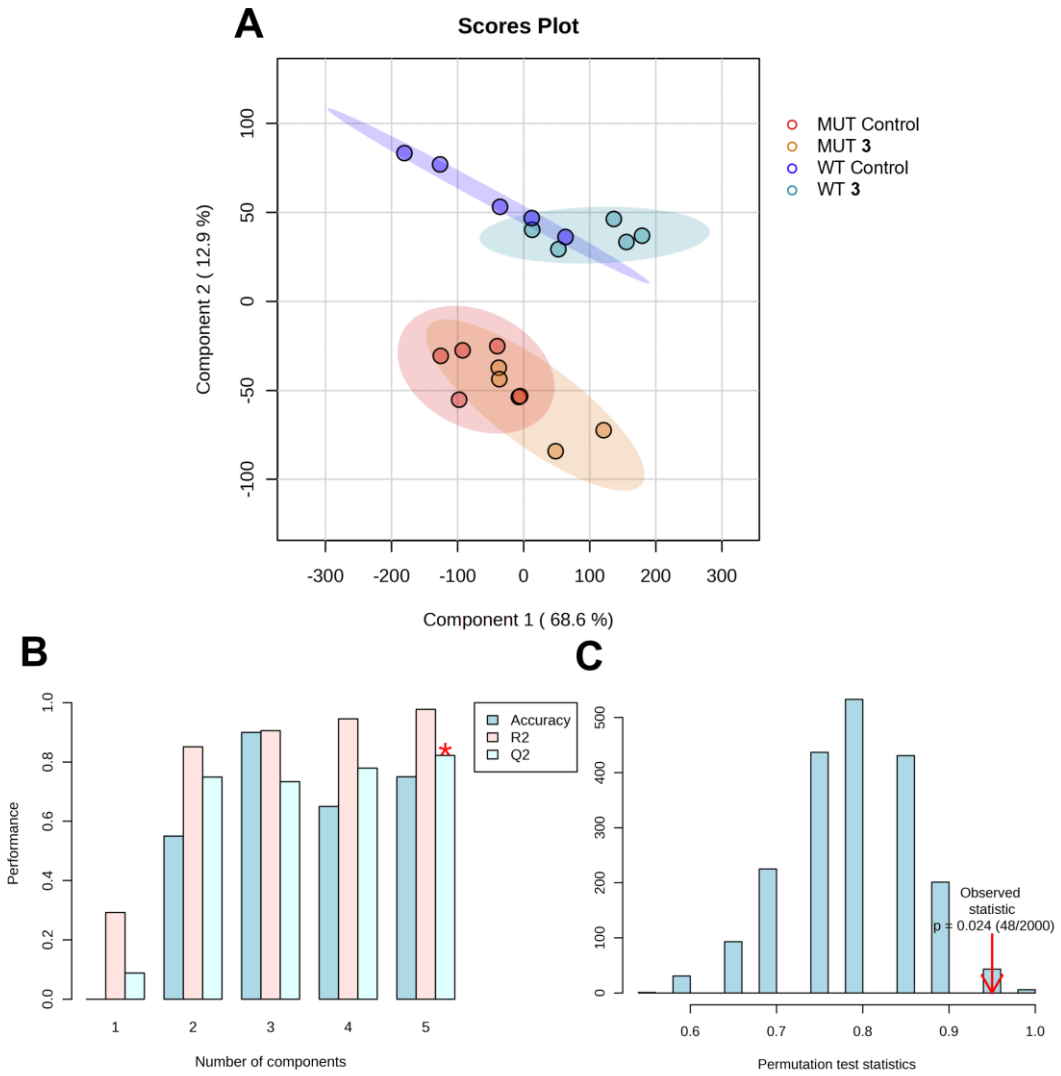

Figure 3.14 *| PLS-DA model of experiment 2. Experimental groups: Control WT cell samples blue (n = 5); WT cell samples treated with **3** are cyan (n = 5); Control MUT cell samples are orange (n = 5); MUT cell samples treated with **3** are orange (n = 5). Control cells were incubated in growth media containing DMSO for 24 hours. Treated cells were incubated in growth media containing **3** (5 μM) for 24 hours.* ***A.*** *PLS-DA scores plot (X axis = component 1, Y axis = component 2). The shaded area for each experimental group represents the 95% confidence region.* ***B.*** *Bar plot summarising the performance of cross-validation (LOOCV, 5 components).* ***C.*** *Bar plot summarising the permutation test (test statistic = prediction accuracy, permutations = 2000).*

The top 15 important features ranked by VIP score contained nine identified metabolites and six unidentified compound features. The identified metabolites comprised 2-HG (1st, 39.60), 6-phosphogluconic acid (3rd, 9.30), glutamic acid (4th, 8.31), βCG (5th, 7.67), glutathione (GSH) (6th, 7.18), *N*-methyl-D-aspartic acid (NMDA, 7th, 6.35), ADP (8th, 5.81), fructose 6-phosphate (9th, 5.35), and uridine 5'-monophosphate (UMP, 15th, 4.03) (**Table 3.7**). The unidentified compound features are labelled with their retention times

and ionic (m/z) or neutral ('n') mass values, as measured by the IC-MS. The unidentified compound features comprised 13.77_97.9767n (2nd, 38.99), 13.61_307.0836n (10th, 5.28), 9.80_333.0229m/z (11th, 5.04), 12.58_339.0735n (12th, 4.19), 13.30_195.0508m/z (13th, 4.03) and 11.04_97.9672n (15th, 3.81) (**Table 3.7**).

Compound	VIP score
2-HG	39.60
13.77_97.9767n	38.99
6PG	9.30
Glutamic acid	8.31
β-CG	7.67
Glutathione (GSH)	7.18
NMDA	6.35
ADP	5.81
F6P	5.35
13.61_307.0836n	5.28
9.80_333.0229m/z	5.04
12.58_339.0735n	4.19
13.30_195.0508m/z	4.03
UMP	4.03
11.04_97.9672n	3.81

Table 3.7 *| Top 15 identified metabolites and compound features ranked by VIP score. VIP scores were generated by the PLS-DA model of WT and MUT cells in* ***Figure 3.14****.*

Important metabolites identified by multivariate analyses are related to significantly altered metabolites identified by univariate analyses

Nine identified metabolites were ranked in the top 15 important features by VIP score. Four metabolites considered important by the PLS-DA model were previously identified as being significantly altered in the univariate analyses (**Table 3.6**), that is 2-HG, β-CG, glutathione, and ADP.

The four remaining identified metabolites (6PG, F6P, UMP, and glutamic acid), although not significantly altered, are associated with pathways containing other significantly altered metabolites (for example, RL5P, R5P, CDP, CTP, UDP, UTP, P5P, 2-OG, β-CG,

γ-glutamylcysteine, *N*-acetylglutamate, and succinic semialdehyde). 6PG and F6P are intermediates in the PPP (**Figure 3.3**); the PPP also includes R5P and RL5P, levels of which were both found to be significantly elevated in MUT cells compared to WT cells.[342, 343] In the *de novo* pyrimidine biosynthesis pathway, UMP is the precursor of UDP, UTP, CDP, and CTP, all four of which exhibited significantly higher abundances in treated WT cells than control WT cells.[409-412]

Glutamic acid participates in several pathways with significantly altered metabolite abundances. Glutamic acid can be transaminated using P5P as a coenzyme, or deaminated, to produce 2-OG in the TCA cycle; the abundances of P5P and 2-OG in treated WT cells were found to be significantly higher than in control WT cells.[180, 189, 413-416] Glutamic acid reacts with citric acid to produce β-CG, acetyl-CoA to produce *N*-acetylglutamate, and cysteine to produce γ-glutamylcysteine during glutathione synthesis; levels of β-CG, *N*-acetylglutamate, γ-glutamylcysteine, and glutathione were each found in treated WT cells to be significantly higher than in control WT cells.[381, 417, 418] Finally, glutamic acid may also be a source of succinic semialdehyde via GABA synthesis.[419]

Uniquely of the metabolites for which a change was observed, *N*-methyl-D-aspartate (NMDA) is not involved in a pathway that had significantly altered metabolites revealed by univariate analyses. Nonetheless, NMDA is a neurotransmitter *N*-methylated derivative of D-aspartate, binding selectively to NMDA glutamate receptors.[420] D-Aspartate is the precursor of *N*-acetylaspartate, which reacts with glutamate to form NAAG; NAAG itself is synthesised by RIMKLA, and to a lesser extent RIMKLB, which also catalyses the synthesis of β-CG.[381] As discussed above, neurotransmitter homeostasis appeared to be affected by the presence of the IDH1 R132H mutation

(**Section 3.3.1**); therefore, here, a related underlying mechanism may inform the VIP score.

3.6.4. Discussion

The results imply that compound **3** exhibits differential effects on WT and MUT cells. In MUT cells treated with compound **3**, no significant changes in abundance were observed when compared to control MUT cells. Conversely, in WT cells, treatment resulted in 29 significantly altered abundances relative to controls. Given that Compound **3** was designed to target IDH2 WT specifically as a PROTAC, the apparent lack of observed inhibition of IDH1 R132H is an interesting outcome. Furthermore, the presence of the IDH1 R132H mutation appears to mitigate the metabolic effects of Compound **3**, a phenomenon similarly noted with the IDH2 WT inhibitor, Compound **2**. Without significant alterations akin to those seen with Compound **1**, it is unlikely that Compound **3** inhibits IDH1 R132H. Therefore, while we can infer some level of selectivity in that Compound **3** likely does not target IDH1 R132H, further investigation is required to conclusively determine its specificity towards IDH2 WT.

Although further work is required, the observed alterations in several metabolites suggest that, as intended, the degradation of IDH2 WT may indeed be taking place. In the mitochondria, IDH2 WT typically facilitates the conversion of 2-OG to ICT, where 2-OG is often sourced from glutamate. Should IDH2 WT undergo degradation, it could result in the accumulation of 2-OG, which was found to be significantly higher in treated WT cells than control WT cells. Elevated levels of 2-OG could potentially lead to a temporarily increased glutamate concentration because the glutamate dehydrogenase catalysed reaction is reversible. This local glutamate surplus might then enhance the synthesis of β-CG, which was found to be significantly elevated in treated WT cells (compared to control WT cells). β-CG facilitates the activation of aconitase by serving as

a chaperone for iron (II), delivering it directly to the enzyme's active site.[225] The chelation of iron (II) by β-CG is mediated through its citric acid derived group, citric acid itself a substrate of aconitase.[225] Treatment with β-CG can reactivate aconitase that has been inactivated by ammonium peroxodisulfate.[225] Given the critical function of the glutamate-glutamine cycle in astrocytes,[190] β-CG might also play a regulatory role in glutamine synthase by acting as a chaperone for magnesium or manganese.[231] This chelation could perhaps be facilitated by the glutamate moiety of β-CG, a substrate of glutamine synthase.

Given that β-CG serves as an enhancer of aconitase, this mechanism would explain the observed rise in *cis*-aconitate levels in treated WT cells (compared to control WT cells) by promoting its synthesis.[225] Even if metabolic flux attempted to progress via IDH2 WT in the forward direction, increased levels of β-CG may still lead to increased levels of *cis*-aconitic acid; accumulation of isocitrate, which then converts back to cis-aconitate or citrate via aconitase, could occur. The link between IDH2 WT and β-CG is less direct in this scenario, but synthesis of β-CG may be influenced by an increase in citrate levels. Accumulation of citrate may stimulate the production of β-CG, which, in turn, activates aconitase and enhances the conversion rate of citrate through the cycle. In the absence of functional IDH2 WT, however, the pathway experiences a bottleneck at isocitrate, leading to elevated levels of cis-aconitate.

Treatment of WT cells with compound **3** was observed to significantly increase (compared to control WT cells) the concentrations of *N*-acetylated amino acids (*N*-Acetyl-aspartate, *N*-acetylglutamate, *N*-acetylglycine, and *N*-acetyl-L-alanine) and 4-hydroxyproline, both of which are typically generated as a result of post-translational modifications, specifically *N*-acetylation and hydroxylation.[421-423] These modifications are generally protein-associated, and their elevated presence in free form strongly

suggests release from protein degradation. This observation is consistent with the proposed mechanism of action of compound **3**, namely, its role as a protein degrader. However, while these data are indicative of protein turnover, they do not definitively establish IDH2 WT as the target of degradation.

The data suggest that treatment with compound **3** induces oxidative stress in cells, as evidenced by elevated levels of γ-glutamylcysteine, 2-ketobutyric acid, and glutathione. Additionally, an increase in the oxidized forms of the nucleotide electron carriers NAD^+ and FAD was observed, which may partly reflect the increased nucleotide synthesis. A possible explanation for this oxidative stress is enhanced protein degradation, potentially involving off-target proteins critical for redox homeostasis. Alternatively, the intended action of compound **3** as a PROTAC targeting IDH2 WT may disrupt mitochondrial NADPH production, directly compromising the cell's ability to maintain redox balance.

Targeting the mitochondrial isoform IDH2 WT could conceivably impair compensatory mechanisms involving IDH1 WT or the pentose phosphate pathway (PPP), both of which might otherwise mitigate the oxidative burden. In cells with the IDH1 R132H mutation, the generation of reducing equivalents appears to shift toward the cytosolic PPP, consistent with the peroxisomal and cytosolic localization of IDH1 R132H. Univariate analysis of control samples reveals significant upregulation of PPP metabolites in the presence of the IDH1 R132H mutation, and variable importance in projection (VIP) scores underscore the PPP's role across all groups. If this scenario holds true, it highlights the critical importance of mitochondrial IDH2 WT in maintaining cellular redox homeostasis.

Treatment with compound **3** resulted in a significant increase in the levels of nearly all nucleotide forms, including ADP, ATP, CDP, CTP, GDP, GMP, dGDP, UDP, and UTP.

The underlying mechanism driving this increase is not immediately apparent, but it may involve the activation of the *de novo* purine and pyrimidine nucleotide synthesis pathways. If **3** targets IDH2 WT, it may indicate that IDH2 WT activity is linked to nucleotide synthesis, but the precise manner in which these pathways are activated remains unclear and warrants further investigation.

The observed increase in fumarate levels could be attributed to elevated 2-oxoglutarate levels progressing through the TCA cycle to fumarate. Alternatively, it might result from enhanced AMP synthesis, releasing fumarate from adenylosuccinate.

Interestingly, the final steps of the lysine, hydroxylysine, and tryptophan degradation pathways were represented by significantly altered metabolites in the pairwise comparative observations of control WT and control MUT cells (glutaconic acid), control WT cells and WT cells treated with **1** (glutaric acid), control MUT cells and MUT cells treated with **1** (glutaconic acid), and control WT cells and WT cells treated with **3** (2-oxoadipic acid). Given that the metabolic effects involved were putatively driven by the IDH1 R132H gain-of-function, IDH1 WT inhibition, and IDH2 WT degradation, further work is warranted to investigate the relationship between IDH isoforms and the shared end phase of lysine, hydroxylysine, and tryptophan degradation pathways. The final steps of these pathways involve the enzymes 2-oxoadipic acid dehydrogenase and glutaryl-CoA dehydrogenase. Changes in local redox homeostasis near the IDH1 R132H mutation or inhibited IDH1/2 WT could impair the activity of these enzymes. Furthermore, considering that 2-oxoadipic acid, glutaric acid, and glutaconic acid are partial structural analogues of 2-OG and 2-HG, there might be enzymatic promiscuity with IDH1/2 WT and/or IDH1 R132H potentially catalysing yet unknown off-target reactions, where 2-oxoadipic acid, glutaric acid, and glutaconic acid could be involved either as substrates or products.

Therefore, while these findings suggest that compound **3** does not target IDH1 R132H, indicating a certain degree of selectivity, we cannot conclusively assess its efficacy against IDH2 WT based solely on this data. Interestingly, compound **3** did not lead to a significant increase in galactose, as observed for treatment with **2**. The results suggest that the IDH1 R132H mutation may exert a dominant metabolic influence that can override disruptions specific to the wild-type enzyme. This observation could represent an adaptive advantage conferred by the IDH1 R132H mutation, potentially locking the cell into a metabolic state that is resilient to external perturbations. However, it is impossible to confidently conclude whether any effects were truly related to IDH2 WT activity without evidence of its degradation by **3**. For the purposes of these studies, this assessment is critical and must be addressed in future work. Similarly, it should be ruled out that any metabolic effects observed after treatment with **3** were not solely due to the activity of the thalidomide moiety, particularly considering thalidomide's reported efficacy as an anti-cancer agent in its own right.[424]

Several important limitations constrain the interpretation of these metabolomic findings. First, the LN18 cell line used in these studies carries a lentivirally introduced IDH1 R132H mutation, rather than a naturally occurring chromosomal mutation; therefore, the cellular context likely does not fully reflect the biology of gliomas harbouring endogenous IDH1 mutations. Second, although compound **3** retains key structural elements of an IDH2 WT inhibitor (compound **2**), its potency against IDH2 WT has not been directly determined, and, critically, no orthogonal evidence, such as immunoblotting or proteomic analysis, has been obtained to confirm degradation of IDH2 WT in treated cells. The absence of direct target engagement data therefore remains a substantial limitation when interpreting the observed metabolic effects. Third, the metabolomics analyses for experiment 2 were conducted using a relatively modest sample size (n=5),

reducing statistical power and increasing the risk of both false positive and false negative findings. Furthermore, the analytical platform used was optimised for the detection of TCA cycle intermediates; therefore, potentially relevant alterations in lipid metabolism may have been under-represented. Additionally, the metabolite identification database employed, while comprehensive, is inevitably incomplete. Consequently, some detected features highlighted as significant may instead correspond to unidentified fragments rather than bona fide metabolites. This limitation, coupled with the use of exogenous glutamine supplementation, which is likely to have influenced glutamine and glutamate metabolism, further complicates the assignment of specific pathway-level perturbations.

Collectively, these factors emphasise the need for complementary approaches, encompassing targeted lipidomics, orthogonal proteomic analyses, and studies in physiologically relevant cellular and tissue contexts, to fully elucidate the molecular and metabolic consequences of compound **3** treatment. While the current observations may be consistent with a role for compound **3** in modulating IDH2 WT function, a more comprehensive evaluation will be required to define its precise mechanism of action and to exclude the contribution of off-target effects or potential independent activities arising from the thalidomide-derived moiety.

3.7. Summary

The IDH1 R132H mutation, frequently occurring in various cancers including gliomas, significantly disrupts cellular metabolism. This mutation leads to increased consumption of 2-OG and NADPH and production of 2-HG, impacting redox balance and biosynthesis.[16] In this chapter, significant and substantial differences in measured metabolite abundances between WT cells and MUT cells were interpreted to suggest dysregulation in the PPP, *de novo* nucleotide synthesis, neurotransmitter homeostasis,

lysine/hydroxylysine/tryptophan degradation, glutathione synthesis, and lipid metabolism pathways. Due to the localisation of IDH1 WT in the peroxisome, the R132H mutation likely impacts peroxisomal function and fatty acid metabolism. The effects appear to be differentiated between effects that involve the peroxisome, and effects that do not.[24]

Treatment of WT and MUT cells with an inhibitor of IDH1 WT, compound **1**, revealed inhibition of IDH1 R132H-induced metabolic effects and putatively IDH1 WT-mediated effects of glutaric acid accumulation.

Treatment of WT and MUT cells with an inhibitor of IDH2 WT, compound **2**, demonstrated effects in WT cells alone, significantly increasing the concentration of galactose. Consistent with the measured *in vitro* selectivity of the inhibitor for IDH2 WT, no effects were observed in MUT cells after treatment, although, galactose was not significantly altered in MUT cells either.

Treatment with a putative IDH2 WT-targeting PROTAC inhibitor, compound **3**, demonstrated widespread effects in WT, but not MUT, cells. Metabolites were significantly altered across multiple areas of metabolism including redox homeostasis, n-acetylated amino acids, nucleotide synthesis, amino acid degradation pathways and niche metabolites such as β-CG. The results suggest that the compound does not inhibit or degrade IDH1 R132H, and may successfully trigger protein degradation, but further investigation is required to conclude if IDH2 WT is being degraded.

Due to the localisation of IDH1 WT in the peroxisome, the R132H mutation likely impacts peroxisomal function and by extension fatty acid metabolism.[24] Indeed, the effects appear to be differentiated between effects that involve the peroxisome, and effects that do not.

Inside the peroxisome, IDH1 R132H likely depletes NADPH levels, leading to increased reactive oxygen species (ROS) production during the initial steps of peroxisomal β-oxidation.[215, 425] This increase in ROS in the peroxisomes is detected by peroxisomal biogenesis factor 2 (PEX2), which, sensing heightened β-oxidation, promotes adipose triglyceride lipase (ATGL) activity, thereby enhancing lipolysis.[379] The first step of lipolysis releases one molecule of DAG and a free fatty acid chain from a molecule of triacylglycerol (TAG).[426] Then, DAG activates a protein kinase, PKCδ, along with c-Abl, and increased levels of H_2O_2.[383, 385] In this way, the IDH1 R132H mutation might influence the activation PKCδ via increasing oxidative stress in the peroxisome; PKCδ may be directly activated by H_2O_2 and c-Abl, and DAG released from lipolysis triggered via PEX2 signalling. Increased lipolysis may then lead to higher rates of fatty acid oxidation; the data discussed previously suggest an increase in overall β-oxidation rates, marked by the depletion of valeric acid, an odd-numbered short chain fatty acid (**Section 3.3.1**). Furthermore, elevated levels of citramalic acid, as observed in the presence of the IDH1 R132H mutation, are a biomarker of propionyl-CoA carboxylase deficiency; propionyl-CoA carboxylase catalyses the conversion of propionyl-CoA to methylmalonyl-CoA following the conversion of valeric acid (in the form pentanoyl-CoA) to propionyl-CoA as the final step of odd-numbered fatty acid β-oxidation.[386, 425]

The R132H mutation also affects NAAG and β-CG levels. The IDH1 R132H mutation's gain-of-function appears to result in increased conversion of glutamate to 2-oxoglutarate (2-OG), potentially reducing the availability of glutamate needed for NAAG and β-CG synthesis.[427] However, glutamate levels themselves are not significantly altered. Alternatively, treatment of cells with a DAG-mimic activator (phorbol ester) of the PKC family is reported to deplete levels of NAAG.[382] This link suggests that oxidative stress, influenced by the mutation, might downregulate NAAG through PKCδ activation.

Outside the peroxisome, several diverse pathways appear to be dysregulated. The pentose phosphate pathway (PPP) appears to be upregulated to restore NADPH levels in MUT cells. Nucleotide synthesis appears to be upregulated, likely to fuel rapid cell proliferation. The GABA recycling pathway appears dysregulated, possibly to produce 2-OG in the presence of IDH1 R132H. The mitochondrial phase of the degradation pathways for amino acids like lysine, hydroxylysine, and tryptophan show signs of dysfunction. Finally, oxidative stress seems to be increased as evidenced by increased glutathione synthesis by-products.

Overall, the IDH1 R132H mutation appears to drive complex changes in peroxisomal dynamics and comprehensive metabolic reprogramming, affecting sugar metabolism, nucleotide synthesis, fatty acid metabolism, neurotransmitter synthesis, and signaling pathways, reflecting its profound impact on cellular metabolic homeostasis. Two treatments that did not target IDH1 R132H, **2** and **3**, led to significant changes in treated WT cells (compared to control WT cells), which were not observed in treated MUT cells (compared to control MUT cells). Therefore, the metabolic effects of the IDH1 R132H mutation are apparently strong enough to override the effects of putative IDH2 WT inhibition.

Further investigation is required (potentially using isotope tracers) to establish the precise mechanism of the relationship between treatment with **1** and glutaric acid, treatment with **2** and galactose, and the precise mechanism of action by which **3** led to widespread metabolic changes in WT cells.

4. The Development of Novel Inhibitors against SARS-CoV-2 Main Protease and Mycobacterium tuberculosis Ldt_{Mt2}

4.1. Introduction

4.1.1. COVID-19, SARS-CoV-2 Main Protease, and Ebselen

The outbreak of SARS-CoV-2 infections in 2020 and the ensuing pandemic caused part of the Schofield Group to shift its focus to potential therapeutic avenues against coronavirus 19 disease (COVID-19). Two thirds of the SARS-CoV-2 genome (~30 kilobases total) is reported to encode for two overlapping polyproteins, pp1a (4405 amino acids) and pp1b (7096 amino acids), which are processed by the SARS-CoV-2 main protease (M^{pro}) and the papain-like protease (PL^{pro}), to release 16 non-structural proteins (NSP 1-16).[428-430] M^{pro} (NSP5) initially releases itself from NSP4 and NSP6 by autolytic cleavage before digesting the remaining polyprotein at more than 11 conserved sites.[429, 430] The mechanism of action of M^{pro} utilises a catalytic dyad of His-41 and Cys-145 to conduct a nucleophilic attack on an amide bond in the natural substrate, forming a thioester linkage that is subsequently hydrolysed by a free water molecule to release the cleaved products.[429, 431] Early studies identified M^{pro} as being essential for viral replication and the nucleophilic cysteine was quickly identified as a potential target for covalent inhibition.[429, 432-435]

Ebselen (**26**) is an organoselenium compound with reported anti-oxidant, anti-inflammatory, anti-bacterial, anti-viral, anti-parasitic, anti-fungal, mood-stabilising, and cytoprotective activity.[436-457] **26** has also been investigated for the treatment of noise-

induced hearing loss, Ménière's disease, cerebral ischaemia, bipolar disorder.[436, 458-461] A high-throughput screen (HTS) with M^{pro} conducted by Jin *et al.* identified six small-molecule hits, including two clinically approved drugs (carmofur, disulfiram), and four pre-clinical candidates (**26**, shikonin, tideglusib, PX-12), of which **26** was the most potent (IC_{50} = 0.67 μM).[429, 462-467] **26** was confirmed by protein-observed mass spectrometry (POMS) to form covalent adducts with cysteine residues of M^{pro} (**Figure 4.1**), leading to clinical trials of **26** as a therapy against COVID-19.[429, 468] **26** may also act beneficially by scavenging reactive oxygen species (ROS), **26** has, however, also been reported to cause cellular toxicity, likely as a result of selenium toxicity and potentially due to the promiscuity of its reaction with cysteines.[449, 469] Studies using POMS have shown that **26** can react with up to 12 cysteines in M^{pro} as well as cysteines in L,D-transpeptidase *Mycobacterium tuberculosis* 2 (Ldt_{Mt2}), an enzyme which catalyses the formation of L-D cross-links in the bacterial cell wall. Subsequent crystallographic studies have suggested that **26** can fragment in the M^{pro} active site after initial reaction, depositing a free selenium atom.[431, 437, 470] The discrepancy in the nature of the final products indicates that the stability of post-reaction adduct is likely condition dependent, and the value of **26** as a clinical therapy against COVID-19 may be limited.

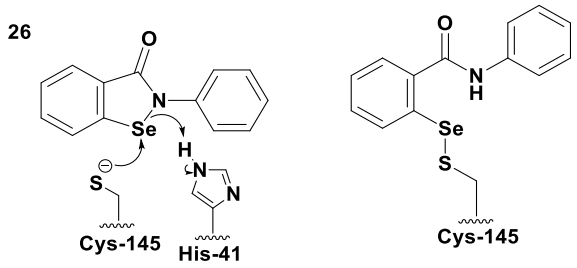

***Figure 4.1** | The hypothesised reaction of Cys-145 (M^{pro}) with **26**, to form a thioselenide bond.*

Substitution of sulfur for the toxic selenium of **26** gives a compound named 'ebsulfur' (**28**), consisting of a benzoisothiazolinone (BIT, **27**) core with an *N*-linked phenyl group

(**Figure 4.2.A**). Previous work by Dr Timothy Suits (Department of Chemistry, University of Oxford) found that **27** may react with the active site nucleophilic cysteine of Ldt_{MT2}; there is evidence from the literature that **27** can react with other cysteine-containing enzymes.[445, 471-473] Therefore, considering that the nitrogen of **27** may bind equivalently to the P1-P2 backbone amide nitrogen of M^{pro} natural substrates (analogous to the P1-P2 amide nitrogen of N3, **Figure 4.2.C**, **Figure 4.2.D**), it was decided to functionalise the core of **27** at the C6, C8, and N2 positions to build favourable interactions in the binding site, and develop covalent inhibitors selective for M^{pro} (**Figure 4.2.B**). The key aim was to decrease the number of cysteines with which an ebsulfur-type compound would react while maintaining potency.

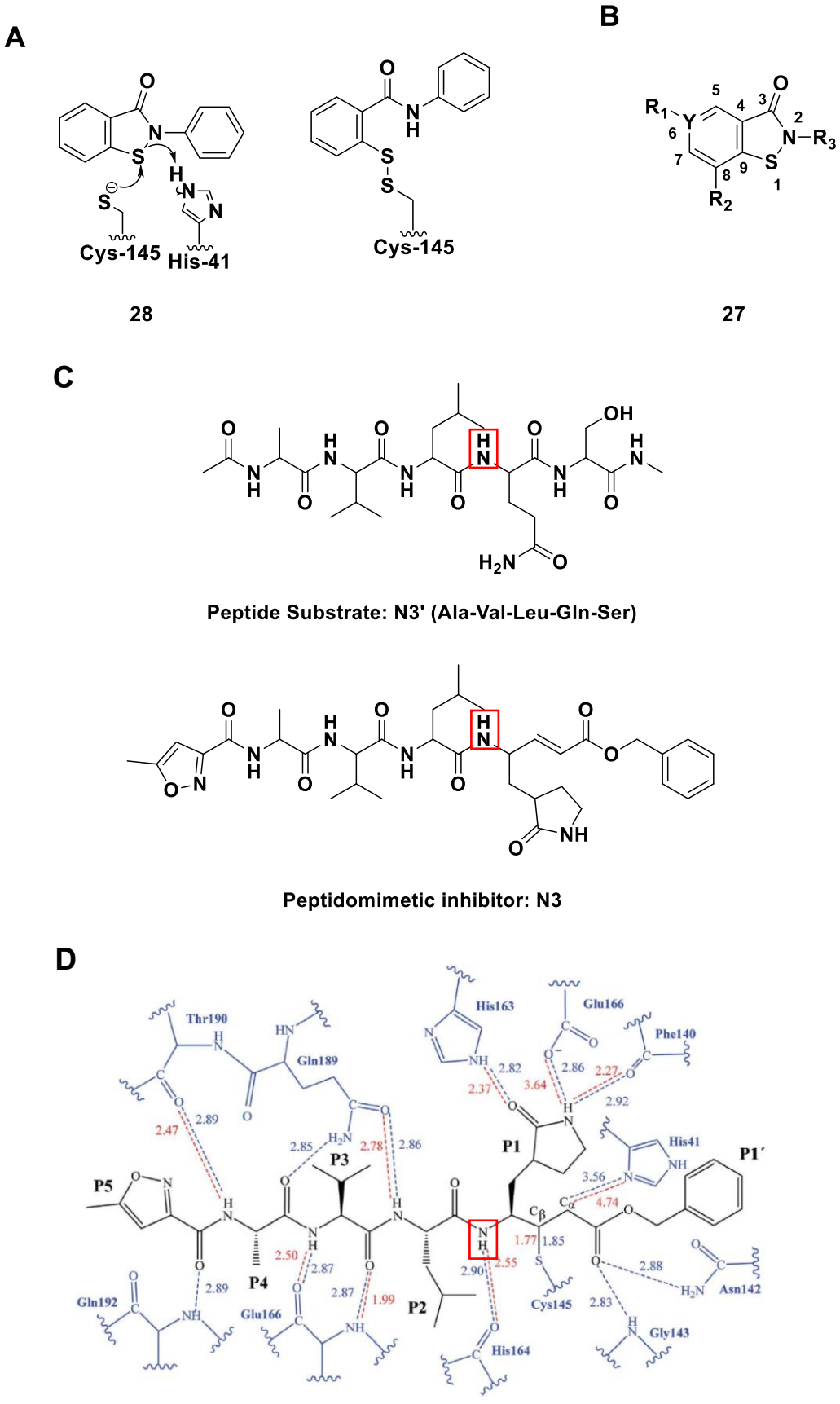

Figure 4.2 | *Overview of **28** as a covalent inhibitor of M^{pro}, the M^{pro} substrate backbone, and N3 as a covalent inhibitor of M^{pro}. **A.** The reaction of **28** with Cys-145 to form a disulfide bond. **B.** BIT core,*

27, and sites of functionalisation. The atom at position 6, Y, was varied between carbon and nitrogen. The variable groups were labelled as follows: R_1 at C6, R_2 at C8, and R_3 at N2. ***C.*** *Structures of a potential M^{pro} substrate fragment (AVLQS) and its inhibitor analogue N3. The P1-P2 backbone amide nitrogen is highlighted. D. The structure and active site interactions of covalent peptide inhibitor N3 and M^{pro}. The P1-P2 backbone amide nitrogen is highlighted. Cys-145 is covalently linked to C_β. 4-(Aminomethyl)pyrrolidine-2-one occupies the P1 position. Panel C was adapted with permission from Mensah et al.[474] Panel D was reproduced from El-Hddad et al. under the Creative Commons Attribution-NonCommercial 3.0 Unported Licence, https://creativecommons.org/licenses/by-nc/3.0/.[475]*

4.2. The Synthesis and Screening of an Initial Series of Ebsulfur Inhibitors

The first derivatives of **27** that were synthesised varied at the N2 position to identify an improved R_3 side chain (**Figure 4.2.B**). Eight compounds (**28** - **36**) were synthesised with a variety of alkyl, aryl, non-polar, and polar side chains. In addition, one compound was synthesised with a 4-(aminomethyl)pyrrolidine-2-one side chain to mimic the natural substrate (**34**), which contained a glutamine residue at the P1 position, and a covalent peptide inhibitor (N3), which also contained a 4-(aminomethyl)pyrrolidine-2-one residue at P1 position (**Figure 4.3**). Synthesis was carried out in conjunction with Dr Tim Suits and his compounds (**28**, **30**, **31**, and **35**, denoted with an asterisk '*') have been included for completeness.

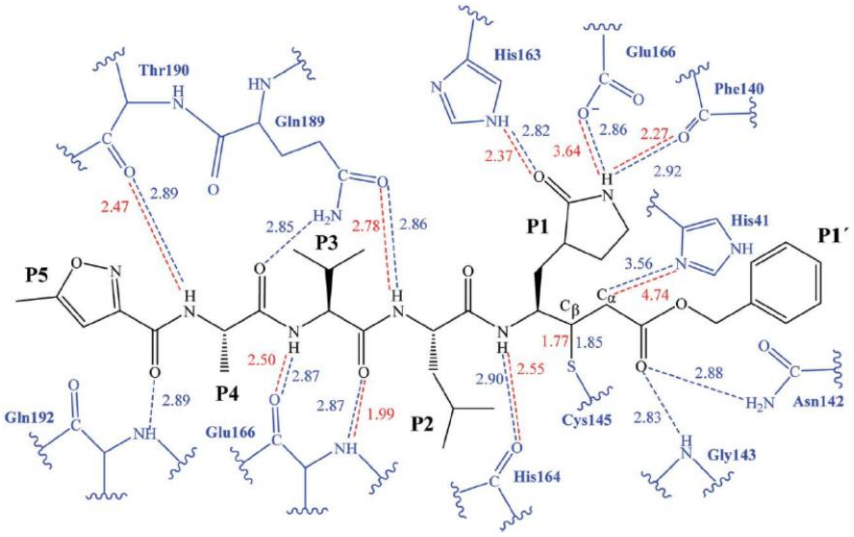

Figure 4.3 *| The structure and active site interactions of covalent peptide inhibitor N3 and M^{pro} are shown again here for reference. 4-(Aminomethyl)pyrrolidine-2-one occupies the P1 position. This figure was*

4.2.1. Synthesis

The initial nine analogues of **28** (**28 - 36**) were synthesised in two steps by first forming an amide from the reaction of a primary amine (R_3-NH_2) and 2-iodobenzoyl chloride, followed by ring closure using a copper-mediated sulfur insertion to give a core with the desired R_3 side chain (**Figure 4.4**, **Table 4.1**).

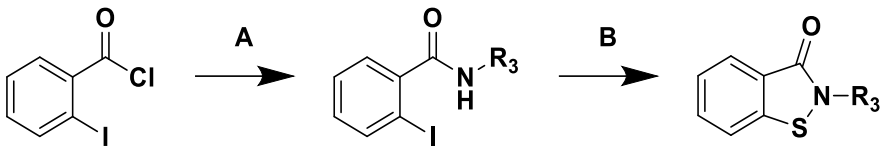

***Figure 4.4** | The general route of synthesis for the initial series of ebsulfur analogues. **A.** R_3-NH_2, DIPEA, CH_2Cl_2, rt, overnight; yields, 13-74%. **B.** CuI, 1,10-phenanthroline, S_8, K_2CO_3, DMF, 110 °C; yields, 30 minutes, 17-81%.*

Compound	Structure	**A.** Yield (%)	**B.** Yield (%)	Overall Yield (%)
28*	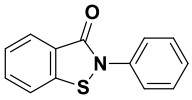	74	70	**52**
29	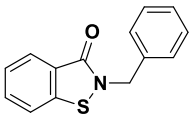	63	49	**31**
30*	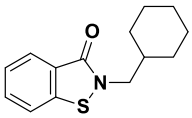	61	20	**12**
31*	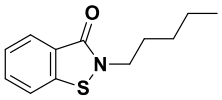	64	81	**52**
32	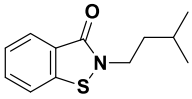	65	28	**18**
33	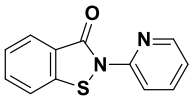	13	65	**8**
34	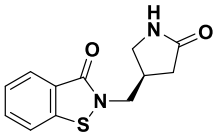	33	17	**6**
35*	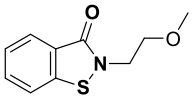	34	62	**21**
36	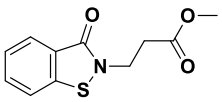	59	80	**47**

Table 4.1 *| Initial ebsulfur* ***(28)*** *analogues that were synthesised. Compounds* ***28****,* ***30****,* ***31****, and* ***35*** *were synthesised by Dr Tim Suits and are denoted with an asterisk '*'. This table was adapted with permission from Dr Tim Suits.*[473]

4.2.2. Inhibition of M^{pro} by the Initial Series of Ebsulfur Analogues

The inhibition of M^{pro} was measured by IC_{50} values as determined by Förster resonance energy transfer (FRET)-based inhibition assays ([M^{pro}] = 50 nM), and solid phase extraction-mass spectrometry (SPE-MS)-based inhibition assays ([M^{pro}] = 2 μM).[429, 470] The FRET-based assay utilised a peptide substrate of M^{pro} (sequence and cleavage

site: AVLQ|SGFRKK) with a fluorophore (5-FAM) at the C terminus (A-1) and a quencher (dabcyl) *N*-linked to the side chain of the penultimate lysine (K-9).[429] The fluorescence emission is internally quenched by FRET while the peptide is intact, but upon cleavage by M^{pro} the distance between the groups normally increases via diffusion and the 5-FAM fluorophore signal is detected.[476] The SPE-MS-based assay directly detects the abundances of cleaved peptide fragments from substrate peptides turned over by M^{pro} (sequence and cleavage site: TSAVLQ|SGFRK). Inhibition is quantified by comparing relative abundances to positive and negative controls.[470] The SPE-MS experiments were kindly carried out by Dr Tika R. Malla (Department of Chemistry, University of Oxford) and Dr Anthony Tumber. (Department of Chemistry, University of Oxford).

The IC_{50} values of compounds **26**, and **28** - **36**, demonstrated potencies against M^{pro} ranging from micromolar to sub-micromolar concentrations (2.55 - 0.04 μM) (**Table 4.2**). Compound **28** (FRET: 0.13 μM, SPE-MS: 0.34 μM) exhibited the lowest IC_{50} value after **26** (FRET: 0.04 μM, SPE-MS: 0.26 μM), closely followed by the other compounds with non-polar side chains (**29** - **32**). Compounds with polar side chains (**33** - **36**) demonstrated slightly lower potency on average compared to **26**, but further evidence is needed for confirmation. The R_3-groups may therefore be able to access a hydrophobic pocket in the M^{pro} active site, possibly corresponding to the P1' (benzyl ester) or P2 (leucine) sites of N3 (**Figure 4.3**).

Compound	Structure	IC_{50} (FRET) (μM)	IC_{50} (SPE-MS) (μM)
26	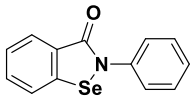	0.04 ± 0.01	0.26 ± 0.15
27	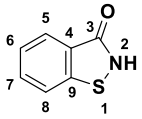	1.51 ± 0.09	0.99 ± 0.15
28*	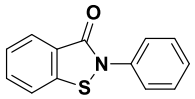	0.13 ± 0.04	0.34 ± 0.06
29	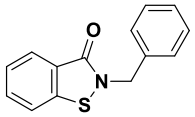	0.19 ± 0.04	0.43 ± 0.03
30*	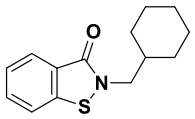	1.00 ± 0.50	0.53 ± 0.05
31*	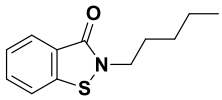	0.41 ± 0.12	0.47 ± 0.02
32	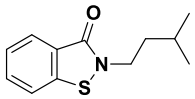	0.32 ± 0.04	0.42 ± 0.03
33	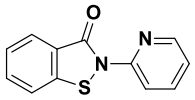	0.22 ± 0.10	0.79 ± 0.09
34	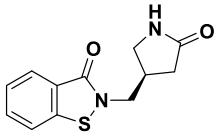	0.51 ± 0.02	2.55 ± 0.57
35*	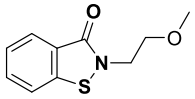	0.95 ± 0.04	0.78 ± 0.18
36	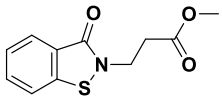	0.25 ± 0.02	0.39 ± 0.05

Table 4.2 *| IC_{50} values exhibiting the measured inhibition of M^{pro} by the initial series of ebsulfur analogues. IC_{50} values shown ± standard deviation. Independent experimental repeats, n = 2. Technical replicates per experiment, n = 3. Compounds* ***28***, ***30***, ***31***, *and* ***35*** *were synthesised by Dr Tim Suits and are denoted with an asterisk '*'. This table is adapted with permission from Thun-Hohenstein et al. under the Creative Commons CC-BY 4.0 license, https://creativecommons.org/licenses/by/4.0 .*[469]

4.2.3. Reaction of the Initial Series of Ebsulfur Analogues with M^{pro}

Ebselen (**26**) has been reported to react promiscuously with cysteine thiols, both those present in M^{pro} (12 cysteines) and other enzymes such as Ldt_{Mt2} (1 cysteine).[431, 437, 477, 478] To investigate whether the R_3-group of ebsulfur (**28**) would impact the number of disulfide adducts formed, POMS experiments with M^{pro} were kindly conducted by Dr Tika R. Malla. M^{pro} (2 μM) was incubated with an ebsulfur analogue (40 μM) then analysed by mass spectrometry after two 2 minutes and 35 minutes, and the number of covalent adducts was calculated (**Figure 4.5**, **Figure 4.6**). Generally, a shift towards fewer adducts was considered to indicate greater selectivity. If a compound were to react once and retain inhibition, it may be inferred that the compound might only have reacted with the active site cysteine.

Compound **26** (in a 20-fold excess) reacted with M^{pro} up to 12 times, with a small proportion of M^{pro} having 11 adducts (**Figure 4.5**). There was little variation in the number of adducts of **26** between the tested time points. **28** reacted with M^{pro} up to 11 times, with a distribution of observed number of adducts down to six. The proportion of M^{pro} with a higher number of adducts of **28** was greater after 35 minutes (**Figure 4.5**). This observation supported the initial hypothesis that a stronger S-N bond would decrease the promiscuity of **28** in comparison to the Se-N bond of **26**.

Compounds **29**, **30**, **32**, **33**, and **35** reacted up to six times with M^{pro} but the number of reactions changed over time. Although the cause was not immediately apparent, the time-dependent variability was likely influenced by several factors including conformational changes in the protein and solubility effects. For example, the reaction with specific M^{pro} cysteine residues could induce structural alterations, thereby exposing additional reactive cysteines and leading to a subsequent increase in adduct formation over time. Alternatively, kinetic dissolution could result in an increased concentration of inhibitor,

further facilitating covalent modification. By contrast, compounds forming less stable adducts and exhibiting poor solubility may dissociate more rapidly, then aggregate, which could reduce the number of adducts as the reaction progresses.

The predominant number of adducts increased over time for **30** and **32** from four to six, and for **33** from two to six, but the predominant numbers of adducts on M^{pro} decreased over time for **29** and **35** from four to two (**Figure 4.5**). For compounds **27** and **36**, which reacted up to five times with M^{pro}, the predominant number adducts decreased over time from four to two. Compound **31** also reacted with M^{pro} up to five times, but the predominant number of adducts remained four after 35 minutes. Compound **34** exhibited the fewest adducts compared to unmodified **26** (3 cf. 12), reacting a maximum of three times, and predominantly reacting once with little variation over time. This suggested the 4-(aminomethyl)pyrrolidine-2-one side chain may mimic the P1 positions of the natural substrate and N3, but additional structural evidence is needed to confirm this hypothesis. All variations of the R_3 group apparently decreased promiscuity relative to **26** and exhibited time dependent behaviour with the exception of compound **34**. Nonetheless, it is likely that compounds **26** – **36** would still be able to react with other exposed biological thiols such as glutathione.

For ebselen-type inhibitors, which exert covalent inhibition, it is ideal to determine the dissociation constant (K_I) for the initial reversible binding event, the inactivation rate constant (k_{inact}), and the ratio of $\frac{K_I}{k_{inact}}$ in order to evaluate the overall efficiency of M^{pro} covalent inhibition.[479] Therefore, future work should seek to address this. A potential approach to derive K_I and k_{inact} involves using a binding assay, such as Surface Plasmon Resonance (SPR), to measure the total occupancy of M^{pro} (%) over time at various inhibitor concentrations.[479] The resulting data could then be analysed by fitting the

observed occupancy to **Eq. 4**. By extracting the observed rate constant (k_{obs}) at each inhibitor concentration, the k_{obs} values can be plotted and fitted to **Eq. 5**, thereby enabling the determination of K_I, k_{inact}, and $\frac{K_I}{k_{inact}}$.[479]

Eq. 4

$$\text{Percentage total occupancy} = 100(1 - \exp(-k_{obs}\, t))$$

Eq. 5

$$k_{obs} = \frac{k_{inact}[I]}{K_I[I]}$$

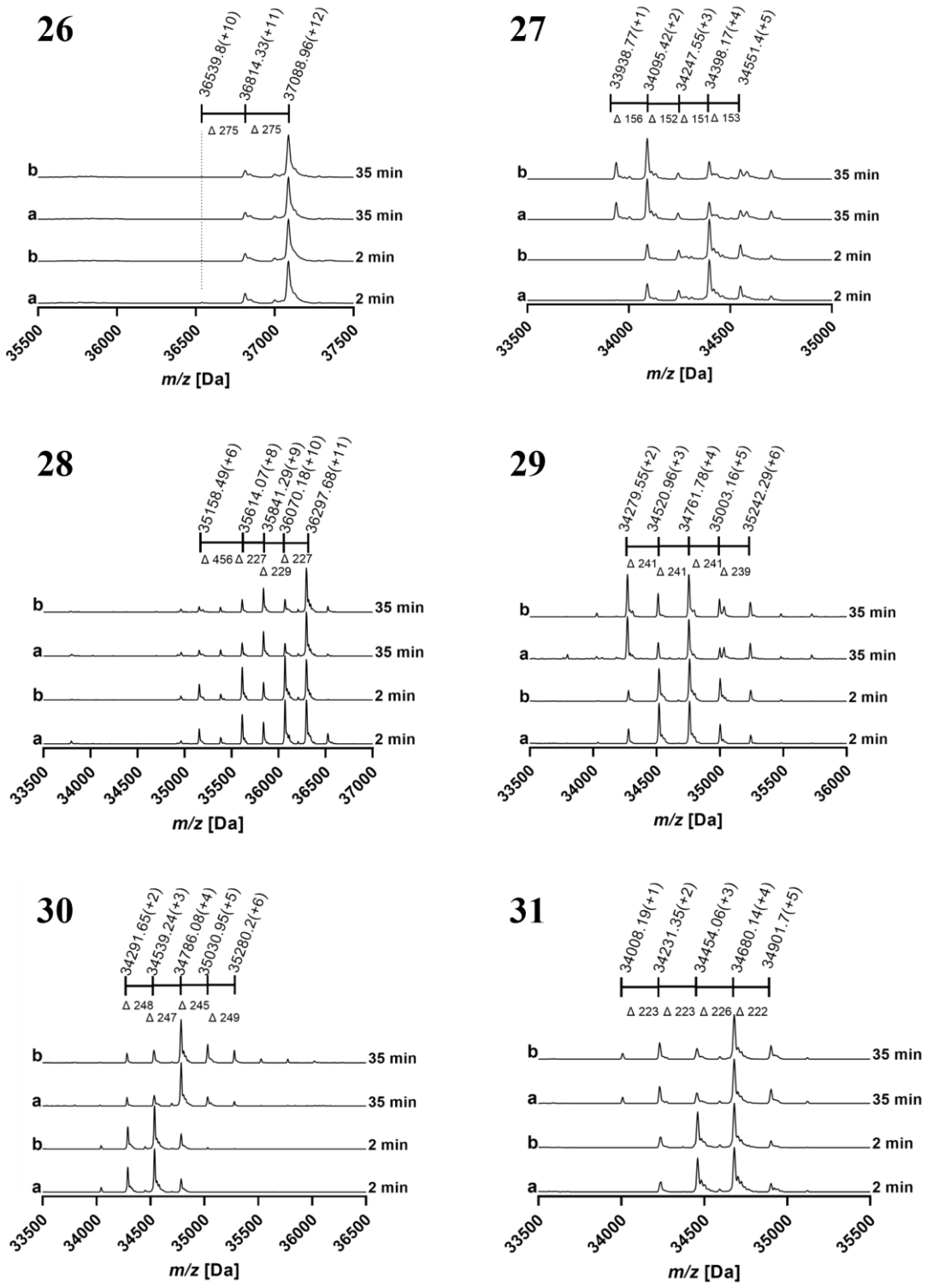

Figure 4.5 | *POMS experiments of M^{pro} (33797 Da) incubated with compounds* ***26 - 31*** *from the initial series. The number of adducts formed is indicated next to the observed mass. Technical repeats are represented by* ***a*** *and* ***b****. This figure was adapted with permission from Dr Tim Suits.*[473]

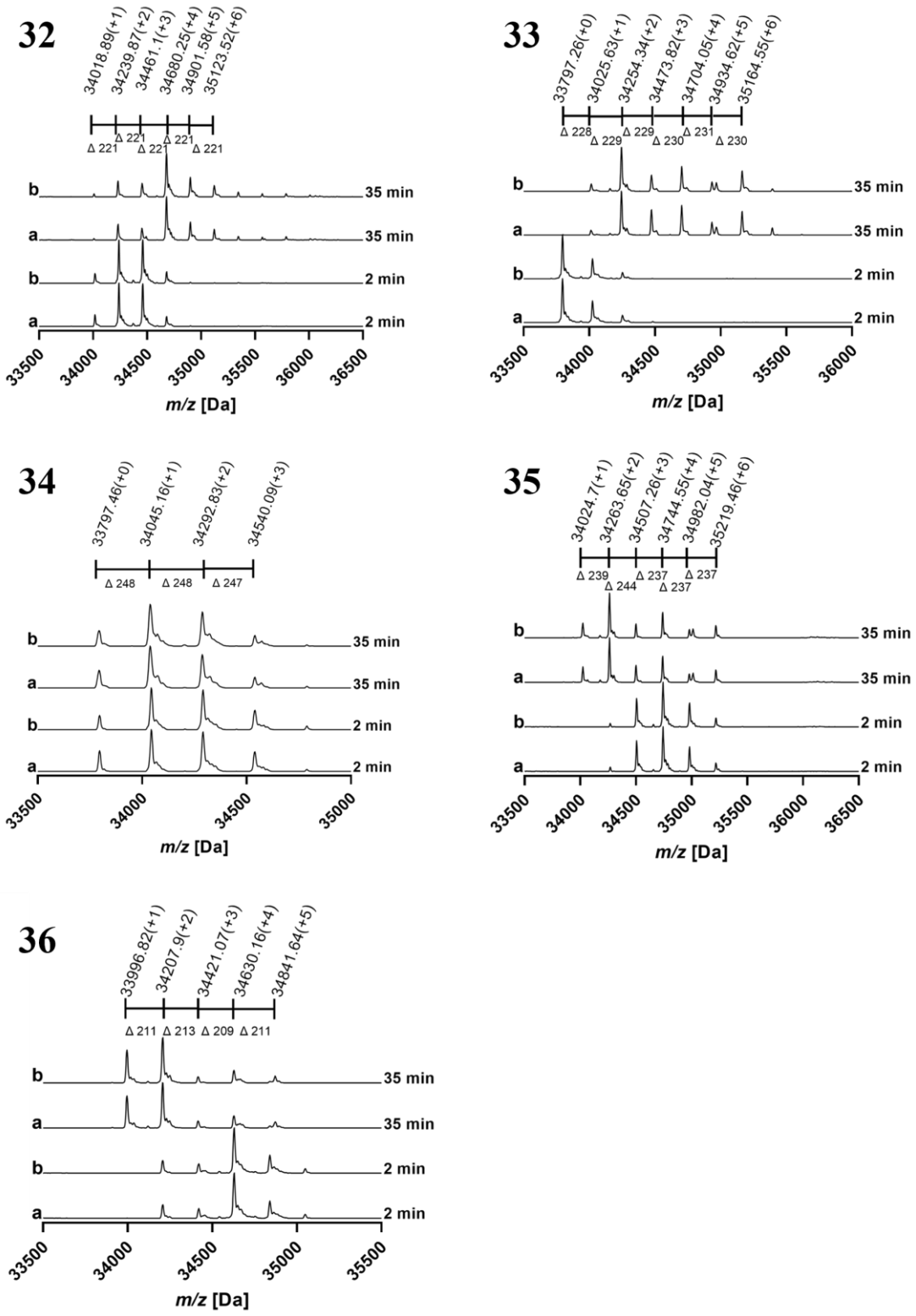

Figure 4.6 | *POMS experiments of M^{pro} (33797 Da) incubated with compounds **32 - 36** from the initial series. The number of adducts formed is indicated next to the observed mass. Technical repeats are represented by **a** and **b**. This figure was adapted with permission from Dr Tim Suits.*[473]

The potency as measured by IC_{50} value for the compounds, **28** – **36**, was lower than for **26**, but the selectivity of **28** – **36** was higher than that of **26** (**Table 4.2**, **Figure 4.5**, **Figure 4.6**). Therefore, an index was devised to combine the potency and selectivity values of ebsulfur analogues for a weighted comparison against **26**; this was labelled 'relative potency'. The relative potency was calculated by dividing the pIC_{50} (FRET) value by the maximum number of adducts formed for each compound; compounds were then ranked accordingly (**Table 4.3**). The compound with the highest value of relative potency was considered to have the most useful combination of selectivity and potency. Unsurprisingly, **26** (0.6) and **28** (0.6) ranked lowest due to their poor selectivity in terms of cysteine reactivity, indicating that high potency comes with a price of promiscuity. Eight out of the nine synthesised analogues (**27**, **29** - **33**, **35**, **36**) were superior to the unmodified **26** and **28**, and exhibited a similar relative potency to each other (1 – 1.3). This result indicates that while any of the tested side chains were superior to a phenyl group, most side chains relative to each other sacrificed as much in potency as they gained in selectivity. Exceptionally, compound **34** exhibited a promisingly higher relative potency (2.1) despite exhibiting one of the lowest potencies (pIC_{50} = 6.29). This observation may support the hypothesis that substrate backbone mimicry might lead to improved selectivity and motivated the synthesis of an expanded series of ebsulfur analogues.

Compound	Structure	pIC_{50} (FRET)	Maximum no. of adducts	Relative potency (pIC_{50} / max no. of adducts)
34	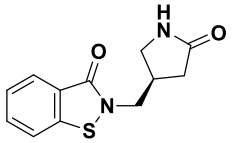	6.29	3	2.1
31*	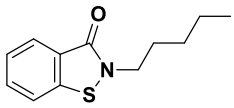	6.39	5	1.3
35*	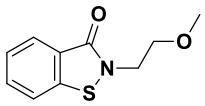	6.11	5	1.2
29	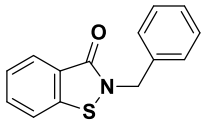	6.75	6	1.1
33	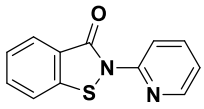	6.67	6	1.1
36	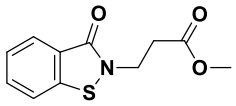	6.61	6	1.1
32	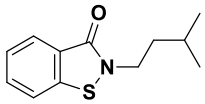	6.5	6	1.1
30*	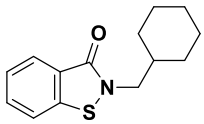	6.03	6	1.0
27	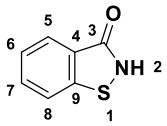	5.82	6	1.0
28*	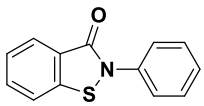	6.89	11	0.6
26	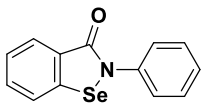	7.4	12	0.6

Table 4.3 | *Compounds **26**, **27**, and the initial series of compounds, **28 - 36**, ranked by relative potency. This table is adapted with permission from Thun-Hohenstein et al. under the Creative Commons CC-BY 4.0 license, https://creativecommons.org/licenses/by/4.0.*[469]

4.3. The Synthesis and Screening of an Expanded Series of Ebsulfur Inhibitors

The results from the initial series of compounds that were synthesised and tested demonstrate that it is possible to decrease the promiscuity of ebsulfur analogues via structural variation. In particular, groups that may resemble components of the natural substrate of M^{pro} or N3 appear to be the most effective. An expanded series of analogues was therefore synthesised with modifications on the core at positions C6 and C8, retaining a phenyl- or isopentyl *N*-linked side chain at position N2 (**Figure 4.7**). The chosen *N*-linked side chains allowed direct comparisons to be made against **26** and **28**. If the *N*-linked side chains of the analogues were to occupy the P1 position, it was hypothesised that groups at C6 may be able to extend into P1', P2, or even P3 positions. Conversely, groups at C8 may sterically hinder general non-specific reaction with cysteines.

4.3.1. Synthesis

The original pathway was adapted to incorporate pre-substituted starting materials and a Pd(0)-catalysed cross-coupling reaction as necessary (**Figure 4.7**). The majority of starting materials with substituents at position C6 or C8 were prohibitively expensive to procure as acyl chlorides, therefore the acyl chloride was generated as necessary via procedure **A**, then subjected as before to procedure **B** (procedure **A.**, **Figure 4.4**). Pre-substituted alkyl- and aryl-bromide starting materials allowed late-stage functionalisation via Pd(0)-catalysed cross-coupling reactions, as carried out in procedure **D.** (**Figure 4.7**), as well as the initial investigation into selectivity via C6 and C8 substituents.[480-482]

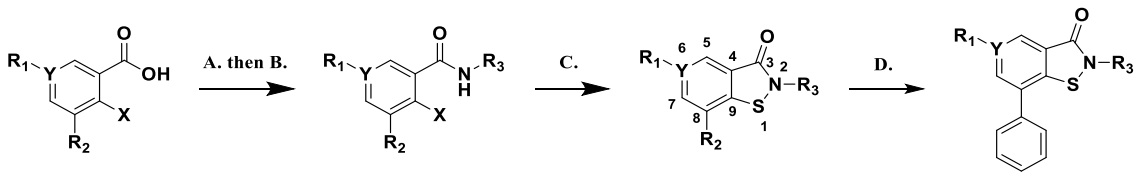

***Figure 4.7** | General synthetic route for the expanded series of ebsulfur analogues. **A.** Oxalyl chloride, DMF, CH_2Cl_2, 0 °C → rt, 3h. **B.** DIPEA, R_3-NH_2, CH_2Cl_2, rt, overnight, 34-70% (**A/B.** combined). **C.** CuI, 1,10-phenanthroline, S_8, K_2CO_3, DMF, 110 °C, 30 min, 7-86%. **D.** Phenylboronic acid, K_2CO_3, $Pd(dppf)Cl_2$, 1,4-dioxane, 80 °C, 3 h, 19%.*

Eight compounds were synthesised to form the expanded series of ebsulfur analogues. Three were varied at position six (**37**, **38**, **42**), and five were varied at position eight (**39**, **40**, **41**, **43**, **44**) (**Table 4.4**).

Compound	Structure	**A/B.** Yield (%)	**C.** Yield (%)	Overall Yield (%)
37	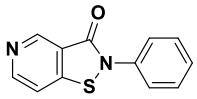	34	58	**20**
38	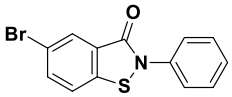	70	86	**60**
39	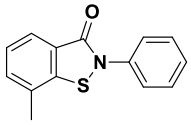	57	7	**4**
40	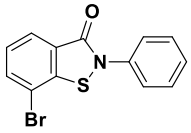	51	52	**27**
41	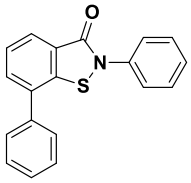	(**D.**) 19		**5**
42	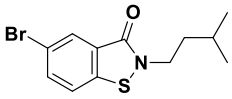	48	15	**7**
43	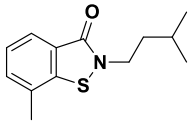	69	61	**42**
44	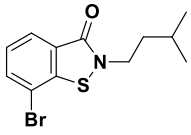	43	29	**12**

***Table 4.4** | The expanded series of ebsulfur analogues. Only the yield of procedure **D.** (19%) is shown for compound **41** because the starting material was **40** and therefore the yields for procedures **A/B.** and **C.** are accounted for.*

4.3.2. Inhibition of M^{pro} by the Expanded Series of Ebsulfur Analogues

The extent of M^{pro} inhibition was assessed by the FRET IC_{50} assay and the SPE-MS IC_{50} assay as before, with the SPE-MS assays being kindly conducted by Dr Tika R. Malla and Dr Anthony Tumber (**Table 4.5**). Compounds **37** (FRET: 0.48 μM, SPE-MS: 0.43 μM), **38** (FRET: 0.03 μM, SPE-MS: 0.34 μM), and **42** (FRET: 0.21 μM, SPE-MS: 0.43 μM) were varied at position six and exhibited potent inhibition, comparable with the respective unsubstituted molecules **28** (FRET: 0.13 μM, SPE-MS: 0.34 μM) and **32** (FRET: 0.32 μM, SPE-MS: 0.42 μM). However, substituents at position eight universally substantially reduced inhibition for all compounds **39** (FRET: > 100 μM, SPE-MS: >100 μM), **40** (FRET: > 100 μM, SPE-MS: 10.88 μM), **41** (FRET: > 100 μM, SPE-MS: > 100 μM), **43** (FRET: > 100 μM, SPE-MS: > 100 μM), and **44** (FRET: > 100 μM, SPE-MS: > 100 μM). This may be due to steric hindrance of bulky groups physically adjacent to the reactive sulfur, preventing access to free thiols of cysteine residues. Differentiated electronic effects of substitution at C6 or C8 by the same group are likely to be minor, comparable to the similar effects of *ortho* and *para* substitution on benzene; ebsulfur's C6 and C8 themselves are *ortho* and *para* to the reactive sulfur.[483] Furthermore, **37** contains a nitrogen at position six and retains similar potency to **28**, supporting the proposal that steric effects had a larger impact than electronic effects on the inhibition of M^{pro}.

Compound	Structure	IC_{50} (FRET) (μM)	IC_{50} (SPE-MS) (μM)
37	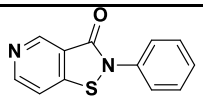	0.48 ± 0.09	0.43 ± 0..01
38	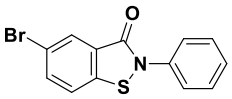	0.03 ± 0.01	0.34 ± 0.01
39	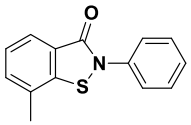	> 100	> 100
40	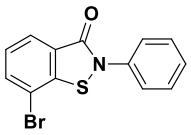	> 100	10.88 ± 0.82
41	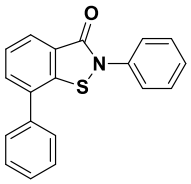	> 100	> 100
42	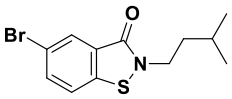	0.21 ± 0.13	0.43 ± 0.01
43	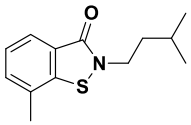	> 100	> 100
44	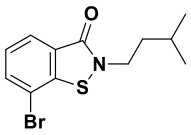	94.50 ± 8.22	> 100

Table 4.5 *| IC_{50} values exhibiting the measured inhibition of M^{pro} by the expanded series of ebsulfur analogues. IC_{50} values shown ± standard deviation. Independent experimental repeats, n = 2. Technical replicates per experiment, n = 3. This figure was adapted with permission from Dr Tim Suits.*[473]

4.3.3. Reaction of the Expanded Series of Ebsulfur Analogues with M^{pro}

Selectivity was assessed as before by POMS experiments with M^{pro}, kindly conducted by Dr Tika R. Malla (**Figure 4.8**, **Figure 4.9**). C8 substituted compounds, **39**, **40**, **41**, **43**, and **44** did not form stable adducts with M^{pro}, mirroring their IC_{50} values and supporting the conclusion that C8 substitution abolishes the activity of ebsulfur analogues. C6 substituted compounds exhibited substantial decreases in the maximum number of adducts compared to their respective unsubstituted analogues (cf. **28** vs **38** (11 → 2), and

32 vs **42** (6 → 2)). Compound **37** (9) exhibited comparable promiscuity to **28** (11), indicating that the electronic effect of nitrogen had a minor effect on the selectivity of the analogue, compared to the steric effect of a bromine substituent. It is likely that the steric bulk incorporated at position six drives the selectivity of **38** and **42**.

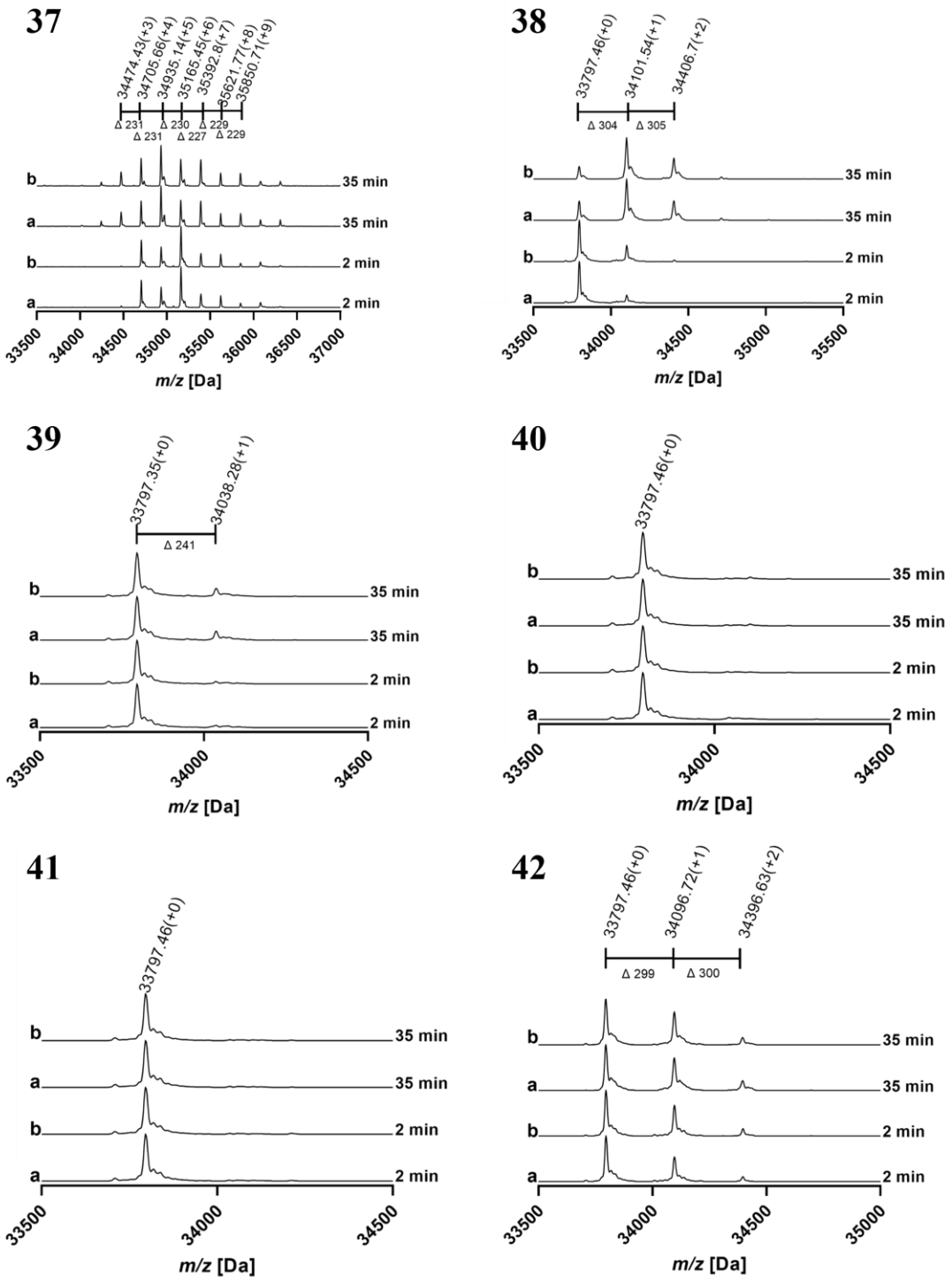

Figure 4.8 *| POMS experiments of* M^{pro} *(33797 Da) incubated with compounds* ***37 - 42****. The number of adducts formed is indicated next to the observed mass. Technical repeats are represented by* ***a*** *and* ***b****. This figure was adapted with permission from Dr Tim Suits.*[473]

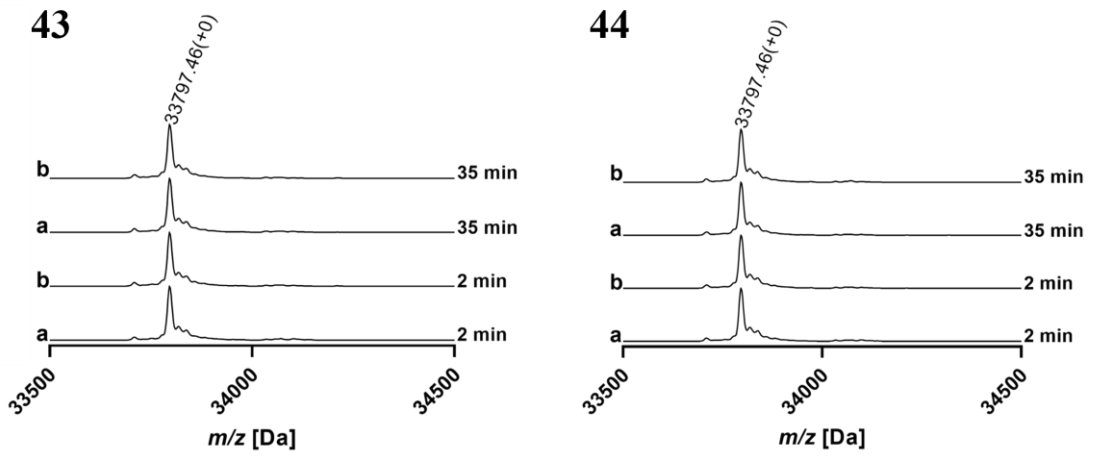

***Figure 4.9** | POMS experiments of M^{pro} (33797 Da) incubated with compounds **43** and **44**. The number of adducts formed is indicated next to the observed mass. Technical repeats are represented by **a** and **b**. This figure was adapted with permission from Dr Tim Suits.[473]*

The expanded series of ebsulfur analogues successfully produced compounds with superior selectivity than the initial series of ebsulfur analogues, as measured by their relative potency (**Table 4.6**). Both compounds with C6 substituents, **38** (3.8) and **42** (3.3), achieved higher relative potencies than the most relatively potent compound in the initial series, compound **34** (2.1). The only other compound modified at the C6 position, **37** (0.7), achieved a similar relative potency to the unmodified analogues, **26** and **28**, in the initial series (1 – 1.3). Compounds substituted at the C8 position were not assigned relative potencies because they did not exhibit covalent reactions or substantial inhibition. The time dependent nature of the reaction of ebsulfur analogues and M^{pro} may lead to more adducts after a longer period than measured here (e.g. **38**), although the precise cause was not immediately apparent. As mentioned previously, future work should assess time-dependent solubility to ascertain whether kinetic dissolution or another mechanism underpins this observation, thereby guiding further investigation. Nonetheless, these data support the proposal that, with respect to relative potency, C6 substitution (e.g. **38**) is superior to both C8 substitution (e.g. **40**) and no substitution (e.g. **28**), particularly because the relative potency index is impacted more greatly by the maximum number of adducts formed than the pIC_{50} value.

Compound	Structure	pIC_{50} (FRET)	Maximum no. of adducts	Relative potency (pIC_{50} / max no. of adducts)
38	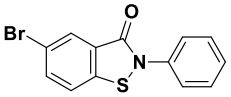	7.51	2	3.8
42	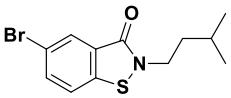	6.68	2	3.3
37	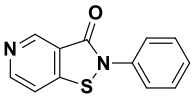	6.32	9	0.7
39	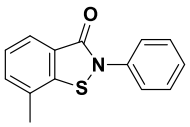	< 3	0	-
40	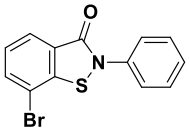	< 3	0	-
41	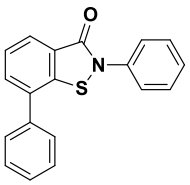	< 3	0	-
43	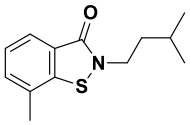	< 3	0	-
44	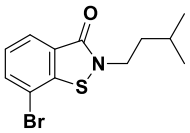	3.02	0	-

Table 4.6 | *The expanded series of compounds,* ***38 - 44****, ranked by relative potency. This was figure was adapted from Thun-Hohenstein et al.*[469]

4.3.4. Future Work to Develop Inhibitors Against M^{pro}

The project aim was to develop novel inhibitors of M^{pro} that combined the potency of the ebsulfur scaffold (**28**) with increased selectivity for reduced toxicity. The initial series of ebsulfur analogues produced **34** (relative potency = 2.1), an ebsulfur analogue containing an *N*-linked 4-(aminomethyl)pyrrolidine-2-one side chain exhibiting an optimal balance

of potency and selectivity. The expanded series of ebsulfur analogues produced **38** (relative potency = 3.8) and **42** (relative potency = 3.3) – ebsulfur analogues containing C6 bromo-substituents with greater potency and selectivity than **34**. Further research should include combining the 4-(aminomethyl)pyrrolidine-2-one side chain with a C6 bromo-substituent in the same compound to determine if greater selectivity could be achieved. Late-stage functionalisation at the C6 position via the bromine substituent could then be leveraged to further improve the affinity of ebsulfur analogues for the active site of M^{pro}. In addition, a crystal structure of **34**, **38**, or **42** displaying the binding pose of the covalent adduct with Cys-145 would greatly inform the accurate design of substrate-mimetics.

4.4. Inhibition of Ldt_{Mt2} by Ebsulfur Analogues

In-house experiments identified the ability of Ebselen (**26**) and ebsulfur analogue **61** to react with the nucleophilic cysteine of Ldt_{Mt2}.[437, 484] Therefore, the initial and expanded series of ebsulfur analogues were subjected to POMS experiments with Ldt_{Mt2} to investigate whether selectivity within M^{pro} had an effect on reactivity with other cysteine containing enzymes (**Figure 4.11**, **Figure 4.12**, **Figure 4.13**). Ldt_{Mt2} contains a single cysteine as part of a histidine-cysteine catalytic dyad, compared to 12 cysteines in M^{pro}.[477] Ideally, compounds selective for M^{pro} would not react with Ldt_{Mt2}. Alternatively, compounds that do react with Ldt_{Mt2} may present antimicrobial activity and serve as potential treatments against *Mycobacterium tuberculosis*. The following POMS experiments were kindly carried out by Dr Tika R. Malla.

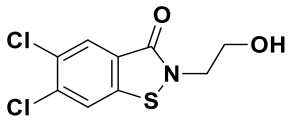

61

Figure 4.10 | *Chemical structure of ebsulfur analogue **61**.*[484]

The initial series of ebsulfur analogues (**28** - **32**, **35**, and **36**) formed adducts with all Ldt_{Mt2} cysteines in solution after five minutes, with the exception of **33** and **34** (**Figure 4.11**, **Figure 4.12**). Compounds **33** and **34** contained cyclic polar side chains, compared to non-polar side chains (**28** - **32**) or linear polar side chains (**35**, and **36**). This finding was encouraging because compound **34** exhibited the highest relative potency in the initial series of ebsulfur analogues, suggesting that the selectivity of high potency compounds could be tailored to a targeted active site. In particular, the 4-(aminomethyl)pyrrolidine-2-one side chain appears to be selectively beneficial in M^{pro}, providing evidence that it accesses the P1 site of M^{pro}.

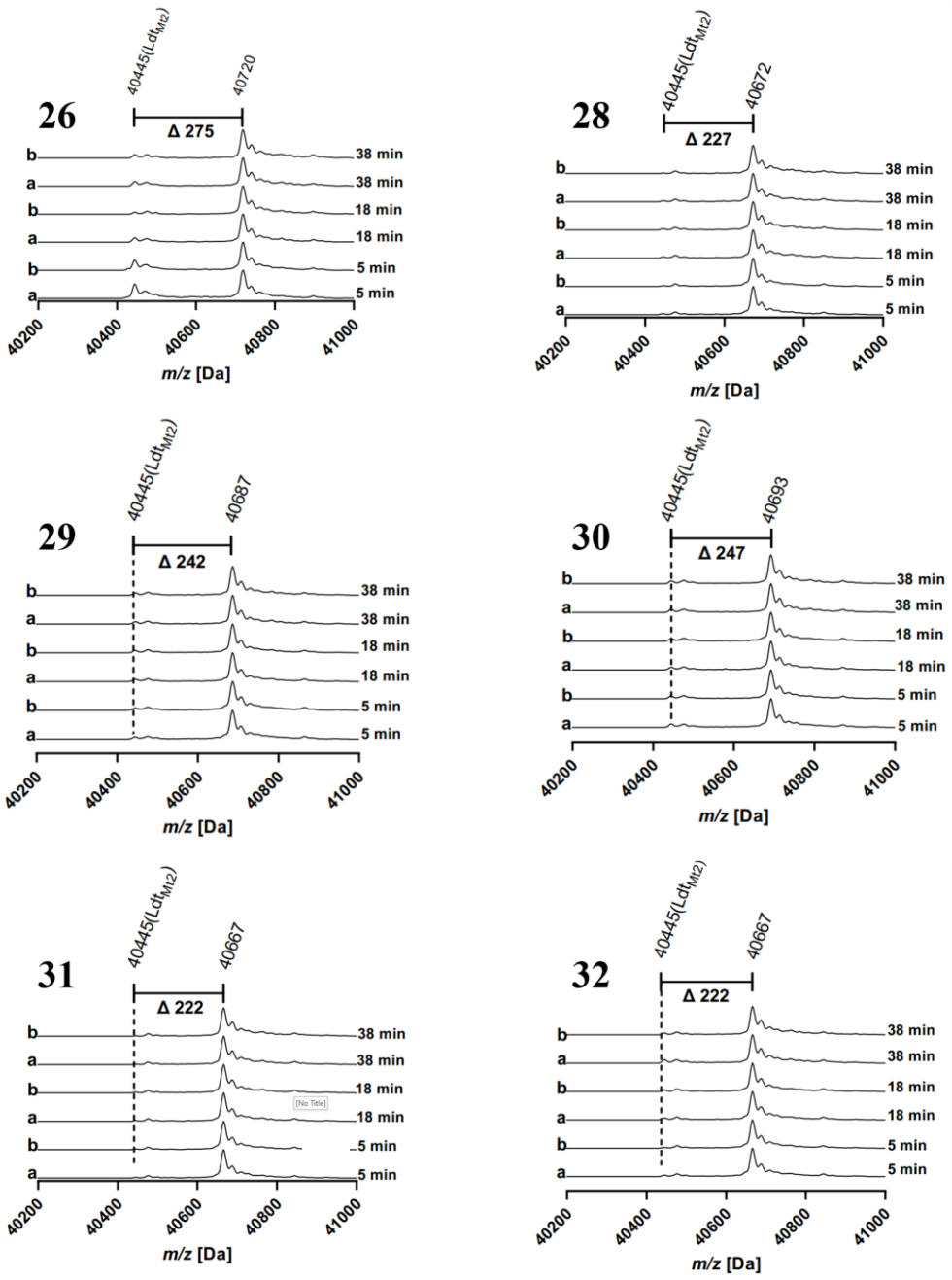

Figure 4.11 | *POMS experiments of Ldt_{Mt2} (40445 Da) incubated with compounds* ***26 - 32****. This figure was adapted with permission from Dr Tim Suits.*[473]

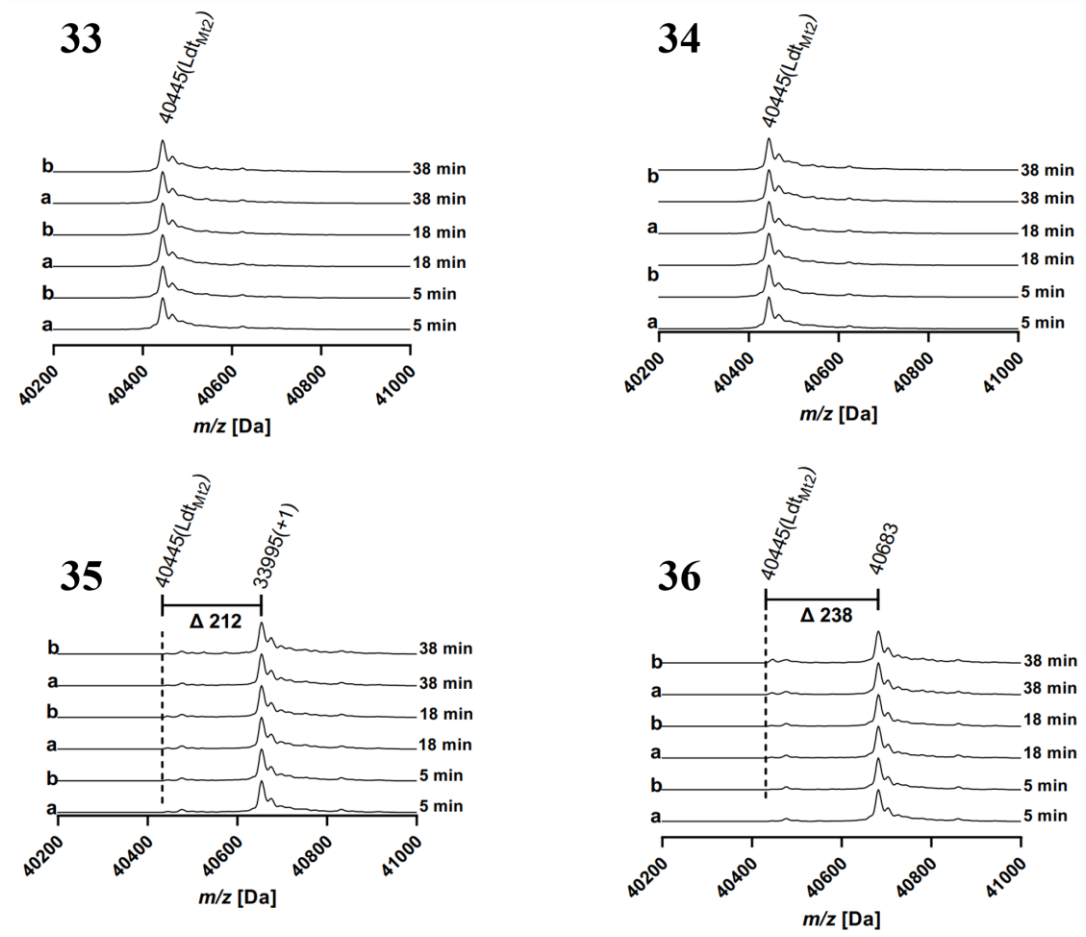

Figure 4.12 *| POMS experiments of Ldt$_{Mt2}$ (40445 Da) incubated with compounds **33 - 36**. This figure was adapted with permission from Dr Tim Suits.*[473]

POMS experiments of the expanded series of ebsulfur analogues with Ldt$_{Mt2}$ demonstrated an absence of adducts for compounds with substituents around the core (**38 - 42**), and fully reacted Ldt$_{Mt2}$ after 38 minutes of incubation with compound **37** (**Figure 4.13**). However, compound **37** reacted with Ldt$_{Mt2}$ slower than **28**, with apparently complete reaction after five minutes. The lack of reaction by compounds with substituents at either the C6 or C8 position indicates that the Ldt$_{Mt2}$ active site did not tolerate steric bulk around the core. This differs from the trend of reactivity between ebsulfur analogues and M^{pro} which did not tolerate C8 substitution, but favoured C6 substitution. The separation of parameters favouring selectivity against M^{pro}, compared to Ldt$_{Mt2}$, supports the hypothesis that ebsulfur analogues may be developed as selective covalent inhibitors to target individual enzymes with nucleophilic cysteine active sites.

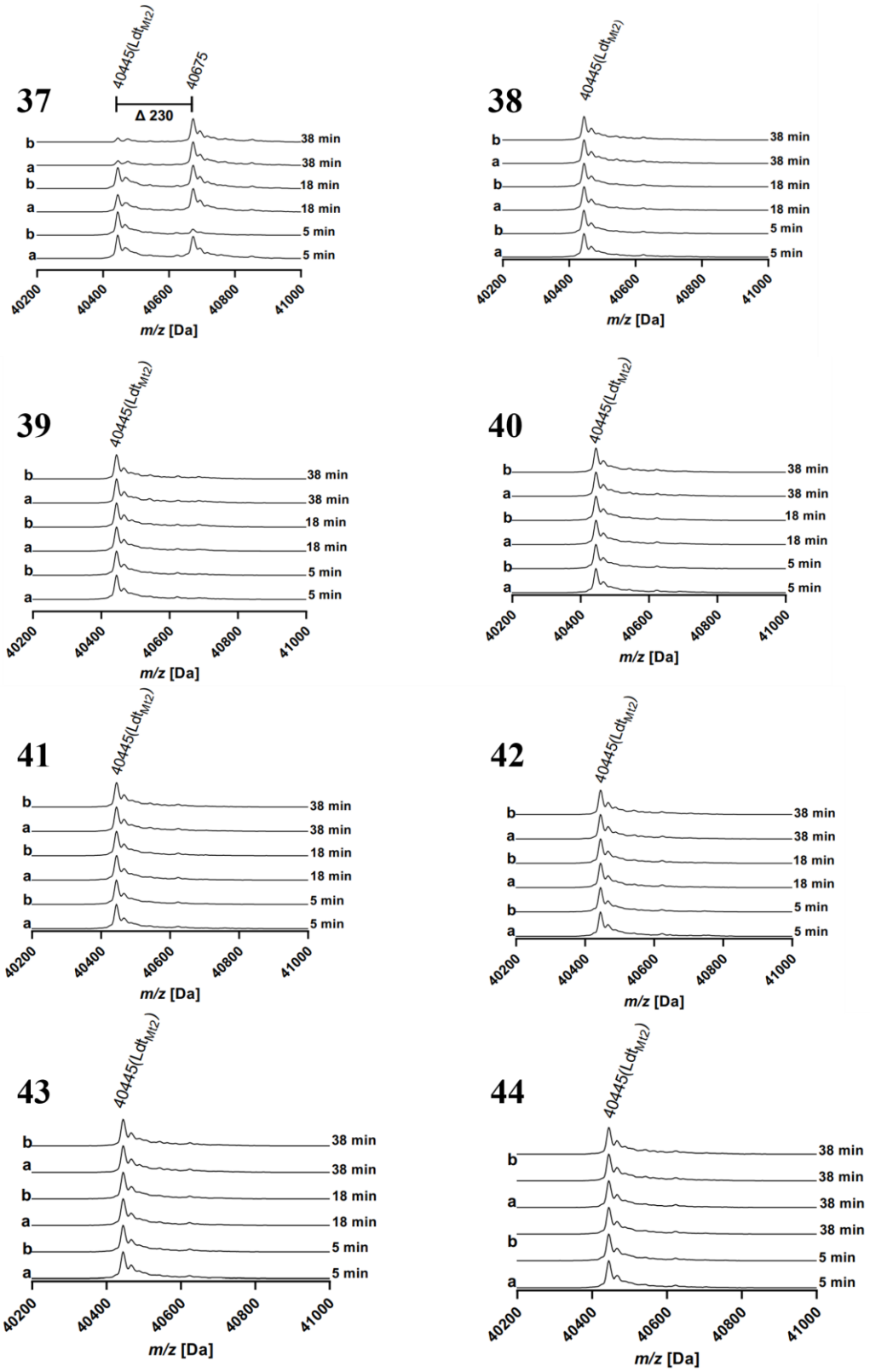

Figure 4.13 | *POMS experiments of Ldt_{Mt2} (40445 Da) incubated with compounds **37 - 42**. This figure was adapted with permission from Dr Tim Suits.*[473]

4.4.1. Antimicrobial Activity of Ebsulfur Analogues Against Multi-drug Resistant *Mycobacterium tuberculosis*

Five compounds from the initial and expanded series of ebsulfur analogues were selected to be screened against *M. tuberculosis* in whole-cell assays. Three compounds that reacted with Ldt_{Mt2} (**28**, **29**, **36**), and two compounds that did not react (**33**, **38**), were chosen. The whole-cell experiments were kindly conducted by collaborators Dr. Chris Moon and Dr. Joanna Bacon et al. (Public Health England).

4.4.2. Flow Cytometry of *M. tuberculosis* Treated with Ebsulfur Analogues

A flow-cytometer channels single cells through the path of a laser, allowing the scattered light to be detected and analysed according to the experiment's parameters. In this case, calcein violet acetoxy-methyl ester (CV-AM) and a fluorophore, Sytox green (SG), were applied to the *M. tuberculosis* cells prior to measurement. CV-AM enters live cells where the ester is hydrolysed to give a fluorophore, calcein violet (CV).[485] The intensity of CV fluorescence is dependent on the number of live cells and therefore representative of cellular proliferation. SG cannot enter live cells with intact membranes but can stain free nucleic acids. The intensity of SG fluorescence is dependent on the abundance of extracellular nucleic acids and therefore representative of cell wall and membrane dysfunction. The flow-cytometer detects and quantifies the intensities of CV and SG per cell to determine the proportion of live cells (via CV), as well as the proportion of cells with compromised cell membranes (via SG).[485] M. tuberculosis cells treated with compounds **28**, **29**, **33**, **36**, and **38** were assessed by flow-cytometry to investigate their effects on cell viability and cell wall integrity (**Figure 4.14**). At a high concentration (100 μM), all compounds (**28**, **29**, **33**, **36**, and **38**) compromised the viability of the cell wall

as observed by the high intensity of SG, and disrupted cell metabolism as seen by the low intensity of CV (cells in upper left quadrant > 70 %) (**Figure 4.14**, **Table 4.7**). In addition, the compounds that reacted with Ldt_{Mt2}**)** exhibited moderate minimum inhibitory concentrations (**28**, **29**, and **36**, MIC ~ 30 μM) but the compounds that did not react with Ldt_{Mt2} exhibited poor MIC values (**33** and **38**, MIC > 100 μM) (**Table 4.7**).

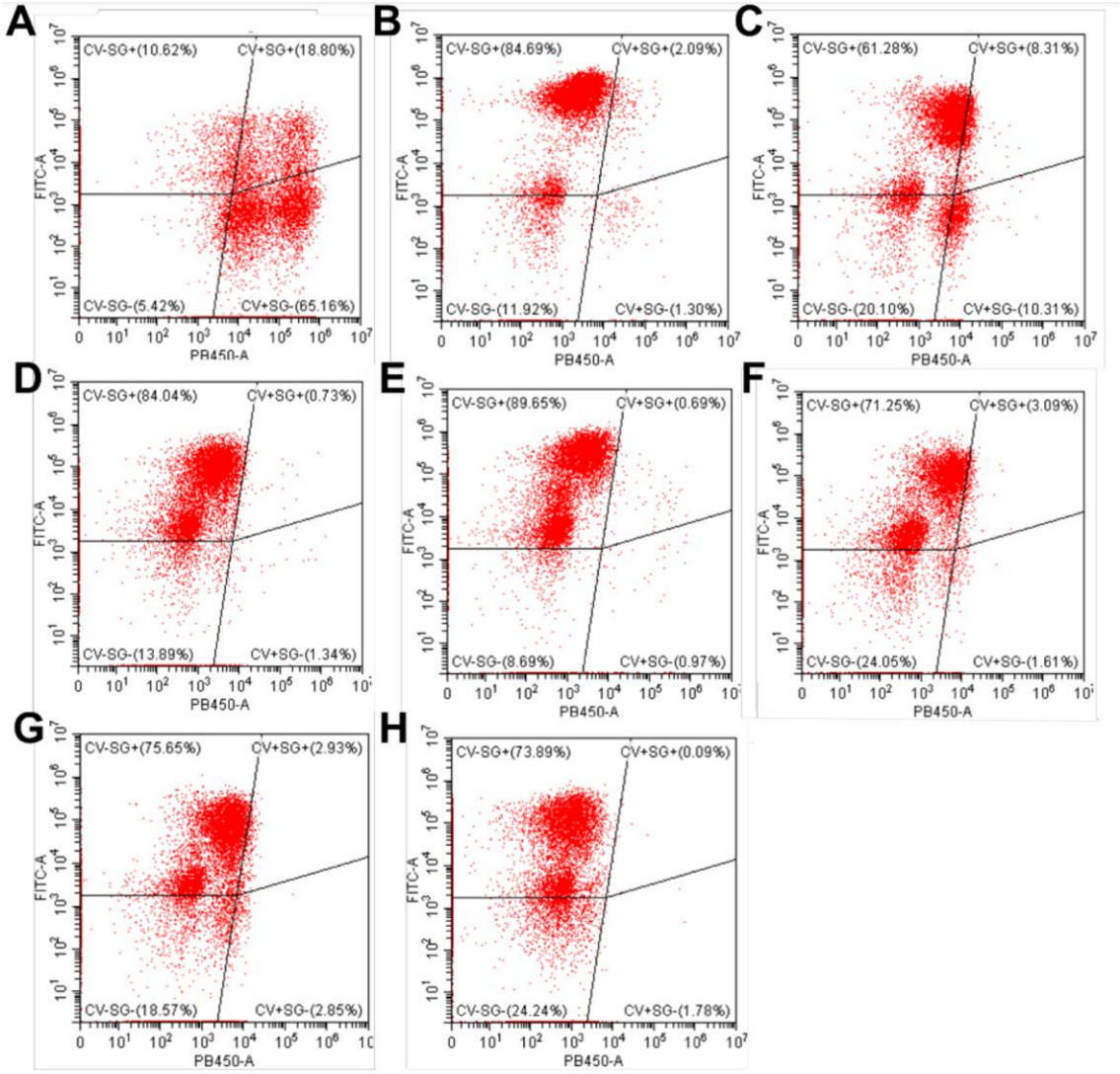

Figure 4.14 *| Flow cytometry experiments of inhibitors against Mycobacterium tuberculosis. Movement along the y axis from bottom to top quadrants represents an increase of detected SG, indicating an increase in the number of compromised cell membranes. Movement along the x axis from left to right quadrants represents an increase of detected CV, indicating an increase in the number of living cells. Movement from the bottom-right quadrant to top-left quadrant represents a transition from high numbers of living cells with intact cell surface membranes to high numbers of dead cells with compromised cell surface membranes.* ***A.*** *Control.* ***B.*** *Imipenem (a carbapenem β-lactam antibiotic).* ***C.*** *SQ109 (an*

inhibitor of mycobacterium membrane protein large 3). ***D. 28****,* ***E. 29****,* ***F. 33****,* ***G. 36****,* ***H. 38****. This figure was adapted with permission from Dr Tim Suits.*[473]

Compound	Structure	MIC (μM)	Cells in upper left quadrant (%)
28*	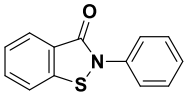	37.04 ± 10.70	84.44
29	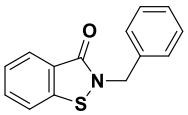	38.25 ± 10.20	89.65
33	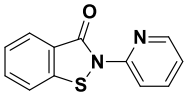	> 100	71.25
36	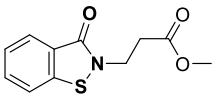	30.80 ± 6.23	75.65
38	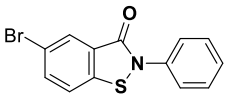	> 100	73.89

Table 4.7 *|MIC values and flow cytometry data for compounds* ***28****,* ***29****,* ***33****,* ***38*** *and* ***36*** *against Mycobacterium tuberculosis. This table was adapted with permission from Dr Tim Suits.*[473]

4.4.3. Future Work to Develop Ebsulfur Analogues Against Ldt_{Mt2}

The flow-cytometry and MIC data from *M. tuberculosis* whole-cell assays indicate that the ebsulfur analogues can exhibit antimicrobial activity. According to the MIC values measured here, compounds previously shown to react with Ldt_{Mt2} (**Figure 4.11.28**, **Figure 4.11.29**, **Figure 4.12.36**) exhibited lower MICs (**Table 4.7**; **28**, MIC ~37 μM; **29**, MIC ~38 μM; **36**, MIC ~31 μM) than compounds which did not react with Ldt_{Mt2} (**Figure 4.12.33**; **Figure 4.13.38**; **Table 4.7**, **33** and **38**, MICs > 100 μM). However, without direct investigation, it is not possible to conclude that compounds **28**, **29**, and **36** achieved lower MIC values via superior Ldt_{Mt2} inhibition. The cell wall of *M. tuberculosis* was also compromised by all compounds at high concentration, suggesting

further experiments are required to confirm whether cell wall dysfunction occurred via slower assembly, or faster degradation.

4.5. Summary and Conclusions

The aim of the work described in this chapter was to help develop a potential small-molecule therapeutic for use in SARS-CoV-2 infections. The project was inspired by the reported potency of Ebselen (**26)** against SARS-CoV-2 M^{pro} (reported IC_{50} = 0.67 μM), and the observed selectivity of the active-site mimetic peptide 'N3'.[429] **26** is known to perform off-target reactions; **26** was measured to react with Ldt_{MT2} and every cysteine in M^{pro} (12).[437, 470] It was proposed that an analogue which reacted fewer times with M^{pro} cysteines, and maintained potency against M^{pro}, may produce fewer off-target reactions.

The scaffold of **26** was substituted at the N1, C6, and C8 positions, and the selenium atom was replaced with a sulfur atom. In comparison with **26**, three compounds were found to form fewer adducts with M^{pro} cysteines and maintain comparable potency against M^{pro}, as measured by relative potency (relative potency = pIC_{50} / max. number of adducts); **34** (relative potency = 2.1), **38** (relative potency = 3.8), and **42** (relative potency = 3.3).

The most relatively potent compound, **38** (relative potency = 3.8), was tested alongside compounds **28** (relative potency = 0.6), **29** (relative potency = 1.1), **33** (relative potency = 1.1), and **36** (relative potency = 1.1), for antimicrobial efficacy against *Mycobacterium tuberculosis* bacteria, which express Ldt_{MT2}.[437] Compound **38** (MIC > 100 μM) demonstrated a poorer MIC than compounds **28** (37 μM), **29** (38 μM), and **36** (31 μM).

In conclusion, **38** exhibited marginally superior potency (IC_{50} = 30 nM) and reduced reactivity (max. number of adducts = 2) against M^{pro} than **26** (IC_{50} = 40 nM, max. number

of adducts = 12). Compound **38** also exhibited relatively poorer antimicrobial activity than **28** (37 μM), **29** (38 μM), and **36** (31 μM), as inferred from their respective MIC values. The higher MIC values exhibited by **38** suggests that modifications putatively beneficial for the selective inhibition of M^{pro} may have a detrimental effect on the growth-inhibitory activity of the ebsulfur scaffold against *M. tuberculosis*. One explanation may be that a reduction in off-target reactions relative to M^{pro} corresponds to fewer reactions with proteins necessary for the growth of *M. tuberculosis*, potentially including Ldt_{Mt2}. Alternatively, considering compound **38** structurally differs from **28** solely through a bromide substituent, **38** may be a substrate for metabolic or efflux pathways in *M. tuberculosis* where **28** is not, thereby diminishing the antimicrobial efficacy of **38**. A substantial amount of further development would be required to derive an approved therapeutic agent from the **26** scaffold. Nonetheless, the results support the proposal that the selectivity of the **26** scaffold can be improved.

5. Conclusions

5.1. Roles and Therapeutic Potential of Isocitrate Dehydrogenase Mutations in Cancer

5.1.1. Summary

The primary objectives of this work were to investigate the roles of IDH1 WT and IDH2 WT in glioma cells with IDH1 R132H mutations, differentiate the effects of the IDH1 R132H gain-of-function and dominant-negative phenotypes, investigate a metabolic link between IDH1 mutations and an oncogenic driver in glioma, and identify novel potential therapeutic avenues enabled by IDH1 mutant-induced changes in metabolism.

Chapter 1 reviewed the significant metabolic effects of IDH1/2 mutations and associated therapeutic strategies. There appeared to be a lack of evidence on the precise mechanistic link between IDH1/2 mutations and specific oncogenic drivers. In addition, the emerging resistance to clinically approved IDH1/2 inhibitors underscores the need for alternative therapeutic approaches that avoid direct targeting of IDH variants. Given the strong metabolic alterations induced by IDH1/2 mutations, strategies targeting metabolically sensitive pathways appear promising, such as IDH1/2 WT inhibition.

Chapter 2 describes the evaluation of existing pre-clinical inhibitor scaffolds targeting IDH1/2 mutations. Inhibition screens against IDH1 WT and IDH2 WT by collaborators yielded two inhibitors: one for IDH1 WT (**1**) and another for IDH2 WT (**2**). The two inhibitors were then synthesised for further investigation. Additionally, a novel small-molecule was synthesized, using elements of **2** as the warhead for a potential PROTAC strategy (**3**). Inhibition assays, including the e-Leaf and NADPH absorbance-based methods, demonstrated that IDH1 WT inhibition with **1** was significantly slower when

the IDH1 WT enzyme had already begun the catalytic cycle, suggesting potential challenges for in vivo efficacy, where enzymatic activity is continuously present. The binding kinetics derivations suggest that **1** binds to IDH1 WT freely, but must wait for IDH1 WT to adopt an open-inactive conformation to trap an inactive conformation and cause inhibition. Studies on compounds incorporating quaternary ammonium ions as potential active-site inhibitors indicated minimal impact on enzyme activity and only modest inhibition effects.

Chapter 3 describes three metabolomics experiments using LN18 GBM cells, with and without IDH1 R132H mutations. The IDH1 WT inhibitor **1**, the IDH2 WT inhibitor **2**, and the putative IDH2 WT PROTAC **3** were applied separately to cells of each mutational status. The metabolic effects of the IDH1 R132H mutation in cells were compared to the IDH1 WT cells, and the effects of each treatment were compared to a control within each mutational status. The untreated IDH1 R132H cells exhibited alterations to the PPP, nucleotide biosynthesis, neurotransmitter homeostasis, redox homeostasis, lysine/hydroxylysine/tryptophan degradation pathways, fatty acid metabolism, and β-CG (the role of which is still undefined). **1** led to dysregulation of the lysine/hydroxylysine/tryptophan degradation pathways and potent inhibitory activity against IDH1 R132H (as reported in literature).[304] Interestingly, IDH1 WT inhibition, and IDH1 R132H inhibition, appeared to affect the lysine/hydroxylysine/tryptophan degradation pathways by different mechanisms; glutaric acid was significantly elevated in both IDH1 WT and IDH1 R132H cells treated with **1** compared to controls, but glutaconic acid was elevated in control IDH1 R132H cells and decreased in favour of glutaric acid when treated with compound **1**. IDH2 WT inhibition appeared to affect galactose metabolism, but the effects were overridden in the presence of the IDH1 R132H mutation. Compound **3** elicited widespread alterations in metabolite abundances in IDH1

WT cells, but have no apparent effects in IDH1 R132H cells. While these findings confirmed that **3** was at least in part selective as it was not targeting IDH1 R132H, it was not clear if IDH2 WT was the target as galactose was not significantly affected in the treated groups. Nonetheless, multiple areas of metabolism contained significantly altered metabolites including co-/post-translationally modified amino acids, nucleotides, redox homeostasis, the TCA cycle, lysine/hydroxylysine/tryptophan degradation pathways, and the metabolites taurine and β-CG.

5.1.2. Limitations of the Metabolomics Analyses

The LN18 GBM cell line was transfected with a lentiviral vector to express the IDH1 R132H mutation. Ideally, the mutation would be endogenously present in the chromosome to more accurately mimic physiological conditions. It would be ideal to utilise patient-derived samples in which the mutation occurred naturally.

The putative PROTAC compound retained only some structural elements of the original compound, **2**, and the IC_{50} value against IDH2 WT was not measured. Moreover, western blots were not available to investigate the IDH2 WT protein degradation activity. Although there was evidence of a strong effect specific to the IDH1 WT cell line, the mechanistic significance of this observation can only be fully understood once its direct interactions within the cell are confirmed.

The sample size in metabolomics experiment 2 was smaller than experiment 1 ($n = 5$ cf. $n = 10$); ideally, sample sizes should be as large as possible to ensure statistical validity ($n > 10$). Additionally, the number of repetitions for the metabolomics experiments is a common limitation in metabolomics analyses. Repeating the entire experiment could enhance the reliability of the findings. For comprehensive analysis, samples from each experiment should also be preserved for other analyses, particularly proteomics. This

would enable the integration of metabolomic and proteomic data, facilitating the investigation of potential connections, such as the role of PKCδ, which may be a crucial effector in peroxisomal oxidative stress signalling.

The metabolite database is not exhaustive and certain metabolites may have multiple unidentified fragments contributing to their significance, or lack thereof. For example, it is possible that the identifications of 4-hydroxybutyric acid and 4-hydroxyphenylglycine are made on underlying compound features which were fragments of other metabolites, such as 2-HG. The IC-MS is sensitive to TCA cycle metabolites, but less so for lipid metabolites, a critical area of significant metabolic dysfunction in IDH1 mutants. In the future, metabolomics analyses could focus on the detection of fatty acids, especially diacylglycerol (DAG) from lipolysis, perhaps necessitating an alternative chromatography-MS method tailored for lipid analysis.

The use of cell lines supplemented with exogenous glutamine potentially biased the levels of glutamate-glutamine cycle metabolites. It would potentially be more accurate culture cells in physiological conditions akin to the synaptic cleft. This adjustment could provide a more accurate representation of cellular responses and metabolic perturbations.

5.1.3. The Roles of IDH1 WT and IDH2 WT and Differentiating Between the Effects of the IDH1 R132H Gain-of-Function and the Dominant Negative-Phenotype

It is challenging to identify the roles of IDH1 WT and IDH2 WT from the available data due to the overall lack of significant alterations of metabolites in IDH1 WT and IDH1 R132H LN18 cells treated with **1** and **2**. It appears that the effects of the IDH1 R132H are mostly conveyed via the gain-of-function and not the dominant negative phenotype. Although the potential inhibition of IDH1 WT by **1** led to alterations in the

lysine/hydroxylysine/tryptophan degradation pathways, similarly to the IDH1 R132H mutation, different altered metabolites in each condition (glutaric acid cf. glutaconic acid) suggest that the mechanism of action is different, and therefore it is not the dominant negative phenotype of IDH1 R132H causing glutaconic acid to be altered. Treatment with **2** appeared to have no significant effect in IDH1 WT cells on metabolites that were altered in the control IDH1 R132H cells, suggesting that IDH2 WT inhibition did not interact with similar pathways as were affected by the IDH1 R132H mutation. The evidence for potentially stronger IDH2 WT inhibition by **3** is inconclusive without further evidence to suggest that IDH2 WT is being degraded itself. In the absence of significant alterations in the same metabolites as affected by **2**, it seems likely that the effects of **3** may be mediated by off-target effects, if not via IDH2 WT inhibition.

5.1.4. A Proposed Role of IDH1 R132H in Glioma, Linking IDH1 R132H to Polyamines and p53:

IDH1 WT activity is reported to be closely linked to fatty acid metabolism, and the IDH1 R132H mutation is reported to lead to fatty acid metabolism dysregulation.[30, 215, 220-222] The IDH1 R132H mutation consumes NADPH and 2-OG, and causes 2-HG accumulation.[16] The IDH1 R132H mutation is also localised to the peroxisome.[24, 27] Crucially, L-α-hydroxyacid oxidase (HAO, catalyses 2-hydroxyacid + O_2 → 2-oxoacid + H_2O_2) is almost exclusively found in the peroxisome.[23] In the peroxisome, 2-HG produced by IDH1 R132H may be immediately oxidised to 2-OG by HAO, producing H_2O_2; 2-OG may then be reduced to 2-HG again by IDH1 R132H at the expense of another NADPH molecule. The consequent accumulation of ROS can then trigger tyrosine-kinase c-Abl to activate catalase, regenerating O_2 from H_2O_2. Thus, 2-OG and 2-HG may cycle indefinitely in the peroxisome until the local NADPH is depleted, and in the absence of sufficient catalase, H_2O_2 may also accumulate until the available O_2 is

depleted (**Figure 5.1**). The PPP appears to be upregulated to compensate for the depletion of NADPH, but this may not ameliorate the balance in the peroxisome. This cycle could also be relevant in the case of an IDH2 mutation; if 2-HG from the mitochondria were to enter the peroxisomes, NADPH depletion would likely remain localised to the mitochondria, but ROS may accumulate in the peroxisome due to the action of HAO.

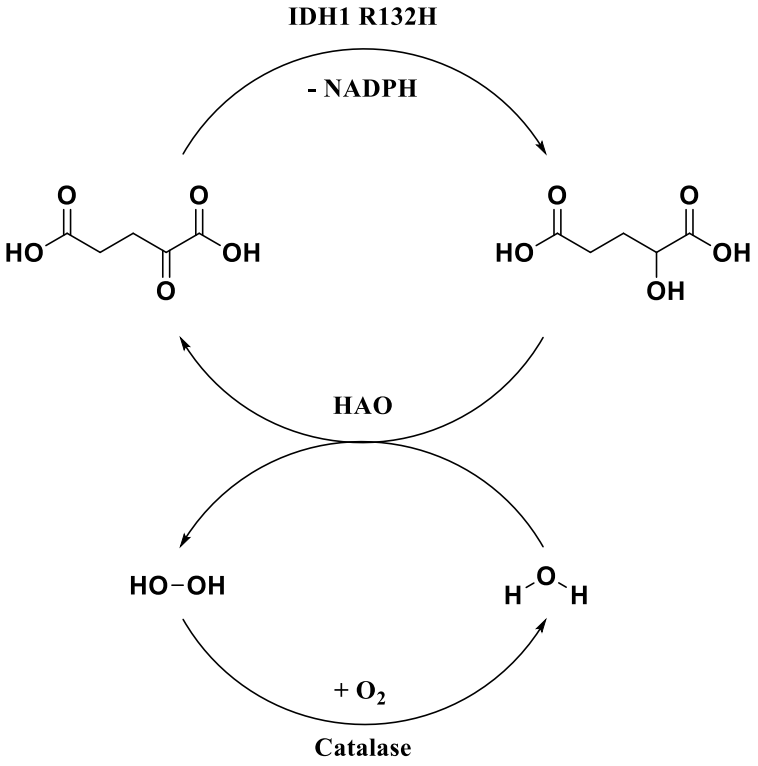

Figure 5.1 *| An overview of the potential cycle between 2-OG and 2-HG in the peroxisome, enabled by IDH1 R132H, HAO, and catalase.*

H_2O_2 and ROS occur at relatively high levels in peroxisomes as a consequence of normal β-oxidation,[486] L-2-hydroxyacid oxidation (here 2-HG),[487] and dysregulated unsaturated fatty acid metabolism;[31] lipid peroxides accumulate, derived from unsaturated fatty acids, which are unable to be reduced without sufficient levels of NADPH. [23, 26, 27, 218, 223] Critically, lipid peroxides in excess cause ferroptosis (iron-dependent programmed cell death);[218] treatment of cells with 2-HG is reported to promote the accumulation of lipid peroxides,[219] and mutant IDH1 is reported to sensitise cells to ferroptosis.[219] Peroxisomal

biogenesis factor 2 (PEX2) senses the accumulation of ROS as a sign of increased β-oxidation and triggers lipolysis via adipose triglyceride lipase, releasing DAG in the first step.[379, 426] H_2O_2, c-Abl, and DAG cooperate to maximally activate protein kinase C delta PKCδ.[383, 385] On activation, PKCδ may deplete NAAG,[382] downregulate glutamine synthase,[488] and activate ornithine decarboxylase (ODC) to produce putrescine.[489-491]

Putrescine is a polyamine and may be converted into longer polyamines through the polyamine cycle.[492] Polyamines are reported to be necessary for rapid proliferation,[493] and are reported to increase the permeability of the blood brain barrier,[494] which in particular suggests effects on glial cells.[495] Inhibition of polyamine synthesis is reported to halt cell growth.[493] Putrescine levels are reported to be elevated in glioma cells expressing IDH1 R132H.[140] Polyamines may not immediately lead to proliferation as they are reported to upregulate p53,[496] however, 2-HG may downregulate p53 via HIF-2α,[497] and IDH1 mutation is reported to frequently co-occur with p53 mutation leading to the suggestion that IDH1 mutation occurs as an initial event in cancer development, with p53 mutation occurring subsequently. [481-483]

PKCδ may be responsible for the observed tissue-specificity of IDH mutations in cancer; PKCδ demonstrates pro-apoptotic effects in the majority of cell studie;.[498] however, PKCδ also demonstrates tissue-specific anti-apoptotic effects, particularly in the skin and brain, which are coincidentally both lipid-rich tissues. Small-molecules inhibitors of PKCδ have been patented as inhibitors of metastatic melanoma,[499] and PKCδ is reported to be anti-apoptotic in glioma cells challenged with virus-induced apoptosis.[500] Inhibition of PKCδ prevents neurite growth,[501] and activation of PKCδ enhances nerve growth factor (NGF) induced neuritogenesis.[502] Hippocampal cells treated with NGF and fibroblast growth factor (FGF) require PKCδ to activate the Mitogen-Activated Protein Kinase (MAPK) for growth.[501]

In conclusion, the IDH1 R132H gain-of-function, and peroxisome-specific cycling of 2-HG and 2-OG by HAO, may maximally activate PKCδ by triggering oxidative stress and lipolysis simultaneously. PKCδ activation may then lead to some of the observations commonly seen in IDH1 R132H mutant cells; namely, glutamine synthetase downregulation, depletion of NAAG (and potentially β-CG), accumulation of polyamines, and p53 co-occurrence. [140, 503-505] Downregulation of glutamine synthase will free glutamate from its recycling pathway making it available as a fuel source. This process may explain the observed net flow of glutamine to glutamate and ultimately 2-HG, as opposed to the physiological direction of glutamate to glutamine. [140, 190-193, 506] NAAG and β-CG are often observed to be depleted in IDH1 R132H cell lines.[140] The accumulation of polyamines may prime the cell in a 'pre-proliferative state', awaiting sufficient p53 downregulation via 2-HG accumulation, or eventual p53 mutation. Upon the mutation of p53, cells may then participate in tumorigenesis.

5.1.5. Therapeutic Avenues for the Treatment of IDH1 R132H Glioma

To date, inhibiting IDH1 WT or IDH2 WT does not seem to be a promising treatment of IDH1 R132H bearing glioma, at least based on the limited metabolic impact identified here. While this study did not clearly delineate the roles of IDH1 WT and IDH2 WT in IDH1 R132H cancers, pathways sensitive to IDH1 mutation appear to include the PPP, nucleotide synthesis, fatty acid metabolism, and lysine/hydroxylysine/tryptophan degradation. Accordingly, future therapeutic avenues may benefit from targeting one of these four metabolic areas.

The pentose phosphate pathway (PPP) is consistently highlighted as key in IDH1 R132H cell lines, likely serving as a compensatory mechanism to regenerate NADPH.[130, 140] Additionally, nucleotide synthesis, linked to the PPP via ribose-5-phosphate, appears to be increased. Targeting the PPP and/or inhibiting de novo nucleotide biosynthesis may

be an effective therapeutic avenue. Recent studies indicate that folate antagonists selectively kill glioma stem cells (GSCs) without affecting fibroblasts or neural stem cells in vitro,[507] underscoring the importance of purine nucleotide biosynthesis in gliomas. Furthermore, glutamine, a key carbon source for accumulated 2-HG and nitrogen source for carbamoyl phosphate in pyrimidine biosynthesis, shows differential utilization in mutant cells.[140] Dr. Ingvild Hvinden's findings suggest that mutant cells exhibit higher resilience to glutaminase inhibition than wild-type cells and it was postulated to be caused by alternative glutamine metabolism pathways; carbamoyl phosphate synthetase II (CPSII) is part of an alternative route glutaminase for the production of glutamate,[508] and increased CPSII activity would promote pyrimidine biosynthesis.[509] An inhibitor targeting the oxidative phase of the PPP could maximise impact in MUT cells by hindering R5P production for nucleotide synthesis and reducing NADPH compensation. Ideally, inhibiting the first enzyme in the PPP, glucose-6-phosphate dehydrogenase, could cease all NADPH production. Alternatively, targeting the third enzyme, 6-phosphogluconate dehydrogenase, which generates the second molecule of NADPH in the PPP and produces RL5P (a pentose), may also be effective.

The IDH1 R132H mutation significantly impacts on fatty acid metabolism and the degradation pathways of lysine, hydroxylysine, and tryptophan. Processes such as peroxisomal β-oxidation in fatty acid metabolism and the pipecolate pathway in lysine degradation, which occur early in peroxisomes, are likely disrupted by the IDH1 R132H mutation's consumption of local NADPH or the increased accumulation of ROS from the action of HAO. Additionally, alterations in metabolites observed exclusively after administering an IDH1 WT inhibitor suggest that normal IDH1 activity is crucial for regulating these pathways. However, the response to the same inhibitor in cells harbouring the IDH1 R132H mutation indicates a distinct mechanism of dysregulation to

the pipecolate pathway, perhaps mediated by the gain-of-function, underscoring the complex interaction between the mutation and metabolic processes. In the case of an IDH2 mutation, HAO may mediate similar downstream effects as an IDH1 R132H mutation via the oxidation of mitochondria-derived 2-HG; although, the relationship between IDH2 WT and lipid metabolism is not clear given conflicting reports on the effect of IDH2 deficiency on lipid metabolism.[32, 33]

5.2. Inhibition of the SARS-CoV-2 Main Protease

5.2.1. Summary

A secondary objective of the work described here was to develop an ebselen-type inhibitor scaffold, which could carry modifications to improve selectivity and potency against the SARS-CoV-2 main protease (M^{pro}). Chapter 4 described the development of the ebselen scaffold into a less reactive, but potent, covalent inhibitor of SARS-CoV-2 M^{pro}. Reactivity was modulated by substituting the selenium atom for a sulfur atom (also known as ebsulfur) and varying substituents on the nitrogen or the benzoisothiazolinone core. For each synthesised compound, IC_{50} values against M^{pro} were measured using FRET and mass-spectrometry, and the number of covalent reactions with M^{pro} were observed by POMS. The most promising hit compound incorporated a bromide substituent at the C6 position of the BIT core, and exhibited comparable potency to ebselen while reacting only twice with M^{pro} (compared to 12 in the case of ebselen). A compound with no modifications to the BIT core, but a 4-(aminomethyl)pyrrolidine-2-one *N*-linked side chain, exhibited slightly reduced potency and substantially reduced reactivity (3 reactions with M^{pro}). The hit compound **38** also exhibited much poorer MIC values against *Mycobacterium tuberculosis* than unmodified ebsulfur, suggesting that

increasing the selectivity against M^{pro} successfully impaired reactivity with other active site cysteine enzymes, here Ldt_{Mt2}.

5.2.2. Limitations

Despite observing a decrease in the number of reactions while maintaining high potency, the absence of a crystal structure containing M^{pro} and **38**, appropriately means it is not possible to say the compounds definitively interact with the active site cysteine. Competition involving irreversible reaction of the active site cysteine with a selective inhibitor will provide insight into selectivity. It remains unclear whether the compounds react with glutathione, other cysteine enzymes, or if they are metabolized during first-pass liver metabolism. Therefore, more specific and detailed biochemical evaluations are required to clarify the compounds' mechanisms of action and stability

5.2.3. A Novel SARS-CoV-2 M^{pro} Inhibitor

The work described here demonstrates the feasibility of modulating the ebselen scaffold reactivity without compromising its potency. By combining optimal BIT core substituents with an optimal *N*-linked side chain, it may be possible to develop a highly selective inhibitor targeting M^{pro}.

6. Materials and Methods

6.1. Chemical Synthesis

6.1.1. General Information

Commercially available reagents and solvents were from Merck, Fluorochem, or Activate Scientific, and were used as received. All manipulations with air- and moisture-sensitive compounds were carried out under a positive pressure of argon in flame-dried glassware.

Chromatographic separation/purifications were performed using a Biotage Isolera system. Unless otherwise specified, the solvent system employed a 0→40% (v/v) ethyl acetate in cyclohexane gradient using Biotage Sfär® HC Duo cartridges. Reactions were monitored by TLC on Merck aluminium backed sheets coated with Merck Kieselgel 60 F254 (230-400 mesh) fluorescent treated silica, and visualised under ultra-violet light (254 nm or 365 nm) and/or stained with ninhydrin.

Melting points were taken on a Stuart® SMP40 automatic melting point instrument. NMR-spectra were acquired using a 2-channel Bruker AVIII HD 400 Nanobay machine equipped with a 5 mm z-gradient BBFO probe (multinuclear with ^{19}F), a 2-channel Bruker AVIII HD 600 equipped with a dedicated 5 mm BB-F/^{1}H Prodigy N_2 cryoprobe optimised for multinuclear observation, or a 2-channel Bruker NEO 600 equipped with a dedicated 5 mm BB-F/^{1}H helium-cooled cryoprobe optimised for multinuclear observation. Chemical shifts were referenced to residual protio- and perdeuterio-solvent resonances (δH 7.26 and δC 77.16 for $CDCl_3$; δH 2.50 and δC 39.52 for DMSO-d6; δH 3.31 and δC 49.00 for CD3OD) as internal standards for ^{1}H NMR and ^{13}C NMR spectra, respectively. All NMR spectra were processed using MestReNova software (version 14.2).

LC-MS (liquid chromatography-mass spectrometry) data were obtained using an Agilent 1200 series LC machine connected to an Agilent 6120 Quadrupole MS using electrospray ionisation (ESI) machine. LC was performed on a C18 reversed-phase column (Acquity UPLC BEH C18, 2.1 mm × 50 mm, 1.7 μm) operated at 30 °C, using a linear gradient of the binary solvent system of buffer A (H_2O:formic acid, 100:0.1 v/v) → buffer B (MeCN:formic acid, 100:0.1 v/v), from 0 to 100% (v/v) B in 8.5 min, then 1 minute at 100% B, maintaining a flow rate of 1.5 mL⁄min. HR-MS (high resolution mass spectrometry) were obtained using a Bruker μTOF (ESI) spectrometer or Waters RDa bench-top TOF used with an Acquity LC system in direct infusion (loop injection) mode for target confirmation. For analysis using a Waters RDa benchtop TOF mcahine, flow injection analysis was performed on an Acquity I-Class PLUS UPLC System (Waters, Milford, MA, USA) coupled to an Acquity RDa mass spectrometer (Waters, Milford, MA, USA) equipped with an ESI probe; analysis was performed in positive or negative ionisation mode. The flow rate was set to 0.300 mL/min using a 50% (v/v) methanol (aq) + 0.1% (v/v) formic acid eluent. Scan parameters were set as follows: analyser mode, full scan; scan range, 50 2000 m/z; scan rate, 2 Hz; cone voltage, 30 V; capillary voltage, 1.5 kV; desolvation temperature, 550 °C; and intelligent data capture, on.

Specific rotations were measured using a Schmidt-Haensch UniPol polarimeter. Values are expressed in 10^{-1} deg cm^2 g^{-1}; concentrations (c) are quoted in g/100 mL; D refers to the D-line of sodium (589 nm).

6.1.2. The Synthesis of 1

1-(4-Chlorophenyl)-1*H*-imidazole-4-carbaldehyde (7a)[510, 511]

A modified version of the literature procedure was used.[510] The atmosphere of a reaction vial was purged with argon, then charged with CuI (350 mg, 1.80 mmol, 0.05 equiv) and

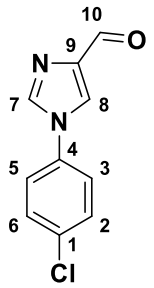

trans-*R*,*R*-*N*,*N*-dimethyl-1,2-cyclohexanediamine (1.03 g, 7.30 mmol, 0.20 equiv). Degassed DMF (69.2 mL, 0.52 M) was cannulated into the vial, forming a green solution. $CsCO_3$ (23.68 g, 70.0 mmol, 2.0 equiv) was added, followed by 4-imidazolecarboxaldehyde (3.46 g, 36.0 mmol, 1.0 equiv); the solution turned blue. 1-chloro-4-iodobenzene (13.0 g, 55.0 mmol, 1.5 equiv) was added and the mixture was stirred for 2.5 h at 110° C. The reaction mixture was cooled to 0° C, washed with saturated NH_4Cl solution (350 mL) and extracted with ethyl acetate (840 mL). The organic layer was separated and dried with Na_2SO_4. Flash chromatography (0-100% ethyl acetate in cyclohexane) followed by concentration *in vacuo* yielded 2.46 g (33%) of **7a** as a yellow solid.

Mp 180-181 °C; **^{1}H NMR** (400 MHz, DMSO) δ 9.82 (s, 1H, *H10*), 8.66 (s, 1H, *Im-H*), 8.50 (s, 1H, *Im-H*), 7.81 (d, *J* = 8.8 Hz, 2H, *H2*, *H6*), 7.64 (d, *J* = 8.8 Hz, 2H, *H3*, *H5*); the **^{1}H NMR** spectroscopic data are consistent with those reported in the literature;[510, 511] **ESI HR-MS**: calcd. for $[C_{10}H_8ON_2Cl+H]^+$: 207.0320, found: 207.0320.

(*S*)-(*E*)-*N*-((1-(4-Chlorophenyl)-1*H*-imidazol-4-yl)methylene)-2-methylpropane-2-sulfinamide (8)[307]

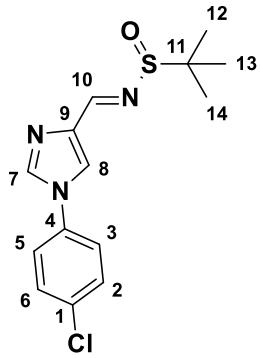

A modified version of the literature procedure was used.[307] A reaction vessel was charged with **7a** (2.45 g, 12.0 mmol, 1.0 equiv) and (S)-2-methylpropane-2-sulfinamide (1.94 g, 12.0 mmol, 1.0 equiv), then the atmosphere was purged with argon. Dichloromethane (23.8 mL, 0.50 M) and pyrrolidine (0.19 mL, 0.20 equiv) were injected sequentially and the reaction mixture was stirred for 3 h at 60° C. The crude mixture was then concentrated in vacuo and

purified using flash chromatography (0-100% ethyl acetate in cyclohexane) to yield 3.22 g (88%) of **8** as a yellow solid.

Mp 179 °C; **^{1}H NMR** (400 MHz, DMSO) δ 8.55 (m, 1H, *Im-H*), 8.48 (m, 1H, *Im-H*), 8.40 (s, 1H, *H10*), 7.80 (m, 2H, *Ar-H*), 7.64 (m, 2H, *Ar-H*), 1.16 (s, 9H, *H12*, *H13*, *H14*); the **^{1}H NMR** spectroscopic data are consistent with those reported in the literature;[307] **ESI HR-MS**: calcd. for $[C_{14}H17ON_3ClS+H]^+$: 310.0776, found: 310.0775.

(*S*)-*N*-((*S*)-1-(1-(4-Chlorophenyl)-1*H*-imidazol-4-yl)ethyl)-2-methylpropane-2-sulfinamide (9a)[308] and **(*S*)-*N*-((*S*)-1-(1-(4-chlorophenyl)-1*H*-imidazol-4-yl)ethyl)-2-methylpropane-2-sulfinamide (9b)**

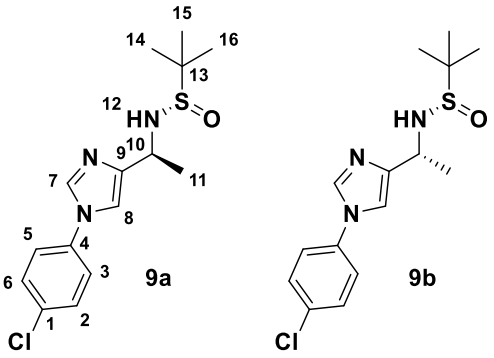

A modified version of the literature procedure was used.[308] A reaction vessel was charged with **8** (620 mg, 2.00 mmol, 1.0 equiv.) then the atmosphere was purged with argon. Dichloromethane (6.10 mL, 0.33 M) was added then the solution was cooled to -70 °C. Methyl magnesium bromide (3 M in Et_2O; 1.33 mL, 4.00 mmol, 2.0 equiv.) was added dropwise, and the mixture was allowed to warm to rt overnight. The reaction was quenched with saturated aqueous NH_4Cl (30.0 mL), then extracted with dichloromethane (30.0 mL). The organic layer was dried with Na_2SO_4 and concentrated *in vacuo*. Purification using flash chromatography (0→100% (v/v) (ethyl acetate + 1% (v/v) Et_3N) in dichloromethane then 0→1% (v/v) (MeOH + 1% (v/v) Et_3N) in (ethyl acetate + 1% Et_3N)) yielded 230 mg (35%) of **9a** (diastereomer ratio **9a**:**9b** 99:1), and 92 mg (14%) of **9b** (diastereomer ratio **9a**:**9b** 5:95) as yellow oils.

9a: **^{1}H NMR** (400 MHz, $CDCl_3$) δ 7.75 – 7.74 (m, 1H, *H7*), 7.44 – 7.41 (m, 2H, *H2*, *H6*), 7.33 – 7.29 (m, 2H, *H3*, *H5*), 7.24 – 7.23 (m, 1H, *H8*), 4.57 (p, *J* = 6.5 Hz, 1H, *H10*), 3.85 – 3.80 (m, 1H, *H12*), 1.57 (d, *J* = 6.67 Hz, 3H, *H11*), 1.23 (s, 9H, *H14*, *H15*, *H16*); the **^{1}H NMR** spectroscopic data are consistent with those reported in the literature.[308] **^{13}C NMR** (101 MHz, $CDCl_3$) δ 146.6, 135.9, 135.3, 133.3, 130.1, 122.7, 114.8, 55.8, 49.6, 22.7, 21.9.

9b: ^{1}H NMR (400 MHz, $CDCl_3$) δ 7.76 (d, *J* = 1.4 Hz, 1H, *H7*), 7.46 – 7.41 (m, 2H, *H2*, *H6*), 7.34 – 7.29 (m, 2H, *H3*, *H5*), 7.17 – 7.15 (m, 1H, *H8*), 4.66 – 4.56 (m, 1H, *H10*), 3.52 (m, 1H, *H12*) 1.66 (d, *J* = 6.8 Hz, 3H, *H11*), 1.22 (s, 9H, *H14*, *H15*, *H16*). **^{13}C NMR** (101 MHz, $CDCl_3$) δ 146.4, 135.8, 135.3, 133.2, 130.0, 122.5, 114.7, 55.8, 50.1, 23.0, 22.6.

ESI HR-MS: calcd. for $[C_{15}H_{20}ClN_3OS+Na]^+$: 348.0908, found: 348.0909.

(*S*)-1-(1-(4-Chlorophenyl)-1*H*-imidazol-4-yl)ethan-1-amine (10)[304]

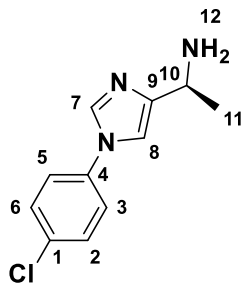

A modified version of the literature procedure was used.[304] The atmosphere of a reaction vessel was purged with argon, then charged with **9a** (650 mg, 2.00 mmol, 1.0 equiv.), MeOH (7.13 mL, 0.28 M) and HCl (4 M in 1,4-dioxane, 1.00 mL, 4.00 mmol, 2 equiv.), then the reaction was stirred at rt for 1 h. The mixture was concentrated *in vacuo* to remove the organic solvents, then re-dissolved in H_2O (15.0 mL). The solution was adjusted to pH 4 with formic acid, then washed with a mixture of isopropanol/$CHCl_3$ (1:3; 20.0 mL), then adjusted to pH 10 with NaOH (4 M in H_2O) and extracted with dichloromethane (30 mL). Concentration *in vacuo* yielded 162 mg (40%) of **10** as a yellow oil.

IR (neat): ν (cm^{-1}) 3470, 3235, 3196, 3102, 2943, 2915, 2848, 1675, 1600, 1535, 1508, 1429, 1378, 1340, 1275, 1216, 1199, 1163, 1126, 1097, 1076, 1028, 1015, 968, 955, 860, 832, 693, 624; **^{1}H NMR** (400 MHz, $CDCl_3$) δ 7.74 (s, *J* = 1.4 Hz, 1H, *H7*), 7.45 – 7.40 (m, 2H, *H2*, *H6*), 7.33 – 7.28 (m, 2H, *H3*, *H5*), 7.08 (s, *J* = 1.5, 0.9 Hz, 1H, *H8*), 4.13 (q, *J* = 6.6, 0.9 Hz, 1H, *H10*), 1.79 (s, 2H, *H12*), 1.46 (d, *J* = 6.6 Hz, 3H, *H11*); **^{13}C NMR** (101 MHz, $CDCl_3$) δ 150.2, 136.1, 135.1, 133.1, 130.1, 122.6, 112.9, 45.6, 23.6; **ESI HR-MS**: calcd. for $[C_{11}H_{12}ClN_3]^-$: 221.0725, found: 221.0728.

(*S*)-3-(2-Chloropyrimidin-4-yl)-4-isopropyloxazolidin-2-one (11)[512]

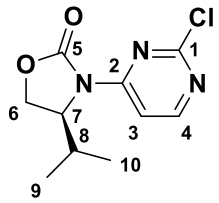

A modified version of the literature procedure was used.[512] The atmosphere of a reaction vessel was purged with argon, then charged with **(S)-4-isopropyloxazolidin-2-one** (1.00 g, 7.70 mmol, 1.0 equiv.), 2,4-dichloropyrimidine (1.15 g, 7.70 mmol, 1 equiv.), and DMF (5.62 mL, 1.37 M). The vessel was cooled to 0 °C and NaH (60% dispersion in mineral oil) was added portionwise. The reaction was stirred at rt for 18 h. The mixture was diluted with H_2O (14.7 mL), then extracted with ethyl acetate (26.6 mL). The organic layer was separated, washed with H_2O (7.34 mL), then dried with Na_2SO_4. Flash chromatography (0→10% (v/v) MeOH in dichloromethane) yielded 637 mg (34%) of **11** as a white solid.

^{1}H NMR (400 MHz, $CDCl_3$) δ 8.46 (d, *J* = 5.8 Hz, 1H, *Ar-H*), 8.18 (d, *J* = 5.9 Hz, 1H, *Ar-H*), 4.79 (ddd, *J* = 8.1, 3.5 Hz, 1H, *H7*), 4.44 – 4.32 (m, 2H, *H6*), 2.59 (hd, *J* = 7.0, 3.7 Hz, 1H, *H8*), 0.99 (d, *J* = 7.1 Hz, 3H, *C-H$_3$*), 0.87 (d, *J* = 7.0 Hz, 3H, *C-H$_3$*); the **^{1}H NMR** spectroscopic data are consistent with those reported in the literature.[512] **^{13}C NMR** (101 MHz, $CDCl_3$) δ 160.3, 159.8, 158.6, 154.5, 107.9, 63.7, 59.0, 27.7, 18.1, 14.5. **ESI HR-MS**: calcd. for $[C_{10}H_{12}ClN_3O_2+Na]^+$: 264.0510, found: 264.0506.

(*S*)-3-(2-(((*S*)-1-(1-(4-Chlorophenyl)-1*H*-imidazol-4-yl)ethyl)amino)pyrimidin-4-yl)-4-isopropyloxazolidin-2-one (1)[304]

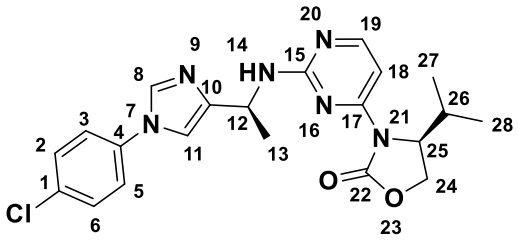

A modified version of the literature procedure was used.[304] The atmosphere of a reaction vessel was purged with argon, then charged with **11** (175 mg, 0.70 mmol, 1.0 equiv.), **10** (177 mg, 0.80 mmol, 1.1 equiv.), DMSO (1.28 mL, 0.63 M), and DIPEA (379 μL, 3 equiv.) were added sequentially, the vessel was heated to 90 °C and stirred for 22 h. The mixture was diluted with dichloromethane (1 mL), then warmed to 40 ° C for 2 h under a stream of nitrogen. The crude mixture was re-dissolved in diethyl-ether, then stirred with ice. The organic layer was separated and dried with Na_2SO_4. Flash chromatography (0→80% (v/v) (95:5 ethyl acetate:MeOH) in cyclohexane) yielded 39 mg (11%) of **1** as a colourless oil.

IR (neat): ν (cm^{-1}) 3354, 3228, 3104, 3069, 2956, 2923, 2852, 1764, 1584, 1504, 1454, 1421, 1390, 1372, 1334, 1315, 1270, 1207, 1147, 1121, 1096, 1069, 1054, 1013, 978, 968, 937, 867, 828, 812, 792, 771, 755, 722, 705, 686, 644, 620; **^{1}H NMR** (600 MHz, $CDCl_3$) δ 8.12 (s, 1H, *H19*), 7.77 (d, *J* = 1.6 Hz, 1H, *H8*), 7.56 (s, 1H, *H18*), 7.46 – 7.43 (m, 2H, *H2*, *H6*), 7.31 – 7.28 (m, 2H, *H3*, *H5*), 7.18 – 7.17 (m, 1H, *H11*), 6.91 (m, 1H, *H14*), 5.17 (m, 1H, *H12*), 4.70 (ddd, *J* = 8.4, 3.3 Hz, 1H, *H25*), 4.34 (m, 1H, *H24'*), 4.28 (dd, *J* = 9.1, 3.0 Hz, 1H, *H24"*), 2.43 (m, 1H, *H26*), 1.65 (d, *J* = 6.9 Hz, 3H, *H13*), 0.87 – 0.77 (m, 6H). **^{13}C NMR** (101 MHz, $CDCl_3$) δ 165.6, 159.9, 158.6, 154.5, 146.3, 135.8, 135.2, 133.5, 130.3, 122.6, 114.1, 99.1, 63.3, 59.0, 46.5, 27.9, 21.6, 14.4. **ESI HR-MS**: calcd. for $[C_{21}H_{23}ClN_6O_2+H]^+$: 427.1644, found: 427.1650.

6.1.3. The Synthesis of 2

6-(2-Fluorophenyl)-*N*^{2},*N*^{4}-dipropyl-1,3,5-triazine-2,4-diamine (2)[306]

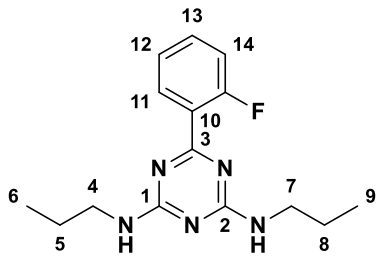

A modified version of the literature procedure was used.[306] A reaction vessel was charged with cyanuric chloride (2.60 g, 14.0 mmol, 1.0 equiv.) and a mixture of 5:1 H_2O:acetone (78 mL, 0.3 M). Propylamine (3.46 mL, 42.12 mmol, 3 equiv.) was added dropwise to the suspension at 0 °C, then the reaction was warmed to 45 °C and stirred for 2 h. The reaction mixture was vacuum-filtered at rt, washed with H_2O and ice-cold diethyl ether, and left to dry under-reduced pressure. This yielded a crude mixture of **15** as a white solid (645 mg, 3.45 mmol, 25%) which was not purified further. A new reaction vessel was purged with argon and charged with the crude mixture (580 mg, 2.50 mmol, 1 equiv.), 2-fluorophenyboronic acid (350 mg, 2.50 mmol, 1 equiv.), $Pd(dppf)Cl_2$ (183 mg, 0.25 mmol, 0.1 equiv.), 1,4-dioxane (25 mL, 0.13 M), and Na_2CO_3 (2M in H_2O, 5 mL, 10.0 mmol, 4 equiv.). The suspension was degassed with argon for 15 min, then stirred at 115 °C for 15 h. The resulting mixture was concentrated *in vacuo*, resuspended in H_2O (25 mL) and extracted with ethyl acetate (40 mL). The combined organic layers were washed with brine (40 mL), dried over Na_2SO_4, then concentrated *in vacuo* again. Flash chromatography (0→30% (v/v) ethyl acetate in cyclohexane) yielded 297 mg (41%) of **2** as a white solid.

^{1}H NMR (400 MHz, DMSO) δ 7.91 – 7.74 (m, 1H), 7.53 – 7.19 (m, 5H), 3.29 – 3.15 (m, 4H, *H4*, *H7*), 1.60 – 1.64 – 1.59 (m, 4H, *H5*, *H8*), 0.92 – 0.83 (m, 6H, *H6*, *H9*); **^{13}C NMR** (101 MHz, DMSO) δ 168.7, 165.5, 161.1, 131.75, 130.9, 127.1, 124.0, 116.4, 41.8, 22.2, 11.5; the **^{1}H** and **^{13}C NMR** spectroscopic data are consistent with those reported in the literature.[306] **ESI HR-MS**: calcd. for $[C_{15}H_{21}FN_5+H]^+$: 290.1776, found: 290.1774.

6.1.4. The Synthesis of 3 and 4

2-(2,6-Dioxopiperidin-3-yl)-4-fluoroisoindoline-1,3-dione (12)[314, 513, 514]

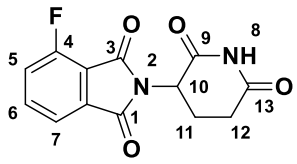

Conditions A: A modified version of the literature procedure was used.[314] 4-Fluoroisobenzofuran-1,3-dione (1115 mg, 6.7 mmol, 1 equiv.) and L-glutamine (980 mg, 6.7 mmol, 1 equiv.) were heated to 170 °C in a reaction vessel and stirred overnight. The mixture was allowed to cool to rt, then stirred with a solution of ethyl acetate (7 mL) and acetonitrile (3 mL) overnight. The resulting solution was washed with HCl (2 M, 15 mL), then dried with Na_2SO_4. Reverse-phase flash chromatography (0→100% (v/v) acetonitrile in H_2O with 0.1% formic acid), followed by concentration under reduced pressure yielded 436 mg (24%) of **12** as a white solid.

Conditions B: A modified version of the literature procedure was used.[315] 4-Fluoroisobenzofuran-1,3-dione (1070 mg, 6.4 mmol, 1 equiv.), 3-aminopiperidine-2,6-dione hydrochloride (826 mg, 6.4 mmol, 1 equiv.), sodium acetate (1050 mg, 12.8 mmol, 2 equiv.), and acetic acid (10 mL, 0.65 M) were added to a reaction vessel, then heated to 120 °C and stirred for 4 h. The mixture was poured into ice-cold H_2O (30 mL) and filtered to give a grey powder. Reverse-phase flash chromatography (0→100% (v/v) acetonitrile in H_2O with 0.1% formic acid), followed by the removal of acetonitrile under reduced pressure, then filtration yielded 849 mg (48%) of **12** as a white solid.

Mp: 253 °C (reported: 255.5-257 °C);[515] **^{1}H NMR** (400 MHz, DMSO) δ 11.15 (s, 1H, *H8*), 7.98 – 7.92 (m, 1H, Ar-*H*), 7.80 – 7.71 (m, 2H, Ar-*H*), 5.16 (dd, *J* = 12.9, 5.4 Hz, 1H, *H10*), 2.94-2.84 (m, 1H, *H12'*), 2.64 – 2.45 (m, 2H, *H11'*, *H12''*), 2.10 – 2.03 (m, 1H, *H11''*); **^{13}C NMR** (101 MHz, DMSO) δ 172.8, 169.7, 166.1, 164.0, 158.1, 155.5, 138.1, 138.0, 133.5, 123.1, 122.9, 120.1, 120.0, 117.1, 117.0, 49.1, 30.9, 21.8; **^{19}F NMR**

(376 MHz, DMSO) δ -114.68; the physical data, and **^{1}H**, **^{13}C**, and **^{19}F NMR** spectroscopic data are consistent with those reported in the literature.[513, 514] **ESI HR-MS**: calcd. for $[C_{13}H_9FN_2O_4\text{-}H]^-$: 275.0474, found: 275.0474.

***tert*-Butyl(4-((2-(2,6-dioxopiperidin-3-yl)-1,3-dioxoisoindolin-4-yl)amino)butyl)-carbamate (13a)**[516-518]

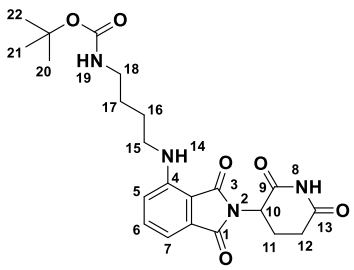

A modified version of the literature procedure was used.[516] A reaction vessel was purged with argon then charged with **12** (40 mg, 0.14 mmol, 1 equiv.), dried *N*-methyl-2-pyrrolidone (320 µL, 0.45 M), *N*-Boc-1,4-butanediamine (30.3 µL, 0.16 mmol, 1.1 equiv.), and DIPEA (75 µL, 0.43 mmol, 3 equiv.), then warmed to 90 °C and stirred overnight. The reaction mixture was diluted with ethyl acetate (2 mL), and washed with citric acid (2 mL, 10% (w/w) in H_2O), then saturated Na_2CO_3 solution (2 mL), then brine (2 mL). Flash chromatography (0→7% (v/v) methanol in dichloromethane) yielded 10 mg (16%) of **13a** as a yellow-green solid.

^{1}H NMR (400 MHz, DMSO) δ 11.09 (s, 1H), 7.57 (dd, *J* = 8.6, 7.1 Hz, 1H), 7.10 (d, *J* = 8.6 Hz, 1H), 7.02 (d, *J* = 7.0 Hz, 1H), 6.83 (t, *J* = 5.8 Hz, 1H), 6.55 (t, *J* = 6.0 Hz, 1H), 5.05 (dd, *J* = 12.8, 5.4 Hz, 1H), 3.34 – 3.26 (m, 2H), 2.97 – 2.86 (m, 3H), 2.62 – 2.52 (m, 2H), 2.06 – 1.98 (m, 1H), 1.56 – 1.50 (m, 2H), 1.48 – 1.41 (m, 2H), 1.36 (s, 9H). **^{13}C NMR** (151 MHz, DMSO) δ 173.3, 170.6, 169.4, 167.8, 156.1, 146.9, 136.7, 132.7, 117.7, 110.9, 109.5, 77.9, 55.4, 49.0, 42.0, 31.5, 28.7, 27.4, 26.6, 22.6; the **^{1}H** and **^{13}C NMR** spectroscopic data are consistent with those reported in the literature.[517-519] **ESI HR-MS**: calcd. for $[C_{22}H_{28}N_4O_6\text{-}H]^-$: 443.1936, found: 443.1937.

4-((4-Aminobutyl)amino)-2-(2,6-dioxopiperidin-3-yl)isoindoline-1,3-dione (14) [304, 520]

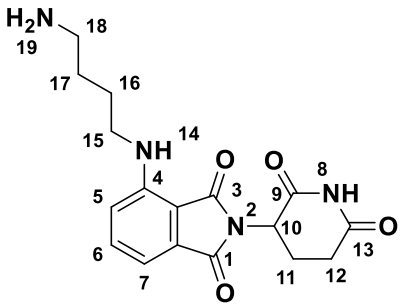

A modified version of the literature procedure was used.[304] A reaction vessel was charged with **13a** (16 mg, 0.04 mmol, 1 equiv.) and HCl (3M in methanol, 0.4 mL, 1.2 mmol, 30 equiv.), then stirred at rt for 2 hours. The reaction mixture was then warmed to 30 °C and dried under a stream of nitrogen to yield 12 mg (97%) of **14** as a yellow-green solid.

^{1}H NMR (400 MHz, DMSO). δ 11.10 (s, 1H), 8.09 (s, 3H), 7.58 (dd, *J* = 8.6, 7.0 Hz, 1H), 7.12 (d, *J* = 8.6 Hz, 1H), 7.02 (d, *J* = 7.0 Hz, 1H), 5.04 (dd, *J* = 12.7, 5.4 Hz, 1H), 3.37 – 3.29 (m, 2H), 2.95 – 2.75 (m, 3H), 2.63 – 2.52 (m, 2H), 2.06 – 1.98 (m, 1H), 1.68 – 1.58 (m, 4H); the **^{1}H NMR** spectroscopic data are consistent with those reported in the literature.[520] **^{13}C NMR** (101 MHz, DMSO) δ 173.3, 170.6, 169.4, 167.8, 146.8, 136.8, 132.7, 117.8, 111.0, 109.5, 49.0, 41.8, 38.9, 31.5, 26.2, 24.9, 22.6. **ESI HR-MS**: calcd. for $[C_{17}H_{20}N_4O_4+H]^+$: 345.1557, found: 345.1550.

6-Chloro-*N*^{2},*N*^{4}-dipropyl-1,3,5-triazine-2,4-diamine (15)[306, 521]

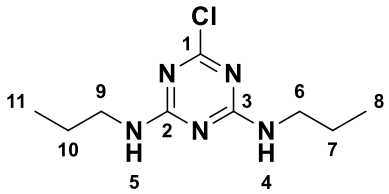

A modified version of the literature procedure was used.[306] A reaction vessel was charged with cyanuric chloride (2.50 g, 13.6 mmol, 1.0 equiv.) and a mixture of 5:1 H_2O:acetone (67 mL, 0.2 M). Propylamine (3.35 mL, 40.07 mmol, 3 equiv.) was added dropwise to the suspension at 0 °C, then the reaction was warmed to 45 °C and stirred for 2 h. The reaction mixture was filtered at rt, washed with H_2O, and the resulting solid was re-dissolved in a mixture of equal parts THF, methanol, and ethyl acetate. The removal of THF and methanol under reduced pressure and subsequent filtration yielded 2.06 g (66%) of **15** as a white solid.

^{1}H NMR (400 MHz, $CDCl_3$) δ 5.57 – 5.25 (m, 2H, *H4*, *H5*), 3.42 – 3.26 (m, 4H, *H6*, *H9*), 1.65 – 1.55 (m, 4H, *H7*, *H10*), 1.00 – 0.91 (m, 6H, *H8*, *H11*); **^{13}C NMR** (101 MHz, $CDCl_3$) δ 169.5, 165.7, 42.7, 22.6, 11.4; the **^{1}H** and **^{13}C NMR** spectroscopic data are consistent with those reported in the literature.[521] **ESI HR-MS**: calcd. for $[C_9H_{17}ClN_5+H]^+$: 230.1167, found: 230.1164.

***tert*-Butyl(4-((4,6-bis(propylamino)-1,3,5-triazin-2-yl)amino)butyl)carbamate (16)[516] and N^2-(4-Aminobutyl)-N^4,N^6-dipropyl-1,3,5-triazine-2,4,6-triamine (17)[304]**

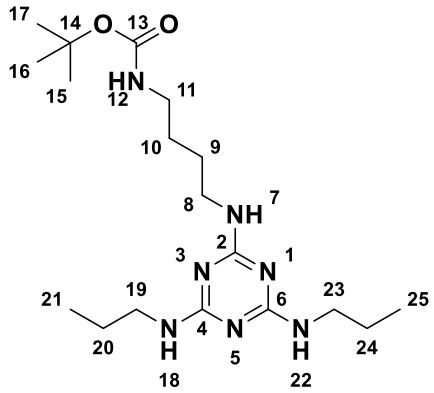

A modified version of the literature procedure was used.[304, 516] A reaction vessel was charged with *N*-Boc-1,4-butanediamine (184 µL, 0.96 mmol, 1.1 equiv.), DIPEA (454 µL, 2.61 mmol, 3 equiv.), and NMP (2 mL, 0.45 M), then degassed with argon for 5 minutes. **15** (200 mg, 0.87 mmol, 1 equiv.) was added last, and the reaction mixture was stirred at 90 °C overnight. The resultant liquid was diluted with ethyl acetate (8 mL), then washed with saturated NH_4Cl solution (8 mL). Vigorous mixing was avoided to prevent an emulsion. The aqueous layer was extracted with ethyl acetate (8 mL, 2 x 4 mL), then the combined organic layers were washed with saturated $NaHCO_3$ solution (8 mL), then brine (3 x 8 mL), then dried over Na_2SO_4. Flash chromatography (0→10% (v/v) methanol in dichloromethane) yielded 158 mg (48%) of the crude intermediate, **16**, identified by ^{1}H NMR, as a white solid.

16: **^{1}H NMR** (400 MHz, $CDCl_3$) δ 5.20 – 4.91 (m, 4H, *H7*, *H12*, *H18*, *H22*), 3.41 – 3.26 (m, 6H, *H8*, *H19*, *H23*), 3.18 – 3.11 (m, 2H, *H11*), 1.63 – 1.50 (m, 8H, *H9*, *H10*, *H20*, *H24*), 1.44 (s, 9H, *H15*, *H16*, *H17*), 0.94 (t, *J* = 7.4 Hz, 6H, *H21*, *H25*).

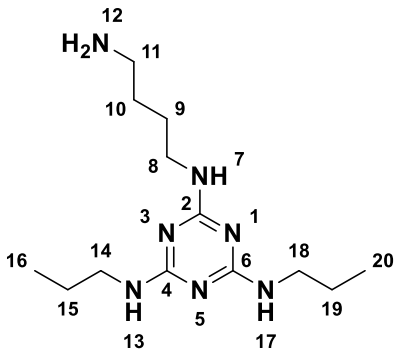

Without further purification, **16** (158 mg, 0.41 mmol, 1 equiv.) and HCl (3M in methanol, 4.1 mL, 12.3 mmol, 30 equiv.) were stirred at rt overnight. The methanol was removed from the reaction mixture under reduced pressure, then the residue was diluted with H_2O, adjusted to pH 12.0, then extracted with mixture of $CHCl_3$:IPA (3:1). Concentration under reduced pressure yielded 100 mg (88%) of **17** as a grey solid.

17: **Mp:** 104 °C; **IR** (neat): ν (cm^{-1}) 3281, 3078, 2960, 2934, 2873, 2797, 2728, 2701, 2541, 2145, 1677, 1660, 1635, 1574, 1513, 1480, 1468, 1429, 1397, 1361, 1348, 1296, 1271, 1166, 1148, 1134, 1042, 961, 886, 813, 785, 673; **^{1}H NMR** (400 MHz, $CDCl_3$) δ 7.93 – 7.79 (m, 3H, *N-H*), 6.67 (s, 1H, *N-H*), 6.14 (s, 1H, *N-H*), 3.47 – 3.25 (m, 6H, *H8*, *H14*, *H18*), 3.11 – 3.04 (m, 2H, *H11*), 1.92 – 1.80 (m, 2H, *H9*), 1.75 – 1.66 (m, 2H, *H10*), 1.64 – 1.53 (m, 4H, *H15*, *H19*), 0.93 (t, *J* = 7.2 Hz, 6H, *H16*, *H20*); **^{13}C NMR** (101 MHz, $CDCl_3$) δ 169.3 (*C2*, *C4*, *C6*), 42.6 (*C14*, *C18*), 39.9 (*C8*), 39.4 (*C11*), 25.9 (*C10*), 24.61 (*C9*), 22.5 (*C15*, *C19*), 11.4 (*C16*, *C20*). **ESI HR-MS**: calcd. for $[C_{13}H_{27}N_7+H]^+$: 282.2401, found: 282.2404.

4-((4-((4,6-Bis(propylamino)-1,3,5-triazin-2-yl)amino)butyl)amino)-2-(2,6-dioxopiperidin-3-yl)isoindoline-1,3-dione (3)[516]

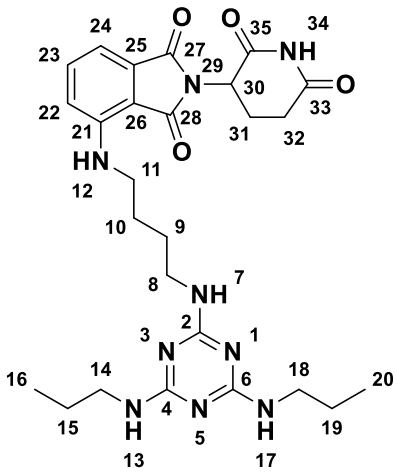

A modified version of the literature procedure was used.[516] A reaction vessel was charged with **17** (100 mg, 0.36 mmol, 1 equiv.) and NMP (0.8 mL, 0.45 M), then degassed with argon for 30 minutes. **12** (98 mg, 0.36 mmol, 1 equiv.) was added last, and the reaction mixture stirred at 90 °C for 4 hours. The reaction mixture was diluted with ethyl acetate (20 mL), then washed with saturated $NaHCO_3$ solution (20 mL). Vigorous mixing was avoided to prevent an emulsion. The aqueous layer was extracted with ethyl acetate (20 mL, 2 x 8 mL), then the combined organic layers were washed with brine (20 mL). Reverse phase flash chromatography (0→100% (v/v) acetonitrile in H_2O, 1% (v/v) ET_3N) produced a mixed fraction which was freeze-dried and re-suspended in a mixture of methanol:acetonitrile:H_2O (5:1:1) to give a pale green precipitate. The precipitate was filtered and dried under reduced to pressure to give 23 mg (12%) of **3** as a green solid.

Mp: 94 °C. **IR** (neat): ν (cm^{-1}) 3549, 3524, 3409, 3393, 3371, 3348, 3327, 3218, 3192, 3100, 2931.27, 2867.02, 1757, 1696, 1624, 1571, 1515, 1459, 1408, 1390, 1356,1252, 1203, 1181, 1113, 1053, 888, 850, 811, 776, 748, 702, 676, 658, 627. **^{1}H NMR** (400 MHz, DMSO) δ 11.08 (s, 1H, *H34*), 7.55 (dd, *J* = 8.6, 7.0 Hz, 1H, *H23*), 7.08 (d, *J* = 8.5 Hz, 1H, *H22*), 7.01 (d, *J* = 7.0 Hz, 1H, *H24*), 6.55 (m, 4H, *H7, H12, H13, H17*), 5.04 (dd, *J* = 12.9, 5.4 Hz, 1H. *H30*), 3.29 (m, 2H, *H8*), 3.22 (m, 2H, *H11*), 3.11 (m, 4H, *H14, H18*), 2.88 (m, 1H, *H32'*), 2.62 – 2.53 (m, 2H, *H31', H32"*), 2.06 – 1.98 (m, 1H, *H31'*), 1.59 – 1.41 (m, 8H, *H9, H10, H15, H19*), 0.83 (t, *J* = 7.4 Hz, 6H, *H16, H20*). **^{13}C NMR** (151 MHz, DMSO) δ 172.8, 170.1, 168.9, 167.29, 165.7, 146.4, 136.2, 132.2, 117.2,

110.3, 109.0, 41.7, 41.6, 39.4 31.0, 26.8, 26.2, 22.6, 22.1, 11.4. **ESI HR-MS**: calcd. for $[C_{26}H_{35}N_9O_4+H]^+$: 538.2885, found: 538.2885.

4,6-Dichloro-*N*-propyl-1,3,5-triazin-2-amine (18)[522]

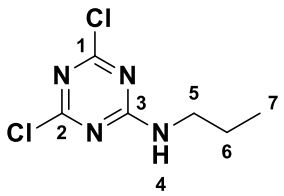

A modified version of the literature procedure was used.[522] A reaction vessel was charged with cyanuric chloride (1.16 g, 6.26 mmol, 1.5 equiv.) and THF (21 mL, 0.2 M), and cooled to 0 °C. Propylamine (342 µL, 4.17 mmol, 0.67 equiv.) was added dropwise to the suspension at 0 °C over 30 minutes, then the reaction was allowed to warm to rt while stirring for 90 minutes. The reaction mixture was filtered at washed with ice cold HCl (0.1 M in H_2O, 20 mL) and dried over Na_2SO_4. Flash chromatography (0→50% (v/v) THF in cyclohexane) yielded 790 mg (53%) of **18** as a white solid.

^{1}H NMR (400 MHz, $CDCl_3$) δ 6.52 (bs, 1H, *H4*), 3.45 (m, 2H, *H5*), 1.70 – 1.57 (m, 2H, *H6*), 0.96 (t, *J* = 7.4 Hz, 3H, *H7*); the **^{1}H NMR** spectroscopic data are consistent with those reported in the literature.[522] **^{13}C NMR** (101 MHz, $CDCl_3$) δ 171.1, 169.9, 166.0, 43.4, 22.5, 11.3. **ESI HR-MS**: calcd. for $[C_6H_8Cl_2N_4+H]^+$: 207.0199, found: 207.0192.

4-Chloro-6-(2-fluorophenyl)-*N*-propyl-1,3,5-triazin-2-amine (19)[306]

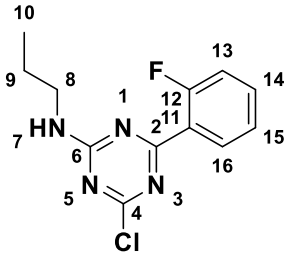

A modified version of the literature procedure was used.[306] A reaction vessel was charged with **18** (4.96 mg, 24.2 mmol, 1.3 equiv.), 2-fluorobenzeneboronic acid (2.6 g, 18.6 mmol, 1 equiv.), $Pd(dppf)Cl_2$ (1.36 g, 1.86 mmol, 0.1 equiv.), and dioxane (149 mL, 0.125 M), then the suspension was degassed with argon for 30 minutes. Caesium carbonate (1.05 g, 3.22 mmol, 4 equiv.) was added and the resulting suspension was degassed with argon for 10 minutes, then warmed to 100 °C and stirred for 1 hour. The reaction mixture was first filtered through a celite pad, then dioxane was removed

under reduced pressure. The solid was resuspended in ethyl acetate (50 mL), then washed with brine (3 x 20 mL), then the combined organic layers were dried with Na_2SO_4. Flash chromatography (0→45% (v/v) ethyl acetate in cyclohexane, then 0→10% (v/v) methanol in dichloromethane), followed by reverse-phase flash chromatography (0→80% (v/v) acetonitrile in H_2O, 0.1% (v/v) formic acid), yielded 660 mg (10%) **19** as a white solid.

Mp: 124 °C; **IR** (neat): ν (cm^{-1}) 3336, 3261, 3164, 3109, 2958, 2927, 2872, 2855, 1735, 1619, 1587, 1556, 1514, 1491, 1465, 1433, 1420, 1378, 1310, 1270, 1254, 1228, 1193, 1170, 1138, 1109, 1080, 1037, 990, 960, 893, 860, 816, 799, 770, 750, 643; **^{1}H NMR** (400 MHz, $CDCl_3$) δ 8.17 – 8.04 (m, 1H, *H16*), 7.54 – 7.45 (m, 1H, *H14*), 7.26 – 7.21 (m, 1H, *H15*), 7.19 – 7.13 (m, H, *H13*), 6.10 – 5.92 (m, 1H, *H7*), 3.54 – 3.44 (m, 2H, *H8*), 1.66 (h, *J* = 7.4 Hz, 2H, *H9*), 0.98 (q, *J* = 7.5 Hz, 3H, *H10*); **^{13}C NMR** (101 MHz, $CDCl_3$) δ 171.2 , 170.6, 166.2, 163.4, 163.0, 160.8, 133.7, 132.0, 124.2, 117.2, 43.2, 22.6, 11.4; **ESI HR-MS**: calcd. for $[C_{12}H_{12}ClFN_4+H]^+$: 267.0807, found: 267.0802.

***tert*-Butyl(4-((4-(2-fluorophenyl)-6-(propylamino)-1,3,5-triazin-2-yl)amino)butyl) carbamate (20)**[516] and ***N*²-(4-aminobutyl)-6-(2-fluorophenyl)-*N*⁴-propyl-1,3,5-triazine-2,4-diamine (21)**[304]

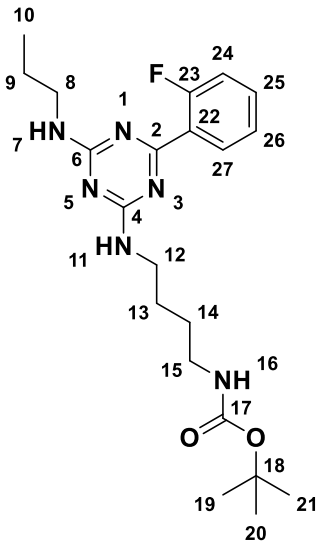

A modified version of the literature procedure was used.[304, 516] A reaction vessel was charged with *N*-Boc-1,4-butanediamine (159 µL, 0.83 mmol, 1.1 equiv.), DIPEA (392 µL, 2.25 mmol, 3 equiv.), and NMP (.167 mL, 0.45 M), then degassed with argon for 5 minutes. **19** (200 mg, 0.75 mmol, 1 equiv.) was added last, and the reaction mixture was stirred at 90 °C overnight. The resultant liquid was diluted with ethyl acetate (8 mL), then washed with saturated NH_4Cl solution (8 mL). Vigorous mixing was avoided to prevent an emulsion. The aqueous layer was extracted with ethyl acetate (8 mL, 2 x 4 mL), then the combined organic layers were washed with saturated $NaHCO_3$ solution (3 x 8 mL), then brine (3 x 8 mL), then dried over Na_2SO_4. Flash chromatography (0→100% (v/v) dichloromethane in cyclohexane, then 0 → 5% (v/v) methanol in dichloromethane) yielded 242 mg (58%) of the crude intermediate, **20**, as a white solid.

20: **^{1}H NMR** (400 MHz, $CDCl_3$) δ 8.05 – 7.81 (m, 1H, *H27*), 7.44 – 7.37 (m, 1H, *H25*), 7.19 (td, *J* = 7.5, 1.1 Hz, 1H, *H26*), 7.12 (ddd, *J* = 11.1, 8.3, 1.1 Hz, 1H, *H24*), 5.64 – 5.50 (m, 2H, *H7, H11*), 4.57 (s, 1H, *H16*), 3.52 – 3.30 (m, 4H, *H12, H15*), 3.20 – 3.11 (m, 2H, *H15*), 1.67 – 1.51 (m, 6H, *H9, H13, H14*), 1.43 (s, 9H, *H19, H20, H21*), 0.97 (t, *J* = 7.4 Hz, 3H, *H10*).

Without further purification, a reaction vessel was charged with **20** (242 mg, 0.58 mmol, 1 equiv.) and HCl (3M in methanol, 5.8 mL, 17.4 mmol, 30 equiv.), then stirred at rt

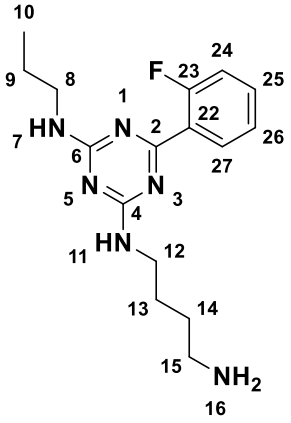

overnight. The methanol was removed from the reaction mixture under a stream of nitrogen, then the residue was diluted with H_2O, adjusted to pH 12.0, then extracted with chloroform (75 mL). Reverse-phase flash chromatography (0→100% (v/v) acetonitrile in H_2O, 1% (v/v) TEA) yielded 76 mg (41%) of **21** as a grey solid.

21: **Mp**: 85 °C; **IR** (neat): ν^{-1} 3255, 3098, 2961, 2928, 2855, 2802, 1733, 1615, 1587, 1546, 1457, 1423, 1378, 1350, 1315, 1297, 1262, 1226, 1177, 1156, 1107, 1038, 983, 948, 863, 822, 810, 768, 756, 722, 706, 670, 638; **^{1}H NMR** (600 MHz, MeOD) δ 7.91 – 7.76 (m, 1H, *H27*), 7.51 – 7.46 (m, 1H, *H25*), 7.24 (t, *J* = 7.4 Hz, 1H, *H26*), 7.17 (dd, *J* = 11.1, 8.3 Hz, 1H, *H24*), 3.45 (t, *J* = 6.8 Hz, 2H, *H12*), 3.38 (t, *J* = 7.0 Hz, 2H, *H8*), 2.69 (t, *J* = 7.2 Hz, 2H, *H15*), 1.70 – 1.59 (m, 4H, *H9, H13*), 1.55 (m, 2H, *H14*), 0.97 (m, 3H, *H10*). **^{13}C NMR** (151 MHz, MeOD) δ 171.0, 170.6, 167.4, 166.9, 163.3, 162.9, 161.3, 133.1, 132.4, 132.2, 127.5, 125.1, 117.4, 117.3, 43.4, 42.3, 42.2, 41.3, 31.1, 30.8, 28.1, 27.9, 24.0, 23.7, 11.8, 11.7. **ESI HR-MS**: calcd. for $[C_{16}H_{23}FN_6+H]^+$: 319.2041, found: 319.2054.

2-(2,6-Dioxopiperidin-3-yl)-4-((4-((4-(2-fluorophenyl)-6-(propylamino)-1,3,5-triazin-2-yl)amino)butyl)amino)isoindoline-1,3-dione (4)[516]

A modified version of the literature procedure was used.[516] A reaction vessel was charged with **21** (69 mg, 0.22 mmol, 1 equiv.), **12** (60 mg, 0.22 mmol, 1 equiv.), and NMP (482 µL, 0.45 M), then degassed with nitrogen for 30 minutes The reaction mixture was stirred at 90 °C for 4 hours, then dried under a stream of nitrogen. The residue was diluted

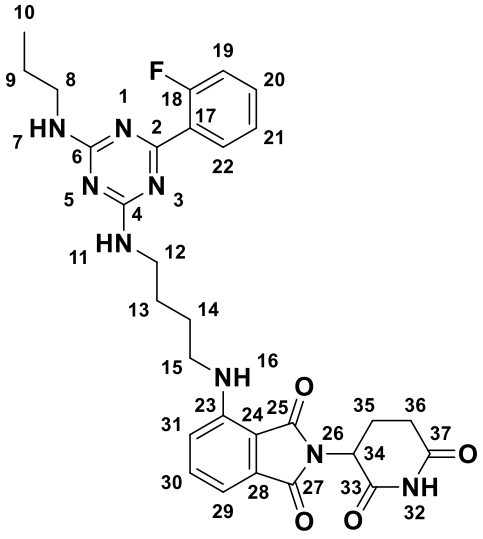

with toluene (20 mL), then washed with saturated NH_4Cl solution (20 mL), then brine (20 mL), then dried with Na_2SO_4. Contact and mixing with aqueous phases was kept as short as possible to avoid hydrolysis of the thalidomide moiety. Flash chromatography (0→5% (v/v) methanol in dichloromethane) produced 15 mg (21%) of **4** as a green solid.

Mp: 205 °C; **IR** (neat): ν^{-1} 3261, 3164, 3109, 2958, 2927, 2872, 2855, 1587, 1556, 1514, 1491, 1465, 1433, 1420, 1378, 1310, 1270, 1254, 1228, 1193, 1170, 1138, 1109, 1080, 1037, 990, 960, 893, 860, 816, 799, 770, 750, 644; **^{1}H NMR** (600 MHz, DMSO) δ 11.07 (s, 1H), 7.89 – 7.76 (m, 1H), 7.58 – 7.52 (m, 1H), 7.50 – 7.29 (m, 3H), 7.26 – 7.21 (m, 2H), 7.10 – 7.05 (m, 1H), 7.01 (d, *J* = 6.7 Hz, 1H), 6.59 – 6.52 (m, 1H), 5.04 (dd, *J* = 12.8, 5.4 Hz, 1H), 3.36 – 3.32 (m, 4H), 3.26 – 3.18 (m, 2H), 2.53 – 2.51 (m, 1H), 2.05 – 1.97 (m, 1H), 1.65 – 1.60 (m, 4H), 1.54 – 1.47 (m, 3H), 0.89 – 0.82 (m, 3H). **ESI HR-MS**: calcd. for $[C_{29}H_{31}FN_8O_4+H]^+$: 575.2525, found: 575.2526.

6.1.5. The Synthesis of Ebsulfur Compounds

The following procedures were reported in Thun-Hohenstein, Suits et al.[469]

General Procedure A – Formation of acyl chlorides (46–49, 51–53)

Oxalyl chloride (1.1 equiv.) was added slowly to a solution (or suspension) of the requisite aryl carboxylic acid (1 equiv.) in anhydrous CH_2Cl_2 (0.3 M) at 0 °C, followed by addition of 1 drop of anhydrous DMF. The mixture was stirred for 1 h at 0 °C. The cooling bath was then removed and the mixture was stirred for a further 2 h at rt

(consumption of the starting aryl carboxylic acid was monitored by TLC and LCMS). The solution was carried forward to the next step without purification.

General Procedure B – Amide coupling (45–60)

Triethylamine (2 equiv.) was either added to the requisite acyl chloride (1 equiv.) in CH_2Cl_2 (0.3 M) (20, 25, 29-35)REF check NUMBERING, or acyl chloride solution using General Procedure A (21-24, 26-28), followed by addition of the requisite primary amine (1.1 equiv). The mixture was stirred at rt overnight (consumption of the starting acyl chloride was monitored by TLC and/or LCMS). The reaction was then diluted with ethyl acetate; the resultant solution was washed with 1 M HCl, then brine. The organic phase was dried over Na_2SO_4, then concentrated *in vacuo*. Purification was achieved using flash chromatography to yield the desired compound.

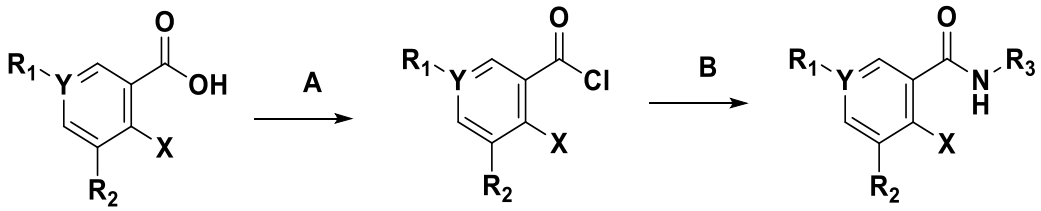

Figure 6.1 *| Synthesis of the secondary amide intermediates (). Conditions:* ***A.*** *$(COCl)_2$, DMF, CH_2Cl_2, 0 °C;* ***B.*** *R_3–NH_2, Et_3N, CH_2Cl_2, rt.*

2-Iodo-*N*-phenylbenzamide (45)[523]

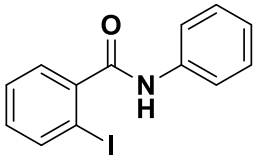

Application of General Procedure B using 2-iodobenzoyl chloride (267 mg, 1 mmol, 1 equiv.) and aniline (100 µL, 1.1 mmol, 1.1 equiv.) yielded 250 mg (74%) of **45** as a white solid.

^{1}H NMR (400 MHz, $CDCl_3$) δ 7.91 (dd, *J* = 8.0, 1.0 Hz, 1H), 7.67 – 7.60 (m, 2H), 7.53 (dd, *J* = 7.5, 1.5 Hz, 1H), 7.46-7.36 (m, 4H), 7.23 – 7.11 ppm (m, 2H); **^{13}C NMR** (101 MHz, $CDCl_3$) δ 167.2, 142.2, 140.1, 137.5, 131.5, 129.2, 128.6, 128.4, 154.0, 120.1, 92.4 ppm; the spectroscopic data are consistent with those reported in the literature.[523]

ESI HR-MS: calcd. for $[C_{13}H_{10}INO+Na]^+$: 345.9699, found: 345.9699. **IR** (neat): ν (cm^{-1}) 3058, 2921, 1655, 1619, 1540, 1440, 1325.

2-Iodo-3-methyl-*N*-phenylbenzamide (46)[524]

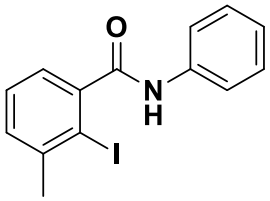

Application of General Procedure A using 2-iodo-3-methyl benzoic acid (262 mg, 1 mmol, 1 equiv.), gave the crude acyl chloride, which was used in the next step without purification.

Application of General Procedure B using triethylamine (167 µL, 1.2 mmol, 1.2 equiv.) and aniline (104 µL, 1.1 mmol, 1.1 equiv.) yielded 193 mg (57%) of **46** as a beige solid.

Mp 149-150 °C; **IR** (neat): ν (cm^{-1}) 3196, 3076, 3017, 2919, 2850, 1647, 1596, 1490, 1335, 1013; **^{1}H NMR** (400 MHz, $CDCl_3$) δ 7.65 – 7.61 (m, 2H), 7.43 – 7.35 (m, 3H), 7.33 – 7.28 (m, 2H), 7.27 – 7.22 (m, 1H), 7.21 – 7.14 (m, 1H), 2.51 ppm (s, 3H); **^{13}C NMR** (101 MHz, $CDCl_3$) δ 168.4, 144.0, 143.2, 137.8, 131.0, 129.3, 128.4, 125.4, 125.0, 120.2, 99.4, 29.3 ppm; **ESI HR-MS**: calcd. for $[C_{14}H_{12}INO+H]^+$: 338.0036, found: 338.0038. The spectroscopic data are consistent with those reported in the literature.[524]

2,3-Dibromo-*N*-phenylbenzamide (47)

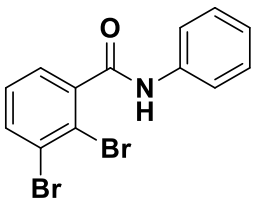

Application of General Procedure A using 2,3-dibromobenzoic acid (280 mg, 1 mmol, 1 equiv.), gave the crude acyl chloride solution, which was used in the next step without purification.

Application of General Procedure B using triethylamine (167 µL, 1.2 mmol, 1.2 equiv.) and aniline (104 µL, 1.1 mmol, 1.1 equiv.) yielded 180 mg (51%) of **47** as a beige solid.

Mp 152-153 °C; **IR** (neat): ν (cm^{-1}) 3201, 3138, 3065, 2962, 2850, 1605, 1578, 1439, 1334; **^{1}H NMR** (400 MHz, $CDCl_3$) δ 7.72 (dd, *J* = 8.0, 1.6 Hz, 1H), 7.64 – 7.58 (m, 2H), 7.55 (s, 1H), 7.47 (dd, *J* = 7.6, 1.6 Hz, 1H), 7.42 – 7.35 (m, 2H), 7.29 – 7.23 (m, 1H),

7.22 – 7.15 ppm (m, 1H); **^{13}C NMR** (101 MHz, $CDCl_3$) δ 165.46, 140.94, 137.45, 135.29, 129.35, 128.92, 127.74, 126.90, 125.26, 122.08, 120.26 ppm; **ESI HR-MS**: calcd. for $[C_{13}H_9Br_2NO+H]^+$: 355.9103, found: 355.9105.

2,5-Dibromo-*N*-phenylbenzamide (48)[525]

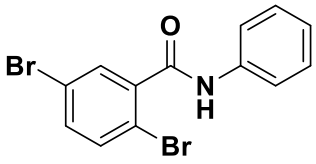

Application of General Procedure A using 2,5-dibromobenzoic acid (625 mg, 2.23 mmol, 1 equiv.), gave the crude acyl chloride solution, which was used in the next step without purification.

General Procedure B was followed with triethylamine (370 µL, 2.68 mmol, 1.2 equiv.) and aniline (232 µL, 2.46 mmol, 1.1 equiv.). Purification by reverse-phase chromatography using a Biotage Sfär® C18 Duo (30 g) cartridge with a solvent system of buffer A (H_2O:formic acid, 100:0.1 (v/v)) to buffer B (MeCN:formic acid, 100:0.1 (v/v)) from 0 to 100% (v/v) B over 29 column volumes, then 7 column volumes at 100% (v/v) B. Concentration in vacuo yielded 553 mg (70%) of **48** as a beige solid.

Mp 149-150 °C; **IR** (neat): ν (cm^{-1}) 3088, 2960, 2921, 1655, 1548, 1444, 1327, 1029; **^{1}H NMR** (400 MHz, $CDCl_3$) δ 7.77 (d, *J* = 2.3 Hz, 1H), 7.69 (s, 1H), 7.64 – 7.60 (m, 2H), 7.49 (d, *J* = 8.5 Hz, 1H), 7.43 (dd, *J* = 8.5, 2.4 Hz, 1H), 7.39 (t, *J* = 7.9 Hz, 2H), 7.22 – 7.16 ppm (m, 1H); **^{13}C NMR** (101 MHz, $CDCl_3$) δ 164.1, 139.5, 137.3, 135.1, 134.8, 132.8, 129.4, 125.3, 121.9, 120.3, 118.1 ppm; **ESI HR-MS**: calcd. for $[C_{13}H_9Br_2NO+H]^+$: 353.9123, found 353.9125. The spectroscopic data are consistent with those reported in the literature.[525]

4-Chloro-*N*-phenylpyridine-3-carboxamide (49)

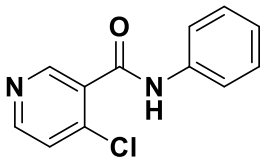

Application of General Procedure A using 4-chloro-nicotinic acid (201 mg, 1 mmol, 1 equiv.), gave the crude acyl chloride solution, which was used in the next step without purification.

Application of General Procedure B using triethylamine (167 µL, 1.2 mmol, 1.2 equiv) and aniline (104 µL, 1.1 mmol, 1.1 equiv.) yielded 80 mg (34%) of **49** as an orange wax.

IR (neat): ν (cm^{-1}) 3017, 2981, 2900, 1635, 1558, 1419, 1305, 1083; **^{1}H NMR** (400 MHz, $CDCl_3$) δ 8.90 (s, 1H), 8.56 (d, *J* = 5.4 Hz, 1H), 8.09 (s, 1H), 7.64 (dd, 2H), 7.42 – 7.36 (m, 3H), 7.20 ppm (m, 1H) **^{13}C NMR** (101 MHz, $CDCl_3$) δ 162.3, 152.0, 151.0, 141.1, 137.3, 131.3, 129.4, 125.5, 125.2, 120.4 ppm; **ESI HR-MS**: calcd. for $[C_{12}H_9ClN_2O+H]^+$: 233.0476, found: 233.0477.

2-Iodo-*N*-(3-methylbutyl)benzamide (50)[526]

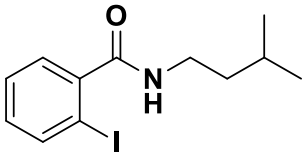

Application of General Procedure B using triethylamine (91 µL, 0.65 mmol, 0.65 equiv), 2-iodobenzoyl chloride (266 mg, 1 mmol, 1 equiv.) and 3-methylbutylamine (126 µL, 1.1 mmol, 1.1 equiv.) yielded 206 mg (65%) of **50** as a beige solid.

Mp 74-75 °C; **IR** (neat): ν (cm^{-1}) 3031, 2920, 2850, 1647, 1586, 1300, 1016; **^{1}H NMR** (400 MHz, $CDCl_3$) δ 7.91 – 7.79 (m, 1H), 7.42 – 7.31 (m, 2H), 7.08 (m, 1H), 5.75 (s, 1H), 3.46 (ddd, *J* = 8.5, 7.4, 5.8 Hz, 2H), 1.73 (m, 1H), 1.57 – 1.47 (m, 1H), 0.95 ppm (d, *J* = 6.6 Hz, 6H); **^{13}C NMR** (101 MHz, $CDCl_3$) δ 169.45, 142.68, 139.93, 131.12, 128.39, 128.29, 92.55, 38.56, 38.34, 26.04, 22.58 ppm; **ESI HR-MS**: calcd. for $[C_{12}H_{16}INO+H]^+$: 318.0349, found: 318.0350. The spectroscopic data are consistent with those reported in the literature.[526]

2-Iodo-3-methyl-*N*-(3-methylbutyl)benzamide (51)

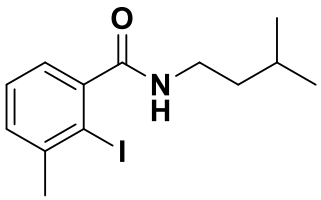

Application of General Procedure A using 2-iodo-3-methylbenzoic acid (262 mg, 1 mmol, 1 equiv.), gave the crude acyl chloride solution, which was used in the next step without purification.

Application of General Procedure B using triethylamine (167 µL, 1.2 mmol, 1.2 equiv.) and 3-methylbutylamine (126 µL, 1.1 mmol, 1.1 equiv.) yielded 230 mg (69%) of **51** as a white solid.

Mp 103-104 °C; **IR** (neat): ν (cm^{-1}) 3267, 3085, 2951, 1633, 1555, 1442, 1338, 1012; **^{1}H NMR** (400 MHz, $CDCl_3$) δ 7.29 – 7.19 (m, 2H), 7.14 – 7.05 (m, 1H), 5.65 (s, 1H), 3.52 – 3.42 (m, 2H), 2.48 (d, *J* = 0.7 Hz, 3H), 1.79 – 1.65 (m, 1H), 1.57 – 1.47 (m, 1H), 0.96 ppm (d, *J* = 6.6 Hz, 6H); **^{13}C NMR** (101 MHz, $CDCl_3$) δ 170.5, 144.4, 143.0, 130.5, 128.2, 125.1, 99.5, 38.5, 38.3, 29.3, 26.1, 22.6 ppm; **ESI HR-MS**: calcd. for $[C_{13}H_{18}INO+H]^+$: 332.0505, found 332.0504.

2,3-Dibromo-*N*-(3-methylbutyl)benzamide (52)[526]

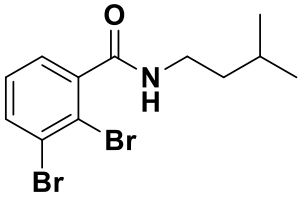

Application of General Procedure A using 2,3-dibromobenzoic acid (280 mg, 1 mmol, 1 equiv.), gave the crude acyl chloride solution, which was used in the next step without purification.

Application of General Procedure B was followed using triethylamine (167 µL, 1.2 mmol, 1.2 equiv) and 3-methylbutylamine (126 µL, 1.1 mmol, 1.1 equiv.) yielded 149 mg (43%) of **52** as a white solid.

Mp 104-106 °C; **IR** (neat): ν (cm^{-1}) 3262, 3052, 2954, 2868, 1640, 1444, 1309, 1230, 1055; **^{1}H NMR** (400 MHz, $CDCl_3$) δ 7.67 (dd, *J* = 8.0, 1.6 Hz, 1H), 7.35 (dd, *J* = 7.6,

1.6 Hz, 1H), 7.23 – 7.18 (m, 1H), 5.78 (s, 1H), 3.52 – 3.42 (m, 2H), 1.70 (m, 1H), 1.57 – 1.47 (m, 2H), 0.96 ppm (d, *J* = 6.6 Hz, 6H); **^{13}C NMR** (101 MHz, $CDCl_3$) δ 167.6, 141.2, 134.8, 128.7, 127.6, 126.7, 122.0, 38.7, 38.3, 26.1, 22.6 ppm; **ESI HR-MS**: calcd. for $[C_{12}H_{15}Br_2NO+H]^+$: 347.9593, found 347.9595. The spectroscopic data are consistent with those reported in the literature.[526]

2,5-Dibromo-*N*-(3-methylbutyl)benzamide (53)

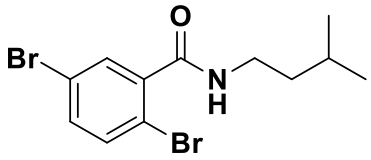

Application of General Procedure A using 2,5-dibromobenzoic acid (280 mg, 1 mmol, 1 equiv.), gave the crude acyl chloride solution, which was used in the next step without purification.

Application of General Procedure B using triethylamine (167 µL, 1.2 mmol, 1.2 equiv.) and 3-methylbutylamine (126 µL, 1.1 mmol, 1.1 equiv.) yielded 166 mg (48%) of **53** as a beige solid.

Mp 117-118 °C; **IR** (neat): ν (cm^{-1}) 3264, 3077, 2957, 2851, 1649, 1548, 1369, 1155, 1085; **^{1}H NMR** (400 MHz, $CDCl_3$) δ 7.64 (d, *J* = 2.4 Hz, 1H), 7.43 (d, *J* = 8.5 Hz, 1H), 7.37 (dd, *J* = 8.5, 2.4 Hz, 1H), 5.94 (s, 1H), 3.51 – 3.42 (m, 2H), 1.70 (m, 1H), 1.56 – 1.46 (m, 2H), 0.96 ppm (d, *J* = 6.6 Hz, 6H); **^{13}C NMR** (101 MHz, $CDCl_3$) δ 166.1, 139.8, 134.9, 134.3, 132.6, 121.7, 118.0, 38.7, 38.3, 26.1, 22.6 ppm; **ESI HR-MS**: calcd. for $[C_{12}H_{15}Br_2NO+H]^+$: 347.9593, found 347.9596.

***N*-Benzyl-2-bromobenzamide (54)**[527]

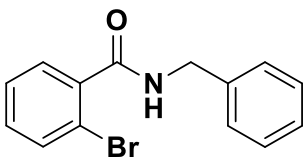

Application of General Procedure B with 2-bromobenzoyl chloride (219 mg, 1 mmol, 1 equiv.), triethylamine (167 µL, 1.2 mmol, 1.2 equiv.), and benzylamine (120 µl, 1.1 mmol, 1.1 equiv.) yielded 184 mg (63%) of **54** as a beige solid.

Mp 115-116 °C; **IR** (neat): ν (cm^{-1}) 3065, 2923, 1639, 1539, 1360. **^{1}H NMR** (400 MHz, $CDCl_3$) δ 7.49 (m, 2H), 7.41 – 7.09 (m, 8H), 6.20 (s, 1H), 4.58 ppm (d, *J* = 5.5 Hz, 2H); **^{13}C NMR** (101 MHz, $CDCl_3$) δ 167.6, 137.8, 137.6, 133.5, 131.5, 129.8, 128.9, 128.2, 127.84 127.7, 119.4, 44.4 ppm; **ESI HR-MS**: calcd. for $[C_{14}H_{12}BrNO+H]^+$: 290.0715, found 290.0717. The spectroscopic data are consistent with those reported in the literature.[527]

***N*-(Cyclohexylmethyl)-2-bromobenzamide (55)**

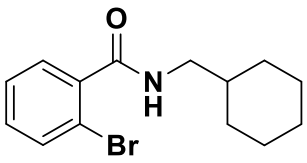

Application of General Procedure B with 2-bromobenzoyl chloride (219 mg, 1 mmol, 1 equiv.), triethylamine (167 µL, 1.2 mmol, 1.2 equiv.), and cyclohexylmethylamine (143 µL, 1.1 mmol, 1.1 equiv.) yielded 180 mg (61%) of **55** as a yellow oil.

IR (neat): ν (cm^{-1}) 3068, 2921, 2850, 1641, 1541, 1367; **^{1}H NMR** (400 MHz, $CDCl_3$) δ 7.62 – 7.49 (m, 2H), 7.34 (td, *J* = 7.5, 1.0 Hz, 1H), 7.30 – 7.21 (m, 2H), 6.03 (s, 1H), 3.30 (dd, *J* = 6.5, 6.0 Hz, 2H), 2.01 – 1.52 (m, 6H), 1.42 – 1.11 (m, 4H), 1.02 ppm (m, 3H); **^{13}C NMR** (101 MHz, $CDCl_3$) δ 167.7, 138.3, 133.5, 131.3, 129.8, 127.7, 119.3, 46.5, 38.0, 31.1, 26.5, 26.0 ppm; **ESI HR-MS**: calcd. for $[C_{14}H_{18}BrNO+H]^+$: 296.0645, found 296.0646.

2-Iodo-*N*-pentylbenzamide (56)[528]

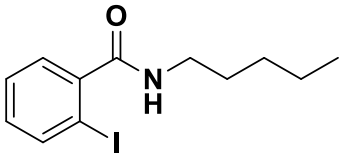

Application of General Procedure B with 2-iodobenzoyl chloride (267 mg, 1 mmol, 1 equiv.), triethylamine (167 µL, 1.2 mmol, 1.2 equiv.), and pentylamine (128 µL, 1.1 mmol, 1.1 equiv.) yielded 203 mg (64%) of **56** as a white solid.

Mp 98-100 °C; **IR** (neat): ν (cm^{-1}) 3066, 2926, 1634, 1546; **^{1}H NMR** (400 MHz, $CDCl_3$) δ 7.88 – 7.81 (m, 1H), 7.43 – 7.32 (m, 2H), 7.08 (ddd, *J* = 8.0, 6.5, 3.0 Hz, 1H), 5.78 (s,

1H), 3.44 (td, *J* = 7.0, 6.0 Hz, 2H), 1.70 – 1.56 (m, 2H), 1.46 – 1.30 (m, 5H), 1.30 – 1.17 (m, 3H), 0.99 – 0.82 (m, 4H) ppm; **^{13}C NMR** (101 MHz, $CDCl_3$) δ 169.3, 142.6, 139.8, 131.0, 128.3, 128.2, 92.4, 40.1, 29.2, 29.1, 22.4, 14.0 ppm; **ESI HR-MS**: calcd. for $[C_{12}H_{16}INO+H]^+$: 318.0349, found 318.0349. The spectroscopic data are consistent with those reported in the literature.[528]

2-Iodo-*N*-(pyridin-2-yl)benzamide (57)[529]

A modified General Procedure B was followed using triethylamine (502 µL, 3.6 mmol, 1.2 equiv.), 2-iodobenzoyl chloride (800 mg, 3 mmol, 1 equiv.) and 2-aminopyridine (310 mg, 3.3 mmol, 1.1 equiv.). The reaction mixture was stirred at rt for 5 min, then diluted in ethyl acetate and washed with HCl (1 M). The aqueous layer was neutralised using NaOH (12 M), extracted with ethyl acetate, and dried over Na_2SO_4. Purification yielded 130 mg (13%) of **57** as a white solid.

Mp 176-177 °C; **IR** (neat): ν (cm^{-1}) 3077, 2956, 1680, 1533, 1434, 1309; **^{1}H NMR** (400 MHz, $CDCl_3$) δ 9.46 (s, 1H), 8.40 (d, *J* = 8.4 Hz, 1H), 7.90 (dd, *J* = 8.0, 1.1 Hz, 1H), 7.85 (dd, *J* = 5.2, 1.9 Hz, 1H), 7.76 (ddd, *J* = 8.8, 7.4, 1.9 Hz, 1H), 7.52 (dd, *J* = 7.6, 1.7 Hz, 1H), 7.41 (td, *J* = 7.5, 1.1 Hz, 1H), 7.15 (td, *J* = 7.7, 1.7 Hz, 1H), 6.99 ppm (ddd, *J* = 7.4, 5.0, 1.0 Hz, 1H); **^{13}C NMR** (101 MHz, $CDCl_3$) δ 167.9, 151.4, 147.3, 141.8, 140.3, 139.1, 131.8, 128.5, 128.5, 120.2, 114.8, 92.7 ppm; **ESI HR-MS**: calcd. for $[C_{12}H_9IN_2O+H]^+$: 324.9843, found 324.9831. The spectroscopic data are consistent with those reported in the literature.[529]

2-Iodo-*N*-([(3*S*)-5-oxopyrrolidin-3-yl]methyl)benzamide (58)

General Procedure B was followed using triethylamine (73.3 µL, 0.53 mmol, 1.3 equiv), 2-iodobenzoyl chloride (106 mg, 0.4 mmol, 1 equiv.) and (4*R*)-4-(aminomethyl)pyrrolidin-2-one

(50 mg, 0.44 mmol, 1.1 equiv). The mixture was stirred for 36 h. The reaction mixture was concentrated in vacuo, then purified with flash chromatography. A solvent system of (0→20% (v/v) methanol in dichloromethane) over 15 column volumes was run to yield 45 mg (33%) of **58** as a beige solid.

Mp 175-176 °C; [α]D25 = -8.1 (c = 0.5, DMSO-d6); **IR** (neat): ν (cm^{-1}) 3284, 3095, 2998, 2964, 1697, 1640, 1560, 1368, 1046; **^{1}H NMR** (400 MHz, DMSO-d6) δ 8.51 (t, *J* = 5.9 Hz, 1H), 7.87 (dd, *J* = 7.9, 1.1 Hz, 1H), 7.52 (s, 1H), 7.44 (td, *J* = 7.5, 1.1 Hz, 1H), 7.31 (dd, *J* = 7.6, 1.7 Hz, 1H), 7.16 (td, *J* = 7.6, 1.7 Hz, 1H), 3.42 – 3.29 (m, 2H), 3.29 – 3.20 (m, 2H), 3.10 – 3.03 (m, 1H), 2.63 (ddd, *J* = 12.1, 9.5, 6.0 Hz, 1H), 2.29 (dd, *J* = 16.7, 8.9 Hz, 1H), 2.00 ppm (dd, *J* = 16.7, 6.4 Hz, 1H); **^{13}C NMR** (101 MHz, DMSO-d6) δ 176.1, 169.2, 143.3, 139.0, 130.7, 128.0, 127.9, 93.4, 45.0, 42.3, 34.4, 33.9 ppm; **ESI HR-MS**: calcd. for $[C_{12}H_{13}IN_2O_2+H]^+$: 345.0094, found 345.0095.

2-Iodo-*N*-(2-methoxyethyl)benzamide (59)

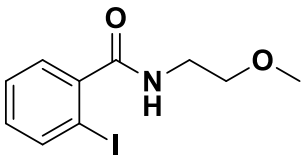

Application of General Procedure B with 2-iodobenzoyl chloride (267 mg, 1 mmol, 1 equiv.), triethylamine (167 µL, 1.2 mmol, 1.2 equiv.), and 2-methoxyethan-1-amine (96 µL, 1.1 mmol, 1.1 equiv.) yielded 105 mg (34%) of **59** as a white wax.

IR (neat): ν (cm^{-1}) 3058, 2924, 1647, 1537, 1360, 1120, 1014. 1H NMR (400 MHz, $CDCl_3$) δ 7.92 – 7.83 (m, 1H), 7.45 – 7.33 (m, 2H), 7.09 (m, 1H), 6.16 (s, 1H), 3.70 – 3.62 (m, 2H), 3.59 (m, 2H), 3.39 ppm (s, 3H); **^{13}C NMR** (101 MHz, $CDCl_3$) δ 169.5, 142.4, 140.0, 131.2, 128.4, 128.3, 92.6, 71.1, 59.0, 39.8 ppm; **ESI HR-MS**: calcd. for $[C_{10}H_{12}INO_2+Na]^+$: 327.9805, found 327.9804.

Methyl 3-[(2-iodophenyl)formamido]propanoate (60)[530]

Application of General Procedure B using triethylamine (169 µL, 1.2 mmol, 1.2 equiv), 2-iodobenzoyl chloride (267 mg, 1 mmol, 1 equiv.), and methyl 3-aminopropanoate (153 mg, 1.1 mmol, 1.1 equiv.) yielded 197 mg (59%) of **60** as a white solid.

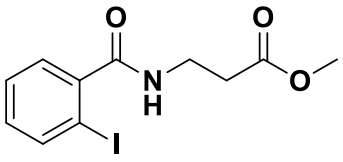

Mp 89-91 °C; **IR** (neat): ν (cm^{-1}) 3031, 2949, 2919, 1731, 1635, 1537, 1330, 1206, 1053; **^{1}H NMR** (400 MHz, $CDCl_3$) δ 7.84 (d, *J* = 8.0 Hz, 1H), 7.36 (m, 2H), 7.14 – 7.03 (m, 1H), 6.38 (s, 1H), 3.77 – 3.68 (m, 6H), 2.70 ppm (t, *J* = 5.9 Hz, 2H); **^{13}C NMR** (101 MHz, $CDCl_3$) δ 173.2, 169.5, 142.2, 140.0, 131.3, 128.3, 128.3, 92.5, 52.1, 35.5, 33.7 ppm; **ESI HR-MS**: calcd. for $[C_{11}H_{12}INO_3+H]^+$: 333.9935, found 333.9935. The spectroscopic data are consistent with those reported in the literature.[530]

General procedure C – Sulfur insertion and ring closure reaction to give 28–40, 38–36.

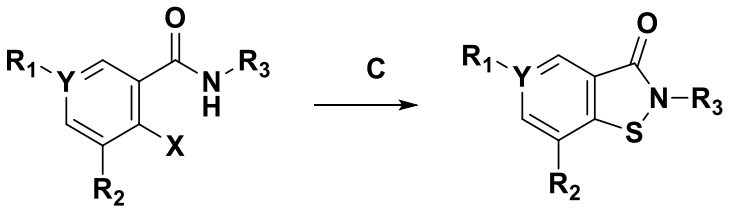

***Figure 6.2** | Sulfur insertion and ring closure (**28**–**40**, **38**–**36**). Conditions: **C.** 1,10-phenanthroline/CuI, S_8, K_2CO_3, DMF, 110 °C.*

Following a modified literature procedure, a reaction vial was charged with CuI (0.3 equiv.) and 1,10-phenanthroline (0.3 equiv).[531] The atmosphere was purged with argon and anhydrous DMF (0.4 M) was added. The suspension was stirred at rt for 15 min, then the appropriate benzamide (1 equiv), S_8 (1.3 equiv), and K_2CO_3 (1.3 equiv) were added. The suspension was stirred for a further 15 minutes at rt, then heated to 110 °C until TLC showed full conversion of the starting material (TLC, MS). The reaction

was cooled to rt and diluted in brine. The resulting mixture was extracted with ethyl acetate. The combined organic phases were dried over Na_2SO_4, then concentrated *in vacuo*. Purification by flash chromatography yielded the desired compound.

2-Benzyl-2,3-dihydro-1,2-benzothiazol-3-one (29)[531]

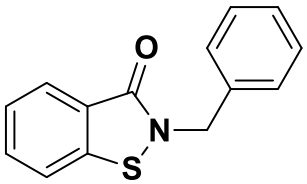

Application of General Procedure C using CuI (29 mg, 0.15 mmol, 0.3 equiv.), 1,10-phenanthroline (27 mg, 0.15 mmol, 0.3 equiv.), **54** (145 mg, 0.5 mmol, 1.3 equiv.), S_8 (22 mg, 0.65 mmol, 1.3 equiv.), and K_2CO_3 (89 mg, 0.65 mmol, 1.3 equiv.) yielded 59 mg (49%) of **29** as a beige solid.

Mp 140-142 °C; **IR** (neat): ν (cm^{-1}) 3063, 2920, 1654, 1447, 1333; **^{1}H NMR** (400 MHz, $CDCl_3$) δ 8.07 (dt, *J* = 7.9, 1.0 Hz, 1H), 7.59 (ddd, *J* = 8.3, 7.1, 1.3 Hz, 1H), 7.49 (dt, *J* = 8.2, 0.9 Hz, 1H), 7.40 (ddd, *J* = 8.0, 7.1, 1.0 Hz, 1H), 7.37 – 7.29 (m, 5H), 5.06 ppm (s, 2H); **^{13}C NMR** (101 MHz, $CDCl_3$) δ 165.5, 140.6, 136.3, 132.0, 129.0, 128.6, 128.4, 127.0, 125.7, 124.7, 120.5, 47.7 ppm; **ESI HR-MS**: calcd. for $[C_{14}H_{11}NOS+Na]^+$: 264.0454, found: 264.0454. The spectroscopic data are consistent with those reported in the literature.[531]

2-(3-Methylbutyl)-2,3-dihydro-1,2-benzothiazol-3-one (32)[472]

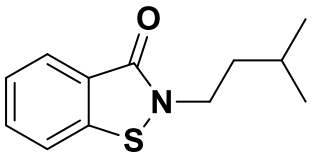

Application of General Procedure C using CuI (28.9 mg, 0.15 mmol, 0.3 equiv.), 1,10-phenanthroline (27.4 mg, 0.15 mmol, 0.3 equiv.), **50** (160 mg, 0.51 mmol, 1 equiv.), S_8 (21.9 mg, 0.66 mmol, 1.3 equiv.), and K_2CO_3 (90.7 mg, 0.66 mmol, 1.3 equiv.) yielded 32 mg (28%) of **32** as an orange solid.

Mp 128-129 °C; **IR** (neat): ν (cm^{-1}) 3075, 2956, 2583, 1647, 1597, 1442, 1347, 1291, 1072; **^{1}H NMR** (400 MHz, $CDCl_3$) δ 8.03 (dt, *J* = 7.9, 1.0 Hz, 1H), 7.65 – 7.51 (m, 2H),

7.39 (ddd, J = 8.0, 6.9, 1.2 Hz, 1H), 4.00 – 3.83 (m, 2H), 1.69 – 1.62 (m, 4H), 0.98 ppm (d, J = 6.3 Hz, 6H).; **^{13}C NMR** (101 MHz, $CDCl_3$) δ 165.4, 140.3, 131.7, 126.8, 125.6, 125.1, 120.4, 42.5, 38.5, 25.8, 22.6 ppm; **ESI HR-MS**: calcd. for $[C_{12}H_{15}NOS+H]^+$: 222.0947, found: 222.0950. The spectroscopic date are consistent with those reported in the literature.[472]

2-(Pyridin-2-yl)benzo[*d*]isothiazol-3(2*H*)-one (33)[532]

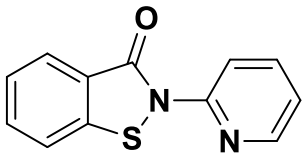

General Procedure C was followed using CuI (21.47 mg, 0.11 mmol, 0.4 equiv.), 1,10-phenanthroline (20.34 mg, 0.11 mmol, 0.4 equiv.), **57** (123 mg, 0.38 mmol, 1 equiv.), S_8 (16.5 mg, 0.49 mmol, 1.3 equiv.), and K_2CO_3 (68.1 mg, 0.49 mmol, 1.3 equiv.). The reaction mixture diluted with HCl (1M) and extracted with ethyl acetate. Purification by flash chromatography (0→45%, ethyl acetate in cyclohexane) yielded 57 mg (65%) mg of **33** as a pink solid.

Mp 191-192 °C; **IR** (neat): ν (cm^{-1}) 3070, 2917, 2849, 1672, 1583, 1450, 1259, 1119; **^{1}H NMR** (400 MHz, $CDCl_3$) δ 8.75 (dt, J = 8.5, 1.0 Hz, 1H), 8.41 (ddd, J = 5.0, 1.8, 0.9 Hz, 1H), 8.06 (dt, J = 7.9, 1.0 Hz, 1H), 7.81 (ddd, J = 8.5, 7.3, 1.8 Hz, 1H), 7.65 (ddd, J = 8.2, 7.1, 1.2 Hz, 1H), 7.58 (dt, J = 8.1, 1.0 Hz, 1H), 7.40 (ddd, J = 8.1, 7.1, 1.1 Hz, 1H), 7.14 ppm (ddd, J = 7.3, 4.9, 1.0 Hz, 1H); **^{13}C NMR** (101 MHz, $CDCl_3$) δ 164.2, 150.6, 147.8, 141.2, 138.6, 133.0, 127.0, 126.8, 125.7, 120.8, 120.5, 114.6 ppm; **ESI HR-MS**: calcd. for $[C_{12}H_8N_2OS+H]^+$: 229.0430, found 229.0433. The spectroscopic data are consistent with those reported in the literature.[532]

(*S*)-2-((5-Oxopyrrolidin-3-yl)methyl)benzo[*d*]isothiazol-3(2*H*)-one (34)

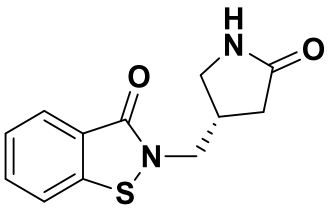

General Procedure C was followed with CuI (24.8 mg, 0.03 mmol, 0.3 equiv.), 1,10-phenanthroline (23.5 mg, 0.03 mmol, 0.3 equiv.), **58** (34.6 mg, 0.1 mmol, 1 equiv.), S_8 (4.4 mg, 0.13 mmol, 1.3 equiv.), and K_2CO_3 (18 mg, 0.13 mmol, 1.3 equiv.). The reaction mixture was filtered through cotton wool and purified using flash chromatography (0→20% MeOH in CH_2Cl_2) to give 4 mg (17%) of **34** as an orange wax.

[α]D25 = +8.8 (c = 1, $CDCl_3$); **IR** (neat): ν (cm^{-1}) 3276, 2927, 1685, 1645, 1447, 1104; **^{1}H NMR** (400 MHz, $CDCl_3$) δ 8.04 (dt, *J* = 7.9, 1.0 Hz, 1H), 7.64 (ddd, *J* = 8.2, 7.0, 1.2 Hz, 1H), 7.56 (dt, *J* = 8.1, 0.9 Hz, 1H), 7.43 (ddd, *J* = 8.0, 7.1, 1.0 Hz, 1H), 5.89 (s, 1H), 4.09 (dd, *J* = 14.2, 8.2 Hz, 1H), 3.87 (dd, *J* = 14.2, 6.5 Hz, 1H), 3.52 (dd, *J* = 9.9, 7.7 Hz, 1H), 3.32 (dd, *J* = 10.0, 5.6 Hz, 1H), 3.11 – 2.97 (m, 1H), 2.53 (dd, *J* = 17.1, 8.8 Hz, 1H), 2.24 ppm (dd, *J* = 17.1, 6.8 Hz, 1H); **^{13}C NMR** (101 MHz, $CDCl_3$) δ 177.0, 165.9, 140.2, 132.3, 127.0, 125.9, 124.3, 120.5, 47.2, 45.6, 35.1, 34.7 ppm; **ESI HR-MS**: calcd. for $[C_{12}H_{12}N_2O_2S+H]^+$: 249.0692, found 249.0692.

Methyl 3-(3-oxo-2,3-dihydro-1,2-benzothiazol-2-yl)propanoate (36)[533]

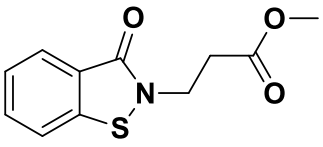

Application of General Procedure C using CuI (32.1 mg, 0.17 mmol, 0.3 equiv.), 1,10-phenanthroline (30.6 mg, 0.17 mmol, 0.3 equiv.), **60** (188.6 mg, 0.57 mmol, 1 equiv.), S_8 (24.5 mg, 0.74 mmol, 1.3 equiv.), and K_2CO_3 (101.6 mg, 0.74 mmol, 1.3 equiv.) yielded 108 mg (80%) of **36** as a pale yellow solid.

Mp 97-98 °C; **IR** (neat): ν (cm^{-1}) 3066, 2951, 2858, 1727, 1649, 1423, 1371, 1176; **^{1}H NMR** (400 MHz, $CDCl_3$) δ 8.02 (dt, *J* = 7.9, 1.1 Hz, 1H), 7.60 (ddd, *J* = 8.3, 7.1, 1.3

Hz, 1H), 7.53 (dt, *J* = 8.1, 0.9 Hz, 1H), 7.39 (ddd, *J* = 8.1, 7.0, 1.0 Hz, 1H), 4.18 (t, *J* = 6.6 Hz, 2H), 3.72 (s, 3H), 2.80 ppm (t, *J* = 6.6 Hz, 2H); **^{13}C NMR** (101 MHz, $CDCl_3$) δ 171.7, 165.6, 140.7, 132.0, 126.8, 125.6, 124.4, 120.4, 52.2, 40.0, 34.0 ppm; **ESI HR-MS**: calcd. for $[C_{11}H_{11}NO_3S+H]^+$: 238.0532 found 238.0534. The spectroscopic data are consistent with those reported in the literature.[533]

2-Phenyl-2*H*,3*H*-[1,2]thiazolo[4,5-*c*]pyridin-3-one (37)[534]

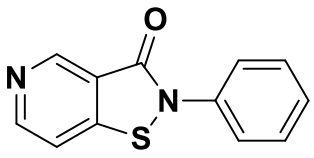

General Procedure C was followed using CuI (5.7 mg, 0.03 mmol, 0.3 equiv.), 1,10-phenanthroline (5.7 mg, 0.03 mmol, 0.3 equiv.), **49** (38.8 mg, 0.11 mmol, 1 equiv.), S_8 (4.8 mg, 0.14 mmol, 1.3 equiv.), and K_2CO_3 (19.7 mg, 0.14 mmol, 1.3 equiv.). Purification by flash chromatography (0→45% (v/v) ethyl acetate in cyclohexane) yielded 15 mg (58%) of **37** as a yellow solid.

Mp 145-147 °C (141-143 °C reported)[534]; **IR** (neat): ν (cm^{-1}) 2922, 2846, 1670, 1584, 1440, 1287, 1031; **^{1}H NMR** (400 MHz, $CDCl_3$) δ 9.29 (s, 1H), 8.75 (d, *J* = 5.4 Hz, 1H), 7.71 – 7.63 (m, 2H), 7.60 (d, *J* = 5.4 Hz, 1H), 7.56 – 7.45 (m, 2H), 7.44 – 7.33 ppm (m, 1H). **^{13}C NMR** (151 MHz, $CDCl_3$) δ 162.8, 149.9, 149.3, 149.1, 136.4, 129.8, 128.0, 125.0, 121.0, 115.2 ppm. **ESI HR-MS**: calcd. for $[C_{12}H_8N_2OS+H]^+$: 229.0430, found: 229.0432. The physical and spectroscopic data are consistent with those reported in the literature.[534]

5-Bromo-2-phenyl-2,3-dihydro-1,2-benzothiazol-3-one (38)

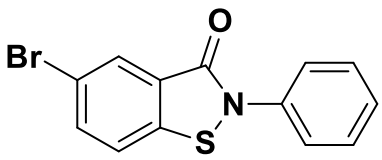

Application of General Procedure C using CuI (89 mg, 0.47 mmol, 0.3 equiv.), 1,10-phenanthroline (84 mg, 0.47 mmol, 0.3 equiv.), **48** (553 mg, 1.56 mmol,

1 equiv.), S_8 (67 mg, 2.03 mmol, 1.3 equiv.), and K_2CO_3 (280 mg, 2.03 mmol, 1.3 equiv.) yielded 412 mg (86%) of **38** as a beige solid.

Mp 188-189 °C; **IR** (neat): ν (cm^{-1}) 3092, 2981, 2884, 1642, 1493, 1444, 1337; **^{1}H NMR** (400 MHz, $CDCl_3$) δ 8.24 (d, *J* = 2.0 Hz, 1H), 7.76 (dd, *J* = 8.5, 2.0 Hz, 1H), 7.68 (dd, *J* = 7.7, 1.6 Hz, 2H), 7.48 (t, *J* = 7.5 Hz, 3H), 7.34 ppm (t, *J* = 7.4 Hz, 1H); **^{13}C NMR** (101 MHz, $CDCl_3$) δ 162.9, 138.7, 137.0, 135.6, 130.1, 129.6, 127.6, 124.8, 121.7, 119.8 ppm; **ESI HR-MS**: calcd. for $[C_{13}H_8BrNOS+H]^+$: 305.9582, found 305.9584.

7-Methyl-2-phenyl-2,3-dihydro-1,2-benzoisothiazol-3-one (39)

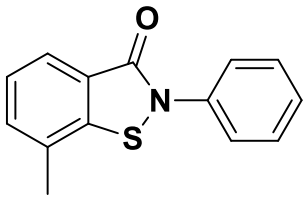

Application of General Procedure C using CuI (23 mg, 0.12 mmol) and 1,10-phenanthroline (22 mg, 0.12 mmol, 0.3 equiv.), **46** (136 mg, 0.4 mmol, 1 equiv.), S_8 (17 mg, 0.52 mmol, 1.3 equiv.), and K_2CO_3 (72 mg, 0.52 mmol, 1.3 equiv.) yielded 7 mg (7%) of **39** as a beige solid.

Mp 113-115 °C; **IR** (neat): ν (cm^{-1}) 2999, 2956, 2917, 1665, 1541, 1377, 1133, 1024; **^{1}H NMR** (400 MHz, $CDCl_3$) δ 7.95 (ddd, *J* = 7.6, 1.3, 0.7 Hz, 1H), 7.78 – 7.69 (m, 2H), 7.51 – 7.42 (m, 3H), 7.39 (t, *J* = 7.5 Hz, 1H), 7.35 – 7.29 (m, 1H), 2.39 ppm (d, *J* = 0.8 Hz, 3H); **^{13}C NMR** (101 MHz, $CDCl_3$) δ 164.9, 140.1, 137.6, 132.7, 129.8, 129.5, 127.1, 126.5, 124.9, 124.8, 18.8 ppm; **ESI HR-MS**: calcd. for $[C_{14}H_{11}NOS+H]^+$: 242.0634, found: 242.0636.

7-Bromo-2-phenyl-2,3-dihydro-1,2-benzothiazol-3-one (40)

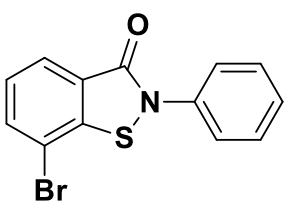

Application of General Procedure C using CuI (27 mg, 0.14 mmol, 0.29 equiv.) and 1,10-phenanthroline (26 mg, 0.14 mmol, 0.29 equiv.), **47** (169 mg, 0.48 mmol, 1 equiv.), S_8 (21

mg, 0.62 mmol, 1.3 equiv.), and K_2CO_3 (85 mg, 0.62 mmol, 1.3 equiv.) yielded 76 mg (52%) of **40** as an orange solid.

Mp 149-150 °C; **IR** (neat): ν (cm^{-1}) 2961, 2918, 2849, 1669, 1488, 1403, 1298, 1072; **^{1}H NMR** (400 MHz, $CDCl_3$) δ 8.09 (dd, *J* = 7.8, 1.0 Hz, 1H), 7.78 (dd, *J* = 7.8, 1.0 Hz, 1H), 7.74 – 7.68 (m, 2H), 7.53 – 7.46 (m, 2H), 7.41 – 7.31 ppm (m, 2H); **^{13}C NMR** (101 MHz, $CDCl_3$) δ 164.1, 142.4, 137.1, 134.8, 129.6, 127.6, 127.5, 127.2, 126.1, 124.9, 114.0 ppm; **ESI HR-MS**: calcd. for $[C_{13}H_8BrNOS+H]^+$: 305.9583, found: 305.9583.

7-Bromo-2-(3-methylbutyl)-2,3-dihydro-1,2-benzothiazol-3-one (42)

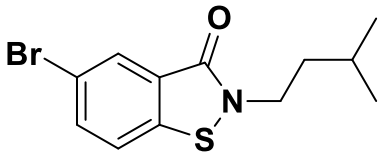

General Procedure C was followed using CuI (25.8 mg, 0.14 mmol, 0.3 equiv.), 1,10-phenanthroline (24.5 mg, 0.14 mmol, 0.3 equiv.), **53** (157.7 mg, 0.45 mmol, 1 equiv.), S_8 (19.6 mg, 0.59 mmol, 1.3 equiv.), and K_2CO_3 (81.1 mg, 0.59 mmol, 1.3 equiv.). Purification by flash chromatography (0→40% (v/v) ethyl acetate in cyclohexane) yielded 20 mg (15%) of **42** as a beige solid.

Mp 107-108 °C; **IR** (neat): ν (cm^{-1}) 3093, 2947, 2849, 1650, 1453, 1308, 1078; **^{1}H NMR** (400 MHz, $CDCl_3$) δ 8.16 (d, *J* = 1.9 Hz, 1H), 7.69 (dd, *J* = 8.5, 2.0 Hz, 1H), 7.42 (d, *J* = 8.4 Hz, 1H), 3.94 – 3.86 (m, 2H), 1.65 (m, 3H), 0.97 (d, *J* = 6.3 Hz, 6H); **^{13}C NMR** (101 MHz, $CDCl_3$) δ 164.1, 138.9, 134.8, 129.6, 126.8, 121.9, 119.4, 42.7, 38.4, 29.8, 25.8, 22.5 ppm; **ESI HR-MS**: calcd. for $[C_{12}H_{14}BrNOS+H]^+$: 300.0052, found 300.0053.

7-Methyl-2-(3-methylbutyl)-2,3-dihydro-1,2-benzothiazol-3-one (43)

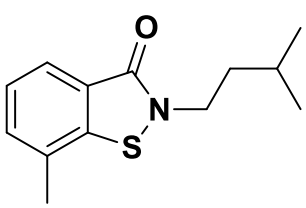

General Procedure C was followed using CuI (37 mg, 0.2 mmol, 0.3 equiv.), 1,10-phenanthroline (35 mg, 0.2 mmol, 0.3 equiv.), **51** (215 mg, 0.65 mmol, 1 equiv.), S_8 (28.2 mg, 0.85 mmol, 1.3 equiv.), and K_2CO_3 (117 mg, 0.85 mmol, 1.3 equiv.). Purification by flash

chromatography (0→40% (v/v) ethyl acetate in cyclohexane) yielded 94 mg (61%) of **43** as a colourless oil.

IR (neat): ν (cm^{-1}) 3066, 2957, 1662, 1478, 1385, 1211; **^{1}H NMR** (400 MHz, $CDCl_3$) δ 7.91 – 7.84 (m, 1H), 7.41 – 7.30 (m, 2H), 3.96 – 3.90 (m, 2H), 2.36 (s, 3H), 1.67 (m, 3H), 1.03 – 0.93 ppm (m, 6H); **^{13}C NMR** (101 MHz, $CDCl_3$) δ 166.1, 140.4, 131.9, 130.0, 126.1, 124.9, 124.9, 42.5, 38.5, 25.8, 22.6, 18.8 ppm; **ESI HR-MS**: calcd. for $[C_{13}H_{17}NOS+H]^+$: 236.1104, found: 236.1105.

5-Bromo-2-(3-methylbutyl)-2,3-dihydro-1,2-benzothiazol-3-one (44)

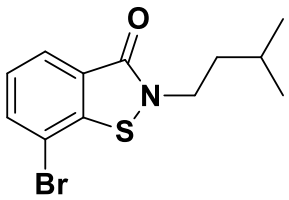

General Procedure C was followed using CuI (21.8 mg, 0.12 mmol, 0.3 equiv.), 1,10-phenanthroline (20.7 mg, 0.12 mmol, 0.3 equiv.), **52** (133.5 mg, 0.38 mmol, 1 equiv.), S_8 (16.6 mg, 0.5 mmol, 1.3 equiv.), and K_2CO_3 (68.6 mg, 0.5 mmol, 1.3 equiv.). Purification by reverse-phase chromatography using a Biotage Sfär® C18 Duo cartridge (buffer A (H_2O:formic acid, 100:0.1 (v/v)) → buffer B (MeCN:formic acid, 100:0.1 (v/v)) from 0 to 100% (v/v) B over 16 column volumes, then 4 column volumes at 100% (v/v) B) gave 33 mg (29%) of **44** as an orange oil.

IR (neat): ν (cm^{-1}) 2962, 2917, 2849, 1669, 1488, 1328. 1089; **^{1}H NMR** (400 MHz, DMSO-d6) δ 7.97 (dd, *J* = 7.7, 1.0 Hz, 1H), 7.94 (dd, *J* = 7.8, 1.0 Hz, 1H), 7.46 (t, *J* = 7.8 Hz, 1H), 3.90 (t, *J* = 7.0 Hz, 2H), 1.64 – 1.48 (m, 3H), 0.97 – 0.87 ppm (m, 6H); **^{13}C NMR** (101 MHz, DMSO-d6) δ 164.1, 141.6, 134.4, 127.9, 126.4, 125.1, 113.7, 41.6, 37.7, 25.0, 22.2 ppm; **ESI HR-MS**: calcd. for $[C_{12}H_{14}BrNOS+H]^+$: 300.0052, found: 300.0054.

General Procedure D – Suzuki-Miyaura cross-coupling reaction

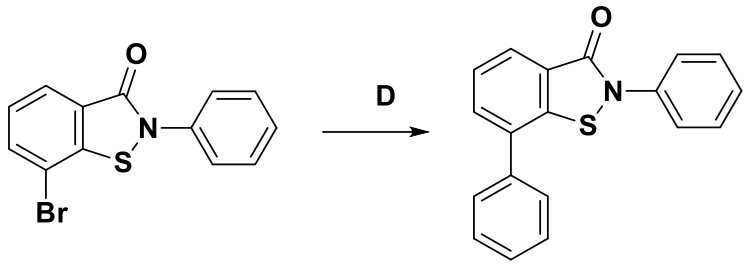

Figure 6.3 *| Suzuki-Miyaura cross-coupling reaction (**41**). Conditions: **D.** phenylboronic acid, K_2CO_3, $Pd(dppf)Cl_2$, 1,4-dioxane, 80 °C.*

A reaction vial was charged with 7-bromo-2-phenylbenzo[*d*]isothiazol-3(2*H*)-one (52.6 mg, 0.17 mmol, 1 equiv), phenylboronic acid (41.9 mg, 0.34 mmol, 2 equiv), K_2CO_3 (118.5 mg, 0.86 mmol, 5 equiv), and $Pd(dppf)Cl_2$ (18.84 mg, 0.026 mmol, 0.15 equiv). The atmosphere was purged with nitrogen and anhydrous, degassed dioxane (11.6 mL, 0.015 M) was transferred to the reaction vial. The vial was sealed and stirred at 80 °C until full conversion of the starting material (3h, TLC, MS). The reaction mixture was filtered using diatomaceous earth, concentrated *in vacuo*, and purified using flash chromatography (0→20% diethyl ether in *n*-pentane) to yield the desired compound.

2,7-Diphenyl-2,3-dihydro-1,2-benzothiazol-3-one (41)

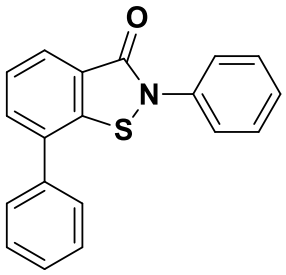

Application of General Procedure D using **40** (52.6 mg, 0.17 mmol, 1 equiv.), phenylboronic acid (41.9 mg, 0.34 mmol, 2 equiv.), and K_2CO_3 (118.5 mg, 0.86 mmol, 5 equiv.) yielded 10 mg (19%) of **41** as a white solid.

Mp153-154 °C; **IR** (neat): ν (cm^{-1}) 3055, 2918, 2850, 1675, 1495, 1327, 1174; **^{1}H NMR** (400 MHz, $CDCl_3$) δ 8.11 (dd, *J* = 7.8, 1.2 Hz, 1H), 7.76 – 7.68 (m, 3H), 7.62 – 7.43 (m, 8H), 7.31 ppm (m, 1H); **^{13}C NMR** (101 MHz, $CDCl_3$) δ 164.6, 139.2, 138.4, 137.4, 134.5, 131.9, 129.6, 129.5, 129.01, 127.2, 127.2, 127.0, 126.1, 126.0, 124.7 ppm; **ESI HR-MS**: calcd. for $[C_{19}H_{13}NOS+H]^+$: 304.0791, found: 304.0792.

6.2. Biochemical Assays

6.2.1. General Information

IDH assays were performed using freshly purified recombinant IDH1 WT, IDH1 R132H prepared by Dr Raphael Reinbold (Department of Chemistry, University of Oxford as reported.[334] M^{pro} assays were performed using freshly purified recombinant M^{pro} solution, provided by Dr Tika R. Malla (Department of Chemistry, University of Oxford), prepared as reported.[470] Thawed aliquots of M^{pro} and IDH were not refrozen, and discarded. Buffers were made up exclusively with LC-MS grade solvents (Merck, Supelco). MS analyses were performed exclusively with LC-MS grade solvents (Merck, Supelco). Reaction buffer was prepared fresh in every instance, including the preparation of enzyme, and substrate stock solutions. Compound stock solutions were prepared to either 10, 2.5, or 1 mM in DMSO and diluted using the relevant reaction buffer.

6.2.2. NADPH Absorbance-Based Assays

IDH catalysis in solution was monitored by changes in the absorbance of NADPH (340 nm, $\varepsilon = 6{,}220\ M^{-1}cm^{-1}$) over time.[283] The measured absorption was converted to NADPH concentration using the Beer-Lamber law: absorbance (A) is equal to the molar absorption coefficient (ε) multiplied by the molar concentration (c) and optical path length (l) (**Eq. 6**).

Eq. 6

$$A = \varepsilon c l$$

DL-Isocitrate trisodium salt (ICT) was procured from ChemCruz. 2-OG disodium salt, NADPH tetrasodium salt, and $NADP^+$ disodium salt were procured from Sigma-Aldrich.

High-Throughput Inhibition Screens and IC_{50} Determination

Assays were carried out using a PHERAstar® FS microplate reader (BMG LabTech) or a CLARIOStar® Plus multi-mode plate reader equipped with an LVis Plate (BMG Labtech) at 25 °C, using clear-bottom 96 well plates. The reaction buffer consisted of Tris HCl, $MgCl_2$, dithiothreitol (DTT), bovine serum albumin (BSA), and tween-20, in varying proportions. Specific reaction conditions are described for each experiment in the relevant chapter (**Chapter 2**). For each assay, one stock solution (4x concentration) each of the IDH isoform and the inhibitor (or control) were prepared, and one stock solution (2x concentration) of the combined substrates was prepared (ICT and $NADP^+$ for IDH1 WT, 2-OG and NADPH for IDH1 variants). All stock solutions were allowed to reach room temperature before dispensation. Each reaction was prepared in at least triplicate. First, 25 µL of the enzyme stock solution (4x) and 25 µL of the inhibitor/control stock solution (4x) were dispensed into the 96 well plate, and incubated together for 12 minutes. Then, the reaction was initiated by dispensing 50 µL of the combined substrate stock solution (2x) into the 96 well plate. The 96 well plate was immediately inserted into the PHERAstar FS microplate reader and the measurement protocol was initiated. The total reaction volume was 100 µL, and the reaction was monitored for a minimum of 15 minutes.

The reaction rate was calculated from the change in concentration over time using Microsoft Excel (Office 2021). The observed activity of a reaction condition was determined by dividing the observed rate of reaction for that condition by the observed rate of reaction in the positive control. To convert activity to a percentage value of inhibition, the activity values were subtracted from one and multiplied by 100 to give a percentage value of inhibition. For IC_{50} determinations, non-linear regression curve fits

were produced using GraphPad Prism (Version 5). Standard error of the mean was calculated using the logarithm of concentration values.

Solution Enzyme Inhibition Kinetic Assays on IDH1 WT

Assays were carried out using a UV/Vis/NIR Lambda 19 Spectrometer (PerkinElmer) at 25 °C in a quartz cuvette. The reaction buffer composition was similar to the high-throughput screen and IC_{50} assay, consisting of Tris, DTT, and varying concentrations of magnesium chloride. BSA and tween-20 were omitted to closer approximate the buffer conditions of the e-Leaf.[249] Specific conditions for each experiment are described in **Chapter 2**. The reaction was initiated by addition of IDH1 WT to the final concentration of 250 pM. 250 pM was identified as a concentration at which a steady-state reaction persisted for >30 minutes. Once the increase in absorbance was linear for at least 1 minute, indicating a steady-state reaction had been achieved, the cuvette was removed and inhibitor was injected to the final concentration (5 – 100 μM) and mixed before replacing the cuvette. The resultant time course data was plotted and analysed using OriginLabs software.

6.2.3. Fluorescence-Based Inhibition Assays

The following procedure was reported in Thun-Hohenstein et al.[469] The inhibitory activities of compounds **26–36** against M^{pro} were determined using a spectroscopic assay, monitoring M^{pro} catalysed hydrolysis of the fluorogenic substrate ([5-FAM]-AVLQSGFR-[Lys(Dabcyl)]-K-amide) as reported.[429] Assays were conducted at rt in clear-bottomed Greiner 384 black well microplates using a ClarioStar or PHERAstar FS microplate reader (BMG LabTech). Compound dilutions were transferred in quadruplicate from a 96 well plate to a 384 well plate (5 μL/well) using a CyBio Liquid Handler (Analytik Jena AG). M^{pro} (5 μl/well) and substrate (10 μL/well) were dispensed

across 384 well plates using a Multidrop Combi dispenser (Thermo Scientific), the plates were then centrifuged (500 g, 15 s, Axygen Plate Spinner Centrifuge, Corning). Final reaction concentrations were 50 nM M^{pro}, 375 nM substrate, 20 mM HEPES, pH 7.3, 50 mM NaCl, 10% (v/v) glycerol, 1% (v/v) DMSO, 0.01% (v/v) Triton X-100. The initial rates of reaction (measured after 15 minutes pre-incubation of the inhibitor with the enzyme) were assessed by monitoring the fluorescence intensity at λ_{ex} = 485 nm and λ_{em} = 520 nm. Following the determination of initial rates of reaction, data were fitted using a four-parameter function: log (inhibitor) vs. response, variable slope in GraphPad Prism 5 to obtain IC_{50} values.

6.2.4. Protein Observed Mass Spectrometry

The following method was reported in Thun-Hohenstein et al.[469] The reactions of compounds **26–36** with recombinant M^{pro} were investigated using protein observed mass spectrometry coupled to solid phase extraction purification as reported.[470] The compounds were dispensed across 384 well plates using an acoustic Echo Dispenser (LabCyte). M^{pro} was dispensed across 384-well plates using a Multidrop Combi dispenser (Thermo Scientific). The plates were then centrifuged (500 g, 15 s, Axygen Plate Spinner Centrifuge, Corning). Final reaction conditions: 40 µM compound, 2 µM M^{pro}, 20 mM HEPES, pH 7.5, 50 mM NaCl, 50µL final volume/well. The mass spectrometer was operated in positive ion mode with the following parameters: drying gas temperature (225 °C), drying gas flow rate (13 L/min), nebulizer pressure (40 psig), sheath gas temperature (350 °C), sheath gas flow rate (12 L/min), capillary voltage (4000 V), nozzle voltage (1000 V).

6.3. Cell Biology Experiments

6.3.1. Benchtop Equipment

Water purification involved the use of a Milli-Q Direct 8 system, which includes a Millipak® Express 40 filter having a 0.22 μM pore size (Merck Millipore). Microscopy examinations of cells were conducted using an AE31E trinocular microscope (Motic). Cell quantification was performed with a Countess™ II FL Automated Cell Counter and Countess™ Cell counting chamber slides, both from (Thermo Fisher Scientific). Spectroscopic analyses of the samples utilized either a NanoDrop One microvolume UV-VIS spectrophotometer (Thermo Fisher Scientific) or a CLARIOStar® Plus multi-mode plate reader equipped with an LVis Plate (BMG Labtech). The samples were centrifuged using a Megafuge 8R Small Benchtop Centrifuge (Thermo Fisher Scientific), which accommodated a 28-sample insert.

6.3.2. Ion-Exchange Chromatography Mass Spectrometry (IC-MS) Equipment

A Dionex™ IonPac™ AS11-HC column (2 × 250 mm, 4 μm particle size) (Dionex, Thermo Fisher Scientific) was utilised with a Q-Exactive HF hybrid quadrupole-Orbitrap (Thermo Fisher Scientific), equipped with a HESI II probe (Thermo Fisher Scientific), connected to an ICS 5000+ HPIC system (Dionex), fitted with a 500e ERS suppressor (Dionex).

6.3.3. General Non-Chemical Consumables

Sterile polypropylene CryoPure tubes (2 mL) featuring QuickSeal screw caps (Sarstedt AG & Co. KG), Sartorius Minisart™ regenerated cellulose (RC) syringe filters with a 0.2 μm pore size and 15 mm filter diameter (Fisher Scientific), Amicon® Ultra

RC filters (0.5 mL) with molecular weight (MW) cut-offs of 3 kDa (Merck), and LCGC clear glass total recovery vials (1 mL) with cap and pre-slit PTFE/silicone septum (Waters), were utilised.

Sterile polystyrene petri dishes (60 mm diameter) designed for adherent cells and equipped with lids (Sarstedt AG & Co. KG), sterile flat-bottom 96-well plates with clear-walls, each individually wrapped with lids featuring condensation rings (Scientific Laboratory Supplies), and non-sterile, untreated, clear, flat-bottomed polystyrene 96-well assay plates with low evaporation lids (Corning Inc), were utilised.

6.3.4. General Chemicals

Purified water was provided by a Millipore MilliQ system, ensuring it met the specifications for type 1 water, including a resistivity of 18.2 MΩ·cm and a low total carbon content of 2 ppb. Unless specified, all utilized water conformed to type 1 standards. Methanol, acetonitrile, and isopropanol, each with a purity of ≥99.9% suitable for HPLC were procured from Sigma Aldrich. Except where noted, all solvents employed in procedures were of HPLC grade.

6.3.5. Cell Culture Chemicals and Growth Media

Foetal bovine serum (FBS) (non-USA origin); liquid Dulbecco's Modified Eagle Medium (DMEM) containing phenol red, sodium bicarbonate (3.7 g/L), sodium pyruvate (1.0 mM), and a low glucose (LG) concentration (1000 mg/L), without glutamine or HEPES; liquid Dulbecco’s phosphate buffered saline (PBS) without calcium chloride or magnesium chloride; and trypsin-EDTA solution (2.5 g porcine trypsin and 0.2 g EDTA·4 Na per litre of Hank’s Balanced Salt solution and phenol red) were obtained from Sigma-Aldrich. GlutaMAX™ (GM™) supplement (200 mM

L-alanyl-L-glutamine in 0.85% NaCl) was acquired from Thermo Fisher Scientific. All solutions and FBS were sterile filtered prior to delivery.

Molecular biology grade dimethyl sulfoxide (DMSO) (99.9%) (Sigma Aldrich) was sterile filtered in-house using a 0.2 μm RC syringe filter. Trypan blue dye for cell staining was included with the Countess™ cell counting chamber slides from Thermo Fisher Scientific.

6.3.6. Cell Culture Treatments

Compounds **1**, **2**, and **3**, were synthesised as described (**Section 6.1.2**, **Section 6.1.3**, **Section 6.1.4**).

6.3.7. Sample Processing Chemicals

Formic acid (99%, for analysis) was obtained from Thermo Fisher Scientific. Ammonium formate (Optima® LC-MS grade) was obtained from Fisher Scientific. Ammonium hydroxide solution (~ 25% NH_3, puriss), ammonium acetate (for MS, eluent additive for LC-MS), and ammonium bicarbonate (BioUltra, ≥ 99.5%) were obtained from Sigma Aldrich. The EGC 500 KOH potassium hydroxide eluent generator cartridge was obtained from Dionex.

6.3.8. General Solutions

Aqueous methanol solution (80%, v/v) was made by combining 80 mL of methanol with 20 mL of water, and stored at 4 °C.

6.3.9. Cell Culture Solutions and Treatment Stocks

Trypsin-EDTA was aliquoted without modification (8-12 mL) and stored at -20 °C prior to use. During use it was stored at 4 °C, used within two weeks, and never refrozen. PBS was not modified and maintained at room temperature at all times. Unopened low glucose

Dulbecco's Modified Eagle Medium (LG DMEM) was stored at 4 °C. FBS (50 mL) and GM™ (5 mL) were aliquoted and stored at -20 °C until use. For use as growth medium, LG DMEM was supplemented with FBS (10%, v/v) and GM™ (1%, v/v), then stored at 4 °C for a maximum of four weeks.

3 (1 mM), **1** (5 mM), **2** (5 mM), MSO (10 mM), phosphinothricin (10 mM), tert-butyl(tert-butyldimethylsilyl)-glyoxylate (10 mM), and ERG240 (10 mM) were dissolved in DMSO to make stock solutions. EGCG (5 mM), and strombine (10 mM), were dissolved in water to make stock solutions. All stock solutions were sterile filtered (0.2 μm pore size) and stored at -80 °C.

6.3.10. Sample Harvest Solutions

Aqueous methanol (80% MeOH, 20% H_2O, v/v) was used as described.

6.3.11. Chromatography Solutions

Mobile phase A consisted of formic acid in water (0.1%, v/v) and was used within one month of preparation. Mobile phase B consisted of formic acid in methanol (0.1%, v/v) and was used within three months of preparation.

6.3.12. Tissue Culture Conditions

Cells were incubated under the same conditions for all experiments (37 °C, 5% CO_2, 20% O_2). Cells were incubated for 24 hours between plating and treatment. Growth media consisted of LG DMEM with FBS (10%, v/v) and GM™ (1%, v/v) unless otherwise specified. Each dish (3 mL, 60 mm diameter) or well (~1 mL) of cells was considered one biological replicate. Each measurement of a sample was considered as one analytical replicate.

6.3.13. Tissue Culture Cell lines

LN18 Glioblastoma multiforme (GBM) cells were utilised for metabolomics experiments. The LN18 GBM cell line was originally from ATCC (CRL-2610). Dr Chiara Bardella and colleagues (Institute of Cancer and Genomic Sciences, University of Birmingham) gifted the cell line to Dr Ingvild Hvinden (Department of Chemistry, University of Oxford). Dr Ingvild Hvinden kindly provided the cell lines for the metabolomic studies described in this project. Dr Chiara Bardella utilised a lentiviral vector (pUltra-Chili) to generate the LN18 GBM cell line expressing IDH1 R132H, and transduced LN18 GBM cells with an empty lentiviral vector to generate the IDH1 WT cell line, as described by Reinbold et al.[283]

6.3.14. Tissue Culture Passaging Procedure

Cells in growth phase in a T75 or T175 flask were removed from the incubator. The confluency was observed by light microscope and noted, then transferred into the laminar flow hood. The ideal confluency for passaging was ~70%. The media was poured out, and the cells were washed twice with PBS (20 mL total), then the PBS was removed by aspiration. Trypsin-EDTA (1 mL for a T75 flask, 2 mL for a T175 flask) was applied to the cells and the flask was incubated for 4 – 7 minutes, or until detachment was observed. Detached cells were suspended by adding LG DMEM (10 mL) and mixing by gentle aspiration. The cells were diluted into a new flask, which was pre-loaded with LG DMEM (final volumes: 10 mL for a T75 flask, 25 mL for a T175 flask). The dilution ratio was chosen from 1:1 to 1:10, according to the observed confluency, aiming for ~25% confluency in a new flask. When necessary, cell lines were scaled up by diluting the suspended cells into larger and/or multiple new flasks.

6.3.15. Tissue Culture Plating Procedure for Metabolomics Experiments

Cells were plated in 60 mm dishes for metabolomics experiments. Cells were first washed, detached, and resuspended as described in the passaging procedure (**Section 6.3.14**), and counted using a Countess™ Automated Cell Counter according to the manufacturer's user guide. The cell suspension was diluted to a maximum of 300 000 cells mL^{-1} and counted again for confirmation. The diluted cell suspension (1 mL) was dispensed into a 60 mm dish pre-loaded with LG DMEM (2 mL), for a final volume of 3 mL per dish (~100 000 cells).

6.3.16. Tissue Culture Treatment Procedure for Metabolomics Experiments

Treatment stock solutions were diluted in LG DMEM to a final concentration of 5 μM. Three at a time, dishes were removed from the incubator for treatment. Old LG DMEM (3 mL) was removed by careful aspiration from each dish and replaced with LG DMEM containing treatment (5 μM, 3 mL). For experiments with treatment stock solutions in DMSO, an equivalent volume of DMSO was diluted in LG DMEM and applied to control replicates. For experiments with aqueous treatment stocks, fresh LG DMEM was applied to control replicates. The dishes were replaced into the incubator and the cells were incubated for 24 hours. The experiments varied in the number of treatments and controls. Therefore, the total number of samples varied per experiment. The table of metabolomic experiments from **Section 3.2** is shown again here for reference (**Table 6.1**)

Expt.	Treatment(s)	DMSO (%, v/v)	IDH Mutation	Biological Replicates	Total Dishes
1	Compound **1**, and Compound **2**	0.1	IDH1 WT, IDH1 R132H	**1** (10), **2** (10), Ctrl (10) **1** (10), **2** (10), Ctrl (10	60
2	Compound **3**	0.50	IDH1 WT, IDH1 R132H	**3** (5), Ctrl (5) **3** (5), Ctrl (5)	20

Table 6.1 | *A summary of all metabolomics experiments. The table contains the experiment number, treatment applied, final percentage of DMSO in the growth media, IDH mutation status (consistent for all groups).*

6.3.17. Tissue Culture Harvest Procedure for Metabolomics Experiments

Three at a time, in random order, dishes were transferred from the incubator into a laminar flow hood. The confluency of each dish was observed by light microscope and noted. Aliquots of media were first saved by pooling samples (100 μL) from each dish in an experimental group. Each dish was then emptied of media and washed with PBS (2 x 5 mL), dabbed with tissue at the rim to remove excess phosphate buffer solution (PBS) without cell contact, then metabolically arrested by the direct addition of liquid nitrogen (5 mL). Careful and efficient handling was necessary to ensure that the liquid nitrogen in the first dish did not completely evaporate before the third dish was frozen. If the liquid nitrogen prematurely evaporated, the dish was stored on dry ice until it's turn. For each dish in order, aqueous methanol (80% (v/v) MeOH, 20% (v/v) H_2O, 180 μL) was added and a cell scraper was firmly applied in circular motions, then the dish was tilted and the cell debris was collected at the bottom of the dish. The dish was rotated clockwise (90°) and the scraping was repeated. Finally, the suspension of cell debris in aqueous methanol was transferred to a microtube (1.5 mL) and stored on ice until the process was complete for all three dishes. Upon completion of all three dishes, harvested

cell contents were stored on dry ice until the process had been completed for all subsequent dishes in the experiment. Once all dishes in the experiment were harvested, samples were stored at -80 °C until processing for metabolomics.

6.3.18. Sample Preparation of Cell Harvest for IC-MS

The centrifuge was pre-cooled to 4 °C, then cell samples harvested for metabolomics were thawed on ice and pelleted (14,000 rpm, 25 minutes, 4 °C). Initially, molecular weight cut-off filters (3 kDA) were centrifuged (14000 rpm, 25 minutes, 4 °C) with H_2O (500 μL) to wash the membrane. Care was taken to remove residual water in the filter before moving on. Before filtration, the concentration of dsDNA (ng/μL) in the supernatant of each cell sample was analysed using a NanoDrop One mcahine (2 μL). The NanoDrop machine was blanked with aqueous MeOH(aq) solution (2 μL), and cleaned between measurements with wetted lint free wipes (H_2O). Blanking was repeated whenever the instrument had been left unattended or measurements were irregular. At least two dsDNA measurements were taken, until two values differed by no more than 6 ng/μL. The cell sample supernatant was transferred to the washed filter and centrifuged (14,000 rpm, 25 minutes, 4 °C), collecting the filtrate in a fresh, labelled, tube. Sample filtrates were then normalise with respect to each other by dilution according to the relative concentrations of dsDNA measured by NanoDrop, then transferred to total recovery vials. Final volumes of samples varied between 30 and 100 μL. Final chromatography-ready samples were stored at 4 °C (< 1 week), or -80 °C (> 1 week).

6.3.19. IC-MS Sample Analysis

The following method, reproduced below, was developed by Dr Walsby-Tickle (Department of Chemistry, University of Oxford) and is reported by Dr Walsby-Tickle and Dr Ingvild Hvinden in the literature.[138, 140, 535]

Sample volume was 5.0 µL with partial-loop injection. The sample manager was set to 4.0 °C and column temperature was 30 °C. Flow rate was 0.250 mL min^{-1} and the following hydroxide gradient was used: 0.0 min, 5 mM; 1.0 min, 5 mM; 15.0 min, 60 mM; 25.0 min, 100 mM; 30.0 min, 100 mM; 30.1 min, 5 mM; 37.0 min, 5 mM. Curve was set to 5 for all gradient steps. The ion suppressor was operated in external water mode with a 0.500 mL min^{-1} flow rate and a continuously regenerated trap column removed ionic contaminants from the eluent. The ion suppressor current was set to 62 mA.

Spray voltage was –3.60 kV (negative polarity), capillary temperature was 320 °C and the probe heater temperature was 350 °C. Gas flow rates were: sheath gas at 60, auxiliary gas was at 20 and spare gas at 0, all arbitrary units (a.u.). S-Lens RF level was set to 70.0%. The method was run with full MS and data dependent (dd) MS2 and the mass range was from 60-900 m/z. The following settings were used for full MS: resolution 7.0 × 104; microscans, 2; AGC target, 1.0 × 106; and maximum IT, 120 ms. The following settings were used for ddMS2: resolution, 1.75 × 103; microscans, 2; AGC target, 1.0 × 105; and maximum IT, 250 ms.

6.3.20. IC-MS Data Pre-Processing

The IC-MS output files were uploaded into Progenesis QI software (Nonlinear Dynamics Waters). The upload parameters were as follows: file format: Thermo Fisher Scientific, instrument type: high resolution mass spectrometer, data format: profile data, ionisation polarity: negative, searched adducts: $[M-H]^-$, $[M-H-H2O]^-$, $[M-2H]^{2-}$ and $[2M-H]^-$.

For each experiment, Progenesis QI identified the sample datafile with the greatest similarity to all other files in the uploaded data as a reference chromatogram, and aligned every other chromatogram accordingly. Sample datafiles were excluded from further processing if their chromatograms did not align ≥ 90%. For each aligned run, Progenesis

QI analysed retention time-m/z pairs (peaks) using a noise estimation algorithm and picked peaks considered to be genuine ions. The peak sensitivity and peak integration settings were set to 'default'. The rt limit and minimum peak width settings were not utilised.

Picked peaks were compared to a database of known metabolite standards in house by retention time (max. error ≤ 2 minutes), m/z (max. error ≤ 5 ppm), fragmentation score (max. error ≤ 12 ppm), isotope similarity (≥ 85%), minimum coefficient of variation (< 50%), and maximum abundance (> 50) (**Section 6.3.25**). Peaks were confidently identified as metabolites in the database according to retention time (max. error ≤ 2 minutes), m/z (max. error ≤ 5 ppm), and isotopic similarity (≥ 90%). Peaks exhibiting an isotopic similarity between 85 – 90% were accepted as putative identifications. Peaks with multiple potential metabolite identifications were differentiated by fragmentation score. Maximum abundance and minimum coefficient of variation were only used to rule out peaks. Finally, all identified metabolites and unidentified peaks (features), and respective peak intensities (ion counts), were outputted in a table for further statistical analysis.

6.3.21. IC-MS Data Processing and Normalisation Procedure in Preparation for Statistical Analysis

For each table output by Progenesis QI, peak intensities (ion counts) were filtered by interquartile range. Near-constant values were removed and the total number of features was limited to 2500. Principal component analysis (PCA) scores were generated using the website www.metaboanalyst.ca, and outliers were removed. Outliers were defined as samples which fell outside of a 95% confidence area. For multivariate statistical analysis, every combination of normalisation (none, median, sum, quantile), transformation (none,

logarithmic, square root), and scaling (none, mean centred, auto-scaling, pareto-scaling) methods was applied to the data. For univariate statistical analysis, data tables were only normalised, not transformed or scaled. The outputs were visualised as unclustered heatmaps, feature distribution plots, and sample distribution plots. The optimal combination of methods produced the most even distribution of colour in a heatmap, and the best possible approximation of a normal distribution in sample and feature distributions.

In a data table, each row 'R' represents a sample (1, 2, 3, …, s) and each columns 'C' represents a metabolite (1, 2, 3, …, m). The notation is as follows:

R_s = the row for a given sample (consisting of the ion counts of all metabolites in the given sample).

C_m = the column for a given metabolite (consisting of the ion counts in all samples of the given metabolite).

x_i = the observed peak intensity/ion count of a metabolite 'm' in a sample 's'

x_i^n = the output value of a normalised/transformed/scaled ion count.

The normalisation, transformation, and scaling functions are defined below.[536-538]

Sum normalisation: ***Eq. 7***

$$x_i^n = \frac{x_i}{\sum_{j=1}^{m} x_{ij}}$$

Median normalisation: ***Eq. 8***

$$x_i^n = \frac{x_i}{median(R_s)}$$

Quantile normalisation:

1. For every column (C), rank the ion count values from lowest to highest.
2. Rearrange the ion count values in each column into rank order from lowest to highest.
3. Calculate the new mean of each row in the table. The output mean values will also necessarily be in rank order from lowest to highest.
4. Assign the values of the means from step '3.' to the ion count values of equivalent rank in step '1.'
5. Replace the ion count values in the original table with the assigned mean values. The table is now quantile normalised.

Log transformation: ***Eq. 9***

$$x_i^n = log_{10}(x_i)$$

Square root transformation: ***Eq. 10***

$$x_i^n = \sqrt{(x_i)}$$

Mean Centring: ***Eq. 11***

$$x_i^n = x_i - mean(C_m)$$

Auto scaling: ***Eq. 12***

$$x_i^n = x_i - \frac{mean(C_m)}{\sigma_{C_m}}$$

Pareto scaling: ***Eq. 13***

$$x_i^n = x_i - \frac{mean(C_m)}{\sqrt{\sigma_{C_m}}}$$

6.3.22. Normalised IC-MS Data Heatmaps, Feature Distributions, and Sample Distributions

Normalisation of IC-MS Data from the Treatment of LN18 Cells with 1 and 2

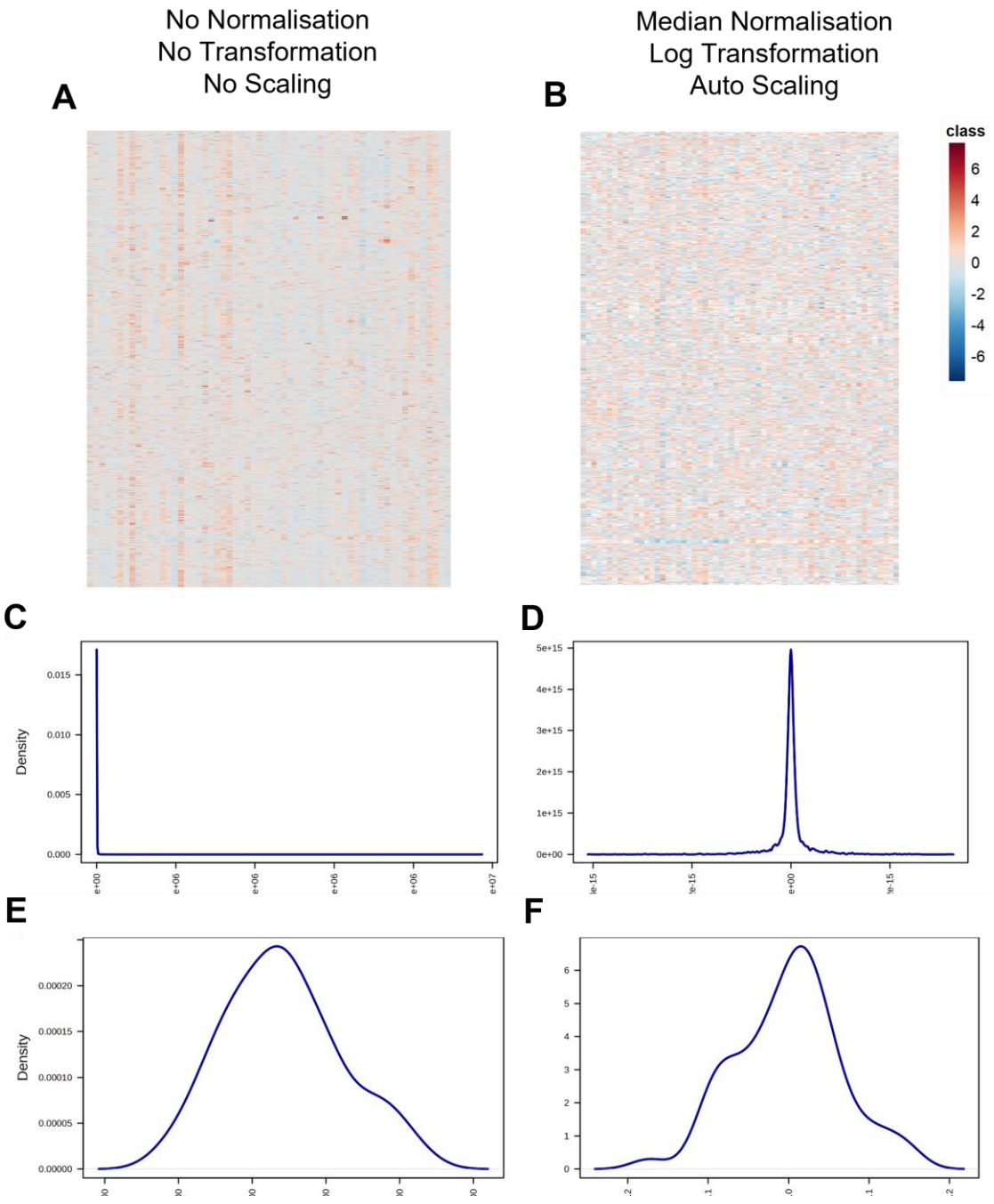

Figure 6.4 *| Heatmap, feature, and sample distribution plots of IC-MS data from IDH1 WT and IDH1 R132H LN18 cells, treated with* ***1*** *or* ***2****. Heatmap before (****A****), and after (****B****), median normalisation with log transformation and auto scaling. Feature distribution before (****C****), and after (****D****), median normalisation with log transformation and auto scaling. Sample distribution before (****E****), and after (****F****), median normalisation*

with log transformation and auto scaling. Normalisation was conducted on the website www.metaboanalyst.ca (version 6.0).

Normalisation of IC-MS Data from the Treatment of LN18 Cells with 3

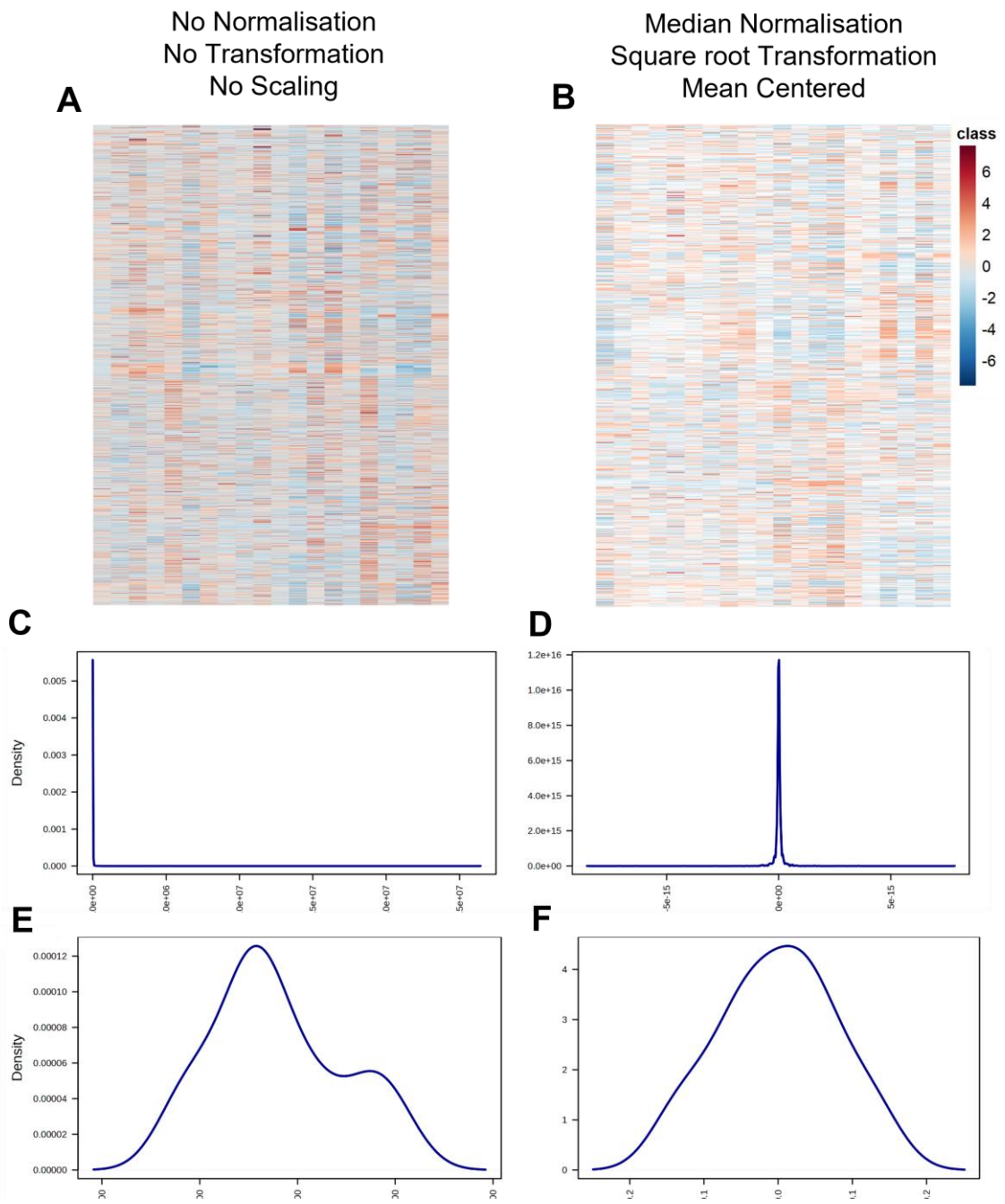

Figure 6.5 *| Heatmap, feature, and sample distribution plots of IC-MS data from IDH1 WT and IDH1 R132H LN18 cells, treated with* ***3****. Heatmap before (****A****), and after (****B****), median normalisation with log transformation and auto scaling. Feature distribution before (****C****), and after (****D****), median normalisation with log transformation and auto scaling. Sample distribution before (****E****), and after (****F****), median normalisation with log transformation and auto scaling. Normalisation was conducted using the website www.metaboanalyst.ca (version 6.0).*

6.3.23. Univariate Statistical Analysis of Processed and Normalised IC-MS Data

Normalised IC-MS data tables were analysed to calculate the relative fold change (FC) and significance of differences between ion abundances in experimental groups. The FC and significance analysis was performed and visualised using the website www.metaboanalyst.ca (version 6.0). FC values for a given feature were calculated for pairwise comparisons of experimental groups by dividing the mean abundances to give a ratio. A substantial difference was defined as FC > 1.2. Significant differences for every feature (n = 2500) were calculated by performing a pairwise t-test between experimental groups with false discovery rate (FDR) correction (FDR adjusted p value cutoff = 0.05).

6.3.24. Multivariate Statistical Analysis of Processed and Normalised IC-MS Data

Normalised, transformed, and scaled IC-MS data tables were used to generate partial least squares-derivative analysis (PLS-DA) models (95% confidence region). PLS-DA models were generated using the website www.metaboanalyst.ca (version 6.0). PLS-DA models were validated by leave-one-out-cross-validation (LOOCV) and permutation testing (2000 permutations, $p < 0.05$). Acceptable LOOCV test statistics were as follows: accuracy > 0.75; R^2 (goodness of fit) > 0.75 (substantial), or 0.50 (moderate), or 0.25 (weak); Q^2 (predictive ability) > 0.8, or $|Q^2 - R^2| < 0.2$).

6.3.25. Metabolite Database

The database used for metabolite identification as described in **Section 3.2** is summarised below (**Table 6.2**). The table includes the 'Human Metabolome Database' (HMDB) ID, compound description, retention time in minutes, neutral mass of the metabolite, and chemical formula.

HMDB ID	Description	RT (min)	Neutral Mass	Formula
N/A	3-[(2,4-Dioxo-1*H*-pyrimidine-6-carbonyl)amino]propanoic acid (DB28)	14.68	227.04690	$C_8H_9N_3O_5$
HMDB0012141	(*R*)-2,3-Dihydroxy-3-methylbutanoate	5.23	134.05790	$C_5H_{10}O_4$
HMDB0060320	(*Z*)-But-1-ene-1,2,4-tricarboxylate	16.88	188.03210	$C_7H_8O_6$
HMDB0013674	1,2,3-Trihydroxybenzene/Pyrogallol	23.21	126.03224	$C_6H_6O_3$
HMDB0000957	1,2-Dihydroxybenzene	25.92	110.03678	$C_6H_6O_2$
HMDB0013593	1,4-Dihydrotheritol	14.86	154.01222	$C_4H_{10}O_2S_2$
HMDB0001213	1-Deoxy-D-xylulose 5-phosphate	10.32	214.02424	$C_5H_{11}O_7P$
N/A	1-Hydroxy-2-methyl-2-butenyl 4-pyrophosphate	16.68	262.00074	$C_5H_{12}O_8P_2$
HMDB0243941	1-Methyl indole	28.33	131.07405	C_9H_9N
N/A	1-Methyl-1*H*-indole-3-carboxamide	33.86	174.07986	$C_{10}H_{10}N_2O$
HMDB0000001	1-Methylhistidine	12.89	169.08513	$C_7H_{11}N_3O_2$
HMDB0001369	1-Pyrroline hydroxycarboxylic acid	4.48	129.04259	$C_5H_7NO_3$
HMDB0001301	1-Pyrroline-5-carboxylic acid	9.37	113.04768	$C_5H_7NO_2$
HMDB0002006	2,3-Diaminopropionic acid	11.75	104.05913	$C_3H_8N_2O_2$
HMDB0001294	2,3-Diphosphoglyceric acid	22.21	265.95927	$C_3H_8O_{10}P_2$
HMDB0062484	2,4-Dihydroxybenzaldehyde	20.55	138.02440	$C_7H_6O_3$
HMDB0125090	2,4,6-Trihydroxybenzaldehyde	24.82	154.01930	$C_7H_6O_4$
HMDB0000152	2,5-Dihydroxybenzoic acid	32.16	154.02661	$C_7H_6O_4$
N/A	2-Amino-5-hydroxybenzoic acid	33.19	153.04314	$C_7H_7NO_3$
HMDB0001123	2-Aminobenzoic acid/Anthranilic acid	25.09	137.04768	$C_7H_7NO_2$
HMDB0001906	2-Aminoisobutyric acid	9.92	103.06333	$C_4H_9NO_2$
HMDB0032059	2-Bromophenol	9.03	171.95293	C_6H_5BrO
N/A	2-Butyl-3-ureido-succinate	11.98	232.10592	$C_9H_{16}N_2O_5$
HMDB0304060	2-*C*-Methyl-D-erythritol-2,4-cyclopyrophosphate	15.28	277.99620	$C_5H_{12}O_9P_2$
HMDB0304061	2-*C*-Methylerythritol 4-phosphate	9.88	214.02424	$C_5H_{13}O_7P$
HMDB0000617	2-Furoate	9.48	112.01600	$C_5H_4O_3$
HMDB0000317	2-Hydroxy-3-methylvaleric acid	7.22	132.07860	$C_6H_{12}O_3$
N/A	2-Hydroxy-4-phenylbutanoic acid	14.39	180.07919	$C_{10}H_{12}O_3$
HMDB0000008	2-Hydroxybutyric acid	5.41	104.04734	$C_4H_8O_3$
HMDB0059655	2-Hydroxyglutarate	10.90	148.03717	$C_5H_8O_5$
HMDB0001624	2-Hydroxyhexanoic acid	11.55	132.07860	$C_6H_{12}O_3$
HMDB0000402	2-Isopropylmalic acid	12.32	176.06847	$C_7H_{12}O_5$

HMDB ID	Description	RT (min)	Neutral Mass	Formula
HMDB0000005	2-Ketobutyric acid	7.86	102.03169	$C_4H_6O_3$
HMDB0000379	2-Methylcitric acid	16.09	206.04320	$C_7H_{10}O_7$
HMDB0000208	2-Oxoglutaric acid	12.85	146.02152	$C_5H_6O_5$
HMDB0000362	2-Phosphoglyceric acid	16.34	185.99294	$C_3H_7O_7P$
HMDB0000397	2-Pyrocatechuic acid	33.01	154.02661	$C_7H_6O_4$
HMDB0002039	2-Pyrrolidinone	13.37	85.05331	C_4H_7NO
HMDB0002441	3,3 Dimethyl glutarate	11.41	160.07356	$C_7H_{12}O_4$
HMDB0012153	3,4,Dihydroxybenzylamine	13.52	139.06388	$C_7H_9NO_2$
HMDB0001336	3,4-Dihydroxyphenyl acetic acid	22.60	168.04226	$C_8H_8O_4$
HMDB0003911	3-Aminoisobutanoic acid	10.32	103.06333	$C_4H_9NO_2$
HMDB0003540	3'-AMP	13.43	347.06254	$C_{10}H_{14}N_5O_7P$
HMDB0012710	3-Dehydroquinate	5.51	190.04774	$C_7H_{10}O_6$
HMDB0001376	3-Deoxy-2-keto-6-phosphogluconic acid	15.93	258.01407	$C_6H_{11}O_9P$
N/A	3-Ethylmalate	10.85	162.05280	$C_6H_{10}O_5$
HMDB0001476	3-Hydroxyanthranilic acid	26.46	153.04314	$C_7H_7NO_3$
HMDB0002466	3-Hydroxybenzoic acid	22.66	138.03224	$C_7H_6O_3$
HMDB0000011	3-Hydroxybutyric acid	5.36	104.04734	$C_4H_8O_3$
HMDB0000023	3-Hydroxyisobutyric acid	5.04	104.04734	$C_4H_8O_3$
HMDB0000754	3-Hydroxyisovaleric acid	5.34	118.06354	$C_5H_{10}O_3$
HMDB0000355	3-Hydroxymethylglutarate	10.76	162.05282	$C_6H_{10}O_5$
HMDB0013188	3-Hydroxypicolinic acid	18.07	139.02694	$C_6H_5NO_3$
HMDB0005784	3-Hydroxytyrosol	15.76	154.06299	$C_8H_{10}O_3$
HMDB0012156	3-Isopropylmalic acid	11.52	176.06850	$C_7H_{12}O_5$
HMDB0059969	3-Methoxyphenylacetic acid	10.04	166.06299	$C_9H_{10}O_3$
HMDB0000491	3-Methyl-2-oxovaleric acid	10.67	130.06299	$C_6H_{10}O_3$
HMDB0001904	3-Nitrotyrosine	8.77	226.05897	$C_9H_{10}N_2O_5$
HMDB0013701	3-Oxoglutarate	11.48	174.05280	$C_7H_{10}O_5$
HMDB0000807	3-Phosphoglyceric acid	15.84	185.99294	$C_3H_7O_7P$
HMDB0061881	4-Acetylbutyrate	5.09	130.06354	$C_6H_{10}O_3$
HMDB0246430	4-Formylbenzoic acid	13.97	150.03169	$C_8H_5O_3$
HMDB0060466	4-Hydroxy-2-oxoglutarate		162.01644	$C_5H_6O_6$
HMDB0000291	4-Hydroxy-3-methoxymandelic acid	15.77	198.05282	$C_9H_{10}O_5$
HMDB0000500	4-Hydroxybenzoic acid	18.86	138.03169	$C_7H_6O_3$
HMDB0000710	4-Hydroxybutyric acid	10.65	104.04734	$C_4H_8O_3$
HMDB0244973	4-Hydroxyphenyl glycine/Oxfenicine	18.59	167.05824	$C_8H_9NO_3$
N/A	4-Hydroxyphenylbutyric acid	17.51	179.07137	$C_{10}H_{12}O_3$
HMDB0000707	4-Hydroxyphenylpyruvic acid	27.88	180.04226	$C_9H_8O_4$
HMDB0000725	4-Hydroxyproline	9.68	131.05824	$C_5H_9NO_3$

HMDB ID	Description	RT (min)	Neutral Mass	Formula
N/A	4-Hydroxypyrrolidinone	2.94	101.04768	$C_4H_7NO_2$
HMDB0001101	4-Methoxybenzoic acid	16.40	152.04730	$C_8H_8O_3$
HMDB0000695	4-Methyl-2-oxovaleric acid (ketoleucine)	9.99	130.06299	$C_6H_{10}O_3$
N/A	4-Methyl-2-ureido-pentanoic acid/Carbamoyl isoleucine	6.36	174.10099	$C_7H_{14}N_2O_3$
HMDB0000873	4-Methylcatechol	29.91	124.05298	$C_7H_8O_2$
HMDB0036619	5,7-Dihydroxyflavone (Chrysin)	4.33	254.05846	$C_{15}H_{10}O_4$
HMDB0001149	5-Aminolevulinic acid	3.89	131.05879	$C_5H_9NO_3$
N/A	5-formyl-2'-deoxyuridine	7.53	256.06954	$C_{10}H_{11}O_6N_2$
N/A	5-Formyl-dCTP	20.45	494.98505	$C_{10}H_{16}N_3O_{14}P_3$
N/A	5-Formylsalicylic acid	19.73	166.02661	$C_8H_5O_4$
N/A	5-Formyluracil	13.36	140.02219	$C_5H_3O_3N_2$
HMDB0000525	5-Hydroxyhexanoic acid	6.83	132.07919	$C_6H_{12}O_3$
HMDB0000763	5-Hydroxyindoleacetic acid	26.83	191.05824	$C_{10}H_9NO_3$
HMDB0246808	5-Hydroxymethyl-2'-deoxyuridine	6.48	258.08500	$C_{10}H_{14}N_2O_6$
N/A	5-Hydroxy-methyl-dCTP	19.40	497.00016	$C_{10}H_{18}N_3O_{14}P_3$
HMDB0001855	5-Hydroxytryptophol	26.62	177.07898	$C_{10}H_{11}NO_2$
HMDB0004096	5-Methoxyindoleacetate	29.66	205.07389	$C_{11}H_{11}NO_3$
N/A	5-Methyl-dCTP	18.96	481.00525	$C_{10}H_{18}N_3O_{13}P_3$
HMDB0038804	6-Hydroxy-2,5,7,8-tetramethylchromane-2-carboxylic acid (Trolox)	29.39	250.12051	$C_{14}H_{18}O_4$
HMDB0001316	6-Phosphogluconic acid	15.18	276.02463	$C_6H_{13}O_{10}P$
HMDB0001127	6-Phosphonoglucono-lactone	11.52	258.01462	$C_6H_{11}O_9P$
HMDB0003333	8-Hydroxy-deoxyguanosine	19.83	283.09167	$C_{10}H_{13}N_5O_5$
HMDB0011615	8-Oxo-dGTP	19.78	522.99011	$C_{10}H_{16}N_5O_{14}P_3$
HMDB0036093	Abscisic acid	11.85	264.13620	$C_{15}H_{20}O_4$
HMDB0000042	Acetic acid	3.85	60.02113	$C_2H_4O_2$
HMDB0000060	Acetoacetate	5.14	102.03169	$C_4H_6O_3$
HMDB0001484	Acetoacetyl-CoA	33.10	851.13634	$C_{25}H_{40}N_7O_{18}P_3S$
N/A	Acetyl-6-formylpterin	15.67	231.05490	$C_7H_4O_2N_5$
HMDB0001206	Acetyl-CoA	7.59	809.12577	$C_{23}H_{38}N_7O_{17}P_3S$
HMDB0001890	Acetylcysteine	11.56	163.03031	$C_5H_9NO_3S$
HMDB0247933	Acetylenedicarboxylic acid	17.10	113.99530	$C_4H_2O_4$
HMDB0000532	Acetylglycine	4.07	117.04259	$C_4H_7NO_3$
HMDB0001494	Acetylphosphate	12.66	139.98801	$C_2H_5O_5P$
HMDB0000034	Adenine	15.32	135.05450	$C_5H_5N_5$
HMDB0011616	Adenosine 2',3'-cyclic phosphate	9.41	329.05197	$C_{10}H_{12}N_5O_6P$
HMDB0001341	Adenosine diphosphate	19.79	427.02941	$C_{10}H_{15}N_5O_{10}P_2$

HMDB ID	Description	RT (min)	Neutral Mass	Formula
HMDB0000045	Adenosine monophosphate (AMP)	13.84	347.06308	$C_{10}H_{14}N_5O_7P$
HMDB0000538	Adenosine triphosphate (ATP)	24.53	506.99575	$C_{10}H_{16}N_5O_{13}P_3$
HMDB0001332	Adenylsuccinate	23.15	463.07404	$C_{14}H_{18}N_5O_{11}P$
HMDB0012882	Adipate semialdehyde	11.34	130.06299	$C_6H_{10}O_3$
HMDB0000508	Adonitol (ribitol)	2.86	152.06847	$C_5H_{12}O_5$
HMDB0006557	ADP Glucose	14.30	589.08224	$C_{16}H_{25}N_5O_{15}P_2$
HMDB0001517	AICAR	12.55	338.06275	$C_9H_{15}N_4O_8P$
HMDB0000462	Allantoin	5.95	158.04454	$C_4H_6N_4O_3$
HMDB0001151	Allose	3.04	180.06339	$C_6H_{12}O_6$
HMDB0000650	α-Aminobutyrate	10.32	103.06333	$C_4H_9NO_2$
HMDB0002166	α-Aminoisobutyrate	10.06	103.06333	$C_4H_9NO_2$
HMDB0000019	α-Ketoisovaleric acid	7.70	116.04734	$C_5H_8O_3$
HMDB0035030	Amygdalin	4.92	457.15840	$C_{20}H_{27}NO_{11}$
HMDB0000539	Arabinonic acid	4.90	166.04774	$C_5H_{10}O_6$
HMDB0029942	Arabinose	3.06	150.05282	$C_5H_{10}O_5$
HMDB0000568	Arabitol	2.71	152.06847	$C_5H_{12}O_5$
HMDB0000044	Ascorbate	12.36	176.03209	$C_6H_8O_6$
HMDB0000191	Aspartate	11.78	133.03751	$C_4H_7NO_4$
N/A	Benzoyl-L-citrulline methyl ester	11.17	293.13810	$C_{14}H_{19}N_3O_4$
HMDB0000056	β-Alanine	4.73	89.04768	$C_3H_7NO_2$
HMDB0013220	β -Citryl-L-glutamic acid	20.62	321.06960	$C_{11}H_{15}NO_{10}$
N/A	Butyl ureidosuccinic acid	10.61	232.10647	$C_9H_{16}N_2O_5$
HMDB0000039	Butyric acid	6.32	88.05243	$C_4H_8O_2$
HMDB0001964	Caffeic acid	29.38	180.04230	$C_9H_8O_4$
HMDB0001847	Caffeine		194.08092	$C_8H_{10}N_4O_2$
HMDB0000535	Caproic acid/Hexanoic acid	8.58	116.08428	$C_6H_{12}O_2$
HMDB0001096	Carbamoyl phosphate	15.06	140.98271	CH_4NO_5P
HMDB0000033	Carnosine	3.93	225.09931	$C_9H_{14}N_4O_3$
HMDB0001564	CDP-ethanolamine	9.60	446.06038	$C_{11}H_{20}N_4O_{11}P_2$
HMDB0003164	Chlorogenic acid		354.09563	$C_{16}H_{18}O_9$
HMDB0011621	Cinnamoylglycine	20.81	205.07334	$C_{11}H_{11}NO_3$
HMDB0000393	*cis*,*cis*-Muconate	12.83	142.02660	$C_6H_6O_4$
HMDB0000072	cis-Aconitic acid	18.12	174.01644	$C_6H_6O_6$
HMDB0001413	Citicoline	3.71	488.10787	$C_{14}H_{26}N_4O_{11}P_2$
HMDB0000634	Citraconic acid	11.96	130.02661	$C_5H_6O_4$
HMDB0000426	Citramalic acid	10.75	148.03717	$C_5H_8O_5$
HMDB0000094	Citric acid	16.91	192.02700	$C_6H_8O_7$
HMDB0000904	Citrulline	4.12	175.09569	$C_6H_{13}N_3O_3$
HMDB0015020	Clomifene	16.22	405.18594	$C_{26}H_{28}ClNO$

HMDB ID	Description	RT (min)	Neutral Mass	Formula
HMDB0001423	Coenzyme A	25.32	767.11521	$C_{21}H_{36}N_7O_{16}P_3S$
HMDB0000058	Cyclic AMP	15.10	329.05252	$C_{10}H_{12}N_5O_6P$
HMDB0001314	Cyclic GMP	24.09	345.04743	$C_{10}H_{12}N_5O_7P$
HMDB0060150	Cysteamine	9.87	77.02992	C_2H_7NS
HMDB0002757	Cysteic acid	12.19	169.00449	$C_3H_7NO_5S$
HMDB0000574	Cysteine	15.66	121.01975	$C_3H_7NO_2S$
HMDB0000089	Cytidine	8.48	243.08607	$C_9H_{13}N_3O_5$
HMDB0001546	Cytidine diphosphate	16.34	403.01763	$C_9H_{15}N_3O_{11}P_2$
HMDB0000095	Cytidine monophosphate	11.78	323.05185	$C_9H_{14}N_3O_8P$
HMDB0001176	Cytidine monophosphate *N*-acetylneuraminic acid	9.79	614.14727	$C_{20}H_{31}N_4O_{16}P$
HMDB0000082	Cytidine triphosphate	21.06	482.98451	$C_9H_{16}N_3O_{14}P_3$
HMDB0000630	Cytosine	5.52	111.04326	$C_4H_5N_3O$
HMDB0001508	dADP	18.27	411.03450	$C_{10}H_{15}N_5O_9P_2$
HMDB0000905	dAMP	12.88	331.06817	$C_{10}H_{14}N_5O_6P$
HMDB0001245	dCDP	30.12	387.02327	$C_9H_{15}N_3O_{10}P_2$
HMDB0001202	dCMP	10.06	307.05694	$C_9H_{14}N_3O_7P$
HMDB0000998	dCTP	19.55	466.98960	$C_9H_{16}N_3O_{13}P_3$
N/A	Dehydrocholic acid		401.23335	$C_{24}H_{34}O_5$
HMDB0000101	Deoxyadenosine	12.14	251.10184	$C_{10}H_{13}N_5O_3$
HMDB0001532	Deoxyadenosine triphosphate	24.33	491.00083	$C_{10}H_{16}N_5O_{12}P_3$
HMDB0000014	Deoxycytidine	4.69	227.09115	$C_9H_{13}N_3O_4$
HMDB0000085	Deoxyguanosine	4.08	283.09222	$C_{10}H_{13}N_5O_4$
HMDB0001031	Deoxyribose 5-phosphate	11.06	214.02424	$C_5H_{11}O_7P$
HMDB0246094	Deoxythymidine	7.67	225.08808	$C_{10}H_{14}N_2O_4$
HMDB0000012	Deoxyuridine	7.62	228.07462	$C_9H_{12}N_2O_5$
HMDB0062739	D-Erythro-3-Methylmalate	10.68	148.03720	$C_5H_8O_5$
HMDB0000960	dGDP	24.67	427.02941	$C_{10}H_{15}N_5O_{10}P_2$
HMDB0001044	dGMP	20.57	347.06308	$C_{10}H_{14}N_5O_7P$
HMDB0001440	dGTP	29.43	506.99520	$C_{10}H_{16}N_5O_{13}P_3$
N/A	Diaminocyclohexane-*N*,*N*,*N*′,*N*′-tetraacetic acid (DCTA)	8.92	345.13034	$C_{14}H_{22}N_2O_8$
HMDB0014724	Diclofenac	1.22	295.01614	$C_{14}H_{11}Cl_2NO_2$
HMDB0003349	Dihydroorotic acid	11.63	158.03276	$C_5H_6N_2O_4$
HMDB0000076	Dihydrouracil	13.43	114.04238	$C_4H_6N_2O_2$
HMDB0001882	Dihydroxyacetone	4.74	90.03169	$C_3H_6O_3$
HMDB0001473	Dihydroxyacetone phosphate	11.36	169.99800	$C_3H_7O_6P$
HMDB0000181	Dihydroxyphenylalanine (L-DOPA)	32.44	197.06881	$C_9H_{11}NO_4$
HMDB0031257	Dimethyl fumarate	13.16	144.04226	$C_6H_8O_4$
HMDB0001120	Dimethylallyl pyrophosphate	18.73	246.00583	$C_5H_{12}O_7P_2$

HMDB ID	Description	RT (min)	Neutral Mass	Formula
HMDB0000092	Dimethylglycine	10.15	103.06333	$C_4H_9NO_2$
HMDB0006555	dIMP	18.99	332.05219	$C_{10}H_{13}N_4O_7P$
N/A	DL-Threo-β-Hydroxyaspartic acid	10.43	148.02515	$C_4H_7NO_5$
HMDB0000073	Dopamine	19.68	153.07898	$C_8H_{11}NO_2$
HMDB0001328	dTDP-D-glucose	17.06	564.07576	$C_{16}H_{26}N_2O_{16}P_2$
HMDB0001000	dUDP	19.60	388.00728	$C_9H_{14}N_2O_{11}P_2$
HMDB0001409	dUMP	17.10	308.04095	$C_9H_{13}N_2O_8P$
HMDB0001191	dUTP	25.45	467.97361	$C_9H_{15}N_2O_{14}P_3$
HMDB0015109	EDTA	10.83	292.09067	$C_{10}H_{16}N_2O_8$
HMDB0000900	Ergocalciferol	4.21	396.33867	$C_{28}H_{44}O$
HMDB0000878	Ergosterol	1.13	396.33867	$C_{28}H_{44}O$
HMDB0001321	Erythrose 4-phosphate	12.91	200.00859	$C_4H_9O_7P$
N/A	Ethionine	33.54	163.06725	$C_6H_{13}NO_2S$
HMDB0000622	Ethylmalonic acid	11.62	132.04226	$C_5H_8O_4$
HMDB0001248	FAD	23.00	785.15713	$C_{27}H_{33}N_9O_{15}P_2$
HMDB0000954	Ferulic acid	27.02	194.05791	$C_{10}H_{10}O_4$
HMDB0014684	Fluorouracil	13.57	130.01786	$C_4H_3FN_2O_2$
HMDB0014615	Fluoxetine	21.52	309.13460	$C_{17}H_{18}F_3NO$
HMDB0000660	Fructose	3.06	180.06339	$C_6H_{12}O_6$
HMDB0001058	Fructose 1,6-bisphosphate	20.44	339.99605	$C_6H_{14}O_{12}P_2$
HMDB0001047	Fructose 2,6 diphosphate	17.52	339.99605	$C_6H_{14}O_{12}P_2$
HMDB0000124	Fructose 6-phosphate	11.88	260.02972	$C_6H_{13}O_9P$
HMDB0000134	Fumarate	13.63	116.01096	$C_4H_4O_4$
HMDB0000639	Galactaric acid (mucic acid)	10.94	210.03757	$C_6H_{10}O_8$
HMDB0000143	Galactose	3.02	180.06339	$C_6H_{12}O_6$
HMDB0000645	Galactose 1-phosphate	9.39	260.02972	$C_6H_{13}O_9P$
N/A	Galactose-6-phosphate	11.77	260.02917	$C_6H_{13}O_9P$
HMDB0002545	Galacturonic acid	6.51	194.04270	$C_6H_{10}O_7$
HMDB0005807	Gallic acid	29.59	170.02150	$C_7H_6O_5$
HMDB0013233	γ-δ-Dioxovaleric acid	10.65	130.02661	$C_5H_6O_4$
HMDB0003559	Gibberellin A3	12.68	346.14164	$C_{19}H_{22}O_6$
HMDB0000625	Gluconate	4.67	196.05830	$C_6H_{12}O_7$
HMDB0000150	Gluconolactone	4.71	178.04774	$C_6H_{10}O_6$
HMDB0001514	Glucosamine	11.58	179.07937	$C_6H_{13}NO_5$
HMDB0001254	Glucosamine 6-phosphate	13.18	259.04570	$C_6H_{14}NO_8P$
HMDB0000122	Glucose	3.43	180.06339	$C_6H_{12}O_6$
HMDB0001586	Glucose 1-phosphate	9.66	260.02972	$C_6H_{13}O_9P$
HMDB0001401	Glucose 6-phosphate	12.38	260.02972	$C_6H_{13}O_9P$
HMDB0000127	Glucuronic acid	8.27	194.04265	$C_6H_{10}O_7$

HMDB ID	Description	RT (min)	Neutral Mass	Formula
HMDB0000620	Glutaconic acid	12.69	130.02661	$C_5H_6O_4$
HMDB0000148	Glutamic acid	14.79	147.05316	$C_5H_9NO_4$
HMDB0000641	Glutamine	11.67	146.06914	$C_5H_{10}N_2O_3$
HMDB0001049	Glutamylcysteine	16.61	250.06289	$C_8H_{14}N_2O_5S$
HMDB0000661	Glutaric acid	10.87	132.04226	$C_5H_8O_4$
HMDB0001339	Glutaryl CoA	19.81	881.14690	$C_{26}H_{42}N_7O_{19}P_3S$
HMDB0000125	Glutathione (GSH)	15.16	307.08381	$C_{10}H_{17}N_3O_6S$
HMDB0001112	Glyceraldehyde 3-phosphate	11.73	169.99802	$C_3H_7O_6P$
HMDB0000139	Glyceric acid	5.23	106.02661	$C_3H_6O_4$
HMDB0000131	Glycerol	2.86	92.04734	$C_3H_8O_3$
HMDB0000126	Glycerol 3-phosphate	9.79	172.01367	$C_3H_9O_6P$
HMDB0003344	Glycoaldehyde	7.52	60.02113	$C_2H_4O_2$
HMDB0000115	Glycolic acid	4.74	76.01600	$C_2H_4O_3$
HMDB0000119	Glyoxylic acid	8.05	74.00039	$C_2H_2O_3$
HMDB0000370	Glyphosate/2-Amino-3-phosphonopropionic acid	14.56	169.01456	$C_3H_8NO_5P$
HMDB0000133	Guanosine	22.22	283.09167	$C_{10}H_{13}N_5O_5$
HMDB0001201	Guanosine diphosphate (GDP)	27.56	443.02378	$C_{10}H_{15}N_5O_{11}P_2$
HMDB0001397	Guanosine monophosphate	22.22	363.05800	$C_{10}H_{14}N_5O_8P$
HMDB0001273	Guanosine triphosphate	30.62	522.99066	$C_{10}H_{16}N_5O_{14}P_3$
HMDB0003466	Gulono-1,4-lactone	4.37	178.04770	$C_6H_{10}O_6$
HMDB0012326	Gulose	3.05	180.06339	$C_6H_{12}O_6$
HMDB0030311	Harmine		212.09551	$C_{13}H_{12}N_2O$
HMDB0005782	Hesperitin	28.50	302.07849	$C_{16}H_{14}O_6$
HMDB0000714	Hippuric acid	11.63	179.05824	$C_9H_9NO_3$
HMDB0000870	Histamine	7.08	111.08020	$C_5H_9N_3$
N/A	Homarine	11.66	137.04768	$C_7H_7NO_2$
HMDB0000130	Homogentisic acid	17.49	168.04226	$C_8H_8O_4$
HMDB0000118	Homovanillic acid	17.21	182.05791	$C_9H_{10}O_4$
HMDB0001212	Hydantoin-5-propionic acid	11.40	172.04786	$C_6H_8N_2O_4$
HMDB0000764	Hydrocinnamic acid	15.63	150.06863	$C_9H_{10}O_2$
HMDB0000528	Hydroorotic acid	10.36	158.03276	$C_5H_6N_2O_4$
HMDB0000023	Hydroxy-isobutyric acid	4.46	104.04734	$C_4H_7O_3$
HMDB0002207	Hydroxyisoheptanoic acid	9.74	146.09484	$C_7H_{14}O_3$
HMDB0000732	Hydroxykynurenine	13.91	224.08026	$C_{10}H_{12}N_2O_4$
N/A	Hydroxy-methyl-dUTP	20.48	497.98418	$C_{10}H_{17}N_2O_{15}P_3$
HMDB0000711	Hydroxyoctanoic acid	7.52	160.11049	$C_8H_{16}O_3$
HMDB0000700	Hydroxypropionic acid	4.88	90.03224	$C_3H_6O_3$
HMDB0001352	Hydroxypyruvic acid	11.64	104.01096	$C_3H_4O_4$
HMDB0000965	Hypotaurine	14.89	109.01975	$C_2H_7NO_2S$

HMDB ID	Description	RT (min)	Neutral Mass	Formula
HMDB0000157	Hypoxanthine	21.34	136.03851	$C_5H_4N_4O$
HMDB0011140	Hypusine	9.42	233.17449	$C_{10}H_{23}N_3O_3$
HMDB0003335	IDP	26.55	428.01343	$C_{10}H_{14}N_4O_{11}P_2$
HMDB0001190	Indole-3-acetaldehyde	27.44	159.06841	$C_{10}H_9NO$
HMDB0000671	Indole-3-lactic acid	27.23	205.07389	$C_{11}H_{11}NO_3$
HMDB0000197	Indoleacetic acid	28.43	175.06333	$C_{10}H_9NO_2$
HMDB0000195	Inosine	5.60	268.08077	$C_{10}H_{12}N_4O_5$
HMDB0000175	Inosine monophosphate	21.97	348.04710	$C_{10}H_{13}N_4O_8P$
HMDB0000189	Inosine triphosphate	30.13	507.97976	$C_{10}H_{15}N_4O_{14}P_3$
HMDB0001143	Inositol 1,3,4-trisphosphate	25.85	419.96238	$C_6H_{15}O_{15}P_3$
HMDB0000193	Isocitrate	17.55	192.02700	$C_6H_8O_7$
HMDB0001347	Isopentenyl pyrophosphate	18.45	246.00583	$C_5H_{12}O_7P_2$
HMDB0000718	Isovaleric Acid	9.43	102.06863	$C_5H_{10}O_2$
HMDB0000678	Isovalerylglycine	6.07	159.08954	$C_7H_{13}NO_3$
HMDB0002092	Itaconic acid	12.13	130.02661	$C_5H_6O_4$
HMDB0032797	Jasmonic acid	12.22	210.12559	$C_{12}H_{18}O_3$
HMDB0032923	Kojic acid	8.81	142.02661	$C_6H_6O_4$
HMDB0000715	Kynurenic acid	27.57	189.04259	$C_{10}H_7NO_3$
HMDB0000684	Kynurenine	8.81	208.08479	$C_{10}H_{12}N_2O_3$
HMDB0000190	Lactic acid	5.05	90.03169	$C_3H_6O_3$
HMDB0000186	Lactose	3.04	342.11676	$C_{12}H_{22}O_{11}$
HMDB0062180	Lactoyl-isoleucine	7.02	203.11631	$C_9H_{17}NO_4$
HMDB0240656	Lanthionine	33.00	208.05233	$C_6H_{12}N_2O_4S$
HMDB0004823	Lanthionine ketimine	30.82	189.01013	$C_6H_7NO_4S$
HMDB0000624	Leucic acid	7.51	132.07919	$C_6H_{12}O_3$
HMDB0254310	Maleamate	5.61	115.02690	$C_4H_5NO_3$
HMDB0000176	Maleic acid	12.43	116.01096	$C_4H_4O_4$
HMDB0000744	Malic acid	10.00	134.02150	$C_4H_6O_5$
HMDB0002928	Malitol	3.08	344.13186	$C_{12}H_{24}O_{11}$
HMDB0006112	Malondialdehyde	8.86	72.02113	$C_3H_4O_2$
HMDB0000691	Malonic acid	11.08	104.01100	$C_3H_4O_4$
N/A	maltose-1-phosphate	8.97	422.27640	$C_{12}H_{22}O_{14}P$
HMDB0060486	Mandelonitrile	29.49	133.05276	C_8H_7NO
HMDB0000765	Mannitol	2.76	182.07904	$C_6H_{14}O_6$
HMDB0000169	Mannose	3.14	180.06339	$C_6H_{12}O_6$
HMDB0001078	Mannose 6-phosphate	12.73	260.02972	$C_6H_{13}O_9P$
HMDB0001892	Menadione	11.43	172.05298	$C_{11}H_8O_2$
HMDB0000749	Mesaconic acid	12.51	130.02661	$C_5H_6O_4$
HMDB0002005	Methionine sulfoxide		165.04596	$C_5H_{11}NO_3S$
HMDB0029965	Methyl β-D-glucopyranoside	2.74	194.07904	$C_7H_{14}O_6$

HMDB ID	Description	RT (min)	Neutral Mass	Formula
HMDB0001167	Methyl glyoxal/Pyruvaldehyde	4.89	72.02168	$C_3H_4O_2$
HMDB0032617	Methyl phenylacetate	14.11	150.06863	$C_9H_{10}O_2$
N/A	Methyl-3-hydroxybenzoic acid	28.57	152.04789	$C_8H_8O_3$
HMDB0004815	Methyl-4-hydroxybenzoic acid	32.63	152.04789	$C_8H_8O_3$
HMDB0000752	Methylglutaric acid	10.73	146.05791	$C_6H_{10}O_4$
HMDB0006471	Methylisocitric acid	15.82	206.04265	$C_7H_{10}O_7$
HMDB0032572	Methylparaben	17.77	152.04734	$C_8H_8O_3$
HMDB0000227	Mevalonic acid	15.14	148.07356	$C_6H_{12}O_4$
HMDB0001343	Mevalonic acid-5P	14.84	228.03989	$C_6H_{13}O_7P$
N/A	Mildronate	1.20	146.10498	$C_6H_4N_2O_2$
HMDB0000211	Myoinositol	2.81	180.06339	$C_6H_{12}O_6$
HMDB0003502	Myo-inositol hexakisphosphate/Phytic Acid	24.31	659.86192	$C_6H_{18}O_{24}P_6$
HMDB0039002	Mytilin A	3.67	332.12251	$C_{13}H_{20}N_2O_8$
HMDB0033442	Mytilin B	3.50	346.13816	$C_{14}H_{22}N_2O_8$
HMDB0033816	Mytilitol	2.58	194.07959	$C_7H_{14}O_6$
N/A	*N*-Acetyl cytosine	8.13	153.05437	$C_6H_7N_3O_2$
HMDB0003357	*N*-Acetyl ornithine	8.73	174.10044	$C_7H_{14}N_2O_3$
HMDB0094701	*N*-Acetyl proline	4.42	157.07444	$C_7H_{11}NO_3$
HMDB0000812	*N*-Acetyl-aspartate	10.03	175.04807	$C_6H_9NO_5$
HMDB0001067	*N*-Acetylaspartylglutamic acid	14.40	304.09067	$C_{11}H_{16}N_2O_8$
HMDB0000215	*N*-Acetyl-D-glucosamine	3.02	221.08994	$C_8H_{15}NO_6$
HMDB0001062	*N*-Acetyl-D-Glucosamine 6-Phosphate	12.41	301.05627	$C_8H_{16}NO_9P$
HMDB0001121	*N*-Acetyl-D-mannosamine 6-phosphate (ManNac-6-P)	12.11	301.05627	$C_8H_{16}NO_9P$
HMDB0001367	*N*-acetyl-glucosamine-1-phosphate	11.66	301.05627	$C_8H_{16}NO_9P$
HMDB0001138	*N*-Acetylglutamate	9.84	189.06427	$C_7H_{11}NO_5$
HMDB0000766	*N*-Acetyl-L-alanine	4.23	131.05824	$C_5H_9NO_3$
HMDB0006488	*N*-Acetyl-L-glutamate 5-semialdehyde	13.97	173.06881	$C_7H_{11}NO_4$
HMDB0006456	*N*-Acetyl-L-glutamyl 5-phosphate		269.03005	$C_7H_{12}NO_8P$
HMDB0011745	*N*-Acetyl-L-methionine	5.91	191.06161	$C_7H_{13}NO_3S$
HMDB0000512	*N*-Acetyl-L-phenylalanine	8.89	207.08954	$C_{11}H_{13}NO_3$
HMDB0001129	*N*-Acetylmannosamine (ManNac)	5.39	221.08994	$C_8H_{15}NO_6$
HMDB0006268	*N*-Acetylneuraminate 9-phosphate	13.98	389.07231	$C_{11}H_{20}NO_{12}P$
HMDB0000230	*N*-acetylneuraminic acid	4.63	309.10600	$C_{11}H_{19}NO_9$
HMDB0013713	*N*-Acetyltryptophan	18.41	246.10044	$C_{13}H_{14}N_2O_3$
HMDB0011757	*N*-Acetylvaline	4.83	159.08954	$C_7H_{13}NO_3$

HMDB ID	Description	RT (min)	Neutral Mass	Formula
HMDB0000902	NAD^+	9.94	663.10912	$C_{21}H_{27}N_7O_{14}P_2$
HMDB0001487	NADH	17.00	665.12477	$C_{21}H_{29}N_7O_{14}P_2$
HMDB0000217	$NADP^+$	16.43	743.07545	$C_{21}H_{28}N_7O_{17}P_3$
HMDB0000221	NADPH	21.37	745.09110	$C_{21}H_{30}N_7O_{17}P_3$
HMDB0002670	Naringenin		272.06902	$C_{15}H_{12}O_5$
HMDB0013287	Ne,Ne dimethyllysine	3.79	174.13683	$C_8H_{18}N_2O_2$
N/A	*N*-Formyl-DL-ethionine	7.53	191.06216	$C_7H_{13}NO_3S$
HMDB0001200	*N*-Formylkynurenine	22.44	236.08026	$C_{11}H_{12}N_2O_4$
HMDB0001015	*N*-Formyl-methionine	6.73	177.04596	$C_6H_{11}NO_3S$
HMDB0001406	Nicotinamide	24.05	122.04801	$C_6H_6N_2O$
HMDB0341363	Nicotinic Acid *N*-Oxide	5.94	139.02694	$C_6H_5NO_3$
HMDB0002393	*N*-Methyl-D-aspartic acid	10.06	147.05316	$C_5H_9NO_4$
HMDB0011717	Nonate	13.85	188.10541	$C_9H_{16}O_4$
HMDB0013716	Norvaline	33.46	117.07953	$C_5H_{11}NO_2$
HMDB0255221	*N*-Oxalylglycine	12.59	147.01680	$C_4H_5NO_5$
HMDB0003011	*O*-Acetylserine	4.36	147.05316	$C_5H_9NO_4$
HMDB0000482	Octanoic acid	19.95	144.11503	$C_8H_{16}O_2$
HMDB0001721	*O*-Phosphoserine	13.70	185.00892	$C_3H_8NO_6P$
HMDB0005765	Ophthalmic Acid	8.51	289.12793	$C_{11}H_{19}N_3O_6$
HMDB0000226	Orotic acid	16.58	156.01711	$C_5H_4N_2O_4$
HMDB0000788	Orotidine	16.11	288.05882	$C_{10}H_{12}N_2O_8$
HMDB0000218	Orotidylic acid/OMP	9.67	368.02624	$C_{10}H_{13}N_2O_{11}P$
HMDB0000223	Oxalacetic acid	10.30	132.00587	$C_4H_4O_5$
HMDB0002329	Oxalic acid	13.40	89.99531	$C_2H_2O_4$
HMDB0000225	Oxoadipic acid	13.08	160.03717	$C_6H_8O_5$
HMDB0001865	Oxovaleric Acid	7.56	116.04789	$C_5H_8O_3$
HMDB0014733	Oxytetracylcine	29.58	460.14818	$C_{22}H_{24}N_2O_9$
HMDB0240389	Pantoic acid	5.56	148.07360	$C_6H_{12}O_4$
HMDB0000210	Pantothenic acid	5.00	219.11067	$C_9H_{17}NO_5$
HMDB0062802	Parabanic Acid/Oxalylyurea	8.17	114.00599	$C_3H_2N_2O_3$
HMDB0002035	*p*-Coumaric acid	29.16	164.04734	$C_9H_8O_3$
HMDB0015050	Phenformin	14.07	241.10997	$C_{10}H_{16}ClN_5$
HMDB0040733	Phenylacetic Acid	13.28	136.05298	$C_8H_8O_2$
HMDB0000821	Phenylacetylglycine/Phenaceturic acid	9.23	193.07444	$C_{10}H_{11}NO_3$
HMDB0000205	Phenylpyruvic acid	30.55	164.04734	$C_9H_8O_3$
HMDB0001511	Phosphocreatine	8.56	211.03636	$C_4H_{10}N_3O_5P$
HMDB0000263	Phosphoenolpyruvic acid	17.96	167.98237	$C_3H_5O_6P$
HMDB0000816	Phosphoglycolic acid	16.32	155.98237	$C_2H_5O_6P$
HMDB0000280	Phosphoribosyl pyrophosphate (PRPP)	22.27	389.95181	$C_5H_{13}O_{14}P_3$

HMDB ID	Description	RT (min)	Neutral Mass	Formula
HMDB0002107	Phthalate	16.51	166.02660	$C_8H_6O_4$
HMDB0000020	*p*-Hydroxyphenylacetic acid	16.97	152.04789	$C_8H_8O_3$
HMDB0000774	Pregnenolone sulfate	21.87	396.19759	$C_{21}H_{32}O_5S$
HMDB0012283	Prephenic Acid	11.47	226.04774	$C_{10}H_{10}O_6$
HMDB0015169	Procainamide	21.97	235.16846	$C_{13}H_{21}N_3O$
HMDB0000237	Propionic acid	5.69	74.03733	$C_3H_6O_2$
HMDB0001275	Propionyl-CoA	10.52	823.14197	$C_{24}H_{40}N_7O_{17}P_3S$
HMDB0000783	Propionyl-glycine	4.27	131.05824	$C_5H_9NO_3$
HMDB0001856	Protocatechuic acid	25.29	154.02661	$C_7H_6O_4$
HMDB0001491	Pyridoxal 5'-phosphate	18.50	247.02457	$C_8H_{10}NO_6P$
HMDB0001431	Pyridoxamine	6.71	168.08988	$C_8H_{12}N_2O_2$
HMDB0000267	Pyroglutamic acid	4.49	129.04314	$C_5H_7NO_3$
HMDB0000243	Pyruvic acid	6.80	88.01604	$C_3H_4O_3$
HMDB0005794	Quercetin	28.65	302.04210	$C_{15}H_{10}O_7$
HMDB0003072	Quinic acid	4.74	192.06339	$C_7H_{12}O_6$
HMDB0000232	Quinolinic acid	13.74	167.02186	$C_7H_5NO_4$
N/A	Quisqualic acid	14.33	189.03912	$C_5H_7N_3O_5$
HMDB0003213	Raffinose	2.80	504.16904	$C_{18}H_{32}O_{16}$
HMDB0001852	Retinoic acid	8.39	300.20948	$C_{20}H_{28}O_2$
HMDB0000244	Riboflavin	24.51	376.13828	$C_{17}H_{20}N_4O_6$
HMDB0000283	Ribose	3.17	150.05282	$C_5H_{10}O_5$
HMDB0001548	Ribose 5-phosphate	13.19	230.01915	$C_5H_{11}O_8P$
HMDB0000621	Ribulose	3.51	150.05282	$C_5H_{10}O_5$
HMDB0011688	Ribulose 1,5,diphosphate	19.79	309.98603	$C_5H_{12}O_{11}P_2$
HMDB0000618	Ribulose 5-phosphate	9.67	230.01915	$C_5H_{11}O_8P$
HMDB0000663	Saccharic acid	12.05	210.03757	$C_6H_{10}O_8$
HMDB0000279	Saccharopine	13.56	276.13214	$C_{11}H_{20}N_2O_6$
HMDB0001185	*S*-adenosyl methionine	8.71	399.14506	$C_{15}H_{23}N_6O_5S$
HMDB0001895	Salicylic acid	32.17	138.03224	$C_7H_6O_3$
HMDB0006088	Scyllitol	2.67	180.06339	$C_6H_{12}O_6$
HMDB0000792	Sebacic acid	18.30	202.12051	$C_{10}H_{18}O_4$
HMDB0060274	Sedoheptulose 1,7-bisphosphate	19.08	370.00661	$C_7H_{16}O_{13}P_2$
HMDB0060509	Sedoheptulose 1-phosphate	10.74	290.04028	$C_7H_{15}O_{10}P$
HMDB0001068	Sedoheptulose 7-phosphate	13.21	290.04028	$C_7H_{15}O_{10}P$
HMDB0003070	Shikimic acid	5.13	174.05282	$C_7H_{10}O_5$
HMDB0032616	Sinapic acid	25.12	224.06847	$C_{11}H_{12}O_5$
HMDB0000247	Sorbitol	2.77	182.07904	$C_6H_{14}O_6$
HMDB0005831	Sorbitol-6-phosphate	9.23	262.04537	$C_6H_{15}O_9P$
HMDB0001266	Sorbose	3.06	180.06339	$C_6H_{12}O_6$
HMDB0006797	Sorbose 1-phosphate	11.96	260.02917	$C_6H_{13}O_9P$

HMDB ID	Description	RT (min)	Neutral Mass	Formula
HMDB0000254	Succinic acid	11.11	118.02661	$C_4H_6O_4$
HMDB0001259	Succinic semialdehyde	5.37	102.03169	$C_4H_6O_3$
HMDB0255868	Succinyl-Homoserine	9.41	219.07400	$C_8H_{13}NO_6$
N/A	sucrose-6'-phosphate	9.45	422.27640	$C_{12}H_{22}O_{14}P$
HMDB0002085	Syringic acid	17.50	198.05282	$C_9H_{10}O_5$
HMDB0029416	Targinine	33.55	188.12787	$C_7H_{16}N_4O_2$
HMDB0000956	Tartaric acid	11.04	150.01640	$C_4H_6O_6$
HMDB0000251	Taurine	5.14	125.01466	$C_2H_7NO_3S$
HMDB0001274	TDP	21.72	402.02293	$C_{10}H_{16}N_2O_{11}P_2$
HMDB0000234	Testosterone	27.34	288.20948	$C_{19}H_{28}O_2$
HMDB0003193	Testosterone glucuronide	8.06	464.24047	$C_{25}H_{36}O_8$
HMDB0002833	Testosterone sulfate	18.09	368.16629	$C_{19}H_{28}O_5S$
HMDB0014897	Tetracycline	20.98	444.15272	$C_{22}H_{24}N_2O_8$
HMDB0002825	Theobromine	17.74	180.06418	$C_7H_8N_4O_2$
HMDB0029178	Thialysine	33.42	164.06250	$C_5H_{12}N_2O_2S$
HMDB0002666	Thiamine monophosphate		344.07026	$C_{12}H_{17}N_4O_4PS$
HMDB0001372	Thiamine pyrophosphate	25.64	425.04497	$C_{12}H_{19}N_4O_7P_2S$
HMDB0004136	Threitol	2.78	122.05791	$C_4H_{10}O_4$
HMDB0001227	Thymidine 5'-phosphate (TMP)	16.77	322.05660	$C_{10}H_{15}N_2O_8P$
HMDB0001342	Thymidine triphosphate	25.42	481.98926	$C_{10}H_{17}N_2O_{14}P_3$
HMDB0000262	Thymine	9.90	126.04293	$C_5H_6N_2O_2$
HMDB0015256	Tolbutamide	15.08	270.10436	$C_{12}H_{18}N_2O_3S$
HMDB0029635	Toluate	20.64	136.05240	$C_8H_8O_2$
N/A	*trans*-2,3-Epoxysuccinic acid	12.02	132.00590	$C_4H_4O_5$
HMDB0000930	*trans*-Cinnamic acid	24.51	148.05243	$C_9H_8O_2$
HMDB0062562	*trans*-Urocanate	18.19	137.03565	$C_6H_5N_2O_2$
HMDB0001124	Trehalose-6-phosphate	8.59	422.27640	$C_{12}H_{22}O_{14}P$
HMDB0062590	Tropic acid	9.33	166.06300	$C_9H_{10}O_3$
HMDB0000303	Tryptamine		160.10060	$C_{10}H_{12}N_2$
HMDB0004284	Tyrosol	17.77	138.06808	$C_8H_{10}O_2$
HMDB0000302	UDP-galactose	18.00	566.05502	$C_{15}H_{24}N_2O_{17}P_2$
HMDB0000935	UDP-glucoronate	24.31	580.03428	$C_{15}H_{22}N_2O_{18}P_2$
HMDB0000286	UDP-glucose	18.40	566.05502	$C_{15}H_{24}N_2O_{17}P_2$
HMDB0013112	UDP-*N*-acetyl-D-mannosamine		607.08157	$C_{17}H_{27}N_3O_{17}P_2$
HMDB0000300	Uracil	8.92	112.02728	$C_4H_4N_2O_2$
HMDB0000026	Ureidopropionic acid	4.46	132.05404	$C_4H_8N_2O_3$
HMDB0000828	Ureidosuccinic acid (*N*-carbamoyl-L-aspartic acid)	10.86	176.04332	$C_5H_8N_2O_5$
HMDB0000289	Uric acid	19.45	168.02834	$C_5H_4N_4O_3$
HMDB0000296	Uridine	9.04	244.06954	$C_9H_{12}N_2O_6$

HMDB ID	Description	RT (min)	Neutral Mass	Formula
HMDB0000295	Uridine 5'-diphosphate	23.85	404.00220	$C_9H_{14}N_2O_{12}P_2$
HMDB0000288	Uridine 5'-monophosphate	18.60	324.03587	$C_9H_{13}N_2O_9P$
HMDB0000290	Uridine diphosphate-*N*-acetylglucosamine	17.77	607.08157	$C_{17}H_{27}N_3O_{17}P_2$
HMDB0000285	Uridine triphosphate	23.43	483.96853	$C_9H_{15}N_2O_{15}P_3$
HMDB0000892	Valeric Acid	9.65	102.06863	$C_5H_{10}O_2$
HMDB0012308	Vanillin		152.04789	$C_8H_8O_3$
HMDB0001554	Xanthylic acid	20.70	364.04256	$C_{10}H_{13}N_4O_9P$
HMDB0002917	Xylitol	2.79	152.06847	$C_5H_{12}O_5$
HMDB0001644	Xylulose	3.64	150.05282	$C_5H_{10}O_5$
HMDB0000868	Xylulose 5-phosphate	13.16	230.01915	$C_5H_{11}O_8P$
HMDB0015464	Yohimbine	26.07	354.19489	$C_{21}H_{26}N_2O_3$

Table 6.2 | *A Summary of the metabolite database used to assign features in the IC-MS data. Compound information includes the HMDB ID, metabolite description, retention time (rt) in minutes, neutral mass, and chemical formula.*

7. References

(1) Hanahan, D.; Weinberg, Robert A. Hallmarks of Cancer: The Next Generation. *Cell* **2011**, *144*, 646-674. DOI: 10.1016/j.cell.2011.02.013.

(2) Hanahan, D.; Weinberg, R. A. The Hallmarks of Cancer. *Cell* **2000**, *100*, 57-70. DOI: 10.1016/S0092-8674(00)81683-9.

(3) Schmidt, C.; Sciacovelli, M.; Frezza, C. Fumarate hydratase in cancer: A multifaceted tumour suppressor. *Semin. Cell Dev. Biol.* **2020**, *98*, 15-25. DOI: 10.1016/j.semcdb.2019.05.002.

(4) Warburg, O. On respiratory impairment in cancer cells. *Science* **1956**, *124*, 269-270. DOI: 10.1126/science.124.3215.269.

(5) Warburg, O. On the origin of cancer cells. *Science* **1956**, *123*, 309-314. DOI: 10.1126/science.123.3191.309.

(6) Fouad, Y. A.; Aanei, C. Revisiting the hallmarks of cancer. *Am. J. Cancer. Res.* **2017**, *7*, 1016-1036.

(7) DeBerardinis, R. J.; Chandel, N. S. Fundamentals of cancer metabolism. *Sci. Adv.* **2016**, *2*, e1600200. DOI: 10.1126/sciadv.1600200.

(8) Jones, R. G.; Thompson, C. B. Tumor suppressors and cell metabolism: a recipe for cancer growth. *Genes Dev.* **2009**, *23*, 537-548. DOI: 10.1101/gad.1756509.

(9) Hsu, P. P.; Sabatini, D. M. Cancer cell metabolism: Warburg and beyond. *Cell* **2008**, *134*, 703-707. DOI: 10.1016/j.cell.2008.08.021.

(10) DeBerardinis, R. J.; Lum, J. J.; Hatzivassiliou, G.; Thompson, C. B. The biology of cancer: metabolic reprogramming fuels cell growth and proliferation. *Cell Metab.* **2008**, *7*, 11-20. DOI: 10.1016/j.cmet.2007.10.002.

(11) Alauddin, M. M. Positron emission tomography (PET) imaging with (18)F-based radiotracers. *Am. J. Nucl. Med. Mol. Imaging.* **2012**, *2*, 55-76.

(12) Sciacovelli, M.; Frezza, C. Oncometabolites: Unconventional triggers of oncogenic signalling cascades. *Free Radic. Biol. Med.* **2016**, *100*, 175-181. DOI: 10.1016/j.freeradbiomed.2016.04.025.

(13) Cascón, A.; Comino-Méndez, I.; Currás-Freixes, M.; de Cubas, A. A.; Contreras, L.; Richter, S.; Peitzsch, M.; Mancikova, V.; Inglada-Pérez, L.; Pérez-Barrios, A.; et al. Whole-exome sequencing identifies MDH2 as a new familial paraganglioma gene. *J. Natl. Cancer Inst.* **2015**, *107*. DOI: 10.1093/jnci/djv053.

(14) Tommasini-Ghelfi, S.; Murnan, K.; Kouri, F. M.; Mahajan, A. S.; May, J. L.; Stegh, A. H. Cancer-associated mutation and beyond: The emerging biology of isocitrate dehydrogenases in human disease. *Science Adv.* **2019**, *5*, eaaw4543. DOI: doi:10.1126/sciadv.aaw4543.

(15) Golub, D.; Iyengar, N.; Dogra, S.; Wong, T.; Bready, D.; Tang, K.; Modrek, A. S.; Placantonakis, D. G. Mutant Isocitrate Dehydrogenase Inhibitors as Targeted Cancer Therapeutics. *Front. Oncol.* **2019**, *9*. DOI: 10.3389/fonc.2019.00417.

(16) Dang, L.; White, D. W.; Gross, S.; Bennett, B. D.; Bittinger, M. A.; Driggers, E. M.; Fantin, V. R.; Jang, H. G.; Jin, S.; Keenan, M. C.; et al. Cancer-associated IDH1 mutations produce 2-hydroxyglutarate. *Nature* **2009**, *462*, 739-744. DOI: 10.1038/nature08617.

(17) Liu, S.; Cadoux-Hudson, T.; Schofield, C. J. Isocitrate dehydrogenase variants in cancer - Cellular consequences and therapeutic opportunities. *Curr. Opin. Chem. Biol.* **2020**, *57*, 122-134. DOI: 10.1016/j.cbpa.2020.06.012.

(18) Al-Khallaf, H. Isocitrate dehydrogenases in physiology and cancer: biochemical and molecular insight. *Cell & Biosci.* **2017**, *7*, 37. DOI: 10.1186/s13578-017-0165-3.

(19) Hvinden, I. C.; Cadoux-Hudson, T.; Schofield, C. J.; McCullagh, J. S. O. Metabolic adaptations in cancers expressing isocitrate dehydrogenase mutations. *Cell Rep. Med.* **2021**, *2*, 100469-100469. DOI: 10.1016/j.xcrm.2021.100469.

(20) Sellés Vidal, L.; Kelly, C. L.; Mordaka, P. M.; Heap, J. T. Review of NAD(P)H-dependent oxidoreductases: Properties, engineering and application. *Biochim. Biophys. Acta Proteins Proteom.* **2018**, *1866*, 327-347. DOI: 10.1016/j.bbapap.2017.11.005.

(21) Chen, X.; Sun, P.; Liu, Y.; Shen, S.; Ma, T.; Ding, J. Structures of a constitutively active mutant of human IDH3 reveal new insights into the mechanisms of allosteric activation and the catalytic reaction. *J. Biol. Chem.* **2022**, *298*, 102695. DOI: 10.1016/j.jbc.2022.102695.

(22) Nekrutenko, A.; Hillis, D. M.; Patton, J. C.; Bradley, R. D.; Baker, R. J. Cytosolic isocitrate dehydrogenase in humans, mice, and voles and phylogenetic analysis of the enzyme family. *Mol. Biol. Evol.* **1998**, *15*, 1674-1684. DOI: 10.1093/oxfordjournals.molbev.a025894.

(23) Leighton, F.; Poole, B.; Beaufay, H.; Baudhuin, P.; Coffey, J. W.; Fowler, S.; De Duve, C. THE LARGE-SCALE SEPARATION OF PEROXISOMES, MITOCHONDRIA, AND LYSOSOMES FROM THE LIVERS OF RATS INJECTED WITH TRITON WR-1339 : Improved Isolation Procedures, Automated Analysis, Biochemical and Morphological Properties of Fractions. *J. Cell. Biol.* **1968**, *37*, 482-513. DOI: 10.1083/jcb.37.2.482.

(24) Yoshihara, T.; Hamamoto, T.; Munakata, R.; Tajiri, R.; Ohsumi, M.; Yokota, S. Localization of Cytosolic NADP-dependent Isocitrate Dehydrogenase in the Peroxisomes of Rat Liver Cells:Biochemical and Immunocytochemical Studies. *J. Histochem. Cytochem.* **2001**, *49*, 1123-1131. DOI: 10.1177/002215540104900906.

(25) Alberts, B.; Johnson, A.; Lewis, J.; Raff, M.; Roberts, K.; Walter, P. Peroxisomes. In *Molecular Biology of the Cell. 4th edition*, Garland Science, 2002.

(26) Schulz, H. Chapter 3 - Oxidation of fatty acids. In *New. Compr. Biochem.*, Vance, D. E., Vance, J. E. Eds.; Vol. 31; Elsevier, 1996; pp 75-99.

(27) Henke, B.; Girzalsky, W.; Berteaux-Lecellier, V.; Erdmann, R. IDP3 Encodes a Peroxisomal NADP-dependent Isocitrate Dehydrogenase Required for the β-Oxidation of Unsaturated Fatty Acids. *J. Biol. Chem.* **1998**, *273*, 3702-3711. DOI: 10.1074/jbc.273.6.3702.

(28) Hua, T.; Wu, D.; Ding, W.; Wang, J.; Shaw, N.; Liu, Z. J. Studies of human 2,4-dienoyl CoA reductase shed new light on peroxisomal β-oxidation of unsaturated fatty acids. *J. Biol. Chem.* **2012**, *287*, 28956-28965. DOI: 10.1074/jbc.M112.385351.

(29) Ye, J.; Gu, Y.; Zhang, F.; Zhao, Y.; Yuan, Y.; Hao, Z.; Sheng, Y.; Li, W. Y.; Wakeham, A.; Cairns, R. A.; et al. IDH1 deficiency attenuates gluconeogenesis in mouse liver by impairing amino acid utilization. *Proc. Natl. Acad. Sci.* **2017**, *114*, 292-297. DOI: 10.1073/pnas.1618605114 (acccessed 2024/05/01).

(30) Chu, B.; Wu, T.; Miao, L.; Mei, Y.; Wu, M. MiR-181a regulates lipid metabolism via IDH1. *Scientific Rep.* **2015**, *5*, 8801. DOI: 10.1038/srep08801.

(31) Bogdanovic, E. IDH1, lipid metabolism and cancer: Shedding new light on old ideas. *Biochim. Biophys. Acta Gen. Subj.* **2015**, *1850*, 1781-1785. DOI: 10.1016/j.bbagen.2015.04.014.

(32) Wang, H.; Xiong, Q.; He, G.; Tang, J.; Sun, L.; Cheng, S.; Ke, M.; Chen, S.; Hu, Y.; Feng, J.; et al. Hepatic IDH2 regulates glycolysis and gluconeogenesis. *Metab.* **2023**, *143*, 155559. DOI: 10.1016/j.metabol.2023.155559.

(33) Lee, J.-H.; Go, Y.; Kim, D.-Y.; Lee, S. H.; Kim, O.-H.; Jeon, Y. H.; Kwon, T. K.; Bae, J.-H.; Song, D.-K.; Rhyu, I. J.; et al. Isocitrate dehydrogenase 2 protects mice from high-fat

diet-induced metabolic stress by limiting oxidative damage to the mitochondria from brown adipose tissue. *Exp. Mol. Med.* **2020**, *52*, 238-252. DOI: 10.1038/s12276-020-0379-z.

(34) Huh, T. L.; Kim, Y. O.; Oh, I. U.; Song, B. J.; Inazawa, J. Assignment of the human mitochondrial NAD+ -specific isocitrate dehydrogenase alpha subunit (IDH3A) gene to 15q25.1-->q25.2by in situ hybridization. *Genom.* **1996**, *32*, 295-296. DOI: 10.1006/geno.1996.0120.

(35) Liu, X.; Qiao, Y.; Ting, X.; Si, W. Isocitrate dehydrogenase 3A, a rate-limiting enzyme of the TCA cycle, promotes hepatocellular carcinoma migration and invasion through regulation of MTA1, a core component of the NuRD complex. *Am. J. Cancer. Res.* **2020**, *10*, 3212-3229.

(36) Sun, P.; Liu, Y.; Ma, T.; Ding, J. Structure and allosteric regulation of human NAD-dependent isocitrate dehydrogenase. *Cell Discov.* **2020**, *6*, 94. DOI: 10.1038/s41421-020-00220-7.

(37) Gregersen, N.; Ingerslev, J.; Rasmussen, K. Low molecular weight organic acids in the urine of the newborn. *Acta Paediatr. Scand.* **1977**, *66*, 85-89. DOI: 10.1111/j.1651-2227.1977.tb07812.x.

(38) Hoffmann, G. F.; Seppel, C. K.; Holmes, B.; Mitchell, L.; Christen, H. J.; Hanefeld, F.; Rating, D.; Nyhan, W. L. Quantitative organic acid analysis in cerebrospinal fluid and plasma: reference values in a pediatric population. *J. Chromatogr. B: Biomed. Sci. Appl.* **1993**, *617*, 1-10. DOI: 10.1016/0378-4347(93)80414-Y.

(39) Janin, M.; Mylonas, E.; Saada, V.; Micol, J. B.; Renneville, A.; Quivoron, C.; Koscielny, S.; Scourzic, L.; Forget, S.; Pautas, C.; et al. Serum 2-hydroxyglutarate production in IDH1- and IDH2-mutated de novo acute myeloid leukemia: a study by the Acute Leukemia French Association group. *J. Clin. Oncol.* **2014**, *32*, 297-305. DOI: 10.1200/jco.2013.50.2047.

(40) Hoffmann, G.; Aramaki, S.; Blum-Hoffmann, E.; Nyhan, W.; Sweetman, L. Quantitative analysis for organic acids in biological samples: batch isolation followed by gas chromatographic-mass spectrometric analysis. *Clin. Chem.* **1989**, *35*, 587-595.

(41) Lindahl, G.; Lindstedt, G.; Lindstedt, S. Metabolism of 2-amino-5-hydroxyadipic acid in the rat. *Arch Biochem.. Biophys.* **1967**, *119*, 347-352. DOI: 10.1016/0003-9861(67)90463-8.

(42) Kaufman, E. E.; Nelson, T.; Fales, H. M.; Levin, D. M. Isolation and characterization of a hydroxyacid-oxoacid transhydrogenase from rat kidney mitochondria. *J. Biol. Chem.* **1988**, *263*, 16872-16879.

(43) Struys, E. A.; Verhoeven, N. M.; Ten Brink, H. J.; Wickenhagen, W. V.; Gibson, K. M.; Jakobs, C. Kinetic characterization of human hydroxyacid-oxoacid transhydrogenase: relevance to D-2-hydroxyglutaric and gamma-hydroxybutyric acidurias. *J. Inherit. Metab. Dis.* **2005**, *28*, 921-930. DOI: 10.1007/s10545-005-0114-x.

(44) Rzem, R.; Vincent, M. F.; Van Schaftingen, E.; Veiga-da-Cunha, M. L-2-hydroxyglutaric aciduria, a defect of metabolite repair. *J. Inherit. Metab. Dis.* **2007**, *30*, 681-689. DOI: 10.1007/s10545-007-0487-0.

(45) Intlekofer, A. M.; Wang, B.; Liu, H.; Shah, H.; Carmona-Fontaine, C.; Rustenburg, A. S.; Salah, S.; Gunner, M. R.; Chodera, J. D.; Cross, J. R.; et al. L-2-Hydroxyglutarate production arises from noncanonical enzyme function at acidic pH. *Nat. Chem. Biol.* **2017**, *13*, 494-500. DOI: 10.1038/nchembio.2307.

(46) Fan, J.; Teng, X.; Liu, L.; Mattaini, K. R.; Looper, R. E.; Vander Heiden, M. G.; Rabinowitz, J. D. Human Phosphoglycerate Dehydrogenase Produces the Oncometabolite d-2-Hydroxyglutarate. *ACS Chem. Biol.* **2015**, *10*, 510-516. DOI: 10.1021/cb500683c.

(47) Intlekofer, Andrew M.; Dematteo, Raymond G.; Venneti, S.; Finley, Lydia W. S.; Lu, C.; Judkins, Alexander R.; Rustenburg, Ariën S.; Grinaway, Patrick B.; Chodera, John D.; Cross, Justin R.; et al. Hypoxia Induces Production of L-2-Hydroxyglutarate. *Cell Metab.* **2015**, *22*, 304-311. DOI: 10.1016/j.cmet.2015.06.023.

(48) Nadtochiy, S. M.; Schafer, X.; Fu, D.; Nehrke, K.; Munger, J.; Brookes, P. S. Acidic pH Is a Metabolic Switch for 2-Hydroxyglutarate Generation and Signaling. *J. Biol. Chem.* **2016**, *291*, 20188-20197. DOI: 10.1074/jbc.M116.738799.

(49) Kranendijk, M.; Struys, E. A.; van Schaftingen, E.; Gibson, K. M.; Kanhai, W. A.; van der Knaap, M. S.; Amiel, J.; Buist, N. R.; Das, A. M.; de Klerk, J. B.; et al. IDH2 mutations in patients with D-2-hydroxyglutaric aciduria. *Science* **2010**, *330*, 336. DOI: 10.1126/science.1192632.

(50) Achouri, Y.; Noël, G.; Vertommen, D.; Rider, M. H.; Veiga-Da-Cunha, M.; Van Schaftingen, E. Identification of a dehydrogenase acting on D-2-hydroxyglutarate. *Biochem. J.* **2004**, *381*, 35-42. DOI: 10.1042/bj20031933.

(51) Rzem, R.; Veiga-da-Cunha, M.; Noël, G.; Goffette, S.; Nassogne, M.-C.; Tabarki, B.; Schöller, C.; Marquardt, T.; Vikkula, M.; Van Schaftingen, E. A gene encoding a putative FAD-dependent L-2-hydroxyglutarate dehydrogenase is mutated in L-2-hydroxyglutaric aciduria. *Proc. Natl. Acad. Sci.* **2004**, *101*, 16849-16854. DOI: 10.1073/pnas.0404840101.

(52) Steenweg, M. E.; Jakobs, C.; Errami, A.; van Dooren, S. J.; Adeva Bartolomé, M. T.; Aerssens, P.; Augoustides-Savvapoulou, P.; Baric, I.; Baumann, M.; Bonafé, L.; et al. An overview of L-2-hydroxyglutarate dehydrogenase gene (L2HGDH) variants: a genotype-phenotype study. *Hum. Mutat.* **2010**, *31*, 380-390. DOI: 10.1002/humu.21197.

(53) Struys, E. A.; Salomons, G. S.; Achouri, Y.; Van Schaftingen, E.; Grosso, S.; Craigen, W. J.; Verhoeven, N. M.; Jakobs, C. Mutations in the D-2-hydroxyglutarate dehydrogenase gene cause D-2-hydroxyglutaric aciduria. *Am. J. Hum. Genet.* **2005**, *76*, 358-360. DOI: 10.1086/427890.

(54) Topçu, M.; Jobard, F.; Halliez, S.; Coskun, T.; Yalçinkayal, C.; Gerceker, F. O.; Wanders, R. J. A.; Prud'homme, J.-F.; Lathrop, M.; Özguc, M.; et al. l-2-Hydroxyglutaric aciduria: identification of a mutant gene C14orf160, localized on chromosome 14q22.1. *Human. Mol. Gen.* **2004**, *13*, 2803-2811. DOI: 10.1093/hmg/ddh300 (acccessed 7/7/2024).

(55) Kranendijk, M.; Struys, E. A.; Gibson, K. M.; Wickenhagen, W. V.; Abdenur, J. E.; Buechner, J.; Christensen, E.; de Kremer, R. D.; Errami, A.; Gissen, P.; et al. Evidence for genetic heterogeneity in D-2-hydroxyglutaric aciduria. *Hum. Mutat.* **2010**, *31*, 279-283. DOI: 10.1002/humu.21186.

(56) Kranendijk, M.; Struys, E. A.; Salomons, G. S.; Van der Knaap, M. S.; Jakobs, C. Progress in understanding 2-hydroxyglutaric acidurias. *J. Inherit. Metab. Dis.* **2012**, *35*, 571-587. DOI: 10.1007/s10545-012-9462-5.

(57) London, F.; Jeanjean, A. Gliomatosis cerebri in L-2-hydroxyglutaric aciduria. *Acta Neurol. Belg.* **2015**, *115*, 749-751. DOI: 10.1007/s13760-015-0489-x.

(58) Patay, Z.; Mills, J. C.; Löbel, U.; Lambert, A.; Sablauer, A.; Ellison, D. W. Cerebral neoplasms in L-2 hydroxyglutaric aciduria: 3 new cases and meta-analysis of literature data. *Am. J. Neuroradiol.* **2012**, *33* (5), 940-943. DOI: 10.3174/ajnr.A2869.

(59) Fourati, H.; Ellouze, E.; Ahmadi, M.; Chaari, D.; Kamoun, F.; Hsairi, I.; Triki, C.; Mnif, Z. MRI features in 17 patients with l2 hydroxyglutaric aciduria. *Eur. J. Radiol. Open.* **2016**, *3*, 245-250. DOI: 10.1016/j.ejro.2016.09.001.

(60) Pietrak, B.; Zhao, H.; Qi, H.; Quinn, C.; Gao, E.; Boyer, J. G.; Concha, N.; Brown, K.; Duraiswami, C.; Wooster, R.; et al. A tale of two subunits: how the neomorphic R132H IDH1 mutation enhances production of αHG. *Biochem.* **2011**, *50*, 4804-4812. DOI: 10.1021/bi200499m.

(61) Balss, J.; Meyer, J.; Mueller, W.; Korshunov, A.; Hartmann, C.; von Deimling, A. Analysis of the IDH1 codon 132 mutation in brain tumors. *Acta Neuropathol.* **2008**, *116*, 597-602. DOI: 10.1007/s00401-008-0455-2.

(62) Parsons, D. W.; Jones, S.; Zhang, X.; Lin, J. C.; Leary, R. J.; Angenendt, P.; Mankoo, P.; Carter, H.; Siu, I. M.; Gallia, G. L.; et al. An integrated genomic analysis of human glioblastoma multiforme. *Science* **2008**, *321*, 1807-1812. DOI: 10.1126/science.1164382.

(63) Losman, J.-A.; Kaelin, W. G. What a difference a hydroxyl makes: mutant IDH, (R)-2-hydroxyglutarate, and cancer. *Genes Dev.* **2013**, *27*, 836-852. DOI: 10.1101/gad.217406.113.

(64) Mardis, E. R.; Ding, L.; Dooling, D. J.; Larson, D. E.; McLellan, M. D.; Chen, K.; Koboldt, D. C.; Fulton, R. S.; Delehaunty, K. D.; McGrath, S. D.; et al. Recurring Mutations Found by Sequencing an Acute Myeloid Leukemia Genome. *N. Engl. J. Med.* **2009**, *361*, 1058-1066. DOI: 10.1056/NEJMoa0903840.

(65) Gross, S.; Cairns, R. A.; Minden, M. D.; Driggers, E. M.; Bittinger, M. A.; Jang, H. G.; Sasaki, M.; Jin, S.; Schenkein, D. P.; Su, S. M.; et al. Cancer-associated metabolite 2-hydroxyglutarate accumulates in acute myelogenous leukemia with isocitrate dehydrogenase 1 and 2 mutations. *J. Exp. Med.* **2010**, *207*, 339-344. DOI: 10.1084/jem.20092506.

(66) Ward, P. S.; Patel, J.; Wise, D. R.; Abdel-Wahab, O.; Bennett, B. D.; Coller, H. A.; Cross, J. R.; Fantin, V. R.; Hedvat, C. V.; Perl, A. E.; et al. The common feature of leukemia-associated IDH1 and IDH2 mutations is a neomorphic enzyme activity converting alpha-ketoglutarate to 2-hydroxyglutarate. *Cancer Cell* **2010**, *17*, 225-234. DOI: 10.1016/j.ccr.2010.01.020.

(67) Yan, H.; Parsons, D. W.; Jin, G.; McLendon, R.; Rasheed, B. A.; Yuan, W.; Kos, I.; Batinic-Haberle, I.; Jones, S.; Riggins, G. J.; et al. IDH1 and IDH2 mutations in gliomas. *N. Engl. J. Med.* **2009**, *360*, 765-773. DOI: 10.1056/NEJMoa0808710.

(68) Hartmann, C.; Meyer, J.; Balss, J.; Capper, D.; Mueller, W.; Christians, A.; Felsberg, J.; Wolter, M.; Mawrin, C.; Wick, W.; et al. Type and frequency of IDH1 and IDH2 mutations are related to astrocytic and oligodendroglial differentiation and age: a study of 1,010 diffuse gliomas. *Acta Neuropathol.* **2009**, *118*, 469-474. DOI: 10.1007/s00401-009-0561-9.

(69) Ichimura, K.; Pearson, D. M.; Kocialkowski, S.; Bäcklund, L. M.; Chan, R.; Jones, D. T.; Collins, V. P. IDH1 mutations are present in the majority of common adult gliomas but rare in primary glioblastomas. *Neuro. Oncol.* **2009**, *11*, 341-347. DOI: 10.1215/15228517-2009-025.

(70) Watanabe, T.; Nobusawa, S.; Kleihues, P.; Ohgaki, H. IDH1 mutations are early events in the development of astrocytomas and oligodendrogliomas. *Am J Pathol* **2009**, *174* (4), 1149-1153. DOI: 10.2353/ajpath.2009.080958.

(71) Wang, H.-Y.; Tang, K.; Liang, T.-Y.; Zhang, W.-Z.; Li, J.-Y.; Wang, W.; Hu, H.-M.; Li, M.-Y.; Wang, H.-Q.; He, X.-Z.; et al. The comparison of clinical and biological characteristics between IDH1 and IDH2 mutations in gliomas. *J. Exp. Clin. Cancer Res.* **2016**, *35*, 86-86. DOI: 10.1186/s13046-016-0362-7.

(72) Amary, M. F.; Bacsi, K.; Maggiani, F.; Damato, S.; Halai, D.; Berisha, F.; Pollock, R.; O'Donnell, P.; Grigoriadis, A.; Diss, T.; et al. IDH1 and IDH2 mutations are frequent events in central chondrosarcoma and central and periosteal chondromas but not in other mesenchymal tumours. *J. Pathol.* **2011**, *224*, 334-343. DOI: 10.1002/path.2913.

(73) Arai, M.; Nobusawa, S.; Ikota, H.; Takemura, S.; Nakazato, Y. Frequent IDH1/2 mutations in intracranial chondrosarcoma: a possible diagnostic clue for its differentiation from chordoma. *Brain Tumor Pathol.* **2012**, *29*, 201-206. DOI: 10.1007/s10014-012-0085-1.

(74) Lu, C.; Venneti, S.; Akalin, A.; Fang, F.; Ward, P. S.; Dematteo, R. G.; Intlekofer, A. M.; Chen, C.; Ye, J.; Hameed, M.; et al. Induction of sarcomas by mutant IDH2. *Genes Dev.* **2013**, *27*, 1986-1998. DOI: 10.1101/gad.226753.113.

(75) Kato Kaneko, M.; Liu, X.; Oki, H.; Ogasawara, S.; Nakamura, T.; Saidoh, N.; Tsujimoto, Y.; Matsuyama, Y.; Uruno, A.; Sugawara, M.; et al. Isocitrate dehydrogenase mutation is frequently observed in giant cell tumor of bone. *Cancer Sci.* **2014**, *105*, 744-748. DOI: 10.1111/cas.12413.

(76) Jin, Y.; Elalaf, H.; Watanabe, M.; Tamaki, S.; Hineno, S.; Matsunaga, K.; Woltjen, K.; Kobayashi, Y.; Nagata, S.; Ikeya, M.; et al. Mutant IDH1 Dysregulates the Differentiation of Mesenchymal Stem Cells in Association with Gene-Specific Histone Modifications to Cartilage- and Bone-Related Genes. *PLOS ONE* **2015**, *10*, e0131998. DOI: 10.1371/journal.pone.0131998.

(77) Lugowska, I.; Mikula, M.; Teterycz, P.; Kulecka, M.; Kluska, A.; Piatkowska, M.; Balabas, A.; Wagrodzki, M.; Pienkowski, A.; Rutkowski, P.; et al. IDH mutations to predict shorter survival in chondrosarcoma. *J. Clin. Oncol.* **2016**, *34*, 11024-11024. DOI: 10.1200/JCO.2016.34.15_suppl.11024.

(78) Cleven, A. H. G.; Suijker, J.; Agrogiannis, G.; Briaire-de Bruijn, I. H.; Frizzell, N.; Hoekstra, A. S.; Wijers-Koster, P. M.; Cleton-Jansen, A.-M.; Bovée, J. V. M. G. IDH1 or -2 mutations do not predict outcome and do not cause loss of 5-hydroxymethylcytosine or altered histone modifications in central chondrosarcomas. *Clin. Sarcoma. Res* **2017**, *7*, 8. DOI: 10.1186/s13569-017-0074-6.

(79) Tallegas, M.; Miquelestorena-Standley, É.; Labit-Bouvier, C.; Badoual, C.; Francois, A.; Gomez-Brouchet, A.; Aubert, S.; Collin, C.; Tallet, A.; de Pinieux, G. IDH mutation status in a series of 88 head and neck chondrosarcomas: different profile between tumors of the skull base and tumors involving the facial skeleton and the laryngotracheal tract. *Hum. Pathol.* **2019**, *84*, 183-191. DOI: 10.1016/j.humpath.2018.09.015.

(80) Abbas, S.; Lugthart, S.; Kavelaars, F. G.; Schelen, A.; Koenders, J. E.; Zeilemaker, A.; van Putten, W. J.; Rijneveld, A. W.; Lowenberg, B.; Valk, P. J. Acquired mutations in the genes encoding IDH1 and IDH2 both are recurrent aberrations in acute myeloid leukemia: prevalence and prognostic value. *Blood* **2010**, *116*, 2122-2126. DOI: 10.1182/blood-2009-11-250878 (acccessed 3/23/2024).Medline.

(81) Marcucci, G.; Maharry, K.; Wu, Y. Z.; Radmacher, M. D.; Mrózek, K.; Margeson, D.; Holland, K. B.; Whitman, S. P.; Becker, H.; Schwind, S.; et al. IDH1 and IDH2 gene mutations identify novel molecular subsets within de novo cytogenetically normal acute myeloid leukemia: a Cancer and Leukemia Group B study. *J. Clin. Oncol.* **2010**, *28*, 2348-2355. DOI: 10.1200/jco.2009.27.3730.

(82) Schnittger, S.; Haferlach, C.; Ulke, M.; Alpermann, T.; Kern, W.; Haferlach, T. IDH1 mutations are detected in 6.6% of 1414 AML patients and are associated with intermediate risk karyotype and unfavorable prognosis in adults younger than 60 years and unmutated NPM1 status. *Blood* **2010**, *116*, 5486-5496. DOI: 10.1182/blood-2010-02-267955.

(83) Wagner, K.; Damm, F.; Göhring, G.; Görlich, K.; Heuser, M.; Schäfer, I.; Ottmann, O.; Lübbert, M.; Heit, W.; Kanz, L.; et al. Impact of IDH1 R132 mutations and an IDH1 single nucleotide polymorphism in cytogenetically normal acute myeloid leukemia: SNP rs11554137 is an adverse prognostic factor. *J. Clin. Oncol.* **2010**, *28*, 2356-2364. DOI: 10.1200/jco.2009.27.6899.

(84) Molenaar, R. J.; Thota, S.; Nagata, Y.; Patel, B.; Clemente, M.; Przychodzen, B.; Hirsh, C.; Viny, A. D.; Hosano, N.; Bleeker, F. E.; et al. Clinical and biological implications of ancestral and non-ancestral IDH1 and IDH2 mutations in myeloid neoplasms. *Leukemia* **2015**, *29*, 2134-2142. DOI: 10.1038/leu.2015.91.

(85) Figueroa, M. E.; Abdel-Wahab, O.; Lu, C.; Ward, P. S.; Patel, J.; Shih, A.; Li, Y.; Bhagwat, N.; Vasanthakumar, A.; Fernandez, H. F.; et al. Leukemic IDH1 and IDH2 Mutations Result in a Hypermethylation Phenotype, Disrupt TET2 Function, and Impair

Hematopoietic Differentiation. *Cancer Cell* **2010**, *18*, 553-567. DOI: 10.1016/j.ccr.2010.11.015.

(86) Paschka, P.; Schlenk, R. F.; Gaidzik, V. I.; Habdank, M.; Krönke, J.; Bullinger, L.; Späth, D.; Kayser, S.; Zucknick, M.; Götze, K.; et al. IDH1 and IDH2 Mutations Are Frequent Genetic Alterations in Acute Myeloid Leukemia and Confer Adverse Prognosis in Cytogenetically Normal Acute Myeloid Leukemia With NPM1 Mutation Without FLT3 Internal Tandem Duplication. *J. Clin. Oncol.* **2010**, *28*, 3636-3643. DOI: 10.1200/JCO.2010.28.3762.

(87) Borger, D. R.; Tanabe, K. K.; Fan, K. C.; Lopez, H. U.; Fantin, V. R.; Straley, K. S.; Schenkein, D. P.; Hezel, A. F.; Ancukiewicz, M.; Liebman, H. M.; et al. Frequent mutation of isocitrate dehydrogenase (IDH)1 and IDH2 in cholangiocarcinoma identified through broad-based tumor genotyping. *Oncolog.* **2012**, *17*, 72-79. DOI: 10.1634/theoncologist.2011-0386.

(88) Kipp, B. R.; Voss, J. S.; Kerr, S. E.; Barr Fritcher, E. G.; Graham, R. P.; Zhang, L.; Highsmith, W. E.; Zhang, J.; Roberts, L. R.; Gores, G. J.; et al. Isocitrate dehydrogenase 1 and 2 mutations in cholangiocarcinoma. *Hum. Pathol.* **2012**, *43*, 1552-1558. DOI: 10.1016/j.humpath.2011.12.007.

(89) Wang, P.; Dong, Q.; Zhang, C.; Kuan, P. F.; Liu, Y.; Jeck, W. R.; Andersen, J. B.; Jiang, W.; Savich, G. L.; Tan, T. X.; et al. Mutations in isocitrate dehydrogenase 1 and 2 occur frequently in intrahepatic cholangiocarcinomas and share hypermethylation targets with glioblastomas. *Oncogene* **2013**, *32*, 3091-3100. DOI: 10.1038/onc.2012.315.

(90) Jiao, Y.; Pawlik, T. M.; Anders, R. A.; Selaru, F. M.; Streppel, M. M.; Lucas, D. J.; Niknafs, N.; Guthrie, V. B.; Maitra, A.; Argani, P.; et al. Exome sequencing identifies frequent inactivating mutations in BAP1, ARID1A and PBRM1 in intrahepatic cholangiocarcinomas. *Nat. Genet.* **2013**, *45*, 1470-1473. DOI: 10.1038/ng.2813.

(91) Ross, J. S.; Wang, K.; Gay, L.; Al-Rohil, R.; Rand, J. V.; Jones, D. M.; Lee, H. J.; Sheehan, C. E.; Otto, G. A.; Palmer, G.; et al. New routes to targeted therapy of intrahepatic cholangiocarcinomas revealed by next-generation sequencing. *Oncolog.* **2014**, *19*, 235-242. DOI: 10.1634/theoncologist.2013-0352.

(92) Farshidfar, F.; Zheng, S.; Gingras, M. C.; Newton, Y.; Shih, J.; Robertson, A. G.; Hinoue, T.; Hoadley, K. A.; Gibb, E. A.; Roszik, J.; et al. Integrative Genomic Analysis of Cholangiocarcinoma Identifies Distinct IDH-Mutant Molecular Profiles. *Cell Rep.* **2017**, *18*, 2780-2794. DOI: 10.1016/j.celrep.2017.02.033.

(93) Lee, J. H.; Shin, D. H.; Park, W. Y.; Shin, N.; Kim, A.; Lee, H. J.; Kim, Y. K.; Choi, K. U.; Kim, J. Y.; Yang, Y. I.; et al. IDH1 R132C mutation is detected in clear cell hepatocellular carcinoma by pyrosequencing. *World J. Surg. Oncol.* **2017**, *15*, 82. DOI: 10.1186/s12957-017-1144-1.

(94) Nepal, C.; O'Rourke, C. J.; Oliveira, D.; Taranta, A.; Shema, S.; Gautam, P.; Calderaro, J.; Barbour, A.; Raggi, C.; Wennerberg, K.; et al. Genomic perturbations reveal distinct regulatory networks in intrahepatic cholangiocarcinoma. *Hepatol.* **2018**, *68*, 949-963. DOI: 10.1002/hep.29764.

(95) Wang, J.; Zhang, Z. G.; Ding, Z. Y.; Dong, W.; Liang, H. F.; Chu, L.; Zhang, B. X.; Chen, X. P. IDH1 mutation correlates with a beneficial prognosis and suppresses tumor growth in IHCC. *J. Surg. Res.* **2018**, *231*, 116-125. DOI: 10.1016/j.jss.2018.04.056.

(96) Cairns, R. A.; Iqbal, J.; Lemonnier, F.; Kucuk, C.; de Leval, L.; Jais, J.-P.; Parrens, M.; Martin, A.; Xerri, L.; Brousset, P.; et al. IDH2 mutations are frequent in angioimmunoblastic T-cell lymphoma. *Blood* **2012**, *119*, 1901-1903. DOI: 10.1182/blood-2011-11-391748.

(97) Odejide, O.; Weigert, O.; Lane, A. A.; Toscano, D.; Lunning, M. A.; Kopp, N.; Kim, S.; van Bodegom, D.; Bolla, S.; Schatz, J. H.; et al. A targeted mutational landscape of

angioimmunoblastic T-cell lymphoma. *Blood* **2014**, *123*, 1293-1296. DOI: 10.1182/blood-2013-10-531509 (acccessed 7/8/2024).

(98) Sakata-Yanagimoto, M.; Enami, T.; Yoshida, K.; Shiraishi, Y.; Ishii, R.; Miyake, Y.; Muto, H.; Tsuyama, N.; Sato-Otsubo, A.; Okuno, Y.; et al. Somatic RHOA mutation in angioimmunoblastic T cell lymphoma. *Nat. Genet.* **2014**, *46*, 171-175. DOI: 10.1038/ng.2872.

(99) Wang, C.; McKeithan, T. W.; Gong, Q.; Zhang, W.; Bouska, A.; Rosenwald, A.; Gascoyne, R. D.; Wu, X.; Wang, J.; Muhammad, Z.; et al. IDH2R172 mutations define a unique subgroup of patients with angioimmunoblastic T-cell lymphoma. *Blood* **2015**, *126*, 1741-1752. DOI: 10.1182/blood-2015-05-644591 (acccessed 7/8/2024).

(100) Dogan, S.; Chute, D. J.; Xu, B.; Ptashkin, R. N.; Chandramohan, R.; Casanova-Murphy, J.; Nafa, K.; Bishop, J. A.; Chiosea, S. I.; Stelow, E. B.; et al. Frequent IDH2 R172 mutations in undifferentiated and poorly-differentiated sinonasal carcinomas. *J. Pathol.* **2017**, *242*, 400-408. DOI: 10.1002/path.4915.

(101) Jo, V. Y.; Chau, N. G.; Hornick, J. L.; Krane, J. F.; Sholl, L. M. Recurrent IDH2 R172X mutations in sinonasal undifferentiated carcinoma. *Mod. Pathol.* **2017**, *30*, 650-659. DOI: 10.1038/modpathol.2016.239.

(102) Riobello, C.; López-Hernández, A.; Cabal, V. N.; García-Marín, R.; Suárez-Fernández, L.; Sánchez-Fernández, P.; Vivanco, B.; Blanco, V.; López, F.; Franchi, A.; et al. IDH2 Mutation Analysis in Undifferentiated and Poorly Differentiated Sinonasal Carcinomas for Diagnosis and Clinical Management. *Am J Surg Pathol* **2020**, *44* (3), 396-405. DOI: 10.1097/pas.0000000000001420.

(103) Chiang, S.; Weigelt, B.; Wen, H. C.; Pareja, F.; Raghavendra, A.; Martelotto, L. G.; Burke, K. A.; Basili, T.; Li, A.; Geyer, F. C.; et al. IDH2 Mutations Define a Unique Subtype of Breast Cancer with Altered Nuclear Polarity. *Cancer Res.* **2016**, *76*, 7118-7129. DOI: 10.1158/0008-5472.Can-16-0298.

(104) Lozada, J. R.; Basili, T.; Pareja, F.; Alemar, B.; Paula, A. D. C.; Gularte-Merida, R.; Giri, D. D.; Querzoli, P.; Cserni, G.; Rakha, E. A.; et al. Solid papillary breast carcinomas resembling the tall cell variant of papillary thyroid neoplasms (solid papillary carcinomas with reverse polarity) harbour recurrent mutations affecting IDH2 and PIK3CA: a validation cohort. *Histopathol.* **2018**, *73*, 339-344. DOI: 10.1111/his.13522.

(105) Nakagawa, M.; Nakatani, F.; Matsunaga, H.; Seki, T.; Endo, M.; Ogawara, Y.; Machida, Y.; Katsumoto, T.; Yamagata, K.; Hattori, A.; et al. Selective inhibition of mutant IDH1 by DS-1001b ameliorates aberrant histone modifications and impairs tumor activity in chondrosarcoma. *Oncogene* **2019**, *38*, 6835-6849. DOI: 10.1038/s41388-019-0929-9.

(106) Pusch, S.; Sahm, F.; Meyer, J.; Mittelbronn, M.; Hartmann, C.; von Deimling, A. Glioma IDH1 mutation patterns off the beaten track. *Neuropathol. Appl. Neurobiol.* **2011**, *37*, 428-430. DOI: 10.1111/j.1365-2990.2010.01127.x.

(107) Gupta, R.; Flanagan, S.; Li, C. C. Y.; Lee, M.; Shivalingham, B.; Maleki, S.; Wheeler, H. R.; Buckland, M. E. Expanding the spectrum of IDH1 mutations in gliomas. *Mod. Pathol.* **2013**, *26*, 619-625. DOI: 10.1038/modpathol.2012.210.

(108) Schneider, T.; Mawrin, C.; Scherlach, C.; Skalej, M.; Firsching, R. Gliomas in adults. *Dtsch Arztebl. Int.* **2010**, *107*, 799-807; quiz 808. DOI: 10.3238/arztebl.2010.0799.

(109) Jäkel, S.; Dimou, L. Glial Cells and Their Function in the Adult Brain: A Journey through the History of Their Ablation. *Front. Cell. Neurosci.* **2017**, *11*, Review. DOI: 10.3389/fncel.2017.00024.

(110) Aschner, M.; Philbert, M. A. 13.12 - Glial Cells. In *Comprehensive Toxicology (Second Edition)*, McQueen, C. A. Ed.; Elsevier, 2010; pp 199-219.

(111) Lee, F. S.; Kim, A. H.; Khursigara, G.; Chao, M. V. The uniqueness of being a neurotrophin receptor. *Curr. Opin. Neurobiol.* **2001**, *11*, 281-286. DOI: 10.1016/S0959-4388(00)00209-9.

(112) Rapalino, O.; Batchelor, T.; González, R. G. Chapter 14 - Intra-axial brain tumors. In *Handb. Clin. Neurol.*, Masdeu, J. C., González, R. G. Eds.; Vol. 135; Elsevier, 2016; pp 253-274.

(113) Youssef, G.; Miller, J. J. Lower Grade Gliomas. *Curr. Neurol. Neurosci. Rep.* **2020**, *20*, 21. DOI: 10.1007/s11910-020-01040-8.

(114) Drevelegas, A.; Karkavelas, G. High-Grade Gliomas. In *Imaging of Brain Tumors with Histological Correlations*, Drevelegas, A. Ed.; Springer Berlin Heidelberg, 2002; pp 109-135.

(115) Louis, D. N.; Perry, A.; Reifenberger, G.; von Deimling, A.; Figarella-Branger, D.; Cavenee, W. K.; Ohgaki, H.; Wiestler, O. D.; Kleihues, P.; Ellison, D. W. The 2016 World Health Organization Classification of Tumors of the Central Nervous System: a summary. *Acta Neuropathol.* **2016**, *131*, 803-820. DOI: 10.1007/s00401-016-1545-1.

(116) Louis, D. N.; Perry, A.; Wesseling, P.; Brat, D. J.; Cree, I. A.; Figarella-Branger, D.; Hawkins, C.; Ng, H. K.; Pfister, S. M.; Reifenberger, G.; et al. The 2021 WHO Classification of Tumors of the Central Nervous System: a summary. *Neuro. Oncol.* **2021**, *23*, 1231-1251. DOI: 10.1093/neuonc/noab106.

(117) Cadoux-Hudson, T.; Schofield, C. J.; McCullagh, J. S. O. Isocitrate dehydrogenase gene variants in cancer and their clinical significance. *Biochem. Soc. Trans.* **2021**, *49*, 2561-2572. DOI: 10.1042/bst20210277.

(118) Suzuki, H.; Aoki, K.; Chiba, K.; Sato, Y.; Shiozawa, Y.; Shiraishi, Y.; Shimamura, T.; Niida, A.; Motomura, K.; Ohka, F.; et al. Mutational landscape and clonal architecture in grade II and III gliomas. *Nat. Genet.* **2015**, *47*, 458-468. DOI: 10.1038/ng.3273.

(119) Chang, C.-M.; Xu, K.; Shu, H. The role of isocitrate dehydrogenase mutations in glioma brain tumors. In *Molecular targets of CNS tumors*, 2011; pp 413-436.

(120) Avellaneda Matteo, D.; Grunseth, A. J.; Gonzalez, E. R.; Anselmo, S. L.; Kennedy, M. A.; Moman, P.; Scott, D. A.; Hoang, A.; Sohl, C. D. Molecular mechanisms of isocitrate dehydrogenase 1 (IDH1) mutations identified in tumors: The role of size and hydrophobicity at residue 132 on catalytic efficiency. *J. Biol. Chem.* **2017**, *292*, 7971-7983. DOI: 10.1074/jbc.M117.776179.

(121) Zhao, S.; Lin, Y.; Xu, W.; Jiang, W.; Zha, Z.; Wang, P.; Yu, W.; Li, Z.; Gong, L.; Peng, Y.; et al. Glioma-Derived Mutations in IDH1 Dominantly Inhibit IDH1 Catalytic Activity and Induce HIF-1α. *Science* **2009**, *324*, 261-265. DOI: 10.1126/science.1170944 (acccessed 2024/03/22).

(122) Xu, X.; Zhao, J.; Xu, Z.; Peng, B.; Huang, Q.; Arnold, E.; Ding, J. Structures of Human Cytosolic NADP-dependent Isocitrate Dehydrogenase Reveal a Novel Self-regulatory Mechanism of Activity. *J. Biol. Chem.* **2004**, *279*, 33946-33957. DOI: 10.1074/jbc.M404298200.

(123) Xu, W.; Yang, H.; Liu, Y.; Yang, Y.; Wang, P.; Kim, S. H.; Ito, S.; Yang, C.; Wang, P.; Xiao, M. T.; et al. Oncometabolite 2-hydroxyglutarate is a competitive inhibitor of α-ketoglutarate-dependent dioxygenases. *Cancer Cell* **2011**, *19*, 17-30. DOI: 10.1016/j.ccr.2010.12.014.

(124) Roman, J. V.; Melkonian, T. R.; Silvaggi, N. R.; Moran, G. R. Correction to "Transient-State Analysis of Human Isocitrate Dehydrogenase I: Accounting for the Interconversion of Active and Non-Active Conformational States". *Biochem.* **2020**, *59*, 3284. DOI: 10.1021/acs.biochem.0c00649 PubMed.

(125) Liu, S.; Abboud, M. I.; John, T.; Mikhailov, V.; Hvinden, I.; Walsby-Tickle, J.; Liu, X.; Pettinati, I.; Cadoux-Hudson, T.; McCullagh, J. S. O.; et al. Roles of metal ions in the selective inhibition of oncogenic variants of isocitrate dehydrogenase 1. *Commun. Biol.* **2021**, *4*, 1243-1243. DOI: 10.1038/s42003-021-02743-5.

(126) Aktas, D. F.; Cook, P. F. A lysine-tyrosine pair carries out acid-base chemistry in the metal ion-dependent pyridine dinucleotide-linked beta-hydroxyacid oxidative decarboxylases. *Biochem.* **2009**, *48*, 3565-3577. DOI: 10.1021/bi8022976.

(127) Quartararo, C. E.; Hazra, S.; Hadi, T.; Blanchard, J. S. Structural, Kinetic and Chemical Mechanism of Isocitrate Dehydrogenase-1 from Mycobacterium tuberculosis. *Biochem.* **2013**, *52*, 1765-1775. DOI: 10.1021/bi400037w.

(128) Rendina, A. R.; Pietrak, B.; Smallwood, A.; Zhao, H.; Qi, H.; Quinn, C.; Adams, N. D.; Concha, N.; Duraiswami, C.; Thrall, S. H.; et al. Mutant IDH1 Enhances the Production of 2-Hydroxyglutarate Due to Its Kinetic Mechanism. *Biochem.* **2013**, *52*, 4563-4577. DOI: 10.1021/bi400514k.

(129) Badur, M. G.; Muthusamy, T.; Parker, S. J.; Ma, S.; McBrayer, S. K.; Cordes, T.; Magana, J. H.; Guan, K. L.; Metallo, C. M. Oncogenic R132 IDH1 Mutations Limit NADPH for De Novo Lipogenesis through (D)2-Hydroxyglutarate Production in Fibrosarcoma Sells. *Cell Rep.* **2018**, *25*, 1018-1026.e1014. DOI: 10.1016/j.celrep.2018.09.074.

(130) Gelman, S. J.; Naser, F.; Mahieu, N. G.; McKenzie, L. D.; Dunn, G. P.; Chheda, M. G.; Patti, G. J. Consumption of NADPH for 2-HG Synthesis Increases Pentose Phosphate Pathway Flux and Sensitizes Cells to Oxidative Stress. *Cell Rep.* **2018**, *22* (2), 512-522. DOI: 10.1016/j.celrep.2017.12.050.

(131) Fong, G. H.; Takeda, K. Role and regulation of prolyl hydroxylase domain proteins. *Cell Death Differ.* **2008**, *15*, 635-641. DOI: 10.1038/cdd.2008.10.

(132) Chowdhury, R.; Yeoh, K. K.; Tian, Y. M.; Hillringhaus, L.; Bagg, E. A.; Rose, N. R.; Leung, I. K.; Li, X. S.; Woon, E. C.; Yang, M.; et al. The oncometabolite 2-hydroxyglutarate inhibits histone lysine demethylases. *EMBO Rep.* **2011**, *12*, 463-469. DOI: 10.1038/embor.2011.43.

(133) Jambhekar, A.; Anastas, J. N.; Shi, Y. Histone Lysine Demethylase Inhibitors. *Cold Spring Harb Perspect Med* **2017**, *7*. DOI: 10.1101/cshperspect.a026484.

(134) Crake, R. L. I.; Burgess, E. R.; Royds, J. A.; Phillips, E.; Vissers, M. C. M.; Dachs, G. U. The Role of 2-Oxoglutarate Dependent Dioxygenases in Gliomas and Glioblastomas: A Review of Epigenetic Reprogramming and Hypoxic Response. *Front. Oncol.* **2021**, *11*, Review. DOI: 10.3389/fonc.2021.619300.

(135) Ohka, F.; Ito, M.; Ranjit, M.; Senga, T.; Motomura, A.; Motomura, K.; Saito, K.; Kato, K.; Kato, Y.; Wakabayashi, T.; et al. Quantitative metabolome analysis profiles activation of glutaminolysis in glioma with IDH1 mutation. *Tumor Biol.* **2014**, *35*, 5911-5920. DOI: 10.1007/s13277-014-1784-5.

(136) Wen, H.; Cho, H. R.; Yun, T.; Kim, H.; Park, C.-K.; Lee, S.-H.; Choi, S. H.; Park, S. Metabolomic comparison between cells over-expressing isocitrate dehydrogenase 1 and 2 mutants and the effects of an inhibitor on the metabolism. *J. Neurochem.* **2015**, *132*, 183-193. DOI: 10.1111/jnc.12950 (acccessed 2024/05/05).

(137) Fack, F.; Tardito, S.; Hochart, G.; Oudin, A.; Zheng, L.; Fritah, S.; Golebiewska, A.; Nazarov, P. V.; Bernard, A.; Hau, A. C. Altered metabolic landscape in IDH-mutant gliomas affects phospholipid, energy, and oxidative stress pathways. *EMBO Mol. Med.* **2017**, *9*, 1681-1695. DOI: 10.15252/emmm.201707729.

(138) Walsby-Tickle, J.; Gannon, J.; Hvinden, I.; Bardella, C.; Abboud, M. I.; Nazeer, A.; Hauton, D.; Pires, E.; Cadoux-Hudson, T.; Schofield, C. J.; et al. Anion-exchange chromatography mass spectrometry provides extensive coverage of primary metabolic

pathways revealing altered metabolism in IDH1 mutant cells. *Commun. Biol.* **2020**, *3*, 247. DOI: 10.1038/s42003-020-0957-6.

(139) Reitman, Z. J.; Jin, G.; Karoly, E. D.; Spasojevic, I.; Yang, J.; Kinzler, K. W.; He, Y.; Bigner, D. D.; Vogelstein, B.; Yan, H. Profiling the effects of isocitrate dehydrogenase 1 and 2 mutations on the cellular metabolome. *Proc. Natl. Acad. Sci.* **2011**, *108* (8), 3270-3275. DOI: 10.1073/pnas.1019393108.

(140) Hvinden, I. Exploring metabolic vulnerability and therapeutic potential in cancers with isocitrate dehydrogenase mutations. University of Oxford, 2022.

(141) Zhou, L.; Wang, Z.; Hu, C.; Zhang, C.; Kovatcheva-Datchary, P.; Yu, D.; Liu, S.; Ren, F.; Wang, X.; Li, Y.; et al. Integrated Metabolomics and Lipidomics Analyses Reveal Metabolic Reprogramming in Human Glioma with IDH1 Mutation. *J. Proteom. Res.* **2019**, *18*, 960-969. DOI: 10.1021/acs.jproteome.8b00663.

(142) Jo, S. H.; Son, M. K.; Koh, H. J.; Lee, S. M.; Song, I. H.; Kim, Y. O.; Lee, Y. S.; Jeong, K. S.; Kim, W. B.; Park, J. W.; et al. Control of mitochondrial redox balance and cellular defense against oxidative damage by mitochondrial NADP+-dependent isocitrate dehydrogenase. *J. Biol. Chem.* **2001**, *276* (19), 16168-16176. DOI: 10.1074/jbc.M010120200.

(143) Heil, C. S.; Wehrheim, S. S.; Paithankar, K. S.; Grininger, M. Fatty Acid Biosynthesis: Chain-Length Regulation and Control. *Chembiochem* **2019**, *20*, 2298-2321. DOI: 10.1002/cbic.201800809.

(144) Lee, S. M.; Koh, H. J.; Park, D. C.; Song, B. J.; Huh, T. L.; Park, J. W. Cytosolic NADP(+)-dependent isocitrate dehydrogenase status modulates oxidative damage to cells. *Free Radic. Biol. Med.* **2002**, *32*, 1185-1196. DOI: 10.1016/s0891-5849(02)00815-8.

(145) Bleeker, F. E.; Atai, N. A.; Lamba, S.; Jonker, A.; Rijkeboer, D.; Bosch, K. S.; Tigchelaar, W.; Troost, D.; Vandertop, W. P.; Bardelli, A.; et al. The prognostic IDH1R132mutation is associated with reduced NADP+-dependent IDH activity in glioblastoma. *Acta Neuropathol.* **2010**, *119*, 487-494. DOI: 10.1007/s00401-010-0645-6.

(146) Lenting, K.; Khurshed, M.; Peeters, T. H.; van den Heuvel, C. N.; van Lith, S. A.; de Bitter, T.; Hendriks, W.; Span, P. N.; Molenaar, R. J.; Botman, D. Isocitrate dehydrogenase 1–mutated human gliomas depend on lactate and glutamate to alleviate metabolic stress. *FASEB J.* **2019**, *33*, 557-571. DOI: 10.1096/fj.201800907RR.

(147) Izquierdo-Garcia, J. L.; Viswanath, P.; Eriksson, P.; Chaumeil, M. M.; Pieper, R. O.; Phillips, J. J.; Ronen, S. M. Metabolic reprogramming in mutant IDH1 glioma cells. *PLOS ONE* **2015**, *10*, e0118781. DOI: 10.1371/journal.pone.0118781.

(148) Jalbert, L. E.; Elkhaled, A.; Phillips, J. J.; Neill, E.; Williams, A.; Crane, J. C.; Olson, M. P.; Molinaro, A. M.; Berger, M. S.; Kurhanewicz, J. Metabolic profiling of IDH mutation and malignant progression in infiltrating glioma. *Scientific Rep.* **2017**, *7*, 44792. DOI: 10.1038/srep44792.

(149) Emir, U. E.; Larkin, S. J.; de Pennington, N.; Voets, N.; Plaha, P.; Stacey, R.; Al-Qahtani, K.; Mccullagh, J.; Schofield, C. J.; Clare, S. Noninvasive quantification of 2-hydroxyglutarate in human gliomas with IDH1 and IDH2 mutations. *Cancer Res.* **2016**, *76*, 43-49. DOI: 10.1158/0008-5472.CAN-15-0934.

(150) Esmaeili, M.; Hamans, B. C.; Navis, A. C.; van Horssen, R.; Bathen, T. F.; Gribbestad, I. S.; Leenders, W. P.; Heerschap, A. IDH1 R132H mutation generates a distinct phospholipid metabolite profile in glioma. *Cancer Res.* **2014**, *74*, 4898-4907. DOI: 10.1158/0008-5472.CAN-14-0008.

(151) Wenger, K. J.; Hattingen, E.; Franz, K.; Steinbach, J.; Bähr, O.; Pilatus, U. In vivo metabolic profiles as determined by 31 P and short TE 1 H MR-spectroscopy: no difference

between patients with IDH wildtype and IDH mutant gliomas. *Clin. Neuroradiol.* **2019**, *29*, 27-36. DOI: 10.1007/s00062-017-0630-8.

(152) Thomas, T.; Thakur, S.; Young, R. Imaging 2-hydroxyglutarate and other brain oncometabolites pertinent to critical genomic alterations in brain tumors. *BJR|Open* **2023**, *5*, 20210070. DOI: 10.1259/bjro.20210070 (acccessed 2/10/2025).

(153) Elkhaled, A.; Jalbert, L. E.; Phillips, J. J.; Yoshihara, H. A. I.; Parvataneni, R.; Srinivasan, R.; Bourne, G.; Berger, M. S.; Chang, S. M.; Cha, S.; et al. Magnetic Resonance of 2-Hydroxyglutarate in IDH1-Mutated Low-Grade Gliomas. *Science Translational Medicine* **2012**, *4*, 116ra115-116ra115. DOI: doi:10.1126/scitranslmed.3002796.

(154) Sudhamalla, B.; Dey, D.; Breski, M.; Islam, K. A rapid mass spectrometric method for the measurement of catalytic activity of ten-eleven translocation enzymes. *Anal. Biochem.* **2017**, *534*, 28-35. DOI: 10.1016/j.ab.2017.06.011.

(155) Selak, M. A.; Armour, S. M.; MacKenzie, E. D.; Boulahbel, H.; Watson, D. G.; Mansfield, K. D.; Pan, Y.; Simon, M. C.; Thompson, C. B.; Gottlieb, E. Succinate links TCA cycle dysfunction to oncogenesis by inhibiting HIF-α prolyl hydroxylase. *Cancer Cell* **2005**, *7*, 77-85. DOI: 10.1016/j.ccr.2004.11.022.

(156) Pickard, A. J.; Sohn, A. S. W.; Bartenstein, T. F.; He, S.; Zhang, Y.; Gallo, J. M. Intracerebral Distribution of the Oncometabolite d-2-Hydroxyglutarate in Mice Bearing Mutant Isocitrate Dehydrogenase Brain Tumors: Implications for Tumorigenesis. *Front. Oncol.* **2016**, *6*.

(157) Colvin, H.; Nishida, N.; Konno, M.; Haraguchi, N.; Takahashi, H.; Nishimura, J.; Hata, T.; Kawamoto, K.; Asai, A.; Tsunekuni, K.; et al. Oncometabolite D-2-Hydroxyglurate Directly Induces Epithelial-Mesenchymal Transition and is Associated with Distant Metastasis in Colorectal Cancer. *Scientific Rep.* **2016**, *6*, 36289. DOI: 10.1038/srep36289.

(158) Kang, Z.; Hou, S.; Gao, K.; Liu, Y.; Zhang, N.; Fang, Z.; Zhang, W.; Xu, X.; Xu, R.; Lü, C.; et al. An Ultrasensitive Biosensor for Probing Subcellular Distribution and Mitochondrial Transport of l-2-Hydroxyglutarate. *Advanced Science* **2024**, *11*, 2404119. DOI: https://doi.org/10.1002/advs.202404119.

(159) Strocchi, S.; Reggiani, F.; Gobbi, G.; Ciarrocchi, A.; Sancisi, V. The multifaceted role of EGLN family prolyl hydroxylases in cancer: going beyond HIF regulation. *Oncogene* **2022**, *41*, 3665-3679. DOI: 10.1038/s41388-022-02378-8.

(160) Fiorini, G.; Schofield, C. J. Biochemistry of the hypoxia-inducible factor hydroxylases. *Curr. Opin. Chem. Biol.* **2024**, *79*, 102428. DOI: 10.1016/j.cbpa.2024.102428.

(161) Semenza, G. L. HIF-1: upstream and downstream of cancer metabolism. *Curr. Opin. Genet. Dev.* **2010**, *20*, 51-56. DOI: 10.1016/j.gde.2009.10.009.

(162) Koivunen, P.; Lee, S.; Duncan, C. G.; Lopez, G.; Lu, G.; Ramkissoon, S.; Losman, J. A.; Joensuu, P.; Bergmann, U.; Gross, S.; et al. Transformation by the (R)-enantiomer of 2-hydroxyglutarate linked to EGLN activation. *Nature* **2012**, *483*, 484-488. DOI: 10.1038/nature10898.

(163) Tarhonskaya, H.; Rydzik, A. M.; Leung, I. K. H.; Loik, N. D.; Chan, M. C.; Kawamura, A.; McCullagh, J. S. O.; Claridge, T. D. W.; Flashman, E.; Schofield, C. J. Non-enzymatic chemistry enables 2-hydroxyglutarate-mediated activation of 2-oxoglutarate oxygenases. *Nat. Commun.* **2014**, *5*, 3423-3423. DOI: 10.1038/ncomms4423.

(164) Acker, T.; Diez-Juan, A.; Aragones, J.; Tjwa, M.; Brusselmans, K.; Moons, L.; Fukumura, D.; Moreno-Murciano, M. P.; Herbert, J.-M.; Burger, A.; et al. Genetic evidence for a tumor suppressor role of HIF-2α. *Cancer Cell* **2005**, *8*, 131-141. DOI: 10.1016/j.ccr.2005.07.003.

(165) Song, L. P.; Zhang, J.; Wu, S. F.; Huang, Y.; Zhao, Q.; Cao, J. P.; Wu, Y. L.; Wang, L. S.; Chen, G. Q. Hypoxia-inducible factor-1α-induced differentiation of myeloid leukemic cells is its transcriptional activity independent. *Oncogene* **2008**, *27*, 519-527. DOI: 10.1038/sj.onc.1210670.

(166) Lawson, H.; Holt-Martyn, J. P.; Dembitz, V.; Kabayama, Y.; Wang, L. M.; Bellani, A.; Atwal, S.; Saffoon, N.; Durko, J.; van de Lagemaat, L. N.; et al. The selective prolyl hydroxylase inhibitor IOX5 stabilizes HIF-1α and compromises development and progression of acute myeloid leukemia. *Nat. Cancer* **2024**, *5*, 916-937. DOI: 10.1038/s43018-024-00761-w.

(167) Kim, T.-D.; Shin, S.; Berry, W. L.; Oh, S.; Janknecht, R. The JMJD2A demethylase regulates apoptosis and proliferation in colon cancer cells. *J. Cell. Biochem.* **2012**, *113*, 1368-1376. DOI: 10.1002/jcb.24009.

(168) Tulstrup, M.; Soerensen, M.; Hansen, J. W.; Gillberg, L.; Needhamsen, M.; Kaastrup, K.; Helin, K.; Christensen, K.; Weischenfeldt, J.; Grønbæk, K. TET2 mutations are associated with hypermethylation at key regulatory enhancers in normal and malignant hematopoiesis. *Nat. Commun.* **2021**, *12*, 6061. DOI: 10.1038/s41467-021-26093-2.

(169) Khurshed, M.; Molenaar, R. J.; Lenting, K.; Leenders, W. P.; van Noorden, C. J. F. In silico gene expression analysis reveals glycolysis and acetate anaplerosis in IDH1 wild-type glioma and lactate and glutamate anaplerosis in IDH1-mutated glioma. *Oncotarget* **2017**, *8*, 49165-49177. DOI: 10.18632/oncotarget.17106.

(170) Dekker, L. J. M.; Wu, S.; Jurriëns, C.; Mustafa, D. A. N.; Grevers, F.; Burgers, P. C.; Sillevis Smitt, P. A. E.; Kros, J. M.; Luider, T. M. Metabolic changes related to the IDH1 mutation in gliomas preserve TCA-cycle activity: An investigation at the protein level. *FASEB J.* **2020**, *34*, 3646-3657. DOI: 10.1096/fj.201902352R.

(171) Tanaka, K.; Sasayama, T.; Irino, Y.; Takata, K.; Nagashima, H.; Satoh, N.; Kyotani, K.; Mizowaki, T.; Imahori, T.; Ejima, Y.; et al. Compensatory glutamine metabolism promotes glioblastoma resistance to mTOR inhibitor treatment. *J. Clin. Invest.* **2015**, *125*, 1591-1602. DOI: 10.1172/jci78239.

(172) Mashimo, T.; Pichumani, K.; Vemireddy, V.; Hatanpaa, Kimmo J.; Singh, Dinesh K.; Sirasanagandla, S.; Nannepaga, S.; Piccirillo, Sara G.; Kovacs, Z.; Foong, C.; et al. Acetate Is a Bioenergetic Substrate for Human Glioblastoma and Brain Metastases. *Cell* **2014**, *159*, 1603-1614. DOI: 10.1016/j.cell.2014.11.025.

(173) Garrett, M.; Sperry, J.; Braas, D.; Yan, W.; Le, T. M.; Mottahedeh, J.; Ludwig, K.; Eskin, A.; Qin, Y.; Levy, R.; et al. Metabolic characterization of isocitrate dehydrogenase (IDH) mutant and IDH wildtype gliomaspheres uncovers cell type-specific vulnerabilities. *Cancer Metab.* **2018**, *6*, 4. DOI: 10.1186/s40170-018-0177-4.

(174) Viswanath, P.; Najac, C.; Izquierdo-Garcia, J. L.; Pankov, A.; Hong, C.; Eriksson, P.; Costello, J. F.; Pieper, R. O.; Ronen, S. M. Mutant IDH1 expression is associated with down-regulation of monocarboxylate transporters. *Oncotarget* **2016**, *7*, 34942-34955. DOI: 10.18632/oncotarget.9006.

(175) Chaumeil, M. M.; Radoul, M.; Najac, C.; Eriksson, P.; Viswanath, P.; Blough, M. D.; Chesnelong, C.; Luchman, H. A.; Cairncross, J. G.; Ronen, S. M. Hyperpolarized (13)C MR imaging detects no lactate production in mutant IDH1 gliomas: Implications for diagnosis and response monitoring. *Neuroimage Clin.* **2016**, *12*, 180-189. DOI: 10.1016/j.nicl.2016.06.018.

(176) Chesnelong, C.; Chaumeil, M. M.; Blough, M. D.; Al-Najjar, M.; Stechishin, O. D.; Chan, J. A.; Pieper, R. O.; Ronen, S. M.; Weiss, S.; Luchman, H. A.; et al. Lactate dehydrogenase A silencing in IDH mutant gliomas. *Neuro. Oncol.* **2014**, *16*, 686-695. DOI: 10.1093/neuonc/not243.

(177) Izquierdo-Garcia, J. L.; Viswanath, P.; Eriksson, P.; Cai, L.; Radoul, M.; Chaumeil, M. M.; Blough, M.; Luchman, H. A.; Weiss, S.; Cairncross, J. G.; et al. IDH1 Mutation Induces Reprogramming of Pyruvate Metabolism. *Cancer Res.* **2015**, *75*, 2999-3009. DOI: 10.1158/0008-5472.Can-15-0840.

(178) Izquierdo-Garcia, J. L.; Cai, L. M.; Chaumeil, M. M.; Eriksson, P.; Robinson, A. E.; Pieper, R. O.; Phillips, J. J.; Ronen, S. M. Glioma Cells with the IDH1 Mutation Modulate Metabolic Fractional Flux through Pyruvate Carboxylase. *PLOS ONE* **2014**, *9*, e108289. DOI: 10.1371/journal.pone.0108289.

(179) Waitkus, M. S.; Pirozzi, C. J.; Moure, C. J.; Diplas, B. H.; Hansen, L. J.; Carpenter, A. B.; Yang, R.; Wang, Z.; Ingram, B. O.; Karoly, E. D.; et al. Adaptive Evolution of the GDH2 Allosteric Domain Promotes Gliomagenesis by Resolving IDH1(R132H)-Induced Metabolic Liabilities. *Cancer Res.* **2018**, *78*, 36-50. DOI: 10.1158/0008-5472.Can-17-1352.

(180) Chen, R.; Nishimura, M. C.; Kharbanda, S.; Peale, F.; Deng, Y.; Daemen, A.; Forrest, W. F.; Kwong, M.; Hedehus, M.; Hatzivassiliou, G.; et al. Hominoid-specific enzyme GLUD2 promotes growth of IDH1R132H glioma. *Proc. Natl. Acad. Sci.* **2014**, *111*, 14217-14222. DOI: 10.1073/pnas.1409653111.

(181) García-Espinosa, M. A.; Wallin, R.; Hutson, S. M.; Sweatt, A. J. Widespread neuronal expression of branched-chain aminotransferase in the CNS: implications for leucine/glutamate metabolism and for signaling by amino acids. *J. Neurochem.* **2007**, *100*, 1458-1468. DOI: 10.1111/j.1471-4159.2006.04332.x.

(182) Ichihara, A.; Koyama, E. Transaminase of branched chain amino acids. I. Branched chain amino acids-alpha-ketoglutarate transaminase. *J. Biochem.* **1966**, *59*, 160-169. DOI: 10.1093/oxfordjournals.jbchem.a128277.

(183) Institute of Medicine Committee on Nutrition, T.; Erdman, J.; Oria, M.; Pillsbury, L. Branched-Chain Amino Acids. In *Nutrition and Traumatic Brain Injury: Improving Acute and Subacute Health Outcomes in Military Personnel*, National Academies Press (US), 2011.

(184) Hull, J.; Hindy, M. E.; Kehoe, P. G.; Chalmers, K.; Love, S.; Conway, M. E. Distribution of the branched chain aminotransferase proteins in the human brain and their role in glutamate regulation. *J. Neurochem.* **2012**, *123*, 997-1009. DOI: 10.1111/jnc.12044.

(185) Castellano, S.; Casarosa, S.; Sweatt, A. J.; Hutson, S. M.; Bozzi, Y. Expression of cytosolic branched chain aminotransferase (BCATc) mRNA in the developing mouse brain. *Gene Expr. Patterns* **2007**, *7*, 485-490. DOI: 10.1016/j.modgep.2006.10.010.

(186) Tönjes, M.; Barbus, S.; Park, Y. J.; Wang, W.; Schlotter, M.; Lindroth, A. M.; Pleier, S. V.; Bai, A. H. C.; Karra, D.; Piro, R. M.; et al. BCAT1 promotes cell proliferation through amino acid catabolism in gliomas carrying wild-type IDH1. *Nat. Med.* **2013**, *19* (Nat. Med.), 901-908. DOI: 10.1038/nm.3217.

(187) McBrayer, S. K.; Mayers, J. R.; DiNatale, G. J.; Shi, D. D.; Khanal, J.; Chakraborty, A. A.; Sarosiek, K. A.; Briggs, K. J.; Robbins, A. K.; Sewastianik, T.; et al. Transaminase Inhibition by 2-Hydroxyglutarate Impairs Glutamate Biosynthesis and Redox Homeostasis in Glioma. *Cell* **2018**, *175*, 101-116.e125. DOI: 10.1016/j.cell.2018.08.038.

(188) Yielding, K. L.; Tomkins, G. M. An effect of L-leucine and other essential amino acids on the structure and activity of glutamic dehydrogenase. *Proc. Natl. Acad. Sci.* **1961**, *47*, 983-989. DOI: 10.1073/pnas.47.7.983.

(189) Aleshin, V. A.; Bunik, V. I.; Bruch, E. M.; Bellinzoni, M. Structural Basis for the Binding of Allosteric Activators Leucine and ADP to Mammalian Glutamate Dehydrogenase. *Int. J. Mol. Sci.* **2022**, *23*. DOI: 10.3390/ijms231911306.

(190) Schousboe, A.; Scafidi, S.; Bak, L. K.; Waagepetersen, H. S.; McKenna, M. C. Glutamate metabolism in the brain focusing on astrocytes. *Adv. Neurobiol.* **2014**, *11*, 13-30. DOI: 10.1007/978-3-319-08894-5_2.

(191) McKenna, M. C.; Sonnewald, U.; Huang, X.; Stevenson, J.; Zielke, H. R. Exogenous glutamate concentration regulates the metabolic fate of glutamate in astrocytes. *J. Neurochem.* **1996**, *66*, 386-393. DOI: 10.1046/j.1471-4159.1996.66010386.x.

(192) McKenna, M. C. Glutamate pays its own way in astrocytes. *Front. Endocrinol.* **2013**, *4*, 72310. DOI: 10.3389/fendo.2013.00191.

(193) Sonnewald, U.; Westergaard, N.; Petersen, S.; Unsgård, G.; Schousboe, A. Metabolism of [U-13C] glutamate in astrocytes studied by 13C NMR spectroscopy: incorporation of more label into lactate than into glutamine demonstrates the importance of the tricarboxylic acid cycle. *J. Neurochem.* **1993**, *61*, 1179-1182. DOI: 10.1111/j.1471-4159.1993.tb03641.x.

(194) Fan, H.; Zhang, S.; Yuan, Y.; Chen, S.; Li, W.; Wang, Z.; Xiang, Y.; Li, J.; Ma, X.; Liu, Y. Glutamine metabolism-related genes predict prognosis and reshape tumor microenvironment immune characteristics in diffuse gliomas. *Front. Neurol.* **2023**, *14*, Original Research. DOI: 10.3389/fneur.2023.1104738.

(195) Caniglia, J. L.; Jalasutram, A.; Asuthkar, S.; Sahagun, J.; Park, S.; Ravindra, A.; Tsung, A. J.; Guda, M. R.; Velpula, K. K. Beyond glucose: alternative sources of energy in glioblastoma. *Theranostics* **2021**, *11*, 2048-2057, Review. DOI: 10.7150/thno.53506.

(196) Matés, J. M.; Campos-Sandoval, J. A.; Santos-Jiménez, J. d. l.; Márquez, J. Dysregulation of glutaminase and glutamine synthetase in cancer. *Cancer Lett.* **2019**, *467*, 29-39. DOI: 10.1016/j.canlet.2019.09.011.

(197) Tardito, S.; Oudin, A.; Ahmed, S. U.; Fack, F.; Keunen, O.; Zheng, L.; Miletic, H.; Sakariassen, P. Ø.; Weinstock, A.; Wagner, A.; et al. Glutamine synthetase activity fuels nucleotide biosynthesis and supports growth of glutamine-restricted glioblastoma. *Nat. Cell. Biol.* **2015**, *17*, 1556-1568. DOI: 10.1038/ncb3272.

(198) Palmieri, E. M.; Menga, A.; Martín-Pérez, R.; Quinto, A.; Riera-Domingo, C.; De Tullio, G.; Hooper, D. C.; Lamers, W. H.; Ghesquière, B.; McVicar, D. W.; et al. Pharmacologic or Genetic Targeting of Glutamine Synthetase Skews Macrophages toward an M1-like Phenotype and Inhibits Tumor Metastasis. *Cell Rep.* **2017**, *20*, 1654-1666. DOI: 10.1016/j.celrep.2017.07.054.

(199) Ruiz-Rodado, V.; Lita, A.; Dowdy, T.; Celiku, O.; Saldana, A. C.; Wang, H.; Yang, C. Z.; Chari, R.; Li, A.; Zhang, W.; et al. Metabolic plasticity of IDH1-mutant glioma cell lines is responsible for low sensitivity to glutaminase inhibition. *Cancer Metab.* **2020**, *8*, 23. DOI: 10.1186/s40170-020-00229-2.

(200) Choi, C.; Ganji, S. K.; DeBerardinis, R. J.; Hatanpaa, K. J.; Rakheja, D.; Kovacs, Z.; Yang, X. L.; Mashimo, T.; Raisanen, J. M.; Marin-Valencia, I.; et al. 2-hydroxyglutarate detection by magnetic resonance spectroscopy in IDH-mutated patients with gliomas. *Nat. Med.* **2012**, *18*, 624-629. DOI: 10.1038/nm.2682.

(201) An, Z.; Ganji, S. K.; Tiwari, V.; Pinho, M. C.; Patel, T.; Barnett, S.; Pan, E.; Mickey, B. E.; Maher, E. A.; Choi, C. Detection of 2-hydroxyglutarate in brain tumors by triple-refocusing MR spectroscopy at 3T in vivo. *Magn. Reson. Med.* **2017**, *78*, 40-48. DOI: 10.1002/mrm.26347.

(202) Chen, L.; Zhang, Z.; Hoshino, A.; Zheng, H. D.; Morley, M.; Arany, Z.; Rabinowitz, J. D. NADPH production by the oxidative pentose-phosphate pathway supports folate metabolism. *Nat. Metab.* **2019**, *1*, 404-415. DOI: 10.1038/s42255-019-0043-x.

(203) Charitou, P.; Rodriguez-Colman, M.; Gerrits, J.; van Triest, M.; Groot Koerkamp, M.; Hornsveld, M.; Holstege, F.; Verhoeven-Duif, N. M.; Burgering, B. M. FOXOs support the metabolic requirements of normal and tumor cells by promoting IDH1 expression. *EMBO Rep.* **2015**, *16*, 456-466. DOI: 10.15252/embr.201439096.

(204) Lee, J. H.; Kim, S. Y.; Kil, I. S.; Park, J.-W. Regulation of Ionizing Radiation-induced Apoptosis by Mitochondrial $NADP^+$-dependent Isocitrate Dehydrogenase. *J. Biol. Chem.* **2007**, *282*, 13385-13394. DOI: 10.1074/jbc.M700303200.

(205) Han, S. J.; Choi, H. S.; Kim, J. I.; Park, J. W.; Park, K. M. IDH2 deficiency increases the liver susceptibility to ischemia-reperfusion injury via increased mitochondrial oxidative injury. *Redox Biol* **2018**, *14*, 142-153. DOI: 10.1016/j.redox.2017.09.003.

(206) Han, S. J.; Jang, H. S.; Noh, M. R.; Kim, J.; Kong, M. J.; Kim, J. I.; Park, J. W.; Park, K. M. Mitochondrial NADP(+)-Dependent Isocitrate Dehydrogenase Deficiency Exacerbates Mitochondrial and Cell Damage after Kidney Ischemia-Reperfusion Injury. *J. Am. Soc. Nephrol.* **2017**, *28*, 1200-1215. DOI: 10.1681/asn.2016030349.

(207) Ku, H. J.; Ahn, Y.; Lee, J. H.; Park, K. M.; Park, J. W. IDH2 deficiency promotes mitochondrial dysfunction and cardiac hypertrophy in mice. *Free Radic. Biol. Med.* **2015**, *80*, 84-92. DOI: 10.1016/j.freeradbiomed.2014.12.018.

(208) Park, J. H.; Ku, H. J.; Lee, J. H.; Park, J. W. Idh2 Deficiency Exacerbates Acrolein-Induced Lung Injury through Mitochondrial Redox Environment Deterioration. *Oxid. Med. Cell Longev.* **2017**, *2017*, 1595103. DOI: 10.1155/2017/1595103.

(209) Biedermann, J.; Preussler, M.; Conde, M.; Peitzsch, M.; Richter, S.; Wiedemuth, R.; Abou-El-Ardat, K.; Krüger, A.; Meinhardt, M.; Schackert, G.; et al. Mutant IDH1 Differently Affects Redox State and Metabolism in Glial Cells of Normal and Tumor Origin. *Cancers (Basel)* **2019**, *11*. DOI: 10.3390/cancers11122028.

(210) Tang, X.; Fu, X.; Liu, Y.; Yu, D.; Cai, S. J.; Yang, C. Blockade of Glutathione Metabolism in IDH1-Mutated Glioma. *Mol. Cancer. Ther.* **2020**, *19*, 221-230. DOI: 10.1158/1535-7163.Mct-19-0103.

(211) Cano-Galiano, A.; Oudin, A.; Fack, F.; Allega, M. F.; Sumpton, D.; Martinez-Garcia, E.; Dittmar, G.; Hau, A. C.; De Falco, A.; Herold-Mende, C.; et al. Cystathionine-γ-lyase drives antioxidant defense in cysteine-restricted IDH1-mutant astrocytomas. *Neurooncol. Adv.* **2021**, *3*, vdab057. DOI: 10.1093/noajnl/vdab057.

(212) Tiburcio, P. D. B.; Gillespie, D. L.; Jensen, R. L.; Huang, L. E. Extracellular glutamate and IDH1(R132H) inhibitor promote glioma growth by boosting redox potential. *J. Neurooncol.* **2020**, *146*, 427-437. DOI: 10.1007/s11060-019-03359-w.

(213) Wise, D. R.; Ward, P. S.; Shay, J. E. S.; Cross, J. R.; Gruber, J. J.; Sachdeva, U. M.; Platt, J. M.; DeMatteo, R. G.; Simon, M. C.; Thompson, C. B. Hypoxia promotes isocitrate dehydrogenase-dependent carboxylation of α-ketoglutarate to citrate to support cell growth and viability. *Proc. Natl. Acad. Sci.* **2011**, *108*, 19611-19616. DOI: 10.1073/pnas.1117773108.

(214) Metallo, C. M.; Gameiro, P. A.; Bell, E. L.; Mattaini, K. R.; Yang, J.; Hiller, K.; Jewell, C. M.; Johnson, Z. R.; Irvine, D. J.; Guarente, L.; et al. Reductive glutamine metabolism by IDH1 mediates lipogenesis under hypoxia. *Nature* **2011**, *481*, 380-384. DOI: 10.1038/nature10602.

(215) Koh, H.-J.; Lee, S.-M.; Son, B.-G.; Lee, S.-H.; Ryoo, Z. Y.; Chang, K.-T.; Park, J.-W.; Park, D.-C.; Song, B. J.; Veech, R. L.; et al. Cytosolic $NADP^+$-dependent Isocitrate Dehydrogenase Plays a Key Role in Lipid Metabolism. *J. Biol. Chem.* **2004**, *279*, 39968-39974. DOI: 10.1074/jbc.M402260200.

(216) Grassian, A. R.; Parker, S. J.; Davidson, S. M.; Divakaruni, A. S.; Green, C. R.; Zhang, X.; Slocum, K. L.; Pu, M.; Lin, F.; Vickers, C.; et al. IDH1 mutations alter citric acid cycle metabolism and increase dependence on oxidative mitochondrial metabolism. *Cancer Res.* **2014**, *74* (12), 3317-3331. DOI: 10.1158/0008-5472.Can-14-0772-t.

(217) Leonardi, R.; Subramanian, C.; Jackowski, S.; Rock, C. O. Cancer-associated isocitrate dehydrogenase mutations inactivate NADPH-dependent reductive carboxylation. *J. Biol. Chem.* **2012**, *287*, 14615-14620. DOI: 10.1074/jbc.C112.353946.

(218) Jiang, X.; Stockwell, B. R.; Conrad, M. Ferroptosis: mechanisms, biology and role in disease. *Nat. Rev. Mol. Cell. Biol.* **2021**, *22*, 266-282. DOI: 10.1038/s41580-020-00324-8.

(219) Wang, T.-X.; Liang, J.-Y.; Zhang, C.; Xiong, Y.; Guan, K.-L.; Yuan, H.-X. The oncometabolite 2-hydroxyglutarate produced by mutant IDH1 sensitizes cells to ferroptosis. *Cell Death & Dis.* **2019**, *10*, 755. DOI: 10.1038/s41419-019-1984-4.

(220) Ciafrè, S. A.; Galardi, S.; Mangiola, A.; Ferracin, M.; Liu, C. G.; Sabatino, G.; Negrini, M.; Maira, G.; Croce, C. M.; Farace, M. G. Extensive modulation of a set of microRNAs in primary glioblastoma. *Biochem. Biophys. Res. Commun.* **2005**, *334*, 1351-1358. DOI: 10.1016/j.bbrc.2005.07.030.

(221) Shi, L.; Cheng, Z.; Zhang, J.; Li, R.; Zhao, P.; Fu, Z.; You, Y. hsa-mir-181a and hsa-mir-181b function as tumor suppressors in human glioma cells. *Brain Res.* **2008**, *1236*, 185-193. DOI: 10.1016/j.brainres.2008.07.085.

(222) Thomas, D.; Wu, M.; Nakauchi, Y.; Zheng, M.; Thompson-Peach, C. A. L.; Lim, K.; Landberg, N.; Köhnke, T.; Robinson, N.; Kaur, S.; et al. Dysregulated Lipid Synthesis by Oncogenic IDH1 Mutation Is a Targetable Synthetic Lethal Vulnerability. *Cancer Discov.* **2023**, *13*, 496-515. DOI: 10.1158/2159-8290.Cd-21-0218 (acccessed 5/1/2024).

(223) Lita, A.; Pliss, A.; Kuzmin, A.; Yamasaki, T.; Zhang, L.; Dowdy, T.; Burks, C.; de Val, N.; Celiku, O.; Ruiz-Rodado, V.; et al. IDH1 mutations induce organelle defects via dysregulated phospholipids. *Nat. Commun.* **2021**, *12*, 614. DOI: 10.1038/s41467-020-20752-6.

(224) Miyake, M.; Kakimoto, Y.; Sorimachi, M. Isolation and identification of β-citryl-L-glutamic acid from newborn rat brain. *Biochim. Biophys. Acta Gen. Subj.* **1978**, *544*, 656-666. DOI: 10.1016/0304-4165(78)90340-9.

(225) Hamada-Kanazawa, M.; Narahara, M.; Takano, M.; Min, K. S.; Tanaka, K.; Miyake, M. β-Citryl-L-glutamate Acts as an Iron Carrier to Activate Aconitase Activity. *Biol. Pharm. Bull.* **2011**, *34*, 1455-1464. DOI: 10.1248/bpb.34.1455.

(226) Collard, F.; Stroobant, V.; Lamosa, P.; Kapanda, C. N.; Lambert, D. M.; Muccioli, G. G.; Poupaert, J. H.; Opperdoes, F.; Van Schaftingen, E. Molecular Identification of N-Acetylaspartylglutamate Synthase and β-Citrylglutamate Synthase. *J. Biol. Chem.* **2010**, *285*, 29826-29833. DOI: 10.1074/jbc.M110.152629.

(227) Collard, F.; Vertommen, D.; Constantinescu, S.; Buts, L.; Van Schaftingen, E. Molecular Identification of β-citrylglutamate Hydrolase as Glutamate Carboxypeptidase 3. *J. Biol. Chem.* **2011**, *286*, 38220-38230. DOI: 10.1074/jbc.M111.287318.

(228) Lodder-Gadaczek, J.; Becker, I.; Gieselmann, V.; Wang-Eckhardt, L.; Eckhardt, M. N-Acetylaspartylglutamate Synthetase II Synthesizes N-Acetylaspartylglutamylglutamate. *J. Biol. Chem.* **2011**, *286*, 16693-16706. DOI: 10.1074/jbc.M111.230136.

(229) Morland, C.; Nordengen, K. N-Acetyl-Aspartyl-Glutamate in Brain Health and Disease. *Int. J. Mol. Sci.* **2022**, *23*, 1268-1268. DOI: 10.3390/ijms23031268.

(230) Neale, J. H.; Bzdega, T.; Wroblewska, B. N-Acetylaspartylglutamate: the most abundant peptide neurotransmitter in the mammalian central nervous system. *J. Neurochem.* **2000**, *75*, 443-452. DOI: 10.1046/j.1471-4159.2000.0750443.x.

(231) Hamada-Kanazawa, M.; Kouda, M.; Odani, A.; Matsuyama, K.; Kanazawa, K.; Hasegawa, T.; Narahara, M.; Miyake, M. .BETA.-Citryl-L-glutamate Is an Endogenous Iron Chelator That Occurs Naturally in the Developing Brain. *Biol. Pharm. Bull.* **2010**, *33*, 729-737. DOI: 10.1248/bpb.33.729.

(232) Vallianatou, T.; Lin, W.; Bèchet, N. B.; Correia, M. S.; Shanbhag, N. C.; Lundgaard, I.; Globisch, D. Differential regulation of oxidative stress, microbiota-derived, and energy metabolites in the mouse brain during sleep. *J. Cereb. Blood Flow Metab.* **2021**, *41*, 3324-3338. DOI: 10.1177/0271678x211033358.

(233) Wen, S.; Tu, X.; Zang, Q.; Zhu, Y.; Li, L.; Zhang, R.; Abliz, Z. Liquid chromatography–mass spectrometry-based metabolomics and fluxomics reveals the metabolic alterations in glioma U87MG multicellular tumor spheroids versus two-dimensional cell cultures. *Rapid Commun. Mass Spectrom.* **2024**, *38*, e9670. DOI: 10.1002/rcm.9670.

(234) Chen, M.; Li, Y.; Xu, X.; Wang, S.; Liu, Z.; Qi, S.; Si, D.; Man, Z.; Deng, S.; Liu, G.; et al. Metabolic differences in MSTN and FGF5 dual-gene edited sheep muscle cells during myogenesis. *BMC Genom.* **2024**, *25*, 637. DOI: 10.1186/s12864-024-10494-w.

(235) Liu, H.; Xie, T.; Wang, J.; Wang, X.; Han, J.; Huang, Z.; Jiang, L.; Nie, Z. In situ analysis of metabolic changes under hypoxic-ischemic encephalopathy via MALDI mass spectrometry imaging. *Talanta* **2024**, *268*, 125306. DOI: 10.1016/j.talanta.2023.125306.

(236) Gehlert, S.; Weinisch, P.; Römisch-Margl, W.; Jaspers, R. T.; Artati, A.; Adamski, J.; Dyar, K. A.; Aussieker, T.; Jacko, D.; Bloch, W.; et al. Effects of Acute and Chronic Resistance Exercise on the Skeletal Muscle Metabolome. *Metabolites* **2022**, *12*, 445. DOI: 10.3390/metabo12050445.

(237) Westbrook, R.; Zhang, C.; Yang, H.; Tian, J.; Guo, S.; Xue, Q.-L.; Walston, J.; Le, A.; Abadir, P. M. Metabolomics-Based Identification of Metabolic Dysfunction in Frailty. *J. Gerontol: Ser. A* **2021**, *77*, 2367-2372. DOI: 10.1093/gerona/glab315 (acccessed 7/18/2024).

(238) Pipino, C.; Shah, H.; Prudente, S.; Di Pietro, N.; Zeng, L.; Park, K.; Trischitta, V.; Pennathur, S.; Pandolfi, A.; Doria, A. Association of the 1q25 Diabetes-Specific Coronary Heart Disease Locus With Alterations of the γ-Glutamyl Cycle and Increased Methylglyoxal Levels in Endothelial Cells. *Diabetes* **2020**, *69*, 2206-2216. DOI: 10.2337/db20-0475 (acccessed 7/18/2024).

(239) Wang-Eckhardt, L.; Sylvester, M.; Becker, I.; Allam, J.-P.; Eckhardt, M. Citrylglutamate synthase deficient male mice are subfertile with impaired histone and transition protein 2 removal in late spermatids. *Biochem. J.* **2022**, *479*, 953-972. DOI: 10.1042/BCJ20210844 (acccessed 7/18/2024).

(240) Piper, T.; Mehling, L.-M.; Spottke, A.; Heidbreder, A.; Young, P.; Madea, B.; Hess, C.; Schänzer, W.; Thevis, M. Potential of GHB phase-II-metabolites to complement current approaches in GHB post administration detection. *Forensic Sci. Int.* **2017**, *279*, 157-164. DOI: 10.1016/j.forsciint.2017.08.023.

(241) Maekura, K.; Tsukamoto, S.; Hamada-Kanazawa, M.; Takano, M. Rimklb mutation causes male infertility in mice. *Scientific Rep.* **2021**, *11*, 4604. DOI: 10.1038/s41598-021-84105-z.

(242) Bunse, L.; Schumacher, T.; Sahm, F.; Pusch, S.; Oezen, I.; Rauschenbach, K.; Gonzalez, M.; Solecki, G.; Osswald, M.; Capper, D.; et al. Proximity ligation assay evaluates IDH1R132H presentation in gliomas. *J. Clin. Invest.* **2015**, *125*, 593-606. DOI: 10.1172/jci77780.

(243) Schumacher, T.; Bunse, L.; Pusch, S.; Sahm, F.; Wiestler, B.; Quandt, J.; Menn, O.; Osswald, M.; Oezen, I.; Ott, M.; et al. A vaccine targeting mutant IDH1 induces antitumour immunity. *Nature* **2014**, *512*, 324-327. DOI: 10.1038/nature13387.

(244) *IDH1 Peptide Vaccine for Recurrent Grade II Glioma (RESIST)*. 2020. https://clinicaltrials.gov/study/NCT02193347 (accessed 16/02/2025).

(245) Platten, M.; Bunse, L.; Wick, A.; Bunse, T.; Le Cornet, L.; Harting, I.; Sahm, F.; Sanghvi, K.; Tan, C. L.; Poschke, I.; et al. A vaccine targeting mutant IDH1 in newly diagnosed glioma. *Nature* **2021**, *592*, 463-468. DOI: 10.1038/s41586-021-03363-z.

(246) Lin, J.; Lu, W.; Caravella, J. A.; Campbell, A. M.; Diebold, R. B.; Ericsson, A.; Fritzen, E.; Gustafson, G. R.; Lancia, D. R., Jr.; Shelekhin, T.; et al. Discovery and Optimization of Quinolinone Derivatives as Potent, Selective, and Orally Bioavailable Mutant Isocitrate Dehydrogenase 1 (mIDH1) Inhibitors. *J. Med. Chem.* **2019**, *62*, 6575-6596. DOI: 10.1021/acs.jmedchem.9b00362.

(247) Ma, R.; Yun, C. H. Crystal structures of pan-IDH inhibitor AG-881 in complex with mutant human IDH1 and IDH2. *Biochem. Biophys. Res. Commun.* **2018**, *503*, 2912-2917. DOI: 10.1016/j.bbrc.2018.08.068.

(248) Herold, R.; Schofield, C.; Armstrong, F. Electrochemical Nanoreactor Provides a Comprehensive View of Isocitrate Dehydrogenase Cancer-drug Kinetics. *Angew. Chem. Int. Ed.* **2023**, *62*. DOI: 10.1002/anie.202309149.

(249) Herold, R. Expanding the scope of powerful electrochemical methods by exploiting nanoconfined cascade catalysis. University of Oxford, 2023.

(250) Konteatis, Z.; Artin, E.; Nicolay, B.; Straley, K.; Padyana, A. K.; Jin, L.; Chen, Y.; Narayaraswamy, R.; Tong, S.; Wang, F.; et al. Vorasidenib (AG-881): A First-in-Class, Brain-Penetrant Dual Inhibitor of Mutant IDH1 and 2 for Treatment of Glioma. *ACS Med. Chem. Lett.* **2020**, *11*, 101-107. DOI: 10.1021/acsmedchemlett.9b00509.

(251) Popovici-Muller, J.; Lemieux, R. M.; Artin, E.; Saunders, J. O.; Salituro, F. G.; Travins, J.; Cianchetta, G.; Cai, Z.; Zhou, D.; Cui, D.; et al. Discovery of AG-120 (Ivosidenib): A First-in-Class Mutant IDH1 Inhibitor for the Treatment of IDH1 Mutant Cancers. *ACS Med. Chem. Lett.* **2018**, *9*, 300-305. DOI: 10.1021/acsmedchemlett.7b00421.

(252) Mellinghoff, I. K.; Penas-Prado, M.; Peters, K. B.; Burris, H. A., III; Maher, E. A.; Janku, F.; Cote, G. M.; de la Fuente, M. I.; Clarke, J. L.; Ellingson, B. M.; et al. Vorasidenib, a Dual Inhibitor of Mutant IDH1/2, in Recurrent or Progressive Glioma; Results of a First-in-Human Phase I Trial. *Clin. Cancer. Res.* **2021**, *27*, 4491-4499. DOI: 10.1158/1078-0432.Ccr-21-0611.

(253) *Servier Receives Regulatory Filing Acceptances from FDA and EMA for Vorasidenib in the Treatment of IDH-Mutant Diffuse Glioma*. Servier Pharmaceuticals (U.S.), 2024. https://servier.us/blog/vorasidenib-ema-fda-release/ (accessed 3/22/2024).

(254) *FDA approves vorasidenib for Grade 2 astrocytoma or oligodendroglioma with a susceptible IDH1 or IDH2 mutation*. The U.S. Food and Drug Administration, 2024. https://www.fda.gov/drugs/resources-information-approved-drugs/fda-approves-vorasidenib-grade-2-astrocytoma-or-oligodendroglioma-susceptible-idh1-or-idh2-mutation (accessed.

(255) *FDA approves first targeted treatment for patients with relapsed or refractory acute myeloid leukemia who have a certain genetic mutation*. The U.S. Food and Drug Administration, 2018. https://www.fda.gov/news-events/press-announcements/fda-approves-first-targeted-treatment-patients-relapsed-or-refractory-acute-myeloid-leukemia-who (accessed 3/22/2024).

(256) *FDA approves new targeted treatment for relapsed or refractory acute myeloid leukemia*. The U.S. Food and Drug Administration, 2017. https://www.fda.gov/news-events/press-announcements/fda-approves-new-targeted-treatment-relapsed-or-refractory-acute-myeloid-leukemia (accessed 3/22/2024).

(257) Yen, K.; Travins, J.; Wang, F.; David, M. D.; Artin, E.; Straley, K.; Padyana, A.; Gross, S.; DeLaBarre, B.; Tobin, E.; et al. AG-221, a First-in-Class Therapy Targeting Acute Myeloid Leukemia Harboring Oncogenic IDH2 Mutations. *Cancer Discov.* **2017**, *7*, 478-493. DOI: 10.1158/2159-8290.Cd-16-1034 (acccessed 3/22/2024).

(258) Alshiekh Nasany, R.; de la Fuente, M. I. Therapies for IDH-Mutant Gliomas. *Curr. Neurol. Neurosci. Rep.* **2023**, *23*, 225-233. DOI: 10.1007/s11910-023-01265-3 From NLM.

(259) Solomou, G.; Finch, A.; Asghar, A.; Bardella, C. Mutant IDH in Gliomas: Role in Cancer and Treatment Options. *Cancers (Basel)* **2023**, *15*. DOI: 10.3390/cancers15112883 From NLM.

(260) Lin, M. D.; Tsai, A. C. Y.; Abdullah, K. G.; McBrayer, S. K.; Shi, D. D. Treatment of IDH-mutant glioma in the INDIGO era. *npj Precision Oncology* **2024**, *8*, 149. DOI: 10.1038/s41698-024-00646-2.

(261) Harding, J. J.; Lowery, M. A.; Shih, A. H.; Schvartzman, J. M.; Hou, S.; Famulare, C.; Patel, M.; Roshal, M.; Do, R. K.; Zehir, A.; et al. Isoform Switching as a Mechanism of Acquired Resistance to Mutant Isocitrate Dehydrogenase Inhibition. *Cancer Discov.* **2018**, *8*, 1540-1547. DOI: 10.1158/2159-8290.Cd-18-0877.

(262) Choe, S.; Wang, H.; DiNardo, C. D.; Stein, E. M.; de Botton, S.; Roboz, G. J.; Altman, J. K.; Mims, A. S.; Watts, J. M.; Pollyea, D. A.; et al. Molecular mechanisms mediating relapse following ivosidenib monotherapy in IDH1-mutant relapsed or refractory AML. *Blood Adv.* **2020**, *4*, 1894-1905. DOI: 10.1182/bloodadvances.2020001503.

(263) Oltvai, Z. N.; Harley, S. E.; Koes, D.; Michel, S.; Warlick, E. D.; Nelson, A. C.; Yohe, S.; Mroz, P. Assessing acquired resistance to IDH1 inhibitor therapy by full-exon *IDH1* sequencing and structural modeling. *Mol. Case Stud.* **2021**, *7*, a006007. DOI: 10.1101/mcs.a006007.

(264) Intlekofer, A. M.; Shih, A. H.; Wang, B.; Nazir, A.; Rustenburg, A. S.; Albanese, S. K.; Patel, M.; Famulare, C.; Correa, F. M.; Takemoto, N.; et al. Acquired resistance to IDH inhibition through trans or cis dimer-interface mutations. *Nature* **2018**, *559*, 125-129. DOI: 10.1038/s41586-018-0251-7.

(265) Li, J.; Eu, J. Q.; Kong, L. R.; Wang, L.; Lim, Y. C.; Goh, B. C.; Wong, A. L. A. Targeting Metabolism in Cancer Cells and the Tumour Microenvironment for Cancer Therapy. *Molecules* **2020**, *25*. DOI: 10.3390/molecules25204831.

(266) Suijker, J.; Oosting, J.; Koornneef, A.; Struys, E. A.; Salomons, G. S.; Schaap, F. G.; Waaijer, C. J. F.; Wijers-Koster, P. M.; Briaire-de Bruijn, I. H.; Haazen, L.; et al. Inhibition of mutant IDH1 decreases D-2-HG levels without affecting tumorigenic properties of chondrosarcoma cell lines. *Oncotarget* **2015**, *6*. DOI: 10.18632/oncotarget.3723.

(267) Tateishi, K.; Wakimoto, H.; Iafrate, A. J.; Tanaka, S.; Loebel, F.; Lelic, N.; Wiederschain, D.; Bedel, O.; Deng, G.; Zhang, B.; et al. Extreme Vulnerability of IDH1 Mutant Cancers to NAD+ Depletion. *Cancer Cell* **2015**, *28*, 773-784. DOI: 10.1016/j.ccell.2015.11.006.

(268) Molenaar, R. J.; Coelen, R. J. S.; Khurshed, M.; Roos, E.; Caan, M. W. A.; van Linde, M. E.; Kouwenhoven, M.; Bramer, J. A. M.; Bovée, J.; Mathôt, R. A.; et al. Study protocol of a phase IB/II clinical trial of metformin and chloroquine in patients with IDH1-mutated or IDH2-mutated solid tumours. *BMJ Open* **2017**, *7*, e014961. DOI: 10.1136/bmjopen-2016-014961.

(269) Emadi, A.; Jun, S. A.; Tsukamoto, T.; Fathi, A. T.; Minden, M. D.; Dang, C. V. Inhibition of glutaminase selectively suppresses the growth of primary acute myeloid leukemia cells with IDH mutations. *Exp. Hematol.* **2014**, *42*, 247-251. DOI: 10.1016/j.exphem.2013.12.001.

(270) Seltzer, M. J.; Bennett, B. D.; Joshi, A. D.; Gao, P.; Thomas, A. G.; Ferraris, D. V.; Tsukamoto, T.; Rojas, C. J.; Slusher, B. S.; Rabinowitz, J. D.; et al. Inhibition of glutaminase preferentially slows growth of glioma cells with mutant IDH1. *Cancer Res.* **2010**, *70*, 8981-8987. DOI: 10.1158/0008-5472.Can-10-1666.

(271) Elhammali, A.; Ippolito, J. E.; Collins, L.; Crowley, J.; Marasa, J.; Piwnica-Worms, D. A High-Throughput Fluorimetric Assay for 2-Hydroxyglutarate Identifies Zaprinast as a

Glutaminase Inhibitor. *Cancer Discov.* **2014**, *4*, 828-839. DOI: 10.1158/2159-8290.Cd-13-0572.

(272) Cuyàs, E.; Fernández-Arroyo, S.; Corominas-Faja, B.; Rodríguez-Gallego, E.; Bosch-Barrera, J.; Martin-Castillo, B.; De Llorens, R.; Joven, J.; Menendez, J. A. Oncometabolic mutation IDH1 R132H confers a metformin-hypersensitive phenotype. *Oncotarget* **2015**, *6*, 12279-12296. DOI: 10.18632/oncotarget.3733.

(273) Kizilbash, S. H.; McBrayer, S.; Port, J.; Reid, J. M.; Lanza, I.; Allred, J. B.; Chakravarti, A.; Kunos, C.; Adjei, A. A. A phase Ib trial of CB-839 (telaglenastat) in combination with radiation therapy and temozolomide in patients with IDH-mutated diffuse astrocytoma and anaplastic astrocytoma (NCT03528642). *J. Clin. Oncol.* **2019**, *37*, TPS2075-TPS2075. DOI: 10.1200/JCO.2019.37.15_suppl.TPS2075.

(274) Harding, J. J.; Telli, M.; Munster, P.; Voss, M. H.; Infante, J. R.; DeMichele, A.; Dunphy, M.; Le, M. H.; Molineaux, C.; Orford, K.; et al. A Phase I Dose-Escalation and Expansion Study of Telaglenastat in Patients with Advanced or Metastatic Solid Tumors. *Clin. Cancer. Res.* **2021**, *27*, 4994-5003. DOI: 10.1158/1078-0432.Ccr-21-1204.

(275) Mukhopadhyay, S.; Goswami, D.; Adiseshaiah, P. P.; Burgan, W.; Yi, M.; Guerin, T. M.; Kozlov, S. V.; Nissley, D. V.; McCormick, F. Undermining Glutaminolysis Bolsters Chemotherapy While NRF2 Promotes Chemoresistance in KRAS-Driven Pancreatic Cancers. *Cancer Res.* **2020**, *80*, 1630-1643. DOI: 10.1158/0008-5472.Can-19-1363.

(276) Romero, R.; Sayin, V. I.; Davidson, S. M.; Bauer, M. R.; Singh, S. X.; LeBoeuf, S. E.; Karakousi, T. R.; Ellis, D. C.; Bhutkar, A.; Sánchez-Rivera, F. J.; et al. Keap1 loss promotes Kras-driven lung cancer and results in dependence on glutaminolysis. *Nat. Med.* **2017**, *23*, 1362-1368. DOI: 10.1038/nm.4407.

(277) ACTIVITY of a new antimalarial agent, chloroquine (SN 7618). *J. Am. Med. Assoc.* **1946**, *130*, 1069. DOI: 10.1001/jama.1946.02870160015006.

(278) Pascolo, S. Time to use a dose of Chloroquine as an adjuvant to anti-cancer chemotherapies. *Eur. J. Pharmacol.* **2016**, *771*, 139-144. DOI: 10.1016/j.ejphar.2015.12.017.

(279) Choi, M. M.; Kim, E. A.; Choi, S. Y.; Kim, T. U.; Cho, S. W.; Yang, S. J. Inhibitory properties of nerve-specific human glutamate dehydrogenase isozyme by chloroquine. *J. Biochem. Mol. Biol.* **2007**, *40*, 1077-1082. DOI: 10.5483/bmbrep.2007.40.6.1077.

(280) Firat, E.; Weyerbrock, A.; Gaedicke, S.; Grosu, A.-L.; Niedermann, G. Chloroquine or Chloroquine-PI3K/Akt Pathway Inhibitor Combinations Strongly Promote γ-Irradiation-Induced Cell Death in Primary Stem-Like Glioma Cells. *PLOS ONE* **2012**, *7*, e47357. DOI: 10.1371/journal.pone.0047357.

(281) *FDA approves olutasidenib for relapsed or refractory acute myeloid leukemia with a susceptible IDH1 mutation*. The U.S. Food and Drug Administration, 2022. https://www.fda.gov/drugs/resources-information-approved-drugs/fda-approves-olutasidenib-relapsed-or-refractory-acute-myeloid-leukemia-susceptible-idh1-mutation (accessed 10/08/2024).

(282) Kang, C. Olutasidenib: First Approval. *Drugs* **2023**, *83*, 341-346. DOI: 10.1007/s40265-023-01844-1.

(283) Reinbold, R.; Hvinden, I. C.; Rabe, P.; Herold, R. A.; Finch, A.; Wood, J.; Morgan, M.; Staudt, M.; Clifton, I. J.; Armstrong, F. A.; et al. Resistance to the isocitrate dehydrogenase 1 mutant inhibitor ivosidenib can be overcome by alternative dimer-interface binding inhibitors. *Nat. Commun.* **2022**, *13*, 4785. DOI: 10.1038/s41467-022-32436-4.

(284) Zhuang, X.; Pei, H. Z.; Li, T.; Huang, J.; Guo, Y.; Zhao, Y.; Yang, M.; Zhang, D.; Chang, Z.; Zhang, Q.; et al. The Molecular Mechanisms of Resistance to IDH Inhibitors in Acute Myeloid Leukemia. *Front. Oncol.* **2022**, *12*, 931462. DOI: 10.3389/fonc.2022.931462.

(285) Mellinghoff Ingo, K.; van den Bent Martin, J.; Blumenthal Deborah, T.; Touat, M.; Peters Katherine, B.; Clarke, J.; Mendez, J.; Yust-Katz, S.; Welsh, L.; Mason Warren, P.; et al. Vorasidenib in IDH1- or IDH2-Mutant Low-Grade Glioma. *N. Engl. J. Med.* **2023**, *389*, 589-601. DOI: 10.1056/NEJMoa2304194.

(286) Atai, N. A.; Renkema-Mills, N. A.; Bosman, J.; Schmidt, N.; Rijkeboer, D.; Tigchelaar, W.; Bosch, K. S.; Troost, D.; Jonker, A.; Bleeker, F. E.; et al. Differential Activity of NADPH-Producing Dehydrogenases Renders Rodents Unsuitable Models to Study IDH1R132 Mutation Effects in Human Glioblastoma. *J. Histochem. Cytochem.* **2011**, *59*, 489-503. DOI: 10.1369/0022155411400606.

(287) Lee, S. H.; Jo, S. H.; Lee, S. M.; Koh, H. J.; Song, H.; Park, J. W.; Lee, W. H.; Huh, T. L. Role of $NADP^+$-dependent isocitrate dehydrogenase ($NADP^+$-ICDH) on cellular defence against oxidative injury by γ-rays. *Int. J. Radiat. Biol.* **2004**, *80*, 635-642. DOI: 10.1080/09553000400007680.

(288) Kim, S. Y.; Lee, S. M.; Tak, J. K.; Choi, K. S.; Kwon, T. K.; Park, J.-W. Regulation of singlet oxygen-induced apoptosis by cytosolic $NADP^+$-dependent isocitrate dehydrogenase. *Mol. Cell. Biochem.* **2007**, *302*, 27-34. DOI: 10.1007/s11010-007-9421-x.

(289) Jo, S.-H.; Lee, S.-H.; Suk Chun, H.; Min Lee, S.; Koh, H.-J.; Lee, S.-E.; Chun, J.-S.; Park, J.-W.; Huh, T.-L. Cellular Defense against UVB-Induced Phototoxicity by Cytosolic $NADP^+$-Dependent Isocitrate Dehydrogenase. *Biochem. Biophys. Res. Commun.* **2002**, *292*, 542-549. DOI: 10.1006/bbrc.2002.6667.

(290) Shin, S. W.; Kil, I. S.; Park, J.-W. Silencing of mitochondrial $NADP^+$-dependent isocitrate dehydrogenase by small interfering RNA enhances heat shock-induced apoptosis. *Biochem. Biophys. Res. Commun.* **2008**, *366*, 1012-1018. DOI: 10.1016/j.bbrc.2007.12.067.

(291) Shin, A. H.; Kil, I. S.; Yang, E. S.; Huh, T. L.; Yang, C. H.; Park, J.-W. Regulation of high glucose-induced apoptosis by mitochondrial NADP+-dependent isocitrate dehydrogenase. *Biochem. Biophys. Res. Commun.* **2004**, *325*, 32-38. DOI: 10.1016/j.bbrc.2004.09.218.

(292) Kil, I. S.; Kim, S. Y.; Lee, S. J.; Park, J.-W. Small interfering RNA-mediated silencing of mitochondrial NADP+-dependent isocitrate dehydrogenase enhances the sensitivity of HeLa cells toward tumor necrosis factor-α and anticancer drugs. *Free Radic. Biol. Med.* **2007**, *43*, 1197-1207. DOI: 10.1016/j.freeradbiomed.2007.07.009.

(293) Kim, S. Y.; Yoo, Y. H.; Park, J.-W. Silencing of mitochondrial NADP+-dependent isocitrate dehydrogenase gene enhances glioma radiosensitivity. *Biochem. Biophys. Res. Commun.* **2013**, *433*, 260-265. DOI: 10.1016/j.bbrc.2013.02.093.

(294) Haider, A. S.; Ene, C. I.; Palmisciano, P.; Haider, M.; Rao, G.; Ballester, L. Y.; Fuller, G. N. Concurrent IDH1 and IDH2 mutations in glioblastoma: A case report. *Front. Oncol.* **2023**, *13*. DOI: 10.3389/fonc.2023.1071792.

(295) Wang, H.-Y.; Tang, K.; Liang, T.-Y.; Zhang, W.-Z.; Li, J.-Y.; Wang, W.; Hu, H.-M.; Li, M.-Y.; Wang, H.-Q.; He, X.-Z.; et al. The comparison of clinical and biological characteristics between IDH1 and IDH2 mutations in gliomas. *Journal of Experimental & Clinical Cancer Research* **2016**, *35* (1), 86. DOI: 10.1186/s13046-016-0362-7.

(296) Urban, D. J.; Martinez, N. J.; Davis, M. I.; Brimacombe, K. R.; Cheff, D. M.; Lee, T. D.; Henderson, M. J.; Titus, S. A.; Pragani, R.; Rohde, J. M.; et al. Assessing inhibitors of mutant isocitrate dehydrogenase using a suite of pre-clinical discovery assays. *Scientific Rep.* **2017**, *7*, 12758. DOI: 10.1038/s41598-017-12630-x.

(297) Okoye-Okafor, U. C.; Bartholdy, B.; Cartier, J.; Gao, E. N.; Pietrak, B.; Rendina, A. R.; Rominger, C.; Quinn, C.; Smallwood, A.; Wiggall, K. J.; et al. New IDH1 mutant inhibitors for treatment of acute myeloid leukemia. *Nat. Chem. Biol.* **2015**, *11*, 878-886. DOI: 10.1038/nchembio.1930.

(298) Deng, G.; Shen, J.; Yin, M.; McManus, J.; Mathieu, M.; Gee, P.; He, T.; Shi, C.; Bedel, O.; McLean, L. R.; et al. Selective Inhibition of Mutant Isocitrate Dehydrogenase 1 (IDH1) via Disruption of a Metal Binding Network by an Allosteric Small Molecule. *J. Biol. Chem.* **2015**, *290*, 762-774. DOI: 10.1074/jbc.M114.608497.

(299) Chaturvedi, A.; Herbst, L.; Pusch, S.; Klett, L.; Goparaju, R.; Stichel, D.; Kaulfuss, S.; Panknin, O.; Zimmermann, K.; Toschi, L.; et al. Pan-mutant-IDH1 inhibitor BAY1436032 is highly effective against human IDH1 mutant acute myeloid leukemia in vivo. *Leukemia* **2017**, *31*, 2020-2028. DOI: 10.1038/leu.2017.46.

(300) Pusch, S.; Krausert, S.; Fischer, V.; Balss, J.; Ott, M.; Schrimpf, D.; Capper, D.; Sahm, F.; Eisel, J.; Beck, A.-C.; et al. Pan-mutant IDH1 inhibitor BAY 1436032 for effective treatment of IDH1 mutant astrocytoma in vivo. *Acta Neuropathol.* **2017**, *133*, 629-644. DOI: 10.1007/s00401-017-1677-y.

(301) Brooks, N.; DeWalt, R.; Boulet, S.; Lu, Z. H.; Kays, L.; Cavitt, R.; Gomez, S.; Strelow, J.; Milligan, P.; Roth, K.; et al. Identification and characterization of LY3410738, a novel covalent inhibitor of cancer-associated mutant Isocitrate Dehydrogenase 1 (IDH1). *Cancer Res.* **2019**, *79*. DOI: 10.1158/1538-7445.Am2019-lb-274.

(302) Cho, Y. S.; Levell, J. R.; Liu, G.; Caferro, T.; Sutton, J.; Shafer, C. M.; Costales, A.; Manning, J. R.; Zhao, Q.; Sendzik, M.; et al. Discovery and Evaluation of Clinical Candidate IDH305, a Brain Penetrant Mutant IDH1 Inhibitor. *ACS Med. Chem. Lett.* **2017**, *8*, 1116-1121. DOI: 10.1021/acsmedchemlett.7b00342.

(303) Levell, J. R.; Caferro, T.; Chenail, G.; Dix, I.; Dooley, J.; Firestone, B.; Fortin, P. D.; Giraldes, J.; Gould, T.; Growney, J. D.; et al. Optimization of 3-Pyrimidin-4-yl-oxazolidin-2-ones as Allosteric and Mutant Specific Inhibitors of IDH1. *ACS Med. Chem. Lett.* **2017**, *8*, 151-156. DOI: 10.1021/acsmedchemlett.6b00334.

(304) Zhao, Q.; Manning, J. R.; Sutton, J.; Costales, A.; Sendzik, M.; Shafer, C. M.; Levell, J. R.; Liu, G.; Caferro, T.; Cho, Y. S.; et al. Optimization of 3-Pyrimidin-4-yl-oxazolidin-2-ones as Orally Bioavailable and Brain Penetrant Mutant IDH1 Inhibitors. *ACS Med. Chem. Lett.* **2018**, *9*, 746-751. DOI: 10.1021/acsmedchemlett.8b00182.

(305) Liu, X. The Studies on the Mechanism and Inhibition of Isocitrate Dehydrogenases. Oxford, 2022.

(306) Lee, L. Structure-Activity Relationship Studies of Almitrine and its Analogues as Pulmonary Vasoconstrictors. Oxford, 2021.

(307) Jiang, L.; Geng, M.; Zheng, Q.; Huang, M.; Wan, H.; Tang, S.; Fu, X.; Lan, X.; Cao, J.; Liu, F.; et al. Compound having mutant IDH inhibitory activity, preparation method and use thereof. US10682352B2, 2020.

(308) Cho, Y. S.; Levell, J. R.; Liu, G.; Shultz, M. D.; Van, D. P. S. C. 3-Pyrimidin-4-Yl-Oxazolidin-2-Ones as Inhibitors of Mutant Idh. WO2014141153A1, 2014.

(309) Luh, L. M.; Scheib, U.; Juenemann, K.; Wortmann, L.; Brands, M.; Cromm, P. M. Prey for the Proteasome: Targeted Protein Degradation-A Medicinal Chemist's Perspective. *Angew. Chem. Int. Ed.* **2020**, *59*, 15448-15466. DOI: 10.1002/anie.202004310.

(310) Sakamoto, K. M.; Kim, K. B.; Kumagai, A.; Mercurio, F.; Crews, C. M.; Deshaies, R. J. Protacs: chimeric molecules that target proteins to the Skp1-Cullin-F box complex for ubiquitination and degradation. *Proc. Natl. Acad. Sci.* **2001**, *98*, 8554-8559. DOI: 10.1073/pnas.141230798.

(311) Békés, M.; Langley, D. R.; Crews, C. M. PROTAC targeted protein degraders: the past is prologue. *Nat. Rev. Drug. Discov.* **2022**, *21*, 181-200. DOI: 10.1038/s41573-021-00371-6.

(312) Mainolfi, N.; Ji, N.; Kluge, A. F.; Weiss, M. M.; Zhang, Y. Irak Degraders and Uses Thereof. US2019192668A1, 2019.

(313) Dong, Y.; Ma, T.; Xu, T.; Feng, Z.; Li, Y.; Song, L.; Yao, X.; Ashby, C. R.; Hao, G.-F. Characteristic roadmap of linker governs the rational design of PROTACs. *Acta Pharm. Sin. B.* **2024**. DOI: 10.1016/j.apsb.2024.04.007.

(314) Hu, Z.; Wang, Q.; Hu, S.; Su, H. Preparation method of 5-aminolevulinic acid hydrochloride intermediate. CN111592484A, 2020.

(315) Zhang, J.; Che, J.; Luo, X.; Wu, M.; Kan, W.; Jin, Y.; Wang, H.; Pang, A.; Li, C.; Huang, W.; et al. Structural Feature Analyzation Strategies toward Discovery of Orally Bioavailable PROTACs of Bruton's Tyrosine Kinase for the Treatment of Lymphoma. *J. Med. Chem.* **2022**, *65*, 9096-9125. DOI: 10.1021/acs.jmedchem.2c00324.

(316) Zhou, F.; Chen, L.; Cao, C.; Yu, J.; Luo, X.; Zhou, P.; Zhao, L.; Du, W.; Cheng, J.; Xie, Y.; et al. Development of selective mono or dual PROTAC degrader probe of CDK isoforms. *Eur. J. Med. Chem.* **2020**, *187*, 111952-111952. DOI: 10.1016/j.ejmech.2019.111952.

(317) Li, L.; Wu, Y.; Yang, Z.; Xu, C.; Zhao, H.; Liu, J.; Chen, J.; Chen, J. Discovery of KRas G12C-IN-3 and Pomalidomide-based PROTACs as degraders of endogenous KRAS G12C with potent anticancer activity. *Bioorg. Chem.* **2021**, *117*, 105447. DOI: 10.1016/j.bioorg.2021.105447.

(318) Petersen, T.; Larsen, A.; Ritzén, A.; Ulven, T. Continuous Flow Nucleophilic Aromatic Substitution with Dimethylamine Generated in Situ by Decomposition of DMF. *J. Org. Chem.* **2013**, *78*. DOI: 10.1021/jo400390t.

(319) Garcia, J.; Sorrentino, J.; Diller, E. J.; Chapman, D.; Woydziak, Z. R. General method for nucleophilic aromatic substitution of aryl fluorides and chlorides with dimethylamine using hydroxide-assisted decomposition of N,N-dimethylforamide. *Synth. Commun.* **2016**, *46*, 475-481. DOI: 10.1080/00397911.2016.1147051.

(320) Schumacher, H.; Smith, R. L.; Williams, R. T. The Metabolism of Thalidomide: The spontaneous Hydrolysis of Thalidomide in Solution. *Br. J. Pharmacol. Chemother.* **1965**, *25*, 324-337. DOI: 10.1111/j.1476-5381.1965.tb02053.x (acccessed 2024/04/26).

(321) Sissung, M. T.; Thordardottir, S.; Gardner, R. E.; Figg, D. W. Current Status of Thalidomide and CC-5013 in the Treatment of Metastatic Prostate Cancer. *Anti-Cancer Agents Med. Chem.* **2009**, *9*, 1058-1069. DOI: 10.2174/187152009789735017.

(322) Armstrong, F. A.; Cheng, B.; Herold, R. A.; Megarity, C. F.; Siritanaratkul, B. From Protein Film Electrochemistry to Nanoconfined Enzyme Cascades and the Electrochemical Leaf. *Chem. Rev.* **2023**, *123*, 5421-5458. DOI: 10.1021/acs.chemrev.2c00397.

(323) Herold, R.; Reinbold, R.; Megarity, C.; Abboud, M.; Schofield, C.; Armstrong, F. Exploiting Electrode Nanoconfinement to Investigate the Catalytic Properties of Isocitrate Dehydrogenase (IDH1) and a Cancer-Associated Variant. *J. Phys. Chem. Lett.* **2021**, *12*, 6095−6101. DOI: 10.1021/acs.jpclett.1c01517.

(324) Herold, R.; Reinbold, R.; Schofield, C.; Armstrong, F. NADP(H)-dependent biocatalysis without adding NADP(H). *Proc. Natl. Acad. Sci.* **2022**, *120*. DOI: 10.1073/pnas.2214123120.

(325) Herold, R. Expanding the Scope of Powerful Electrochemical Methods by Exploiting Nanoconfined Cascade Catalysis. University of Oxford, 2023.

(326) Babu, A. N.; Cheng, T. P.; Zhang, A.; Altura, B. T.; Altura, B. M. Low concentrations of ethanol deplete type-2 astrocytes of intracellular free magnesium. *Brain Res. Bull.* **1999**, *50*, 59-62. DOI: 10.1016/s0361-9230(99)00091-x.

(327) Sun, L.; Kosugi, Y.; Kawakami, E.; Piao, Y.-S.; Hashimoto, T.; Oyanagi, K. Magnesium concentration in the cerebrospinal fluid of mice and its response to changes in

serum magnesium concentration. *Magnes. Res.* **2009**, *22*, 266-272. DOI: 10.1684/mrh.2009.0186.

(328) Xie, X.; Baird, D.; Bowen, K.; Capka, V.; Chen, J.; Chenail, G.; Cho, Y.; Dooley, J.; Farsidjani, A.; Fortin, P.; et al. Allosteric Mutant IDH1 Inhibitors Reveal Mechanisms for IDH1 Mutant and Isoform Selectivity. *Structure* **2017**, *25*, 506-513. DOI: 10.1016/j.str.2016.12.017.

(329) Yang, B.; Zhong, C.; Peng, Y.; Lai, Z.; Ding, J. Molecular mechanisms of "off-on switch" of activities of human IDH1 by tumor-associated mutation R132H. *Cell. Res.* **2010**, *20*, 1188-1200. DOI: 10.1038/cr.2010.145.

(330) Zhao, S.; Guan, K.-L. IDH1 mutant structures reveal a mechanism of dominant inhibition. *Cell. Res.* **2010**, *20*, 1279-1281. DOI: 10.1038/cr.2010.160.

(331) Tan, E. H. L.; Govender, D. S. K.; Birge, R. R. Large Organic Cations Can Replace Mg2+ and Ca2+ Ions in Bacteriorhodopsin and Maintain Proton Pumping Ability. *J. Am. Chem. Soc.* **1996**, *118*, 2752-2753. DOI: 10.1021/ja953491+.

(332) Baker, J. R.; Chaykin, S. The Biosynthesis of Trimethylamine-N-Oxide. *J. Biol. Chem.* **1962**, *237*, 1309-1313. DOI: 10.1016/S0021-9258(18)60325-4.

(333) Zou, Q.; Bennion, B. J.; Daggett, V.; Murphy, K. P. The Molecular Mechanism of Stabilization of Proteins by TMAO and Its Ability to Counteract the Effects of Urea. *J. Am. Chem. Soc.* **2002**, *124*, 1192-1202. DOI: 10.1021/ja004206b.

(334) Reinbold, R. Studies on human cancer variant and mycobacterial isocitrate dehydrogenases. University of Oxford, 2021.

(335) Kirsch, P.; Hartman, A. M.; Hirsch, A. K. H.; Empting, M. Concepts and Core Principles of Fragment-Based Drug Design. *Molecules* **2019**, *24*. DOI: 10.3390/molecules24234309 From NLM.

(336) Salamanca-Cardona, L.; Shah, H.; Poot, A. J.; Correa, F. M.; Di Gialleonardo, V.; Lui, H.; Miloushev, V. Z.; Granlund, K. L.; Tee, S. S.; Cross, J. R.; et al. In Vivo Imaging of Glutamine Metabolism to the Oncometabolite 2-Hydroxyglutarate in IDH1/2 Mutant Tumors. *Cell Metab.* **2017**, *26*, 830-841.e833. DOI: 10.1016/j.cmet.2017.10.001.

(337) Li, L.; Paz, A. C.; Wilky, B. A.; Johnson, B.; Galoian, K.; Rosenberg, A.; Hu, G.; Tinoco, G.; Bodamer, O.; Trent, J. C. Treatment with a Small Molecule Mutant IDH1 Inhibitor Suppresses Tumorigenic Activity and Decreases Production of the Oncometabolite 2-Hydroxyglutarate in Human Chondrosarcoma Cells. *PLOS ONE* **2015**, *10*, e0133813. DOI: 10.1371/journal.pone.0133813.

(338) Chaturvedi, A.; Goparaju, R.; Gupta, C.; Weder, J.; Klünemann, T.; Araujo Cruz, M. M.; Kloos, A.; Goerlich, K.; Schottmann, R.; Othman, B.; et al. In vivo efficacy of mutant IDH1 inhibitor HMS-101 and structural resolution of distinct binding site. *Leukemia* **2020**, *34*, 416-426. DOI: 10.1038/s41375-019-0582-x.

(339) Molloy, A. R.; Najac, C.; Viswanath, P.; Lakhani, A.; Subramani, E.; Batsios, G.; Radoul, M.; Gillespie, A. M.; Pieper, R. O.; Ronen, S. M. MR-detectable metabolic biomarkers of response to mutant IDH inhibition in low-grade glioma. *Theranostics* **2020**, *10*, 8757-8770, Research Paper. DOI: 10.7150/thno.47317.

(340) Radoul, M.; Hong, D.; Gillespie, A. M.; Najac, C.; Viswanath, P.; Pieper, R. O.; Costello, J. F.; Luchman, H. A.; Ronen, S. M. Early Noninvasive Metabolic Biomarkers of Mutant IDH Inhibition in Glioma. *Metabolites* **2021**, *11*, 109. DOI: 10.3390/metabo11020109.

(341) Andronesi, O. C.; Arrillaga-Romany, I. C.; Ly, K. I.; Bogner, W.; Ratai, E. M.; Reitz, K.; Iafrate, A. J.; Dietrich, J.; Gerstner, E. R.; Chi, A. S.; et al. Pharmacodynamics of mutant-

IDH1 inhibitors in glioma patients probed by in vivo 3D MRS imaging of 2-hydroxyglutarate. *Nat. Commun.* **2018**, *9*, 1474. DOI: 10.1038/s41467-018-03905-6.

(342) Kruger, N. J.; von Schaewen, A. The oxidative pentose phosphate pathway: structure and organisation. *Curr. Opin. Plant. Biol.* **2003**, *6*, 236-246. DOI: 10.1016/S1369-5266(03)00039-6.

(343) Horecker, B. L. The Pentose Phosphate Pathway. *J. Biol. Chem.* **2002**, *277*, 47965-47971. DOI: 10.1074/jbc.X200007200.

(344) Li, S.; Lu, Y.; Peng, B.; Ding, J. Crystal structure of human phosphoribosylpyrophosphate synthetase 1 reveals a novel allosteric site. *Biochem. J.* **2006**, *401*, 39-47. DOI: 10.1042/bj20061066.

(345) Zhang, Y.; Desharnais, J.; Greasley, S. E.; Beardsley, G. P.; Boger, D. L.; Wilson, I. A. Crystal Structures of Human GAR Tfase at Low and High pH and with Substrate β-GAR. *Biochem.* **2002**, *41*, 14206-14215. DOI: 10.1021/bi020522m.

(346) Hartman, S. C.; Buchanan, J. M. Biosynthesis of the purines. XXVI. The identification of the formyl donors of the transformylation reactions. *J. Biol. Chem.* **1959**, *234*, 1812-1816.

(347) Melnick, I.; Buchanan, J. M. BIOSYNTHESIS OF THE PURINES: XIV. CONVERSION OF (α-N-FORMYL)GLYCINAMIDE RIBOTIDE TO (α-N-FORMYL)GLYCINAMIDINE RIBOTIDE; PURIFICATION AND REQUIREMENTS OF THE ENZYME SYSTEM. *J. Biol. Chem.* **1957**, *225*, 157-162. DOI: 10.1016/S0021-9258(18)64918-X.

(348) Welin, M.; Grossmann, J. G.; Flodin, S.; Nyman, T.; Stenmark, P.; Trésaugues, L.; Kotenyova, T.; Johansson, I.; Nordlund, P.; Lehtiö, L. Structural studies of tri-functional human GART. *Nucleic Acids Res.* **2010**, *38*, 7308-7319. DOI: 10.1093/nar/gkq595 (acccessed 8/25/2024).

(349) Li, S.-X.; Tong, Y.-P.; Xie, X.-C.; Wang, Q.-H.; Zhou, H.-N.; Han, Y.; Zhang, Z.-Y.; Gao, W.; Li, S.-G.; Zhang, X. C.; et al. Octameric Structure of the Human Bifunctional Enzyme PAICS in Purine Biosynthesis. *J. Mol. Biol.* **2007**, *366*, 1603-1614. DOI: 10.1016/j.jmb.2006.12.027.

(350) Spiegel, E. K.; Colman, R. F.; Patterson, D. Adenylosuccinate lyase deficiency. *Mol. Genet. Metab.* **2006**, *89*, 19-31. DOI: 10.1016/j.ymgme.2006.04.018.

(351) Cheong, C.-G.; Wolan, D. W.; Greasley, S. E.; Horton, P. A.; Beardsley, G. P.; Wilson, I. A. Crystal Structures of Human Bifunctional Enzyme Aminoimidazole-4-carboxamide Ribonucleotide Transformylase/IMP Cyclohydrolase in Complex with Potent Sulfonyl-containing Antifolates. *J. Biol. Chem.* **2004**, *279*, 18034-18045. DOI: 10.1074/jbc.M313691200.

(352) Rayl, E. A.; Moroson, B. A.; Beardsley, G. P. The Human purH Gene Product, 5-Aminoimidazole-4-carboxamide Ribonucleotide Formyltransferase/IMP Cyclohydrolase: CLONING, SEQUENCING, EXPRESSION, PURIFICATION, KINETIC ANALYSIS, AND DOMAIN MAPPING (∗). *J. Biol. Chem.* **1996**, *271*, 2225-2233. DOI: 10.1074/jbc.271.4.2225.

(353) Brayton, K. A.; Chen, Z.; Zhou, G.; Nagy, P. L.; Gavalas, A.; Trent, J. M.; Deaven, L. L.; Dixon, J. E.; Zalkin, H. Two genes for de novo purine nucleotide synthesis on human chromosome 4 are closely linked and divergently transcribed. *J. Biol. Chem.* **1994**, *269*, 5313-5321. DOI: 10.1016/S0021-9258(17)37689-5.

(354) Ireland, L. S.; Harrison, D. J.; Neal, G. E.; Hayes, J. D. Molecular cloning, expression and catalytic activity of a human AKR7 member of the aldo-keto reductase superfamily: evidence that the major 2-carboxybenzaldehyde reductase from human liver is a homologue

of rat aflatoxin B1-aldehyde reductase. *Biochem. J.* **1998**, *332 (Pt 1)*, 21-34. DOI: 10.1042/bj3320021.

(355) Tunnicliff, G. 4-Aminobutyrate Transaminase. In *Neurotransm. Enzym.*, Boulton, A. A., Baker, G. B., Yu, P. H. Eds.; Humana Press, 1986; pp 389-420.

(356) Rashmi, D.; Zanan, R.; John, S.; Khandagale, K.; Nadaf, A. Chapter 13 - γ-Aminobutyric Acid (GABA): Biosynthesis, Role, Commercial Production, and Applications. In *Stud. Nat. Prod. Chem.*, Atta ur, R. Ed.; Vol. 57; Elsevier, 2018; pp 413-452.

(357) Kaufman, E. E.; Nelson, T. An overview of γ-hydroxybutyrate catabolism: The role of the cytosolic NADP+-dependent oxidoreductase EC 1.1.1.19 and of a mitochondrial hydroxyacid-oxoacid transhydrogenase in the initial, rate-limiting step in this pathway. *Neurochem. Res.* **1991**, *16*, 965-974. DOI: 10.1007/BF00965839.

(358) Navrátil, M.; Tykvart, J.; Schimer, J.; Pachl, P.; Navrátil, V.; Rokob, T. A.; Hlouchová, K.; Rulíšek, L.; Konvalinka, J. Comparison of human glutamate carboxypeptidases II and III reveals their divergent substrate specificities. *FEBS J.* **2016**, *283*, 2528-2545. DOI: 10.1111/febs.13761.

(359) Boyko, A. I.; Karlina, I. S.; Zavileyskiy, L. G.; Aleshin, V. A.; Artiukhov, A. V.; Kaehne, T.; Ksenofontov, A. L.; Ryabov, S. I.; Graf, A. V.; Tramonti, A.; et al. Delayed Impact of 2-Oxoadipate Dehydrogenase Inhibition on the Rat Brain Metabolism Is Linked to Protein Glutarylation. *Front. Med.* **2022**, *9*, Original Research. DOI: 10.3389/fmed.2022.896263.

(360) Fu, Z.; Wang, M.; Paschke, R.; Rao, K. S.; Frerman, F. E.; Kim, J.-J. P. Crystal Structures of Human Glutaryl-CoA Dehydrogenase with and without an Alternate Substrate: Structural Bases of Dehydrogenation and Decarboxylation Reactions. *Biochem.* **2004**, *43*, 9674-9684. DOI: 10.1021/bi049290c.

(361) Amaral, A. U.; Ferreira, G. C.; Seminotti, B.; Leipnitz, G.; Wajner, M. Glutaric Acid Neurotoxicity: Mechanisms and Actions. In *Handb Neurotox.*, Kostrzewa, R. M. Ed.; Springer International Publishing, 2021; pp 1-35.

(362) Wajner, M. Glutaric Acidemia Type 1: An Inherited Neurometabolic Disorder of Intoxication. In *Handb. Neurotox.*, Kostrzewa, R. M. Ed.; Springer International Publishing, 2021; pp 1-25.

(363) Shen, H.; Campanello, G. C.; Flicker, D.; Grabarek, Z.; Hu, J.; Luo, C.; Banerjee, R.; Mootha, V. K. The Human Knockout Gene CLYBL Connects Itaconate to Vitamin B(12). *Cell* **2017**, *171*, 771-782.e711. DOI: 10.1016/j.cell.2017.09.051.

(364) Strittmatter, L.; Li, Y.; Nakatsuka, N. J.; Calvo, S. E.; Grabarek, Z.; Mootha, V. K. CLYBL is a polymorphic human enzyme with malate synthase and β-methylmalate synthase activity. *Human. Mol. Gen.* **2013**, *23*, 2313-2323. DOI: 10.1093/hmg/ddt624 (acccessed 8/19/2024).

(365) Zuhra, K.; Augsburger, F.; Majtan, T.; Szabo, C. Cystathionine-β-Synthase: Molecular Regulation and Pharmacological Inhibition. *Biomol.* **2020**, *10*. DOI: 10.3390/biom10050697.

(366) Gall, W. E.; Beebe, K.; Lawton, K. A.; Adam, K.-P.; Mitchell, M. W.; Nakhle, P. J.; Ryals, J. A.; Milburn, M. V.; Nannipieri, M.; Camastra, S.; et al. α-Hydroxybutyrate Is an Early Biomarker of Insulin Resistance and Glucose Intolerance in a Nondiabetic Population. *PLOS ONE* **2010**, *5*, e10883. DOI: 10.1371/journal.pone.0010883.

(367) Lord, R. S.; Bralley, J. A. Clinical applications of urinary organic acids. Part 2. Dysbiosis markers. *Altern. Med. Rev.* **2008**, *13*, 292-306.

(368) Koltai, T.; Reshkin, S. J.; Baltazar, F.; Fliegel, L. Chapter 4 - Lipid metabolism part I: an overview. In *Prostate Cancer Metab.*, Koltai, T., Reshkin, S. J., Baltazar, F., Fliegel, L. Eds.; Academic Press, 2021; pp 71-135.

(369) Horecker, B. L.; Smyrniotis, P. Z.; Seegmiller, J. E. THE ENZYMATIC CONVERSION OF 6-PHOSPHOGLUCONATE TO RIBULOSE-5-PHOSPHATE AND RIBOSE-5-PHOSPHATE. *J. Biol. Chem.* **1951**, *193*, 383-396. DOI: 10.1016/S0021-9258(19)52464-4.

(370) Apel, T. W.; Scherer, A.; Adachi, T.; Auch, D.; Ayane, M.; Reth, M. The ribose 5-phosphate isomerase-encoding gene is located immediately downstream from that encoding murine immunoglobulin kappa. *Gene* **1995**, *156*, 191-197. DOI: 10.1016/0378-1119(94)00901-4.

(371) Sonoda, Y.; Kumabe, T.; Nakamura, T.; Saito, R.; Kanamori, M.; Yamashita, Y.; Suzuki, H.; Tominaga, T. Analysis of IDH1 and IDH2 mutations in Japanese glioma patients. *Cancer Sci.* **2009**, *100*, 1996-1998. DOI: 10.1111/j.1349-7006.2009.01270.x.

(372) Modrek, A. S.; Golub, D.; Khan, T.; Bready, D.; Prado, J.; Bowman, C.; Deng, J.; Zhang, G.; Rocha, P. P.; Raviram, R.; et al. Low-Grade Astrocytoma Mutations in IDH1, P53, and ATRX Cooperate to Block Differentiation of Human Neural Stem Cells via Repression of SOX2. *Cell Rep.* **2017**, *21*, 1267-1280. DOI: 10.1016/j.celrep.2017.10.009.

(373) Kim, Y. G.; Lee, S.; Kwon, O. S.; Park, S. Y.; Lee, S. J.; Park, B. J.; Kim, K. J. Redox-switch modulation of human SSADH by dynamic catalytic loop. *EMBO J.* **2009**, *28*, 959-968. DOI: 10.1038/emboj.2009.40.

(374) Li, Q.; Yang, C.; Feng, L.; Zhao, Y.; Su, Y.; Liu, H.; Men, H.; Huang, Y.; Körner, H.; Wang, X. Glutaric Acidemia, Pathogenesis and Nutritional Therapy. *Front. Nutr.* **2021**, *8*, 704984. DOI: 10.3389/fnut.2021.704984.

(375) Kölker, S.; Koeller, D. M.; Okun, J. G.; Hoffmann, G. F. Pathomechanisms of neurodegeneration in glutaryl-CoA dehydrogenase deficiency. *Ann. Neurol.* **2004**, *55*, 7-12. DOI: 10.1002/ana.10784.

(376) Hallen, A.; Jamie, J. F.; Cooper, A. J. L. Lysine metabolism in mammalian brain: an update on the importance of recent discoveries. *Amino Acids* **2013**, *45*, 1249-1272. DOI: 10.1007/s00726-013-1590-1.

(377) Violante, S.; Achetib, N.; van Roermund, C. W. T.; Hagen, J.; Dodatko, T.; Vaz, F. M.; Waterham, H. R.; Chen, H.; Baes, M.; Yu, C.; et al. Peroxisomes can oxidize medium- and long-chain fatty acids through a pathway involving ABCD3 and HSD17B4. *FASEB J.* **2019**, *33*, 4355-4364. DOI: 10.1096/fj.201801498R.

(378) Lazarow, P. B. Rat liver peroxisomes catalyze the beta oxidation of fatty acids. *J. Biol. Chem.* **1978**, *253*, 1522-1528. DOI: 10.1016/S0021-9258(17)34897-4.

(379) Ding, L.; Sun, W.; Balaz, M.; He, A.; Klug, M.; Wieland, S.; Caiazzo, R.; Raverdy, V.; Pattou, F.; Lefebvre, P.; et al. Peroxisomal β-oxidation acts as a sensor for intracellular fatty acids and regulates lipolysis. *Nat. Metab.* **2021**, *3*, 1648-1661. DOI: 10.1038/s42255-021-00489-2.

(380) Li, X.; Xu, Z.; Lu, X.; Yang, X.; Yin, P.; Kong, H.; Yu, Y.; Xu, G. Comprehensive two-dimensional gas chromatography/time-of-flight mass spectrometry for metabonomics: Biomarker discovery for diabetes mellitus. *Analytica Chim. Acta.* **2009**, *633*, 257-262. DOI: 10.1016/j.aca.2008.11.058.

(381) Collard, F.; Stroobant, V.; Lamosa, P.; Kapanda, C. N.; Lambert, D. M.; Muccioli, G. G.; Poupaert, J. H.; Opperdoes, F.; Van Schaftingen, E. Molecular identification of N-acetylaspartylglutamate synthase and beta-citrylglutamate synthase. *J. Biol. Chem.* **2010**, *285*, 29826-29833. DOI: 10.1074/jbc.M110.152629.

(382) Arun, P.; Madhavarao, C. N.; Moffett, J. R.; Namboodiri, M. A. A. Regulation of N-acetylaspartate and N-acetylaspartylglutamate biosynthesis by protein kinase activators. *J. Neurochem.* **2006**, *98*, 2034-2042. DOI: 10.1111/j.1471-4159.2006.04068.x.

(383) Kikkawa, U.; Matsuzaki, H.; Yamamoto, T. Protein Kinase Cδ (PKCδ): Activation Mechanisms and Functions. *J. Biochem.* **2002**, *132*, 831-839. DOI: 10.1093/oxfordjournals.jbchem.a003294.

(384) Goel, G.; Makkar, H. P.; Francis, G.; Becker, K. Phorbol esters: structure, biological activity, and toxicity in animals. *Int. J. Toxicol.* **2007**, *26*, 279-288. DOI: 10.1080/10915810701464641.

(385) Sun, X.; Wu, F.; Datta, R.; Kharbanda, S.; Kufe, D. Interaction between Protein Kinase C δ and the c-Abl Tyrosine Kinase in the Cellular Response to Oxidative Stress. *J. Biol. Chem.* **2000**, *275*, 7470-7473. DOI: 10.1074/jbc.275.11.7470.

(386) Greter, J.; Lindstedt, S.; Seeman, H.; Steen, G. 2-Hydroxy-2-methylsuccinic acid — a urinary metabolite in propionyl-CoA carboxylase deficiency. *Clin. Chim. Acta.* **1980**, *106*, 103-106. DOI: 10.1016/0009-8981(80)90380-0.

(387) Shechter, I.; Dai, P.; Huo, L.; Guan, G. IDH1 gene transcription is sterol regulated and activated by SREBP-1a and SREBP-2 in human hepatoma HepG2 cells: evidence that IDH1 may regulate lipogenesis in hepatic cells. *J. Lipid. Res.* **2003**, *44*, 2169-2180. DOI: 10.1194/jlr.M300285-JLR200 (acccessed 2024/03/23).

(388) Li, S.; Sun, C.; Gu, Y.; Gao, X.; Zhao, Y.; Yuan, Y.; Zhang, F.; Hu, P.; Liang, W.; Cao, K.; et al. Mutation of IDH1 aggravates the fatty acid-induced oxidative stress in HCT116 cells by affecting the mitochondrial respiratory chain. *Mol. Med. Rep.* **2019**, *19*, 2509-2518. DOI: 10.3892/mmr.2019.9903.

(389) Calvert, A. E.; Chalastanis, A.; Wu, Y.; Hurley, L. A.; Kouri, F. M.; Bi, Y.; Kachman, M.; May, J. L.; Bartom, E.; Hua, Y.; et al. Cancer-Associated IDH1 Promotes Growth and Resistance to Targeted Therapies in the Absence of Mutation. *Cell Rep.* **2017**, *19*, 1858-1873. DOI: 10.1016/j.celrep.2017.05.014.

(390) Reitman, Z. J.; Yan, H. Isocitrate Dehydrogenase 1 and 2 Mutations in Cancer: Alterations at a Crossroads of Cellular Metabolism. *J. Natl. Cancer Inst.* **2010**, *102*, 932-941. DOI: 10.1093/jnci/djq187 (acccessed 3/23/2024).

(391) Danhauser, K.; Sauer, S. W.; Haack, T. B.; Wieland, T.; Staufner, C.; Graf, E.; Zschocke, J.; Strom, T. M.; Traub, T.; Okun, J. G.; et al. DHTKD1 mutations cause 2-aminoadipic and 2-oxoadipic aciduria. *Am. J. Hum. Genet.* **2012**, *91*, 1082-1087. DOI: 10.1016/j.ajhg.2012.10.006.

(392) Thoden, J. B.; Timson, D. J.; Reece, R. J.; Holden, H. M. Molecular Structure of Human Galactose Mutarotase. *J. Biol. Chem.* **2004**, *279*, 23431-23437. DOI: 10.1074/jbc.M402347200 (acccessed 2024/09/22).

(393) Holden, H. M.; Rayment, I.; Thoden, J. B. Structure and Function of Enzymes of the Leloir Pathway for Galactose Metabolism. *J. Biol. Chem.* **2003**, *278*, 43885-43888. DOI: 10.1074/jbc.R300025200.

(394) Berry, G. T. Classic Galactosemia and Clinical Variant Galactosemia. In *GeneRev*, Adam, M. P., Feldman, J., Mirzaa, G. M., Pagon, R. A., Wallace, S. E., Bean, L. J. H., Gripp, K. W., Amemiya, A. Eds.; University of Washington, Seattle

(395) Holton, J. B. Galactose disorders: An overview. *J. Inherit. Metab. Dis.* **1990**, *13*, 476-486. DOI: 10.1007/BF01799505.

(396) Li, J.-j.; Yu, T.; Zeng, P.; Tian, J.; Liu, P.; Qiao, S.; Wen, S.; Hu, Y.; Liu, Q.; Lu, W.; et al. Wild-type IDH2 is a therapeutic target for triple-negative breast cancer. *Nat. Commun.* **2024**, *15*, 3445. DOI: 10.1038/s41467-024-47536-6.

(397) Van Damme, P.; Hole, K.; Pimenta-Marques, A.; Helsens, K.; Vandekerckhove, J.; Martinho, R. G.; Gevaert, K.; Arnesen, T. NatF contributes to an evolutionary shift in protein N-terminal acetylation and is important for normal chromosome segregation. *PLOS Genet.* **2011**, *7*, e1002169. DOI: 10.1371/journal.pgen.1002169.

(398) Goh, D. L. M.; Patel, A.; Thomas, G. H.; Salomons, G. S.; Schor, D. S. M.; Jakobs, C.; Geraghty, M. T. Characterization of the human gene encoding α-aminoadipate aminotransferase (AADAT). *Mol. Genet. Metab.* **2002**, *76*, 172-180. DOI: 10.1016/S1096-7192(02)00037-9.

(399) Nishizuka, Y.; Ichiyama, A.; Gholson, R. K.; Hayaishi, O. Studies on the Metabolism of the Benzene Ring of Tryptophan in Mammalian Tissues: I. ENZYMIC FORMATION OF GLUTARIC ACID FROM 3-HYDROXYANTHRANILIC ACID. *J. Biol. Chem.* **1965**, *240*, 733-739. DOI: 10.1016/S0021-9258(17)45237-9.

(400) Nemeria, N. S.; Gerfen, G.; Nareddy, P. R.; Yang, L.; Zhang, X.; Szostak, M.; Jordan, F. The mitochondrial 2-oxoadipate and 2-oxoglutarate dehydrogenase complexes share their E2 and E3 components for their function and both generate reactive oxygen species. *Free Radic. Biol. Med.* **2018**, *115*, 136-145. DOI: 10.1016/j.freeradbiomed.2017.11.018.

(401) Chow, S. L.; Rohan, C.; Morris, A. A. M. Case Report: Rhabdomyolysis in Glutaric Aciduria Type I. *J. Inherit. Metab. Dis.* **2003**, *26*, 711-712. DOI: 10.1023/B:BOLI.0000005635.89043.8a.

(402) Winter, S. C. Treatment of carnitine deficiency. *J. Inherit. Metab. Dis.* **2003**, *26*, 171-180. DOI: 10.1023/A:1024433100257.

(403) Pineda, M.; Ribes, A.; Busquets, C.; Vilaseca, M. A.; Aracil, A.; Christensen, E. Glutaric aciduria type I with high residual glutaryl-CoA dehydrogenase activity. *Dev. Med. Child. Neurol.* **1998**, *40*, 840-842. DOI: 10.1111/j.1469-8749.1998.tb12362.x.

(404) Christensen, E.; Ribes, A.; Merinero, B.; Zschocke, J. Correlation of genotype and phenotype in glutaryl-CoA dehydrogenase deficiency. *J. Inherit. Metab. Dis.* **2004**, *27*, 861-868. DOI: 10.1023/B:BOLI.0000045770.93429.3c.

(405) Nguyen, T.; Kirsch, B. J.; Asaka, R.; Nabi, K.; Quinones, A.; Tan, J.; Antonio, M. J.; Camelo, F.; Li, T.; Nguyen, S.; et al. Uncovering the Role of N-Acetyl-Aspartyl-Glutamate as a Glutamate Reservoir in Cancer. *Cell Rep.* **2019**, *27* (2), 491-501.e496. DOI: 10.1016/j.celrep.2019.03.036.

(406) Ripps, H.; Shen, W. Review: taurine: a "very essential" amino acid. *Mol. Vis.* **2012**, *18*, 2673-2686.

(407) Stipanuk, M. H.; Ueki, I.; Dominy, J. E., Jr.; Simmons, C. R.; Hirschberger, L. L. Cysteine dioxygenase: a robust system for regulation of cellular cysteine levels. *Amino Acids* **2009**, *37*, 55-63. DOI: 10.1007/s00726-008-0202-y.

(408) Sbodio, J. I.; Snyder, S. H.; Paul, B. D. Regulators of the transsulfuration pathway. *Br. J. Pharmacol.* **2019**, *176*, 583-593. DOI: 10.1111/bph.14446.

(409) Pal, S.; Kaplan, J. P.; Nguyen, H.; Stopka, S. A.; Savani, M. R.; Regan, M. S.; Nguyen, Q.-D.; Jones, K. L.; Moreau, L. A.; Peng, J.; et al. A druggable addiction to de novo pyrimidine biosynthesis in diffuse midline glioma. *Cancer Cell* **2022**, *40*, 957-972.e910. DOI: 10.1016/j.ccell.2022.07.012.

(410) Pesini, A.; Iglesias, E.; Bayona-Bafaluy, M. P.; Garrido-Pérez, N.; Meade, P.; Gaudó, P.; Jiménez-Salvador, I.; Andrés-Benito, P.; Montoya, J.; Ferrer, I.; et al. Brain pyrimidine nucleotide synthesis and Alzheimer disease. *Aging* **2019**, *11*, 8433-8462. DOI: 10.18632/aging.102328 (acccessed 2024/05/01/22:20:06). From www.aging-us.com.

(411) Schild, T.; Keshari, K. R. Revealing de novo pyrimidine synthesis as a key vulnerability in brain tumors. *Cancer Cell* **2022**, *40*, 1457-1458. DOI: 10.1016/j.ccell.2022.10.023.

(412) Shi, D. D.; Savani, M. R.; Levitt, M. M.; Wang, A. C.; Endress, J. E.; Bird, C. E.; Buehler, J.; Stopka, S. A.; Regan, M. S.; Lin, Y.-F.; et al. De novo pyrimidine synthesis is a targetable vulnerability in IDH mutant glioma. *Cancer Cell* **2022**, *40*, 939-956.e916. DOI: 10.1016/j.ccell.2022.07.011.

(413) Liao, R. Z.; Ding, W. J.; Yu, J. G.; Fang, W. H.; Liu, R. Z. Theoretical studies on pyridoxal 5'-phosphate-dependent transamination of alpha-amino acids. *J. Comput. Chem.* **2008**, *29*, 1919-1929. DOI: 10.1002/jcc.20958.

(414) Cooper, A.; Jeitner, T. Central Role of Glutamate Metabolism in the Maintenance of Nitrogen Homeostasis in Normal and Hyperammonemic Brain. *Biomol.* **2016**, *6*, 16-16. DOI: 10.3390/biom6020016.

(415) Cooper, A. J. The role of glutamine synthetase and glutamate dehydrogenase in cerebral ammonia homeostasis. *Neurochem. Res.* **2012**, *37*, 2439-2455. DOI: 10.1007/s11064-012-0803-4.

(416) Li, C.; Allen, A.; Kwagh, J.; Doliba, N. M.; Qin, W.; Najafi, H.; Collins, H. W.; Matschinsky, F. M.; Stanley, C. A.; Smith, T. J. Green Tea Polyphenols Modulate Insulin Secretion by Inhibiting Glutamate Dehydrogenase. *J. Biol. Chem.* **2006**, *281*, 10214-10221. DOI: 10.1074/jbc.M512792200.

(417) Caldovic, L.; Ah Mew, N.; Shi, D.; Morizono, H.; Yudkoff, M.; Tuchman, M. N-acetylglutamate synthase: structure, function and defects. *Mol. Genet. Metab.* **2010**, *100 Suppl 1*, S13-19. DOI: 10.1016/j.ymgme.2010.02.018.

(418) Franklin, C. C.; Backos, D. S.; Mohar, I.; White, C. C.; Forman, H. J.; Kavanagh, T. J. Structure, function, and post-translational regulation of the catalytic and modifier subunits of glutamate cysteine ligase. *Mol. Asp. Med.* **2009**, *30*, 86-98. DOI: 10.1016/j.mam.2008.08.009.

(419) Buzzi, A.; Wu, Y.; Frantseva, M. V.; Perez Velazquez, J. L.; Cortez, M. A.; Liu, C. C.; Shen, L. Q.; Gibson, K. M.; Snead, O. C. Succinic Semialdehyde Dehydrogenase Deficiency: GABAB receptor-mediated function. *Brain Res.* **2006**, *1090*, 15-22. DOI: 10.1016/j.brainres.2006.02.131.

(420) Hansen, K. B.; Yi, F.; Perszyk, R. E.; Furukawa, H.; Wollmuth, L. P.; Gibb, A. J.; Traynelis, S. F. Structure, function, and allosteric modulation of NMDA receptors. *J. Gen. Phys.* **2018**, *150*, 1081-1105. DOI: 10.1085/jgp.201812032.

(421) Ree, R.; Varland, S.; Arnesen, T. Spotlight on protein N-terminal acetylation. *Exp. Mol. Med.* **2018**, *50*, 1-13. DOI: 10.1038/s12276-018-0116-z.

(422) Luo, S.; Surapaneni, A.; Zheng, Z.; Rhee, E. P.; Coresh, J.; Hung, A. M.; Nadkarni, G. N.; Yu, B.; Boerwinkle, E.; Tin, A.; et al. NAT8 Variants, N-Acetylated Amino Acids, and Progression of CKD. *Clin. J. Am. Soc. Nephrol.* **2020**, *16*, 37-47. DOI: 10.2215/cjn.08600520.

(423) Pihlajaniemi, T.; Myllylä, R.; Kivirikko, K. I. Prolyl 4-hydroxylase and its role in collagen synthesis. *J. Hepatol.* **1991**, *13 Suppl 3*, S2-7. DOI: 10.1016/0168-8278(91)90002-s.

(424) Latif, T.; Chauhan, N.; Khan, R.; Moran, A.; Usmani, S. Z. Thalidomide and its analogues in the treatment of Multiple Myeloma. *Experimental Hematology & Oncology* **2012**, *1*, 27. DOI: 10.1186/2162-3619-1-27.

(425) Talley, J. T.; Mohiuddin, S. S. Biochemistry, Fatty Acid Oxidation. In *StatPearls*, StatPearls Publishing, 2024.

(426) Duncan, R. E.; Ahmadian, M.; Jaworski, K.; Sarkadi-Nagy, E.; Sul, H. S. Regulation of lipolysis in adipocytes. *Annu. Rev. Nutr.* **2007**, *27*, 79-101. DOI: 10.1146/annurev.nutr.27.061406.093734.

(427) Dekker, L. J. M.; Verheul, C.; Wensveen, N.; Leenders, W.; Lamfers, M. L. M.; Leenstra, S.; Luider, T. M. Effects of the IDH1 R132H Mutation on the Energy Metabolism: A Comparison between Tissue and Corresponding Primary Glioma Cell Cultures. *ACS Omega* **2022**, *7*, 3568-3578. DOI: 10.1021/acsomega.1c06121.

(428) Osipiuk, J.; Azizi, S.-A.; Dvorkin, S.; Endres, M.; Jedrzejczak, R.; Jones, K. A.; Kang, S.; Kathayat, R. S.; Kim, Y.; Lisnyak, V. G.; et al. Structure of papain-like protease from SARS-CoV-2 and its complexes with non-covalent inhibitors. *Nat. Commun.* **2021**, *12*, 743. DOI: 10.1038/s41467-021-21060-3.

(429) Jin, Z.; Du, X.; Xu, Y.; Deng, Y.; Liu, M.; Zhao, Y.; Zhang, B.; Li, X.; Zhang, L.; Peng, C.; et al. Structure of Mpro from SARS-CoV-2 and discovery of its inhibitors. *Nature* **2020**, *582*, 289-293. DOI: 10.1038/s41586-020-2223-y.

(430) Jamison, D. A.; Anand Narayanan, S.; Trovão, N. S.; Guarnieri, J. W.; Topper, M. J.; Moraes-Vieira, P. M.; Zaksas, V.; Singh, K. K.; Wurtele, E. S.; Beheshti, A. A comprehensive SARS-CoV-2 and COVID-19 review, Part 1: Intracellular overdrive for SARS-CoV-2 infection. *Eur. J. Hum. Genet.* **2022**, *30*, 889-898. DOI: 10.1038/s41431-022-01108-8.

(431) Amporndanai, K.; Meng, X.; Shang, W.; Jin, Z.; Rogers, M.; Zhao, Y.; Rao, Z.; Liu, Z.-J.; Yang, H.; Zhang, L.; et al. Inhibition mechanism of SARS-CoV-2 main protease by ebselen and its derivatives. *Nat. Commun.* **2021**, *12*, 3061-3061. DOI: 10.1038/s41467-021-23313-7.

(432) Liu, X.; Wang, X.-J. Potential inhibitors against 2019-nCoV coronavirus M protease from clinically approved medicines. *J. Genet. Genom. = Yi chuan xue bao* **2020**, *47*, 119-121. DOI: 10.1016/j.jgg.2020.02.001.

(433) Wu, F.; Zhao, S.; Yu, B.; Chen, Y.-M.; Wang, W.; Song, Z.-G.; Hu, Y.; Tao, Z.-W.; Tian, J.-H.; Pei, Y.-Y.; et al. A new coronavirus associated with human respiratory disease in China. *Nature* **2020**, *579*, 265-269. DOI: 10.1038/s41586-020-2008-3.

(434) Zhou, P.; Yang, X.-L.; Wang, X.-G.; Hu, B.; Zhang, L.; Zhang, W.; Si, H.-R.; Zhu, Y.; Li, B.; Huang, C.-L.; et al. A pneumonia outbreak associated with a new coronavirus of probable bat origin. *Nature* **2020**, *579*, 270-273. DOI: 10.1038/s41586-020-2012-7.

(435) Hegyi, A.; Ziebuhr, J. Conservation of substrate specificities among coronavirus main proteases. *J. Gen.. Virol* **2002**, *83*, 595-599. DOI: 10.1099/0022-1317-83-3-595.

(436) Singh, N.; Sharpley, A. L.; Emir, U. E.; Masaki, C.; Herzallah, M. M.; Gluck, M. A.; Sharp, T.; Harmer, C. J.; Vasudevan, S. R.; Cowen, P. J.; et al. Effect of the Putative Lithium Mimetic Ebselen on Brain Myo-Inositol, Sleep, and Emotional Processing in Humans. *Neuropsychopharmacol.* **2016**, *41*, 1768-1778. DOI: 10.1038/npp.2015.343.

(437) de Munnik, M.; Lohans, C. T.; Lang, P. A.; Langley, G. W.; Malla, T. R.; Tumber, A.; Schofield, C. J.; Brem, J. Targeting the Mycobacterium tuberculosis transpeptidase LdtMt2 with cysteine-reactive inhibitors including ebselen. *Chem. Commun.* **2019**, *55*, 10214-10217. DOI: 10.1039/C9CC04145A.

(438) Maślanka, M.; Mucha, A. Antibacterial Activity of Ebselen. *Int. J. Mol. Sci.* **2023**, *24*. DOI: 10.3390/ijms24021610.

(439) Thangamani, S.; Younis, W.; Seleem, M. N. Repurposing ebselen for treatment of multidrug-resistant staphylococcal infections. *Scientific Rep.* **2015**, *5*, 11596. DOI: 10.1038/srep11596.

(440) Saha, T.; Lyons, N.; Yue Yung, D. B.; Quiñones-Mateu, M. E.; Pletzer, D.; Das, S. C. Repurposing ebselen as an inhalable dry powder to treat respiratory tract infections. *Eur. J. Pharm. Biopharm.* **2024**, *195*, 114170. DOI: 10.1016/j.ejpb.2023.12.010.

(441) Thangamani, S.; Younis, W.; Seleem, M. N. Repurposing Clinical Molecule Ebselen to Combat Drug Resistant Pathogens. *PLOS ONE* **2015**, *10*, e0133877. DOI: 10.1371/journal.pone.0133877.

(442) Shaikh, S. A.; Patel, B.; Priyadarsini, I. K.; Vavilala, S. L. Combating planktonic and biofilm growth of Serratia marcescens by repurposing ebselen. *Int. Microbiol.* **2023**, *26*, 693-704. DOI: 10.1007/s10123-022-00301-5.

(443) Sies, H.; Parnham, M. J. Potential therapeutic use of ebselen for COVID-19 and other respiratory viral infections. *Free Radic. Biol. Med.* **2020**, *156*, 107-112. DOI: 10.1016/j.freeradbiomed.2020.06.032.

(444) Hüther, A.; Zhang, Y.; Sauer, A.; Parnham, M. Antimalarial properties of ebselen. *Parasitol. Res.* **1989**, *75*, 353-360. DOI: 10.1007/BF00931130.

(445) Lu, J.; Vodnala, S. K.; Gustavsson, A. L.; Gustafsson, T. N.; Sjöberg, B.; Johansson, H. A.; Kumar, S.; Tjernberg, A.; Engman, L.; Rottenberg, M. E.; et al. Ebsulfur is a benzisothiazolone cytocidal inhibitor targeting the trypanothione reductase of Trypanosoma brucei. *J. Biol. Chem.* **2013**, *288*, 27456-27468. DOI: 10.1074/jbc.M113.495101.

(446) Ren, X.; Zou, L.; Lu, J.; Holmgren, A. Selenocysteine in mammalian thioredoxin reductase and application of ebselen as a therapeutic. *Free Radic. Biol. Med.* **2018**, *127*, 238-247. DOI: 10.1016/j.freeradbiomed.2018.05.081.

(447) Sies, H. Ebselen, a selenoorganic compound as glutathione peroxidase mimic. *Free Radic. Biol. Med.* **1993**, *14*, 313-323. DOI: 10.1016/0891-5849(93)90028-s.

(448) Mukherjee, S.; Weiner, W. S.; Schroeder, C. E.; Simpson, D. S.; Hanson, A. M.; Sweeney, N. L.; Marvin, R. K.; Ndjomou, J.; Kolli, R.; Isailovic, D.; et al. Ebselen Inhibits Hepatitis C Virus NS3 Helicase Binding to Nucleic Acid and Prevents Viral Replication. *ACS Chem. Biol.* **2014**, *9*, 2393-2403. DOI: 10.1021/cb500512z.

(449) Azad, G. K.; Tomar, R. S. Ebselen, a promising antioxidant drug: mechanisms of action and targets of biological pathways. *Mol. Biol. Rep.* **2014**, *41*, 4865-4879. DOI: 10.1007/s11033-014-3417-x.

(450) Schewe, T. Molecular actions of ebselen—an antiinflammatory antioxidant. *Gen. Pharmacol.: Vasc. Syst.* **1995**, *26*, 1153-1169. DOI: 10.1016/0306-3623(95)00003-j.

(451) Augsburger, F.; Filippova, A.; Rasti, D.; Seredenina, T.; Lam, M.; Maghzal, G.; Mahiout, Z.; Jansen-Dürr, P.; Knaus, U. G.; Doroshow, J. Pharmacological characterization of the seven human NOX isoforms and their inhibitors. *Redox Biol.* **2019**, *26*, 101272. DOI: 10.1016/j.redox.2019.101272.

(452) Zhao, R.; Masayasu, H.; Holmgren, A. Ebselen: a substrate for human thioredoxin reductase strongly stimulating its hydroperoxide reductase activity and a superfast thioredoxin oxidant. *Proc. Natl. Acad. Sci.* **2002**, *99*, 8579-8584. DOI: 10.1073/pnas.122061399.

(453) Kalantari, P.; Narayan, V.; Natarajan, S. K.; Muralidhar, K.; Gandhi, U. H.; Vunta, H.; Henderson, A. J.; Prabhu, K. S. Thioredoxin reductase-1 negatively regulates HIV-1 transactivating protein Tat-dependent transcription in human macrophages. *J. Biol. Chem.* **2008**, *283*, 33183-33190. DOI: 10.1074/jbc.M807403200.

(454) Haddad, E.-B.; McCluskie, K.; Birrell, M. A.; Dabrowski, D.; Pecoraro, M.; Underwood, S.; Chen, B.; De Sanctis, G. T.; Webber, S. E.; Foster, M. L.; et al. Differential Effects of Ebselen on Neutrophil Recruitment, Chemokine, and Inflammatory Mediator Expression in a Rat Model of Lipopolysaccharide-Induced Pulmonary Inflammation. *J. Immunol.* **2002**, *169*, 974-982. DOI: 10.4049/jimmunol.169.2.974 (acccessed 8/7/2024).

(455) Thangamani, S.; Eldesouky, H. E.; Mohammad, H.; Pascuzzi, P. E.; Avramova, L.; Hazbun, T. R.; Seleem, M. N. Ebselen exerts antifungal activity by regulating glutathione

(GSH) and reactive oxygen species (ROS) production in fungal cells. *Biochim. Biophys. Acta Gen. Subj.* **2017**, *1861*, 3002-3010. DOI: 10.1016/j.bbagen.2016.09.029.

(456) Satheeshkumar, K.; Mugesh, G. Synthesis and Antioxidant Activity of Peptide-Based Ebselen Analogues. *Chem. Eur. J.* **2011**, *17*, 4849-4857. DOI: 10.1002/chem.201003417.

(457) Kurebayashi, Y.; Tabuchi, Y.; Akasaki, M. Gastric cytoprotection by ebselen against the injury induced by necrotizing agents in rats. *Arzneimittelforschung* **1989**, *39*, 250-253.

(458) Parnham, M.; Sies, H. Ebselen: prospective therapy for cerebral ischaemia. *Expert Opin. Investig. Drugs* **2000**, *9*, 607-619. DOI: 10.1517/13543784.9.3.607.

(459) Kil, J.; Lobarinas, E.; Spankovich, C.; Griffiths, S. K.; Antonelli, P. J.; Lynch, E. D.; Le Prell, C. G. Safety and efficacy of ebselen for the prevention of noise-induced hearing loss: a randomised, double-blind, placebo-controlled, phase 2 trial. *Lancet* **2017**, *390*, 969-979. DOI: 10.1016/S0140-6736(17)31791-9.

(460) Yamaguchi, T.; Sano, K.; Takakura, K.; Saito, I.; Shinohara, Y.; Asano, T.; Yasuhara, H. Ebselen in Acute Ischemic Stroke. *Stroke* **1998**, *29*, 12-17. DOI: 10.1161/01.STR.29.1.12 (acccessed 2024/08/07).

(461) Pharmaceuticals, S. *Sound Pharma initiates enrollment in pivotal Phase 3 clinical trial of SPI-1005 for the treatment of hearing loss and tinnitus in Meniere's disease*. https://www.prnewswire.com/news-releases/sound-pharma-initiates-enrollment-in-pivotal-phase-3-clinical-trial-of-spi-1005-for-the-treatment-of-hearing-loss-and-tinnitus-in-menieres-disease-301595208.html (accessed.

(462) Meraz-Torres, F.; Plöger, S.; Garbe, C.; Niessner, H.; Sinnberg, T. Disulfiram as a Therapeutic Agent for Metastatic Malignant Melanoma-Old Myth or New Logos? *Cancers (Basel)* **2020**, *12*. DOI: 10.3390/cancers12123538.

(463) Sharpley, A. L.; Williams, C.; Holder, A. A.; Godlewska, B. R.; Singh, N.; Shanyinde, M.; MacDonald, O.; Cowen, P. J. A phase 2a randomised, double-blind, placebo-controlled, parallel-group, add-on clinical trial of ebselen (SPI-1005) as a novel treatment for mania or hypomania. *Psychopharmacol. (Berl)* **2020**, *237*, 3773-3782. DOI: 10.1007/s00213-020-05654-1.

(464) Sakamoto, J.; Oba, K.; Matsui, T.; Kobayashi, M. Efficacy of oral anticancer agents for colorectal cancer. *Dis. Colon Rectum* **2006**, *49*, S82-91. DOI: 10.1007/s10350-006-0601-7.

(465) Boulos, J. C.; Rahama, M.; Hegazy, M. F.; Efferth, T. Shikonin derivatives for cancer prevention and therapy. *Cancer Lett.* **2019**, *459*, 248-267. DOI: 10.1016/j.canlet.2019.04.033.

(466) Lovestone, S.; Boada, M.; Dubois, B.; Hüll, M.; Rinne, J. O.; Huppertz, H. J.; Calero, M.; Andrés, M. V.; Gómez-Carrillo, B.; León, T.; et al. A phase II trial of tideglusib in Alzheimer's disease. *J. Alzheimers Dis.* **2015**, *45* (1), 75-88. DOI: 10.3233/jad-141959.

(467) Baker, A. F.; Adab, K. N.; Raghunand, N.; Chow, H.; Stratton, S. P.; Squire, S. W.; Boice, M.; Pestano, L. A.; Kirkpatrick, D. L.; Dragovich, T. A phase IB trial of 24-hour intravenous PX-12, a thioredoxin-1 inhibitor, in patients with advanced gastrointestinal cancers. *Invest New Drugs* **2013**, *31*, 631-641. DOI: 10.1007/s10637-012-9846-2.

(468) Haritha, C. V.; Sharun, K.; Jose, B. Ebselen, a new candidate therapeutic against SARS-CoV-2. *Int. J. Surg.* **2020**, *84*, 53-56. DOI: 10.1016/j.ijsu.2020.10.018.

(469) Thun-Hohenstein, S. T. D.; Suits, T. F.; Malla, T. R.; Tumber, A.; Brewitz, L.; Choudhry, H.; Salah, E.; Schofield, C. J. Structure-Activity Studies Reveal Scope for Optimisation of Ebselen-Type Inhibition of SARS-CoV-2 Main Protease. *ChemMedChem* **2021**, e202100582-e202100582. DOI: 10.1002/cmdc.202100582.

(470) Malla, T. R.; Tumber, A.; John, T.; Brewitz, L.; Strain-Damerell, C.; Owen, C. D.; Lukacik, P.; Chan, H. T. H.; Maheswaran, P.; Salah, E.; et al. Mass spectrometry reveals

potential of β-lactams as SARS-CoV-2 Mpro inhibitors. *Chem. Commun.* **2021**, *57*, 1430-1433. DOI: 10.1039/D0CC06870E.

(471) Su, J.; Liu, J.; Chen, C.; Zhang, Y.; Yang, K. Ebsulfur as a potent scaffold for inhibition and labelling of New Delhi metallo-β-lactamase-1 in vitro and in vivo. *Bioorg. Chem.* **2019**, *84*, 192-201. DOI: 10.1016/j.bioorg.2018.11.035.

(472) Ngo, H. X.; Shrestha, S. K.; Garneau-Tsodikova, S. Identification of ebsulfur analogues with broad-spectrum antifungal activity. *ChemMedChem* **2016**, *11*, 1507-1507. DOI: 10.1002/cmdc.201600236.

(473) Suits, T. The development of non-β-lactam inhibitors of bacterial transpeptidases. University of Oxford, 2022.

(474) Mensah, J. O.; Ampomah, G. B.; Gasu, E. N.; Adomako, A. K.; Menkah, E. S.; Borquaye, L. S. Allosteric Modulation of the Main Protease (MPro) of SARS-CoV-2 by Casticin—Insights from Molecular Dynamics Simulations. *Chemistry Africa* **2022**, *5*, 1305-1320. DOI: 10.1007/s42250-022-00411-7.

(475) El-Hddad, S. S. A.; Sobhy, M. H.; El-morsy, A.; Shoman, N. A.; El-Adl, K. Quinazolines and thiazolidine-2,4-dions as SARS-CoV-2 inhibitors: repurposing, in silico molecular docking and dynamics simulation. *RSC Adv.* **2024**, *14*, 13237-13250, 10.1039/D4RA02029D. DOI: 10.1039/D4RA02029D.

(476) Li, H.; Zhang, D.; Gao, M.; Huang, L.; Tang, L.; Li, Z.; Chen, X.; Zhang, X. Highly specific C–C bond cleavage induced FRET fluorescence for in vivo biological nitric oxide imaging. *Chem. Sci.* **2017**, *8*, 2199-2203, 10.1039/C6SC04071C. DOI: 10.1039/C6SC04071C.

(477) Böth, D.; Steiner, E. M.; Stadler, D.; Lindqvist, Y.; Schnell, R.; Schneider, G. Structure of LdtMt2, an L,D-transpeptidase from Mycobacterium tuberculosis. *Acta Crystallogr. D. Biol. Crystallogr.* **2013**, *69*, 432-441. DOI: 10.1107/s0907444912049268.

(478) Zhao, Y.; Zhu, Y.; Liu, X.; Jin, Z.; Duan, Y.; Zhang, Q.; Wu, C.; Feng, L.; Du, X.; Zhao, J.; et al. Structural basis for replicase polyprotein cleavage and substrate specificity of main protease from SARS-CoV-2. *Proc. Natl. Acad. Sci.* **2022**, *119*, e2117142119. DOI: doi:10.1073/pnas.2117142119.

(479) Strelow, J. M. A Perspective on the Kinetics of Covalent and Irreversible Inhibition. *SLAS Discov.* **2017**, *22* (1), 3-20. DOI: 10.1177/1087057116671509 From NLM.

(480) Jagtap, S. Heck Reaction—State of the Art. *Catal* **2017**, *7*, 267. DOI: 10.3390/catal7090267.

(481) Beletskaya, I.; Dr, F.; Tyurin, V. The Suzuki-Miyaura reaction after the Nobel prize. *Coord. Chem. Rev.* **2019**, *385*, 137-173. DOI: 10.1016/j.ccr.2019.01.012.

(482) Dorel, R.; Grugel, C. P.; Haydl, A. M. The Buchwald–Hartwig Amination After 25 Years. *Angew. Chem. Int. Ed.* **2019**, *58*, 17118-17129. DOI: 10.1002/anie.201904795.

(483) Clark, D. T.; Murrell, J. N.; Tedder, J. M. 234. The magnitudes and signs of the inductive and mesomeric effects of the halogens. *J. Chem. Soc.* **1963**, 1250-1253, 10.1039/JR9630001250. DOI: 10.1039/JR9630001250.

(484) de Munnik, M.; Lang, P. A.; De Dios Anton, F.; Cacho, M.; Bates, R. H.; Brem, J.; Rodríguez Miquel, B.; Schofield, C. J. High-throughput screen with the l,d-transpeptidase Ldt(Mt2) of Mycobacterium tuberculosis reveals novel classes of covalently reacting inhibitors. *Chem. Sci.* **2023**, *14*, 7262-7278. DOI: 10.1039/d2sc06858c.

(485) Hendon-Dunn, C. L.; Doris, K. S.; Thomas, S. R.; Allnutt, J. C.; Marriott, A. A.; Hatch, K. A.; Watson, R. J.; Bottley, G.; Marsh, P. D.; Taylor, S. C.; et al. A Flow Cytometry Method for Rapidly Assessing Mycobacterium tuberculosis Responses to Antibiotics with Different

Modes of Action. *Antimicrob. Agents. Chemother.* **2016**, *60*, 3869-3883. DOI: 10.1128/aac.02712-15.

(486) Mierke, C. T. Lysosomes and Peroxisomes. In *Cellular Mechanics and Biophysics: Structure and Function of Basic Cellular Components Regulating Cell Mechanics*, Springer International Publishing, 2020; pp 277-332.

(487) Blanchard, M.; Green, D. E.; Nocito-Carroll, V.; Ratner, S. l-HYDROXY ACID OXIDASE. *J. Biol. Chem.* **1946**, *163*, 137-144. DOI: 10.1016/S0021-9258(17)41353-6.

(488) Brodie, C.; Bogi, K.; Acs, P.; Lorenzo, P. S.; Baskin, L.; Blumberg, P. M. Protein kinase C delta (PKCdelta) inhibits the expression of glutamine synthetase in glial cells via the PKCdelta regulatory domain and its tyrosine phosphorylation. *J. Biol. Chem.* **1998**, *273*, 30713-30718. DOI: 10.1074/jbc.273.46.30713.

(489) Jones, M. E. Conversion of Glutamate to Ornithine and Proline: Pyrroline-5-Carboxylate, a Possible Modulator of Arginine Requirements. *J. Nutrition* **1985**, *115*, 509-515. DOI: 10.1093/jn/115.4.509.

(490) Otieno, M. A.; Kensler, T. W. A Role for Protein Kinase C-δ in the Regulation of Ornithine Decarboxylase Expression by Oxidative Stress. *Cancer Res.* **2000**, *60*, 4391-4396.

(491) Wheeler, D. L.; Reddig, P. J.; Dreckschmidt, N. E.; Leitges, M.; Verma, A. K. Protein kinase Cdelta-mediated signal to ornithine decarboxylase induction is independent of skin tumor suppression. *Oncogene* **2002**, *21*, 3620-3630. DOI: 10.1038/sj.onc.1205451.

(492) Seiler, N. Polyamine metabolism. *Digest* **1990**, *46 Suppl 2*, 319-330. DOI: 10.1159/000200405.

(493) Wang, C.; Delcros, J.-G.; Cannon, L.; Konate, F.; Carias, H.; Biggerstaff, J.; Gardner, R. A.; Phanstiel. Defining the Molecular Requirements for the Selective Delivery of Polyamine Conjugates into Cells Containing Active Polyamine Transporters. *J. Med. Chem.* **2003**, *46*, 5129-5138. DOI: 10.1021/jm030223a.

(494) Zhang, L.; Lee, H.-K.; Pruess, T. H.; White, H. S.; Bulaj, G. Synthesis and Applications of Polyamine Amino Acid Residues: Improving the Bioactivity of an Analgesic Neuropeptide, Neurotensin. *J. Med. Chem.* **2009**, *52*, 1514-1517. DOI: 10.1021/jm801481y.

(495) Gao, L.; Pan, X.; Zhang, J. H.; Xia, Y. Glial cells: an important switch for the vascular function of the central nervous system. *Front. Cell. Neurosci.* **2023**, *17*, Review. DOI: 10.3389/fncel.2023.1166770.

(496) Huang, Y.; Pledgie, A.; Rubin, E.; Marton, L. J.; Woster, P. M.; Sukumar, S.; Casero, R. A., Jr.; Davidson, N. E. Role of p53/p21(Waf1/Cip1) in the regulation of polyamine analogue-induced growth inhibition and cell death in human breast cancer cells. *Cancer Biol. Ther.* **2005**, *4*, 1006-1013. DOI: 10.4161/cbt.4.9.1970.

(497) Jiang, B.; Zhao, W.; Shi, M.; Zhang, J.; Chen, A.; Ma, H.; Suleman, M.; Lin, F.; Zhou, L.; Wang, J.; et al. IDH1 Arg-132 mutant promotes tumor formation through down-regulating p53. *J. Biol. Chem.* **2018**, 9747-9758. DOI: 10.1074/jbc.RA117.001385.

(498) Brodie, C.; Blumberg, P. M. Regulation of cell apoptosis by protein kinase c delta. *Apoptosis* **2003**, *8*, 19-27. DOI: 10.1023/a:1021640817208.

(499) Simmons, D. P. Us of a Pkc-Delta Inhibitor for the Inhibition of Metastatic Melanoma. WO2005065666A1, 2005.

(500) Zrachia, A.; Dobroslav, M.; Blass, M.; Kazimirsky, G.; Kronfeld, I.; Blumberg, P. M.; Kobiler, D.; Lustig, S.; Brodie, C. Infection of glioma cells with Sindbis virus induces selective activation and tyrosine phosphorylation of protein kinase C delta. Implications for Sindbis virus-induced apoptosis. *J. Biol. Chem.* **2002**, *277*, 23693-23701. DOI: 10.1074/jbc.M111658200.

(501) Corbit, K. C.; Foster, D. A.; Rosner, M. R. Protein Kinase Cδ Mediates Neurogenic but Not Mitogenic Activation of Mitogen-Activated Protein Kinase in Neuronal Cells. *Mol. Cell. Biol.* **1999**, *19*, 4209-4218. DOI: 10.1128/MCB.19.6.4209.

(502) O'Driscoll, K. R.; Teng, K. K.; Fabbro, D.; Greene, L. A.; Weinstein, I. B. Selective translocation of protein kinase C-delta in PC12 cells during nerve growth factor-induced neuritogenesis. *Mol. Biol. Cell.* **1995**, *6*, 449-458. DOI: 10.1091/mbc.6.4.449.

(503) Lai, A.; Kharbanda, S.; Pope, W. B.; Tran, A.; Solis, O. E.; Peale, F.; Forrest, W. F.; Pujara, K.; Carrillo, J. A.; Pandita, A.; et al. Evidence for Sequenced Molecular Evolution of IDH1 Mutant Glioblastoma From a Distinct Cell of Origin. *J. Clin. Oncol.* **2011**, *29*, 4482-4490. DOI: 10.1200/JCO.2010.33.8715.

(504) Murnyak, B.; Huang, L. E. Association of TP53 Alteration with Tissue Specificity and Patient Outcome of IDH1-Mutant Glioma. *Cells* **2021**, *10*. DOI: 10.3390/cells10082116.

(505) Geramizadeh, B.; Kohandel-Shirazi, M.; Soltani, A. A Simple Panel of IDH1 and P53 in Differential Diagnosis Between Low-Grade Astrocytoma and Reactive Gliosis. *Clin. Pathol.* **2021**, *14*, 2632010x20986168. DOI: 10.1177/2632010x20986168.

(506) Miyata, S.; Tominaga, K.; Sakashita, E.; Urabe, M.; Onuki, Y.; Gomi, A.; Yamaguchi, T.; Mieno, M.; Mizukami, H.; Kume, A.; et al. Comprehensive Metabolomic Analysis of IDH1R132H Clinical Glioma Samples Reveals Suppression of β-oxidation Due to Carnitine Deficiency. *Scientific Rep.* **2019**, *9*, 9787. DOI: 10.1038/s41598-019-46217-5.

(507) Okada, M.; Suzuki, S.; Togashi, K.; Sugai, A.; Yamamoto, M.; Kitanaka, C. Targeting Folate Metabolism Is Selectively Cytotoxic to Glioma Stem Cells and Effectively Cooperates with Differentiation Therapy to Eliminate Tumor-Initiating Cells in Glioma Xenografts. *Int. J. Mol. Sci.* **2021**, *22*, 11633-11633. DOI: 10.3390/ijms222111633.

(508) Meek, T. D.; Karsten, W. E.; DeBrosse, C. W. Carbamoyl-phosphate synthetase II of the mammalian CAD protein: kinetic mechanism and elucidation of reaction intermediates by positional isotope exchange. *Biochem.* **1987**, *26*, 2584-2593. DOI: 10.1021/bi00383a026.

(509) Reardon, M. A.; Weber, G. Increased synthesis of carbamoyl-phosphate synthase II (EC 6.3.5.5) in hepatoma 3924A. *Cancer Res.* **1986**, *46*, 3673-3676.

(510) Chakravarty, S.; Pendharkar, D.; Ramachandran, S. a.; Bathula, C.; Soni, S.; Kumar, V.; Saeed, U.; Danodia, A. K.; Sharma, A.; Jadhavar, P. S. Heterocyclic Compounds as Mutant Idh Inhibitors. US2020206233A1, 2020.

(511) Huber, G.; Schier, O.; Druey, J. Imidazolderivate aus 1-Amino-1-desoxy-D-fructosen. 4. Mitteilung über Aminozucker. *Helva. Chim. Acta.* **1960**, *43*, 1787-1795. DOI: 10.1002/hlca.19600430641.

(512) Jia, P.; Wu, Y.; Du, H.; Yang, L.; Zhang, Z.; Ma, T.; Li, S.; Yuan, S.; Lu, L.; Zha, X. I-8, a novel inhibitor of mutant IDH1, inhibits cancer progression in vitro and in vivo. *Eur. J. Pharm. Sci.* **2019**, *140*, 105072-105072. DOI: 10.1016/j.ejps.2019.105072.

(513) Yang, X.; Wang, Z.; Pei, Y.; Song, N.; Xu, L.; Feng, B.; Wang, H.; Luo, X.; Hu, X.; Qiu, X.; et al. Discovery of thalidomide-based PROTAC small molecules as the highly efficient SHP2 degraders. *Eur. J. Med. Chem.* **2021**, *218*, 113341-113341. DOI: 10.1016/j.ejmech.2021.113341.

(514) Cooper, M. S.; Norley, M. C.; Armitage, S.; Cresser-Brown, J. O.; Edmonds, A. K.; Goggins, S.; Hopewell, J. P.; Karadogan, B.; Knights, K. A.; Nash, T. J.; et al. Efficient, multi-hundred-gram scale access to E3 ubiquitin ligase ligands for degrader development. *Org. Biomol. Chem.* **2023**, *21*, 8344-8352, 10.1039/D3OB00983A. DOI: 10.1039/D3OB00983A.

(515) Huang, J.-T.; Fang, J.-M.; Chern, Y.-J.; Tseng, Y.-L.; Huang, Y.-A. Compounds and Their Uses for Treating Neurodegenerative Disease. WO2023039010A1, 2023.

(516) Zhou, F.; Chen, Y. Compound for selectively degrading CDK subtype in targeted manner and application thereof. CN110938060A, 2020.

(517) Jin, J.; Burakoff, S.; Kaniskan, H. U.; Sawasdikosol, S.; Witter, D. Heterobifunctional Compounds as Hpk1 Degraders. WO2023097020A1, 2023.

(518) Sang, R.; Fan, R.; Deng, A.; Gou, J.; Lin, R.; Zhao, T.; Hai, Y.; Song, J.; Liu, Y.; Qi, B.; et al. Degradation of Hexokinase 2 Blocks Glycolysis and Induces GSDME-Dependent Pyroptosis to Amplify Immunogenic Cell Death for Breast Cancer Therapy. *J. Med. Chem.* **2023**, *66*, 8464-8483. DOI: 10.1021/acs.jmedchem.3c00118.

(519) Ji, N.; Yin, N.; Qiu, H. KRAS G12D Proteolysis Targeting Chimeras. US2025051364A1, 2025.

(520) Liu, J.; Plewe, M. B.; Wang, J.; Han, X.; Chen, L.; Zhang, C. Cyclic-Amp Response Element Binding Protein (cbp) and/or Adenoviral E1a Binding Protein of 300 Kda (p300) Degradation Compounds and Methods of Use. WO2022042707A1, 2022.

(521) Aldilla, V. R.; Bhadbhade, M.; Bhattacharyya, S.; Kumar, N.; Rich, A. M.; Marjo, C. E. Controlling the distance between hydrogen-bonded chloro-s-triazine tapes: crystal engineering using N-alkyl chains and the influence of temperature. *CrystEngComm.* **2017**, *19*, 4749-4758. DOI: 10.1039/C7CE01049D.

(522) Mannion, J. C.; Dax, S. L.; Golder, F. J.; Macintyre, D. E.; McLeod, J.; Ozola, V.; Suna, E.; Shubin, K.; Mencel, J. J.; Peng, S. X. Novel Orally Bioavailable Breathing Control Modulating Compounds, and Methods of Using Same. WO2014078575A2, 2014.

(523) Mehta, S.; Brahmchari, D. Phosphazene Superbase-Mediated Regio- and Stereoselective Iodoaminocyclization of 2-(1-Alkynyl)benzamides for the Synthesis of Isoindolin-1-ones. *J. Org. Chem.* **2019**, *84*, 5492-5503. DOI: 10.1021/acs.joc.9b00452.

(524) Bhakuni, B. S.; Kumar, A.; Balkrishna, S. J.; Sheikh, J. A.; Konar, S.; Kumar, S. KOtBu Mediated Synthesis of Phenanthridinones and Dibenzoazepinones. *Org. Lett.* **2012**, *14*, 2838-2841. DOI: 10.1021/ol301077y.

(525) Yadav, L.; Tiwari, M. K.; Shyamlal, B. R. K.; Chaudhary, S. Organocatalyst in Direct C(sp2)–H Arylation of Unactivated Arenes: [1-(2-Hydroxyethyl)-piperazine]-Catalyzed Inter-/Intra-molecular C–H Bond Activation. *J. Org. Chem.* **2020**, *85*, 8121-8141. DOI: 10.1021/acs.joc.0c01019.

(526) Pacuła, A. J.; Ścianowski, J.; Aleksandrzak, K. B. Highly efficient synthesis and antioxidant capacity of N-substituted benzisoselenazol-3(2H)-ones. *RSC Adv.* **2014**, *4*, 48959-48962. DOI: 10.1039/C4RA08631G.

(527) Hellal, M.; Cuny, G. D. Microwave assisted copper-free Sonogashira coupling/5-exo-dig cycloisomerization domino reaction: access to 3-(phenylmethylene)isoindolin-1-ones and related heterocycles. *Tetrahedron Lett.* **2011**, *52*, 5508-5511. DOI: 10.1016/j.tetlet.2011.08.070.

(528) Kumar, J. S.; Reddy, G. S.; Medishetti, R.; Ray, A.; Bele, S. D.; Hossain, K. A.; Thirupataiah, B.; Edwin, R. K.; Behera, P.; Joseph, A.; et al. Sonochemical synthesis of rosuvastatin based novel 3-methyleneisoindolin-1-one derivatives as potential anticancer agents. *J. Mol. Struct.* **2021**, *1240*, 130574-130574. DOI: 10.1016/j.molstruc.2021.130574.

(529) Landgraf, A. D.; Alsegiani, A. S.; Alaqel, S.; Thanna, S.; Shah, Z. A.; Sucheck, S. J. Neuroprotective and Anti-neuroinflammatory Properties of Ebselen Derivatives and Their Potential to Inhibit Neurodegeneration. *ACS Chem. Neurosci.* **2020**, *11*, 3008-3016. DOI: 10.1021/acschemneuro.0c00328.

(530) Viani, F.; Rossi, B.; Panzeri, W.; Merlini, L.; Martorana, A. M.; Polissi, A.; Galante, Y. M. Synthesis and anti-bacterial activity of a library of 1,2-benzisothiazol-3(2H)-one (BIT)

derivatives amenable of crosslinking to polysaccharides. *Tetrahedron* **2017**, *73*, 1745-1761. DOI: 10.1016/j.tet.2017.02.025.

(531) Bhakuni, B. S.; Balkrishna, S. J.; Kumar, A.; Kumar, S. An efficient copper mediated synthetic methodology for benzo[d]isothiazol-3(2H)-ones and related sulfur–nitrogen heterocycles. *Tetrahedron Lett.* **2012**, *53*, 1354-1357. DOI: 10.1016/j.tetlet.2012.01.003.

(532) Yang, L.; Song, L.; Tang, S.; Li, L.; Li, H.; Yuan, B.; Yang, G. Co-Catalyzed Intramolecular S-N Bond Formation in Water for 1,2-Benzisothiazol-3(2H)-ones and 1,2,4-Thiadiazoles Synthesis. *Eur. J. Org. Chem.* **2019**, *2019*, 1281-1285. DOI: 10.1002/ejoc.201801642.

(533) Yang, K.; Zhang, H.; Niu, B.; Tang, T.; Ge, H. Benzisothiazol-3-ones through a Metal-Free Intramolecular N–S Bond Formation. *Eur. J. Org. Chem.* **2018**, *2018*, 5520-5523. DOI: 10.1002/ejoc.201801090.

(534) Wright, S. W.; Petraitis, J. J.; Abelman, M. M.; Batt, D. G.; Bostrom, L. L.; Corbett, R. L.; Decicco, C. P.; Di Meo, S. V.; Freimark, B.; Giannaras, J. V.; et al. Heteroaryl-fused 2-phenylisothiazolone inhibitors of cartilage breakdown. *J. Med. Chem.* **1994**, *37*, 3071-3078. DOI: 10.1021/jm00045a012.

(535) Walsby-Tickle, J. Investigating isocitrate dehydrogenase mutations in cancer using new metabolomics methods. University of Oxford, 2020.

(536) Karaman, I. Preprocessing and Pretreatment of Metabolomics Data for Statistical Analysis. *Adv. Exp. Med. Biol.* **2017**, *965*, 145-161. DOI: 10.1007/978-3-319-47656-8_6.

(537) Wulff, J.; Mitchell, M. A Comparison of Various Normalization Methods for LC/MS Metabolomics Data. *Adv. Biosci. Biotechnol.* **2018**, *09*, 339-351. DOI: 10.4236/abb.2018.98022.

(538) van den Berg, R. A.; Hoefsloot, H. C. J.; Westerhuis, J. A.; Smilde, A. K.; van der Werf, M. J. Centering, scaling, and transformations: improving the biological information content of metabolomics data. *BMC Genom.* **2006**, *7*, 142. DOI: 10.1186/1471-2164-7-142.